University of Wollongong

Research Online

University of Wollongong Thesis Collection 1954-2016

University of Wollongong Thesis Collections

2014

Chronologies in context: reconciling the optical dating of quartz with its sedimentary environment

Nathan R. Jankowski
University of Wollongong

Follow this and additional works at: https://ro.uow.edu.au/theses

University of Wollongong

Copyright Warning

You may print or download ONE copy of this document for the purpose of your own research or study. The University does not authorise you to copy, communicate or otherwise make available electronically to any other person any copyright material contained on this site.

You are reminded of the following: This work is copyright. Apart from any use permitted under the Copyright Act 1968, no part of this work may be reproduced by any process, nor may any other exclusive right be exercised, without the permission of the author. Copyright owners are entitled to take legal action against persons who infringe their copyright. A reproduction of material that is protected by copyright may be a copyright infringement. A court may impose penalties and award damages in relation to offences and infringements relating to copyright material. Higher penalties may apply, and higher damages may be awarded, for offences and infringements involving the conversion of material into digital or electronic form.

Unless otherwise indicated, the views expressed in this thesis are those of the author and do not necessarily represent the views of the University of Wollongong.

Recommended Citation

Jankowski, Nathan R., Chronologies in context: reconciling the optical dating of quartz with its sedimentary environment, Doctor of Philosophy thesis, School of Earth and Environmental Sciences, University of Wollongong, 2014. https://ro.uow.edu.au/theses/4428

Research Online is the open access institutional repository for the University of Wollongong. For further information contact the UOW Library: research-pubs@uow.edu.au

Chronologies in context: reconciling the optical dating of quartz with its sedimentary environment

A thesis submitted in fulfilment of the requirements for the award of the degree

Doctor of Philosophy

from

University of Wollongong

by

Nathan R. Jankowski

BSc. Advanced (Honours) University of Wollongong

Centre for Archaeological Science

School of Earth & Environmental Sciences

2014

Certification

1, Nathan R. Jankowski, declare that this thesis, submitted in fulfilment of the requirements for the award of Doctor of Philosophy, in the School of Earth & Environmental Sciences, University of Wollongong, is wholly my own work unless otherwise referenced or acknowledged. This document has not been submitted for qualifications at any other academic institution.

Nathan R. Jankowski

Statement of Authorship

Chapters 1 to 9 of this thesis are the products of the research carried out by the PhD candidate, Nathan Jankowski, during the period of candidature. One of these chapters (Chapter 5) has been accepted for publication by Earth Surface Processes and Landforms following major and, subsequently, minor revisions. In these chapters, Nathan was the main contributor of the study design and responsible for data collection and analysis, and largely responsible for data interpretation. The candidate also wrote the first draft of each manuscript and was then responsible for addressing the editorial suggestions made by the co-authors – Zenobia Jacobs, Richard G. Roberts and Paul Goldberg. With respect to Chapter 5, Nathan was solely responsible for submitting this manuscript to the relevant journal and addressing the reviewer's comments with the aid of the co-authors.

Appendix I contains the submitted manuscript of the Pech de l'Azé I, II and IV single-grain OSL chronologies. This paper was written by Dr Zenobia Jacobs and uses the findings of Chapter 8 (carried out by Nathan) to provide the foundation upon which the single-grain OSL study was conducted.

Chapters 5, 6, 7 and 8 are written in the style of journal articles. We are aware that these, in their current form, are significantly longer than is typically acceptable for journal submissions. The chapters were, however, written in such a way under an agreement between Nathan Jankowski and the principal supervisor, Dr Zenobia Jacobs, that the journal article thesis style was to be used.

Signed

Nathan Jankowski	Zenobia Jacobs
PhD candidate	Principal Supervisor
July 2014	July 2014

ABSTRACT

The occurrence of overdispersion (OD) in single-grain optically stimulated luminescence (OSL) equivalent dose (D_e) distributions is an issue affecting both natural and laboratory irradiated grains of quartz. The presence of this additional spread beyond statistical expectations is often explained as the result of factors either intrinsic or extrinsic to the grains being dated, or a combination of both. The designation of one, or both, of these factors to explain the OD is compounded by the destruction of the sedimentary context during sample preparation. With the original context destroyed, the De distribution and associated OD are disconnected from the sedimentary environment. The explanation of OD is often made using either macroscopic field observations or by comparison to previously published data. This thesis is motivated by the overarching aim to reconcile the De distribution, and the associated OD, with the sedimentary context from which the samples were collected.

To address this aim, two locations – MacCauley's Beach and Pech de l'Azé IV – were chosen as study sites. The former is a geogenic receded barrier beach deposit located near Wollongong, New South Wales, Australia, whereas the latter is a Neanderthal occupation site containing anthropogenic sediments located in the Department of the Dordogne, France. A total of 12 samples, six from each site, were collected as part of a broad aim to construct temporal frameworks and assess the site formation processes at each site. In 11 of the 12 samples the resulting De distributions were overdispersed, with OD values between 27 ± 2 and 87 ± 5%.

Beyond intrinsic characterisation studies, a series of approaches was developed in an attempt to elucidate the possible extrinsic factors responsible for the observed OD. These methods included soil micromorphological analysis, beta dose rate (β-Dr) measurement of fractionated sediment components based on grain size and mineralogy, β-Dr modelling using microphotograph analysis, portable X-ray fluorescence (pXRF) analysis, aluminium oxide (Al_2O_3:C) dosimetry and micro-computer tomography (μ-CT).

Soil micromorphological analysis was used to qualitatively establish post-depositional mixing and beta microdosimetry as likely processes responsible for the observed OD. Furthermore, the fractionation and β-Dr measurement of two samples

from both localities (SP2, SP5, PdAIV-01-C and PdAIV-02) quantitatively showed that β-Dr variability existed, both with respect to grain size and mineralogy. This method, however, destroyed the original sedimentary context. Modelling of the β-Dr using thin-section microphotographs taken from these same four samples demonstrated spatial variability in β-Dr but could not account entirely for the spread in D_e values. Portable XRF and Al2O3:C dosimetry analyses both supported the β-Dr modelling findings but had their own associated limitations. These limitations included the 4 μg/g detection limit for U and Th of the pXRF, and dim luminescence signals from single-grains of Al2O3:C. Micro-CT analysis of the MacCauley's Beach samples, only, was able to resolve the high β-Dr heavy mineral sand fraction but also deposited dose into the light-shielded quartz grains. Although each of these methods has its own series of limitations, taken collectively, they provide a greater depth of understanding of the sedimentary environment than what is currently appreciated or observed.

Using both the qualitative and quantitative insights into sedimentary context, the processes responsible for the observed OD could be evaluated and robust interpretations made with regards to the De distribution patterns, and hence OSL ages. Beta microdosimetry was proposed to be an influential process, with post-depositional mixing and intrinsic variability also playing a role. With this understanding, the onset of the mid-Holocene sea level high stand at MacCauley's Beach was dated to between 7.7 ± 0.5 and 7.5 ± 0.4 ka ago, consistent with regional sea level models. At Pech IV, the period of time between the deposition of the basal unit (Layer 8) and the highest sampled sedimentary layer (Layer 4A) is bracketed by the OSL ages of 95 ± 5 (a weighted mean of 4 ages) and 65 ± 5 ka.

The procedures developed and presented in this thesis contribute towards our understanding of the sedimentary environment, with regards to pre-, syn- and post-depositional processes, and the influence that such processes have on the single-grain OSL De distributions. By placing the sand-sized grains being dated in their original sedimentary context more robust interpretations can be made about the amount of spread within these distributions and, in turn, the single-grain OSL ages. This contextualisation, therefore, is the key to greater understanding.

ACKNOWLEDGMENTS

This thesis has been a long time in the making and would not have been completed without the help and support of many people. These people I would like to take this opportunity to thank here.

First of all, I would like to extend my heartfelt thanks and gratitude to my supervisors Zenobia Jacobs and Richard 'Bert' Roberts. I would like to thank you both for taking me on as an undergraduate, honours and now PhD student. Without your wisdom and patience this thesis would not have been a reality. Thank you for showing me the 'light.' To my associate supervisor, Paul Goldberg, I would like to thank you for giving me the soil micromorphological skills required to complete this thesis and providing constant and ongoing encouragement particularly towards the 'twilight' days of this thesis.

I would like to thank my family, Mum and Dad, Celise and Granny. For constantly being there to remind me to keep calm, chin up and carry on. Thank you from the bottom of my heart.

There are a number of friends that I also wish to thank. These people have helped, encouraged, grounded, laughed (both at and with me) and been a constant source of joy and happiness. So to the members of the Tuesday morning coffee crew; Deirdre Ryan, Brent 'Pinky' Koppel, Daniela Müller, Florian Dux, Venera Espanon, Sarah Eccleshall, Mika Puspaningrum, Amy Blakemore, Claire Perrette, Anna Harbeck-Fardy and Stephanie Jane Kermode, thank you all so very much for keeping me sane (or at least as sane as possible). I also wish to thank my dear friend Nerida Brown for all her help and support; thanks Dotty.

I would like to thank a number of staff at the University of Wollongong. To Terry Lachlan, Brian Jones, Paul Carr, Penny Williamson, Colin Murray-Wallace, Tim Cohen, Jan 'Henne' May, Luke Gliganic, Richard Fullagar and Kat Szabó thank you for your time and helpful, informative and constructive conversations.

To the Carsac crew, Harold Dibble, Shannon McPherron, Dennis Sandgathe, Vera Aleias, Sam Lin, Luíseach Nic Eoin, Lauren Jones, Vanessa Hillman and Virginie Sinet-Mathiot, thank you for accepting me as an honorary crew member and

making me feel welcome during my field seasons abroad. Those that known me as 'Shorty' or use my height as a standardised unit of measurement shall hold a special place in my life.

I would also like to pay a special tribute to three very special women in my life. The first is Mrs Margaret Carriage. To you, I wish thank you for igniting my enthusiasm for learning and instilling a spirit to always endeavour to achieve greater things. The second is Mrs Kerry Kimbrey. Without your love of science and your passion for teaching I would not have chosen the path that I currently tread. I would, however, like to apologise for abandoning penguin ecology for sand grains. The third is Mrs Gabriella Dalton: ex-nun, teacher, mathematician and life-long learner; your zest for life and constant encouragement throughout my high school years drives me onwards to this day. I miss our cups of tea, piano lessons, maths classes and interminable smiling and laughter throughout.

I have, however, saved the biggest and most sincere thanks for last. To Kathleen Dawes, my partner, fiancé (now wife) and best friend, you have been with me on this journey right from the start. As I have travelled along this roller-coaster ride, you have remained a steady and constant point throughout the entire journey. Thank you for believing in me, for helping and guiding me, for being a constant source of warmth, friendship and joy through the tears and the smiles. Without you by my side and holding my hand this thesis would have never been finished.

Table of Contents

List of Figures

List of Tables

List of common abbreviations

AAR	Amino acid racemisation
AHD	Australian height datum
^{14}C	Radiocarbon
Al_2O_3:C	Aluminium oxide doped with carbon
BM	Beta microdosimetry
CAM	Central Age Model
D_e	Equivalent dose
ESR	Electron spin resonance
FMM	Finite mixture model
Gy	Gray
Gy/ka	Gray per thousand years
HRGS	High-resolution gamma spectrometry
ICP-OES/MS	Inductively-coupled plasma optical emission spectrometry/ mass spectrometry
MAM	Minimum age model
MAX	Maximum age model
OD	Overdispersion
OSL	Optically stimulated luminescence
PMSL	Present mean sea level
pXRF	Portable x-ray fluorescence
TL	Thermoluminescence
U-series	Uranium series
β-D_r	Beta dose rate
μ-CT	Micro-computer tomography

Chapter 1

Introduction and Scope

This chapter outlines the scope of the thesis and presents the overarching, broad and specific aim that it intends to address. I also comment on the thesis style selected for this body of work and how this has been employed here. Finally, I present the outline of thesis chapters to be encountered.

1.1 THESIS SCOPE

This study examines in detail the importance of sedimentary geometry and environment for samples collected for OSL dating. This absolute dating determines the burial age of sedimentary deposits as a function of radiation dose stored within constituent sediment grains. To determine the burial age for a sample using current practice, however, requires the collection of a light-shielded sediment sample that is prepared under dim red light conditions and a particular mineral (typically quartz and K-feldspar) and grain size extracted for OSL measurement. Herein lays the issue. As the OSL signal measured from each grain is the direct result of the surrounding radiation field, by deliberately removing the 'wanted' grain size fraction, and disregarding the remaining portions, all evidence of the sedimentary context within which they were deposited is destroyed. The outcome of this is that the distribution and spread observed in the radiation doses absorbed by the grains are, at best, inferences based on field observations or previously described examples, rather than examination of the sediments themselves.

1.2 THESIS AIMS

The overarching aim of this thesis is to contribute towards the advancement of the OSL method by integrating sedimentological studies with the standard OSL practice and procedures. It has a broad aim of assessing site formation processes, sedimentary geometry and chronology of two stratigraphic profiles. To address this broad aim, two study sites were selected for single-grain OSL dating. These sites were not only geographically removed from one another, but formed under distinctly different processes. Additionally, the questions that can be answered through the chronological and sedimentological investigation of these two sites places further impetus for their inclusion to this study.

The first site is a receded-barrier beach deposit located at MacCauley's Beach on the New South Wales (NSW) coastline of south-eastern Australia. This site was

first investigated more than 20 years ago by Bryant *et al.* (1992b) and is the product of entirely geogenic site formation processes. The chronology for the site was constructed using the thermoluminescence (TL) dating method – an absolute dating technique that was state-of-the-art during the early 1990s but shown to be not so accurate when dealing with unburnt sediments, particularly in depositional environments where the complete resetting of the TL signal cannot be ensured. Such settings include fluvial, deltaic, or lacustrine settings where light intensities under turbulent water flows have been shown to be ~10^4 times less at 4m water depth than at the surface (Berger & Luternauer 1987, Berger 1990). When the reduced light intensities of these environments are considered with the finding that a reduction of the TL signal to 20% of its original intensity requires ~200 min of direct sunlight exposure (Godfrey-Smith *et al.* 1988) it becomes increasingly apparent that the possibility for unreliable TL chronologies is significant. Furthermore, the stratigraphic interpretations presented by Bryant *et al.* (1992b) are lacking in detail.

By re-evaluating this site, it is not only possible to address the reliability of the TL chronology and stratigraphic interpretations, but also to comment on the late Quaternary evolution of the NSW coastline and the timing and nature of the mid-Holocene sea level high stand recorded at a number of surrounding coastal locations. The selection of this site, also, was based on the 'tyranny of distance.' Given the methodological nature of this thesis it is important that at least one study location be readily accessible for further experimentation and sample collection (should it be required). The location of MacCauley's Beach is no more than ~12 km from the University of Wollongong, equating to about 20 min by car. This ease of access was not afforded by the second study site.

The second site to be investigated is a Neanderthal occupation site of Pech de l'Azé IV (Pech IV). This site is located in the south-west of France in the Department of the Dordogne. Unlike the 'purely' geogenic sediments of MacCauley's Beach, Pech IV has a strong anthropogenic signature preserved within its sedimentary record in the form of hearths, stone tools and bone fragments. Originally excavated in the 1970s by F. Bordes, the site was shown to contain a long and variable sequence of Mousterian stone tool industries. The work conducted at

this site was made in conjunction with a larger ARC-funded project to Z. Jacobs that aimed to provide a temporal framework using single-grain OSL for a number of sites within this region of France. The previous chronological constraints at Pech IV used multiple techniques on multiple materials and gave an incomplete chronological record for the site. By evaluating the Pech IV site we can address questions of the nature of Mousterian stone tool variability, the influence that the intensive anthropogenic signature had on the Pech IV sediments, and the OSL signal that we are measuring.

With these two sedimentary sequences in mind, this thesis aims to address a number of specific aims. These aims are to:

1. Develop novel sampling techniques that allow the investigation and assessment of sedimentary characteristics from which the single-grain OSL samples have been collected,
2. Develop a method of evaluating the spatial variability of the beta dose rate throughout the sediments,
3. Investigate the association between the distribution of radioactive mineral species in 3-dimensions and the amount of spread overdispersion (OD) in a single-grain OSL D_e distribution,
4. Investigate how the site formation processes influence the intrinsic OSL signal behaviour of quartz; and
5. Investigate the sediments preserved at MacCauley's Beach and Pech IV to evaluate the extent and causes of the OD present in the single-grain D_e distributions.

1.3 THESIS STYLE

The style that this thesis is presented in is unorthodox. It was initially considered, and approved, by my supervisor (Z. Jacobs) that the 'Thesis with chapters written in the form of journal articles' style was to be used. However, it was noted in the final stages of preparation that this style was rather constrictive if word limits for journal articles (7 to 8 thousand words) were adhered to. Reducing the amount of text would translate into a lack of 'wiggle room' to present the logical development of arguments that were made.

The chapters that make up the original contributions to the OSL field are presented as self-contained studies and remain written in the style of journal articles, with each having an abstract, introduction, methods, results, discussion and conclusions. These headings are, however, not necessarily presented in this order or under these exact headings. I, myself, and my supervisor are aware that these chapters are significantly longer than would be permissible for journal articles. We expect, however, that following thesis submission these can be reworked into a format and word limit suitable for journal article publication.

In each section, the referring style used is consistent with that used for the Australian Journal of Earth Sciences. By using this style the comma following the abbreviation *et al.* in 'in text' citations is not included e.g., (Roberts *et al.* 1999) rather than (Roberts *et al.,* 1999).

The beginning and end of each chapter have been 'book-ended' to aid the reader of this thesis to follow the developmental logic behind the range of studies undertaken. The aims to be addressed are presented before each chapter and how these have, or in some cases, have not been achieved are outlined after each chapter as well as how these findings can be improved upon in the future.

1.4 THESIS ORGANISATION

This thesis is split into three parts: A, B, C and D. Part A represents the review of the literature surrounding both the study sites and the main methodological

approaches used throughout this thesis. Part B is the main body of work conducted throughout the period of candidature. Part C presents a synthesis of the main findings of this thesis. Part D is an appendix section includes the OSL dating paper of Jacobs *et al.* (submitted). The remainder of this thesis is organised as follows:

PART A

- Chapter 2 – Two sites, two stories

This chapter contains substantive reviews of the study sites being investigated in this thesis and placing these into their respective contexts. They are by no means intended to be exhaustive or in depth, but provide adequate foundation of both sites. First, the literature surrounding the late Quaternary coastal evolution is appraised and the previous study by Bryant *et al.* (1992b) assessed. This is followed by an examination of the Pech IV site paying particular attention to the stratigraphy, site formation processes and chronology; and how these relate to the question of Mousterian variability.

- Chapter 3 – OSL dating and measurement techniques

This chapter delves into the OSL literature to provide an understanding of the physical background, dose rate evaluation and D_e measurement procedures. It also examines the intrinsic and extrinsic factors that influence the amount of spread observed within D_e distributions. Particular attention here is paid to recent studies in the field of beta microdosimetry. The section concludes with an overview of age models used in D_e determination and the method for calculating OSL ages.

- Chapter 4 – Soil micromorphology: terminology, methods and approach

This final chapter of Part A reviews soil micromorphology as a method for analysing thin sections of soils/sediments. Particular attention is given to the

terminological framework of Stoops (2003), the collection, preparation and processing of samples and the scaffold for reporting soil micromorphological data.

PART B

- Chapter 5 – Optical dating and soil micromorphology at MacCauley's Beach, New South Wales, Australia

This chapter examines the chrono- and lithostratigraphy of MacCauley's Beach. Here, a new integrated approach to optical dating is introduced that sees soil micromorphology samples collected in tandem with those for OSL dating. The results of this study provide qualitative insights into the sedimentary context of the OSL samples, thereby, allowing more robust interpretations of the D_e distributions to be made.

- Chapter 6 – Variation in beta-dose rates within a sample and its implications for OSL dating of individual quartz grains

This chapter builds upon the results from Chapter 3 using samples from both MacCauley's Beach and Pech IV by providing quantitative, rather than qualitative, results. Here, measurements of the beta dose rates of constituent minerals and grain size fractions were investigated, with the results showing significant variability in the measured beta-dose rates. This variability was also spatially examined using portable X-ray florescence and aluminium oxide dosimetry of resin-impregnated sediment slabs. The spatial variability was also modeled using concentrations of U, Th and K determined for constituent mineralogies and grain sizes in conjunction with microphotographs of the sediments.

- Chapter 7 – Micro-computer tomography (μ-CT) of sediments and its applicability to optically stimulated luminescence studies

The results of Chapter 4 investigated a two dimensional geometry, this chapter build upon this and aims to determine whether the same spatial distribution of beta-dose rate can also be observed in three dimensions. Here the applicability (and influence) of the μ-CT technique to digitally resolve sediment components is investigated with the aim to then use these same samples in OSL age determination.

- Chapter 8 – Shedding light on a burning question: luminescence characteristics, dosimetry and OSL ages of quartz grains from Pech de l'Azé IV, France

This chapter presents the results of the investigations into the intrinsic behaviour of the quartz grains collected from Pech IV, with particular attention focused onto how the post-depositional and sedimentary environments influence these characteristics. I also reports age for six samples collected from three sedimentologically distinct layers and how these fit into the previously published chronology for the site.

PART C

- Chapter 9 – Synthesis

This chapter is separated into four sections. The first section outlines the main implications to OSL dating in terms of the findings, shortcomings and implications for the studies conducted in this thesis. Section two outlines the questions that could potentially be addressed by future work. Section three revisits the aims outlined in

Chapter 1 and critically assess whether these had been met or not. The final section provides the concluding remarks of this thesis.

PART D

- Appendix I – Additional OSL methods, measurement procedures and equipment

This appendix contains the further information regarding: 1) rejection criteria, 2) sample preparation methods, and 3) environmental dose rate determination methods and procedures.

- Appendix II – Soil micromorphology: Further information

This appendix contains an additional review of the literature with respect to the historical development of soil micromorphology as a means of investigations sediments, the terminological framework of Stoops (2003) and the method of reporting soil micromorphological data according to Goldberg & Macphail (2006).

- Appendix III – Chapter 6 Supplementary Information

This appendix contains the supplementary information of the paper reported in Chapter 6.

- Appendix IV – Chapter 8 Supplementary Information

This appendix contains the supplementary information of the paper reported in Chapter 8.

- Appendix V – Jacobs *et al.* (submitted)

This appendix contains the OSL dating paper of Jacobs *et al.* (submitted) for the three Pech de l'Azé sites (Pech I, II and IV). This paper is included as the work conducted at the Pech IV site in this thesis formed part of this larger chronological investigation.

CHAPTER SUMMARY

This chapter has provided details on the motivation behind the body of work presented here. It also presents the overarching aim of this study – to contribute to the advancement of the OSL method through the integration of sedimentological analysis of OSL samples. More broadly, this study aims to investigate and provide robust chronologies for the two locations of MacCauley's Beach and Pech IV. The five specific aims to be addressed by this study have also been presented. The slightly unorthodox and hybridised nature of this thesis has been addressed and acknowledged. Finally, the outline of the chapters to follow has been presented to aid the reader to follow the development of this thesis.

PART A

Chapter 2

Two sites, two stories

This chapter reviews the literature surrounding the two key questions that can be answered through the stratigraphic and chronological reassessment of the MacCauley's Beach and Pech IV study sites. The two study sites investigated in this thesis are fundamentally different, in terms of their formation and sedimentological characteristics. The site of MacCauley's Beach, Australia, was considered by Bryant et al. (1992b) to be the result of fluctuating sea level heights over the period between MIS 5e and the mid-Holocene. As such, these deposits represent geogenically-derived material as a direct result of Later Quaternary sea level changes. In contrast, the Pech IV site was deposited under an admixture of colluvial and anthropogenic mechanisms between ~100 and 20 ka ago (Turq et al. *2011). Thus, the coastal evolution of the NSW coastline over the last glacial cycle will be reviewed in section 1, and the Mousterian stone tool variability and site formation at Pech IV reviewed in section 2.*

2.1 RISE UP: LATE QUATERNARY COASTAL EVOLUTION OF NEW SOUTH WALES

MacCauley's Beach is one of the study sites that this thesis is concerned about. The aim at this location is to investigate both the chronology and site formation processes as a response to sea level fluctuations over the last glacial cycle. This section does not aim to provide a complex and exhaustive review of sea level change for the late Quaternary, but rather aims to place MacCauley's Beach into the context of sea level history along the NSW coast and how this coastline has responded to such changes. To do this, I touch upon the role of climatic forcing in sea level fluctuations as well as the components that comprise relative sea level curves. I then discuss the sedimentary infilling successions that typify the NSW coastline before outlining how these respond the sea level fluctuations. This section concludes by presenting the formative work carried out by Bryant *et al.* (1992b) at MacCauley's Beach and why it is important that this site be re-evaluated.

2.1.1 RELATIVE SEA LEVEL THEORY

Quaternary coastal landscape evolution is inextricably linked to fluctuations in the relative height of sea level to dry land. These fluctuations in sea level height have been shown to be climatically driven as a result of orbital forcing. Deviations in Earth's orbital eccentricity, obliquity and procession lead to differences in the amount of insolation energy reaching Earth's surface, with periods of ~100, 41 and 23 ka for each orbital force, respectively (Milankovitch 1930). The link between climatic forcing and sea level height is through the waxing and waning of large continental ice sheets (Nakada *et al.* 2000, Lambeck & Chappell 2001, Fleming & Lambeck 2004, Brunnabend *et al.* 2012, Roberts *et al.* 2012, Hay *et al.* 2014). In the most basic terms, high insolation leads to an input of ice sheet melt water into the ocean basin thereby increasing the volume of water, whereas low insolation periods

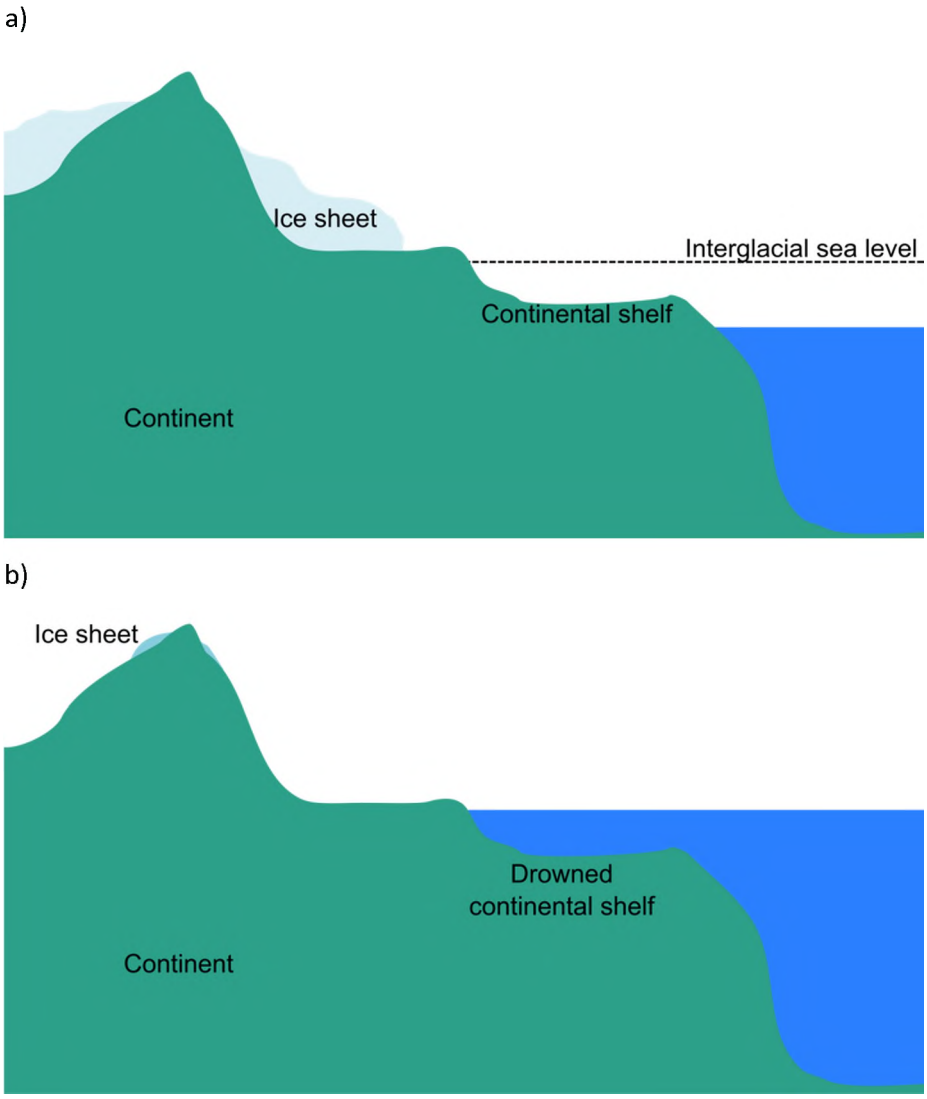

Figure 2.1.1. a) During glacial periods, large amounts of water are locked up as continental ice sheets reducing the volume of oceanic water thereby lowering sea level. b) warming conditions during interglacial periods melt the continental ice sheets releasing the water back into the oceans resulting in a higher sea level.

result in oceanic water being locked into continental ice sheets and reducing the oceans volume (Figure 2.1.1). This signature of oceanic sea level fluctuations is locked up in the oxygen isotope records of both marine and ice cores (Imbrie *et al.* 1992, EPICA community members 2004).

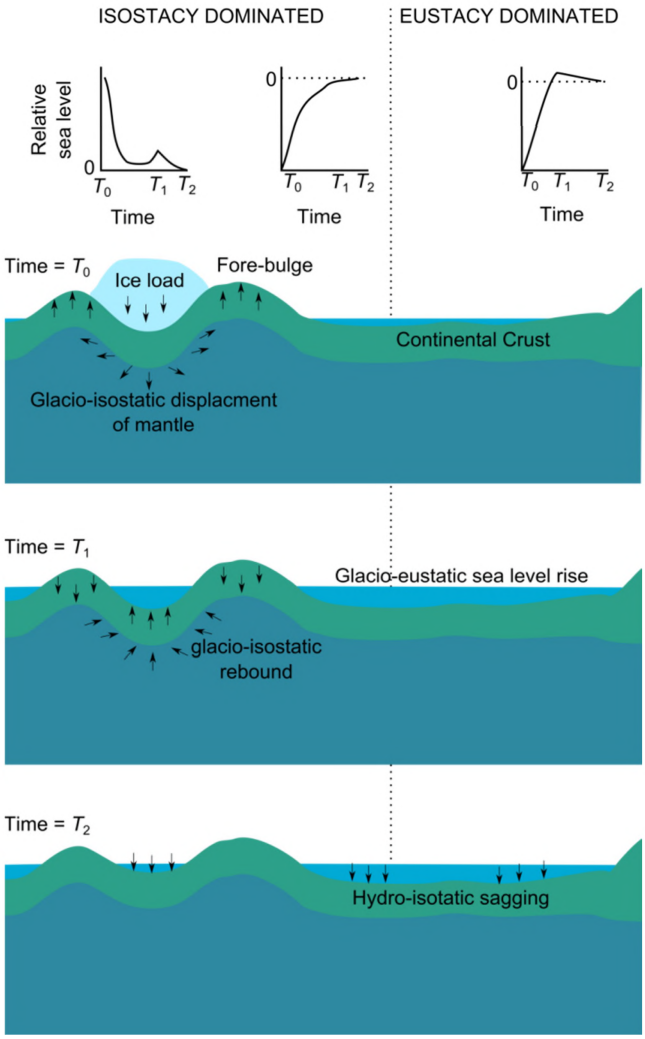

Figure 2.1.2. Relative sea level signatures of near field (isostacy dominated) localities under the ice load and the associated mantle bulges; and far field (eustacy dominated) regions.

Time T_0) The ice load at the near field depresses the underlying mantle which produces the characteristic fore-bulge surrounding it. The far field is not affected by these isostatic adjustments.

Time T_1) once the ice load melts, the far field records a steady eustatic sea level rise. In contrast, the relative sea level records for the near field locations under the ice load and on top of the mantle bulge that are heavily influenced by the respective isostatic rebound and relaxation and record a steady fall or rise of sea level for those regions, respectively.

Time T_2) the water loaded into the ocean basins results in hydro-isostatic 'sagging' of the sea floor, which results in the falling sea level signature in the far field and also the near field under the previous ice sheet.

The relative sea-level history signature, however, comprises of three separate components, these being: I) tectonic, II) glacio-hydro-isostatic and III) glacio-eustatic adjustment (Figure 2.1.2; (Lambeck 1993, Lambeck 2001, Lambeck 2004)). The tectonic component (i.e., the rise of dry land with respect to sea level) gives the appearance of a lowering of sea level. This component is typically estimated from independent sources and can (in some cases) be corrected for in the sea level height data for the region.

The second component is that of isostatic adjustment due to loading of the Earth's crust with either ice or water. The loading of the crust with ice or water results in the redistribution of the viscous underlying mantle as equilibrium is attained. In terms of ice loading, the depression of the crust directly under the ice sheet produces a bulging effect in the surrounding region (Figure 2.1.2 at T_0) – termed the near field. Thus, in the near field the relative sea level is dominated by glacio-hydro-isostatic adjustments – i.e., rebounding of the crust from under the ice load and a relaxing of the crust over the mantle bulge. In these two instances, the former results in a relative sea level fall whereas the latter produces a signature of relative sea level rise (Figure 2.1.2 at T_1). The loading of the oceanic crust (either sea floor or continental shelves) with water results in an isostatic 'sagging' or depression of the crust and gives the impression of the lowering of sea level (Figure 2.1.2 at T_2).

Finally, the glacio-eustatic component is the result of worldwide changes in the volume of ocean water and hence sea level height due to the input of glacial melt water (Figure 2.1.2 at T_2). This relative sea level signature is most clearly seen in regions that are tectonically stable and isolated from the ice sheet cover, such as Australia, and are termed the far field regions.

2.1.2 RELATIVE SEA LEVEL HISTORY FOR NSW

The position of the NSW coastline in the far field provides an excellent opportunity to study (almost exclusively) the glacio-eustatic change in ocean water volume and sea level over the past glacial cycle. The position of NSW away from

major continental ice sheets and plate boundaries has two consequences. The first is that the influence of the glacio-hydro-isostatic effects (as experienced in the near field) is minimal. The second is that the region is considered to be tectonically stable. Given the tectonic stability, the fluctuations of relative sea level height produce a coastal landscape where younger sedimentary deposits are stacked on top of, or against, older sediments. This section reviews the sea level history for the NSW region over the last ~125 ka by compartmentalising this record into three sections: 1) last interglacial (marine isotope stage; MIS 5); 2) last glacial maximum (MIS 2); and 3) the Holocene (MIS 1).

2.1.2.1 LAST INTERGLACIAL MAXIMUM (MIS 5)

Sedimentary deposits dating to MIS 5 are present right along the NSW coast. South of Sydney, these deposits are often encountered as relict MIS 5 barrier sediments found directly underlying the Holocene-age barrier and can be found at Lake Illawarra (Sloss *et al.* 2004, Sloss *et al.* 2005, Sloss *et al.* 2006a), Minnamurra River estuary (Panayotou *et al.* 2007), Lake Conjola (Sloss *et al.* 2010), Narrawallee Inlet (Nichol & Murray-Wallace 1992) and Burril Lake (Sloss *et al.* 2006b). However there are two issues that surround these localities with respect to the sea level high stand during MIS 5e. Firstly, the chronology of these barriers is typically determined using TL and often produce ages that are considerably younger than MIS 5e, often MIS 3 (Sloss *et al.* 2006a). These younger ages are often explained as the aeolian reworking of the barrier sands during periods of lowered sea level. This point, consequently, raises the second issue surrounding these barrier features. Given the significant aeolian reworking of the barrier sands, it is likely that these features are no longer at the original elevation that they achieved during MIS 5e – i.e., they have been flattened and depressed. The presence of the last interglacial barriers, therefore, only provides evidence of the spatial position of the MIS 5 sea level but gives no indication of absolute previous sea level heights.

Only the two localities at Evan's Head (Pickett 1981, Pickett *et al.* 1989) and Largs (Thom & Murray-Wallace 1988) are known to preserve stratigraphically-

controlled evidence for the height of MIS 5e sea levels in the form of fossils. At both locations, the fossils were found inland of Pleistocene-age barrier sequences –Thom *et al.* (1981) referred to these barrier structures as the 'Inner Barrier.'

At Evan's Head, located on the coast between Ballina and Yamba, a suite of fossil corals were recovered from ~9 km upstream of the Evans River mouth, ~5 km from the present day coast. Here, the corals were exposed on the south bank of the river at low tide as a thin layer of *in situ* fossils (Pickett 1981). Previous work by Marshall & Thom (1976) suggested that the preservation of the fossils at this locality was due to the sheltering effect of a nearby bedrock ridge and headland. The species assemblage of corals led Pickett (1981) to propose a sheltered marine environment during the time of coral growth and a water depth of no more than 10 m. Uranium series dating of a number of corals by Marshall & Thom (1976) provided radiometric ages of 114 ± 9 and 127 ± 18 ka for reworked material, and a concordant age of 118 ± 9 ka for an *in situ* fossil coral. This led Marshall & Thom (1976) to hypothesise that these corals formed during MIS 5 when sea level was between 4 and 6 m above present sea level based upon the location they were found in, (i.e., between sand barrier and lagoonal mud facies). Their 5 ± 1 m MIS 5e sea level is not inconsistent with that of <10 m determined from the fossil coral assemblage by Pickett (1981).

At Largs, near Maitland, *in situ* shell material (*Anadara trapizia*) was recovered from the Inner Barrier central mud basin facies (Murray-Wallace *et al.* 1988). The site is a narrow terrace remnant containing both Pleistocene and Holocene units: the latter butting up against the former. The fossil shells were recovered within a ~1.2 m thick layer under ~4 m of brown silty clay. The contact between these units is abrupt and irregular suggesting an erosion surface. The ~2 m of sediment underlying the shell bed are dominated by muddy sands, with reworked shell material found only in the upper ~0.5 m. Amino acid racemisation (AAR) ages for the shell assemblage provide ages that are concordant with the MIS 5 age presented in Marshall & Thom (1976) for the nearby Grahams Town location. Using the present height of the shell bed (+2–3 m above present mean sea level: APMSL) and the ecology of the shelly fauna, Thom & Murray-Wallace propose a water depth

of 4 ± 1 m during MIS 5 for the region (Murray-Wallace *et al.* 1988, Thom & Murray-Wallace 1988).

The evidence for the absolute height of MIS 5e sea level along the NSW coast therefore, is tied to only two localities of Evans Head and Largs. Both of these sites provide the only evidence for *absolute* sea level of ~5 m APMSL experience during MIS 5e for the NSW coast. It is for this reason that I have given such emphasis to both of these important sites.

2.1.2.2 LAST GLACIAL MAXIMUM (MIS 2)

The coastal evolutionary picture between MIS 5 and MIS 2 is poorly understood, simply because the transitional nature of these deposits (from high stand to low stand of sea level) would mean that that have been subsequently reworked since their original deposition and is under the water on the continental shelf. All that can be deduced for the time period MIS 5e (~125 ka) and the height of the last glacial maximum (~21 ka) is sea level regressed from its maximum of +5 m APMSL as a result of glacio-eustatic sea level change to between -120–130 m below PMSL based on AAR ages from vibracores (Murray-Wallace *et al.* 1996, Murray-Wallace *et al.* 2005). At this position, the active shoreline would be located 20 to 30 km east of its current position.

The post-glacial marine transgression (PMT) was the result of glacio-eustatic sea level rise. There is a distinct paucity of material and research during the early stages of the PMT along the NSW coast. Presumably, this is due to the inability, and difficulty, of collecting samples from the submerged continental shelf. The review by Lewis *et al.* (2013), however, provides a generalised sea level envelope for the Australasian region from the LGM through to 7 ka ago (Figure 2.1.3). This model of sea level rise is drawn from a number of data sets collected from Australia, New Guinea, New Zealand and the Sunda shelf. The initial period of the PMT (between the LGM and ~15 ka ago) is relatively slow at a rate of ~4 m/ka. The rate of the PMT seems to increase substantially to ~20 m/ka between 15 ka and the start of the

Holocene. The implications for the PMT along the NSW coast are shown graphically in Figure 2.1.5. Off the coast of Wollongong, sea level during the LGM was ~20 km east of its present position (Figure 2.1.4a), this distance decreases to 15 km by ~15 ka (Figure 2.1.5b), between 10 and 12 km by 13 ka (Figure 2.1.4c and d), and between 2 and 4 km away at the Pleistocene/Holocene boundary (Figure 2.1.4e and f).

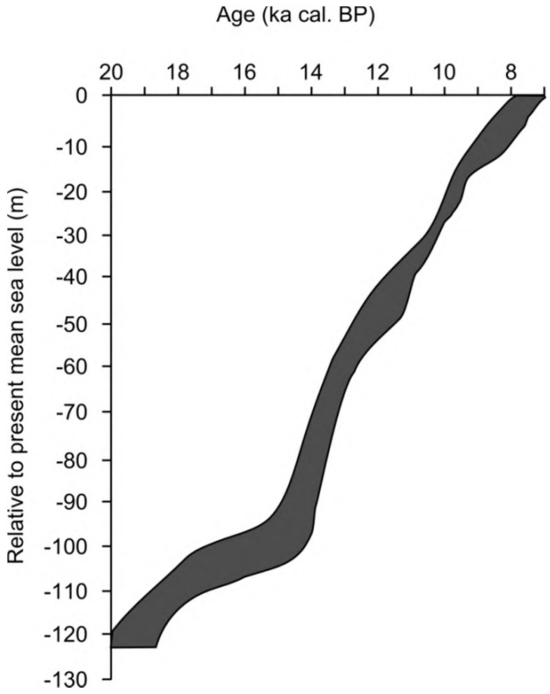

Figure 2.1.3. Post-glacial marine transgression sea level curve presented in and modified from Lewis *et al.* (2013). The relative sea level envelope was drawn to incorporate intertidal indicators and the zone between the terrestrial and marine directional indicators.

2.1.2.3 The Holocene (MIS 1)

The NSW Holocene sea level history is significantly better constrained both in terms of time and relative sea level height. A model for Holocene sea level rise specific to the south-eastern coastline of Australia was presented by Thom & Chappell (1975).

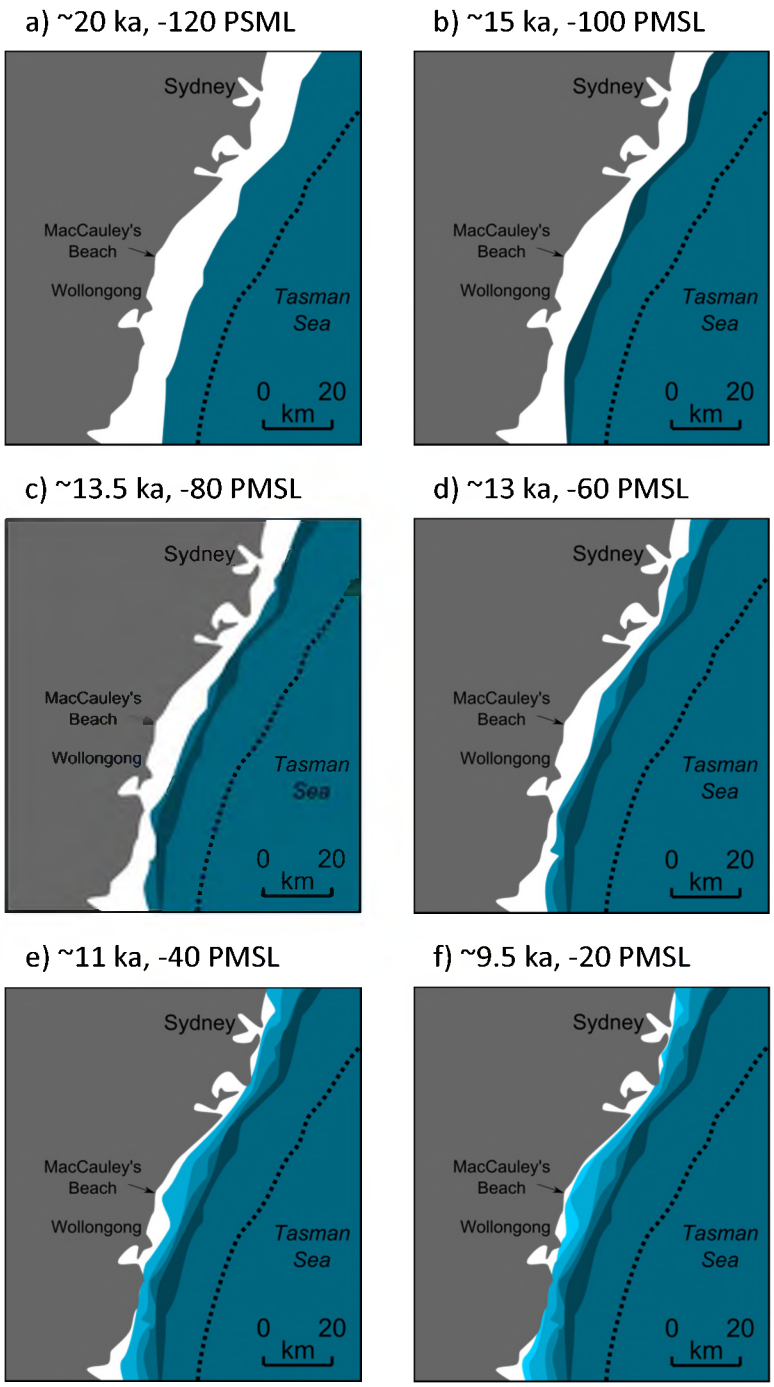

Figure 2.1.4. Position of sea level with respect to the present day coastline (grey) for a section of the NSW coast relatively to this study during the post-glacial marine transgression from 20 to 9.5 ka. Also shown is the relative position of the continental shelf edge (dashed line). This figure uses the bathymetric data presented in Murray-Wallace *et al.* (2005) and the Australasian post-glacial marine transgression curve of Lewis *et al.* (2013)

This sea level curve underwent several iterations before it was finalised and presented by Thom & Roy (1985). The Holocene sea level envelope proposed by Thom & Roy (1985) was based upon 69 ^{14}C ages for samples that had been collected from estuarine sedimentary facies from a variety of depths below PMSL to a maximum depth of ~80 m. The ^{14}C ages of these shell, wood and charcoal samples were corrected for the marine reservoir effect and produced ages that were all older than 5 ka BP (uncalibrated). Although the ^{14}C ages require calibration to sidereal years, the sea level model proposed by Thom & Roy (1985) shows as smooth rise to PMSL by 7–6 ka BP – calibration would push this range back to between 7.9 and 6.7 ka cal BP.

However, the Thom & Roy (1985) model failed to recognise the significance of the radiocarbon ages presented in Jones *et al.* (1979) for two receded barrier beach deposits. These deposits were located at South Thirroul and North Bulli beaches, ~12 km north of Wollongong. A radiocarbon age on an *in situ* mangrove stump at North Bulli (later calibrated by Sloss *et al.* 2007) gave an age of 7.7 ± 0.3 ka cal BP. A concordant ^{14}C age of 7.8 ± 0.3 ka cal BP was returned for an *in situ* mangrove root from South Thirroul. In both instances, the ^{14}C samples were recovered from an elevation of > +1 m PMSL. Yet, despite this fact, Thom & Roy (1985) took a conservative view that after reaching PMSL, sea levels remained relatively stable and fluctuated less than ± 1 m PMSL.

A re-evaluation of the NSW Holocene sea level history was conducted by Sloss *et al.* (2007) some 30 years later. In their review Sloss *et al.* (2007) calibrated 112 previously published ^{14}C ages from along the NSW coast, presented 37 new ^{14}C ages from seven sites, and 50 complementary AAR ages from six of these seven sites. A comparison of the new chronologies presented in Sloss *et al.* (2007) with that from Thom & Roy (1985) reveals the same trend in sea level history over the Holocene period, with PMSL attained by 7.9 to 7.7 ka (Figure 2.1.5). Beyond this point, Sloss *et al.* (2007) give precedence to the radiocarbon ages of Jones *et al.* (1979) and posit that the PMT continued to a height of ~1.5 m above PMSL by 7.4 ka ago. This rise in sea level is consistent with the model for glacio-eustatic sea level adjustment presented by Lambeck & Nakada (1990) for the NSW coastline. Here, the rise, and

subsequent fall of sea level above PMSL is a result of the hydro-isostatic adjustment of the oceanic basin to the increased water loading. Sloss *et al.* (2007) suggest that sea level remained at a higher elevation than PMSL, with small oscillations, until ~2.0 ka ago, before regressing to PMSL (Lewis *et al.* 2013, Sloss *et al.* 2007).

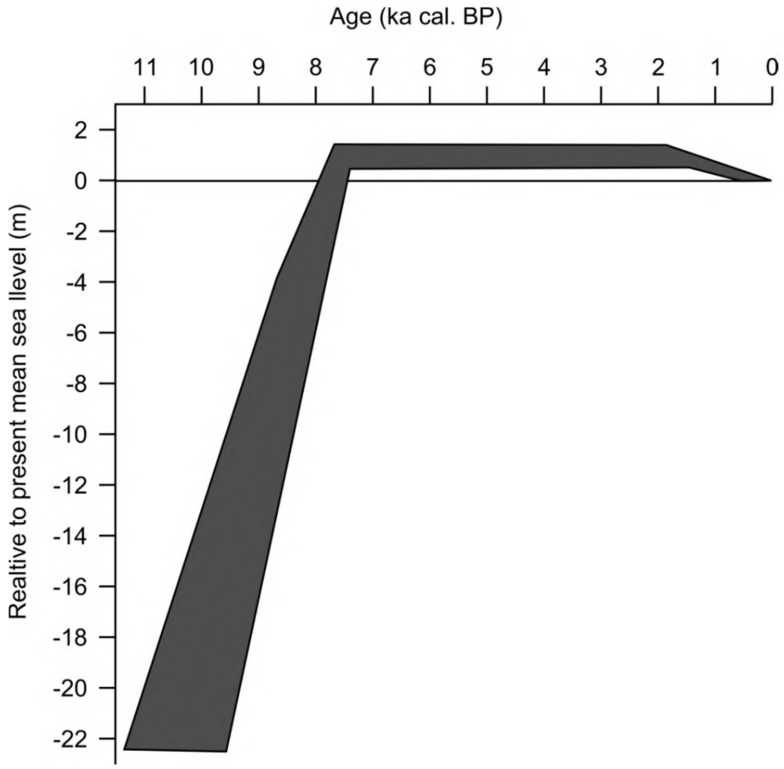

Figure 2.1.5. Holocene sea level curve for south eastern Australia. Modified from Sloss *et al.* (2007).

2.1.3 ESTUARIES AND COASTAL INFILL ALONG THE NSW COAST

The interaction between terrestrial landscapes and marine environments produces, in some instances, estuary sequences. These sedimentologically-distinctive environments record past sea level fluctuations and coastline morphodynamics through biological and geological indicators. The sedimentary deposits located at MacCauley's Beach are the result of such processes. It is therefore important to understand the formation and processes active within these estuarine environments.

The continental margin off the east coast of Australia was produced during the rifting event that opened up the Tasman Sea between the Australian continent and the islands of New Zealand, New Caledonia and Lord Howe Rise during the Late Cretaceous/Palaeogene (Haynes & Ringis 1973). Erosion accompanying and following this process produced an embayed coastline with rocky headlands separated by incised river valleys that have infilled with estuarine sedimentary facies. Pritchard (1967) defined an estuary as:

'*a semi-enclosed coastal water body which had free connection to the open sea and within which sea water is measurably diluted with freshwater derived from land drainage.*'

Yet, this definition failed to outline the geological and sedimentological variability of these environments. In contrast, the definition given by Dalrymple *et al.* (1992) provides a more geomorphologically-centred outline of estuaries as:

'*The seaward portion of a drowned valley system which receives sediments from both fluvial and marine sources and which contains facies influenced by tide, wave and fluvial processes. The estuary is considered to extend from the landward limit of tidal facies at its head to the seaward limit of the coastal facies at its mouth.*'

The authors went on to say that if the rate of sea level rise is greater than the rate of sedimentation then the estuary will submerge and drown.

Three types of estuary were outlined in Dalrymple *et al.* (1992) with the distinctive morphologies produced as a result of the dominant energy coming from wave, tide or river processes. The microtidal climate of the NSW coastline in conjunction with the relatively small fluvial systems results in the NSW estuaries being classified as wave-dominated. Within this estuary classification, a number of distinct categories exist that are based upon the bay-barrier mouth morphology and embayment shape. Roy *et al.* (1980) outline three categories that include: open ocean, drowned river valleys (open estuaries) and barrier estuaries. In a

reassessment, Roy *et al.* (2001) added an additional category of saline coastal lake – this is a barrier estuary that had become permanently cut off from marine influenced due to the infilling of the inlet channel. This last estuary type, however, was combined with the bay-barrier category by Yassini & Jones (1995) due to their

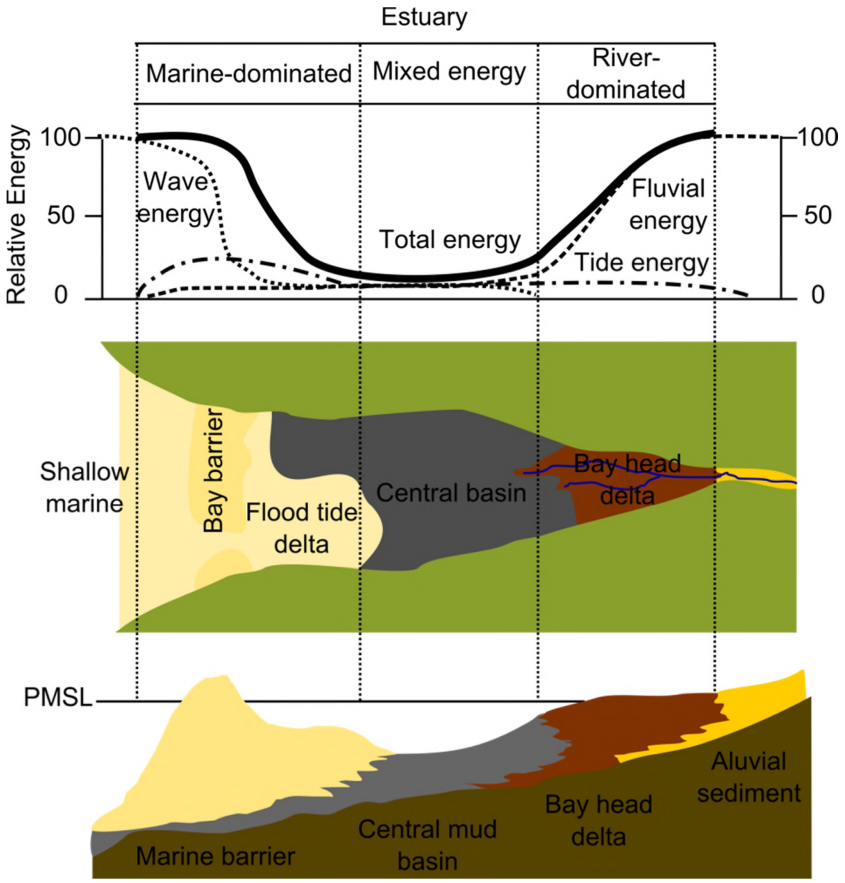

Figure 2.1.6. Schematic of the energy distribution, plan-form and facies changes within a wav-dominated estuary. Modified from Dalrymple *et al.* (1992).

similar genetic histories. These authors added sheltered oceanic embayments as an additional category of estuary along the coast of NSW.

The geomorphology of the wave-dominated estuaries, as the name suggests, is a reflection of dominant wave energy at the estuary mouth. A profile of the total energy across a typical wave-dominated estuary is given in Figure 2.1.6. Wave

energy results in the onshore movement of sandy sediments to produce barriers that inhibit the wave energy from entering the embayment. In microtidal climates, the low energy of the tide can occasionally result in the 'choking' of the barrier inlet channel with sediment producing a saline coastal lagoon as described by Roy *et al.* (2001). Where tides are sufficient to maintain the inlet channel, a flood-tide delta can be produced over the back barrier facies on the landward side of the barrier, with an ebb-tide delta forming seaward of the barrier. The fluvial energy entering the back-barrier lagoon is dominant only where the flow is channelised, but quickly reduces once it enters the back-barrier lagoon.

The variability in total energy across the estuary gives rise to distinct packages of sediments with their own unique sedimentological characteristics and creates the distinctive progression of tripartite facies (Boyd *et al.* 1992, Dalrymple *et al.* 1992, Nichol & Murray-Wallace 1992). A stylised schematic of a wave-dominated estuary and the tripartite facies zonation is shown in Figure 2.1.6.

At the seaward limit of the estuary, the marine facies are typified by coarse marine sands, reflecting the high energy environment of the near-shore zone. This marine sand consists of a core of transgressive sub-tidal shoals with associated wash-over deposits producing a barrier/beach complex. This barrier feature is often cut by a tidal inlet channel. If the tidal energy is sufficient a flood-tide delta of marine sands can be formed on the landward side of the inlet channel.

Headward of the coastal facies is a low energy lagoon that contains the central mud basin facies. This central estuary component accumulates fine-grained sediments, predominantly silts and clay, with minor sands, and is typified by a dark, usually black, colouration reflecting the high proportion of organic matter being deposited within the basin. The source of the fine-grained sediments is not from the marine zone, but rather the fluvial inputs from the hinterland. In this light, the central mud basin facies can be considered the pro-delta region of the terrestrial sediment infilling the basin.

A fluvial bay-head delta, at the headward end of the central lagoon, forms as a result of the infilling of the basin with terrestrial hinterland-derived sediments. The sedimentology of this facies is complex and shows a characteristic coarsening upwards sequence of sediments; from the fine muds of the prodelta region, into the fine sands of the crevasse splay sands and levee bank deposits into the coarse sand and gravel components of the river channel proper. Along the NSW coastline, these sediments are sourced from the western hinterlands. The morphology of the bay-head deltas can be categorised into either fluvial-, wave- or tide-dominated, depending on the prevailing process.

The alluvial sediment component marks the edge of the estuary itself. Beyond this region, fluvial processes dominate. Here, sands and gravels dominate the in channel sediments, with silts, clays and fine sands forming overbank sequences. Swampy environments are generally associated with fluvial muds and peats.

2.1.4 THE RESPONSE OF THE NSW COASTLINE MORPHOLOGY TO SEA LEVEL CHANGE OVER THE LAST GLACIAL CYCLE

It must be recognised that the spatial context of estuaries along the coastline is not static and fixed. Rather these depositional environments are dynamic and have the ability to translate either landwards with transgressing sea levels or seawards under regressing sea level conditions (Roy *et al.* 1994). Thus, these bedrock valley infill sequences are constantly moving towards equilibrium with the relative height of sea level dictating their position. That being said, the morphology and type of estuary produced is the expression of controlling geological and physical context within which these environments form. The model presented for the tectonically stable (Bryant 1992a) coastline along NSW by Roy & Thom (1981) recognised two morpho-dynamically distinct districts: a 'rugged' coastline south of Newcastle (~33°S) – the southern sector; and a 'subdued' coastline to the north – the northern sector (Figure 2.1.7). The distinctive behaviour of these environments to sea level change, was proposed by Roy & Thom (1981) to be the result of three formative,

geologically-inherited factors: 1) substrate slope; 1) wave energy potential; and 3) rate of sediment supply.

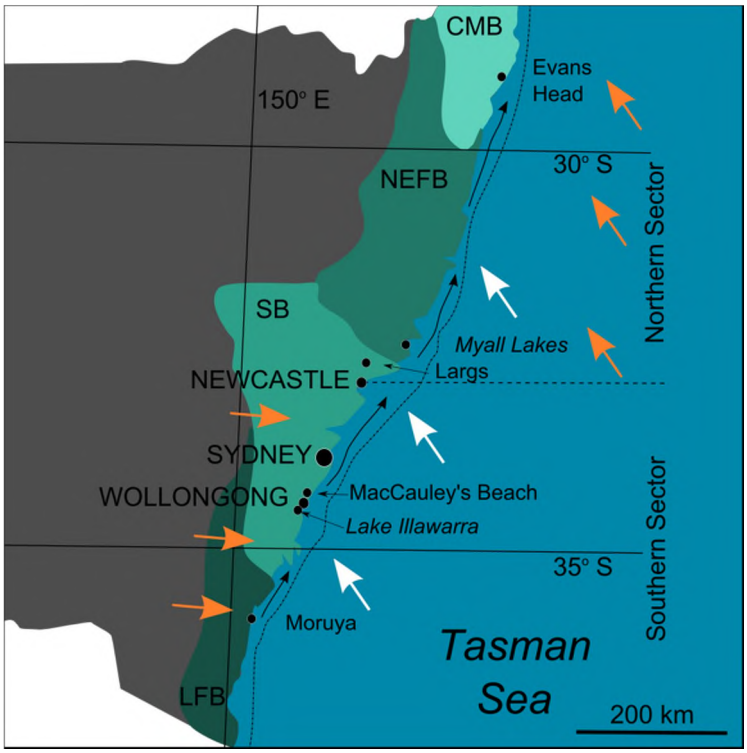

Figure 2.1.7. Schematic of the New South Wales coastline modified from Roy & Thom (1981). Dominant wave climate is sourced from swell and wind-waves generated from the south-east (white arrows), producing a littoral drift (black arrows) that transports sediments from south to north along the inner continental shelf (edge delimited by the dashed black line running sub-parallel with the coast). The southern sector (south of the dashed horizontal line) has a geology dominated by the Lachlan Fold Belt (LFB) and Sydney Basin (SB), and is highly compartmentalised. The northern sector (north of the dashed horizontal line) was formed with the New England Fold Belt (NEFB) and Clarence-Moreton Basin (CMB), is typified by broad, wide and shallow bedrock valleys giving the coastline a more 'subdued' morphology. During glacial periods, the main wind direction for the southern sector was from the west, whereas in the northern sector, the main wind direction was from the south-east.

The geologically inherited substrate slope plays an important role in not only the potential for sediment preservation within NSW bedrock valley's but also the rate and morphology of the sedimentary infill itself (Wright 1976, Cowell *et al.* 1992, Roy *et al.* 1994). The morphology of the NSW continental shelf, in general, becomes wider and shallower from south to north. In the southern sector, ~80% of the continental shelf lies at a depth greater than -50 m below PMSL and is rarely more than 50 km wide (Roy & Thom 1981, Murray-Wallace *et al.* 2005). Thus, the profile across the southern sector continental shelf is considered deep and narrow, producing a steep substrate slope. Although roughly the same width as in the southern sector, the majority of the continental shelf in the northern sector is found at less than 100 m below PMSL – producing a shallow substrate slope (Marshall 1983).

The wave climate along the NSW coastline provides the energy required to shape and modify the coastal landscape. The incident wave climate is set up by pressure systems sitting in the Tasman Sea (Thom *et al.* 1973) producing swell and wind-waves that act upon the coast from the S–SE (Wright 1976) (Figure 2.1.7). The roughly normal orientation of the NSW coastline (NNE–SSW) to this dominant wave climate (SE) results in the high energy, wave-dominated coastline morphology of the region and a south-to-north littoral drift of sediment (Thom 1978, Roy *et al.* 1980, Roy & Thom 1981, Chapman *et al.* 1982).

The continental shelf has significantly different characteristics with regards to the northern and southern sectors. The south sector has a steep profile, whereas the northern sector has a relatively shallower profile. This disparity in slope gives rise to a differential in wave energy potential along the coast. In the southern sector, the deep and narrow continental shelf produces negligible frictional loss of the incident wave energy seaward of the breaker zone (Wright 1976). Modelling studies conducted by Griffin *et al.* (2008) found that only the maximum recorded wave height could mobilise medium–fine sand on the inner and mid continental shelf and the non-cohesive muds beyond the shelf break, reemphasising the dominance of wave energy on sediment transport along the inner shelf. Given the shallower continental shelf profile in the northern sector, frictional energy losses are more pronounced, therefore, the incident wave energy is somewhat less than in the

southern sector. This difference in wave energy, therefore, results in greater energy available to shape (and erode) the coastline of the southern sector, with substantially less energy available for coastal modification in the north.

The rate of sediment supply and the ability to transport sediment along the coast produces distinct morphological differences between the southern and northern sectors. The factors controlling the rate of sediment supply and transport, however, are dictated by the regional geology. In the southern sector, the main geological formations of the Lachlan Fold Belt and Sydney Basin (Figure 2.1.7) are relatively hard and geologically stable, whereas those of the New England Fold Belt and Clarence-Moreton Basin (Figure 2.1.7) in the north are relatively soft and easily weathered (Roy & Thom 1981). The eastern edges of these geological provinces continue beyond the coastline as submerged bedrock promontories or reefs onto the mid-continental shelf plain. These reefs are aligned to the main structural trends in the associated geological formation and are most prominent in the Sydney Basin province where the structural trends run transverse to the coastline. In the south, pocket beaches and small embayments are common, with the short distance between successive headland/reef promontories acting as sediment compartments that have relatively minor losses of sediment to littoral (south-to-north) drift. Thus, the southern sector has a deficient supply of sediment that can be delivered to the coast(i.e., that found within its respective bedrock-defined compartment). In contrast, the lack of headland/reef compartments in the north allows the free movement of sediment as a result of littoral drift processes, producing a sediment surplus.

These three interrelated factors (slope, wave energy and sediment availability) culminate to produce distinctive barrier morphologies. These are shown schematically in Figure 2.1.8. While the term 'barrier' is commonly used to describe an elongate sand body running (sub)parallel to the coast, it can also be used for those sediments that are entirely attached to the mainland such as strand plains and main-land beaches. In general, three broad categories of barrier were described by Roy *et al.* (1994). These categories are based upon the rate and direction of sea level change and include: I) transgressive, 2) regressive and 3) stillstand barriers – these are shown graphically in Figure 2.1.8.

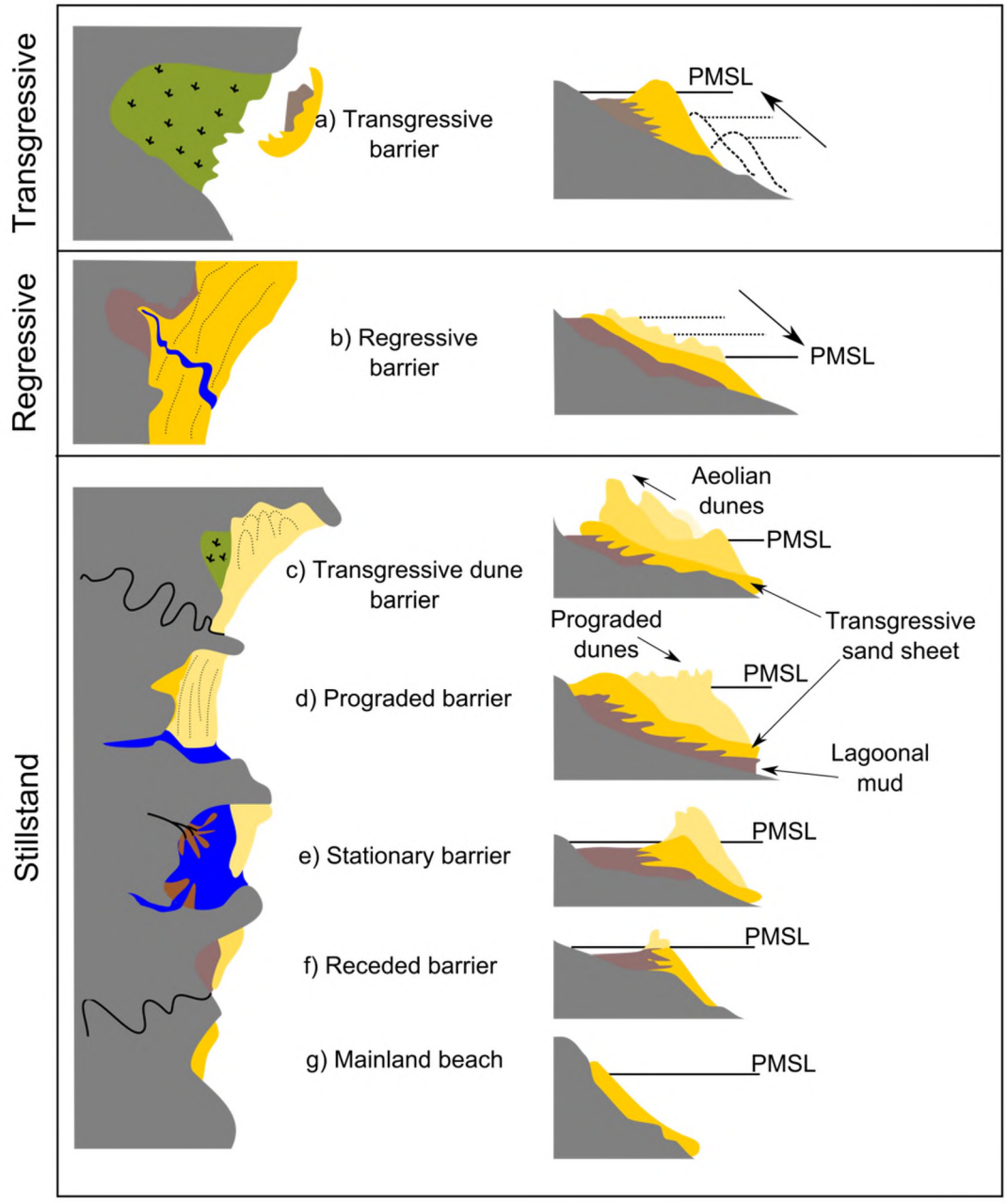

Figure 2.1.8. Transgressive, regressive and stillstand barrier morphologies for wave-dominated barrier estuaries. Modified from Woodroffe (2002) and Roy *et al.* (1994).

Transgressive barriers, also termed barrier islands, are formed under conditions of rising sea levels. These barriers usually occur as detached thin and elongate shore-parallel sand bodies separated from the mainland by either a lagoon or estuary

(Figure 2.1.8a). In contrast, regressive barriers form as a series of beach ridges that step down in elevation sequentially with falling sea level (Figure 2.1.8b). These two types of barrier are uncommon along the NSW coast, if not absent.

Of more importance to NSW barrier morphology are those barrier types found in the stillstand class. Roy *et al.* (1994) presented a number of sub-types of stillstand barrier. However this work, in fact, represents a conglomeration of nearly thirty years of sea level research along the NSW coastline (Thom & Chappell 1975, Thom 1978, Thom *et al.* 1981, Chapman *et al.* 1982, Thom 1984a, 1984b, Thom *et al.* 1992, Roy *et al.* 1994). The continuum of stillstand sub-classes presented in Figure 2.1.8. are ordered according to increasing wave energy and substrate slope; and decreasing sediment supply from top (Figure 2.1.8c) to bottom (Figure 2.1.8g). Thus, the layout of the stillstand barrier systems in Figure 2.1.8 roughly equates to the prevalence of these types of barrier systems in the northern and southern sectors.

Transgressive dune and prograded barriers result from an excess of sediments being delivered to the shore-face. In the case of transgressive barriers, these sands are then mobilised by onshore winds that blow the sand farther inland over the central mud basin facies to generate large dune fields (Figure 2.1.8c). In contrast, prograded barriers (or strand plains) are typified by a succession of relict beach ridges that young towards the modern beach face (Figure 2.1.8d). While, there is sufficient wind energy to provide each beach ridge with an aeolian dune cap, the climatic conditions are more favourable for primary colonising plants that stabilise the dune before it, and the underlying beach ridge, can be blown farther inland. The formation of prograded barrier systems, therefore, can be seen as an accretionary process that effectively builds out the barrier complex seawards from the original transgressive barrier at the headward side of the complex.

Stationary barriers are the result of a balance between sediment supply and loss. These stationary barriers were formed from a limited supply of sediments that experienced periods of erosion and accretion (Figure 2.1.8e). However, the sediment loss is never major as the bedrock reefs that form the underwater compartment prevents sand being lost to longshore drift processes. These barriers are typically

associated with major lagoonal (back-barrier) facies and are often anchored to, or overlie, antecedent barrier structures. Given their stability, the associated dunes often show evidence of soil development.

The receded barrier type is the sedimentary deficient relative of the stationary barrier. The lack of sediment, and the high incident wave energy, results in the barrier sands translating up and onto the relict central mud basin facies (Figure 2.1.9f). Thus, it is common in these settings that the muds and peats are often seen outcropping on the adjoining beach. Typically, barriers of this nature are of low relief and less than 10 m thick. The barrier dune often encloses a small lagoon, such as at Dee Why, Sydney (Thom 1984b), with the inlet channel that drains the lagoon occasionally being blocked with sediments.

Finally, the mainland beach barrier type represents a barrier end member. Comprising a thin covering of sediments, typically sands and gravels, these barriers are subjected to the highest amount of wave energy and receive the least amount of sediment (Figure 2.1.8g). Thus, these environments represent regions of continued sediment reworking.

The fluctuation of relative sea level height along the NSW coast (as described in section 2.1.1) forces the bedrock-valley confined estuarine system to adjust (in time and space) to maintain equilibrium. The distinctive differences in substrate slope, wave energy and sediment supply between the southern and northern sectors of the NSW coast results in equally characteristic responses of the coast to sea level changes. This led Roy & Thom (1981) to propose two separate models to account for the disparity between the northern and southern sector coastal landscapes. These are shown graphically in Figure 2.1.9.

In the northern sector, the higher than present sea level of MIS 5 allowed large deposits of sediment to accumulate along the coast as wave-dominated bay-barrier estuaries. Their large size was due, in part, to the large space available to accommodate these sediments but also the surplus of sediments being delivered (Figure 2.1.9a). MIS 2 sea level low stands shift the active region of sedimentation

eastwards (Figure 2.1.9b). Although cut into by fluvial processes, the MIS 5 barrier sediments remain intact and are, potentially, fed by sandy sediments sourced from the continental shelf by the intensification of south-east winds. The net result, therefore, is that the MIS 5 barrier remains fairly *in situ*. Thus, the PMT results in the translation of the coastal estuary system back towards its MIS 5 position. However, here, during the Holocene, the zone of sedimentation abuts against the previous valley infill (Figure 2.1.9c). Thus according to Roy & Thom (1981), these coasts represent a *depositional* transgressive stratigraphic pattern.

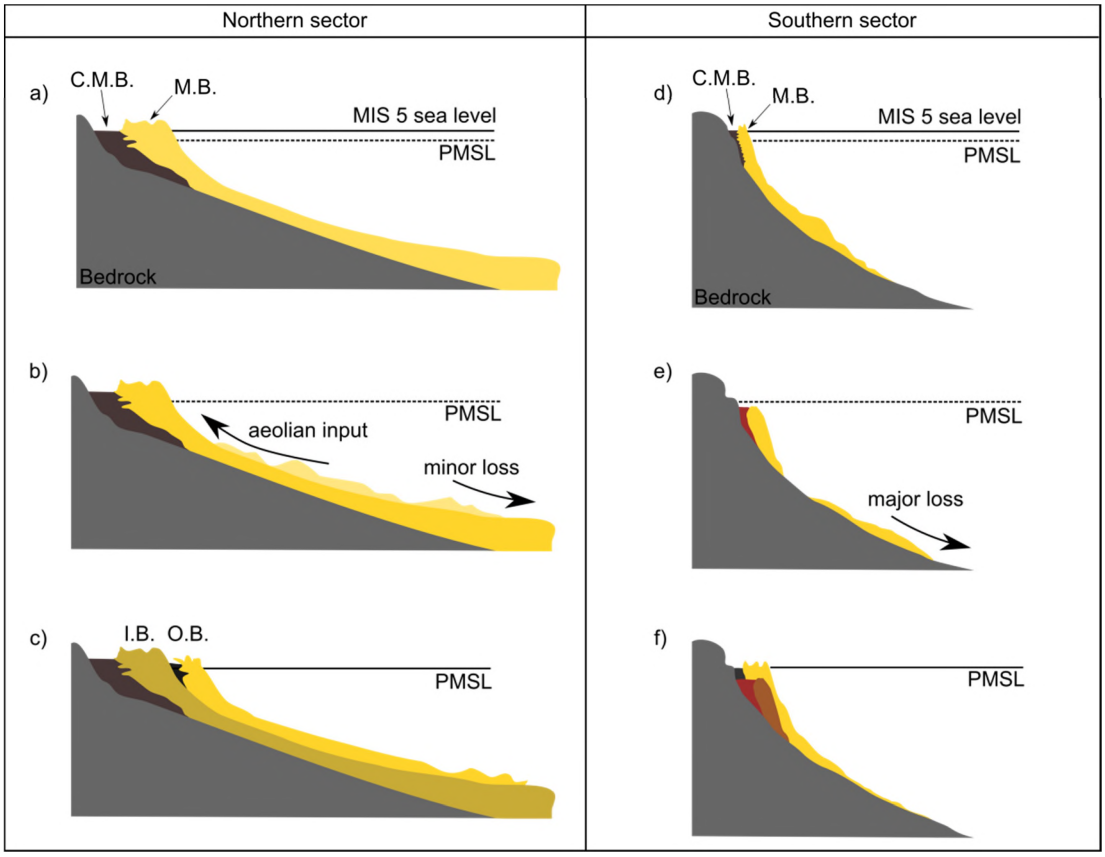

Figure 2.1.9. Model of sediment accumulation and preservation potential along the NSW coastline for the northern (left) and southern (right) sectors. Central mud basin (C.M.B.) facies can be found landward of the Inner Barrier (I.B.) or Outer Barrier (O.B.) sand-dominated marine sediments. Modified from Roy & Thom (1981).

In contrast, the southern sector was identified as an *erosional* transgressive stratigraphic pattern by Roy & Thom (1981). Here they considered that during the MIS 2 low stand the entire the MIS 5 valley infill was eroded onto the continental shelf. This concept is no longer supported with detailed drilling and TL dating of barrier systems along the southern sector revealing an inner 'core' of MIS 5 deposits (Sloss *et al.* 2006b, Sloss *et al.* 2010). The model for coastline response has been revised as follows. During MIS 5 the estuarine facies filled, or partially filled, the available accommodation space in the small, deep and narrow coastal valleys (Figure 2.9d). Given the steep gradient of this coastline, during the MIS 2 sea level low stand, a substantial proportion of the valley infill is removed as the MIS 5 barrier complex was cut into by fluvial activity (Sloss *et al.* 2006a) and flattened by aeolian processes (Bowler 1976) leaving behind a 'relict' barrier system (Figure 2.9e). The PMT following the LGM refilled these valleys with a 'new' Holocene-aged estuary (Figure 2.9f).

2.1.5 MacCauley's Beach: Previous work

The site of MacCauley's Beach (MB), located immediately north of Sandon Point (Figure 2.1.10), is situated directly in between the North Bulli (to the south) and South Thirroul (to the north) study sites outlined in Jones *et al.* (1979). Given the regional significance of these two sites (see Section 2.1.2.3.), containing the earliest known records for the Holocene sea levels at a height greater than PMSL, Bryant *et al.* (1992b) conducted a limited stratigraphic and chronological investigation at MB. Below, I present both the litho- and chrono-stratigraphy constructed by Bryant *et al.* (1992b). In their investigations, Bryant *et al.* (1992b) subdivided the sedimentary sequence at MB into four broad stratigraphic units: the Pleistocene mud, dune humate, loose sand and modern dune unit. These are shown schematically in the original block diagram presented by Bryant *et al.* (1992b; Figure 2.1.10).

2.1.5.1 Pleistocene mud unit

The lowest stratigraphic unit at MacCauley's Beach comprises two layers. Texturally, both layers are similar comprising entirely of silts and clays and a small proportion of fine sand. However, Bryant *et al.* (1992b) delimited this unit into two, separating a lower, highly mottled unit, from an upper, less mottled unit. The lowest unit was described as dark grey/red in colour, directly overlying the bedrock at the southern end of the beach, and contained unweathered angular clasts, quartz sand and carbonised roots and iron oxide nodules. Bryant *et al.* (1992b) note that the upper surface of this unit rises to a height of 3.5 m APMSL and dips towards the north (Figures 2.1.10). A sharp contact separates the two mud units with the upper less mottled off lapping from the underlying mottled mud. The upper less mottled mud unit was described as dipping to the north before levelling off at a height of 2.5 m APMSL at the northern end of the beach. No thickness for this unit was given.

Two TL samples were taken from the Pleistocene mud succession, but the exact locations and units were not specified. The TL age of the Pleistocene material was determined to be 71 ± 23 and 45 ± 17 ka, using a multi-grain and multi-aliquot approach. Bryant *et al.* (1992b) interpreted this unit as an estuarine (central mud basin) facies deposited during a period when sea level was higher than PMSL. The authors tentatively assign this unit to MIS 5, with the potential of being even older, citing the poor TL temperature plateaux curves as evidence for this age. This presumably means that the ratio of the natural TL curve to that of a natural + laboratory dose (similar to Figure 1.3 in Aitken 1985) is not giving a plateau region, thereby suggesting the likelihood of partial bleaching.

2.1.5.2 DUNE HUMATE UNIT

Bryant *et al.* (1992b) provided details of two separate layers that overlie the Pleistocene mud. The first layer is a section of indurated, iron-cemented 'beach rock' composed of quartz sand. This unit sits atop a scarp that has been eroded into the Pleistocene mud (Figure 2.1.10). Bryant *et al.* (1992b) state that this deposit was located ~5 m seaward of the MacCauley's Beach sedimentary cliff section. Given the 22 years that have passed since this original study, it can be assumed that this deposit

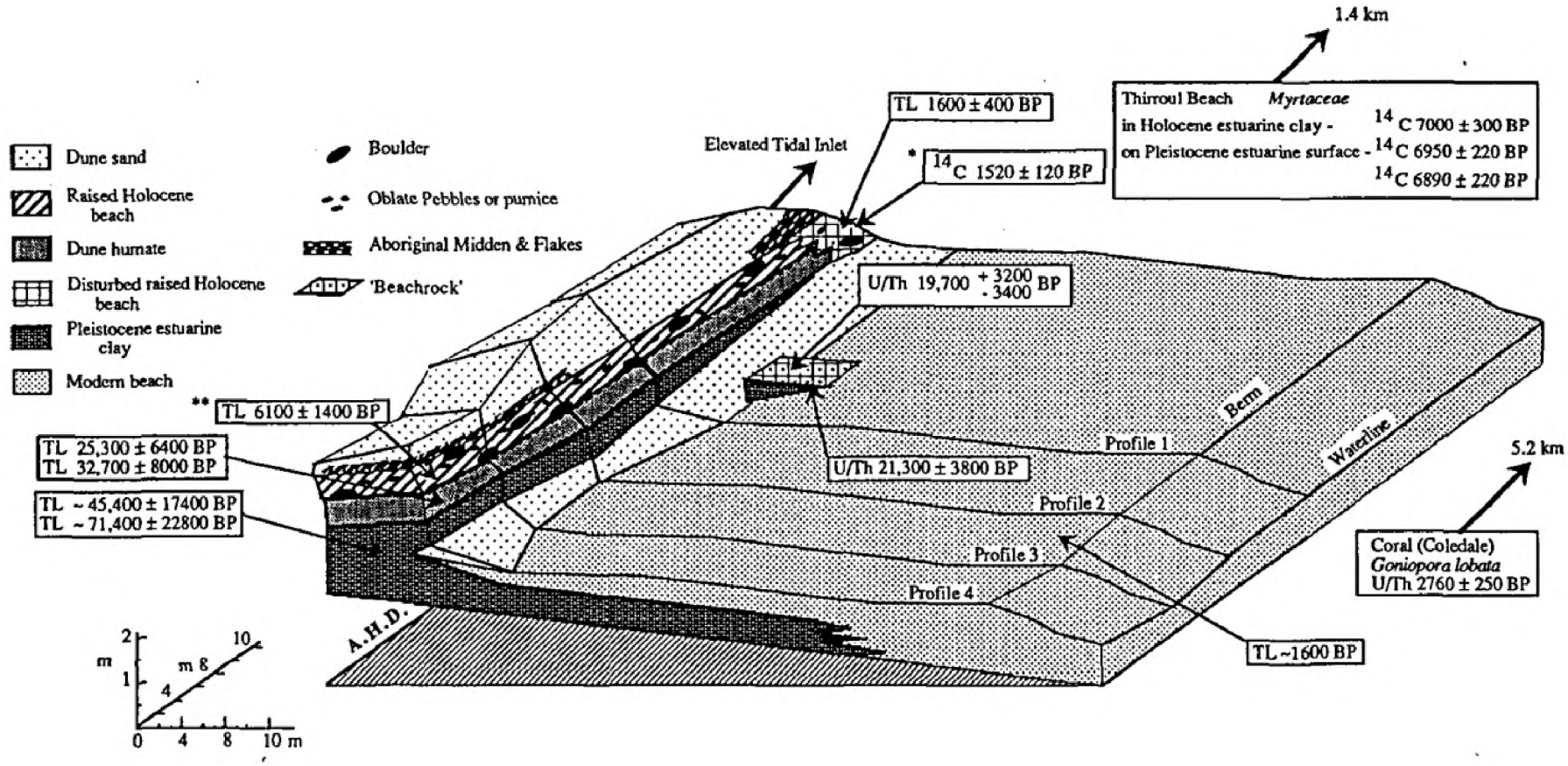

Figure 2.1.10. MacCauley's Beach stratigraphy as presented by Bryant *et al.* (1992b). Please note that there is an error in the original figure. Here, the x- and y-axes read 10 m but ought to read 12 m.

has since been eroded. A Uranium (U)-series age for two portions of 'beach rock' provided ages of 21.3 ± 3.8 and 19.7 ka with uncertainties of +3.2 and -3.4 ka. It should be recognised that these ages are for the formation age of the carbonates, rather than the deposition of the sediments themselves. Furthermore, the carbonate systems are typically considered to be open to U uptake and leaching, so the accuracy of these ages, with respect to the target event being dated, ought to be considered tentative until supported by another means (Schwarcz 1989, Blackwell & Schwarcz 1995).

The second layer was found in the sedimentary section proper. The unit had a thickness of between 0.5 and 0.6 m and was composed almost entirely of quartz sand that had been partially cemented with organic and humic residues (Figure 2.1.10). Numerous pebbles and boulders punctuate the unit. Two TL samples were collected from the dune humate unit and gave ages of 33 ± 8 and 25 ± 6 ka. This unit, as well as the sediments on the eroded scarp, are considered by Bryant *et al.* (1992b) to be the result of 'significant aeolian sand movement' as sea level regressed during the LGM. The authors posited, therefore, that the site recorded two separate Pleistocene sea level stands: one to deposit the Pleistocene clay unit and one to cut into it.

2.1.5.3 LOOSE SAND AND MODERN DUNE UNIT

The loose sand unit overlies the dune humate unit, according to the descriptions provided in Bryant *et al.* (1992b). This unit consists of an ash grey/brown predominantly quartz sand unit that has a thickness of 0.5 m (Figure 2.1.10). The quartz grains are loosely packed and unconsolidated. Only one TL sample was collected from this unit and provided an age of 6 ± 1 ka. The loose sand unit also showed evidence of shell midden usage at the northern end of the beach, with a shell collected from this region returning a ^{14}C age of 1.4 ± 0.1 ka cal BP. The dune capping that overlies the midden deposits was not dated. Bryant *et al.* (1992b) interpreted these units as a raised Holocene beach deposit and its associated foredune. They go on to say that the presence of the large pebbles and cobbles are the result of multiple tsunami – the presence of which they had previously shown along

the length of the Illawarra coastline (Young *et al.* 1993, Price *et al.* 1999, Switzer *et al.* 2005).

It is interesting to note, also that a TL age of ~1.6 ka was obtained from a modern beach sample collected at the site. While this will have no bearing on the TL ages for the Pleistocene units (i.e., Pleistocene mud and dune humate) given the large uncertainties on these estimates, it will have a larger effect on the accuracy of the 6 ± 1 ka age for the loose sand unit.

2.1.6 MACCAULEY'S BEACH: AN EARLY RISER?

The question, then, is what makes MacCauley's Beach such an important site to warrant re-evaluation? The answer to this question can be answered from three separate angles; 1) the merit of the original research conducted by Bryant *et al.* (1992b), 2) the context of the site with regards to chronology, and 3) the context of the site with respect to sea level history.

The initial study by Bryant *et al.* (1992b) was innovative at the time but has two notable flaws that can be highlighted. The first issue surrounds the reporting and interpretation of the stratigraphy. Beyond the sedimentological characteristics described in the text, the authors present no laboratory data to confirm these field observations. It follows that the interpretation of the stratigraphy and depositional environments should be viewed with caution until such data are presented. The second point is the dating sample context or, rather, lack thereof. The positions of the TL and U-series samples are only vaguely shown in the block diagram presented for the site (Figure 2.1.10). It remains unclear as to whether these arrows are indicative of sample position or the unit from which they were collected. Given the 20 years that have passed since its initial investigation, it is unlikely that the original context of these samples remain as the sedimentary section has eroded considerably over this time period.

The chronology presented by Bryant *et al.* (1992b) used state-of-the-art techniques (TL and U-series) to provide temporal constraints on the deposition of

these units. With respect to the TL chronology, this method has since been shown to be unsuitable for sediments that have not experienced heating, or exceptionally long periods of sunlight exposure (Godfrey-Smith *et al.* 1988), prior to burial. This inference is also supported by the apparent ~1.6 ka age for the 'modern' beach sand from the location. While this residual TL signal will have little effect on the Pleistocene age determination, it is significantly more important for the Holocene units. Furthermore, the uncertainties on these age estimates are large (between ~20 and 30% relative error), thus the precision of these ages can be further improved upon. Are these ages credible or are they over or underestimates of the true burial age of the unit? With respect to the U-series ages for the 'beach rock,' these formations are effectively pedogenic carbonates that are known to be open to U uptake and leaching and should be viewed with caution (Blackwell & Schwarcz 1995).

Finally, the physical context of MacCauley's Beach, between the sites of North Bulli and South Thirroul beaches, makes this site regionally important. These two bounding locations have the earliest reported ^{14}C ages for the onset of Holocene sea level attaining and continuing beyond PMSL (see Section 2.1.2.3; Jones *et al.* 1979). Given the locality of MacCauley's Beach it is possible that this site also records the same early onset of the mid-Holocene high stand. However, the stratigraphic and chronological framework that currently exists requires considerable improvement. As a side note, Sloss *et al.* (2007) report ^{14}C ages for 'Sandon Point' in their revision of the Holocene sea level curve, citing Bryant *et al.* (1992b) as the source. However, it should be noted that these ages, in fact, relate to the South Thirroul Beach site ~1.5 km north of MacCauley's Beach, beyond the next rocky headland.

For a site of such regional importance as MacCauley's Beach, the previous stratigraphic investigation presented only a brief overview of the site stratigraphy and sedimentology, and provided no insights into the depositional and post-depositional processes that produced the MacCauley's Beach site. The depositional ages for the sediments are poorly constrained and imprecise, and the stratigraphic relationships between the sediments, ^{14}C and U-series ages are tenuous. It is these issues that are to be resolved in this thesis.

SECTION SUMMARY

In this section the literature surrounding the climatic forcing of global sea level fluctuations was outlined and the basic components of tectonic, glacio-hydro-isostatic and glacio-eustatic signatures explained. The positioning of Australia in the far field, away from continental ice sheets, and away from tectonically active plate boundaries results in the sea level signature for the NSW coastline to provide a record of sea level that can be attributed entirely to glacio-eustatic adjustment. The sea level history for the NSW coastline implies that sea levels attained heights of + 5 m and -120 m PMSL during MIS 5 and MIS 2, respectively. During these transgressive and regressive periods, the estuarine sedimentary facies that infill the coastal valleys sort to readjust their position along the continental shelf to achieve equilibrium – moving inland during high stands and out onto the continental shelf during low stands. The mid-Holocene high stand at ~7.9 ka ago saw sea levels reached PSML and continued to rise to +1.5 m PMSL, with two locations close to Wollongong (North Bulli and South Thirroul beaches) providing the earliest published ^{14}C ages for this height. These two sites effectively enclose MacCauley's Beach, a site with the potential of also preserving evidence for the early onset of the mid-Holocene high stand. However, given to limitations of the original stratigraphic and temporal frameworks presented by Bryant et al. (1992b), both the stratigraphy and chronology for the site require re-evaluation.

2.2 PECH DE L'AZÉ IV: THE LEGACY OF NEANDERTHAL MAN

The archaeological site of Pech de l'Azé IV (Pech IV) contains many of the different Mousterian lithic traditions (the stone tool industry typically associated with Neanderthals). This site, in conjunction with the two neighbouring Pech I and Pech II locations, have played an important part in the debate about the nature and variability of the Mousterian industry of south-western France. This section aims to contextualise the Pech IV site with respect to the historical and recent excavations at the site. I then review the litho-, archaeo- and chrono-stratigraphy for the site. I then describe the site formation processes for the site as proposed in Turq *et al.* (2011). I close this section with a summary of the importance of the Pech IV site and why OSL investigation ought to be carried out here.

2.2.1 DIGGING DEEP: A HISTORY OF EXCAVATIONS AT PECH IV

The excavations carried out at Pech IV have a long and complex history. Originally discovered in the spring of 1952 by François Bordes, a major systematic excavation of Pech IV was not undertaken until the 1970-1977 field seasons. In his eight years at Pech IV, Bordes excavated an area of ~52 m^2, removing ~115 m^3 of sediment and rock from the site. Prior to this, however, a trench was excavated by a local dentist, Mortureux, in the 1950s. Following his excavations, Bordes (1975) believed that the deposits of Pech IV had formed in a rockshelter, unlike that of the neighbouring Pech de l'Azé I and II, which he knew were cave deposits. Bordes' excavations recovered a large amount of archaeological material, with lithic artefacts alone numbering ~92,000 pieces. Furthermore, each artefact was digitally recorded using a 3-dimensional coordinate system. This note-taking would prove to be advantageous for future researchers at the site, after the passing of Bordes in 1981.

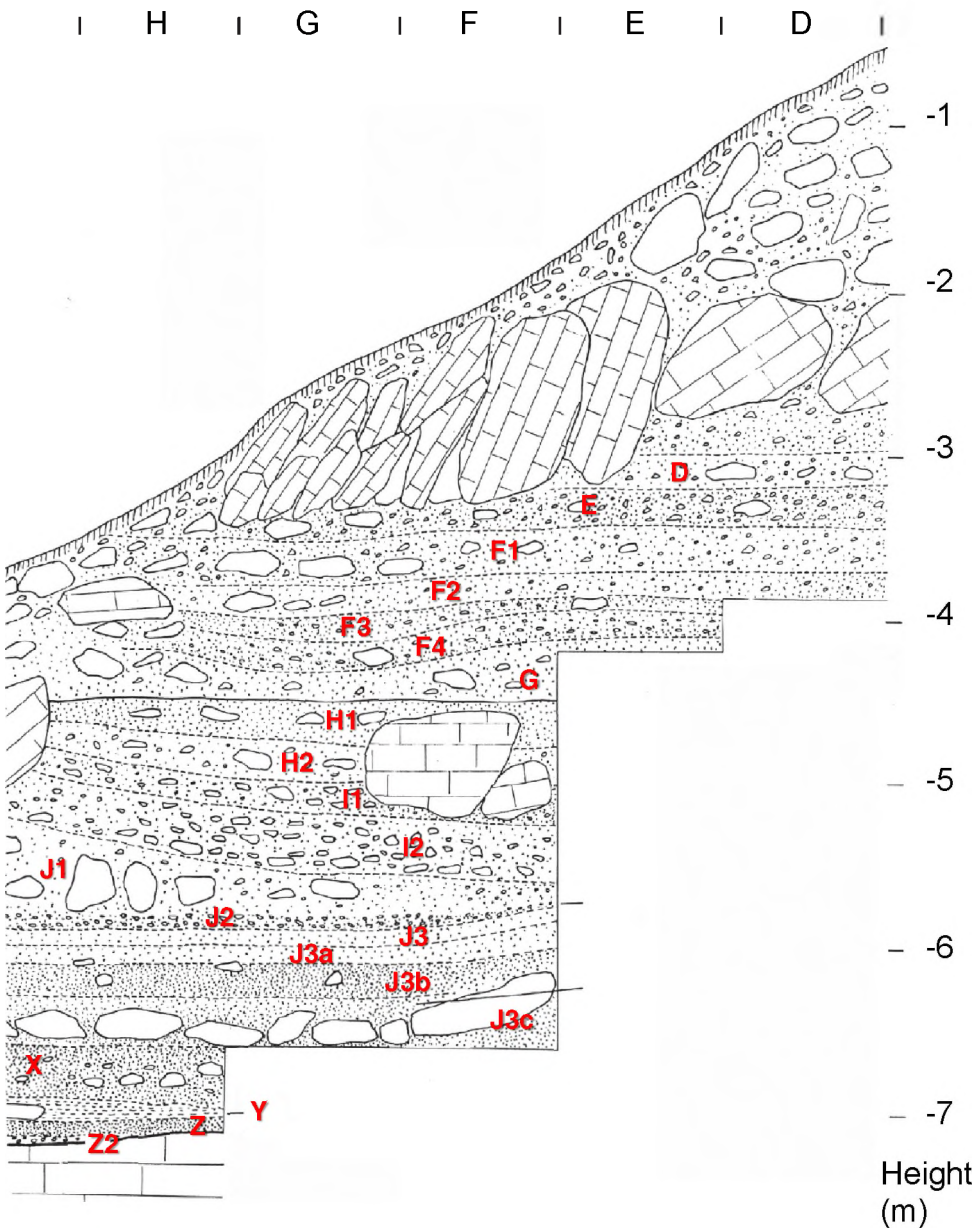

Figure 2.2.1. Stratigraphic framework of Pech IV as determined by Bordes. Modified from Turq et al. (2011).

The stratigraphy of Pech IV was first described in a preliminary note by Bordes in 1975 (see Table 2.2.1). Bordes (1975) remarked that classification of sedimentary layers was particularly difficult due to the abundance of large limestone blocks (known by the French term *éboulis*), disrupting the stratigraphic succession. This

difficulty was further compounded by the lateral variations found in a number of excavated layers with distance from the northern wall. His proposed stratigraphy was comprised of 13 layers (A–J and X–Z) based on geological characteristics, with a number of layers further subdivided (Figure 2.2.1). These subdivisions were made according to changes in stone tool typology, while others were simply arbitrary (Bordes 1975, Turq *et al.* 2011). Prior to the advent of a number of modern dating techniques, the chronology of the site was based upon the correlation of the lithic and faunal assemblages with those of nearby Pech de l'Azé II. As such, Bordes (1978) tentatively classified the basal layers of Pech IV, from layer Z through to layer F, as being deposited between 87 to 54 thousand years (ka) ago.

At the time of Bordes death in 1981, the Pech IV assemblages were in various states of preservation and curation. The curated collection (consisting of numbered lithics and faunal remains along with several hundred bags of small finds), was housed at the Institut de Préhistoire et de Géologie du Quaternaire at the University of Bordeaux and remained largely incomplete until 1996 when McPherron & Dibble (2000) began their own investigations at Pech IV. They found roughly half the collection washed, labelled, organised and in good condition, while the remaining artefacts were at various stages in the curation process. One major issue with the collection was the degradation of labels, in some instances beyond recognition, making stratigraphic positioning of the artefacts difficult to determine. Also a number of drawers had been labelled incorrectly, and therefore, when plotted in 3-dimensions using computer software, they were placed in the wrong stratigraphic layer. Using the original field notebooks of Bordes, McPherron & Dibble (2000) were able to reassign the artefacts to their correct stratigraphic positions.

In their review of Bordes' original work at Pech IV, McPherron & Dibble (2000) remarked that a number of issues still required addressing before the Pech IV site could be put to rest. The first issue is one of sedimentology. Unfortunately, none of the sedimentological work carried out by H. Laville at Pech IV was published, except for that presented in Bordes' preliminary note of 1975. Therefore, questions pertaining to stratigraphic integrity, palaeoclimatology and site formation were unable to be answered. The second issue is related to the proposed stratigraphy for

Table 2.2.1. Comparison of the stratigraphic framework set out by Bordes (1975) and Turq *et al.* (2011). Also shown are the probable MIS, the current radiometric ages presented in Dibble *et al.* (2009) and Turq et al. (2011), Mousterian Industry variant and sedimentology of each layer. Industry abbreviations are Typical Mousterian (MT), Asinipodian (AP), Quina (MQ) and Mousterian of Acheulian Tradition (MTA)

Bordes stratigraphy 1975	MIS	Industry (Bordes 1975)	Stratigraphy (Turq *et al.* 2011)	Ages (ka)	Sedimentology
A to E	?		1		Part of modern soil profile. Dark brown, organic rich silty to sandy layers with rounded and dissolving limestone fragments.
F1	?	MTA-B	2		Spatially restricted unit of rounded pebbles, and limestone fragments in a sandy, silty matrix.
F2	3	MTA-B	3A	47 – 56 (ESR) 44 – 45 cal BP (^{14}C)	Red/yellow silty-sand with limestone fragments more compacted and less cemented than underlying layer 4. Limestone fragments are rounded and appear to be dissolved.
F3		MTA-A/B			
F4		MTA-A	3B	44 – 56 (ESR) ~50 BP. (^{14}C) 50 ± 3 (TL)	Red/yellow silty-sand with limestone fragments more compacted and less cemented than underlying layer 4. Limestone fragments are rounded and appear to be dissolved.
G		MT	4A		Red/yellow silty-sand with limestone fragments. Strongly cemented with calcite in some regions produced a breccia.
H1/H2		MQ			
I1	4	MT	4B		Red/yellow silty-sand with greater concentration of limestone fragments than the overlying 4A layer.
rock shelter roof collapse					Limestone slabs and blocks
I2	4	MT	4C	70 ± 5 (TL)	Silty-sand with higher concentrations of small eroded limestone fragments and bone fragments.
J1	5a	MT	5A	74 ± 5 (TL)	Red/yellow silty-sand with angular limestone blocks
J2		MT	5B		Red/yellow silty-sand with limestone fragments, some of which are well-rounded.
J3A		AP	6A	71 ± 4 (TL)	Dark brown to red/yellow silty-sand with large block of limestone occurring in the upper portion
J3B		AP			
J3C		AP	6B		Silty-sand with varying sizes of limestone blocks
vault collapse					Limestone slabs and blocks
X top	5b	MT	7		Thin layer of coarse sand with edge damaged stone tools.
X base	5c	MT	8	96 ± 5 (TL)	Black, bedded clayey-sand with major organic anthropogenic component. Charcoal and ash lenses with burnt and unburnt bone fragments.
Y		MT			
Z		MT			

the site. Bordes excavated Pech IV in a period when the importance of site formation processes was not fully appreciated. Thus, the excavation design and the demarcation of strata may be the result of subjective, rather than objective, decisions. Evidence of post-depositional reworking of sediments may have also been overlooked. The final concern expressed by McPherron & Dibble (2000) is that of absolute chronology.

Although tentative correlations between layers in Pech IV with those from Pech de l'Azé I and II (Bordes 1978), no absolute dating of the site had been undertaken.

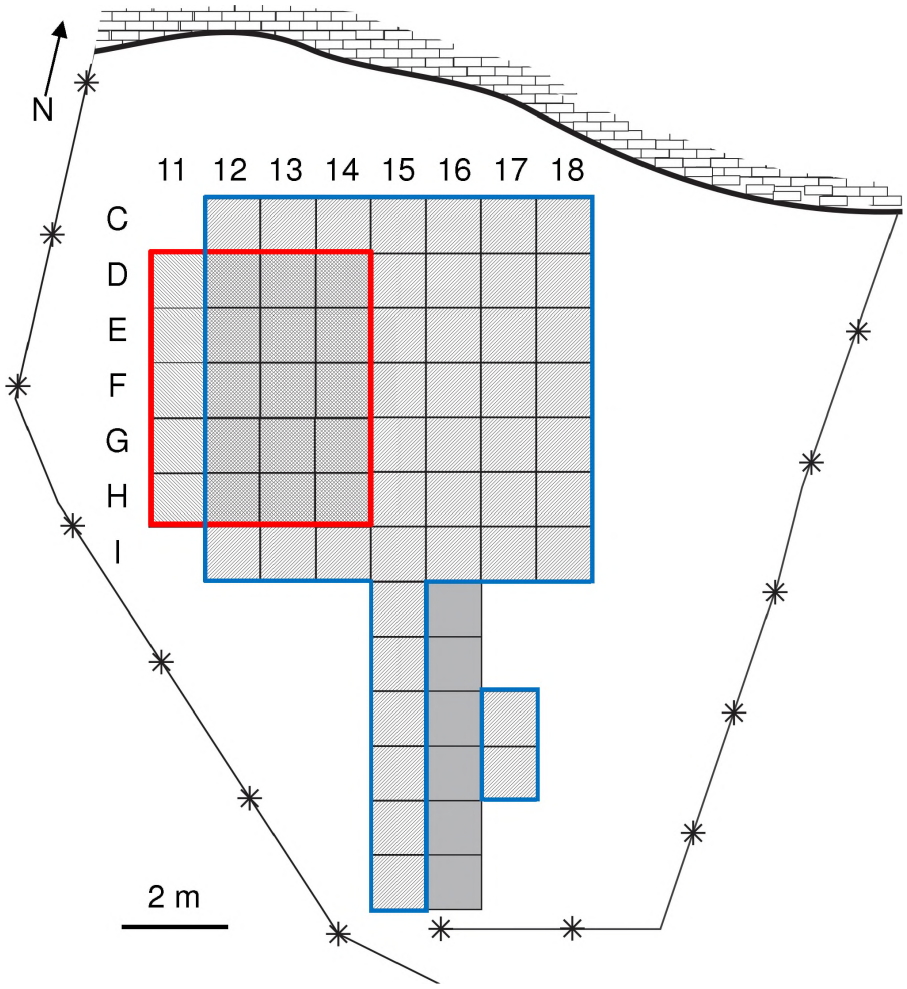

Figure 2.2.2. Site map of the Pech IV excavations. Red outline indicates squares excavated by Dibble and McPherron from 2000 and 2003. Blue outline indicates area excavated by Bordes. Remaining area excavated trench by Mortureux during the 1950s.

Without an absolute chronology, the progression of lithic industries could not be compared with other similar archaeological sites or with palaeoclimatic records. To resolve these issues, Pech IV was reopened for four field seasons (2000–2003), headed by Harold Dibble of the University of Pennsylvania. The results of their

investigations addressing these three issues of stratigraphy, site formation and chronology are presented below.

2.2.2 REVISION OF PECH IV STRATIGRAPHY

The initial revision of the original Bordes (1975) litho- and archaeo-stratigraphy of Pech IV was presented in Dibble *et al.* (2009) following the end of their work at the Pech IV site. The site map presented in Figure 2.2.2 shows the regions of the original Bordes excavation as well as the area excavated by Dibble and others during the 2000–2003 field seasons. The Dibble *et al.* (2009) paper was mainly concerned with the sediments at the base of the deposit and gave no detail regarding the remaining units. A complete and detailed review of the new stratigraphic framework (including both litho- and archaeostratigraphy) was not published until 2011 by Turq and colleagues (Turq *et al.* 2011). The development of the new stratigraphy employed a number of modern excavation techniques (Dibble *et al.* 2007, McPherron & Dibble 2007). Like Bordes (1975), the stratigraphic classification presented in Dibble *et al.* (2009) has delimited distinct packages of sediments, some of which have been further subdivided according to sedimentology. This new stratigraphic framework will be used throughout this thesis and will now be reviewed in stratigraphic order (Figure 2.2.3). Table 2.2.1 compares the Bordes (1975) and Dibble *et al.* (2009) stratigraphy and also provides information on the associated Mousterian Industry, chronology, climatology and sedimentology.

Unit 8 correlates to Bordes' levels Z, Y and the base of X (Figure 2.2.3). The unit is composed of clayey-sand with little limestone and a major organic component (Goldberg *et al.* 2012). It is typically dark brown to black in colour, with some regions more grey or red than others. The organic component, derived from anthropogenic burning at the site, is comprised of hearth features containing fragments of burnt and unburnt bone, charcoal and ash (Turq *et al.* 2011). It is, therefore, not surprising that ~20% of all lithic tools recovered from this unit show evidence of heating. The hearth features are present as thin, laterally continuous, lenses of ash, occasionally associated with underlying charcoal material. However,

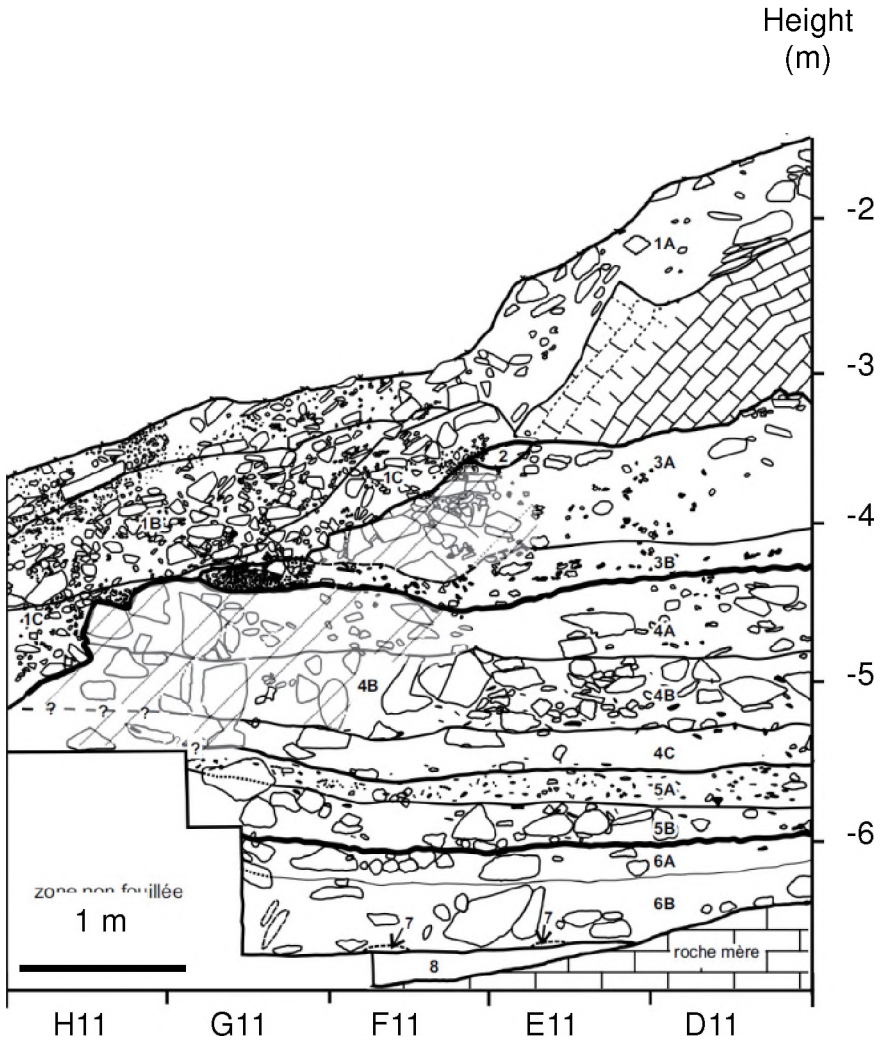

Figure 2.2.3. Stratigraphic framework for Pech IV western wall following the recent excavations (From Turq *et al.* 2011)

this lenticular morphology makes it difficult to distinguish from one another, even at a microscopic level. Micromorphological analysis of thin sections revealed that *in situ* hearth features are rare. Those preserved hearths are typically compacted and laminated bands of cemented ash and charcoal, with few rhombohedral crystals of calcite - a pseudomorph after calcium oxalate found in plant material (Turq *et al.* 2011, Goldberg *et al.* 2012). More commonly, ashes appear as chaotically-orientated angular fragments or disseminated calcite crystals mixed with other hearth materials.

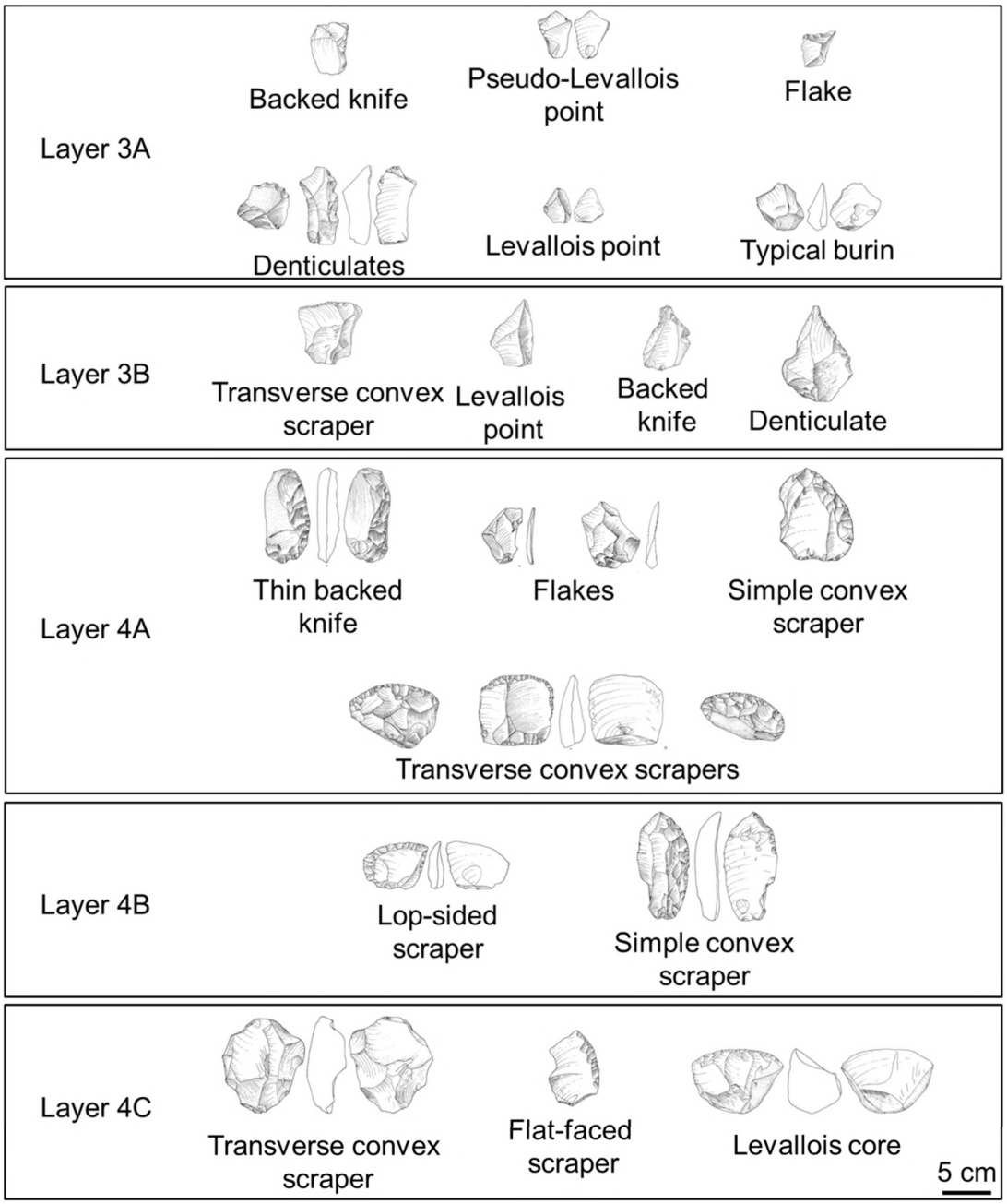

Figure 2.2.4a. A selection of Mousterian stone tools recovered from Layers 3A to 4C of Pech IV during the recent excavations. All images use the same scale in the bottom right hand corner of figures. Modified from Turq *et al.* (2011).

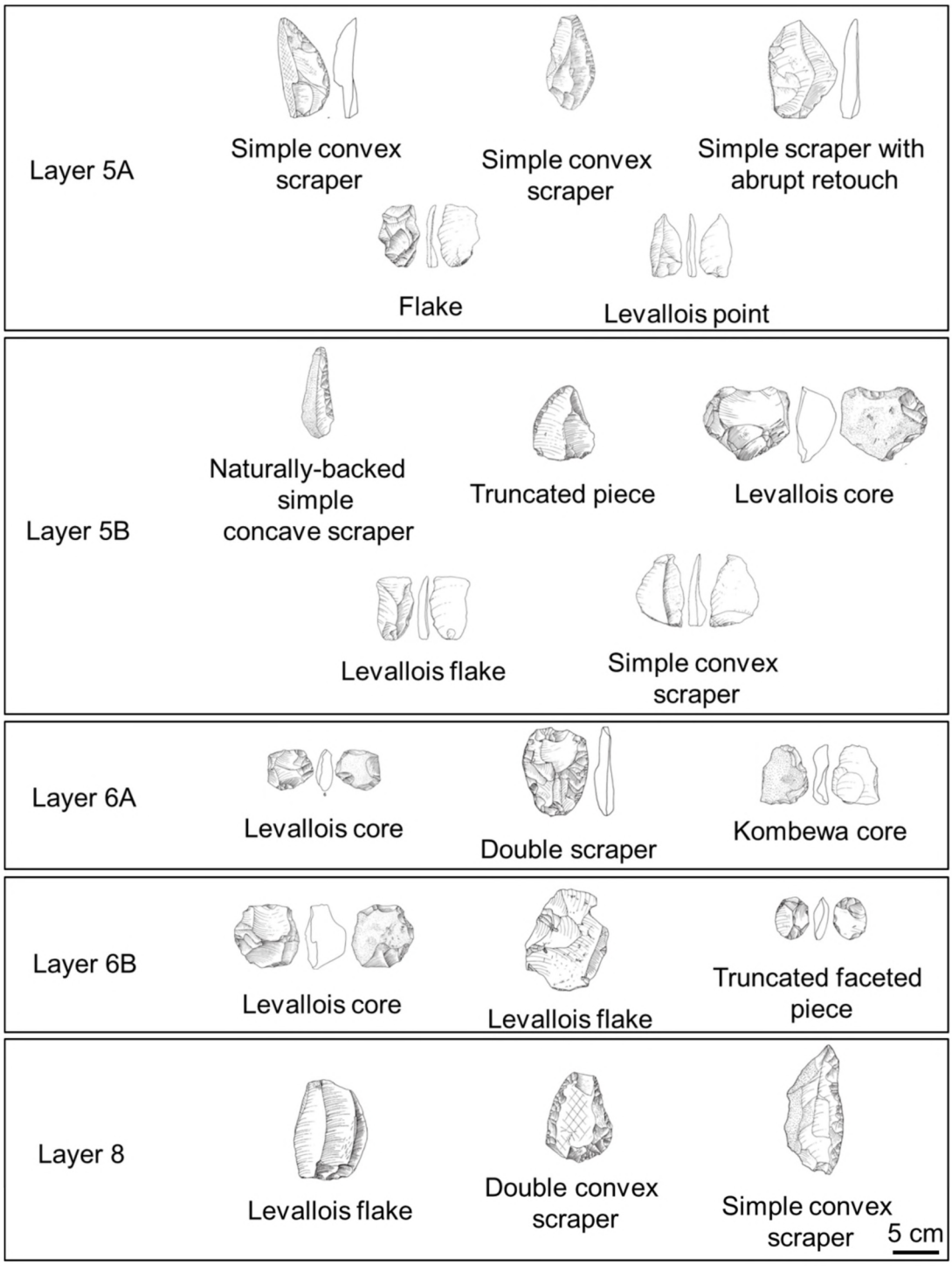

Figure 2.2.4b. A selection of Mousterian stone tools recovered from Layers 5A to 8 of Pech IV during the recent excavations. All images use the same scale in the bottom right hand corner of Figures. Modified from Turq *et al.* (2011).

In terms of archaeology, Unit 8 was classified by Bordes (1975) as belonging to a Typical Mousterian (MT) facies, a classification supported by Turq *et al.* (2011). The lithic tools are dominated by linear and convex scrapers (Figure 2.2.4b); however, the total percentage of tools present within this layer is the lowest for the site (7%). Interestingly, Unit 8 also had the highest amount of tools produced using 'exotic' material, ~14% as opposed to the average of ~4%, and the second highest blank-to-core ratio (~32%) (Turq *et al.* 2011).

Unit 7 is present in the western section of Pech IV as small pockets between roof fall blocks, and corresponds to the upper part of level X (Bordes 1975). Although containing less organic matter and fine fraction than the underlying Unit 8, the anthropogenic sediment is similar in composition (i.e., burnt and raw bone fragments, flints, ashes, charcoal, etc). The coarse sediment fraction is composed of coarse sands and edge-damaged lithic tools. Although Unit 7 produced the highest number and volume of stone tools for the site during the recent excavations, Turq *et al.* (2011) state that the damage sustained by the vast majority of tools recovered from this unit makes drawing robust conclusions difficult. As such, they do not classify the Unit 7 assemblage into any Mousterian Industry type.

Unit 6 has been subdivided into two layers, 6A and 6B, based upon the relative amount of limestone within each layer (Figure 2.2.3). Layer 6B, corresponding to layer J3c of Bordes' (1975) classification, is composed of large limestone slabs resting on top of Unit 7. These limestone slabs are generally 20–30 cm thick and up to 120 cm long. The void space between each slab is filled with loose and friable sands, hosting a similar anthropogenic component as described for the underlying units. The colour of this layer grades from grey at the base to red/yellow at the top. Layer 6A, equivalent to Bordes' (1975) layers J3a and J3b, is compositionally similar to that of 6B, apart from the paucity of large limestone slabs, and is red/yellow to dark brown in colour. The presence of burnt bone and small pieces of charcoal found throughout both this layer and 6B suggest that anthropogenic activities still occurred at the site. The upper part of this layer contains a number of large limestone blocks.

The lithic tool assemblage of Unit 6 was thought by Bordes (1975) to represent an entirely new Mousterian facies, termed the Asinipodian. The Asinipodian, a Latin translation of Pech de l'Azé (or Donkey Hill in English), is similar in composition to a Denticulate Mousterian (MD) facies, with the percentage of notches and denticulates greater than scrapers(Figure 2.2.4b) (Bordes 1975, McPherron & Dibble 2000). Unlike a MD industry, however, this unit is also rich in truncated-faceted pieces, Kombewa cores and flakes, and very small Levallois flakes (Figure 2.2.4b). The assemblage also revealed a low percentage of utilised flakes, and low blank-to-core and tool-to-flake ratios (Turq *et al.* 2011).

The contact between Unit 6 and Unit 5 is sharp and irregular, suggesting a significant break in sedimentation according to Turq *et al.* (2011). Unit 5 is also subdivided into 2 layers, 5A and 5B (Figure 2.2.3). The basal part of Layer 5B contains coarse sand and well-rounded limestone pebbles, and correlated to the J2 layer of the original stratigraphy (Bordes 1975). The sediments are dominated by red/yellow silts and sands that thicken to the south/southwest where they onlap onto several large limestone boulders. The degree of rounding and abrasion of the lithic tools is more apparent at the front of the site. The sediments in Layer 5A are indistinguishable from those of 5B except for the relatively scarce limestone blocks. Those blocks that are present protrude through the Unit 5/4 boundary. The lithic industry of Unit 5 returns to that of MT (Figure 2.2.4b). The assemblage is moderately high in scrapers, a relatively low frequency of notches and denticulates, and a strong representation of Levallois tools (Bordes 1975, McPherron & Dibble 2000).

The Unit 4 complex (Figure 2.2.3), subdivided into 4A, 4B and 4C, is a package of sediments distinct from the underlying Unit 5. Correlated to layers G through to I2 of Bordes (1975), the sediments are more abundant in red-brown, silty-clays and locally are cemented with carbonates. The basal layer, 4C, is the least cemented, and contains abundant rounded and dissolving limestone pebbles. In contrast, Layers 4B and 4A show a higher incidence of cementation with stark lateral variation. The southern end of both layers has been strongly cemented into a breccia,

while the northern end remains relatively carbonate free. Layer 4B contains the most numerous limestone blocks, compared with the remaining 2 layers from Unit 4.

Although originally assigned to the MT by Bordes (1975), the lithic assemblage from the recent excavation of Unit 4 has led Turq *et al.* (2011) to reassign it to Mousterian of Quina type (MQ) (Figure 2.2.4a). Using modern excavation techniques, Turq *et al.* (2011) were able to isolate and recognise a lense of Quina Industry in layer 4A previously overlooked by Bordes (1975). Layer 4 is relatively poor in lithics, with the tools dominated by end scrapers and having a moderate Levallois component. The flakes recovered from this layer are the largest in dimension at Pech IV (McPherron & Dibble 2000, Turq *et al.* 2011).

The Unit 4 deposits are truncated by a sharp erosional contact, separating Unit 4 from Unit 3. Unlike the underlying units, Unit 3 is the most heavily weathered. Again separated into 2 layers, 3A and 3B (Figure 2.2.3), the overall appearance is sandy due to the dissolution of the limestone rubble. Layer 3B and 3A, equate to layer F4 and layers F2 and F3, respectively (Bordes 1975). Both layers are red and show the same lateral variation in carbonate content as the underlying Unit 4. The archaeological materials are concentrated in Layer 3B. Unit 3 is the last unit of the Pech IV site containing *in situ* Mousterian-aged archaeological material.

Bordes (1975) assigned this Unit to the Mousterian of Acheulian Tradition (MTA) which grades from Type A at the base to Type B at the top (Figure 2.2.4a). However, according to Turq *et al.* (2011), this unit is not easy to assign to any particular Mousterian industry facies. Although the number of Upper Palaeolithic tool types, such as chisels and backed knives are higher than in any other layer, the number of bifacial tools is poor. Additionally, this increase in atypical and typical backed knives is not followed by an increase in blade technologies. The remainder of the assemblage is dominated by notches and denticulates, with a high representation of pseudo-Levallois products and has a low proportion of scrapers. Turq *et al.* (2011) to assign this unit to the MTA-A, albeit one poor in bifaces.

Unit 2 is present only as a small isolated pocket of material. From the witness section along the western section of the Pech IV, Unit 2 represents a cut and fill feature (Figure 2.2.3). Corresponding to Bordes' F1, Unit 2 is composed of limestone fragments and sediments with similar composition and colour to those of Unit 3.

The remaining layers of Bordes' stratigraphy, layers A through to E, have been assigned to Unit 1 in the stratigraphy presented in Turq *et al.* (2011). Following a large hiatus in deposition, Unit 1 is comprised of organic-rich sandy-silts of dark brown colour and dates to Medieval and younger periods (Figure 2.2.3).

2.2.3 SITE FORMATION PROCESSES

2.2.3.1 ORIGIN OF SEDIMENTS

The sediments of Pech IV are comprised of both anthropogenic and geogenic materials. The majority of the coarse fraction (i.e., sand, pebbles, cobbles, etc), which make up the deposit, is derived from the weathering of the host limestone (Goldberg *et al.* 2012). This geogenic coarse fraction, however, is accompanied by fragments of burnt and raw bones, charcoal and ashes originating from anthropogenic activities (Turq *et al.* 2011).

The fine fraction (silts and clays), is also geogenic, but their origin of which is not known. Two models for their presence at the Pech IV site have been proposed in Turq *et al.* (2011). The first is that the fine fraction is derived from the weathering of mineral grains into clays (e.g., feldspars, glauconite, etc found in the host limestone). The second model proposes that the fine fraction is derived from the 'sidérolithique' soil profile mantling the top of the host limestone. This model posits that water percolating through the soil entrains the fine clay particles that are then transported through the karstic network of joints in the host limestone before being deposited into the site as part of the cave infilling process.

2.2.3.2 SEQUENCE OF SITE FORMATION

From the literature, it is possible to classify the formation of the Pech IV archaeological site into 4 broad phases. These phases relate to the morphology of the host limestone (Figure 2.2.5) and are as follows.

Phase 1

Phase 1 corresponds to the development of the karstic tube as part of the phreatic system during the pre-Quaternary (Figure 2.2.5a). Similar to the formation of the karstic tube that separates Pech de l'Azé I and II (Texier 2009), the tube at Pech IV is suggested to have formed as a result of groundwater percolation through joint spaces within the host limestone. Turq *et al.* (2011) point out that the Pech IV tube is almost certainly a continuation of the karstic system associated with that at Pech de l'Azé I and II, based upon the strike and dip of the tube, along with the proximity of the sites. At some latter point, the cliff line retreated, exposing parts of the tube to the valley below.

Phase 2

Phase 2 begins with the exposure of the karstic tube and the initial infilling of sediments (Figure 2.2.5b). At this point in time the morphology of the site is more like that of a cave system (Goldberg *et al.* 2012), rather than a rockshelter as suggested by Bordes (1975).

Unit 8 represents a period of intense anthropogenic activity in the cave. Numerous hearth features, clustered towards the south-eastern end closer to the cave mouth, show that the cave was used for an extended period of time. It is also apparent that the occupants had built their fireplaces directly on top of the cave floor, as some sections of floor show tell-tale rubification and cracking associated with heating. Micromorphological analyses of thin sections show that some hearth features remain *in situ*, while others have been mixed with surrounding sediments. The ashes of *in situ* hearths have been locally cemented and generally display

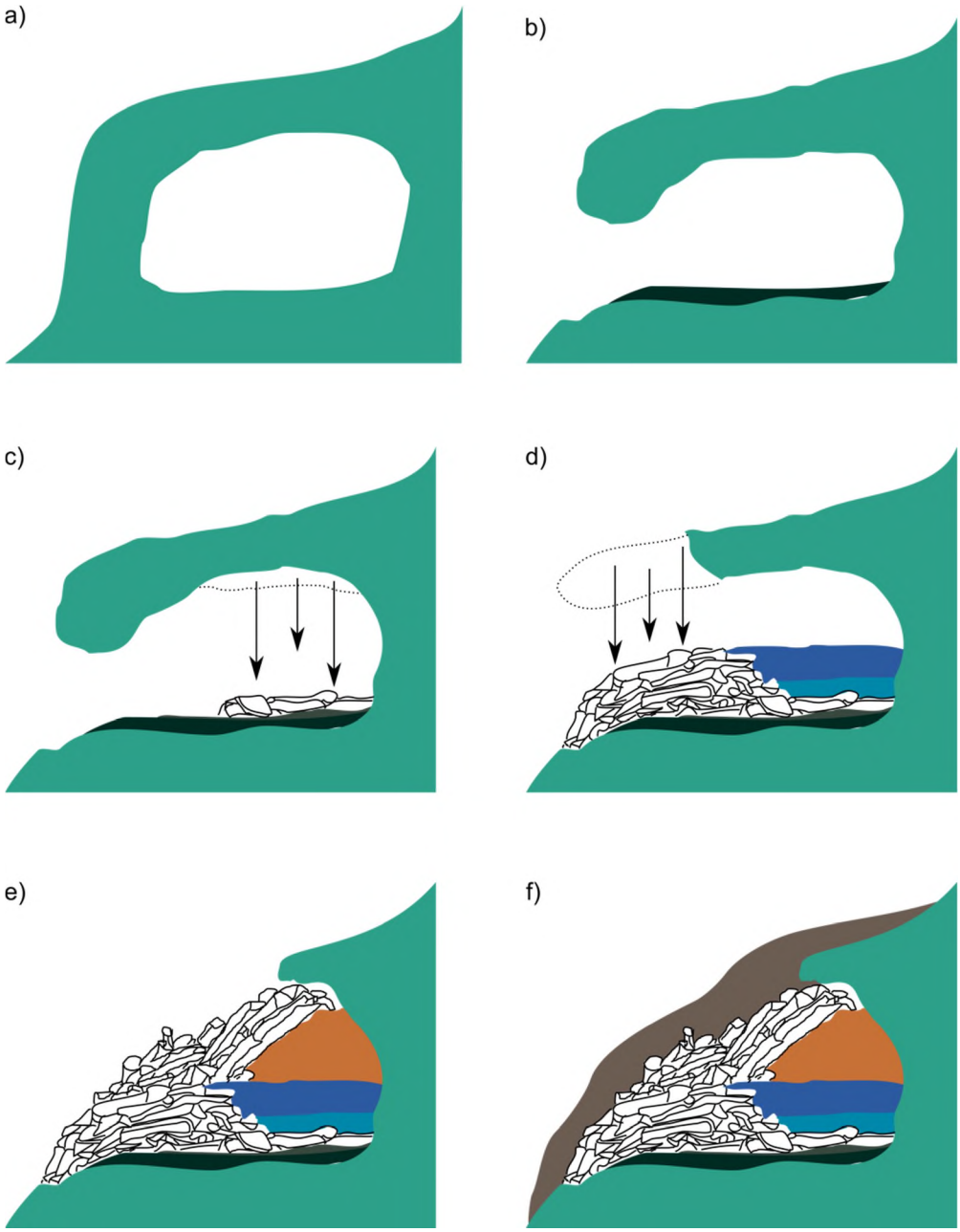

Figure 2.2.5. Sequence of Pech IV site formation based on Figures provided by P. Goldberg. a) Phase 1 – kartic tube development; b) Phase 2 – cliff retreat cuts into karstic tube allowing sediments from beyond the cave to begin infilling; c) Phase 2 – cave vault collapse prior to deposition of Layer 6B; d) Phase 3 – cave awning collapse after the deposition of Layer 5A changing morphology of the site from cave to rock shelter; e) Phase 4 – complete collapse of limestone ceiling preventing further occupation; and f) Phase 4 – colluvial sediments cover and preserve cave/rock shelter sequence.

accommodating fracture planes, infilled by fine clays and micritic calcite. These fracture patterns are suggested to be the result of trampling by the site occupants. Further evidence of trampling has also been noted in a number of burnt bone fragments. The hearths that have been disturbed are regarded by Turq *et al.* (2011) as the product of domestic rake-out and cleaning of hearth space. Some of the hearth ash has dissolved and reprecipitated as secondary calcite in the void space at the base of Unit 8, giving it a grey colour.

Unit 7 represents a thin, possibly cryoturbated, lobe of sediment that then has been deformed by the subsequent rockfall. The chaotic orientation of both the artefacts and limestone fragments found within this unit makes the determination of the direction of movement of these sediments difficult. It remains uncertain if the sediments were flowing out of the cave or *vice-versa*. However the former is more likely given the dip of the deposit (i.e., towards the southwest and towards where the original cave mouth is considered to have been situated, away from the bedrock cliff and supposed interior of the cave).

Layer 6B marks the first major collapse of the cave ceiling (Figure 2.2.5c). The large fallen limestone slabs created a pavement over the underlying sediments, acting as a physical and chemical barrier, preserving Units 8 and 7 from further trampling and carbonate dissolution (Turq *et al.* 2011). The collapse of the ceiling resulted in a more open configuration of the cave and a possible enhancement of the lighting conditions. The non-calcareous sands within Layers 6A and 6B are most probably the result of cave infilling (Goldberg *et al.* 2012). The uppermost section of layer 6A contains a number of large limestone blocks indicative of continued ceiling collapse. Anthropogenic activities, such as burning, continue in the Unit 6 layers. However, preservation is much poorer than in the underlying units, as the primary carbonates have dissolved, leaving only small pieces of charcoal and burnt artefacts, tools and bones, as suggestive evidence of their presence (Turq *et al.* 2011).

The contact between Units 6 and 5 is thought to be an unconformity surface. Bordes (1975) tentatively described this contact as the result of cryoturbation on the basis of the contact's geometry, sharp and irregular. However, the lag deposit of

rounded pebbles and lithic tools within the sandy gravel matrix at the base of layer 5B, have led Turq *et al.*(2011) to suggest that this contact was produced as a result of water reworking sediments in the cave.

The formation of Unit 5 is thought by Turq *et al.* (2011) to be the result of cryoturbation processes. Layer 5B is believed to represent a lobe of sediments that have slowly migrated towards to cave mouth from the interior of the cave. The lateral thickening towards the south/southwest, accompanied with the chaotic orientations of well-rounded pebble and severely abraded lithic tools, suggests that this layer is the result of periglacial processes, in particular solifluction (Bordes 1975, Turq *et al.* 2011). Interestingly, the micromorphology of this unit does not provide any evidence to this end, with no solifluction structures evident within the thin sections.

Phase 3

Phase 3 commenced with the collapse of the cave ceiling centred over the cave mouth (Figure 2.2.5d). This event resulted in the enlargement of the cave aperture, dramatically changing the morphology of the site from a poorly-illuminated and sheltered cave to something more akin to a rock shelter (Turq *et al.* 2011).

The Unit 4 complex and Unit 3 show a distinct change in their sedimentology compared with the underlying units. Not only does the fine fraction of the sediments increase (i.e., the silt and clay content) but the carbonate content also varies with distance from the north wall of the deposit. This lateral variability in the carbonate content of these sediments has been explained by Turq *et al.* (2011) to be the result of water running off the rock shelter brow. Over time, the carbonate-rich water falling from the awning onto the sediments directly below results in the formation of a hard, strongly-cemented breccia. The retreat of the rock shelter can be traced by following this cementation, and the associated roof fall blocks, from the southern limits of the site northwards. Layer 4B, in particular, was a major awning collapse event, with an abundance of large limestone blocks found within this layer.

The contact between Units 4 and 3 is sharp and irregular, similar to that of the Unit 5/6 boundary. This is believed to be the result of cryoturbation truncating the

lower layer 4A. Correspondingly, the angular pebbles found overlying this contact are considered to be an agglomeration of heavily weathered and redeposited cryoturbated material (Turq *et al.* 2011).

The boundary between 3B and 3A shows a cut-and-fill feature similar to the boundary delimiting layer 3A from Unit 2. Turq *et al.* (2011) suggest that this type of feature is, again, the result of the relative position of the rock shelter awning. Water running off the awning, cuts into the underlying deposit, creating a gutter that becomes filled with large pebbles and material from the surrounding sedimentary unit. Turq *et al.* (2011) suggest that this process is solely responsible for the formation of Unit 2.

Phase 4

The final phase of site development, Phase 4, occurs after the deposition of Unit 2, with the complete collapse of the rock shelter awning (Figure 2.2.5e). This event effectively sealed off and preserved the Pech IV site and its archaeological sequence. Thus, the Unit 1 complex is the result of colluvial processes (Figure 2.2.5f), with sediments migrating slowly downhill, mantling the collapsed roof deposits of the site (Turq *et al.* 2011).

2.2.4 CHRONOLOGICAL FRAMEWORK

The timing of the archaeological sequence at Pech IV represents one of the better temporally-constrained sites in the region. Bordes (1975) originally used the sedimentology and the faunal successions from Pech IV to assign certain layers to regional climatic phases by comparison to other sites in the Perigord region of France (e.g., Pech de l'Azé I and II and Combe-Grenal). This method of providing relative ages, however, is no longer appropriate given the range of modern absolute dating techniques now available.

One of the key focusses of the Dibble-lead excavations was to carry out absolute dating at Pech IV to accurately place the sequence preserved here into a

regional chronostratigraphic framework. At present, three independent dating techniques have been used at Pech IV, these include: 1) TL dating of burnt flints, 2) ESR dating of fossil teeth,; and 3) radiocarbon dating of bone. The ages obtained from each of these three methods are shown in Figure 2.2.6.

In their preliminary report focussing on Unit 8, Dibble *et al.* (2009) presented TL ages for a number of burnt flints. In total, 5 burnt flints were dated giving a spread of ages between 108 ± 12 ka and 92 ± 9 ka, and weighted mean of 100 ± 5 ka. Continued work on burnt flints in Unit 8 has refined the weighted mean TL age of Unit 8 to 96 ± 5 ka (Richter *et al.* 2013). Further TL ages are presented for Layer 6A (71 ± 4 ka; Goldberg *et al.* 2012), Layer 5A (88 ± 10 to 69 ± 6 ka, Richter *et al.* 2013), Layer 4C (72 ± 7 to 69 ± 7 ka; Richter *et al.* 2013) and Layer 3B (55 ± 5 to 46 ± 4 ka; Richter *et al.* 2013).

A number of ESR ages for fossil teeth collected from Unit 3 have also been produced (Turq *et al.* 2011). In total, three teeth were collected from Unit 3 (2 from Layer 3A and 1 from 3B). Based on early- (EU) and linear-uptake (LU) models , weighted mean ages of 49 ± 2 ka (EU) and 50 ± 2 ka (LU) for Layer 3A, and 50 ± 3 ka (EU) and 52 ± 5 ka (LU) for Layer 3B were determined. Turq *et al.* (2011), consequently, assigned an age range of 47–57 ka to Unit 3.

Radiocarbon ages of bone material have also been used to date the age of Unit 3. Of the 10 ages produced, only seven were considered to be reliable, citing low collagen as reasons for the rejection of the remaining three samples (McPherron *et al.* 2012). Bayesian age distribution modelling carried out by McPherron *et al.* (2012), determined that the beginning of sedimentation of Unit 3 began at ~50.6 ka B.P. (uncalibrated) to 44.5 ka calibrated B.P., agreeing well with the ESR and TL ages also obtained from teeth and burnt flints found in these layers.

From these chronological investigations, age estimates for six of the 11 layers of sediment preserved at Pech IV have been determined. Perhaps the most important outcome of these investigations is that the likely range in the age profile of the site can be assessed. Thus, the deposit at Pech IV began to accumulate at ~95 ka ago with

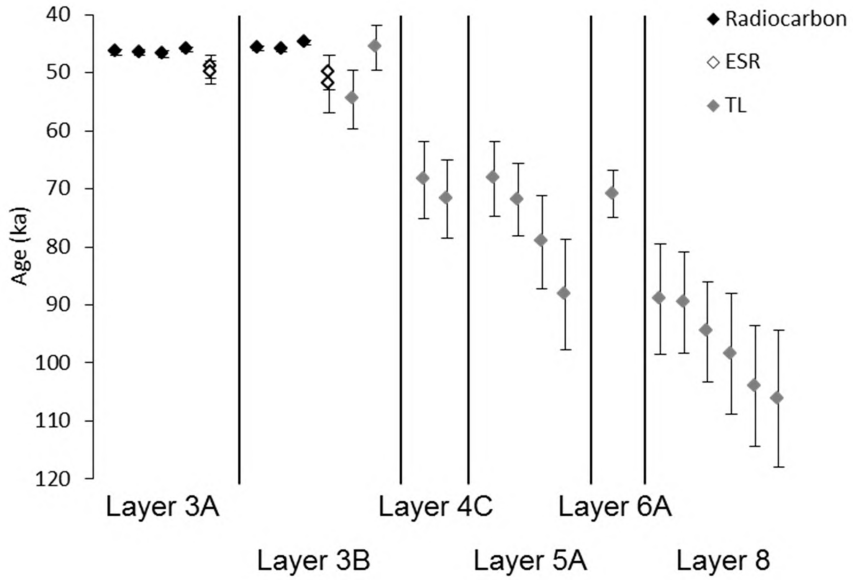

Figure 2.2.6. Previously published radiometric ages for Pech IV. Of the 11 Mousterian layers preserved at Pech IV, only 6 have so far been examined using either ^{14}C, ESR or TL on burnt flints.

the deposition of Unit 8 and culminated with the deposition of Unit 3 at ~45 ka. However, our understanding of the age profile between these two end points is relatively limited because of the paucity of datable materials. Furthermore, the methods used thus far rely upon the recovery of specific material upon which to date, require calibration or assumptions to be made based upon the uptake and leaching of uranium. Furthermore, without a complete understanding the Pech IV age profile, the sequence of Mousterian Industries cannot be resolved in time. Therefore, the use of single-grain OSL dating of sand-sized grains of quartz provides an opportunity to systematically date each layer of Pech IV due to the ubiquitous presence of this mineral.

2.2.5 MOUSTERIAN MAKERS: THE IMPORTANCE OF THE PECH IV SEQUENCE

The Pech IV site contains a long and stratigraphically-controlled sequence of many different Mousterian stone tool industry variants. The variability in the Mousterian industry has long been the subject of debate (Bordes 1961, Binford 1962, 1965, Binford & Binford 1966, Mellars 1970, Bordes 1978, Rolland & Dibble 1990, Mellars 1996, Richter *et al.* 2013) with a number of models proposed to explain this variation. Bordes (1961) suggests that the contemporaneous differences in ethnicity and cultural tradition were responsible for the observed variability. On the other hand, Binford (1962) viewed the Mousterian variability as reflecting the differences in the functional 'tool kits' used for different activities carried out by different portions of internally-divided cultural groups at the same time. Alternatively, Mellars (1970) considered the variation in Mousterian Industries to represent cultural evolution over time. In each of these models, the importance of the temporal constraints provides one way of assessing their relative applicability.

The current chronology for Pech IV is incomplete (Figure 2.2.6) and a function of the dating methods used (^{14}C, ESR and TL). Each of these methods of age determination requires that specific material be present in the deposit, and, for ^{14}C dating only, that the deposit is no older than ~45–50 ka. As such, where these specific materials are absent, temporal 'gaps' in the chronology of the site, and by extension Mousterian industries exist. Richter *et al.* (2013) concluded from their TL investigation of Pech IV that the Mellars (1970) model of cultural evolution was not supported, despite a number of chronological 'gaps.' One way to fill these temporal 'gaps' is through the use of single-grain OSL dating, which has remained largely unexplored in this region of France. The applicability of the OSL method to sediments in the Périgord region, therefore, remains to be assessed.

SECTION SUMMARY

The archaeological assemblage recovered from Pech IV shows a distinct succession of Mousterian stone tool industries; in stratigraphic order Typical Mousterian, Asinipodian, Typical Mousterian, Quina and Mousterian of Archeulian Tradition. The recent excavations have provided a wealth of information about the processes of site formation, the origin of the sediments (derived from the same source lithology) and a chronological framework that provides boundary ages of between ~95 to ~45 ka for the archaeological deposits at Pech IV. It is considered that the use of single-grain OSL dating on ubiquitous quartz grains can provide a complete and robust age scaffold for the site onto which the various Mousterian Industries can be placed, thereby allowing comparison with other sites in the region

Chapter 3

OSL dating

This section will introduce the method of OSL dating of quartz and the underlying conduction band theory. The total environmental dose rate is, first, reviewed. Along with an outline of the major contributing radiation types, I also outline the methods used in the measurement of the environmental dose rate in this thesis. I then look at the methods and equipment used in the measurement of the D_e of the sand-sized grains of quartz using the single aliquot regenerative–dose (SAR) procedure. I also describe the rejection criteria used to screen the data to ensure that the D_e values used in the final age determination are meaningful. Particular attention is paid to a discussion of the variability and spread within D_e datasets obtained for a single sample both in terms of intrinsic and extrinsic factors. I then review the age models used to combine the individual D_e values to obtain a reliable estimate of the burial dose for the sample which is then used in the OSL age equation. Finally, I outline the steps taken in the calculation of an OSL age using the D_e and total environmental dose rate.

3.1 TESTING TIME: BASIC NOTIONS OF THE OSL DATING METHOD

3.1.1 THE OSL DATING METHOD: AN OVERVIEW

Optically stimulated luminescence (OSL) dating provides an estimate of the amount of time elapsed since the mineral grains were last exposed to sunlight or heat (Huntley *et al.* 1985, Aitken 1998). This method has been widely applied throughout the field of Quaternary science to answer both geological and archaeological questions. This increase is driven by the fact that the material used for age determination is the sediments themselves.

Mineral grains of quartz and feldspar are typically utilised for OSL dating and act as a natural dosimeter. These grains begin to accumulate an electron charge once it has been deposited and is no longer exposed to sunlight or elevated temperatures. This electron charge (known as the burial dose) increases as a result of exposure to ionising radiation and cosmic rays. The ionising radiation is the result of the decay of ^{235}U, ^{238}U, ^{232}Th and ^{40}K (and their radioactive daughters, apart from ^{40}K) found in the surrounding sediment matrix. The rate at which the burial dose increases is dictated by the rate at which the ionising radiation is delivered. The total amount of radiation delivered to the mineral grains is termed the environmental dose rate.

When the irradiated-minerals are exposed to sunlight, the burial dose is evicted from the light-sensitive electron traps. These evicted electrons are emitted as photons of light (luminescence) through a process of radiative recombination at luminescence centres. Thus, the event being dated using the OSL method is the last time the grains were exposed to natural sunlight and subsequently buried. The method, therefore, presupposes that, prior to the last burial period, the signal held within the minerals grains was completely zeroed, or 'bleached,' via sunlight exposure.

To determine the burial age of the naturally-irradiated minerals requires a measurement of the amount of charge present within the grains as well as the environmental dose rate. The luminescence signal is measured from the naturally-irradiated mineral to determine the 'natural' luminescence signal. For regenerative procedure, the mineral then receives a series of laboratory irradiations, of various sizes, to determine the amount of laboratory radiation that gives a luminescence signal that is 'equivalent' to that of the natural signal. This is termed the equivalent dose and is abbreviated to D_e. It should be noted that laboratory irradiations are usually of one type (e.g., beta or gamma) rather than a combination of alpha, beta, gamma and cosmic radiation and orders of magnitude higher than natural systems. The regenerative dose process is elaborated upon in Section 3.2. An estimate of the dose rate can be determined in a number of ways that are outlined in Section 3.4.

If both the D_e, measured in Gray (Gy; where 1 Gy is equal to the absorption of 1 joule of energy per 1 kg of matter), and the dose rate (measured in Gy/ka) are known, then the age of the sediment (in thousands of years; ka) can be determined using the following (much simplified) equation:

$$Age \text{ estimate } (ka) = \frac{D_e\ (Gy)}{Total\ dose\ rate\ (Gy/ka)} \qquad \text{equation 2.1}$$

It should be appreciated, however, that in order of a dozen measurements are required to calculate the age estimate, not just the two stated above. This

3.1.2 PHYSICAL BASIS OF OSL DATING

The physical basis for the luminescence dating methods derives from the energy band theory of solids (Aitken 1985, Bailey *et al.* 1997, Aitken 1998, Bailey 2001). A schematic of the energy band model is shown in Figure 3.1. In the crystalline lattice of a quartz grain, atoms are arranged periodically in three dimensions, within which electrons can only occupy discrete ranges of energy bands (Aitken 1985). A forbidden zone separates the lowest energy band, known as the valence band, and the next highest energy band, termed the conduction band. The crystal lattice, constructed from interconnected SiO_4 tetrahedra (Figure 3.1a), is

rarely perfect and contains defects as a result of missing or replaced atoms and/or distortion of the lattice itself. For example, the SiO_4 may have Si or O vacancies within the tetrahedron structure (Figure 3.1b) or contains substitutions of impurities including Al, Fe, P, Ti, etc (Figure 3.1.b) (Preusser *et al.* 2009). Some of these defects allow the capture of electron charge within the forbidden zone, and are commonly referred to as 'traps' (Aitken 1985, 1998).

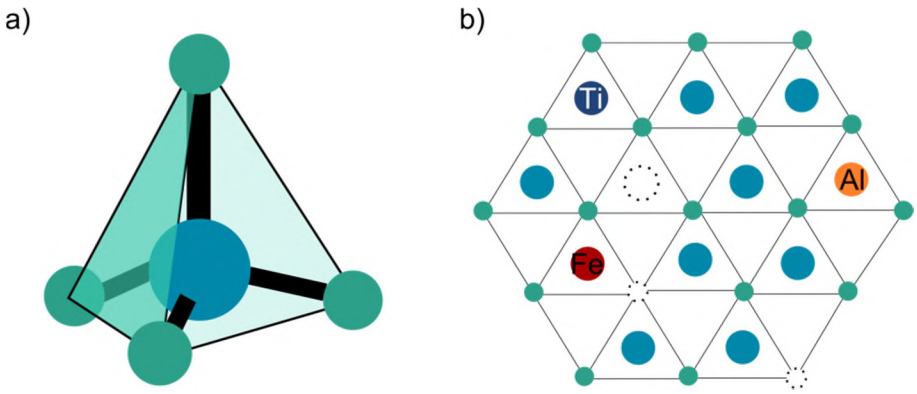

Figure 3.1. a) Stylised silicate tetrahedron comprising of four oxygen atoms (green) surrounding a larger Si atom (blue) at the centre. The crystalline lattice of quartz is composed of interconnected tetrahedron covalently bonded at each apex, as shown in b). Here, a heavily simplified single crystalline plane is shown, as well as the possible vacancies (dashed outlines) of Si and O atoms and also the atomic substitutions that can occur. For example, in three positions, the Si atom has been substituted by Ti (dark blue), Al (orange) and Fe (red) atoms.

During burial, the crystal lattice of the quartz grain is bombarded with ionising radiation. The radiation provides enough energy to elevate electrons from the valence band to the conduction band leaving behind 'holes', or electron vacancies (Figure 3.2) (Aitken 1985, 1998). Once the electron reaches the conduction band it can either return to the valence band directly, or become trapped within the defects in the forbidden zone. If an electron hole becomes trapped within the forbidden zone it can act as a recombination centre.

For electrons to be useful for OSL dating, they are required to be captured in sufficiently deep traps. Capture of the electrons, or their associated holes, into 'shallow' traps is likely to result in their eviction through the natural vibration of the crystal lattice over the age span of the sample (Aitken, 1998). Once lodged within a sufficiently deep trap, heating and/or light exposure is required to elevate the electrons back into the conduction band.

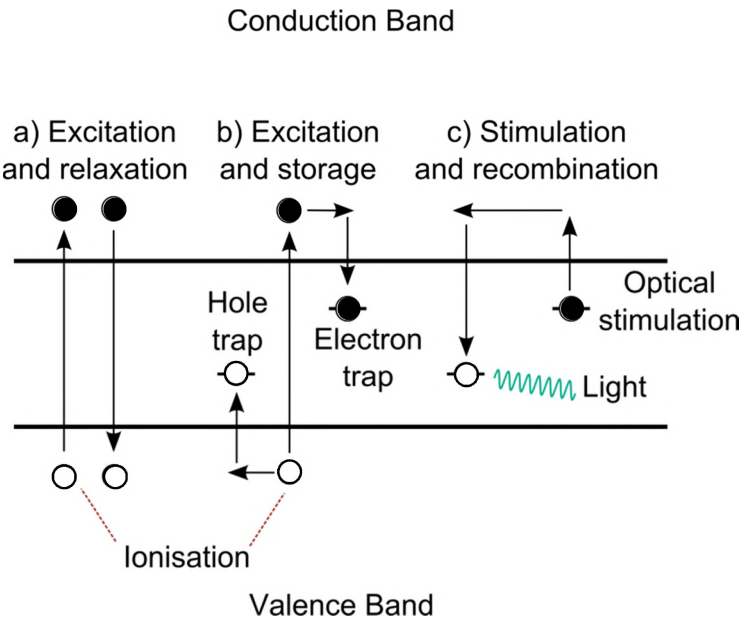

Figure 3.2. Energy band diagram for OSL production based on Figure 3.2 in Aitken (1985). Following irradiation, a) electrons (filled circles) can be excited into the conduction band and return directly to their original position, or b) electrons and holes (open circles) can be generated and become trapped within defects in the forbidden zone. c) Following optical stimulation, the electrons are elevated back into the conduction band, where they can recombine within trapped holes with the potential of producing a photon of light.

During optical or heat stimulation, the electrons are elevated back into the conduction band and are free to diffuse around the crystal until a recombination centre is encountered. Luminescence occurs if recombination results in the dissipation of excess energy by emitting photons of light (Aitken, 1985, 1998). As

such, the amount of luminescence is proportional to the amount of electrons trapped within crystal defects and, hence, the amount of radiation energy absorbed over the period of burial (Aitken 1998).

Subsequent research has considered that, beyond the luminescence recombination centre, there are a number of different recombination centre types that can be found within natural dosimeter minerals. Such recombination centres include 'reservoir' and 'killer' recombination centres. These centres compete for the same electron charge that becomes diffused into the conduction band during stimulation but do not produce a photon emission upon recombination. Rather, these recombination centres release the excess energy as heat.

The luminescence signal of a quartz grain that is stimulated using a constant power results in an OSL decay curve. If only one type of light-sensitive trap were in existence the decay curve would follow a first order rate of decay. Smith & Rhodes (1994), however, were able to explain the OSL decay curve for an aliquot of quartz from Chaperon Rouge, Morocco, as having three components: a fast, medium and slow, based on their respective rate of decay. Thus, they posited that more than one 'type' of trap was responsible for their OSL decay curve. This finding was supported by the work of Bailey *et al.* (1997) using quartz grains from the same location. This is further discussed in Section 3.2.5.1.2.

The proportion of the various OSL components is of importance to the accurate determination of burial ages for sediments. The fast component is of most importance, as it is this component that is used in the single-aliquot regenerative-dose (SAR) procedure that determines the burial age of the sediments. The SAR procedure and the various OSL decay components are further discussed in Section 3.2.4.

3.2 D_e DETERMINATION, MEASUREMENT AND EQUIPMENT

3.2.1 MEASURING D_e: THE RISØ TL/OSL READER

All OSL measurements carried out in this thesis where made on one of two automated Risø TL/OSL readers; Risø 3 is a DA-15 model, whereas Risø 5 is a DA-20 model. Both readers were fitted with single-grain laser attachments (Figure 3.3). Both single-aliquot and single-grain measurements were conducted. For single-grain measurements, individual sand-sized grains of quartz were loaded into specifically designed aluminium discs measuring 9.7 mm in diameter (Bøtter-Jensen *et al.* 2000). Each disc holds 100 single grains of ~200 μm in diameter in separate chambers 300 μm in diameter and 300 μm in depth (Figure 3.3d). The centres of each hole are spaced 600 μm apart and are arranged in a 10 by 10 grid (Bøtter-Jensen *et al.* 2003, Duller 2004). Three larger 500 μm locating holes are positioned on the periphery of the disc in order to determine the orientation of the disc in the Risø reader. The individual quartz grains were loaded into the aluminium discs by pouring the grains over the disc and brushing them into the holes. The discs were then checked under a binocular microscope to ensure that only one grain was in each hole.

For single-aliquot measurements, grains were placed onto stainless steel discs and held in position using an amount of silicon spray oil ('Silkospray'). The silkospray was applied by first placing a stainless steel mask over the top of the discs. These masks have had apertures of varying sizes (e.g., 0.5, 1, 2 and 5 mm diameter holes) drilled into them. The size of the aliquots is then named after the size of the mask aperture (i.e., aliquots made using a 5 mm mask size would be termed a 5 mm aliquot). With the mask in place, an even coating of silkospray is applied. Grains of the chosen size range are then deposited onto the discs as a monolayer and the disc checked under a binocular microscope to ensure that no 'stray' grains are found outside the mask-size area. The bottom of each disc is cleaned to ensure good thermal contact between the heater plate in the Risø reader and the aliquot. This

cleaning was also carried out for the single-grain discs. The discs (either stainless steel or single-grain) were placed onto a 48 position sample carousel, before being positioned inside the Risø automated reader. To reduce the impact of cross-talk, i.e. the percentage dose given to an adjacent non-irradiated disc (Bray *et al.* 2002, Duller 2012a), each sample was separated by one vacant carousel position.

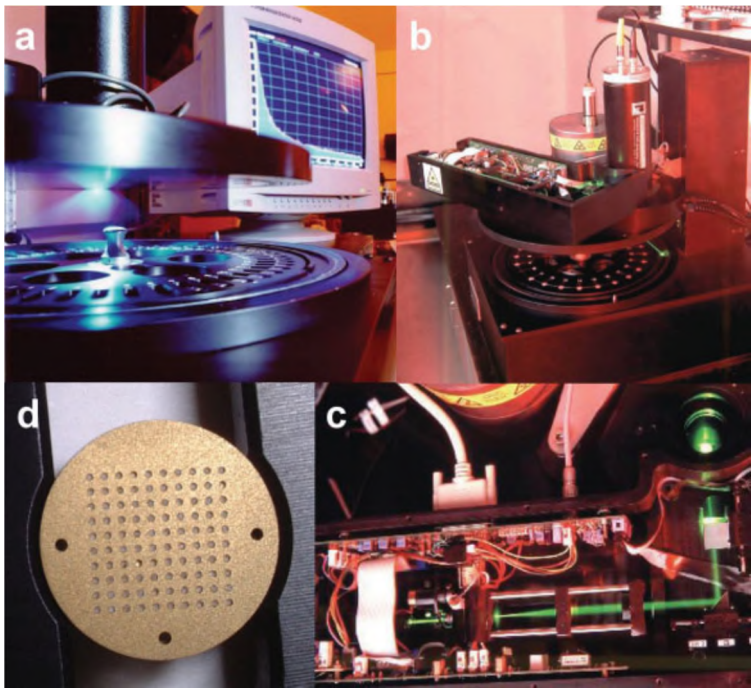

Figure 3.3. Image from Jacobs & Roberts (2007) showing typical set up of a Risø TL/OSL reader with single-grain attachment. a) automated Risø TL/OSL reader with only blue LEDs for optical stimulation. b) another Risø TL/OSL reader fitted with a single-grain laser attachment for single-grain measurement. c) close-up of the internal components within the single-grain attachment showing the three mirrors that focus the green laser. d) typical single-grain aluminium disc.

Laboratory irradiation for all samples, including dose recovery tests, was carried out using a calibrated $^{90}Sr/^{90}Y$ beta-irradiator attachment. The beta dose rate for one of the two Risø readers was ~6.6 Gy/min, whereas the second machine had a beta dose rate of ~7.6 Gy/min. The calibration was carried out using multiple sub-samples of gamma-irradiated calibration quartz and revealed that the spatial

distribution of the beta source was inhomogeneous in all readers used. Thus, the single-grain OSL D_e values were corrected for this beta dose spatial heterogeneity using the methods outlined in Ballarini *et al.* (2006).

Optical stimulation of the samples was achieved using either blue light emitting diodes (LED) (for single aliquots) or a focused green laser beam (for single grains). The blue LEDs (~470 ± 30 nm) are arranged into 4 groups of seven diodes and can deliver a power density of 50 mW/cm^2 when measurements are made at 100% power (Bøtter-Jensen *et al.* 2000, Bøtter-Jensen *et al.* 2003). The single-grain attachments houses a 10 mW 532 nm (green) Nd:YVO4 solid-state diode-pumped laser that is focused onto a spot ~20 μm in diameter delivering a power density of ~50 W/cm^2 at full power (Bøtter-Jensen *et al.* 2000, Bøtter-Jensen *et al.* 2003). This green laser beam can be steered with a precision of ~3 μm using two mirrors. The subsequent luminescence signal was then measured using a bi-alkali EMI 9635Q photomultiplier tube (PMT). The PMT detects individual photons given off during electron charge recombination in the crystal lattice using a photosensitive cathode mounted inside a vacuum tube inside the PMT. However, in order to discriminate the stimulation light source form the quartz luminescence signal two U-340 filters were fitted in front of the PMT. The U-340 filters block the passage of the green and blue stimulation wavelengths but permit the passage of the ultraviolet (UV; 270–370 nm) emissions (Spooner & Questiaux 2000).

3.2.2 THE POWER OF ONE: THE BENEFITS OF USING THE SINGLE-GRAIN METHOD

The single–grain OSL method using the single-grain discs outlined above differs from the previously used multi-grain single-aliquot method in a number of respects. Rather than measuring the OSL signal from a number of grains (~5 to >100), the single-grain method, as the name suggests, involves measuring the OSL signal from individual sand-sized grains (Murray & Roberts 1997, Roberts *et al.* 1999, Duller & Murray 2000, Bateman *et al.* 2007a, Lowick *et al.* 2010, Duller

2012b). The last decade has seen an increase in the use of OSL dating as a powerful tool in determining burial ages for sediments in geological and archaeological contexts. This expansion of the technique is due to advances in both the technology (single-grain laser system) (Bøtter-Jensen *et al.* 2000, Bøtter-Jensen *et al.* 2003) and the single-aliquot regenerative dose procedure (see Section 3.2.4) (Murray & Wintle 2000) allowing rapid and systematic determination of D_e for individual sand-sized grains of quartz. This enables the measurement of many thousands of grains in a routine manner to obtain a statistically representative number of grains from which interpretations can be made.

The single-grain OSL method has a number of inherent benefits, which include; (1) the ability to assess the stratigraphic integrity of the site, (i.e. the degree of mixing within the deposit), (2) check the adequacy of the bleaching event prior to burial, and (3) reject grains with aberrant physical properties from the sample, allowing for a more accurate and precise age determination. A number of studies have shown that the inclusion of such aberrant grains increase the spread of data (i.e. overdispersion, discussed below), and as such produced under- or overestimates of the true burial dose (Roberts *et al.* 1999, Feathers 2003, Thomsen *et al.* 2005, Jacobs *et al.* 2006a, Jacobs *et al.* 2006c, Lomax *et al.* 2007, Galbraith & Roberts 2012).

3.2.3 THE SAR PROCEDURE, REJECTION CRITERIA AND RADIAL PLOTS

3.2.3.1 SINGLE ALIQUOT REGENERATIVE DOSE PROCEDURE

The SAR procedure currently used in the majority of OSL studies to measure D_e is based on that originally proposed by Murray & Wintle (2000). Rather than using the 110 °C TL peak to track sensitivity changes, Murray & Wintle (2000) took advantage of the linear relationship in the sensitisation of the 110 °C TL peak and OSL signal, as shown in both Stoneham & Stokes (1991) and Murray & Roberts (1998), thus, comparing a 'like' signal (i.e., OSL vs. OSL, rather than TL vs. OSL) for sensitivity correction. Numerous studies have revealed that accurate age estimates

can be obtained using the SAR procedure (Roberts *et al.* 1999, Turney *et al.* 2001, Banerjee *et al.* 2003, Jacobs *et al.* 2003a, Arnold *et al.* 2008, Fornós *et al.* 2009, Guérin *et al.* 2012a), providing that the necessary tests have been performed and that the measurement parameters used as part of the procedure are appropriate for the samples measured (Murray & Olley 2002).

The SAR procedure of Murray & Wintle (2000) entails making a number of OSL measurements (L_X and T_X; Figure 3.4) to construct a dose-response curve, from which the D_e can be determined by projecting the natural luminescence signal (L_N and T_N) onto the curve. The fundamental assumption of this procedure is that the OSL response to a small dose, termed the test dose (T_X), administered immediately after the L_N and L_X measurements, provides an appropriate measure of the sensitivity changes during measurement of the main L_X signal relating to a regeneration dose (R_X). The samples are preheated, following irradiation and prior to stimulation, to remove the charge accumulated within thermally unstable traps during laboratory irradiation that would otherwise be eroded away in the natural setting. Similarly, a further preheat is applied after the test dose for the same reason. Thus, a sensitivity-corrected OSL response (L_N/T_N or L_X/T_X) can be determined for the L_N and L_x intensities by dividing them by their associated T_N or T_X OSL responses.

Using the sensitivity-corrected OSL signals, a sensitivity-corrected dose-response curve can be constructed (Figure 3.4). A dose-response curve typically contains three or more R_X points. The R_X are given so as to bracket the expected D_e of the sample; however further measurements can be made if required. A 0 Gy dose is given to monitor for the thermal transfer of charge from light-insensitive into light-sensitive traps due to heating – termed recuperation. A repeated R_X of the same magnitude as the R_1 is given to ensure that the T_D is suitably monitoring and correcting for the sensitivity changes throughout the SAR procedure (Murray & Wintle 2003). Finally, an OSL infrared (IR)-depletion ratio check is conducted to distinguish between quartz and feldspar grains (Duller 2003). Here, prior to OSL measurement, the grains are typically stimulated for 40 s using IR diodes at 50 °C to deplete the OSL signal in any contaminant feldspar grains which are relatively more sensitive to IR-stimulation than quartz.

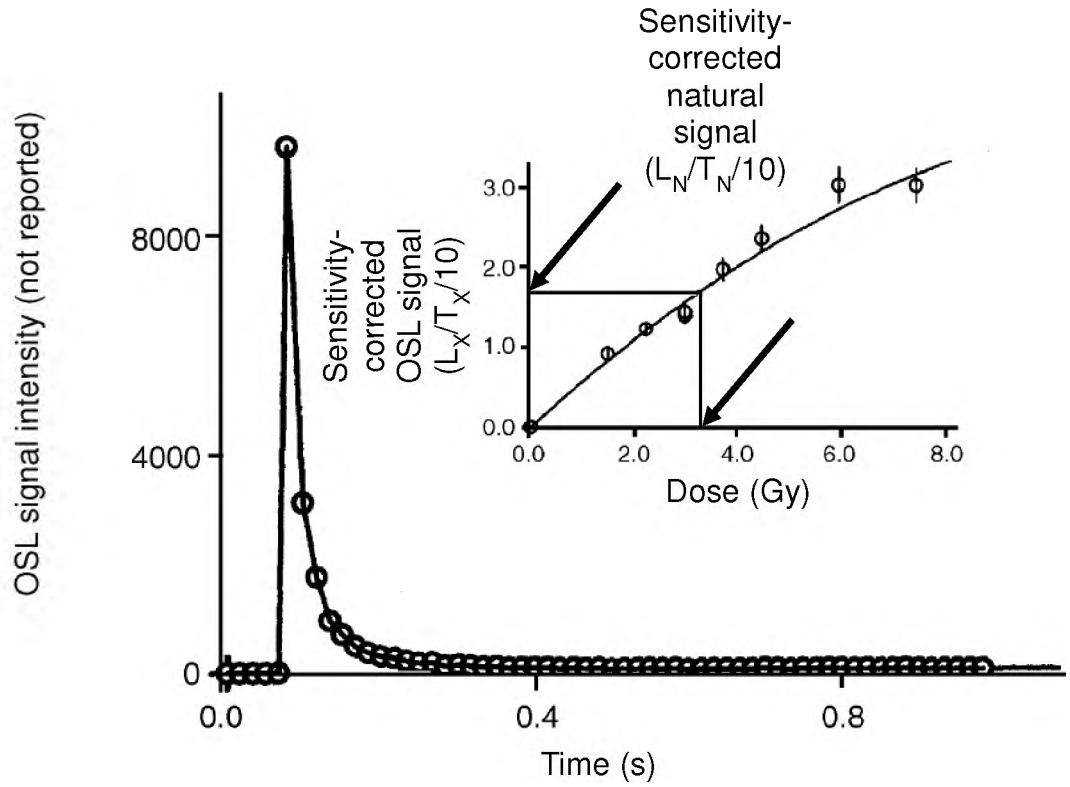

Figure 3.4. OSL decay curve for a single-grain of quartz (sample UW436) coming from a Pleistocene layer of Cactus Hill, Virginia, USA – published in Feathers *et al.* (2006). Also shown is the associated dose-response curve for the grain showing the sensitivity-corrected natural dose and 8 regenerative doses. The D_e for this grain can be determined by projecting the sensitivity-corrected natural dose onto the dose response curve and interpolating onto the dose (x) axis.

3.2.3.2 Rejection criteria

The tests incorporated into the SAR procedure are used to check the suitability of the individual quartz grains to the OSL method. Previous studies have documented the variability in the OSL signal of individual grains of quartz from the same sample and showed that not all grains are suitable for the SAR procedure due to underlying aberrant physical properties (Murray & Roberts 1997, Roberts *et al.* 1999, Henshilwood *et al.* 2002, Olley *et al.* 2004b, Thomsen *et al.* 2005, Feathers *et al.*

2006, Lian & Roberts 2006, Jacobs *et al.* 2006a, Arnold & Roberts 2011, Constantin *et al.* 2012, Guérin *et al.* 2012a). These 'poorly-behaved' grains of each sample are required to be removed as the D_e values they provide are, in effect, unreliable.

A set of objective rejection criteria are applied to the single-grain OSL D_e dataset based upon those presented by Jacobs *et al.* (2006c). Grains are considered unreliable, and are rejected, if: 1) the intensity of the T_N signal is shown to be less than three times that of its signal background; 2) the recycling ratio (RR; the ratio of the two identical R_X given at the start and end of each SAR procedure) is not consistent with unity at 2σ; 3) the OSL IR-depletion ratio (the ratio of the OSL signal produced by an additional identical dose following IR-stimulation) is smaller than unity by more than 2σ; 4) the L_X/T_X of a 0 Gy dose is >5% of its corresponding L_N/T_N OSL signal; 5) the L_N/T_N fails to intersect the dose-response curve; and 6) a meaningful dose-response curve could not be constructed. With respect to criterion 5, it is specifically assumed that the effect that causes these high first cycle D_e values does not lead to correspondingly low values which cannot be identified and rejected. Only those individual grains that pass these objective criteria are deemed 'meaningful' in terms of the D_e measured. A full account of these rejection criteria are outlined above is given in Appendix 1.

3.2.3.3 Error estimation

Dose response curves and D_e values can be calculated for each quartz grain using the Analyst software package (v.3.24). Typically, either a single saturating exponential curve or a single saturating exponential curve with a linear function is the most appropriate for OSL dose-response curves. Along with the D_e, the program also calculates the uncertainty associated with the D_e of each grain. The uncertainty consists of several components including:

Counting statistics – the uncertainty associated with the measurement of the L_X/T_X ratios is constrained by the intensity of the integrated OSL signal and the

magnitude of the associated background count. The error calculated following the equations outlined in Galbraith (2005) and (Duller 2007).

Instrumental reproducibility – a random 2% error is assigned for all samples and is based on experimental studies involving the repeated irradiation and measurement of the same sample (Jacobs *et al.* 2006a).

Curve fitting – after the errors of counting statistics and instrumental reproducibility are propagated, Monte Carlo simulations (Yoshida *et al.* 2003, Duller 2007) were used to determine the uncertainty on the curve fitting of the dose response curve. By using the Monte Carlo method (Yoshida *et al.* 2003), the dose-response curve is refitted repeatedly drawing the D_e from a Gaussian distribution whose width is set by the calculated standard deviation of the sensitivity-corrected regenerative dose points.

Spatially-resolved beta dose rate – for single grain studies, the spatial inhomogeneity of the beta source was determined using the procedure outlined in Ballarini *et al.* (2006). The uncertainty on calibration for each of the 100 single-grain disc positions was added in quadrature to the pre-existing signal, curve fitting and instrument reproducibility errors.

Beta source calibration– a systematic 3% error is added in quadrature to the final D_e value. This error is to account for the uncertainty in the calibration of the beta irradiator of each Risø reader.

3.2.3.4 RADIAL PLOTS

The use of radial plots, as described by Galbraith (1990), provides a means of visually evaluating the D_e distribution of samples in terms of its overall patterning and precision of the individual accepted D_e (Figure 3.5). A distinctive feature of the radial plot is that all D_e values lying along a radial line from the standardised estimate axis to the log D_e axis arc on the right hand side of the plot have the same

D_e (Galbraith 1990). Furthermore, a 95% confidence interval can be fitted to the plot, extending +2σ and -2σ from the standardised D_e estimate. Where these intervals cross the log dose axis, the 95% confidence interval can be read off (Galbraith *et al.* 1999). In addition, the precision associated with the D_e values can also be read from the radial plot. Relative precision arises from the inherent difference in the luminescence intensities between quartz grains (i.e., counting statistics) along with errors associated with variability in the fitted dose-response curve and instrument reproducibility (Duller 2007). Through the use of radial plots, the range of precisions can be easily observed as the imprecise grains fall to the left of the plot, whereas the higher precision grains fall towards the right, along the relative error axis at the base of the plot.

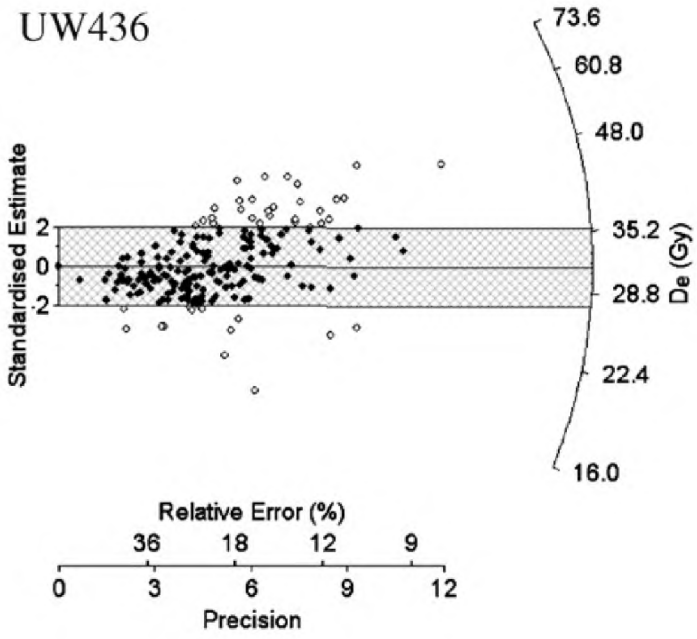

Figure 3.5. A radial plot for the sample UW436 from Cactus Hill, Virginia, USA – published in Feathers *et al.* (2006). If the D_e estimates in this distribution were statistically consistent (at 2σ) with a common value, then 95% of the points should fall within any grey band projecting ± 2σ from the standardised estimate axis on the left hand side. The D_e values of this sample are more dispersed than this. The 2σ grey band around the standardised estimate is centred on the weighted mean measured D_e value of 32 ± 1 Gy.

3.2.4 OVERDISPERSION IN SINGLE-GRAIN OSL DATING: A MEASURE BEYOND THE EXPECTED

The determination of the D_e for single-grains of naturally-irradiated quartz do not, for the most part, conform to the expectation that 95% of the data should fall between ± 2σ of the sample mean. Rather, the distribution of D_e values is often described as being overdispersed, i.e., having a spread that is greater than statistical expectation once all sources of known measurement uncertainty has been accounted for. For example, Olley *et al.* (2004b) have shown that, for a variety of geomorphic settings throughout the south-eastern corner of the Australian continent, the 'additional' spread can range from 1–85% for fluvial settings (n=6), 24–47% for aeolian environments (n=5) and 27% (n=1) for a marine setting. It is considered that this 'additional' spread, or overdispersion (OD), is the result of a combination of both intrinsic and extrinsic factors associated with the quartz grains being measured. This section we will first review the intrinsic variations in quartz grain behaviour; followed by our current understanding and methods used in the explanation for OD arising from extrinsic processes.

3.2.4.1 WE ARE ALL INDIVIDUALS: INTRINSIC VARIATIONS IN SINGLE-GRAIN OSL BEHAVIOURS

The production of a luminescence signal and its inherent intrinsic variability are inextricably linked. This inherent variability has been suggested to be, at least in part, the result of the geochemical conditions under which the quartz grains undergo crystallisation (Preusser *et al.* 2009). Depending on the processes involved (i.e., plutonic, hydrothermal, volcanic, etc) various amount of impurities are either incorporated into (as in the rapid cooling of volcanic quartz) or expelled from (during the slow cooling of plutonic rocks) the atomic structure of the quartz grains, resulting in the presence or absence of various luminescence-centres and differences in the absolute abundance of electron traps (Westaway 2010). Thus, the myriad of possible defect compositions (be they substitutions or vacancies within the quartz crystal

lattice) gives rise to a range of possible OSL behaviours and, as a result, intrinsic variability in the luminescence behaviour. This variability includes: grain brightness, the rate of OSL decay and the timing of the onset of dose saturation, amongst others. These three aspects of variability will be reviewed below.

3.2.4.1.1 Signal intensity

Signal intensity (or the brightness of individual grains) is an important intrinsic factor to consider when undertaking OSL dating studies. It is the brightness of the individual grains that dictates the precision of the determined D_e value and, by extension, the burial dose for the sample. However, not all grains are luminescent, with only a small proportion of the total number of grains producing an OSL signal (Roberts *et al.* 1998, Duller & Murray 2000, Jacobs *et al.* 2003b, Thomsen *et al.* 2005, Arnold & Roberts 2011, Thomsen *et al.* 2012, Duller 2012b). Duller *et al.*(2000) demonstrated that, by presenting a cumulative brightness plot, ~90% of the total light sum comes from ~5% of the grains for a number of samples presented. In contrast the WIDG8 sample from Australia falls closer to the 1:1 line, with more grains (40–50%) producing ~90% of the total luminescence (Duller *et al.* 2000). Jacobs *et al.*(2003b) found that ~90% of the total luminescence for their samples of South African quartz from Blombos Cave was produced by ~5% of the grians. An additional study at Blombos Cave by Jacobs *et al.* (2013) found that, on average ~4% of the grains measured could be classified as 'bright' – an arbitrary distinction made on the basis a grain having >1000 counts/0.2 s following a 12 Gy test dose. The remaining grains falling roughly equally between the 'moderate' (100–1000 counts/0.2 s) and 'dim' (<100 counts/0.2 s) categories.

An extension of intrinsic OSL signal intensity is that of OSL sensitivity. Whereas signal intensity is the total number of OSL counts over the period of optical stimulation, OSL sensitivity is the OSL intensity per unit dose. Thus, OSL sensitivity is the efficacy with which electron charge can be trafficked from storage in OSL traps through the conduction band and into recombination centres per unit dose (Gy). Even within an individual samples, the sensitivity of grains fluctuates dramatically

(Duller *et al.* 2000). Duller *et al.* (2000) also notes that those grains with the highest sensitivities provided more accurate estimate of laboratory-administered dose. It can be said, therefore, that as OSL sensitivity increases, the ability of the grain to produce a reliable measure of D_e also increases.

While the chemical composition plays a role in OSL sensitivity, it should be noted that the geological history of the sample has also been suggested to be important in the sensitisation of quartz grains. An increase in OSL sensitivity has also been associated with increasing number of cycles of burial, irradiation and transportation increase (Murray & Wintle 2000, Pietsch *et al.* 2008, Fitzsimmons *et al.* 2010). Pietsch *et al.* (2008) found that the sensitivity of quartz grains collected along the Castlereagh River in NSW, Australia, increased with increased distance from the head of the catchment. Furthermore, the sedimentary inputs here were all derived from the same source lithology. They also showed that the sensitisation process could be carried out in the laboratory, increasing the sensitivity of the grains ~2.5 times following 25 cycles of 2 Gy irradiation, preheating to 50 °C and blue LED stimulation for 100 s.

The signal intensity and sensitivity to radiation dose, therefore, is a result of both the crystalline composition of the quartz grains in combination with its geological history. Those grains that are highly sensitive, in general, appear to provide more accurate and precise estimate of the true radiation dose accrued during burial. This finding, however, may not be true under conditions of trap saturation.

3.2.4.1.2 Rate of OSL decay: OSL signal components

The decay of the OSL signal is the result of exponential exhaustion of trapped electrons from within the defects of the quartz crystal lattice. However, continued investigation into the OSL signal reveals this understanding to be an oversimplification of the processes involved, with numerous separate OSL components comprising the OSL signal.

Variations in quartz 'bleachability' were first posited by Smith & Rhodes (1994) and Bailey *et al.* (1997), both using quartz collected from Chaperon Rouge, Morocco. Using a constant light intensity, these authors were able to show that OSL decay curves could be explained by the sum of three decaying exponential components (Figure 3.6); termed the 'Fast', 'Medium' and 'Slow,' and had mean half-life values of ~2.45 s, 7.71 s and 788 s, respectively, using a halogen lamp with a power density of ~12 mW/cm^2. This led Bailey *et al.* (1997), and later Bailey (2001), to propose that the OSL signal coming from quartz is due to multiple electron trap types present in the quartz grains (Figure 3.2).

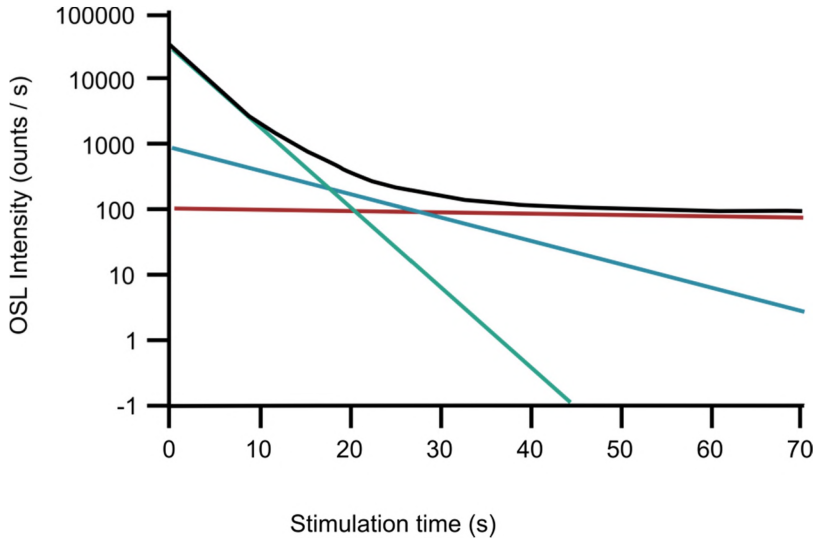

Figure 3.6. OSL decay curve (black) presented in Bailey *et al.* (1997) and the mathematically deconvoluted Fast (green), Medium (blue) and Slow (red) components.

The advent of linear-modulated OSL (LM-OSL) by Bulur (1996), built upon the concepts developed by Smith & Rhodes (1994). Bulur (1996) suggested rather than exposing the quartz grains to a constant photon flux (known as continuous-wave OSL; as was carried out by Bailey *et al.* (1997), that by linearly increasing the photon flux from 0 to some predetermined endpoint (usually 90% power output) over a period of time, a picture of OSL peaks, with respect to optical 'bleachability,' could

be drawn in a similar way that TL peaks were resolved with respect to heating rate. The LM-OSL method rests upon the understanding that the various traps responsible for OSL production have different photo-ionisation cross-sections (or PICs). These are equivalent to detrapping probability or signal 'bleachability' of Bailey *et al.* (1997). Thus, the PIC of the 'Fast' decaying component is larger than that of both the 'Medium' and 'Slow' components, requiring less energy to move the trapped electrons into the conduction band (Jain *et al.* 2003). The LM-OSL curve can then be deconvoluted into representative components using the equations presented in Bulur *et al.* (2000).

$$L(t) = Ab\frac{t}{P}e^{\left(-\frac{bt^2}{2P}\right)} \qquad \text{equation 2.3}$$

Where: A is equal to the amplitude and proportional to the trap population n_0, b is the detrapping probability (where b is equal to PIC (σ) multiplied by the maximum stimulation light intensity (I_0)) and P is the total stimulation period. Example of LM-OSL curves are shown in Figure 3.7, along with the deconvoluted signal components.

Component analysis of the OSL signal of quartz grains from globally distinct regions shows significant variations (Jain *et al.* 2003, Singarayer 2003, Singarayer & Bailey 2003, 2004, Choi *et al.* 2006, Jain *et al.* 2008). A comparison of the OSL signal component from a number of these studies is presented in Table 3.1. These variations are not only in the magnitude of the components, but also the number of components present and the sensitivities of each. Jain *et al.* (2003), in their investigation of single-aliquots of quartz from 12 different samples from Australia to Sweden, found that seven different components could be resolved from the LM-OSL signal: Ultrafast, Fast, Medium, Slow 1, Slow 2, Slow 3 and Slow 4. Furthermore, they showed that each of the samples investigated did not always have the full complement of components, with some (Denmark and Scotland) dominated entirely by the 'Slow' components. Jacobs *et al.* (2008c) found that a number of individual grains within their samples from South Africa were also dominated entirely by a slow component.

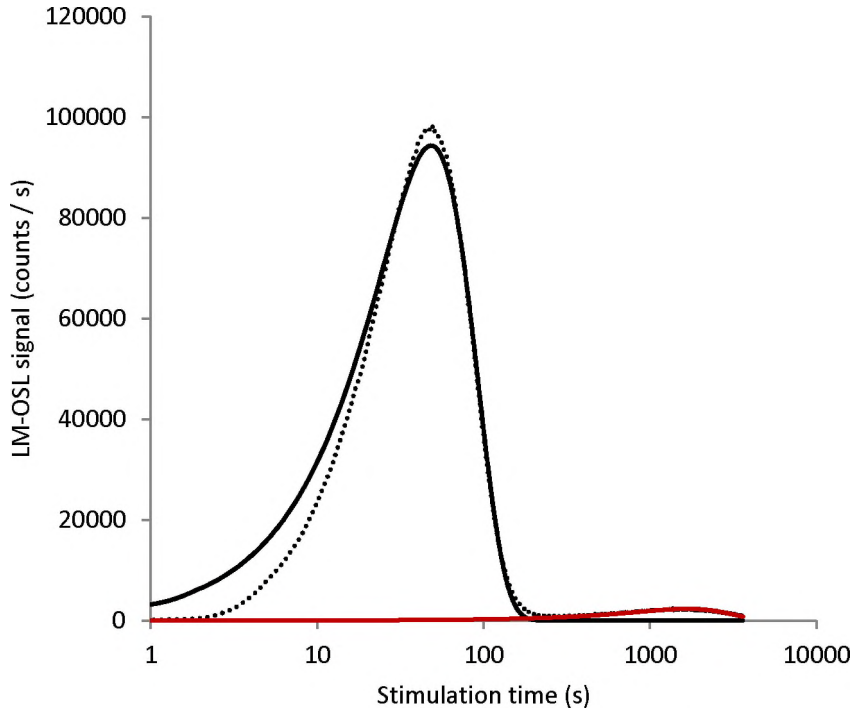

Figure 3.7. LM-OSL curve (dotted line) displayed on a semi-log scale. Also shown are the mathematically deconvoluted Fast (black) and Slow (red) components.

Perhaps most importantly, Jain *et al.* (2003) showed that each of these components sensitised (i.e., luminescence produced per unit dose increased) at different rates. The presence and absence of a component/s, the magnitude of each and the rate of sensitisation can be linked back to the intrinsic variability of the crystal lattice. This in turn affects the rate of OSL decay; the greater the proportion of Medium and Slow components, the longer it takes for the OSL signal to reach background levels. Furthermore, seeing as these components sensitise at different rates, it is possible that the rate of OSL decay can also change over successive SAR cycles.

Table 3.1. Table of LM-OSL resolved components presented in Jain *et al.* (2003) and Singarayer & Bailey (2003) showing PIC and Relative PIC values for each component and D0 values, where applicable.

Jain *et al.* (2003)			Singarayer & Bailey (2003)			
Component	PIC (cm^2)	Relative PIC	Component	PIC (cm^2)	Relative PIC	D_0 (Gy)
Ultrafast	2.9×10^{-16}	13	Ultrafast	7.0×10^{-15}	280	-
Fast	2.32×10^{-17}	1	Fast	2.5×10^{-17}	1	190
Medium	5.59×10^{-18}	0.2	Medium	5.9×10^{-18}	0.2	258
Slow 1	1.33×10^{-18}	0.06				
Slow 2	2.08×10^{-19}	0.01	S_1	2.1×10^{-19}	0.01	250
Slow 3	2.06×10^{-20}	0.001	S_2	1.2×10^{-20}	0.0005	28
Slow 4	2.76×10^{-21}	0.0001	S_3	1.9×10^{-21}	0.0001	850

3.2.4.1.3 *Dose response curve shape*

Variability in the dose response curve shape and the onset of dose saturation has been noted extensively in the OSL literature (Duller *et al.* 2000, Burbidge *et al.* 2006, Jacobs *et al.* 2008c, Lowick *et al.* 2010, Timar-Gabor *et al.* 2012, Demuro *et al.* 2013, Jacobs *et al.* 2013). In general, it is possible to fit either a single saturation exponential plus linear function to the dose response data using the following equation:

$$I = I_0 + I_{MAX}\left(1 - e^{-D/D_0}\right) + kD \qquad \text{equation 2.4}$$

Where: I is the sensitivity-corrected luminescence intensity, I_0 is the luminescence signal intensity at 0 Gy dose, I_{MAX} is the maximum luminescence intensity at signal saturation, k is a constant, D is dose (Gy), and D_0 is the characteristic saturation dose at which point the signal intensity has reached 63% (or 1- $1/e^1$) of its saturation intensity (Bøtter-Jensen *et al.* 2003). Occasionally, just a

saturating exponential function provides a better fit and can be found by dropping the linear term (*kD*) from the above equation.

Of particular interest are the differences present in the 'characteristic saturation dose' (D_0) value as this provides a measure for the onset of dose saturation. Murray and Wintle & Murray (2006) suggest that any measure of D_e that is $>2D_0$ ought to be treated with caution due to the likelihood of a large asymmetric uncertainty being produced as a result of a saturated dose response curve. Galbraith & Roberts (2012) argue, contrary to this advice, stating that these grains should not be rejected (out of hand) as they: 1) provide an useful lower bound estimate of the true value, and 2) provide evidence for the range of D_e values present within the population.

Good examples of why such D_es should not be rejected is given in the study of 'super-grains' by Yoshida *et al.* (2000) and OSL component work undertaken by Bailey *et al.* (1997). The former study found that significant variability exists in the rate of saturation between their class 1, 2 and 3 grains (although they do not report D_0 values). Their class 1 grains show continued growth in the OSL response beyond 300 Gy, whereas the remaining classes saturated at much lower values (100–200 Gy). The differences in the onset of saturation between grains can be attributed to the underlying OSL signal components. Bailey *et al.* (1997) showed that D_0 values varied significantly between the Fast (117 ± 18 Gy), Medium (328 ± 91 Gy) and Slow (889 ± 717 Gy) components determined from CW-OSL decay curves. This relationship has also been shown to exist in LM-OSL component resolved dose response curves (Table 3.1) where the Medium and Slow components have substantially larger D_0 values of between 258–850 Gy than the Fast component (D_0 = 190 Gy) (Singarayer & Bailey 2003).

One notable exception to this rule is the Slow 3 (or S_2) (Table 3.1.) which has a characteristic saturating dose value of 28 Gy (Singarayer & Bailey 2003). This early saturation behaviour mimics that of the Yoshida *et al.* (2000) class 3 grains, which were shown to saturate at doses of <100 Gy. The composition of the OSL decay curve can be seen to be the result of the combination of various components with each component having its own dose saturation characteristics. There variability in

the dose-response curves is more than likely the manifestation of the dominance of one or more of these components.

3.2.4.1.4 Overdispersion and intrinsic variability

So how does the intrinsic variation in quartz grains give rise to OD in single-grain D_e data sets? The combination of crystal defects in the crystal lattice produces intrinsic variations through: 1) the brightness of the grain (amount of electron traps); 2) the rate of OSL decay (the number and type of OSL components); and 3) the rate of sensitisation (the sensitisation of various OSL components). The end result is that the physical behaviours of individual grains to optical stimulation are as varied as the chemical constituents that make up its crystal lattice. Of all the grains measured, therefore, an unknown proportion will have OSL characteristics that are unfavourable for OSL measurement either as a result of dim luminescence, signal behaviour or sensitivity and come to the fore during D_e determination. The aim, therefore, is to identify and remove these grains using the rejection criteria provided in Section 3.2.4.2.

3.2.4.1.5 Measuring intrinsic OD using dose-recovery tests

The amount of intrinsic OD, to some extent, can be estimated using a dose-recovery test of Murray & Roberts (1998). Such tests are often used to determine if the measurement procedures (such as preheat temperature) are appropriate and that the analytical process and error estimation are adequate. Dose recovery tests involve bleaching the natural signal of a representative sample using natural sunlight before applying a known laboratory dose to the bleached grains. This laboratory administered dose is treated as an 'unknown,' surrogate natural dose. The SAR procedure is then applied to see if the given dose can be recovered using the specified measurement conditions. If the known dose is not recovered then it is unlikely that the D_e values for the natural samples using the same procedure will be accurate. The ratio of measured-to-given dose should, therefore, be consistent with

unity if the measurement conditions used in the SAR procedure are suitable for the sample. As each grain is given the same laboratory dose, any 'additional' scatter (OD) beyond measurement expectations in the D_e distributions could be the result of the underlying intrinsic characteristics of each grain.

Yet, for the OD resulting from a dose-recovery test to be an accurate representation of true intrinsic variability requires that the quartz grains used remain 'true' to the context in which they were found. This is highlighted by two dose-recovery tests carried out by Thomsen *et al.* (2005) and Jacobs *et al.* (2006a). The former study, prior to administering a small 7 Gy dose, annealed the quartz grains at high temperature as a means of optimising the sensitivity of each grain – a process rarely achieved in nature. Using these annealed grains Thomsen *et al.* (2005) were able to completely account for all variability in their D_e distribution, i.e., the OD was equivalent to 0%. In contrast, Jacobs *et al.* (2006a) using a sunlight-bleached quartz sample, administered ~108 Gy dose (to replicate that accrued during burial) and obtained an OD value of 7%. This 7% OD was explained as either: 1) an unaccounted source of random error, or 2) the presence of grains that are unsuitable to the SAR procedure despite the application of a series of rejection criteria. The use of dose-recovery tests, when used in conjunction with rejection criteria, provides an estimate of the minimum amount of OD present in a sample that is due to *intrinsic variability* in the mineral grain. Thus, any OD value greater than this obtained from naturally irradiated quartz is likely to be the result of extrinsic processes occurring during and following deposition.

3.2.4.2 Against the grain: extrinsic factors effecting D_e distributions of single grains of quartz

The extrinsic OD can be assessed following the screening of the data using the rejection criteria (Section 3.2.4.2) and generating an estimate of the minimum amount of intrinsic OD using a dose-recovery test (Section 3.2.5.1.5). It can be considered that any OD within a sample that is in addition to that measured using a dose-recovery test (or a modern analogous sample) is due to pre-, syn- and post-

depositional processes. To assess the possible impact of any of these processes on the burial dose of the individual grains from a specific sample, the individual D_e values are plotted on a radial plot (Section 3.2.4.4).

The past two decades of theoretical and experimental research has shown that a number of different 'types' of D_e distribution pattern can be observed within naturally-irradiated samples. In an ideal world, the different D_e distribution pattern types are the result of the dominant depositional or post-depositional processes at play. However, in natural systems, there is usually a degree of overlap where similar processes can generate similar D_e distribution patterns. Such variations and overlaps in D_e distribution patterns illustrates why first-hand knowledge of the site, site stratigraphy and site formation processes are fundamental when interpreting single-grain D_e distributions.

That being said, four broad D_e distribution pattern types can be recognised when the D_e values are graphically displayed as radial plots. Under ideal circumstances, these four patterns relate to: 1) well-bleached grains that have remained undisturbed over the period of burial; 2) grains that were partially bleached prior to burial; 3) distinct populations of grains that have been post-depositionally mixed; and 4) grains that have experienced micro-scale variations in the β-D_r. For an accurate age to be produced, a method of meaningfully combining to single-grain D_e values is required. The choice of age model (Section 3.3.3) to use rests upon determining the dominant extrinsic factor at play and the bleaching event being dated. It should be noted, however, that distribution shape alone is can only rarely be used to identify the underlying causes of dispersion.

3.2.4.2.1 D_e distribution patterns for samples containing well-bleached grains

The OSL dating technique is founded upon the assumption that the electron traps were emptied completely prior to the final period of burial. Godfrey-Smith *et al.* (1988) showed that, for quartz, only about 1% of the signal remains after 10 s of sunlight exposure. Thus, aeolian sand deposits and loess are considered to be

comprised of 'well-bleached' grains prior to deposition and burial. In these instances the radial plot D_e distribution pattern typically shows a distribution that is similar to those of a dose recovery test – where that individual D_e points are distributed symmetrically around a central mean value. This is not to say that such D_e distribution patterns are not overdispersed – as they typically are with OD value of between 0 and 40% (Murray & Roberts 1997, Roberts *et al.* 1998, Olley *et al.* 2004a, Olley *et al.* 2004b, Feathers *et al.* 2006, Olley *et al.* 2006, Jacobs *et al.* 2006a, Jacobs *et al.* 2006b, Arnold *et al.* 2007, Bateman *et al.* 2007a, Demuro *et al.* 2008, Jacobs & Roberts 2008, Turney *et al.* 2008, Jacobs *et al.* 2008b, Jacobs *et al.* 2012, Gliganic *et al.* 2012b). The use of a definitive threshold to delimit those samples that comprise of grains that were well bleached prior to burial from those that are partially bleached is not appropriate. The statistical modelling, therefore, should not be conducted in isolation of information pertaining to site formation processes and depositional content – as suggested by Galbraith *et al.* (2005).

A number of methods have been proposed in the literature to combine the D_e values from samples containing well-bleached grains. Some authors consider that the arithmetic or weighted mean to be sufficient (Fuchs & Lang 2001, Feathers 2003, Thomas *et al.* 2005, Ou *et al.* 2010, Constantin *et al.* 2012, Kreutzer *et al.* 2012, Medialdea *et al.* 2014). While these estimates may be appropriate, the issue of how to account for the OD within the distribution is often overlooked, as suggested by Galbraith & Roberts (2012). The use of the central age model (CAM) of Galbraith *et al.* (1999) provides not only a statistically sound and tests means of determining the weighted mean D_e for the sample, but also accounts for the OD in the standard error term. The CAM is further discussed in Section 3.3.3.

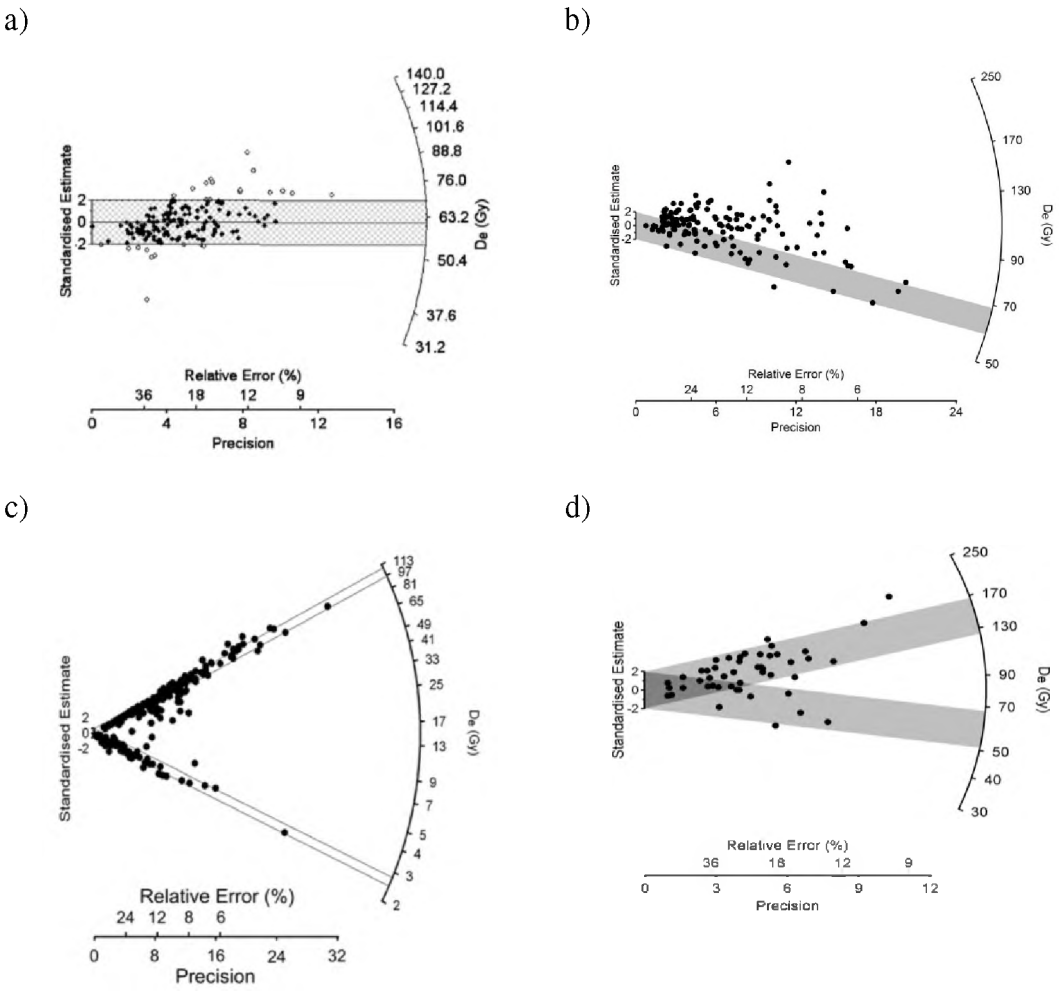

Figure 3.8. Radial plots displaying four general distribution patterns for a) well-bleached grains, UW438, OD = 24 ± 2% – Feathers *et al.* (2006); b) D_e distribution comprising of partially-bleached grains, TEC99 – Unit D, OD = 33 ± 3% - Prideaux *et al.* (2010); c) D_e distribution of a post-depositionally mixed sample, SIB11, OD = 174 ± 8% - Jacobs *et al.* (2008b), d) beta microdosimetry-influenced D_e distribution for a sample of well-bleached quartz, MR7, OD = 40 ± 6% - Gliganic *et al.* (2012b).

3.2.4.2.2 D_e distribution patterns for samples containing partially-bleached grains

In aqueous depositional environments, there is a possibility that the OSL signal in all of the grains within a sample is not reduced to zero prior to deposition. This is not only due to the decrease in light intensity and UV component attenuation (Berger & Luternauer 1987, Berger 1990), with water depth, e.g., river channel sands deposited under turbid water conditions.

In such samples, the degree of optical resetting is considered to form a continuum from those grains that are more completely, or totally, reset to those that are only marginally bleached. The latter set of grains still hold a substantial (but unknown) proportion of charge from the previous burial period. The D_e distribution pattern of such samples when displayed as a radial plot often show a continuous smear of D_e values from low to high dosed grains (Figure 3.8b). The low D_e grains are considered to be those that most accurately record the latest depositional event and burial periods.

A number of models have been suggested to combine the D_e values from partially-bleached grains to provide an estimate of the time elapsed since the latest burial period. These include the leading edge model (Lepper *et al.* 2000, Woda & Fuchs 2008) and the lowest 5% rule (Olley *et al.* 1999). Again, these models are not statistically robust. I consider the minimum age model (MAM) of Galbraith *et al.* (1999) – see Section 2.3.3. – to be the most appropriate means of estimating the D_e dose of samples displaying partially-bleached characteristics.

3.2.4.2.3 D_e distributions for samples containing post-depositionally-mixed grains

The burial history experienced by some quartz grains does not cease at the time of deposition. Rather, the process of post-depositional mixing can occur as either a

punctuated or protracted event since the time of deposition resulting in a number of different radial plot distribution patterns. In the case of a singular, punctuated event of mixing event results in a D_e distribution pattern akin to spokes on a bicycle wheel, with each spoke being associated with individual populations of grains (see Figure 3.8c). Here, the finite mixture model (FMM), as outlined and statistically verified in Roberts *et al.* (2000), can be used to mathematically determine discrete D_e components and calculate a weighted mean (and standard error) for each component. Worked examples of the FMM are presented in David *et al.* (2007) and Jacobs *et al* .(2008b).

In contrast, the D_e value distribution for those samples that have undergone continuous mixing display a continuum of D_e values with no discrete D_e components evident. In situations such as these, it is most likely that the true age of the deposit cannot be determined because the event being dated is not known. It is, therefore, more applicable to present a range of possible ages for the sample using the MAM and its inversion, the maximum age model (MAX) (Olley *et al.* 2006) – see Section 2.3.3, or to suggest that the targeted event is undetectable by OSL dating.

3.2.4.2.4 D_e distribution patterns influenced by beta microdosimetry

The importance of the beta particle and its contribution to the total environmental dose rate has become a significant field of research in single-grain OSL studies (Murray & Roberts 1997, Nathan *et al.* 2003, Mayya *et al.* 2006, Nathan & Mauz 2008, Jacobs *et al.* 2008c, Cunningham *et al.* 2012, Guérin *et al.* 2012a) . This significance is due to the fact that the beta dose rate in sediments can vary across the range of several micrometers to several millimeters as a result of the non-uniform spatial distribution of radionuclide-bearing minerals. Furthermore, the composition of the sediments, in terms of non-radioactive mineral species and mineral densities, also plays a role in BM (Olley *et al.* 1997, Nathan *et al.* 2003, Nathan & Mauz 2008).

Prior to the advent of single-grain OSL dating, multi-grain studies (which provide an average D_e value across a number of grains ranging from 10 to 1000s of grains) could supply an average beta dose rate roughly equal to what is termed the 'infinite matrix' assumption (Aitken 1985, 1998, Guérin *et al.* 2012b) to the average D_e to obtain an optical age. However, the infinite matrix beta dose rate is no longer applicable when dating single-grains as each grain now has its own beta sphere of influence which can vary due to spatial heterogeneity of beta particle emitting materials (such as K-feldspar, zircons, etc.) (Nathan *et al.* 2003, Guérin *et al.* 2012a, Guérin *et al.* 2012b).

The influence of BM on D_e distributions is not easily identifiable. The distribution of individual D_e fall roughly symmetrically around a mean value similar to well-bleached quartz D_e distributions (as shown in Figure 3.8d). In some instances, discrete bands of D_e values fall further away from the central mean; the 'scattered' D_e distributions of Jacobs *et al.* (2008c) and Gliganic *et al.* (2012a) show a number of D_e values with significantly lower D_e values than the mean. The authors of these studies suggest that the presence of radioactively 'inert' minerals are responsible for lower beta dose rate and, hence, D_e values. BM is typically invoked but rarely investigated beyond this point. At present, the most appropriate means of combing the D_e values for a sample of grains effected by BM is the same as those assumed to be well-bleached at deposition, using the central age model (CAM) of Galbraith *et al.* (1999) – see Section 2.3.3.

Before this, however, I present a review of the current investigations in BM.

3.2.4.3 Recent investigations into beta microdosimetry

BM studies appear to fall into two broad categories; being either empirical or computational. While both methods have their benefits, they also both have their own weaknesses. The study carried out at Allen's Cave, Western Australia, by Murray & Roberts (1997) in conjunction with the intensive dosimetry study of Olley *et al.* (1997) at the same site, was the first study to recognize BM in single-grain

OSL D_e distributions. Although published prior to the term OD being introduced into the literature, Murray & Roberts (1997) posited that variations in the contribution of the beta dose rate as a result of spatial heterogeneity of mineral grains with differing radioactivities was likely to be responsible for the observed spread in their D_e distribution. The work of Olley *et al.* (1997) had previously determined that 70% of the deposit was comprised of aeolian grains and the remaining 30% was carbonate derived from the disintegration of the limestone host rock, with each fraction having their own beta dose rate; 4 Gy/ka vs. 0.25 Gy/ka, respectively. Those quartz grains found within 2-3 mm of carbonate spall would receive a beta dose ~60% less than the average beta dose rate according to the authors, while those quartz grains surrounded entirely by aeolian-derived sediment would receive a beta dose rate ~30% more than the average. These combined studies were able to determine the likely range of beta dose rate values for sediment found at that specific site which are then directly applicable to the D_e values measured. The downside is that the relative positions of the grains within their respective beta dose rate spheres are destroyed in the process of beta dose rate evaluation.

Computer simulation and modeling studies have become increasingly popular in the literature and are a sophisticated way of understanding the effect of BM in OSL samples (Nathan *et al.* 2003, Nathan & Mauz 2008, Cunningham *et al.* 2012, Guérin *et al.* 2012b). These modeling studies have used various mathematical software packages (MCNP-4C or GEANT4) to construct geometries, and determine beta dose rates to individual grains using Monte Carlo simulations. Using such simulations, the total interaction of one source particle (i.e., a beta particle) beginning with a constant energy, is tracked through the modeled geometry until that particle and all induced secondary radiations are below the cutoff energy level threshold or have exited the geometry. Certain 'cells' (equivalent to grains) in the model can be selected to act as dosimeters, thereby recording the amount of energy deposited during the experiment and therefore the dose rate of the sediment matrix.

The modeling study of Nathan *et al.* (2003) provided the foundational work for Monte Carlo simulations in BM research with respect to OSL dating. Three separate experiments were modeled using Monte Carlo simulations. The first investigated the

density of attenuating grains (plastic beads, glass and steel balls) with the results showing that the average beta dose rate decreased as a function of increasing density of the attenuating bodies. The second investigated the effect of varying sizes of non-radioactive minerals had on the mean beta dose rate. The results showed that as the size of the non-radioactive bodies increases (from 1 mm, to 4 mm and 10 mm diameters) the mean beta dose rate decrease, while OD increased. The third was effectively the reverse of the second, i.e. looking at the effect of highly radioactive minerals of different sizes. Here, as the diameter of the radioactive grain increased, the D_e distribution became more asymmetrical, with a greater number of high dose grains present and having a greater OD. Interestingly, the D_e distribution becomes much broader as the size of the granite bodies decreases with the mean beta dose rate coming closer to that of the infinite matrix dose rate.

Subsequent computational BM studies, however, have become increasingly interested in the presence of K-feldspars as the sole inducer of BM. Using this assumption, Monte Carlo simulation investigation was undertaken by Guérin *et al.* (2012b) to model the BM environment of an OSL sample coming from a Danish beach. Using a number of assumptions including: grain packing (0.635); grain size distribution and shape (100 to 600 µm diameter spheres); and K-content of feldspar grains (those grains with > 6% K content as determined by SEM-EDS analysis were classed as 'pure' K-feldspar grains with a content of 14%; and dosimeter size (207 µm diameter); the simulated D_e distribution displays a positively skewed asymmetric distribution (similar to that present for the radioactive bodies simulation in Nathan *et al.* 2003). Additionally, the D_e dataset show a degree of OD, a function of distance of the dosimeter relative to the hotspot grains. In terms of the infinite matrix dose delivered to the dosimeter quartz grains, the model of Guérin *et al.* (2012b) suggests that the majority of the grains received significantly less than the infinite matrix dose, while the remaining grains actually receive more (similar to the "empiric" findings of Murray & Roberts some 15 years previous).

A similar experiment carried out by Cunningham *et al.* (2012) also focused on K-feldspar grains. However, K-feldspars were substituted with spherical sodium hydroxide grains (650 to 800 µm diameter) that had been bombarded with neutrons

to produce the ^{24}Na isotope that has a beta-energy spectra similar to ^{40}K, and that produces large amounts of beta dose in a relatively short period of time and is water soluble. This experiment was run using both an experimental set-up and a Monte Carlo model. The results of the experiment set-up show a D_e distribution ranging from 0.26 to 19.2 Gy and an OD of 82%. The corresponding Monte Carlo simulation yielded an OD value of 50%, severely underestimating the amount of OD in the experimental result. However, both the experimental and simulated data show the same asymmetrical distribution of D_e values.

The use of Monte Carlo simulation and computer modelling represents a sophisticated and elegant solution to determining the distribution of beta dose rate within the sedimentary environment. However, the modelled results are only as good as the assumptions upon which they are built. For example, how likely is it that the presence of K-feldspars, alone, produces BM? Isn't it equally likely that beta dose rate hotspots can be the result of U and Th? The results of these modelling studies provide valuable insights into the effect that BM has on D_e distributions however the results obtained are only applicable to the model that produced them and not universally applicable to naturally formed sediments.

3.3 THE USE OF AGE MODELS IN D_E DETERMINATION OF THE BURIAL DOSE

Many different age models have been used in OSL dating to combine the individual D_e values meaningfully. The age models proposed by Galbraith *et al.* (1999) are the only available models based on sound statistical principles and tested using computer simulations and known age samples. Therefore, in this study only these models have been applied and will be discussed below. One critical aspect of the Galbraith *et al.* (1999) age models is that the D_e are first log-transformed to overcome problems associated with errors that increase in proportion to dose.

The central age model (CAM) provides a weighted mean of the sample population and its standard error takes into account the OD that cannot be explained by measurement uncertainties alone (Galbraith *et al.* 1999). This is important since it has been shown experimentally that well-bleached samples have OD values of between 10 and 20% (Murray & Roberts 1997, Roberts *et al.* 1998, Olley *et al.* 2004a, Olley *et al.* 2004b, Feathers *et al.* 2006, Olley *et al.* 2006, Jacobs *et al.* 2006a, Jacobs *et al.* 2006b, Arnold *et al.* 2007, Bateman *et al.* 2007a, Demuro *et al.* 2008, Jacobs & Roberts 2008, Turney *et al.* 2008, Jacobs *et al.* 2008b, Jacobs *et al.* 2012, Gliganic *et al.* 2012b). The full equation and statistical explanation of the model is presented in Galbraith *et al.* (1999). The CAM model is most appropriately applied to samples of grains that have been well bleached prior to burial and remained undisturbed after deposition (Figure 3.8a). It is assumed that, by taking the weighted mean of the D_e distribution, the mean beta dose rate measured (Section 3.4.3.4.2) can be used in the final age determination for the sample.

The minimum age model (MAM; Galbraith *et al.* 1999) is most appropriate for samples where bleaching of the grains has been incomplete or non-uniform prior to burial (Figure 3.8b), resulting in significant OD. If one were to apply the CAM to such a data set an overestimate of the D_e will be obtained. The MAM provides an appropriate means of estimating the D_e specific to the most recent bleaching event. The model assumes that the true log D_e values are drawn from a truncated normal distribution, where the lower truncation point corresponds to the log D_e of the population of fully-bleached grains and, hence, the target dating event. The model also has three additional parameters which represent the unknown proportion of fully-bleached grains, and the mean and standard deviation of the population if the normal distribution was not truncated, respectively. The latter can be omitted if the number of D_e values is small, or if there is little OD, resulting in a three parameter model that may, in some circumstances, provide a more robust fit to the data. In applying the model, an estimation of the intrinsic OD (determined using dose-recovery tests or the OD coming from an analogous well-bleached sample) is required to be added to each individual standard error, in quadrature, to take into account the degree of OD presented in well-bleached samples.

On occasions the inverse of the MAM, termed the maximum age model (MAX; Olley *et al.* 2006), is warranted to estimate the maximum dose population of D_e values in a sample. Here, the natural log of the D_e values is taken and multiplied by -1 to create a mirror image of the D_e dataset. The exponent of each D_e value is then taken and the MAM applied once the appropriate relative error has been combined in quadrature to each of the standard errors to account for the OD present in a population of well-bleached grains. The results of the MAM are then transformed by taking the natural log, multiplying by -1 and taking the exponent to determine the mean and standard error of the maximum dose population of D_e values.

The use of age models is central to determining the D_e of single-grain OSL samples. However, other considerations, such as burial histories and site context are required to be addressed before applying statistical age models to ensure the best, and most informed, estimate.

3.4 ENVIRONMENTAL DOSE RATE COMPONENTS AND MEASUREMENT

3.4.1 ENVIRONMENTAL DOSE RATE: AN OVERVIEW

Naturally occurring ionising radiation, primarily from potassium (^{40}K), and the decay of uranium (^{235}U and ^{238}U) and thorium (^{232}Th) and their respective daughter products, is responsible for the movement of electrons into traps in the crystal lattice of the quartz grain (Aitken 1985, 1998). The half-lives of the U and Th parent isotopes and of ^{40}K are suitably long (~10^9 years) so that their natural abundance is, in effect, constant over the time range of OSL dating interest. This allows the estimation of the total environmental dose rate experienced during the burial period of the sediments to be made by measurement of the current radiation flux.

Measurement of the environmental dose rate, the denominator in the OSL age equation, is thus of equal importance to the measurement of the D_e.

The total environmental dose rate can be broken down into four constituent radiation types. These include: 1) alpha-particle, 2) beta-particle, 3) gamma-ray, and 4) cosmic-ray radiation (Aitken 1985). A schematic of the penetrating potential of these various radiation types in sediment can be found in Figure 3.9. Alpha particles are heavily energetic, have a short range of influence no more than several μm, and result from the nuclear fission of ^{235}U, ^{238}U, ^{232}Th, and their radioactive daughters. Beta particles have a range of between 2–3 mm in sediment an comprise of high-energy electrons and positrons, whereas gamma rays can penetrate up ~30 cm and are a form of electro-magnetic radiation (i.e., they have no mass or charge) (Aitken 1985). Both beta particles and gamma rays are produced from the nuclear fission of ^{235}U, ^{238}U and ^{232}Th (and their radioactive progeny) with a contribution also made by the radioactive decay of ^{40}K. The cosmic ray flux, unlike alpha, beta and gamma radiation, is derived from intergalactic protons interacting with Earth's Upper atmosphere and is the most penetrating (>30m) of any radiation type discussed here (Prescott & Hutton 1994).

The environmental dose rate of a given sample can be divided into: 1) an internal dose rate; and 2) an external dose rate. The internal dose rate represents that radiation coming from within the quartz grains themselves. The external dose rate is derived from the alpha, beta and gamma radiation in the bulk sediment matrix surrounding the grain, and also cosmic rays. Below I outline these internal and external radiation sources and, where applicable, give a description of the methods used to evaluate their contribution to the total environmental dose rate.

Further discussion of dose rate determination methods and equipment is provided in Appendix 1.

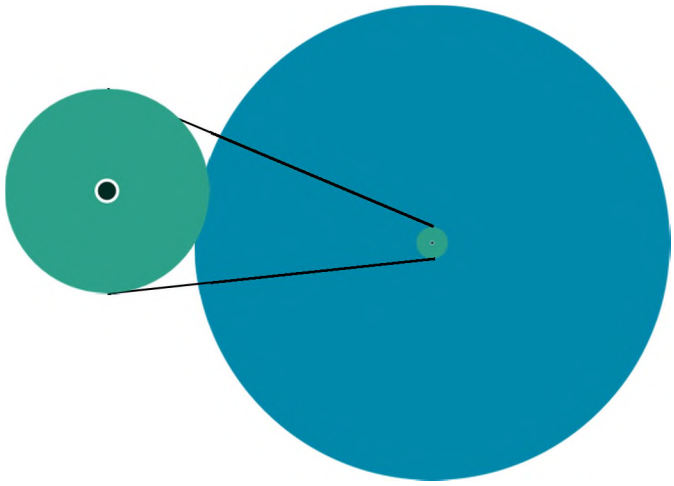

Figure 3.9. Radiation spheres (to scale) surrounding a single grain of quartz (black circle). The quartz grain measures 180 µm in diameter and received an external radiation dose from alpha (white), beta (green) and gamma (blue) radiation from the decay of radiogenic isotopes in the surrounding sediments. External alpha particles have a range of ~25 µm from the emitting nucleus, beta particles have a range of 2–3 mm, whereas gamma rays have a range of ~30 cm. Not shown is the contribution of cosmic rays.

3.4.1.1 Correction factors: moisture content and beta dose attenuation

A number of corrections are needed to be made prior to the determination of the total environmental dose rate. Of particular importance is the correction of the beta dose rate to account for attention of beta particles as they pass through the quartz grains (Mejdahl 1979, Bell 1979a, Aitken 1985, 1998, Brennan 2003). It is also important that the fluctuations in the sediment water content over the period of burial be accounted for or OSL age underestimates will be produced (Aitken 1985, Aitken & Xie 1990, Aitken 1998).

The amount of attenuation experienced by a beta particle is dependent upon the radionuclide it is being released from and the size of the grain it is penetrating. In this

thesis, 180–212 μm grain size was used exclusively in D_e determinations and, hence, the values used below are directly applicable to this grain size fraction. The attenuation factors presented by Brennan (2003) are the most recent revision of the original attenuation factors presented by Mejdahl (1979). This paper, however, is difficult to use in its current form given the graphical representation of the data and the, at time, confusing nature of the HF-acid etching effects. However, the tabulated values can be obtained from the author through written communication (as is suggested in the acknowledgements). The average attenuation factors for a beta particle coming from the U and Th decay chains or ^{40}K are 0.850, 0.798 and 0.924, respectively. However, the practice of HF-etching the quartz grains must also be considered and accounted for. As such, the attenuation coefficients decrease to 0.839, 0.782 and 0.918 for U, Th and K, respectively. These attenuation coefficients were used in instances where the individual concentrations of U, Th and K were known (e.g., ICP-MS data). In cases where the individual contribution of U, Th and K to the beta dose rate were not known (such as in beta counting), the mean of the three HF-etch corrected attenuation coefficients (0.846) was used. A systematic 3% error is added in quadrature to the random beta dose rate uncertainty to account for systematic uncertainty in the attenuation factors.

Account of sediment water content is also required to be accounted for. The sediment water content (either held in pores or bound in clay) absorbs a proportion of the incoming beta and gamma radiation, and also cosmic-rays. As a general rule, a ~1% increase in sediment water content decreases the total environmental dose rate by ~1%; producing an increase in OSL age by ~1%. Thus, the beta, gamma and cosmic dose rate (which are measured or estimated as 'dry') are required to be corrected.

An estimate of sediment water content can be made by collecting a portion of sediment as the time of sample collection and weighing the sample before and after a period of oven drying. The difference between these two measurements can be expressed as a percentage of the dried sample mass. An uncertainty is then required to be added to encompass the likely range of water contents experience over the period of burial. At the University of Wollongong laboratory, a typical uncertainty of

25% (1σ) is assigned to each sediment water content estimate. However, uncertainties of between 4 to 50% can be found in the literature (Munyikwa *et al.* 2011, Reimann *et al.* 2012, Guérin *et al.* 2012a, Medialdea *et al.* 2014), or simply not stated.

The correction coefficients for water content can be calculated using the equations set out in Aitken (1985); where the water-corrected dose rate can be found by dividing the dry dose rate by one plus a correction factor specific to the radiation type (F) that has been multiplied by the measured water content (W). This is expressed in the equation below:

$$water - corrected\ dose\ rate = \frac{dry\ dose\ rate}{1+WF} \qquad \text{equation 2.2}$$

For beta, gamma and cosmic rays, the correction factor F is 1.25, 1.14, and 1.176, respectively. The total environmental dose rate, therefore, is the sum of the moisture-corrected external cosmic, gamma and (attenuated) beta dose rates and the internal alpha dose rate.

3.5 AGE AND ERROR CALCULATIONS

With the determination of the D_e and the total environmental dose rate, the optical age of the sample can be obtained by dividing the former by the latter (as in equation 2.1). Calculating the total uncertainty, however, is not so straight forward.

The total uncertainty associated with the D_e and dose rate consists of both random and systematic components, which have been discussed in Sections 3.2 and 3.4. However, prior to determining the total uncertainty on the dose rate some additional systematic errors need to be accounted for. In terms of the D_e, a 2% systematic error is added, in quadrature, to the previously determined random errors to account for beta source calibration. The uncertainty of the dose rate is found by adding in quadrature all the known errors associated with each of the dose rate

components (i.e., beta, gamma, cosmic and internal). However, allowances need to be made for sediment water content over the period of burial using equation 2.2 for the external radiation components. It is probably best to illustrate this process through example.

A wet and attenuated beta dose rate of 1.00 ± 0.03 Gy/ka was measured for a sample that has a total environmental dose rate of 2.11 Gy/ka and a moisture content of 10 ± 2.5%. The water attenuation coefficient for the 10% mean water content was calculated to be 0.89, with values of 0.91 and 0.87 were obtained using a mean water content minus 1σ and water content plus 1σ, respectively. The fraction systematic error on the water content was then calculated by taking the difference of 0.91 and 0.87 (0.91-0.87 = 0.04) and dividing the result by 2 (0.04/2 = 0.02), before dividing the result by the coefficient of the mean water content (0.02/0.89 = 0.02). The fractional contribution of the systematic water content error to the beta dose was then found by dividing the wet and attenuated beta dose rate by the total dose rate (1.00/2.11 = 0.47) and multiplying by the systematic water content error (0.47×0.02 = 0.01). This series of calculations are then carried out for the gamma and cosmic contributions. The calculated water content systematic errors for all three components are then summed and the total error added in quadrature to the uncertainty calculated previously (i.e., the quadratic sum of the random and systematic uncertainties on each of the individual components).

The total uncertainty on the optical age is then calculated from the relative standard errors on both the D_e and total environmental dose rate terms being propagated accordingly, by adding them in quadrature, as suggested by Aitken (1985).

SECTION SUMMARY

The OSL dating technique can be used to determine the amount of time elapsed since sediment grains were last exposed to sunlight. A revolution in OSL method, procedures and technologies now allows for the rapid assessment of De from individual grains. However, the spread between D_e values form the same sample can, most often, be overdispersed. This OD is often assumed to be the result of intrinsic or extrinsic factors. The intrinsic component of OD, which relates to signal brightness sensitivity and dose response can, to some extent, be quantified using dose-recovery tests. In contrast the influence of extrinsic factors is often based on the appearance of the D_e distribution pattern (as a radial plots) or assumed from macroscopic observations of the sediments. Typically, three processes are evoked to explain the remaining OD in naturally-irradiated D_e distributions; these include partial-bleaching, post-depositional mixing or beta microdosimetry. The accuracy of the final OSL age hinges upon the interpretation of both sources of OD and the age model used to combine the individually measured D_e values.

Chapter 4

Under the microscope: soil micromorphological analysis and application

The following sections provide more of a practical and methodological review of the soil micromorphological technique, rather than a theoretical one – besides which a review of that nature would be beyond the scope of this thesis. Here, I outline a brief overview of the technique followed by sampling practices and preparation of thin sections.

4.1 SOIL MICROMORPHOLOGICAL TECHNIQUE

The application of soil micromorphology is often used to elucidate complex, and compound, sedimentary problems in archaeological and geological contexts. The technique requires the collection of intact and orientated sediment block samples from which thin sections are produced and analysed. Through thin section analysis the origin of sediments, the mode of formation, and the processes that may have influenced it since its original depositional event can be observed. The power of this technique, therefore, can be better illustrated through a comparison with sedimentological analysis using bulk sediment samples.

Investigations carried out by earth scientists (e.g., soil scientists, geologists, physical geographers, and geoarchaeologists) generally use a suite of analysis techniques conducted on bulk sediment samples. These techniques include, but are not limited to: grains size particle analysis, x-ray florescence, x-ray diffraction, carbonate content analysis, soil organic matter content, etc. While each of these methods provide an invaluable insight into the sedimentary composition as a whole, it is not possible to deconvolute complex or superimposed depositional events within the one sample. For example, a grain size analysis of a sample containing sand-sized pelletal clay grains would provide an erroneous representation of the sedimentary make-up leading to inaccurate interpretations of the depositional events. Or, a bulk carbonate content analysis is unable to differentiate between primary calcite (e.g., limestone clasts) and secondary calcite formed during a pedogenic event (e.g., micritic calcite). Soil micromorphology, in contrast, is able to unravel these compound site formation events as the sedimentary geometry and fabric remain intact.

4.2 FIELD SAMPLING PRACTICE AND SAMPLE PREPARATION

4.2.1 FIELD DESCRIPTIONS

The micromorphological investigation should not be viewed as purely a laboratory-based exercise, but rather as a continuation of the sedimentological observations carried out in the field. As such, sample collection begins with detailed and systematic descriptions of the field section being examined and its position in the landscape. Descriptions of the wider site context, therefore, allow for questions regarding sediment origin (or provenience) to be addressed, along with the probable mode of deposition (e.g., fluvial, colluvial, aeolian, karstic, etc.). The description of the site stratigraphy or profile should also be carried out to not only allow for later interpretation but also for providing context for the samples collected and the type of sampling strategy used in their collection. Descriptions of field stratigraphy should follow general soil/sedimentological descriptions, sediment moisture, colour and colour variation, texture and stoniness, bedding and bedding features, sedimentary structures, soil structure and character, and porosity. In addition to writing descriptions and field notes, it is important also to produce a scaled drawing of the section or stratigraphic column showing the main boundaries and textural changes between the various units within the site.

4.2.2 SAMPLING STRATEGY

The sampling strategy employed at a site ought to reflect the questions being addressed. Courty *et al.* (1989) outlines a number of different strategies that can be employed with regards to the research question being conducted. These strategies include: systematic and selective sampling methods.

Systematic sampling involves the collection of samples from a single column, a number of columns collected one on top of the other without any gap, or as number of offset and overlapping blocks that cover the entire height of the stratigraphic section being investigated.

Selective sampling is often used when specific questions are required to be addressed. Typically, this is done subsequent to the continuous sampling technique to: 1) address lateral variations within a unit, and/or 2) to provide a better understanding of an archaeological (sub)unit or living floor. Here, specific features or layers are selectively targeted for analysis. This approach was used exclusively throughout this thesis.

4.2.3 SAMPLING METHODS

Once a sampling strategy has been determined, sediment block samples can then be collected. There are two different methods used in sample collection: 1) tin box, or 2) 'loose' sediment block approach. The type of sampling method used is dependent upon the type of sediment being sampled.

The use of a metal tin, commonly referred to as 'Kubiena tins,' is often employed in the sampling of poorly consolidated materials. However, plastic or metal downpipe, and even aluminium cans, can be used if traditional 'Kubienas' are unavailable. Sampling with a tin requires that it be carefully inserted into the sediment/soil section. The sediment surrounding the tin is then carefully removed using a knife, trowel or similar implement, and the sample detached from the section. The restriction of this sampling method is highly heterogeneous contexts (such as highly stony sediments) may not allow the tin to be inserted into the section.

In contexts where the sediments are more consolidated, or too coarse and heterogeneous for sampling tins to be used, an alternative method is to excise a sediment block directly out of the sedimentary profile using a sharp knife. In this case, it is best to outline an area that is larger than the expected size of the sample

being collected. Using a sharp knife, the sediments are methodically removed from all four sides of the block until a sufficient depth (~10 cm) is reached. The sediment block can be stabilised with a casing made from quick-drying plaster bandages – these are made of a gauze mesh impregnated with plaster of Paris and readily available from pharmacies and art supply stores. The bandages are wetted and applied to the outer surface of the block and allowed to dry (between 1–2 hr) before a second layer is applied. Given the malleability of bandages, irregular surfaces can be easily covered and stabilised. Once dried, the block can be carefully removed from the sediment section by incising into a section at an angle from the sides of the block that will converge roughly at the centre of the sample. At this point, a bricklayers trowel can be used to lever the block out of the section.

Once the samples have been removed from the section, using either of the above methods, they are carefully wrapped in tissue paper. Care should be taken, however, to maintain the orientation of the samples with respect to the section. Once wrapped with tissue, the entire compliment is then stabilised with plastic packing tape to prevent disaggregation during transport to the laboratory. The sample is then labelled to preserve the orientation of the block in the field. Markings and notes are written on the outer surface of the samples to designate the top and bottom, and also the side that was facing into the deposit and which face was point outwards.

4.2.4 SAMPLE PREPARATION

The sediment block samples are then prepared for thin sectioning using the techniques outlined in Courty *et al.* (1989). First, the blocks need to be dried so that the resin used to impregnate the samples properly cures. This can be achieved either by air drying the samples (e.g., under a fume hood) or in a low temperature oven (40–60 °C). Drying the blocks at higher temperatures can cause the cracking and changes in the original morphology (and mineralogy) of the samples. Once dried, the blocks can be impregnated with polyester resin. The blocks were placed into a deep, leak-proof container and polyester resin added in increments. Goldberg & Macphail (2006) suggest using styrene to dilute the resin in a 7 parts resin to 3 parts styrene ratio as a means of decreasing the viscosity of the resin. The polymerisation reaction

is aided using a 2-butanone peroxide ($C_8H_{16}O_4$) catalyst. The first pouring of the resin should fill the container to about half-way up the side of the samples and then leaving them to allow the resin to 'wick' up and into the sediments; this usually takes several hours, depending on the texture of the material. This process is repeated until the top of each sediment block sample appears 'moist' with resin, typically the following day. The final pouring of resin should totally cover the samples. The samples can then be left to harden and the curing process finished by placing then in a low temperature oven at ~60°C. Caution is required during the impregnation process with all work carried out under a fume hood or a well-ventilated area as the styrene and resin fumes are toxic.

4.2.5 PROCESSING FOR THIN SECTIONING

Soil micromorphology thin sections are larger than those used in standard petrographic studies, measuring 5×7.5 cm, 9×6 cm or larger, depending upon the equipment used. Slices of resin-impregnated sediments from each block are generally cut to this size and ~0.5 cm thick using a cooled, diamond saw. The stages outlined up to this point were conducted by the candidate at the University of Wollongong. It is at this point that the 'thick-sections' can be sent off for commercial processing (which was done in this thesis) into thin sections. All thin sections described in this thesis were produced at Spectrum Petrographics, Vancouver, Washington state, USA.

Further details regarding the history, terminological framework of Stoops (2003) and the analysis and reporting of thin sections (based upon those set out in Goldberg & Macphail 2006) are given in Appendix 2.

SECTION SUMMARY

Soil micromorphology requires the collection of intact and orientated samples. The strength of soil micromorphology is that the basic components of the soil/sediment can be contextualised and resolved definitively in space and time in relation to other components. This ability to spatially resolve components cannot be achieved using other sedimentological techniques that 'destroy' the geometric relationships among constituent components. Soil micromorphology, therefore, can be used to determine not only basic sedimentological parameters (e.g., grain size and sorting, etc.) but also to infer microstratigraphic sequencing, including depositional environment, sediment provenience, mode of formation and any post-depositional modifications.

PART B

Chapter 5

Optical dating and soil micromorphology at MacCauley's Beach, New South Wales, Australia

Nathan R. Jankowski, Zenobia Jacobs & Paul Goldberg

Accepted for publication in Earth Surface Processes and Landforms

This chapter investigates the sedimentary environment at MacCauley's Beach, a coastal geogenic deposit that straddles the Pleistocene/Holocene boundary. While the single-grain OSL dating of this site has important implications for the timing of Holocene sea-level rise on Australia's eastern sea board, more importantly this study demonstrates how the use of soil micromorphology and the microscopic examination of sediments can aid in the both the interpretation of De distribution patterns and the explanation of OD present. The results of this study demonstrate that the integration of soil micromorphology with single-grain OSL dating has mutually beneficial outcomes for both these techniques.

Aims for this chapter:

- *develop a sampling strategy to allow qualitative assessment of sedimentary geometry of samples to be dating with single-grain OSL*
- *determine the site formation processes that led to the accumulation of MacCauley's Beach*
- *construct a more robust, accurate and precise chronology for MacCauley's Beach using single-grain OSL dating*

ABSTRACT

The ability to position landscapes in a context of time and space is a particular goal of Quaternary science research. The lack of context for dating samples published previously for MacCauley's Beach, an important site for the reconstruction of Australian sea levels, warranted a re-evaluation of both the site stratigraphy and chronology. In this study, we combined optically stimulated luminescence (OSL) dating of sedimentary quartz grains and soil micromorphology of the same samples to improve our understanding of the depositional history and chronology of the sediments. This combination allowed the contextualisation of samples not only in time and space, but also in terms of their depositional histories. The latter is important in OSL dating, where pre-, syn- and post-depositional processes can all influence the accuracy and precision of the final age estimates. The sediment profile at MacCauley's Beach is made up of three major units. The basal mottled mud layer has undergone extensive pedogenesis since deposition, and only a minimum age of 14.7 ± 2.7 ka could be calculated. The overlying grey mud, with OSL ages from the bottom and top of the unit of 10.0 ± 0.7 and 7.7 ± 0.5 ka respectively, shows evidence of soil structure collapse. This unit correspond to the onset of the mid-Holocene sea-level highstand for this region. The overlying sand layer was first deposited at 7.5 ± 0.4 ka, with deposition continuing beyond 6.6 ± 0.4 ka. Not only does the chronology presented constrain the timing of deposition (and the extent of post-depositional processes) at MacCauley's Beach, but the methodological approach used here can be applied to any site to aid in the interpretation of formation processes and assess their influence on OSL age determination.

5.1 INTRODUCTION

Optically stimulated luminescence (OSL) dating is commonly used to determine the depositional age of coastal barriers and dune sequences (e.g., Bateman *et al.* 2004, Rhodes *et al.* 2006, Fornós *et al.* 2009), and has been pivotal in many reconstructions of past coastal landscapes, placing them into their correct stratigraphic and chronological context (e.g., Banerjee *et al.* 2003). In Australia, however, there remains a paucity of OSL dating studies of sedimentary deposits that may shed light on the development and evolution of coastal landscapes and sea level fluctuations. Holocene chronologies are mostly based on radiocarbon (^{4}C) dating of charcoal and shell material (e.g., Thom *et al.* 1978, Roy & Thom 1981, Chapman *et al.* 1982, Sloss *et al.* 2007) and Pleistocene chronologies on thermoluminescence (TL) dating of sediment (e.g., Bryant *et al.* 1990b, 1992b, 1994, Nott *et al.* 1994).

The New South Wales (NSW) coastline provides an ideal setting for the study of coastal landform response to sea level fluctuations due to its relative tectonic stability and position in a "far field" location, distant from continental ice. The coastal landscape evolution is, therefore, driven by eustatic sea-level rise, rather than isostatic adjustment (Lambeck & Nakada 1990). The Pleistocene sea level history for this region is poorly constrained. Sedimentary deposits pre-dating marine isotope stage (MIS) 5 are rare; only one location, Red Point south of Wollongong (Figure 5.1), has preserved aeolian dune sediments older than the last interglacial at ~125 ka (using TL: Bryant *et al.* 1990a). Fossil coral from Evan's Head near Newcastle dated to 119 ± 4 ka (Pickett *et al.* 1989), and amino acid racemisation (AAR) ages for fossil shell (*Anadara trapizia*) preserved at Largs in the Hunter Valley estuary (Murray-Wallace *et al.* 1988, Thom & Murray-Wallace 1988) provide limited evidence that sea levels during MIS 5e might have attained heights of ~3–6 m above present mean sea level (PMSL) (Murray-Wallace & Belperio 1991). AAR ages of fossil shell material recovered from drowned deposits on the continental shelf dating to the last glacial maximum (LGM) place the then shoreline ~20 km east of its current position (Murray-Wallace *et al.* 1996) and at ~120–130 m below PMSL

using known, present day ecological parameters of the fossil shell fauna (in particular *Glycymeris radians*) as a proxy for palaeo-water depth (Murray-Wallace *et al.* 2005).

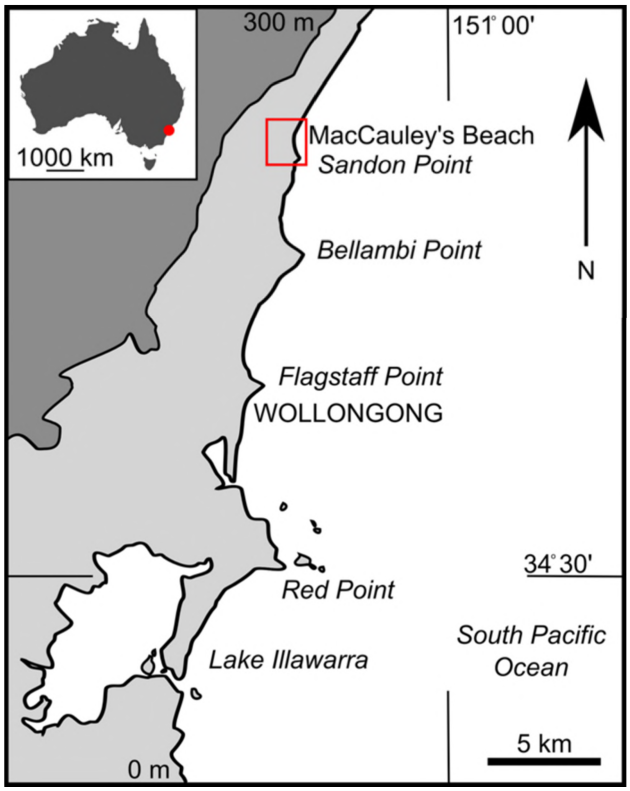

Figure 5.1. Schematic map showing the location of MacCauley's Beach in relation to Wollongong. The 300 m contour interval represents the position of the Illawarra escarpment. Top left inset: study site in relation to the Australian mainland shown by red circle. Map after Bowman (1974).

The Holocene sea level history is better constrained (e.g., Thom *et al.* 1978, Roy & Thom 1981, Roy 1984, Sloss *et al.* 2004, Murray-Wallace *et al.* 2005, Sloss *et al.* 2006a, 2007, Lewis *et al.* 2013). Following the melting of continental ice sheets, sea level transgressed over the NSW coastline to PMSL by 7.9 to 7.7 ka, after which it continued to rise to ~1.5 m above PMSL by 7.4 ka, and remained at that level until ~2.0 ka ago, before regressing to PMSL (Sloss *et al.* 2007, Lewis *et al.* 2013). Our understanding of this initial rapid rise of Holocene sea level to above PMSL is based on records from only a small number of sites in the northern Illawarra

region, namely MacCauley's Beach, North Bulli and South Thirroul, all located in proximity of each other and ~12 km north of Wollongong, NSW (Figure 5.1).

The MacCauley's Beach site is the subject of this study. For a site of such regional importance, the stratigraphic investigations are too coarse, the depositional and post-depositional processes that led to the formation of the site are poorly understood, and the existing chronology is imprecise. In this study, we aim to: 1) re-evaluate the stratigraphy and site formation processes of the site through a combination of field observations, grain particle size analysis and soil micromorphology (Fedoroff *et al.* 1987, FitzPatrick 1993), 2) test the existing chronology and construct a reliable temporal framework for the preserved sediment sequence using OSL dating of individual grains of quartz, and 3) combine soil micromorphology and single grain OSL dating to improve the accuracy of the chronological framework for this site.

5.1.1 REGIONAL SETTING AND STUDY SITE

The continental margin off the east coast of Australia was produced during the rifting event that opened up the Tasman Sea between Australia and New Zealand during the Late Cretaceous/Palaeogene (Haynes & Ringis 1973). The continental shelf of the Illawarra region of NSW is considered tectonically stable (Bryant 1992a), and known to be deep and narrow (Roy & Thom 1981). Due to the depth of the continental shelf, there is negligible frictional loss of wave energy seaward of the breaker zone; the dominant wave climate come from S–SE swell and wind waves generated in the Tasman Sea and Southern Ocean. The deep continental shelf and approximately normal orientation of the coastline (NNE–SSW) to the dominant wave climate (SE) gives rise to the high energy, wave-dominated coastline morphology of the region (Roy & Thom 1981, Roy 1984).

The rifting of the eastern margin of the Australian continent has produced an embayed coastline with numerous micro-tidal estuaries. In the Illawarra region, successive cycles of sea level fluctuations have resulted in the incision of the

Permian-aged Sydney Basin geological sequences by small, eastward flowing rivers and the formation of coastal bedrock valleys. The sediment currently preserved within these embayments are Quaternary in age and show a distinctive progression of tripartite facies (Boyd *et al.* 1992, Dalrymple *et al.* 1992) consisting of marine quartz-rich sand, central basin muds and fluviatile sediment moving landward from the present coastline. These preserved sedimentary successions are thought to be the product of consecutive cycles of climatically driven sea level fluctuations (Lewis *et al.* 2013).

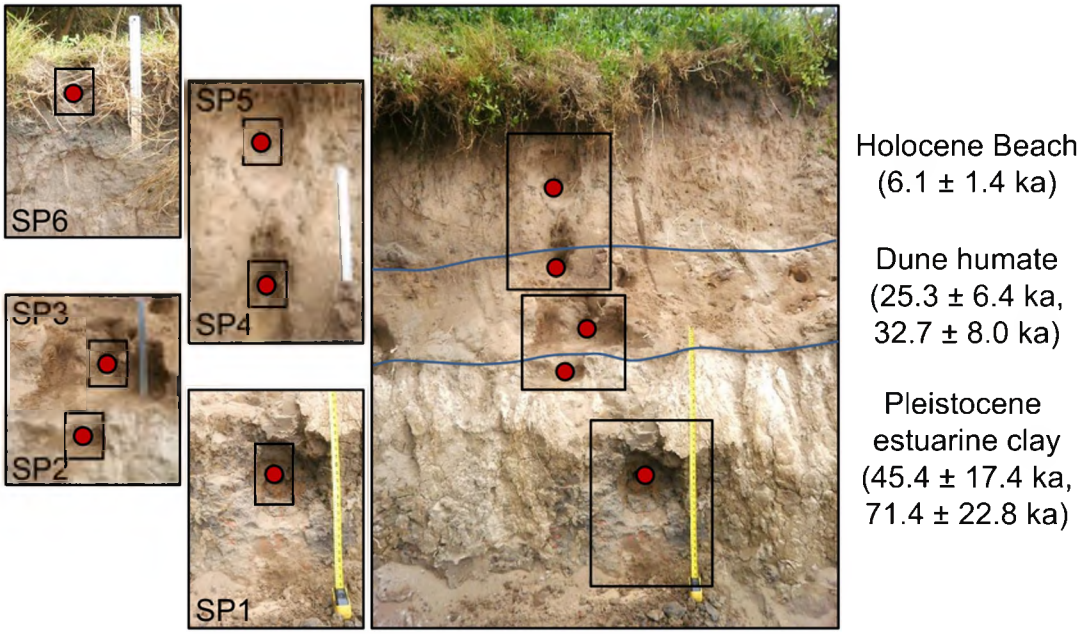

Figure 5.2. Photograph of the MacCauley's Beach sampling column showing the position of soil micromorphology and OSL samples used in this study, and stratigraphic classification and TL ages presented in Bryant *et al.* (1992b) (right-hand column). Sample SP6 was collected from ~2 m to the left of the profile shown. The yellow measuring tape is 1 m in height. Metal ruler in inset images measures 30 cm in length. The postion of the micromorphological samples is indicated by the black squares in the images to the left of the main profile.

The coastal dune sequence preserved at MacCauley's Beach (Figure 5.1), forms part of the much larger southeast Australian dune field (Lees 2006). Here, two small creeks (Tramway and Woodland) drain eastwards from the hinterland of a small 53 ha catchment to a shallow lagoon located directly behind the modern beach face at the north of the beach. Bryant *et al.* (1992b) first investigated the MacCauley's Beach site and subdivided the sedimentary sequence into four broad stratigraphic units (Figure 5.2). They classified the basal layer as mottled estuarine clay overlain by similarly textured sediment with slightly fewer mottles. These two sedimentary layers were collectively referred to as the 'Pleistocene estuarine clay' unit. A sandy quartz and organic residue-rich 'dune humate' deposit was recognised above the Pleistocene estuarine clay, which in turn was overlain by a raised Holocene beach unit. Modern dune sand and an associated shell midden capped the stratigraphic sequence. This arrangement of lithofacies led Bryant *et al.* (1992b) to classify the MacCauley's Beach deposits as a receded barrier beach in the terminology of Thom *et al.* (1978). This lithostratigraphy is analogous to that presented by Jones *et al.* (1979) for the deposits at North Bulli and South Thirroul located directly to the south and north of MacCauley's Beach, respectively (Figure 5.1) from which the earliest ages (^{14}C) for the onset of the mid-Holocene sea level high stand have been reported.

Bryant *et al.* (1992b) also presented a temporal framework for the MacCauley's Beach site. TL dating of unheated sediment gave ages of 71 ± 23 and 45 ± 17 ka for the Pleistocene estuarine clay unit, 33 ± 8 and 25 ± 6 ka for the 'dune humate' unit, 6.1 ± 1.4 ka for the raised beach deposit and ~1.6 ka for the modern beach face at the site (Figure 5.2). Two Uranium (U)-series ages of 21.3 ± 3.8 and 19.7 $\pm \frac{3.2}{3.4}$ ka were also reported for a portion of beach rock perched on top of an eroded scarp of the Pleistocene estuarine clay, found ~5 m further seaward from the exposed section (not visible in Figure 5.2, and currently buried under the modern beach face).

5.2 METHODS

5.2.1 SEDIMENTOLOGY AND STRATIGRAPHY

The total 2.0 m height of the section above the present beach face was cleaned and textural and colour changes recorded, as well as any sedimentary features. Nineteen bulk sediment samples were collected every 10 cm down the sample column for grain size analysis, measuring grain particle size distribution, mean grain size and sorting of the <2 mm in diameter grain size fraction. These samples were measured using a Malvern Mastersizer 2000. The samples were diluted to the appropriate detection level (10–20% laser obscuration) and ultrasonic diffuser switched on for a minimum of 1 min to disperse the fine particulate matter prior to measurement. Sediment colour for each unit was recorded on dry sediments collected at the six sampling positions shown in Figure 5.2 using a Munsell soil colour chart.

5.2.2 SOIL MICROMORPHOLOGY

Soil micromorphology is the study of undisturbed sediments and soils in thin section (Courty *et al.* 1989). As this method studies intact and orientated sediment samples, the original integrity of the materials is preserved. By assessing the texture (sized and sorting) and fabric (the geometric and spatial organisation of mineral and organic clasts and voids), the origin of sediments can be inferred, along with mode of deposition and post-depositional modification (Kubiëna 1938, Courty *et al.* 1989, Stoops 2003, Goldberg *et al.* 2009).

A total of six undisturbed sediment block samples were collected for soil micromorphology from a single stratigraphic column (Figure 5.2) (56 H 0309015 E, 6199655 S, UTM GDA94). All, except SP1, were collected using rectangular 5 x 10 cm aluminium downpipe, cut into 10 cm lengths. Sample SP1 was collected by cutting out a 5 x 5 x 10 cm block of sediment. The samples were wrapped in tissue

paper and sealed with packing tape to prevent disturbance and disintegration of the sample during transport to the laboratory.

The sediment block samples were prepared using techniques outlined in Courty *et al.* (1989). The blocks were oven dried at 60°C for at least one week and then impregnated with polyester resin, diluted with styrene in a ratio of 7:3, with 2-butanone peroxide ($C_8H_{16}O_4$) catalyst. The blocks were returned to the oven to cure before being cut into slabs ~1-2 cm thick. Thin sections, 50 x 75 mm, were processed at Spectrum Petrographics (Vancouver WA, USA). In total, 6 thin sections were observed in plane-polarised and cross-polarised light (PPL and XPL, respectively) at magnifications ranging from 0.63 to 4x with an Olympus SZ61 binocular microscope fitted with polarising filters and from 20 to 400x using an Olympus BX51 polarising binocular microscope with an Infinity-1, 1.3 megapixel colour digital camera attached. Descriptive nomenclature of thin sections followed that of Stoops (2003). Point counting of thin section constituents was conducted using the 'Point Counting' function in JMicroVision freeware package (Roduit 2013). Point counting was completed using a plain polarised light image of each sample measuring 2.2 by 1.6 cm, a recursive grid pattern and 500 points counted for each sample.

5.2.3 OSL DATING

OSL dating provides an estimate of the time since mineral grains such as quartz or feldspar were last exposed to sunlight (Huntley *et al.* 1985, Aitken 1998). The method is based on the increase in number of trapped electrons in mineral grains with increasing time after burial, in response to the energy supplied by background levels of ionizing radiation from environmental sources. The time elapsed since sediments were last exposed to sufficient sunlight to empty the relevant electron traps can be estimated from measurements of the OSL signal, together with determinations of the radioactivity of the sample and the material surrounding it to a distance of ~40 cm. The burial dose ('equivalent dose', D_e) can be measured using the OSL signal from a sample of sediment and represents the radiation dose to which sedimentary grains have been exposed in their burial environment. The dose rate (D_r)

represents the rate of exposure of these grains to ionizing radiation over the entire period of burial; this dose can be divided into 3 sources: 1) those internal to the mineral grains, 2) those found in the surrounding sediment matrix, and 3) those coming from cosmic-rays. The internal dose to quartz grains is derived from inclusions that contain trace amounts of ^{238}U, ^{235}U and ^{232}Th (and their radioactive daughters). The external dose is again derived from the radioactive decay of ^{238}U, ^{235}U, ^{232}Th (and their daughter products) but also includes a contribution from ^{40}K. The burial age of grains that were well bleached by sunlight at the time of deposition and remained undisturbed thereafter can be calculated by dividing the D_e by the D_r (Aitken 1998, Bøtter-Jensen *et al.* 2003, Duller 2004, Lian & Roberts 2006, Jacobs & Roberts 2007). Further information regarding sample collection and prepartion, D_e measurement and D_r evaluation are presented in Supplemenetary Material (Seciton 5.7).

5.3 RESULTS AND INTERPRETATION

5.3.1 FIELD DESCRIPTION AND GRAIN SIZE ANALYSIS

The currently exposed ~2 m high profile (Figure 5.2) is comprised of a basal clay-rich sediment unit (~0.7 m), capped by a quartz-rich sand unit (~1.3 m). This variation in sediment texture is also reflected in grain size distribution (Figure 5.3). The clay-rich sediment at the base of the profile can be divided into two layers, based primarily on colour. The bottom 0.5 m of exposed sediment consists of a dark bluish grey clay (Gley 2 4/5PB) with yellowish red (5YR 5/8) mottles (mottled mud). This layer is punctuated by numerous dark red (10R 3/6) to yellowish brown (10YR 5/8) nodules of iron oxides. The sediment is relatively poorly sorted, with mean grain size of <100 μm, but also contains significant amounts of sand and silt (Figure 5.3). The high clay content, coupled with modern-desiccation, has resulted in the opening up of surficial fissures and cracks producing a blocky pedality.

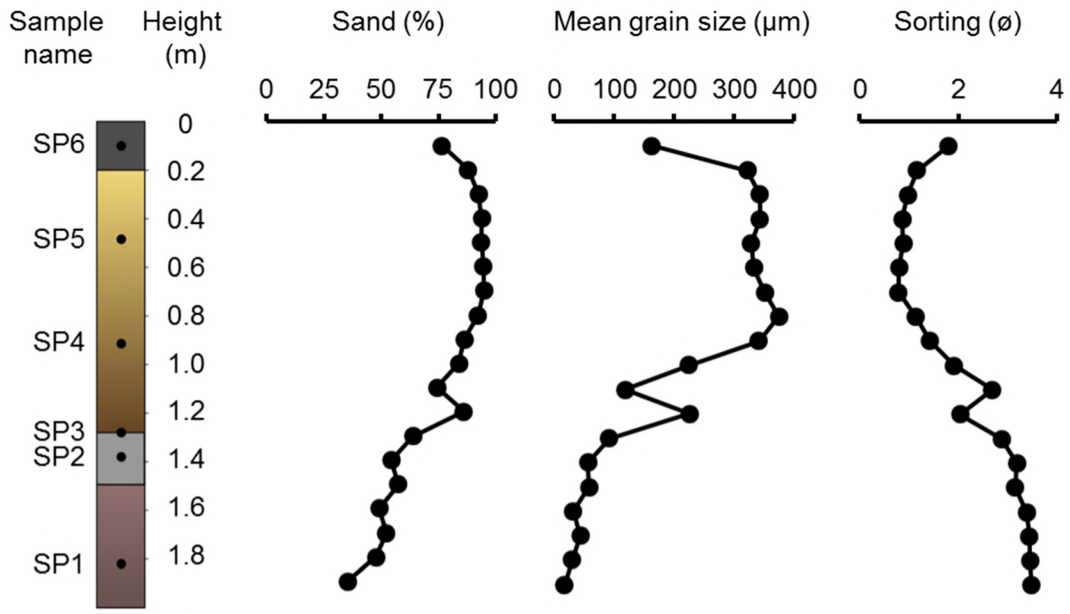

Figure 5.3. Stratigraphic column and grain size analysis results from the MacCauley's Beach profile. Lithostratigraphic units of Bryant *et al.* (1992b), in ascending order: 1) Pleistocene estuarine clay incorporating mottled (1.5 to 2.0 m) and less mottled (1.3 to 1.5 m) layers, 2) dune humate (0.9 to 1.3 m), and 3) raised Holocene beach (0.0 to 0.9 m). The current beach face intersects the stratigraphic section at 2.0 m depth. The sand fraction is defined as those grains with a diameter greater than 63 µm and less than 2 mm. Mean grain size shows a relatively constant decrease with depth down profile. The standard deviation is a proxy of sedimentary sorting and given in phi (ø) units. The greater the standard deviation, the more poorly sorted the sediment. The sample collected from 1.2 m depth is not representative of the sediments at this level as this sample was collected within the vicinity of an ant nest.

The mottled mud grades upward into a ~0.2 m thick indurated, greyish brown (2.5Y 5/2) sandy mud, containing a high number of charcoal fragments (<5 mm) and numerous nodules similar in colour to those of the underlying mottled mud (grey mud). It should be noted that this unit reaches higher elevations towards the southern end of the beach where it eventually pinches out. Beyond this point the sand-dominated unit sits directly on top of the mottled mud. At the current sedimentary

section, the top of this unit become less indurated and grades into more sand-dominated sediment. The top of this transition zone, marked by brown colouration (7.5YR 5/2), defines the lower contact of ~1.3 m of quartz-rich sand.

The lowermost 0.7 m of the quartz-rich sand unit, equivalent to the 'dune humate' unit of Bryant *et al.* (1992b), is the most clay-rich of the quartz sand sediments and is punctuated by numerous pebbles and cobbles, and rounded clasts of indurated darker brown sands (brown sands). The brown sands are overlain by 0.4 m of greyish brown (10YR 5/2) sands with very little clay content (equivalent to the raised Holocene beach unit of Bryant *et al.* 1992b) (clean sands). The entire sequence is capped by 0.2 m of dark grey (10YR 4/1) organic-rich sand (black sand). Grain size analysis reveals that the sediment is relatively well sorted with mean grain sizes of >100 μm and that the amount of sand remains fairly constant throughout the upper 1.3 m of the profile (Figure 5.3).

5.3.2 SOIL MICROMORPHOLOGY RESULTS

In the following sections the general sedimentary components of the deposit are described. Table 1 presents a summary of the features outlined below, and detailed observations of each of the six samples are provided in Supporting Material.

5.3.2.1 SAND SIZE FRACTION

The sand-sized fraction can be divided into two categories: siliciclastic and biogenic. The siliciclastic component is dominated by ubiquitous quartz sand. The sorting and roundedness of the sand-size fraction reveals a distinct change between samples SP4 and SP3 (Figure 5.4a and 5.4b). This trend is also reflected in the grain size analysis results (Figure 5.3). The three lowermost samples (SP1–SP3) are more poorly sorted (Figures 5.4a, c to f) relative to the three uppermost samples (SP4–SP6) (Figures 5.4b, g and h). Additionally, the rounding of the sand grains changes

Table 5.1. Sedimentary characteristics and soil micromorphological features as determined by thin section analysis.

Sample name	Sorting	Rounding	Coarse fraction						Fine Fraction	Textural pedofeatures		
			Quartz	Heavy Minerals	Calcite	Coal	Charcoal	Rootlets		Complex Void coatings	Nodules	Intercalations
SP6	Poor	Subrounded to rounded	X	X	X	X	X	X	Impure dark brown to black clays forming coatings and bridges			
SP5	Well sorted	Subrounded to rounded	X	X	X			X	Thin impure clay coatings of grains			
SP4	Moderate	Subrounded to rounded	X	X	X			X	Dark brown, impure to dusty clay coatings			
SP3	Poor	Subangular to subrounded	X	X			X	X	Speckled, dark brown to light grey impure clay	X	X	
SP2	Poor	Subangular to subrounded	X	X			X	X	Light grey clay	X	X	
SP1	Poor	Subangular to subrounded	X	X					Poro- and granostriated b-fabric		X	X

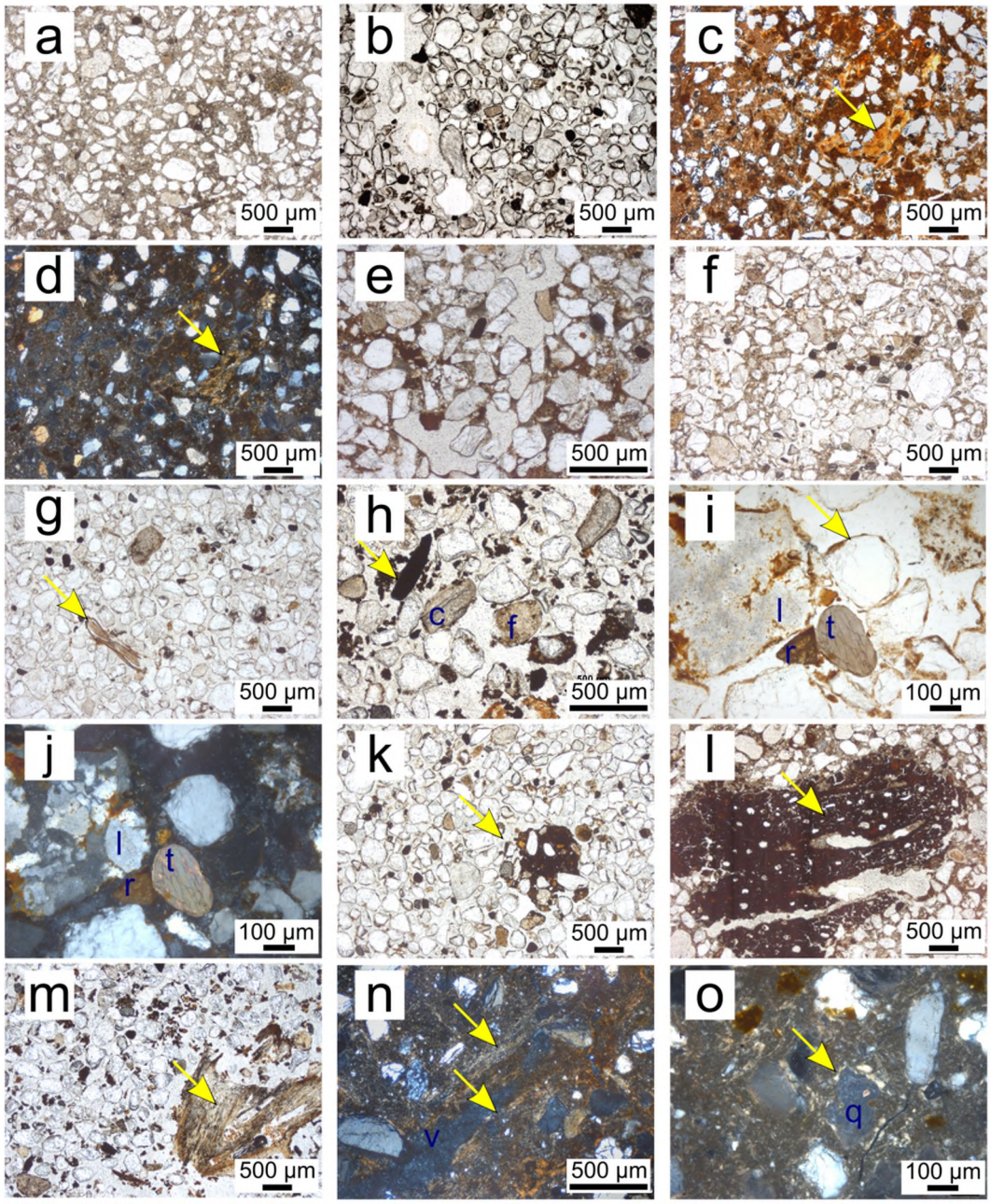

Figure 5.4. Thin section microphotographs of resin-impregnated sediment samples from MacCauley's Beach. **a)** SP3 – poorly sorted quartz sand and silt in a light grey, undifferentiated clay groundmass. Image is of the lower part of SP3 thin section (plane-polarised light; ppl). **b)** SP4 – moderately sorted quartz sand and few heavy minerals. Of particular note are the continuous clay coatings around the sand (ppl). **c)** SP1 – coarse fraction comprised of predominantly of quartz sands with clay groundmass that is more iron stained towards the right than the left of the image. Arrow indicates the location of simple intercalation with distinctive colour difference

to that of surrounding groundmass (ppl). **d)** as in a) but in cross-polarised light (xpl). Arrow indicates the simple intercalation with well-developed b-fabric suggesting slow eluviation of clay from further up profile. **e)** SP2 – polyconcave voids with poorly sorted quartz sand and silt and few heavy minerals (ppl).**f)** SP3 – as in a) but note the browner colour of the clay groundmasses this is from the top of the thin section with the sample collected along the transition zone between the greyish brown sandy mud and overlying brown sand (ppl). **g)** SP5 – moderately sorted quartz sands and silts. Arrow indicates a rootlet (ppl). **h)** SP6 – samples coming from the top of the raised beach unit, comprising of quartz sands with few calcite (c) and feldspar (f) grains. Arrow indicates rounded coal fragment. Note the clay fraction here is present as black-stained crumb between the coarse fraction and coating some of the finer grains (ppl). **i)** SP4 – Heavy mineral fraction from within the upper sand unit; rutile (r), tourmaline group species (t) and lithic fragment (l). Arrow indicates clay coatings (ppl). **j)** as in i) but in xpl. **k)** SP4 – anorthic, iron oxide nodule comprised of quartz sand and silt in an iron stained clay groundmass (ppl). **l)** SP2 – charcoal fragment with silty clay coating of tubule voids (ppl). **m)** SP6 – rootlet with mite activity indicated by arrow (ppl). **n)** SP1 – fissure void (v) with moderately developed porostriated and parallel-striated b-fabric along both sides of fissure, indicative of shrink and swell processes (xpl). **o)** SP1 – granostriated b-fabric surrounding a quartz (q) grain, moderate iron staining present in top left hand corner of image but groundmass mostly devoid of iron (xpl).

from more sub-rounded/sub-angular below sample SP3, becoming more rounded/sub-rounded in the three uppermost samples. Point counting of thin sections reveals the abundance of heavy mineral grains increases above the upper surface of the clay-rich sediments at ~1.3 m depth (Table 5.2). The stratigraphically highest sample (SP6) contains the smallest proportion of heavy minerals (0.8%). Non-opaque heavy mineral species include rutile, zircon and tourmaline-group minerals (Figures 5.4i and j), some of which are undergoing dissolution, with preferential weathering occurring along cleavage planes. Opaque heavy minerals include ilmenite, hematite and pyrite. Lithic fragments are very few (<0.2%), and comprise of subrounded to rounded feldspar-bearing lithologies and iron-stained micro-

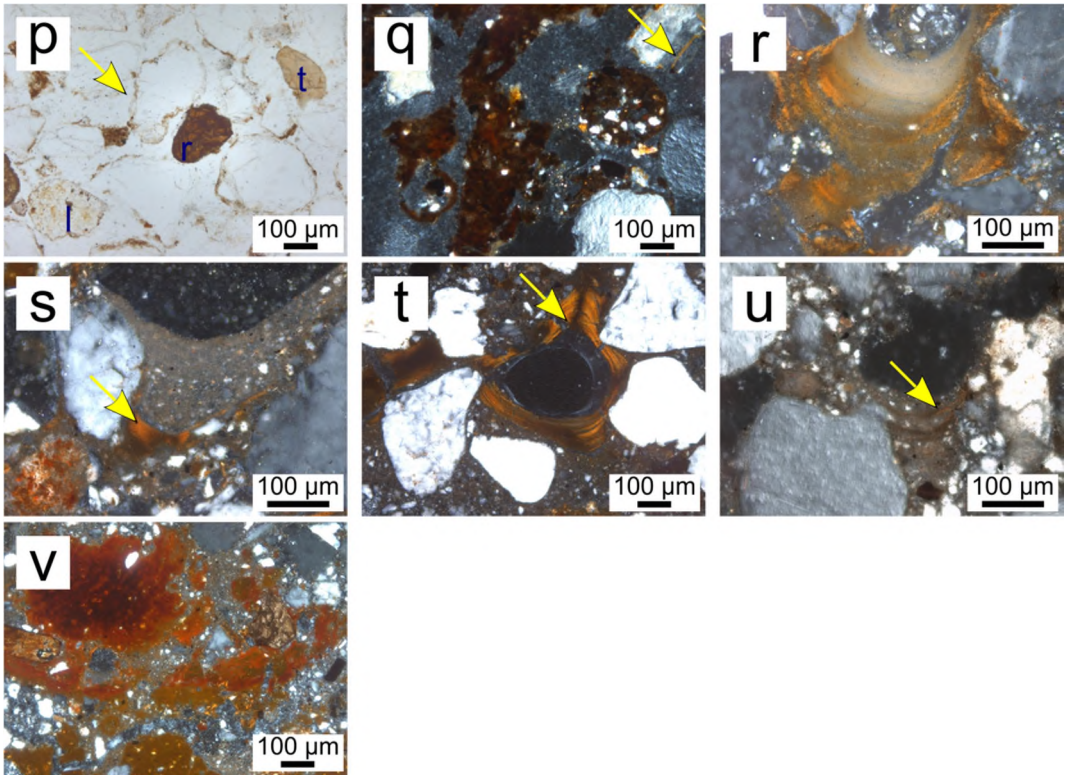

Figure 5.4 (continued). **p)** SP5 – heavy mineral fraction with rutile (r), tourmaline group (t) and microcrystalline quartz lithic fragment (l). Note the discontinuous clay coatings surrounding the coarse fraction indicated by arrow (ppl). **q)** SP6 – clay is stained dark brown to black and embedded with quartz silts and organic fragments. Arrow indicates clay coating of quartz sand grain (xpl). **r)** SP2 – complex, layered void coating shows rhythmic deposition of iron-stained limpid clays (red-orange) with dusty and silty clay (buff grey) (xpl). **s)** SP2 – complex, layered void coating, arrow indicates thick limpid clay layer with wavy extinction lines, overlain by more silt-rich sediments (xpl). **t)** SP2 – iron-stained laminated limpid clay void coatings indicative of low energy eluviation of material. Note the sharp extinction line indicated by arrow (xpl). **u)** SP3 – predominantly silty void coatings with some thin limpid clay layers indicated by arrow (xpl). **v)** SP2 – moderately impregnative orthic iron and manganese nodule (xpl).

crystalline quartz (probably jasper). The occurrence of anorthic nodules of iron and manganese is restricted to samples SP4,SP5 and SP6 (Figures 5.4k). These nodules are equidimensional and contain subangular to subrounded sand and silt in an iron-

stained clay matrix. Coal and charcoal fragments, rootlets and carbonate grains constitute the biogenic components observed at MacCauley's Beach. The presence of coal is exclusive to sample SP6, coming from the organic-rich black sands (Figures 5.4h), and appears as black, opaque, subangular to subrounded clasts, ranging in size from fine to medium sand. Charcoal fragments are distinguished from coal by the preservation of vascular tubules often filled with fine sediments and coated in iron-stained clays and found only in samples SP2, SP3 and SP6 (Figures 5.4l). Rootlets are found in all samples except SP1 (Figures 5.4g and m). Sparry calcium carbonate grains are found only in sample SP6 as subrounded to rounded grains of fine to medium sand (Figure 5.4h).

5.3.2.2 Silt and clay fraction

The silt and clay fraction is considerably more variable than the sand-sized fraction. The silt-sized component is more abundant in the basal three samples (SP1–SP3), with the mineralogy mirroring that of the sand-sized fraction. In these samples, the silt grains are found encased in the surrounding clay matrix. For samples collected higher in the profile (SP4–SP6), the silt grains are found either as individual grains (when the clay fraction is absent, SP5) or incorporated into clay coatings (when clay fraction is present, SP4).

The clay fraction varies in both colour and abundance with depth. In the lowermost 0.7 m of the profile, the silt and clay particles represents roughly half of the total grain size distribution (Figure 5.3) and is supported in the point counting data (Table 5.2), resulting in matrix-supported sediment. The clay in sample SP1 (Figure 5.4c) shows a marked difference in colouration moving from red into grey.

Also, the development of b-fabric (the pattern of orientation of the clays and resulting distribution of interference colours in the fine fraction; Stoops 2003) is found only in sample SP1. Here the clay has a well-developed poro- and granostriated b-fabric (Figure 5.4n and o).The clay in SP2, in contrast, is uniformly grey, as is sample SP3 (Figures 5.4a and f), collected at the contact between the grey

Table 5.2. JMicroVision point counting results for the six thin sections analysed in this study.

Sample	Quartz/Feldspar[a]	Clay[b]	Void	Heavy minerals	Lithic fragments	Charcoal/Coal	Calcite
SP6	42.00	9.00	42.00	0.80	0.60	4.40	1.20
SP5	64.00	-	32.00	3.40	0.80	-	-
SP4	61.60	-	32.20	3.80	2.00	-	-
SP3	60.20	30.40	7.60	1.40	0.40	-	-
SP2	41.52	43.31	10.58	1.20	0.80	2.59	-
SP1	29.80	65.00	3.40	1.20	0.60	-	-

[a] The quartz and feldspar minerals have been categorised together due to the inability to differentiate between these minerals (particularly quartz and orthoclase) at the resolution used.

[b] The clay fraction of samples SP4 and SP5 were not counted because the thin clay coatings surrounding larger grains could not be resolved at the resolution used.

mud and brown sands. In sample SP4, at a depth of 0.9 m, the silts and clay grain size fraction are found as 3–6 μm thick coatings surrounding the larger sand-sized particles (Figure 5.4b). In contrast, the clay fraction of SP5 is found as thin (<1 μm) discontinuous coatings surrounding only the larger sand grains (Figure 5.4p). Sample SP6 contains dark brown to black clay. Here the clay is found as aggregates with quartz silt, or as coatings around grains (Figure 5.4q).

5.3.2.3 PEDOFEATURES

A number of pedofeatures are found in the samples from MacCauley's Beach. These features consist of: 1) void coatings and infillings, 2) intercalations, and 3) redoximorphic features. Void coatings are restricted to samples SP2 and SP3 in the grey mud layer. These complex void coatings and infillings are comprised of rhythmically interbedded, iron-stained and laminated limpid clay coatings with dusty clay and silt lenses (Figures 5.4r–u). Intercalations are found only in sample SP1, where large domains of clay exhibit moderate orientation. These clays contrast with those of the surrounding groundmass, being yellow and without striated b-fabrics (Figures 5.4c and d). Redoximorphic features are found within the three lowermost samples, SP1, SP2 and SP3 (Figure 5.2) coming from the grey and mottled mud layers. The redoximorphic features of SP1 from the mottled mud contain iron-depleted hypocoatings and impregnative orthic sesquioxide nodules (Figure 5.4k). A number of domains surrounding the fissures within this sample have been depleted in iron oxides, resulting in buff-coloured clay domains (Figures 5.4n). The redoximorphic features in samples SP2 and SP3, from the grey mud, consist of moderately to strongly impregnative orthic iron nodules, similar to those in the underlying sample SP1 (Figure 5.4v).

5.3.3 OSL DATING

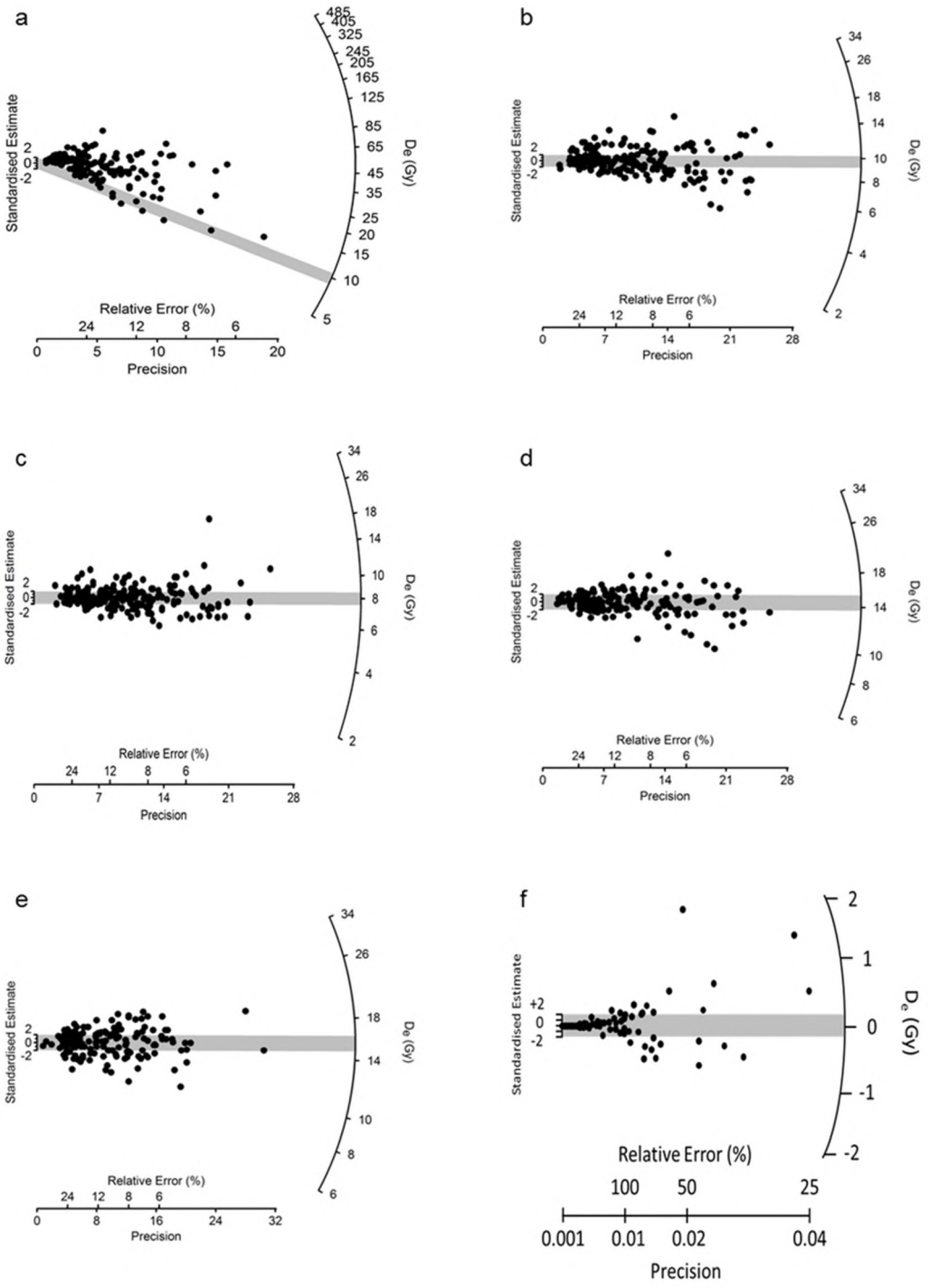

Figure 5.5. Radial plots of single-grain D_e distributions for all six samples collected from MacCauley's Beach. If the D_e estimates in each distribution were statistically consistent (at 2σ) with a common value, then 95% of the points should fall within any grey band projecting ± 2 units from the standardised estimate axis. The D_e values of all samples are more dispersed than this (see text). The OSL ages were

estimated using the central age model (CAM), except (a) for which the minimum D_e values were calculated. The grey bands are centred on the CAM weighted mean D_e values, except (a), and specified in Table 5.3. a) SP1, b) SP2, c)SP3, d) SP4, e) SP5, and f) SP6.

The results of the OSL study, including D_e, D_r and OSL ages are presented in Table 5.3. In this study, 4400 individual sand-sized grains of quartz were measured. Of these grains, between 16 and 35% of those measured for each of the samples were accepted for D_e determination (Table S5.1). The D_e values estimated for the accepted grains (N=1010; ~23% of the total grains measured) were deemed to be meaningful in terms of the dose absorbed during burial. The accepted D_e values from each sample are displayed as radial plots (Galbraith 1990) in Figures 5.5a to f. Such plots aid in the visual assessment of the D_e distribution patterns, and are used to help determine which statistical model to use in order to combine the individual D_e values meaningfully for final age determination (e.g., Jacobs & Roberts 2007).

If all grains were deposited at the same time, had their signals completely reset prior to burial, were exposed to a uniform radiation fields and remained undisturbed thereafter, then each independent estimate of D_e should be consistent with statistical expectations. This means that, on a radial plot, 95% of the D_e values should scatter within a band of width ±2 units projecting from the left-hand ("standardised estimate") axis to any chosen D_e value on the right-hand, radial axis (Figure 5.5). This may not be true if all quantifiable uncertainties are not correctly accounted for, or the variability in intrinsic luminescence characteristics is not sufficiently explained. We believe that the overdispersion (OD) values of 9 ± 2% and 8 ± 3% obtained from our dose recovery experiments at 12 and 105 Gy, respectively, (Figure S5.2) provide a *minimum* estimate for the OD that can be measured under laboratory conditions. The OD within a given sample needs to be quantified and should be included in the uncertainty estimates of the D_e. The central age model (CAM) of Galbraith *et al.* (1999) takes this into account (see Supplementary Material Section 5.7.1 for details).

It is, however, apparent from the radial plots in Figure 5.5 that all the samples (except SP6: 6 ± 14%) show a larger spread in D_e values than observed in the dose recovery tests; OD values range from 27 ± 2 (SP4) to 87 ± 5% (SP1) (Table 5.3). This 'additional' OD (beyond the ~10% obtained for the dose recovery tests) is commonly assumed to be due to extrinsic factors such as the incomplete removal of charge from electron traps ('partial bleaching') prior to deposition (Olley *et al.* 1999), mixing of different age grains after burial, either as a discrete event(s) or on a continuous basis (e.g., bio- or pedo-turbation) (Bateman *et al.* 2007a, Bateman *et al.* 2007b, David *et al.* 2007), and variations in millimetre scale beta dose delivered to individual grains (Murray & Roberts 1997, Olley *et al.* 1997, Nathan *et al.* 2003, Guérin *et al.* 2012). A detailed understanding of the depositional and burial history of the sediments is, thus, imperative where the pre-, syn- and post-depositional processes may all influence the accuracy and precision of the resulting OSL age estimates. To improve our understanding and better inform our interpretations of the D_e distributions we have examined each D_e data set in tandem with its corresponding micromorphological results. We used this information to determine how to meaningfully combine the individual D_e values for age determination. Our interpretations and decisions are discussed below for each of the samples.

5.3.3.1 Sample SP1 at 1.8 m below current ground surface – mottled mud (Figure 5.3)

The distribution of D_e values for sample SP1 show the largest OD (87 ± 5%). The radial plot shows a continuous smear of D_e values ranging from ~6 to ~400 Gy (Figure 5.5a). Micromorphological analysis of this sample showed the presence of poro- and granostriated b-fabrics (Figures 5.4n and o), a diagnostic feature produced by shrink and swell processes in soils with vertic properties and associated with pedoturbation (Yaalon & Kalmar 1978). The striated b-fabrics also suggests that a series of fissure cracks were periodically opening and closing in this sediment (Kovda & Mermut 2010), which may have allowed material to be incorporated into the sediments from the then land surface. The lack of any D_e values <6 Gy, however, suggests that this process is not currently operating at the site and that the

incorporation of modern grains into the sediment is no longer taking place. From the sedimentological data, it is clear that the original depositional environment for this sample was within the central mud basin facies of a barrier estuary. Thus, partial bleaching of the sediment and subsequent bioturbation of the deposit also potentially occurred, further contributing to the complex D_e distribution pattern obtained for sample SP1.

The original depositional age of the mottled mud sediments cannot be determined with accuracy. Only a minimum D_e value for this sample can be estimated to determine when pedoturbation may have terminated. We used the 3-parameter minimum age model (MAM) of Galbraith *et al.* (1999), and added in quadrature an additional 40% to the uncertainty of each D_e value (based on the OD of the overlying samples that are thought to be well-bleached) prior to running the model to allow for additional overdispersion that would be present in a well-bleached sample and that would otherwise be taken into account using the central age model (CAM) of Galbraith *et al.* (1999).

Table 5.3. Results of the single-grain OSL investigation carried out at MacCauley's Beach. The dose rate components and ages of sample SP5 marked with an (*) were obtained using high resolution gamma spectrometry measurements.

Sample Code	Field and (mean ± 1σ) moisture content (%)[a]	Dose rate (Gy/ka)[b]			Total Dose Rate (Gy/ka)[c]	Number of Grains (N)[d]	D_e (Gy)[e]	Age Model[f]	Over-dispersion (%)	OSL age (ka)[g]
		Gamma	Beta	Cosmic						
SP6	11 (9 ± 2)	0.80 ± 0.03	0.82 ± 0.05	0.19 ± 0.02	1.91 ± 0.10	105	0.02 ± 0.04	UCAM	6 ± 14	0.01 ± 0.02
SP5	4 (5 ± 1.3)	1.16 ± 0.05 0.95 ± 0.02*	0.92 ± 0.07 0.74 ± 0.03*	0.19 ± 0.02 0.19 ± 0.02	2.37 ± 0.13 1.98 ± 0.06*	170	15.62 ± 0.46	CAM	35 ± 2	6.60 ± 0.42 7.90 ± 0.38*
SP4	7 (8 ± 2)	0.84 ± 0.04	0.82 ± 0.05	0.18 ± 0.02	1.94 ± 0.10	172	14.57 ± 0.34	CAM	27 ± 2	7.52 ± 0.44
SP3	14 (11 ± 3)	0.47 ± 0.02	0.32 ± 0.03	0.17 ± 0.02	1.05 ± 0.06	207	8.09 ± 0.21	CAM	36 ± 2	7.69 ± 0.52
SP2	13 (13 ± 3)	0.41 ± 0.02	0.31 ± 0.03	0.16 ± 0.02	0.99 ± 0.06	193	9.84 ± 0.30	CAM	40 ± 2	9.99 ± 0.71
SP1	29 (28 ± 7)	0.42 ± 0.02	0.33 ± 0.02	0.14 ± 0.01	0.99 ± 0.07	163	14.50 ± 2.40	MAM	87 ± 5	14.70 ± 2.69

a. Field water content was calculated as the % mass of water per unit of dried sediment. The dried dose rates were then adjusted to the weighted mean (± 1σ) water content for age determination. The weighted mean water content values were calculated using a number of samples collected over a period of 6 months from the time of sampling.

b. Measured and calculated dose rates ± (1σ). Gamma dose rate measured using a 2-inch gamma detector. Beta dose rate measured with a GM-25-5 beta counter using dried, powdered and homogenised sediment samples. Cosmic dose rate determined using the equations of Prescott & Hutton (1994) and assigned a ± 10% uncertainty.

c. Mean ± total (1σ) uncertainty. Uncertainty calculated as the quadratic sum of all known and estimated random and systematic uncertainties associated with each dose rate component. Total dose rate includes an assumed internal alpha dose rate value of 0.10 ± 0.02 Gy/ka for all samples; determined using thick-source alpha counting on a HF-etched sample of 180–212 µm quartz from sample SP2 and SP5, respectively.

d. The number of accepted grains used in the calculation of the sample D_e.

e. Mean ± total (1σ) uncertainty. The uncertainty of this term includes a ± 2% uncertainty associated with the calibration of the beta source irradiator.

f. Age models used in the determination of sample D_e. Where: MAM is the 3-parameter minimum age model; (U)CAM is the (unlogged) central age model. An additional 40% uncertainty was added in quadrature to each D_e value prior to running the MAM to account of overdispersion.

g. Mean ± total (1σ) uncertainty. Uncertainty calculated as the quadratic sum of the random and systematic uncertainties associated with D_e and dose rate estimates.

5.3.3.2 SAMPLE SP2 AT 1.4 M – GREY MUD (FIGURE 5.3)

The D_e distribution pattern and OD value of sample SP2 (Figure 5.5b), collected from the grey mud (Figure 5.2), is different to that obtained for SP1. The sample has an OD value of 40 ± 2% and has D_e values ranging between ~4 and ~34 Gy (Figure 5.5b). Visual assessment of the D_e distribution for SP2 reveals that the majority of grains are spread symmetrically around a central value with the exception of a few higher D_e values >25 Gy. Micromorphological evidence has shown that heavy mineral species associated with high concentrations of U, Th and K (such as rutile, zircon and feldspar-bearing lithic fragments) are present in small, but significant, quantities and distributed heterogeneously throughout the sample. This suggests that the effect of localised variations in the beta dose rate (i.e., beta microdosimetry) may be one possible cause for the wider spread in D_e values found for this sample. To test this, the fine sand-sized heavy mineral fraction (63–180 μm) was separated from a bulk sediment sample of SP2; this made up 0.5% of the total sample weight. A moisture content and grain size corrected beta dose rate of 8.31 ± 0.50 Gy/ka was measured for the heavy mineral separates using a GM-25-5 beta counter (Bøtter-Jensen & Mejdahl 1988); this means that 13% of the beta dose rate comes from only 0.5% of the grains. This may not have a significant effect on the overall beta dose rate, but quartz grains positioned close to these heavy mineral grains will have received a higher-than-average beta dose rate, resulting in a higher D_e value, compared to those located further away. We, thus, consider the sample well-bleached at deposition but affected by beta microdosimetry. Because our bulk sample beta dose rate includes all grains, the CAM weighted mean sample D_e was considered the most appropriate method of combining the individual D_e values for this sample.

5.3.3.3 SP3 AT 1.3 M – GREY MUD (FIGURE 5.3)

The D_e distribution, OD value (36 ± 2%), range of D_e values (~4 to 30 Gy), and shape of the radial plot (Figure 5.5c) is very similar to that of SP2. The D_e values

are spread almost symmetrically between 4 and 18 Gy, with a few values centred at ~30 Gy. The micromorphology of the sample shows a similar distribution and abundance of heavy mineral grains such as rutile, feldspar-bearing lithic fragments and zircon as was found for SP2 (Table 5.2). The similarities between this sample and SP2 are not surprising given that both samples were collected from the same layer (grey mud) and within 10 cm of each other. Our interpretation and method for combining the D_e value is the same as for SP2: using the CAM.

5.3.3.4 SP4 AT 0.9 M - BROWN SAND (FIGURE 5.3)

The range of D_e values (Figure 5.5d) for sample SP4 range from ~8 to 30 Gy, and the OD value is 27 ± 2% (Table 5.3). Micromorphology reveals that the sedimentology of this sample changed significantly from the underlying layers, becoming clast-supported rather than matrix-supported (Figures 5.4a and b). Different factors may, therefore, have influenced the shape of the radial plot and the amount of scatter in D_e values. The two major factors that may have contributed to the larger than expected scatter (OD) in the D_e values, is the presence of thick clay coatings (Figure 5.4i) found around individual quartz grains, and the increase in the abundance (3.8% of the total) of heavy minerals in this sample (Figures 5.4j; Table 5.2). So, it is again micro-scale differences in beta radiation received by individual grains that appears to be the primary cause of OD (Olley *et al.* 1997, Nathan *et al.* 2003). The most appropriate method of combining the individual D_e values is again thought to be the CAM.

5.3.3.5 SP5 AT 0.5 M – CLEAN SANDS (FIGURE 5.3)

The range of D_e values (Figure 5.5e) for sample SP5 is also between ~8 and 30 Gy, very similar to that of SP4. The calculated OD value of this sample is slightly higher at 35 ± 2% (Table 5.3). Like SP4, the random distribution of heavy minerals (Figure 5.4j and p) throughout the sample is the likely cause of scatter in D_e values due to the inhomogeneous distribution of the beta dose rate delivered to individual

grains. While the distribution of heavy minerals as a group may be random, not all minerals in this group are radioactive, or of equal radioactivity, meaning that this random distribution may be more regular than appreciated at face value. It is where the radioactively 'hot' minerals are spaced at 5 – 6 mm intervals, that the influence on beta dose heterogeneity is most apparent. Using a separate bulk sediment sample, the 63–180 μm heavy mineral fraction was separated (making up 2.9% of the total sample weight), powdered, homogenised and measured using the GM-25-5 beta counter, resulting in a beta dose rate of 22.0 ± 0.7 Gy/ka; this means that ~69% of the beta dose rate comes from only 2.9% of the grains. The clay coatings may also contribute to the beta micro-dosimetry effect, but they are much thinner (Figure 5.4p) in this sample compared to the brown sand sample (SP4). The individual D_e values were combined using CAM to obtain a weighted mean D_e.

5.3.3.6 SP6 AT 0.1 M – BLACK SANDS (FIGURE 5.3)

Sample SP6 was collected from the black sands at a depth of 10 cm below the modern day surface and contains a number of grains that have D_e values consistent with 0 Gy (Figure 5.5f) with large associated uncertainties. The OD of this sample was calculated to be 6 ± 14%. Given the presence of D_e values consistent with 0 Gy, D_e values were combined using the unlogged CAM (Arnold *et al.* 2009).

5.3.4 DOSE RATE RESULTS

D_r estimates are presented in Table 5.3. The moisture content estimates are the mean of multiple field values determined on sediment collected both at the time of sampling, and several months afterwards. The mottled and grey muds may have had higher moisture contents at the time of deposition. Thin section analysis, however, shows that these sediments have very little pore space; a saturated moisture content is accommodated within the 1σ limits of our estimate. In contrast, the brown, clean and black sands are more porous allowing water to rapidly drain through them. This difference is reflected in the distinct shift in moisture content across the grey

mud/brown sand boundary that appears to be linked with clay content (Figure 5.3; Table 5.2). The range of mean moisture content values for the site varies between 5 and 9% for sand dominated sediments (SP4, SP5 and SP6), and 11 to 28% for clay-rich samples (SP1, SP2 and SP3).

A comparison of the gamma dose rates determined using five independent methods are shown graphically in Figure S5.3 and are provided in Table S5.2. Good reproducibility has been obtained between all methods except when gamma dose rates were determined from concentrations of U, Th and K obtained from ICP-OES/MS measurements for all samples and high resolution gamma spectrometry (HRGS) for SP5. The discrepant ICP-OES/MS is thought to be the result of incomplete dissolution of uranium from the heavy mineral fraction in the samples, in particular highly resistant zircon and rutile grains (Intertek Genalysis Laboratory, pers. comm.). Those samples showing the biggest discrepancy (SP4 and SP5) are also the samples with the highest proportion of heavy minerals (Table 5.2; Figure S5.3).

The inconsistency with the HRGS for SP5 is attributed to of the presence of disequilibrium in the U-series in this sample. Further information regarding the HRGS results is presented in Supplementary Material and Table S5.3. We have chosen to use the gamma dose rates derived using the 2-inch gamma detector for age determination because this was measured at the point of sampling and would take into account any inhomogeneity present in the gamma dose sphere of influence. Substituting the gamma dose rates derived from any of the other methods (except ICP-OES/MS and HRGS for SP5), give ages that are statistically consistent with the ages presented in Table 5.3. The OSL age for SP5 determined using HRGS for both beta and gamma dose rate is also given in Table 5.3 to show the effect that U-series disequilibrium has on the age of this sample. The severity, cause and discussion of the disequilibrium effects are discussed in section 5.7.1.3.

The beta and gamma D_r values for the site also reveal a dichotomy between the clay-rich and sand-dominated sediments. The three lowermost samples (SP1–SP3) have D_r values of between 0.92 ± 0.06 and 1.03 ± 0.09 Gy/ka. In contrast, the

sand-dominated samples (SP4–SP5) have D_r values roughly double those of the underlying clay-dominated samples, ranging from 1.87 ± 0.11 to 2.41 ± 0.14 Gy/ka. It is thought that the silt and clay matrix of SP1 to SP3 dominates the D_r for these samples whilst, in SP4 and SP5, it is the heavy mineral fraction that provides the majority of the D_r (Figures 5.4a and 4g).

5.3.5 OSL AGE ESTIMATES AND COMPARISONS WITH EXISTING CHRONOLOGY

Single-grain OSL ages for six samples were calculated by dividing the sample D_e values by their corresponding D_r. These ages, and their 1σ uncertainties, are presented in Table 5.3. The uncertainties were calculated by combining in quadrature all known and estimated uncertainties.

We demonstrated a complex burial history for the basal mottled mud unit and could not obtain an age for its initial deposition. Based on our interpretation of the burial history of this sediment we believe that the TL ages of 71 ± 23 and 45 ± 17 ka presented in Bryant *et al.* (1992b) are not meaningful. Instead, these ages represent the mean of many grains with different burial histories and should be discarded as it is not dating the target event (i.e., original deposition of the unit). The age of the original depositional event of this unit, thus, remains unknown. Instead, we obtained a minimum age for the mottled mud (SP1) to determine that the last incorporation of material into the unit occurred on the Pleistocene/Holocene boundary at 14.7 ± 2.7 ka ago, which is also the maximum age for the overlying grey mud unit, for which an age of 10.0 ± 0.7 ka was obtained for sample SP2 near its base. Sample SP3, collected from near the top of the grey mud gave an OSL age of 7.7 ± 0.5 ka.

The open-system U-series ages of 21.3 ± 3.8 and 19.7 $\pm \frac{3.2}{3.4}$ ka for the beach rock are also considered unreliable. No spatial reference beyond ~5 m further towards the ocean is given, so the context of these ages remains unclear. Additionally, the open geochemical system of the beach rock, in essence a pedogenic

carbonate, would readily allow U uptake or leaching over time. These ages should be treated with caution until confirmed by alternative methods (Blackwell & Schwarcz 1995).

We obtained an age of 7.5 ± 0.4 ka for sample SP4 from the brown sand unit, which is inconsistent with the previous TL ages of 32.7 ± 8.0 and 25.3 ± 6.4 ka obtained for the 'dune humate' unit of Bryant *et al.* (1992b). There are two possible explanations: 1) the sediments sampled by Bryant *et al.* (1992b) were not sampled in this study and may still be preserved elsewhere, or 2) the TL traps were not completely emptied prior to burial, resulting in an age overestimate. The ages of sample SP2 and SP3 suggests that the final deposition of the grey mud unit occurred at 7.7 ± 0.5 ka. If this conclusion is correct, the age of the overlying 'dune humate' unit is required to be younger than this age, which is not the case. It appears as though the second of these two possibilities (incomplete bleaching) is best supported by our new data.

The age of the sample collected from SP5 in the clean sands gave an OSL age of 6.6 ± 0.4 ka, and is consistent with the corresponding TL age of 6.1 ± 1.4 ka (Bryant *et al.* 1992b). If however, we take into account the disequilibrium in the U-series for the SP5 sample and assume that this has been the case over the sample's entire burial period, an age of 7.9 ± 0.4 ka is obtained. Although the older SP5 OSL age is inconsistent with the former, it is, however, consistent with the TL age of Bryant *et al.* (1992b). Finally, an age of 10 ± 20 years was obtained for the sample coming from the black sand (SP6) collected from the top of the MacCauley's Beach sediment profile (Figure 5.2).

The initial chronological investigation carried out by Bryant *et al.* (1992b) was innovative at the time of publication. We were able to expand that investigation by providing greater resolution in time and space and a more detailed understanding of the site formation processes, resulting in a more accurate and precise chronology.

5.4 DISCUSSION

The sampling strategy employed in this study allows sediments to be placed in context in terms of time, space and depositional processes. This method of investigation, therefore, provides a more detailed understanding of the processes involved in site formation. In the following section, we describe the formation of the site in four broad stages. Each stage is also schematically presented (not to scale) in Figure 5.6(I-IV).

5.4.1 STAGE IA– DEPOSITION OF THE MOTTLED MUD UNIT

Although the timing of the original depositional event for the mottled mud unit cannot be accurately determined, it is hypothesised that this unit was laid down during MIS 5e (~125 ka). It is thought that a bay barrier, akin to the present-day barrier found at nearby Lake Illawarra (Figure 5.1), was in place at this time (Figure 5.6(Ia)), enclosing what is now MacCauley's Beach and allowing the deposition of the clay-rich sediments in a low-energy lagoonal setting. The exact location and nature of this Pleistocene barrier cannot be determined; no evidence for Pleistocene-age barrier sediments was identified in this study, or has been reported previously for MacCauley's Beach.

The assignation of the mottled mud unit to MIS 5 is drawn from three lines of evidence: 1) the physical context of the MacCauley's Beach mottled mud unit, 2) similarities that this unit shares with those at nearby locations, and 3) the presence of Pleistocene-age barrier sediments at similar settings further south along the coastline.

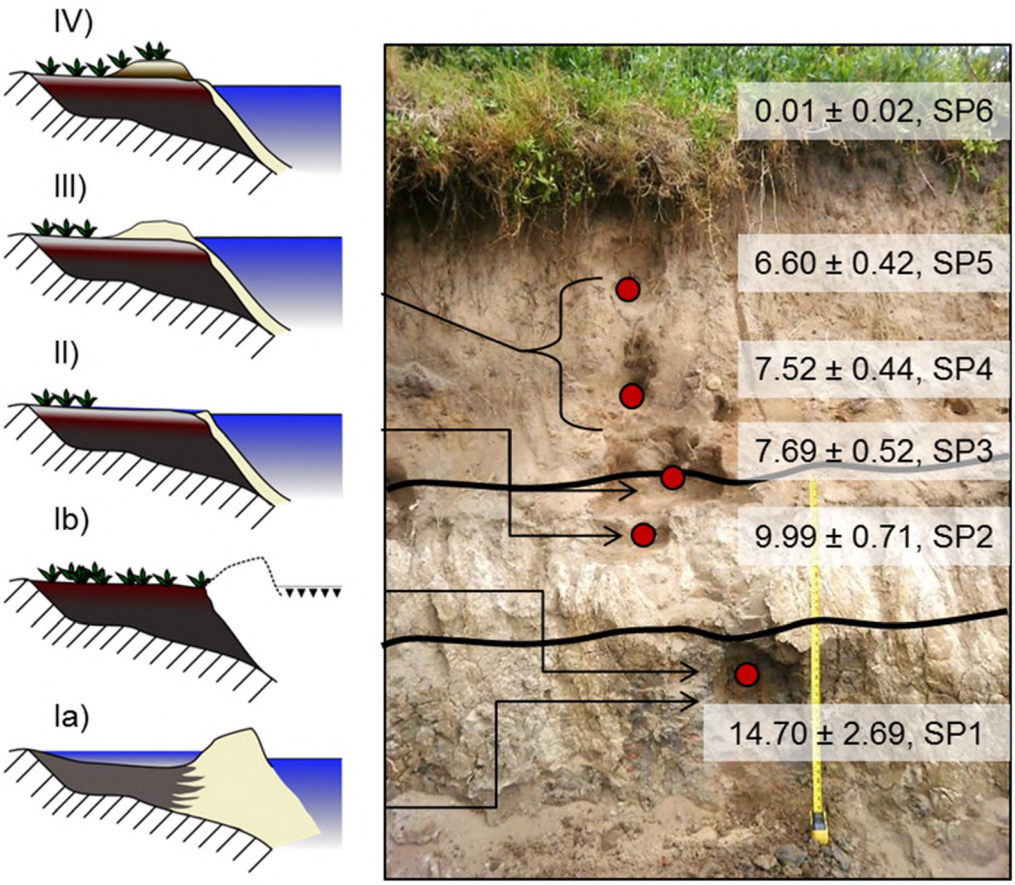

Figure 5.6. OSL chronology and site formation history for MacCauley's Beach. Section photograph shows the positions of soil micromorphology and OSL samples. OSL ages (in ka) are reported at ± 1σ. The thick black lines delimit the contact between the mottled mud, grey mud and overlying sand units. Schematic drawings (not to scale) to the left of the stratigraphic column show formation history for the site as determined from micromorphology and the associated single-grain OSL ages (see text).

The upper contact of the mottled mud unit at MacCauley's Beach was determined to have a maximum elevation of 3.5 m above PMSL, levelling off to a height of 2.5 m above PMSL (Bryant *et al.* 1992b). This height is consistent with other Pleistocene-aged (MIS 5) platforms in the Illawarra region (Bryant 1992a). Analogous mottled mud units to that found at MacCauley's Beach have reported by Jones *et al.* (1979) from South Thirroul and North Bulli also have erosive upper contacts that reach

elevations of 5 m above PMSL and considered to be MIS 5 in age. For the central mud basin facies to be deposited at this elevation requires sea level to be at an equivalent height, which, along the NSW coastline, was last at this elevation during MIS 5 (Murray-Wallace & Belperio 1991). Similar mottled, and deeply incised and weathered, mud facies of MIS 5 age and associated eroded barrier sediments, both underlying Holocene material, have also been found at Lake Illawarra (Sloss *et al.* 2006a), Lake Conjola (Sloss *et al.* 2010) and Narrawallee Inlet (Nichol & Murray-Wallace 1992), all located further south along the NSW coastline.

5.4.2 Stage Ib – incision and exposure of the central basin mud facies

By the LGM, sea level has regressed by ~120–130 m PMSL (Murray-Wallace *et al.* 2005) as a function of oceanic waters being locked up into large continental ice sheets. Murray-Wallace *et al.* (2005) concluded that along the NSW coastline this regression in sea level resulted in a lowering of sea level by between 120 to 130 m PMSL and a concomitant shift of the coastline ~20 km to the east compared to its current position. We argue that this would have affected the configuration of the MacCauley's Beach site in two important ways.

First, the fall in sea level would have caused the Tramway and Woodlands Creeks to erode the surface of, and incise into, the mottled mud unit and moving the active zone of sediment deposition to the re-established sea level baseline ~20 km away. Dendritic incision patterns have previously been reported for the upper surface of MIS 5-aged muds from Lake Illawarra (Sloss *et al.* 2006a). At MacCauley's Beach, although it not visible, it is likely that the Tramway and Woodlands Creeks incised at the northern end of the beach where these streams currently drain from the small back barrier lagoon. Second, the regression of sea level resulted in the destruction of the MIS 5 barrier. Intensification of westerly (offshore) trade winds during the LGM would have actively reworked the barrier sediments onto the continental shelf, having removed the source of sediment for barrier construction

(Bowler 1976, Roy & Thom 1981). This aeolian reworking was possibly enhanced by fluvial processes associated with the Tramway and Woodland Creeks.

The incision of the mottled mud and removal of the Pleistocene barrier system ultimately resulted in the draining and subaerial exposure of the central mud basin facies (Figure 5.6(Ib)). Exposure of the clay-rich, mud basin sediments led to extensive pedogenesis. Evidence for pedogenesis includes: 1) absence of bedding structures (such as laminations or sand lenses) that would be expected in a low-energy depositional environment of a back-barrier lagoon; and 2) well-developed poro- and grano-striated b-fabrics in the clay matrix (Figures 5.4n and o) surrounding both sediment voids and sand-sized grains. These features have previously been linked to swell-shrink processes occurring within clay-rich soils due to cyclical wetting and drying (Yaalon & Kalmar 1978). Such processes are also associated with surficial cracking and development of large fissures, diagnostics typical of soils with vertic properties (Mermut *et al.* 1988, Kovda & Mermut 2010). Thus, pedoturbation, due to cyclical wetting and drying of sediments, is considered to have incorporated surface material into the soil through surface cracks, but also to have churned previously deposited and buried soil material towards the surface. The wetting and drying of the sediment also allowed the development of redoximorphic features such as the impregnative orthic sesquioxide nodules (Figure 5.4v), most probably through the oxidation of pyrite, giving the sediment its distinctive red/yellow mottles (Figures 5.1 and 5.6(Ib)). Single-grain OSL dating of SP1 (Figure 5.5, Table 5.2) suggests that the period of pedogenesis, as seen in the D_e distribution pattern (Figure 5.5a) and the soil micromorphological results (Figure 5.4d), terminated near the Holocene/Pleistocene boundary at 14.7 ± 2.7 ka. This age further supported by the concordant single-grain OSL age for the overlying grey mud unit of 10.0 ± 0.7 ka (SP2) (Figure 5.6, Table 5.2).

5.4.3 Stage II – deposition and formation of the grey mud unit

The origin of the grey mud (Figure 5.3 and 5.6(II)) has never been established in previous publications for MacCauley's Beach (Bryant *et al.* 1992b). The two samples collected from the grey mud unit gave depositional ages of 10.0 ± 0.7 (SP2) and 7.7 ± 0.5 ka (SP3). Over this time period (10–7 ka ago), sea level gradually transgressed from -50 m below PSML to PMSL. Soil micromorphological analysis of these sediments revealed the presence of complex, rhythmic void coatings, redoximorphic sesquioxide nodules, and significant amounts of charcoal and rootlets (particularly at the base of the unit). Grain roundness is consistent with the mottled mud unit (subangular to subrounded), but heavy mineral species like rutile and zircon (Figure 5.4v) appear in greater abundance and are typically associated with sediments derived from the continental shelf (Roy & Crawford 1977, Roy & Thom 1981).

It is argued that the grey mud unit was produced from the hydromorphic reorganisation and reworking of the mottled mud unit in conjunction with sediment inputs coming from the continental shelf; the latter process become more important over time. The association of charcoal, sesquioxide nodules and complex, rhythmic void coatings have previously been documented for marine-inundated Holocene archaeological sites in the United Kingdom (Allen *et al.* 2002, Goldberg & Macphail, 2006, Macphail *et al.* 2010). Furthermore, these features are commonly associated with wetland soil formation processes (Stoops & Eswaran 1985). For such an environment to form requires that the site be periodically inundated or flooded.

It is posited, therefore, that the incised channel of the Tramway and Woodlands Creek at the north of MacCauley's Beach was periodically choked with sandy continental shelf-derived sediments causing water to become impounded behind the choke point. This would have led to the periodic inundation, and hydromorphic overprinting, of the palaeosol. The complex rythmic void coatings (Figures 5.4r, s and u) and distinctive grey colouration of this unit were produced as a result of the deflocculation and translocation of iron-stained clays down profile and the resulting downward movement of fine silt, aided by Na+ ions in sea water (Levy 2011). Indirect evidence for inundation is given by the northerly dip direction of this unit towards the present day outlet of the Tramway and Woodlands Creeks and the

pinching out of the grey mud to the south of the beach. A similar depositional environment was concluded by Jones *et al.* (1979) for their grey mud equivalent units at South Thirroul and North Bulli. Here, the authors proposed that their grey sandy muds were subjected to marine influences and that a substantial barrier system was required to allow for the deposition of a sandy mud unit close to a high-energy coastline, that had subsequently been destroyed. In effect, this unit was deposited within an estuarine environment, such as those present along this section of the NSW coastline.

5.4.4 STAGE III – DEPOSITION OF MARINE-DERIVED SEDIMENTS

The inundation of the Pleistocene mottled mud and deposition of the grey mud sediments was followed by the deposition of marine-sourced sediments derived from the continental shelf. This is shown schematically in Figure 5.6(III). The 'marine' derived sediment (Figure 5.4b) was deposited over the antecedent topography at 7.5 ± 0.4 ka (SP4), an age also consistent with the mid-Holocene sea-level high stand (Sloss *et al.* 2007, Lewis *et al.* 2013). If account is taken of the disequilibrium in the U-series (using the HRGS dose rate; Table S5.3) for SP5 then an age of 7.9 ± 0.4 ka, an age that is consistent at 1σ with both SP3 and SP4, suggesting a rapid accumulation of ~0.8 m of sand. However, if no account of the U-series disequilibrium is made, and the current dose rate (Table 5.3) is assumed to have existed throughout the entire period of burial, then an age of 6.6 ± 0.4 ka is obtained for SP5, with a more gradual rate of sand accumulation. Bryant *et al.* (1992b) describe this unit as a raised beach deposit. The lack of either macro- or microscopic sedimentary structures, however, means that such a conclusion cannot be drawn from this study. It is thought that deposition of the 'marine' sand continued until ~2 ka when sea level regressed back to PMSL (Sloss *et al.* 2007, Lewis *et al.* 2013), but sediment of this age is not present at MacCauley's Beach.

5.4.5 STAGE IV – DUNE STABILISATION

Subsequent dune stabilisation has resulted in the podzolisation of the sand-dominated parent material (Figure 5.6(IV)). The change in colour of the sand-dominated sediments from black organic rich sediments at the surface (SP6), to pale 'albic' sands (SP5) and brown clayey sands at the base (SP4) is associated with clay content, stained to greater or lesser extents by iron oxides and/or humic residues, that are translocated down profile, producing a progression of clay coating features (Figures 5.4h, g and b) similar to those outlined in Kühn *et al.* (2010, p. 231). The outcome of this is the development of a weakly podzolic soil, a soil type prevalent on the beach ridges along the coast of New South Wales (Nott *et al.* 1994).

5.5 CONCLUSIONS

This study involved the collection of six intact and orientated sediment block samples from equivalent stratigraphic positions as six complimentary OSL samples. The sedimentary fabric, composition and depositional context were determined using soil micromorphological analysis of thin sections. This analysis provided information about possible causes of spread in D_e values by providing information regarding both pre- and post-depositional sediment histories for each sample. The interpretation of the D_e distribution patterns, and the choice of statistical age models for each sample, was aided by the integration of the soil micromorphology data. The combined application of these two techniques is considered to be mutually beneficial.

The chronology for MacCauley's Beach presented in this study is considered to be more reliable than previous work at the locality due to the more robust methods utilised in this study. The mottled mud unit is proposed to have been deposited during MIS 5, before undergoing a period of extensive pedogenesis, producing the distinctive mottled coloration. The pedogenic processes active in the mottled mud unit had ceased by 14.7 ± 2.7 ka (SP1). This termination is considered to be the result of the periodic inundation of the mottled mud unit, resulting in soil structure collapse, and the subsequent deposition of the grey mud unit between 10.0 ± 0.7 (SP2) and 7.7 ± 0.5 ka (SP3) as sea level returned to a height similar to the present. This inundation was followed immediately by a 'marine' derived unit blanketing the

site (7.5 ± 0.4; SP4 and 7.9 ± 0.4 or 6.6 ± 0.4 ka; SP5). The current colouration of the sand-dominated sediment is due to podzolisation of the sandy parent material.

While the single-grain OSL ages presented in this study are more precise than the TL ages presented in Bryant *et al.* (1992b), they are still too coarse to refine the Holocene sea level curve of Sloss *et al.* (2007). We note, however, that these ages are consistent with those presented in the sea level history model for the NSW coastline presented by Lewis *et al.* (2013). OSL ages show great potential to provide reliable constraints for coastal sediment landscapes throughout NSW and Australia.

5.6 ACKNOWLEDGMENTS

Financial support was provided by the University of Wollongong and an Australian Postgraduate Award scholarship. We also acknowledge the useful and constructive discussions had with Associate Professor Brian Jones and Professor Colin Murray-Wallace. We would like to thank the anonymous reviewers for their constructive reviews that greatly improved the original manuscript.

5.7 SUPPLEMENTARY MATERIAL

5.7.1 OSL DATING

5.7.1.1 SAMPLE PREPARATION AND D_e MEASUREMENT PROCEDURES

An OSL dating sample was collected from directly behind each of the soil micromorphology samples (Figure 5.2), using 20 cm lengths of 5 cm diameter opaque PVC pipe. Thus, each OSL sample can be directly associated with the corresponding micromorphology sample in time and space.

All OSL samples were prepared under dim red-light conditions to preserve the light-sensitive OSL signal. A subsample of 180-212 μm diameter quartz grains was obtained for each sample by standard chemical pre-treatment, heavy liquid separation and sieving procedures (Wintle 1997). The quartz subsamples were etched in 48% hydrofluoric acid for 40 min to remove the alpha-irradiated rind of each of the quartz grains, and to dissolve any residual feldspar grains that may not have been removed during sample pre-treatment.

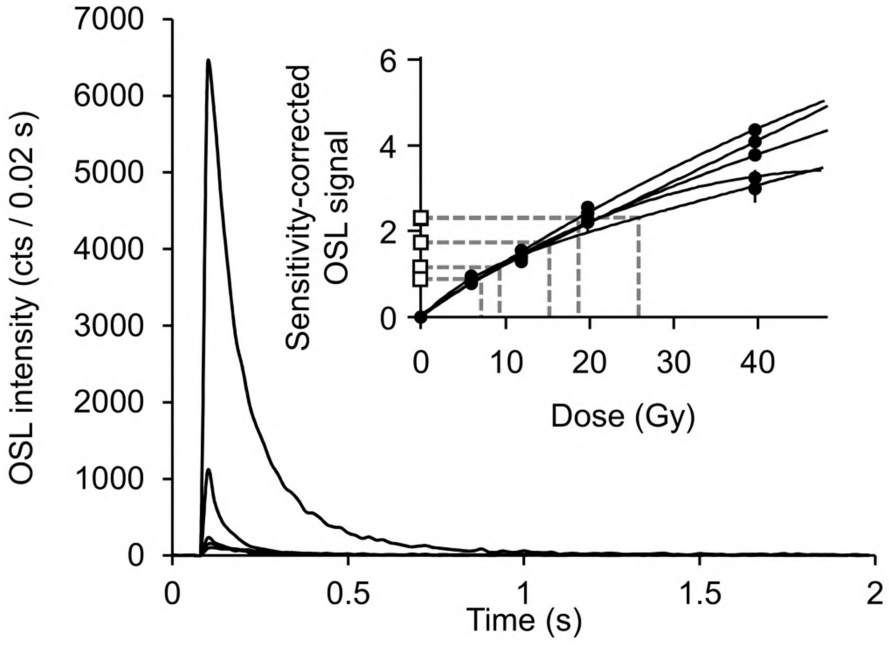

Figure S5.1. Optical decay curves for the natural dose of five accepted grains from SP5. Note the variation in the initial OSL intensity and the rate of OSL depletion. Inset: Dose-response curves for the same five grains fitted using a single saturated exponential function.

OSL measurements were carried out using an automated Risø TL/OSL-DA-15 reader fitted with a focussed green (532 nm) laser and $^{90}Sr/^{90}Y$ beta-irradiator. Individual grains were loaded into standard purpose-made single grain aluminium discs (Bøtter-Jensen *et al.* 2000). Optical stimulation of all grains measured in this

study was for 2 s. The induced luminescence signal was measured using an EMI 9635Q photomultiplier tube fitted with two Hoya U-340 filters.

The single-aliquot regenerative-dose (SAR) procedure (Murray & Wintle 2000) was used to obtain D_e estimates for each invidual grain. Measurement of the natural and regenerative dose OSL signals was preceded by a preheat of 180°C for 10 s and each test dose OSL measurement by a preheat of 180°C for 5 s. All OSL signals were measured at 125°C for 2 s. A selection of optical decay curves and dose-response curves of grains from sample SP5 are presented in Figure S5.1. The dose response curves were fitted using either a single saturating exponential with an additional linear term or just a single saturating exponential function. The uncertainty associated with each D_e value takes into account the counting statistics, instrument reproducibility and variability in the fitted dose-response curve. Each measured grain was subjected to a set of formal rejection criteria (Jacobs *et al.* 2006a, Jacobs *et al.* 2006c), as not every grain provides useful information of the absorbed radiationdose. Table S5.1 provides details for all samples and reasons for why single grains were rejected.

The measurement and analytical parameters used in this study were tested using a dose recovery test (Murray & Roberts 1997, Galbraith *et al.* 1999). A sub-sample of grains from sample SP5 was bleached in natural sunlight for several days and then given a known laboratory beta dose of 12 Gy. The measured dose values of all accepted grains are plotted as a radial plot (Figure S5.2). A measured-over-given dose ratio of 1.00 ± 0.02, and overdispersion (OD) value of 9 ± 2% was obtained. OD is the amount of scatter left after allowance was made for all quantifiable measurement uncertainties (Galbraith *et al.* 1999). An additional dose recovery test was also conducted on a subsample of SP1. Here, a laboratory beta dose of 105 Gy was delivered to the natural sunlight-bleached grains. A measured-over-given dose ratio of 0.97 ± 0.03 was obtained with an OD value of 8 ± 3%.

5.7.1.2 Dose rate and water content measurements

To obtain estimates of the environmental dose rate for each of the samples, the additional samples collected from the back of each OSL sample position were weighed and dried to obtain an estimate of field water content (at the time of sampling) and then ground to a fine powder. Beta dose rates were measured directly from triplicate samples of dried, homogenised and powdered sediment, using a GM-25-5 multi-counter system (Bøtter-Jensen & Mejdahl 1988). All beta dose rates were adjusted for grains size and moisture content (Aitken 1985, Brennan 2003). Gamma dose rates for each sample were measured *in situ* at the point of sampling using a 2-inch in diameter Na(Tl) detector. The detector was calibrated using the concrete blocks at Oxford (Rhodes & Schwenninger 2007) and the gamma dose rate was determined using the 'threshold' technique (Løvborg & Kirkegaard 1974, Murray *et al.* 1978, Mercier & Falguères 2007). A total uncertainty of 5% was assigned to each gamma dose rate using this instrument.

To test the reliability of our gamma dose estimates, we also made measurements using four independent methods. These included: 1) a 5-inch in diameter Exploranium GC-320 gamma detector (except for SP6 where this was not possible) calibrated using the Fugro Instruments flatpad calibration facility in Sydney; 2) a combination of thick-source alpha counting (TSAC) and GM-25-5 beta counting of the same powdered and homogenised samples used for beta dose rate determination, 3) inductively-coupled plasma optical emission spectrometry (ICP-OES) for determination of K and ICP-mass spectrometry (MS) for determination of U and Th at Genalysis Intertek Laboratory in Perth, Australia. and 4) high resolution gamma spectrometry measurements for two of the samples (SP2 and SP5). The results are shown in Table S5.2.

The cosmic-ray dose rates were determined using the equations presented in Prescott & Hutton (1994), allowing for altitude (4 m), geomagnetic latitude (42.9°), and the density (1.8 g cm^{-3}) and thickness (variable) of sedimentary overburden.

Table S5.1. Distribution of rejected grains for each of the six SP samples investigated in this study based upon the rejection criteria outlined in Jacobs et al. (2003, 2006a; 2006b).

Sample name	No. of grains measured	No. of grains rejected on the basis of:					Total no. of rejected grains	Total no. of usable grains
		Brightness[a]	Recycling Ratio[b]	IR ratio[c]	Failure to intersect dose response curve[d]	Recuperation[e]		
SP1	500	226	23	14	2	72	337	163
SP2	600	284	49	31	11	32	407	193
SP3	600	261	60	14	4	54	393	207
SP4	1100	781	57	38	8	44	928	172
SP5	1000	698	57	30	2	43	830	170
SP6	600	467	15	13	0	-	495	105

a) The OSL signal determined for the test dose given directly after measurement of the natural OSL signal was less than 3 times the respective background count.
b) The 'recycling ratio' (the ratio of sensitivity-corrected OSL signals produced by 2 identical regenerative dose points) differed from unity by more than 2σ.
c) The OSL signal resulting from an identical dose to that given in the recycling ratio following a 40 s infrared stimulation at room temperature was less than 2σ from unity.
d) The sensitivity-corrected natural OSL signal failed to intercept the dose-response, termed a Class 3 grain of Yoshida *et al.* (2000).
e) The sensitivity-corrected OSL signal measured after preheating a regenerative dose of 0 Gy was greater than 5% of the sensitivity-corrected natural OSL signal. This was not applied to sample SP6 given the 'young' age of this sample.

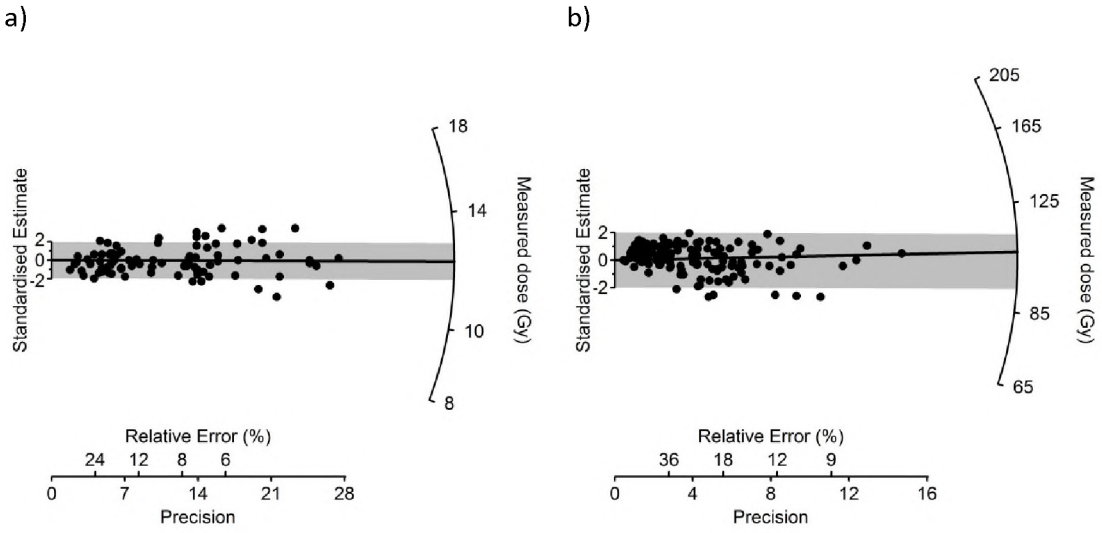

Figure S5.2. Radial plots of single grain measured dose values for a sub-sample of grains from a) SP5 and b) SP1 that were first sun-bleached to remove all trapped charge. SP5 was then given a known laboratory beta dose of ~12 Gy, while SP1 was given a beta dose of ~105 Gy. The given doses of ~12 and 105 Gy are shown by the solid black line. The 2σ grey band around the standardised estimate is centred on the weighted mean measured dose value of 12.2 ± 0.2 Gy for SP5 and 102.0 ± 2.1 Gy for SP1 determined sing the central age model of Galbraith et al. (1999). OD values of 9 ± 2% for SP5 and 8 ± 3% SP1 were calculated.

Table S5.2. Comparison of the gamma dose rates (Gy/ka) determined using four independent measurement techniques.

Sample name	2-inch detector[a]	Exploranium GR320	TSAC + GMBC	ICP-OES/ICP-MS	HRGS
SP6	0.79 ± 0.03	-	0.77 ± 0.08	0.46 ± 0.01	
SP5	1.17 ± 0.05	1.15 ± 0.04	1.10 ± 0.13	0.77 ± 0.02	0.95 ± 0.02
SP4	0.84 ± 0.04	0.71 ± 0.02	0.72 ± 0.03	0.51 ± 0.01	
SP3	0.45 ± 0.02	0.41 ± 0.02	0.37 ± 0.04	0.32 ± 0.01	
SP2	0.41 ± 0.02	0.36 ± 0.01	0.37 ± 0.04	0.28 ± 0.01	0.36 ± 0.03
SP1	0.42 ± 0.02	0.39 ± 0.02	0.39 ± 0.04	0.38 ± 0.01	

[a] The values from the 2-inch gamma detector were used in the calculation of the OSL ages for all samples measured in this study.

Table S5.3. Activities for selected Uranium and Thorium series radionuclides; and ^{40}K determined using HRGS for samples SP2 and SP5 (± 1σ). Also shown is the gamma dose rate calculated using these concentrations.

Sample name	Uranium series (Bq.kg)			Thorium series (Bq.kg)		^{40}K (Bq/kg)	Gamma dose rate (Gy/ka)
	^{238}U	^{226}Ra	^{210}Pb	^{228}Ra	^{228}Th		
SP5	47.2 ± 1.6	51.9 ± 0.5	44.5 ± 1.8	48.0 ± 0.8	52.3 ± 1.0	30.9 ± 2.0	0.95 ± 0.02
SP2	18.3 ± 0.9	19.6 ± 0.2	17.9 ± 0.9	18.4 ± 0.4	20.7 ± 0.5	34.6 ± 1.7	0.36 ± 0.03

The presence of water in the sediment effectively absorbs a small portion of the incoming external environmental dose. The external beta and gamma dose rates, therefore, are required to be corrected according to the average water content experienced by the sediment over the period of burial. A mean water content was calculated for each sample from a number of samples collected over a period of 6 months. Given the likely fluctuations in sediment moisture content over its burial period, a relative uncertainty of 25% at 1σ was applied to each sample mean. These mean moisture contents are thought to be realistic when considered together with the soil micromorphology data. For example, the sandy nature of some of the deposit (e.g., SP5) means that water moves relatively rapidly through the pore space network after heavy rainfall, the period of saturation can, therefore, be considered insignificant throughout its burial history. Using these moisture content values, the external radiation dose rates were then adjusted using the equations provided in Aitken (1985).

The internal alpha dose rate was measured directly with TSAC for two of the samples (SP2 and SP5). Estimates of U and Th were obtained for purified, dried and powdered, HF-acid etched quartz grains of 180-212 μm in diameter (Aitken 1985, Aitken & Xie 1990).

5.7.1.3 DISEQUILIBRIUM ASSESSMENT

To assess the state of (dis)equilibrium in the sediments of MacCauley's Beach, two samples (SP2 and SP5) were analysed using high resolution gamma spectrometry (HRGS) at the Australian Government's Department of the Environment Jabiru Field Station Facility, Northern Territory. These samples were chosen based on their sedimentology; one from the lower clay-rich unit and one from the upper sand-rich unit. For HRGS analysis, 0.5 kg of sediment were dried, powdered and homogenised before being pressed at the Jabiru facility. The samples were then stored for a minimum of three weeks to allow the ingrowth of radionuclides, and measured for two days. The HRGS-determined concentrations of

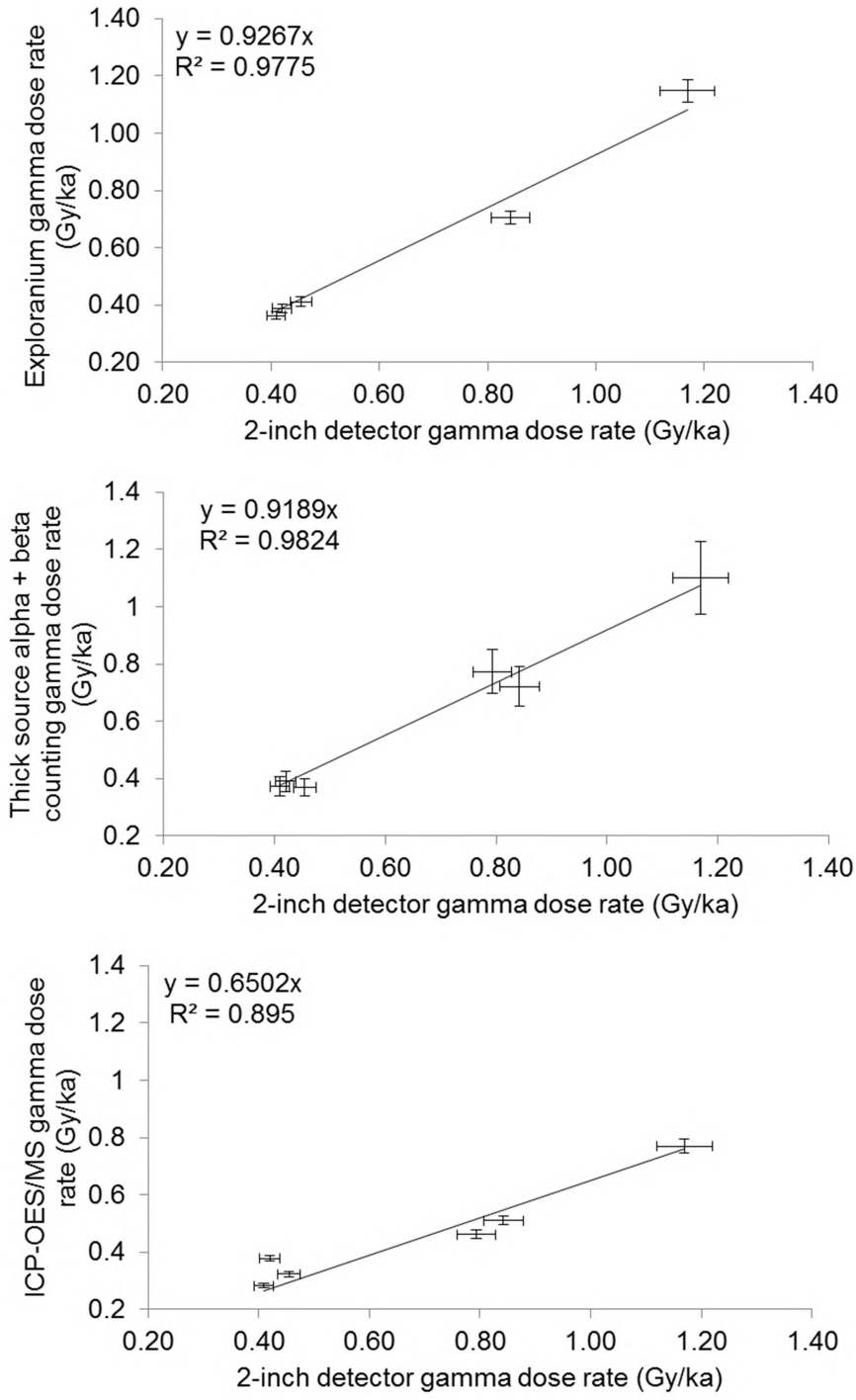

Figure S5.3. Comparison of gamma dose rates determined using three independent techniques: a) Exploranium GR320 gamma detector; b) Thick source alpha + beta counting; and c) ICP-OES/MS against the 2-inch NaI(Tl) gamma detector. The line of best fit (with y-intercept set to 0) and R^2 value are shown on each plot.

U, Th and K (as well as the resulting gamma dose rates) are shown below in Table S5.3.

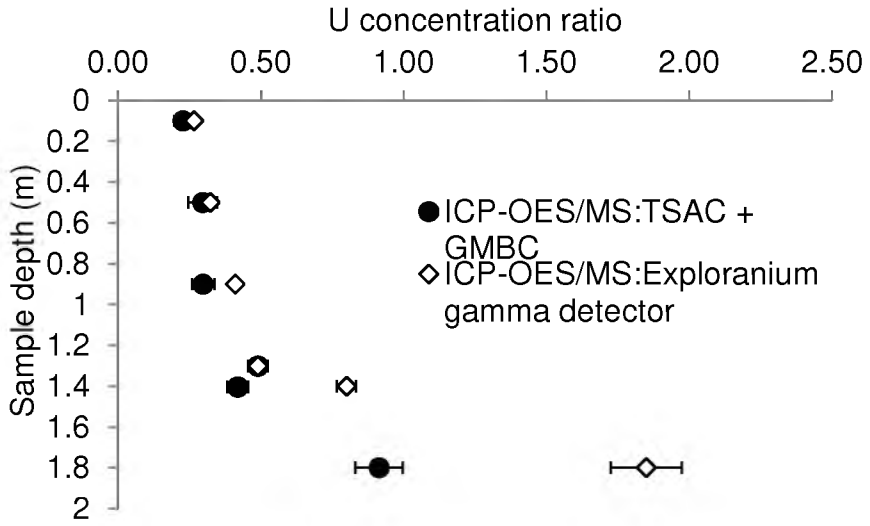

Figure S5.4. U concentration ratios of ICP-OES/MS with respect to Thick source alpha + beta counting (filled circles) and the Exploranium gamma detector (open diamonds). Error bars shown are at 1σ.

A small degree of disequilibrium in the U-series is present in the two samples tested; affecting sample SP5 more than SP2. The resulting gamma dose rate for SP2 is consistent with that of the other measurement techniques, except ICP-OES/MS (Table S5.2). In contrast, the gamma dose rate of SP5 is not statistically equivalent to any other measurement technique used (Table S5.2). The exact mechanism responsible for this state of disequilibrium is not known, nor is the time when it began. However, it is likely coupled with the leaching of radionuclides by percolating ground water through the sediments. Although we cannot account for this disequilibrium, we do present an additional age for SP5 in Table 5.3 that was calculated using the HRGS-determined gamma and beta dose rates. The age of this sample increases from 6.6 ± 0.4 to 7.9 ± 0.4 ka; an age that is consistent with the

underlying SP4 sample from this unit and also that of SP3 from the top of the underlying grey mud. For SP2, the effect of disequilibrium is almost negligible, producing an age of 10.8 ± 0.7 ka that is equivalent to the age of this sample using the 2-inch detector and GMBC as well as the underlying SP1. We, therefore, continue to use the 2-inch detector and GMBC age.

5.7.2 SOIL MICROMORPHOLOGY

The samples are outlined in descending stratigraphic order, i.e., from SP6 to SP1 (Figures 5.2 and 5.3). The terminology used throughout the micromorphological descriptions follows that of Stoops (2003).

5.7.2.1 SAMPLE SP6

FIELD DESCRIPTION

Sample SP6 was collected from 0.05 m depth (Figures 5.2 and 5.3). The sediments are comprised mainly of partially broken down plant material and quartz sand, resulting in a dark brown/black to ashy grey colour. Numerous granules of coal and charcoal are evident throughout, and well as extensive bioturbation in the form of rootlet activity.

MICROMORPHOLOGY

The SP6 sample has a fine, single-spaced enaulic related distribution, with complex packing voids. No bedding structures are evident in this sample, with grains arranged randomly with no preferential orientation. The coarse material is dominated by subrounded to rounded fine to medium quartz sands, with few calcite and lithic fragments, showing the same degree of rounding. Some of the lithic fragments range in size up to coarse sand. The silt size fraction is also dominated by quartz, with few calcite and heavy minerals, such as rutile, ilmenite and tourmaline group species. The clay fraction, with chitonic and gefuric related distribution is impure, with very fine

silt inclusions of quartz and organic matter giving them a dusty appearance. The clay is undifferentiated and stained dark brown to black by humic material.

5.7.2.2 SAMPLE SP5

FIELD DESCRIPTION

Sample SP5 was collected at 0.45 m depth (Figures 5.2 and 5.3). The sediments of this horizon are also dominated by pale yellow, friable quartz sand. The non-cohesive texture indicates low clay content, while the pale colour suggests little or no organic matter. Numerous roots are evident, often protruding from the sediment surface.

MICROMORPHOLOGY

The micromorphology of this sample is similar to that of SP6, apart from the clear reduction in the concentration of opaque bioclastic material (e.g., coal, charcoal) and reduced abundance of the fine fraction. The coarse grain fraction is dominated by subrounded to rounded, moderately to well sorted, fine to medium sand. Other coarse fraction constituents include few calcite grains, rock fragments and heavy minerals, as well as very few feldspar grains. A number of anorthic, iron-stained sandy, silty nodules are also present. The calcite grains show evidence of dissolution along cleavage planes. The fine fraction is again dominated by quartz silts with very few calcite grains. Very little clay is present within the section only found as very thin, undifferentiated coatings surrounding larger sand grains. Numerous roots are observed in thin section. The void space is dominated by simple packing voids. The overall related distribution is fine, close enaulic.

5.7.2.3 SAMPLE SP4

FIELD DESCRIPTION

This sample was collected from within the upper part of the brown sandy sediments (0.90 m) (Figures 5.2 and 5.3). The majority of the horizon is dark brown in colour, with patches of black and orange sands. The dark colouration is interpreted as the result of illuviation of clays and also iron and manganese oxides. The horizon is punctuated with laterally discontinuous lumps of dark brown to black, indurated sands with mammilate edges. These lumps of indurated sands are termed 'coffee rock,' as they closely resemble compressed coffee grinds, and found in the greatest abundance at a depth of 1.10 m.

MICROMORPHOLOGY

The coarse fraction is composed of rounded to subrounded, fine to coarse quartz sands. Few rock fragments are also present, as well as calcite and heavy mineral grains and anorthic, Fe-stained silty, sandy nodules. The fine fraction is dominated by quartz silts and clays. The majority of the clay coating surrounding the larger sand grains is predominantly undifferentiated. The void space is dominated by complex packing voids. The related distribution is close to single-spaced chitonic.

5.7.2.4 SAMPLE SP3

FIELD DESCRIPTION

Sample SP3 was collected from along the gradational contact between the dark brown sand into the underlying greyish brown sandy mud at 1.30 m depth (Figures 5.2 and 5.3). This change in colour is interpreted as the result of a perched water table sitting atop the underlying clay-rich mottled mud unit. This water logging of the sediments maintains reducing conditions, allowing soluble iron and manganese oxides to be mobilized. This boundary represents the contact between the overlying dune humate and underlying Pleistocene estuarine clay of Bryant *et al.* (1992).

MICROMORPHOLOGY

The coarse fraction for the sample is dominated by subangular to subrounded, moderately sorted, fine to coarse quartz sand. There are few weathering sand-sized gains of tourmaline and feldspars. In the porphyric regions, the clay fabric is generally undifferentiated, containing quartz silts and ferromagnesian oxide flecks. The clay fraction of the upper portion of the sample is stained dark brown. Textural pedofeatures found within this sample include complex, layered coatings of impure, dusty clays are interbedded with silty clays. Strongly impregnative, concentric and typic iron and manganese oxide nodules are present but rare. Furthermore, the edges appear undulating to mammillate, cracked and, in some cases, reworked and fragmented. The close to single spaced porphyric related distribution with vughy microstructure remains constant throughout the sample, regardless of depth along the gradational boundary. Some of the vughs are polyconcave in nature. Some domains have greatly reduced fine fraction content, resulting in a more chitonic related distribution, dominated by simple packing voids. This change in related distribution is attributed to bioturbation of the sediments.

5.7.2.5 SAMPLE SP2

FIELD DESCRIPTION

The SP2 sample was collected from a depth of 1.40 m (Figures 5.2 and 5.3). The sediments here are greyish brown sandy mud, similar to those found at sample SP3. Yet, unlike the SP3 sample, the sediments here are not only cohesive but indurated and associated with the cracking of the lower part of the unit into prismatic peds. Charcoal and iron oxide nodules are present and increases with depth.

MICROMORPHOLOGY

The coarse fraction, like all other samples, is dominated by moderately sorted, subangular to subrounded, fine to coarse quartz sand. There are few heavy minerals, such as rutile, and calcite is absent. The silts are also dominated by quartz. The clay fraction is stipple speckled, unlike the undifferentiated clays of all the overlying

samples. Limpid, Fe-stained clays form void coatings with clear extinction lines. Some regions show complex, layered coatings of dusty and limpid clays. It is typical for the limpid clay coatings to be juxtaposed by a thick accumulation dusty/silty clay as pore space is infilled. Orthic moderate to strongly impregnative nodules of both manganese and iron oxides are common, the edges are typically diffuse to mammillate. The related distribution for this sample is close to single-spaced porphyric, with a predominantly vughy (some polyconcave) microstructure.

5.7.2.6 SAMPLE SP1

FIELD DESCRIPTION

The sample SP1 was collected from the top of the mottled mud unit, at a depth of 1.85 m (Figures 5.2 and 5.3). The unit is comprised of mainly muds, showing extensive evidence of gleying; the unit is typically dark grey/blue and punctuated with numerous red/orange mottles. The mud is not pure with notable inclusions of sand. The surface of the mud has become cracked, as a result of dehydration, producing blocky to prismatic peds separated by deep fissure cracks.

MIRCROMORPHOLOGY

The coarse fraction of this sample is dominated by subangular to subrounded, fine to medium sands. These sands are typically quartz however there are rare heavy minerals, e.g., rutile and tourmaline group species. The fine fraction silts are of the same composition as the coarse fraction, dominated by quartz. The clay groundmass has been reworked to produce moderately developed grano- and porostriated b-fabric. Rather than the complex, layered clay coating of the overlying units, intercalations, with moderately developed extinction lines, are present within the samples. Some regions of clay have been stained with iron oxides producing orthic, iron oxide nodules and giving the clay a deep red colour. In contrast, some regions have iron oxide depletion hypocoatings, with buff to off white colours

predominating. The related distribution of this sample is slightly more open than SP3 or SP2, having a single to double-spaced porphyric related distribution.

CHAPTER SUMMARY

Here I have provided an updated chronological framework for the deposition of MacCauley's Beach. Unlike the previous TL and U-series ages, the single-grain OSL ages have been tied directly into the macro and microscopic sedimentary context of the site. This contextualisation was achieved through the use of soil micromorphology in conjunction with OSL to provide qualitative insights into the role that (potential) extrinsic factors might play in relation to the measured D_e distributions. The tandem collection of OSL and soil micromorphology samples at the same stratigraphic position meant that one data set could be directly compared to the other.

Future work at this site is required to definitively determine the timing of the deposition for the mottled Pleistocene mud unit. Presently, the absolute age of this sedimentary facies remains unknown and based on other sources of evidence. This goal could be achieved by sampling below sample SP1– i.e., beyond the zone affected by pedogeneic processes. Unless the sediments are cored, the timing of this sampling will be constrained by timing of storm-induced erosion of the modern beach sands that currently cover the lowest deposits.

Chapter 6

Variations in β-dose rates within a sample and its implications for OSL dating of individual quartz grains

In Chapter 5, soil micromorphological examination of the sediments preserved at MacCauley's Beach allowed for the qualitative identification of beta microdosimetry as the likely cause of the OD in the majority of the single-grain OSL D_e distributions. Using Chapter 5 as a foundation upon which to build, this chapter investigates the beta dosimetric environment for two of the MacCauley's Beach samples (SP2 and SP5), along with two samples from Pech IV (PdAIV-01-C and PdAIV-02). Here, procedures are developed to explore the variability in the β-D_r: 1) for different grain size fractions and mineralogies using standard OSL laboratory equipment; and 2) across intact sedimentary blocks using novel quantitative approaches.

Aims for this chapter:

- *investigate the variability in β-D_r between different mineralogies and grains sizes within the same sample;*
- *develop methods of assessing the two dimensional distribution of β-D_r across sediment slabs;*
- *use this information on β-D_r magnitude and variability to inform the interpretation of OD for the four selected samples*

ABSTRACT

Variation in the beta dose rate (β-D_r) delivered to individual quartz grains (termed beta microdosimetry: BM) has been recognised in single-grain OSL luminescence studies as producing scatter (termed overdispersion: OD) in the resultant equivalent dose (D_e) values. The OD observed in four studied samples; two from MacCauley's Beach and two from Pech IV, was considered to be due to BM. To investigate this further, examination of β-D_r variability and magnitude and spatial distribution of the related 'hotspots' using bulk (disturbed) sediments and resin-impregnated (undisturbed) sediment slabs was conducted. First, thick-source alpha-counting, beta counting and inductively coupled plasma optical emission and mass spectrometry (ICP-OES/MS) measurements of constituent components (e.g., coarse sand quartz, fine sand heavy minerals, etc.) of the bulk sediment samples was used to assess β-D_r variability within each sample. Second, the spatial distribution of β-D_r distributions was studied using portable x-ray fluorescence (pXRF), aluminium oxide (Al_2O_3:C) dosimetry, and image analysis modelling techniques. The results of the β-D_r variability study show significant variation in beta flux of sedimentary components. At MacCauley's Beach this is dominated by Uranium in the heavy mineral fraction, whereas at Pech IV potassium dominates within the clay and mica fractions. Portable XRF measurements, image analysis modelling and Al_2O_3:C dosimetry maps revealed heterogeneous distribution in β-Dr 'hotspots.' Using the minimum and maximum β-D_rs obtained from spatial β-D_r measurements, the OD in all four samples could be explained as the effect of BM effects, with the exception of image analysis modelling that could not fully account for the OD. It was concluded that BM plays a significant role in the OD of the single-grain OSL D_e distributions of those samples investigated. It is recommended that the characterisation of the beta dosimetric environment be carried out before the assignation of BM is applied to D_e distributions.

6.1 INTRODUCTION

The advent of single-grain optically stimulated luminescence (OSL) dating brought about renewed appreciation for small-scale differences in β-D_r within a sample. In their formative single-grain OSL study of sediment from Allen's Cave in Australia, Murray & Roberts (1997) suggested that the greater-than-expected spread in single-grain equivalent dose (D_e) distributions was the result of variations in the β-D_r received by individual quartz grains in their natural burial environment. This conclusion was based on the detailed investigation of the dosimetric properties of the same sediment carried out by Olley *et al.* (1997). Variation in the β-D_r resulting in increased spread in the distribution of D_e values has since become known as BM.

The aim of this study (read Chapter) is to describe, demonstrate and discuss the BM investigations of disturbed and undisturbed sediment samples using two samples collected from MacCauley's Beach, Australia and two samples from Pech de l'Azé IV, France. The disturbed sediment investigation largely mimics the work of Olley *et al.* (1997), whereas the undisturbed sediments enable determination of spatially-resolved β-D_r using a portable XRF (pXRF), image analysis modelling and Al_3O_2:C grains. These results will be integrated with the reported soil micromorphology and single-grain OSL dating results of these two locations (Chapter 5 and 8). This will enable us to test our interpretation of the observed D_e OD. It was an explicit aim to keep the analytical tools simple (i.e., using generally available and standard equipment), so that implementation of these procedures is feasible for any OSL practitioner. It is acknowledged that there are superior methods to probe deeper into specific aspects of sediment diagenesis and temporal dimensions of dose rates, but such methods require specialised equipment and expertise and, as such, would form the next level of analytical enquiry.

6.2 REGIONAL SETTING

6.2.1 STUDY SITES AND PREVIOUS RESEARCH

The samples studied in this investigation come from distinctly different sedimentological contexts. The first is the receded barrier-beach deposit located at MacCauley's Beach on the south coast of New South Wales, Australia and formed solely as the result of geogenic processes (Figure 6.1a). Detailed descriptions of the site stratigraphy and single-grain OSL chronology were provided in Chapter 5. For this study, two samples were selected (SP2 and SP5; Figure 6.1a) on the basis of their contrasting sedimentary characteristics and the possibility of BM being the major contributor to OD. The remaining two samples come from Pech IV in the Périgord of southwestern France. The stratigraphy and archaeological assemblages for this site have been reported previously in Turq *et al.* (2011), and single-grain OSL investigation reported in Jacobs *et al.* (submitted). For this study, two samples (PdAIV-01-C and PdAIV-02; Figure 6.1b) where chosen for further investigation due to their contrasting and complex sedimentological characteristics. The radial pots for these samples are shown in Figure 6.2. Further discussion regarding these samples with respect to their sedimentology and D_e distribution characteristics can be found in Appendix 3.

6.2.2 SAMPLE COLLECTION

To determine the different sources of radioactivity that give rise to the β-D_r and to quantify the variation in β-D_r within these four samples, these samples were collected in two different ways: 1) as intact and orientated samples and, 2) also as 'disturbed' sediment samples.

Intact and orientated sediment block samples were collected from the SP2 and SP5 sample positions (Figure 6.1a) using 5 x 10 cm aluminium downpipe, cut into 10

cm lengths. The Pech IV samples were excised from the section using a sharp knife and supported using plaster bandages, before being completely removed (Figure 6.1b). Each of the four blocks were wrapped in tissue paper and packing tape to prevent sample disturbance during transport to the laboratory where they were impregnated with polyester resin. It is from these resin-impregnated blocks that the undisturbed sediment samples were taken. Further details on sample collection are outlined in Section 6.4.3.

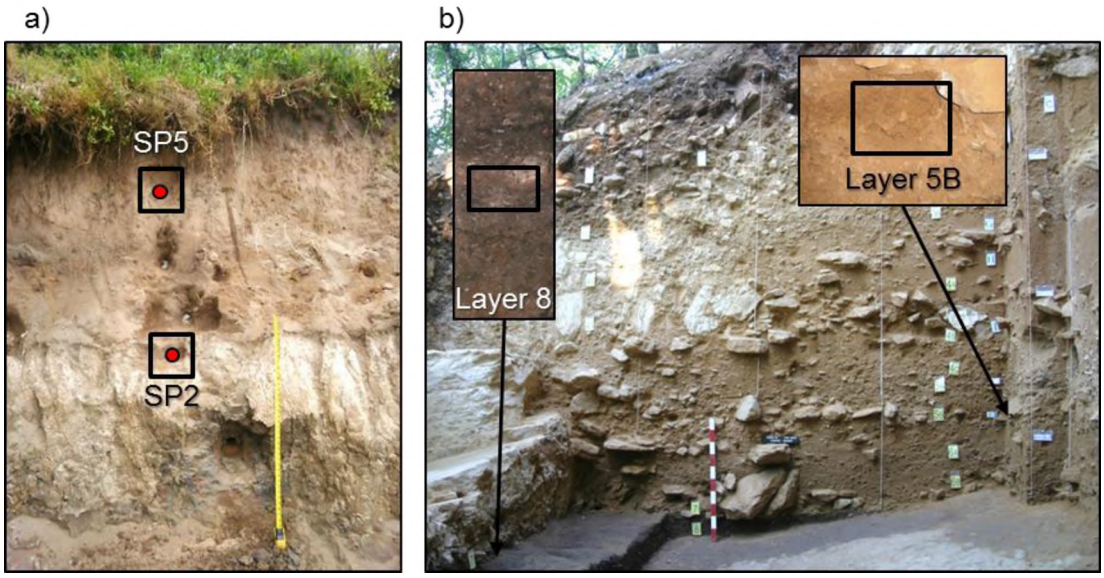

Figure 6.1. a) Photograph of the stratigraphy and sample column at MacCauley's Beach showing the locations of SP2 in the indurated mud unit and SP5 in the 'clean' sand. Yellow tape measure is 1 m. b) Photograph of stratigraphy and sample block locations for Layer 8 and Layer 5B at Pech IV. Layer 8 column shown is 30 cm in height. Layer 5B block location (black box) is 30 cm in width. Pech IV stratigraphy photograph courtesy of P. Goldberg.

Disturbed sediment samples were collected from stratigraphically-equivalent heights as their undisturbed counterparts. At MacCauley's Beach, sediment samples were collected from the same location as the intact blocks, but deeper into the profile. This method was not considered appropriate at Pech IV so as to preserve the

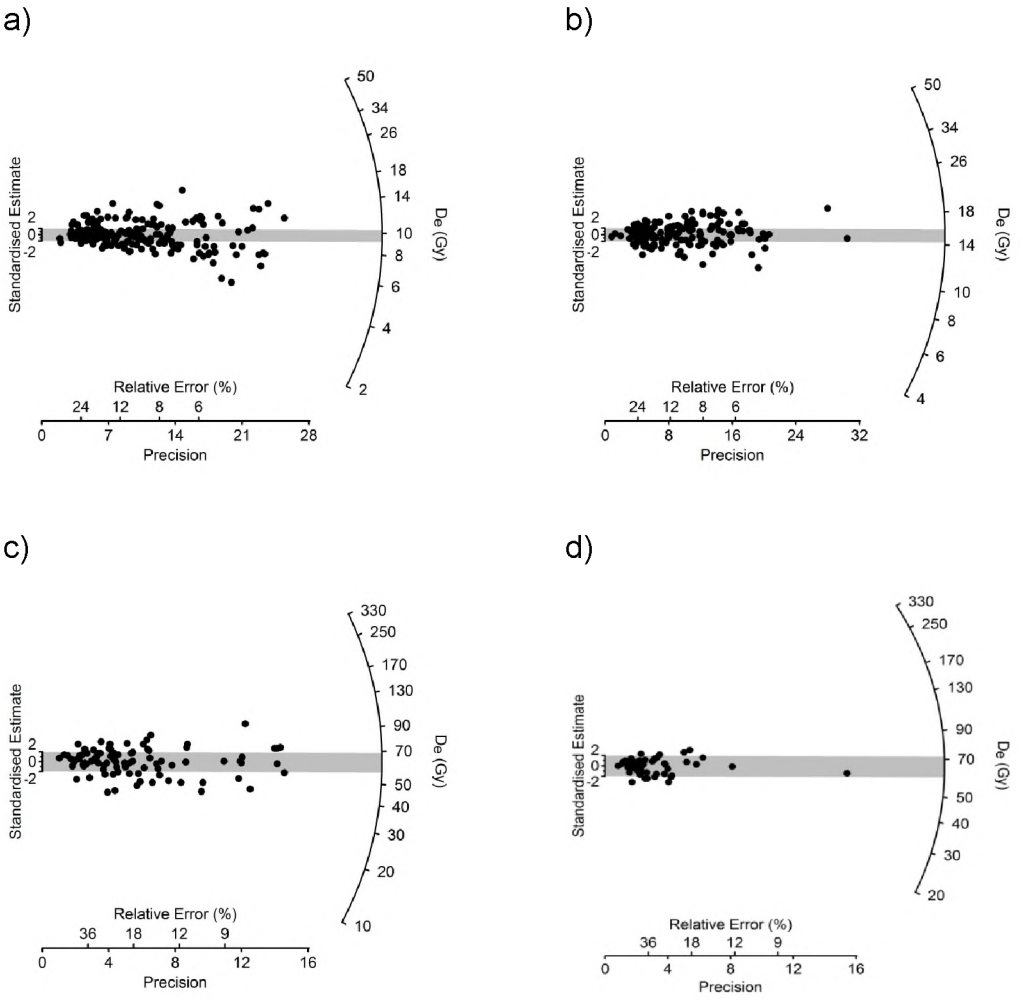

Figure 6.2. Radial plots for a) SP2; b) SP5; c) Layer 8; and d) Layer 5B. Grey bands centre on the determined sample D_e values for the samples: SP2, 9.8 ± 0.3 Gy; SP5, 15.6 ± 0.5 Gy; Layer 8, 63 ± 4 Gy; and d) Layer 5B, 64 ± 4 Gy.

site due to its archaeological significance. Instead our disturbed sediments were sampled from the intact blocks at stratigraphically equivalent heights as both the OSL samples (PdAIV-01-C and PdAIV-02; Chapter 8). This sampling was done prior to resin impregnation for the Layer 5B sediment block but after resin impregnation of the Layer 8 block.

A 6 mm thick resin-impregnated slice was removed from the Layer 8 sediment block and bisected. Half the slice was used for D_e measurement and age estimation, the remaining half used for β-D_r determination. This approach for the Layer 8 sample was taken to restrict the vertical extent of the sampling and ensure that the beta dose rate measurements directly relate to the sediment being dated. The polyester resin was removed using toluene, followed by acetone.

In all four samples investigated, this disturbed sediment sampling results in the destruction of the sedimentary context, and, therefore, any spatial information of the β-D_r is lost. Different experiments have been conducted on the two types of samples (disturbed vs. undisturbed) and are referred to in the following sections as undisturbed sediment block samples and disturbed bulk sediment samples, respectively. By collecting the samples in these two ways, it is hoped that a quantitative understanding of the both the spatial variability in the β-D_r (undisturbed samples) and the magnitude of β-D_r variability (disturbed samples) will be achieved.

6.3 DISTURBED SEDIMENT SAMPLES

6.3.1 SAMPLE PREPARATION

The disturbed sediment samples from MacCauley's Beach were sieved using graduated sieves into grain size fractions of >2 mm (fine gravel; FG), 2 mm–180 μm (coarse sand; CS), 180–63 μm (fine sand; FS) and <63 μm. The <63 μm fraction was further divided into polymineral silt (63–4 μm) and polymineral clay (<4 μm) fractions using a water column. The CS and FS fractions were further separated into mineral components to determine if any one mineralogical fraction was significantly more radioactive. The heavy mineral component was separated from quartz and feldspar using heavy liquid (sodium polytungstate) at a specific gravity of 2.7. The feldspar component was then separated from the quartz using heavy liquid at a specific gravity of 2.62.

The loose sediment samples from Pech IV were not separated into the same mineralogical subdivisions as those from MacCauley's Beach. Both the Layer 8 and 5B were separated using graduated sieves into three fractions: >2 mm, 2 mm–180 μm and <180 μm. Additionally, individual components of flint and burnt bone from Layer 8 and limestone and unburnt bone from Layer 5B, all greater than 2 mm, were collected from the site during sample collection.

Following separation, the weight of each fraction was recorded and expressed as a proportion of the total weight of the sample. Each fraction was then crushed into a fine powder using a ball mill. For MacCauley's Beach, a sub-sample of HF-acid etched 180–212 μm quartz used for D_e determination and a bulk (unseparated) powdered and homogenised sub-sample of both samples was also analysed. Throughout this paper, the term 'sample' was used to refer to the sediments as a whole, 'fraction' to refer to a specific grain size class, and 'component' to refer to a fraction with a specific mineralogy. A summary of the fractions, their respective

grain size ranges, components and proportions are provided in Table 6.1 for MacCauley's Beach and Table 6.2 for Pech IV.

Table 6.1. Grains size, fraction name and mineral components and proportion of each obtained from SP2 and SP5 collected from MacCauley's Beach.

Grain size range	Fraction name	Component	SP2 (%)	SP5
> 2 mm	Fine gravel (FG)	Polymineral	3.9	-
2 mm – 180 µm	Coarse sand (CS)	Quartz	50.0	84.6
2 mm – 180 µm	Coarse sand (CS)	Feldspar	5.2	5.5
2 mm – 180 µm	Coarse sand (CS)	Heavy Mineral	2.0	2.5
180 – 63 µm	Fine sand (FS)	Quartz	4.1	1.9
180 – 63 µm	Fine sand (FS)	Feldspar	1.9	0.4
180 – 63 µm	Fine sand (FS)	Heavy Mineral	0.5	2.9
63 – 4 µm	Silt	Polymineral	18.1	0.4
< 4 µm	Clay	Polymineral	14.4	1.7

Table 6.2. Grains size range, fraction name and proportion of each obtained from PdAIV-01-C and PdAIV-02 collected from Pech IV.

Grain size range	Fraction name	PdAIV-01-C (%)	PdAIV-02 (%)
> 2 mm	Fine gravel (FG)	22.5	40.0
2 mm – 180 µm	Coarse sand (CS)	66.1	40.5
<180 µm	Fine sand, silt and clay (FSC)	11.4	19.5

6.3.2 U, TH AND K CONTENT DETERMINATION

To determine the β-D_r for the different fractions (Table 6.1), two methods were used. First, small samples of powdered material from each component (~2 g) from both sites were sent to Intertek Genalysis Laboratory in Perth, Australia for U, Th and K concentration analysis, with two exceptions. The Layer 8 and Layer 5B FG fractions were not analysed with this method, rather the powdered individual

components of burnt and unburnt bone, limestone and flint were measured instead. These components were collected from the site during sample collection therefore no proportion for this is given in Table 6.2. This was done so as to further investigate the radionuclide concentrations of these components and, hence, β-D_r. Each sample was subjected to a four acid digestion to produce a 'near total digestion.' U and Th were measured using inductively-coupled plasma mass spectrometry (ICP-MS), with K measured using ICP-optical emission spectrometry (ICP-OES).

Second, thick-source alpha-counting (TSAC) and GM-25-5 beta counting (GMBC: Bøtter-Jensen & Mejdahl 1988) of the same ground samples was carried out at the University of Wollongong on each of the MacCauley's Beach powdered components, only (Aitken 1985, 1990). GMBC was carried out only on the three grains size fractions of the Pech IV samples.

GMBC was carried out using the standard nylon plastic sample containers ('pots'), but with a false bottom made of polyethylene glycol (PEG) wax. This measure was taken to deal with the small amounts of material available for a number of the components. PEG is a water soluble wax and its low melting point and water solubility make the filling and removal of the 'false bottoms' a simple process. A graduated syringe was used to pour 1 ml of liquid PEG wax into each pot. Each pot was then tapped to ensure an even distribution of wax. Shortly after filling, the wax solidifies leaving a ~3 mm, beta-thick, volume to be filled with powdered sediment on top of the 'false bottom.' All pots were filled to the brim with powder and scraped level to ensure a homogeneous presentation to the detectors.

A number of experiments were undertaken to test whether the PEG false bottoms may affect the GMBC results. These tests were constructed to determine: 1) whether the PEG bottom produced a detectable β-D_r and 2) if the PEG false bottom influenced the β-D_r for a known standard. To test the first condition, an unfilled beta pot containing only the PEG false bottom was used. This unfilled beta pot was measured against a standard (Nussi) with a known β-D_r, together with a sample of magnesium oxide (MgO), normally used as a background measurement. The Nussi standard and MgO powder were both placed in regular pots with no false bottom.

The mean count rate (counts/hr) estimated over 24 one-hour cycles for the PEG false bottom pot (9.4 ± 0.7 counts/hr) was indistinguishable from the MgO sample (9.5 ± 0.6 counts/hr), and both were significantly less than that obtained for the Nussi standard (315 ± 2.9 counts/hr). It was concluded that the PEG false bottom does not contribute to the total β-D_r. To test the second condition, three pots with PEG false bottoms were filled with sub-samples of the Nussi standard and measured against a sub-sample of the Nussi standard packed in the conventional way (i.e., with no false bottom). The average β-D_r measured for the three pots containing the Nussi standard with PEG false bottoms (1.47 ± 0.05 Gy/ka) and the Nussi standard without the PEG false bottom (1.49 ± 0.05 Gy/ka) gave a ratio that was consistent with unity (0.99 ± 0.05). It is clear that the PEG false bottom does not influence the measurement of the β-D_r. For consistency, all GMBC measurements in this study were done using the PEG false bottoms.

All elemental concentrations (U, Th and K) from both the Intertek Genalysis and TSAC and GMBC measurements were converted to β-D_r using the conversion factors of Guérin *et al.* (2011).

6.3.3 DISTURBED SEDIMENT SAMPLE RESULTS

6.3.3.1 MACCAULEY'S BEACH (SP2 AND SP5)

The concentrations of U, Th (both in µg/g) and K (%) and the associated β-D_r values for the fractions and components outlined above are shown in Table 6.3 for SP2 and Table 6.4 for SP5. It should be noted that all β-D_r estimates shown are dry to facilitate a 1:1 comparison between all samples and have not been attenuated or corrected for moisture content.

It was immediately recognised that the FS quartz components for both SP2 (FS1) and SP5 (FS1) were contaminated. The β-D_r for the SP2 sample was measured to be 1.33 ± 0.06 Gy/ka using GMBC. The values were replicated using the TSAC

concentrations of U and Th resulting in a β-D_r of 1.18 ± 0.21 Gy/ka (K excluded). A similar result was obtianed for SP5, where β-D_r values of 3.77 ± 0.12 Gy/ka using GMBC and 3.81 ± 1.58 Gy/ka from the TSAC concentrations of U and Th alone were calculated. A subset of unground SP2 and SP5 FS quartz component were subsequently washed to remove any remaining clay material and density separated again to remove any remaining heavy minerals or feldspar grains.

This second round of treatments had a significant effect on β-D_r values for both sample, reducing them by almost an order of magnitude. Following re-treatment, the SP2 FS quartz component (FS2) had a GMBC β-D_r of 0.16 ± 0.03 Gy/ka and ICP-OES/MS β-D_r of 0.12 ± 0.00 Gy/ka: both consistent with the HF-acid etched 180–212 μm quartz component (see Table 6.3). The GMBC β-D_r for the re-treated SP5 FS quartz component (FS2) was 0.30 ± 0.03 Gy/ka, while the ICP-OES/MS β-D_r was 0.28 ± 0.01 Gy/ka. Yet, these β-D_r values are significantly higher than that of the HF-acid etched 180–212 μm GMBC β-D_r at 0.11 ± 0.04 Gy/ka. It was concluded that the SP5 FS2 component still had some level of contamination.

The β-D_r calculated using TSAC (U and Th) and ICP-OES (K) for sample SP2 range from 0.058 ± 0.004 to 13.03 ± 1.45 Gy/ka. In instances where a coarse and fine grained fraction exists (e.g. for the quartz, feldspar and heavy mineral components), the fine fraction has a higher β-D_r than its coarse fraction counterpart. There is a seven-fold increase in the β-D_r between the CS (0.12 ± 0.01 Gy/ka) and FS (0.84 ± 0.03 Gy/ka) feldspar component. The largest difference, however, is found between the FS (13.03 ± 1.45 Gy/ka) and CS (0.84 ± 0.03 Gy/ka) heavy mineral components. The β-D_r for the polymineral silt, clay and FG components for the SP2 sample were measured to be 0.73 ± 0.06, 0.65 ± 0.05 and 0.54 ± 0.05 Gy/ka, respectively.

The TSAC and ICP-OES β-D_r values determined for the SP5 sample, in contrast, show a significantly greater range from 0.068 ± 0.003 to 29.54 ± 2.51 Gy/ka. For the quartz, feldspar and heavy mineral components, the β-D_r estimates associated with the FS fractions are, once again, significantly higher than the β-D_r

Table 6.3. β-D_r values obtained for sedimentary components of SP2 using GMBC, a combination of TSAC and ICP-OES for K, and ICP-OES/MS. Were appropriate, the concentrations of U, Th and K are shown for each component. The 'combined' β-D_r was determined using the TSAC U concentration with the ICP-OES/MS concentrations of K and Th.

SP2		GMBC	TSAC + ICP-OES K				ICP-OES/MS[c]				'Combined' Beta dose rate (Gy/ka)[d]
Component	Fraction	Beta dose rate (Gy/ka)	U (µg/g)	Th (µg/g)	K (%)	Beta dose rate (Gy/ka)[d]	U (µg/g)	Th (µg/g)	K (%)	Beta dose rate (Gy/ka)[d]	
Quartz	CS	0.04 ± 0.07	0.20 ± 0.01	0.60 ± 0.14	0.01 ± 0.00	0.06 ± 0.00	0.12 ± 0.00	0.54 ± 0.02	0.01 ± 0.00	0.04 ± 0.00	0.06 ± 0.00
Quartz	FS1[a]	1.33 ± 0.06	7.38 ± 1.40	3.91 ± 0.82	-	-	-	-	-	-	-
	FS2[b]	0.16 ± 0.03	-	-	-	-	0.23 ± 0.01	1.09 ± 0.04	0.07 ± 0.00	0.12 ± 0.00	-
Feldspar	CS	0.14 ± 0.03	0.34 ± 0.01	0.41 ± 0.12	0.07 ± 0.00	0.12 ± 0.01	0.20 ± 0.01	0.56 ± 0.02	0.07 ± 0.00	0.10 ± 0.00	0.12 ± 0.00
Feldspar	FS	0.89 ± 0.04	1.03 ± 0.04	1.68 ± 0.30	0.81 ± 0.02	0.84 ± 0.03	0.56 ± 0.02	1.74 ± 0.07	0.81 ± 0.02	0.78 ± 0.03	0.84 ± 0.03
Heavy Minerals	CS	0.19 ± 0.03	0.82 ± 0.04	1.52 ± 0.37	0.07 ± 0.00	0.22± 0.01	0.47 ± 0.01	1.51 ± 0.06	0.07 ± 0.00	0.17 ± 0.01	0.22 ± 0.01
Heavy Minerals	FS	11.13 ± 0.40	56.89 ± 2.07	166.63 ± 49.07	0.16 ± 0.00	13.03 ± 1.45	15.33 ± 0.46	268.74 ± 10.75	0.16 ± 0.00	9.80 ± 0.42	15.86 ± 0.64
Polymineral	Silt	0.64 ± 0.03	2.48 ± 0.31	7.37 ± 1.26	0.21 ± 0.01	0.73 ± 0.06	1.59 ± 0.05	7.16 ± 0.29	0.21 ± 0.01	0.60 ± 0.02	0.73 ± 0.05
Polymineral	Clay	0.61 ± 0.03	1.57 ± 0.18	9.84 ± 1.40	0.18 ± 0.00	0.65 ± 0.05	2.44 ± 0.07	7.06 ± 0.28	0.18 ± 0.00	0.70 ± 0.02	0.57 ± 0.03
Polymineral	FG	0.58 ± 0.03	2.00 ± 0.26	4.94 ± 1.18	0.14 ± 0.00	0.54 ± 0.05	2.39 ± 0.07	5.17 ± 0.21	0.14 ± 0.00	0.60 ± 0.02	0.54 ± 0.04
Quartz	HF	0.13 ± 0.03	0.40 ± 0.01	1.13 ± 0.01	0.06 ± 0.00	0.14 ± 0.01	0.20 ± 0.01	1.01 ± 0.04	0.06 ± 0.00	0.11 ± 0.00	0.14 ± 0.00
Polymineral	Bulk	0.42 ± 0.02	2.16 ± 0.17	3.42 ± 0.62	0.10 ± 0.00	0.49 ± 0.03	0.91 ± 0.03	4.01 ± 0.16	0.10 ± 0.00	0.33 ± 0.01	0.51 ± 0.03

[a] The FS component following only one round of pre-treatment
[b] The FS component following two rounds of pre-treatment
[c] The total uncertainties associated with the concentrations of U, Th and K determined using ICP-OES/MS are based on reproducibility measurements. Thus, all U, Th and K concentrations were assigned an uncertainty of 3, 4 and 2.5%, respectively.
[d] The TSAC + ICP-OES K, ICP-OES/MS and 'combined' β-D_r values were converted from elemental concentrations of U, Th and K to β-D_r using the conversion factors set out in Guérin *et al.* (2011).

Table 6.4. β-D_r values obtained for sedimentary components of SP5 using GMBC, a combination of TSAC and ICP-OES for K, and ICP-OES/MS. Were appropriate, the concentrations of U, Th and K are shown for each component. The 'combined' β-D_r was determined using the TSAC U concentration with the ICP-OES/MS concentrations of K and Th.

SP5		GMBC	TSAC + ICP-OES K				ICP-OES/MS[a]				Combined
Component	Fraction	Beta dose rate (Gy/ka)[b]	U (μg/g)	Th (μg/g)	K (%)	Beta dose rate (Gy/ka)[b]	U (μg/g)	Th (μg/g)	K (%)	Beta dose rate (Gy/ka)[b]	Beta dose rate (Gy/ka)[b c]
Quartz	CS	0.06 ± 0.07	0.29 ± 0.01	0.45 ± 0.10	0.02 ± 0.00	0.07 ± 0.00	0.11 ± 0.00	0.51 ± 0.02	0.02 ± 0.00	0.04 ± 0.00	0.07 ± 0.00
Quartz	FS1	3.77 ± 0.12	23.32 ± 10.79	16.49 ± 2.61	-	-	-	-	-	-	-
	FS2	0.30 ± 0.03	-	-	-	-	0.34 ± 0.01	2.17 ± 0.09	0.21 ± 0.01	0.28 ± 0.01	-
Feldspar	CS	0.29 ± 0.03	0.21 ± 0.01	1.19 ± 0.31	0.28 ± 0.01	0.29 ± 0.01	0.19 ± 0.01	0.71 ± 0.03	0.28 ± 0.01	0.27 ± 0.01	0.27 ± 0.01
Feldspar	FS	1.02 ± 0.05	0.28 ± 0.01	0.76 ± 0.17	1.17 ± 0.03	1.00 ± 0.04	0.21 ± 0.01	0.83 ± 0.03	1.17 ± 0.03	0.99 ± 0.04	1.00 ± 0.04
Heavy Minerals	CS	1.39 ± 0.06	3.82 ± 0.52	13.24 ± 1.69	0.60 ± 0.02	1.41 ± 0.10	2.21 ± 0.06	14.32 ± 0.57	0.60 ± 0.02	1.19 ± 0.04	1.44 ± 0.09
Heavy Minerals	FS	22.03 ± 0.70	163.29 ± 2.39	199.55 ± 83.83	0.28 ± 0.01	29.54 ± 2.51	34.05 ± 1.02	507.73 ± 20.31	0.28 ± 0.01	19.25 ± 0.82	38.07 ± 1.32
Polymineral	Silt	1.08 ± 0.05	2.56 ± 0.37	6.78 ± 1.40	0.78 ± 0.02	1.18 ± 0.08	1.48 ± 0.04	6.60 ± 0.26	0.78 ± 0.02	1.02 ± 0.04	1.18 ± 0.07
Polymineral	Clay	1.38 ± 0.05	2.78 ± 0.32	8.73 ± 1.20	1.12 ± 0.03	1.54 ± 0.08	1.80 ± 0.05	7.03 ± 0.28	1.12 ± 0.03	1.35 ± 0.05	1.50 ± 0.07
Quartz	HF	0.11 ± 0.04	0.45 ± 0.01	1.25 ± 0.17	0.06 ± 0.00	0.15 ± 0.01	0.21 ± 0.01	1.02 ± 0.04	0.06 ± 0.00	0.11 ± 0.00	0.14 ± 0.00
Polymineral	Bulk	1.13 ± 0.06	4.60 ± 0.78	12.74 ± 1.93	0.10 ± 0.00	1.10 ± 0.13	1.36 ± 0.04	13.21 ± 0.53	0.10 ± 0.00	0.64 ± 0.03	1.12 ± 0.12

[a] The FS component following only one round of pre-treatment
[b] The FS component following two rounds of pre-treatment
[c] The total uncertainties associated with the concentrations of U, Th and K determined using ICP-OES/MS are based on reproducibility measurements. Thus, all U, Th and K concentrations were assigned an uncertainty of 3, 4 and 2.5%, respectively.
[d] The TSAC + ICP-OES K, ICP-OES/MS and 'combined' β-D_r values were converted from elemental concentrations of U, Th and K to β-D_r using the conversion factors set out in Guérin *et al.* (2011).

Table 6.5. β-D_r values obtained for sedimentary fractions and components PdAIV-01-C (Layer 8) and PdAIV-02 (Layer 5B) using GMBC andICP-OES/MS. Where appropriate, the concentrations of U, Th and K are shown for each component.

Stratigraphic Unit	Fraction/Component	GMBC	ICP-OES/MS[a]			
		Beta dose rate (Gy/ka)[b]	U (μg/g)	Th (μg/g)	K (%)	Beta dose rate (Gy/ka)[b]
Layer 8	>2 mm (FG)	0.18 ± 0.04	-	-	-	-
	2 mm–180 μm (CS)	0.40 ± 0.03	0.50 ± 0.02	2.60 ± 0.10	0.37 ± 0.01	0.30 ± 0.01
	<180 μm (FSC)	0.53 ± 0.03	0.54 ± 0.02	3.24 ± 0.13	0.48 ± 0.01	0.55 ± 0.02
	Proportionally mixed	0.35 ± 0.02	-	-	-	--
	Burnt bone	-	1.78 ± 0.05	0.04 ± 0.00	0.02 ± 0.00	0.28 ± 0.01
	Flint	-	1.10 ± 0.03	0.45 ± 0.02	0.07 ± 0.00	0.23 ± 0.01
Layer 5B	>2 mm (FG)	0.37 ± 0.02	-	-	-	-
	2 mm–180 μm (CS)	0.52 ± 0.03	0.61 ± 0.02	2.70 ± 0.11	0.44 ± 0.01	0.52 ± 0.02
	<180 μm (FSC)	1.12 ± 0.04	1.47 ± 0.04	8.18 ± 0.33	0.92 ± 0.00	1.17 ± 0.04
	Proportionally mixed	0.57 ± 0.03	-	-	-	-
	Unburnt bone	-	1.28 ± 0.04	0.18 ± 0.01	0.02 ± 0.00	0.21 ± 0.01
	Limestone	-	0.24 ± 0.01	1.31 ± 0.05	0.30 ± 0.01	0.31 ± 0.01

[a] The total uncertainties associated with the concentrations of U, Th and K determined using ICP-OES/MS are based on reproducibility measurements. Thus, all U, Th and K concentrations were assigned an uncertainty of 3, 4 and 2.5%, respectively.

[b] All beta dose rates presented have been wet to6.6 and 6.9% moisture content as used in the age calculations of Jankowski *et al.* (submitted), attenuated for 200 μm diameter quartz grains according to Brennan (2003) and have a systematic uncertainty of 3%added in quadrature to account for the uncertainties in the beta particle attenuation factors.

obtained for the CS fractions. The feldspar components were measured to be 0.29 ± 0.01 and 1.00 ± 0.04 Gy/ka for the CS and FS, respectively. The highest β-D_r determined for this sample was for the FS heavy mineral component at 29.54 ± 2.51 Gy/ka. In contrast, the CS heavy mineral component (1.41 ± 0.10 Gy/ka) is more in line with the remaining β-D_r determined for this sample. The polymineral silt and clay components were measured to be 1.18 ± 0.08 and 1.54 ± 0.08 Gy/ka, respectively.

There seems to be a significant difference in the U concentrations between the TSAC and ICP-MS methods in both the MacCauley's Beach samples (Tables 6.3 and 6.4). It is considered the ICP-MS U concentration as an underestimation, with the majority of the ICP-MS:TSAC U concentration ratios more than 20% below unity. Similar underestimation of ICP-MS-determined U concentrations were found in Chapter 5 where it was concluded that this was a result of incomplete dissolution of the heavy mineral fraction when using a 'four acid digestion' prior to sample measurement (Intertek, pers. com), because zircon and rutile grains are known to be highly resistant. The β-D_r for each component in SP2 and SP5 using the TSAC U estimates in conjunction with the ICP-OES/MS-determined Th and K has therefore been calculated as the 'combined' β-D_r (Table 6.3, 6.4 and 6.5). In doing this, the majority of the β-D_r values become consistent with that produced using the GMBC method.

6.3.3.2 Pech IV (Layer 8 and Layer 5B)

The results for the two samples collected from Pech IV are shown in Table 6.5. The β-D_r values measured using the GMBC for Layer 8 show a β-D_r gradient from 0.18 ± 0.04 and 0.53 ± 0.03 Gy/ka that is associated with grain size reduction from FG to FSC. This gradient is also present in the β-D_r values for the Layer 5B sample, which ranges from 0.37 ± 0.02 Gy/ka for the FG fraction to 1.12 ± 0.04 Gy/ka for the FSC fraction. The ICP-OES/MS data for the CS and FSC provide further insights into the underlying geochemistry responsible for this increase. There is no significant change in U concentration for Layer 8 between CS and FSC fractions, but there is

increase in both the Th and K concentrations by about 20 and 30%, respectively. In contrast, all three radionuclides increase significantly from CS to FSC fraction in Layer 5B. Here, there is a one and half times increase in U, a doubling of K and a tripling of Th concentrations. Given the lack of any significant amounts of heavy minerals or K feldspars in these samples, the increase in β-D_r is considered to be associated with the clay content.

The GMBC β-D_r of both samples can also be explained using the ICP-OES/MS concentration for the separate samples of bone, flint and limestone. In the case of Layer 8, the FG fraction is comprised, predominantly, of an admixture of burnt and unburnt bone, with minor proportions of flint and limestone. The ICP-OES/MS β-D_r for the burnt and unburnt bone components of 0.28 ± 0.01 and 0.21 ± 0.01 Gy/ka, respectively, are consistent with the Layer 8 FG component β-D_r of 0.18 ± 0.05 Gy/ka measured using the GMBC. The FG fraction for the Layer 5B sample returned a β-D_r value of 0.37 ± 0.02 Gy/ka using the GMBC. This fraction was almost entirely comprised of limestone gravel and cobbles with a minor proportion of unburnt bone. The GMBC β-D_r for this fraction of 0.37 ± 0.02 Gy/ka is larger than the ICP-OES/MS β-D_r value for the limestone cobbles (0.31 ± 0.01 Gy/ka) collected from this same layer.

Unlike the MacCauley's Beach samples, in almost every instance where a GMBC and ICP-OES/MS β-D_r were able to be calculated for Pech IV samples, these values are within 2σ of unity. The exception is the GMBC β-D_r for the CS fraction for PdAIV-01-C falls just short of that determined using ICP-OES/MS. This consistency is attributed to the lack of highly resistant heavy minerals being found in these samples, such as zircon and rutile, which, if present, would produce a similar underestimation of U concentration and hence β-D_r. Alternatively, as the ICP-OES/MS method measures the parent radionuclides (U, Th and K) and GMBC measures the total of number of beta particles embittered for each decay chain, it is likely that the consistency of these two results is due to their being no disequilibrium present in the decay chains of these two samples.

6.3.3.3 RELATIVE CONTRIBUTIONS OF U, Th AND K TO BETA DOSE RATES

6.3.3.3.1 SP2 and SP5

It is interesting to compare the relative contributions (%) of U, Th and K to the total β-D_r (as shown in Tables 6.3 and 6.4) for the two locations investigated in this study. For the MacCauley's Beach components, the TSAC-determined U concentrations were used along with the ICP-OES/MS Th and K results. The FS1 quartz components have been excluded from both samples. The results, for both locations are shown graphically in Figure 6.3 as ternary diagrams. For sample SP2 (Figure 6.3a), the β-D_r for both the FS and CS feldspar components are dominated by K, at 76 and 46%, respectively. The clay, silt and HF-acid etched quartz components all fall approximately in the centre of the diagram; having a roughly equal contribution of each radionuclide to their respective β-D_r. The FG, CS quartz, both heavy mineral components, and bulk sample fall outside this central portion, with their β-D_r dominated by the presence of U. Of particular note is the FS heavy mineral component that has roughly equal contributions of both U and Th (52 and 47%, respectively).

A similar distribution exists for SP5 (Figure 6.3b). The β-D_r for the feldspar components are dominated by K, 83% for the CS and 94% for the FS. The β-D_r for the silt and clay components are also dominated by K, 53 and 60%, respectively. Only the CS heavy mineral and HF-acid etched quartz components fall in the central portion of the diagram. The presence of K in the HF-etched samples is most probably the result of grinding the sample with a ceramic pestle and mortar. The two remaining components, FS heavy mineral and CS quartz, have β-D_r that are dominated by U, as is the bulk sample of SP5 sediment.

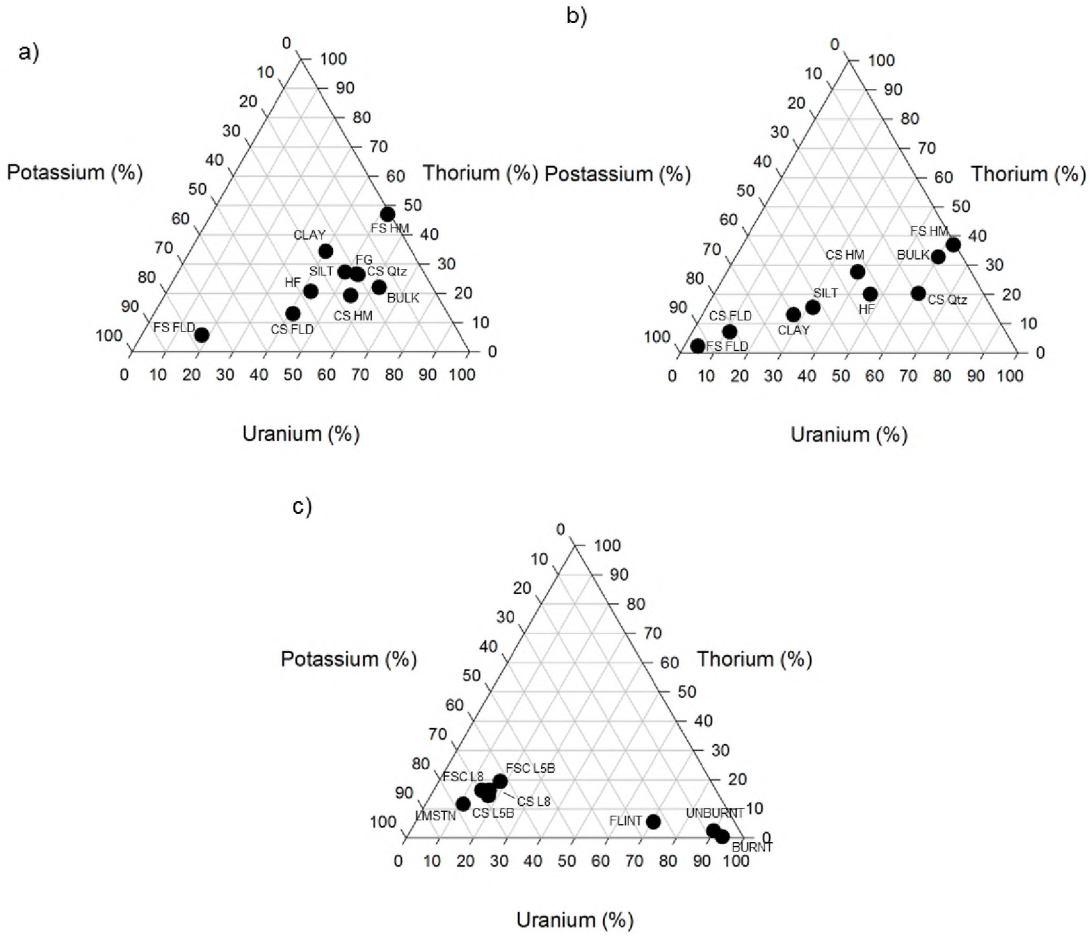

Figure 6.3. Ternary diagrams showing the contribution (%) of U, Th and K to the total β-D_r of sedimentary components for: a) SP2; b) SP5 and c) Pech IV. Here Layer 8 (L8) and Layer 5B (L5B) are shown together. The components shown for the MacCauley's Beach samples (SP2 and SP5) are those determined using TSAC (U and Th) and ICP-OES (K) listed in Tables 6.3 and 6.4. Those components shown for Pech IV were all determined using the ICP-OES/MS shown in Table 6.5.

6.3.3.3.2 Pech IV samples

The Pech IV fractions show a distinctly different contribution of U, Th and K to the total β-D_r values (Figure 6.3c). The concentrations of U, Th and K determined with ICP-OES/MS were used for the Pech IV components. Looking at the FG components, the β-D_r of the limestone pebbles are dominated by K (77%), whereas

those for the burnt and unburnt bone and flints are dominated by U, at 93, 90 and 71%, respectively. Both the CS and FSC fractions for Layer 8 are remarkably similar. Both samples are dominated by K at 67% for CS and 69% for the FSC fractions. The similarities are, presumably, associated with the significant amount of limestone spall being present in the CS fraction pulling the K contribution towards that of the 'pure' limestone K contribution, whereas for the FSC fraction, the clay and mica content would result in the same outcome. This high K contribution is also found in the Layer 5B CS and FSC components at 68 and 62%, respectively, presumably as a result of weathered limestone material being incorporated into the sediments.

6.4 UNDISTURBED SEDIMENT BLOCK SAMPLES

This section has been subdivided into four parts. In Section 6.4.1, the sample preparation and experimental design for the mapping of U, Th and K using a portable X-ray fluorescence (pXRF) device is outlined, the results presented and discussed, and limitations of this method considered. Section 6.4.2 investigates the applicability of modelling the distribution of the U, Th and K and generating a β-D_r map using image analysis techniques and the concentrations for the respective sedimentary components in Tables 6.2, 6.3 and 6.4. The experimental design is presented along with the modelled U, Th, K and β-D_r maps for each sample. These results are discussed and the limitations explained. The question of whether the pXRF and image analysis modelling results (which represent 2π geometries) are representative of natural sedimentary deposits (that present 4π geometries) is then addressed in Section 6.4.3. The final section, Section 6.4.4, examines the use of aluminium oxide (Al_2O_3:C) grains as a means of determining the 4π geometry of the β-D_r environment for all four samples. The experimental design and SAR procedures are outlined, the results presented and discussed.

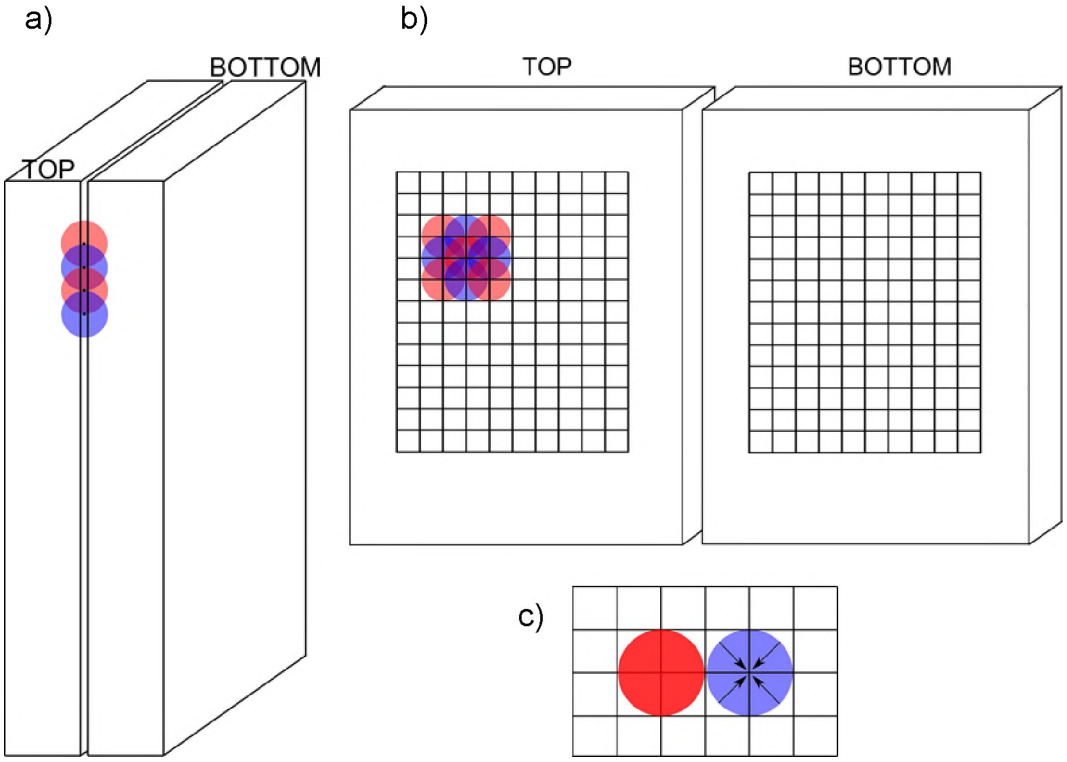

Figure 6.4. Schematics of the resin-impregnated sediment blocks used in the experiments conducted in this study. a) Sediment slabs were bisected to produce a mirror plane and a 'top' and 'bottom' slab using a 0.8 mm thick saw blade. Spheres represent 3 mm radius beta spheres of influence and are drawn in proportion relative to the 0.8 mm bisection width. b) The internal surface of both top and bottom slabs covered in a 3×3 mm grid drawn in pencil measuring 3.0 cm (horizontal) by 3.9 cm (vertical). pXRF, and Al_2O_3:C, measurements were made at each vertex point on the top and bottom slab. c) The pXRF estimates the concentration of U, Th and K of the 3 mm radius sphere (left hand sphere). The Al_2O_3:C grains directly measure the β-D_r delivered to the grains positioned on the vertex of each analysis point.

6.4.1 RADIONUCLIDE DISTRIBUTIONS USING PXRF

6.4.1.1 SAMPLE PREPARATION

The sediment block samples collected from MacCauley's Beach and Pech IV were prepared using the techniques outlined in Courty *et al.* (1989) and in Chapter 4. The resin-impregnated sediment blocks were cut into slabs of ~7 x 5 cm in area and ~2 cm in thickness. These slabs were then bisected using a Buehler Isomet® 1000 precision saw, with a 0.8 mm thick cutting blade to produce 2 slabs of ~1 cm thickness that are the mirror image of each other (Figure 6.4).

6.4.1.2 PXRF INSTRUMENT

A Thermo Scientific Niton (XL3t GOLDD+) handheld pXRF was used to determine the concentrations of U, Th and K. X-rays are generated from an Ag anode X-ray tube at 50 kV and 200 μA. Measurements were made using the 'TestAll Geo' setting for 2 min at each measurement point. This analysis setting effectively determines the concentrations for up to 30 different elements, from Mg to U, that are commonly found in geological and soil samples.

6.4.1.3 EXPERIMENTAL DESIGN

Measurements were made using the pXRF across both internal surfaces of the bisected slabs for all four samples (Figure 6.5). To do this, a 3×3 mm grid was drawn onto the sample in pencil that covered an area 30 mm (11 points) by 39 mm (14 points) (Figure 6.5). A total of 154 points were measured per slab or 308 points per sample (i.e., the two internal faces; Figure 6.4 and 6.5).

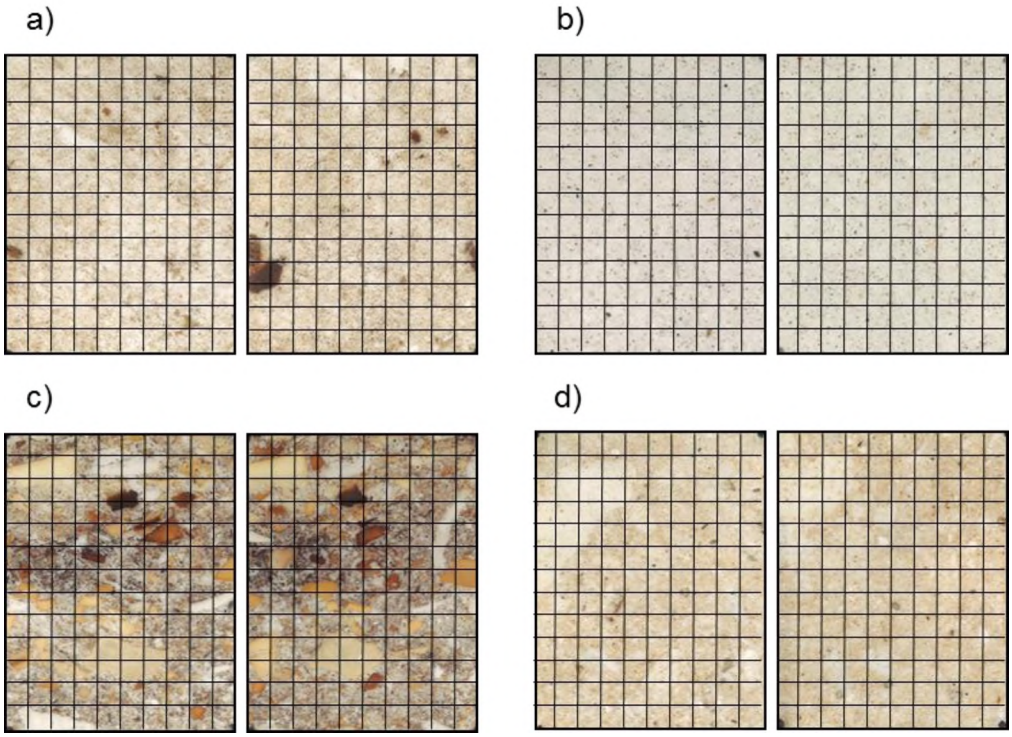

Figure 6.5. Thin section scans of mirror-image faces on the inside of the bisected resin-impregnated slabs of: a) SP2; b) SP5; c) Layer 8; and d) Layer 5B. Each thin section is covered with a 3×3 mm grid, which, including the image borders, is comprised of 11 columns and 14 rows. In each example, the bottom slab is given on the left and the top is on the right.

Table 6.6. Weighted mean concentrations (±1σ se) and relative standard errors (%) for U, Th, K and Si elements in SP5_pp, SiO2 and 'pure' resin samples determined using pXRF. < LOD; less than the level of detection.

	U (µg/g)	Th (µg/g)	K (µg/g)	Si (%)
SP5_pp (n=23)	10.2 ± 0.6 (5.9)	16.0 ± 0.4 (2.5)	874.4 ± 14.9 (1.7)	47.9 ± 0.2 (0.4)
SiO_2 (n=26)	< LOD -	< LOD -	< LOD -	40.1 ± 0.5 (1.2)
Resin	< LOD -	< LOD -	133.4 ± 4.1 (3.1)	0.3 ± 0.0 (1.2)

Measurements were made by moving the 6 mm diameter detection window of the pXRF device systematically along successive vertices of this grid. This approach resulted in the measurement of overlapping 3 mm in diameter spheres, which is roughly the same size as the average penetration range of individual β-particles in sediment (Figure 6.4). It should, however, be kept in mind that the scale of analysis still only represents an average of each sphere and not equivalent to the potential β-D_r received by an individual grain.

6.4.1.4 INSTRUMENT REPRODUCIBILITY

Reproducibility of the pXRF analyser was determined by periodically measuring a blank standard (SiO_2) and a pressed pellet made from a pulverised and homogenised subsample of SP5 (SP5_pp). The weighted mean concentrations and the relative errors for both the SiO_2 blank and SP5_pp are shown in Table 6.6. The reproducibility for U, Th and K measurements of SP5_pp were 5.8, 2.5 and 1.7%, respectively. In the SiO_2 blank, only small amounts of Ti and Ca were measured.

6.4.1.5 CONTRIBUTION OF THE CASTING RESIN

The contribution of the casting resin to the total count rate was also investigated (Table 6.6). Analysis of a 'pure' casting resin sample resulted in detectable levels of K (133.4 ± 4.1 µg/g). No correction to the final K concentrations, however, was made for the K measured for our resin-impregnated sediment blocks because: 1) the volume of resin present in the sediment sample slabs is significantly less than the volume measured from the 'pure' casting resin slab (i.e., 100%); and 2) significant variations in the volume of resin found between successive measurement positions on the sediment slab make the application of a standardised correction factor to each measurement impractical.

6.4.1.6 pXRF Calibration

The measured U, Th and K at each measurement position were then calibrated to provide accurate concentrations of each element. Calibration curves were constructed from a number of known standards for the four elements investigated in this study (Figure 6.6). These standards included two NIST standards (2709a and 2780pp), sub-samples of 105A and 109 (Aitken 1985; p. 306) and four 'in house' sample standards (PDLII-04 and PDLII-16 from Pech de l'Azé II in southwestern France and SP2 and SP5 from MacCauley's Beach Australia), whose elemental concentrations were determined by laboratory XRF analysis (Table 6.7). Each standard was measured five times for 2 min duration using the pXRF. The weighted mean value of the 5 repeats for each standard and their standard errors are plotted for each element against their respective independently determined concentrations in Figure 6.6. If no detectable amount was obtained then the standard was not used in the calibration curve and was omitted from Figure 6.6. A linear function ($y = mx+b$) was fitted to the data to determine the slope and intercept and a goodness of fit (R^2 value). The uncertainties in the fitting of the calibration curves to each data set was estimated using equation 7 in Duller (2007) and calculated to be 1.8% (U; Figure 6.6a), 1.6% (Th; Figure 6.6b) and 0.14% (K; Figure 6.6c).

A worked example of the conversion processes for the K concentration from sample SP2 is given in Table 6.8. The 'raw' pXRF measured concentrations of U, Th and K (Step 1) were then substituted into their respective calibration curve equations (see Figures 6.6a–c; Steps 2 and 3) and solved to obtain calibrated concentrations of each (Step 4). The associated relative standard error for each measurement (Step 5) was then summed in quadrature with its respective calibration curve fitting error (Steps 6 and 7) to provide calibrated concentrations of U, Th and K and an associated uncertainty that takes into account the uncertainty on the fitted calibration curve (Step 8). All uncertainties are reported at 1σ.

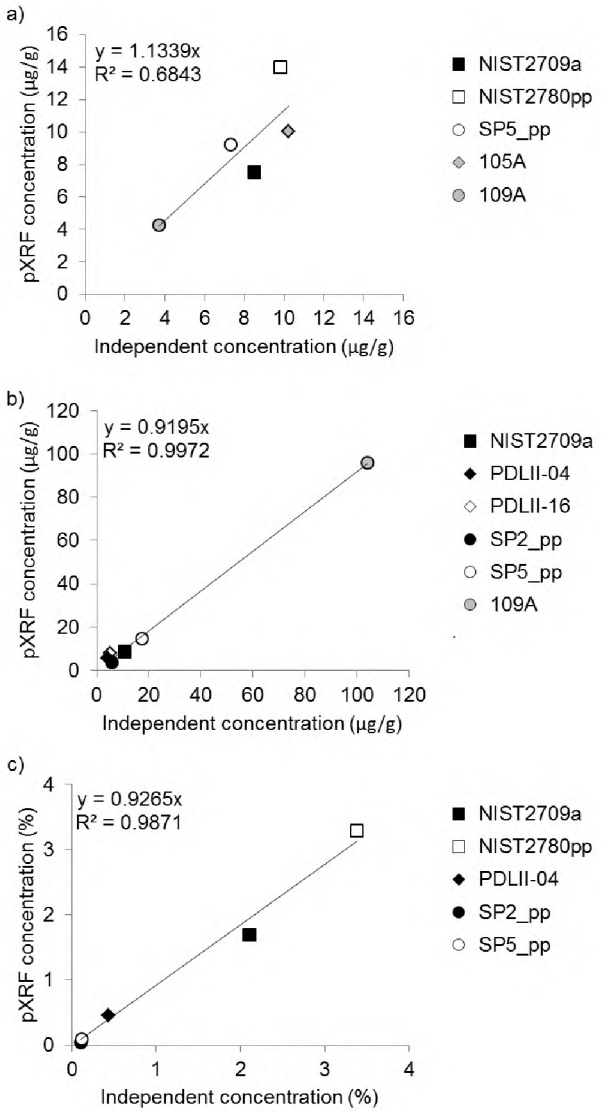

Figure 6.6. Calibration curves for the pXRF used throughout this study for: a) U, b) Th, and c) K.

Table 6.7. Concentrations of U, Th and K determined using laboratory XRF conducted at the University of Wollongong. No uncertainties were provided with these measurements.

Sample name	U (µg/g)	Th (µg/g)	K (%)
SP2	<1.0	5.9	0.11
SP5	7.3	17.5	0.11
PDLII-04	0.3	4.3	0.43
PDLII-16	<1.0	5.1	0.67

Table 6.8. Steps involved in the calibration of 'raw' pXRF K concentration using the calibration curve presented in Figure 6.6c.

Step	Description	Calculation
1	Original K concentration (± 1σ)	0.095 ± 0.005 %
2	K calibration curve equation	y = 0.9265x
3	Substituting K concentration from Step 1 for y in calibration curve equation in Step 2	0.095 = 0.9265x
4	Solve calibration curve equation in Step 3 for x	x = 0.095/0.9265 x = 0.103
5	Find relative standard error (RSE) on the K measurement in Step 1	RSE = 0.005/0.095 ×100 RSE = 5.26%
6	Sum in quadrature with the RSE in Step 5 with K calibration curve fitting error of 0.14%	Sum = SQRT (27.67 + 0.02) Sum = SQRT (27.69) Sum = 5.26%
7	Multiply calibrated K concentration in Step 4 by the sum of squares RSE in Step 6	1σ = 0.103×0.056 1σ = 0.005
8	Calibrated K concentration	0.103 ± 0.005%

6.4.1.7 RESULTS

6.4.1.7.1 K distribution maps for MacCauley's Beach and Pech IV

The K distribution maps for the four samples investigated are presented in Figure 6.7 and 6.8. The K distribution maps presented in Figure 6.7 have been shown drawn to the same scale (0.00–0.06% K) so that the variation *between* samples can be easily identified. In contrast, Figure 6.8 shows the same K distributions as presented in Figure 6.7, however, each sample has been drawn to its own individual scale to highlight the variability in K concentration *within* each sample.

Detectable levels of K were measured at each of the 154 points of analysis on each sediment face examined using the pXRF. At MacCauley's Beach, the K concentrations for SP2 range between 0.06 ± 0.01 and 0.18 ± 0.01%. The concentrations of K in SP5 are comparable and range from 0.04 ± 0.01 to 0.17 ± 0.01%. These K concentrations are equivalent to dry and unattenuated β-D_r values of 0.05 ± 0.01 and 0.14 ± 0.01 Gy/ka for SP2 and 0.03 ± 0.01 and 0.14 ± 0.01 Gy/ka for SP5. These regions are shown as purples and blues in Figures 6.7a and b, respectively, and relatively homogenous at this scale. Yet, closer inspection of Figure 6.8a and b reveal that the distribution of K throughout these samples is heterogeneous. From analysis of the associated thin sections, the area with higher concentrations of K (red and yellows in Figure 6.8a and b) are associated with areas containing a greater proportion of silts and clays rather than the presence of discrete mineral grains (such as K-feldspar). From the disturbed dosimetric information presented in Tables 6.3 and 6.4 for SP2 and SP5, respectively, the silt (0.21% SP2, 0.78 % SP5) and clay (0.18% SP2, 1.12 % SP5) components have K concentrations that are larger than their respective quartz or heavy mineral components and also their CS feldspar fractions. However, in terms of BM, it is considered that the small variations detected using the pXRF would have only a small, if not negligible, effect on the localised variations in β-D_r values.

The Pech IV samples show similarly heterogeneous K. The lowest measured K concentrations were 0.06 ± 0.02% for Layer 8 (Figures 6.7c and 6.8c) and 0.28 ± 0.02% for Layer 5B (Figure 6.7d and 6.8d). In Figures 6.8c and d, these concentrations are shown as dark blue. From analysis of the associated thin sections, these regions of low K concentrations appear to be associated with regions of flint and bone. The highest K values are typically found in regions of sedimentary matrix and were measured to be 0.40 ± 0.03% (Layer 8) and 0.62 ± 0.03% (Layer 5B) and appear as reds and yellows in Figure 6.8c and d. Within the sedimentary matrix, the clays are likely to be responsible for the high concentrations of K as has been shown in Table 6.5 for the FSC components in both samples. As is the case with the MacCauley's Beach samples, it is unlikely that the variations observed in K concentrations are influential in terms of BM.

6.4.1.7.2 U and Th distribution maps for MacCauley's Beach and Pech IV

Using the pXRF, according to the manufacturer, the detection limits for U, Th and K in a typical soil matrix containing Si, Fe and Ca are ~4, 4 and 150 μg/g, respectively. Of a total possible 308 measurements in each of the four samples, U was present above detection limits at 16 positions (5%) for SP2, 64 positions (21%) for SP5, 17 positions (6%) for Layer 8 and 14 positions (5%) for Layer 5B. The detection of Th was substantially better than the U, although this too failed to attain 100% detection. As such, 221 (72%), 254 (82%), 104 (34%) and 206 (67%) positions for SP2, SP5, Layer 8 and Layer 5B had detectable levels of Th. At each of these measurement positions the concentrations of U and Th were above the detection limit of the pXRF detector. For all other measurements positions where no U and Th were able to be detected, it can be assumed that here the concentrations of U and Th range between 0 and 4 μg/g and are all shown as purple in Figure 6.8 and 6.9.

The distribution maps for U for each of the four samples are shown in Figures 6.9 and 6.10. As was the case with K, these two figures display the same data but use different scales, the former standardised, the latter variable. The concentrations of detectable U in SP2 range between 3.32 ± 1.07 and 5.55 ± 1.31 μg/g, shown as dark

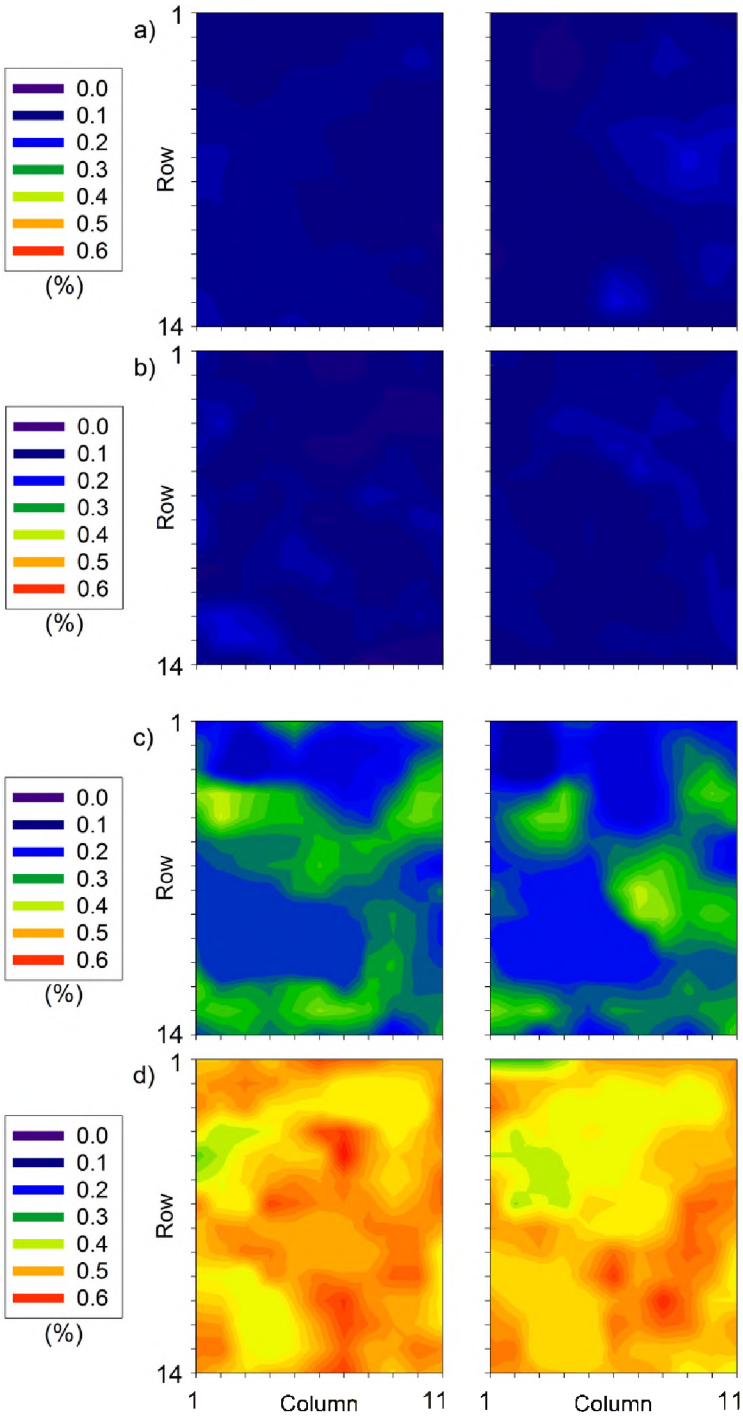

Figure 6.7. Portable XRF-determined K distribution maps for a) SP2, b) SP5, c) Layer 8 and d) Layer 5B. In each example the same K scale (0.00–0.06%) has been used to facilitate comparison ***between*** samples. The bottom slab is given on the left and the top is on the right.

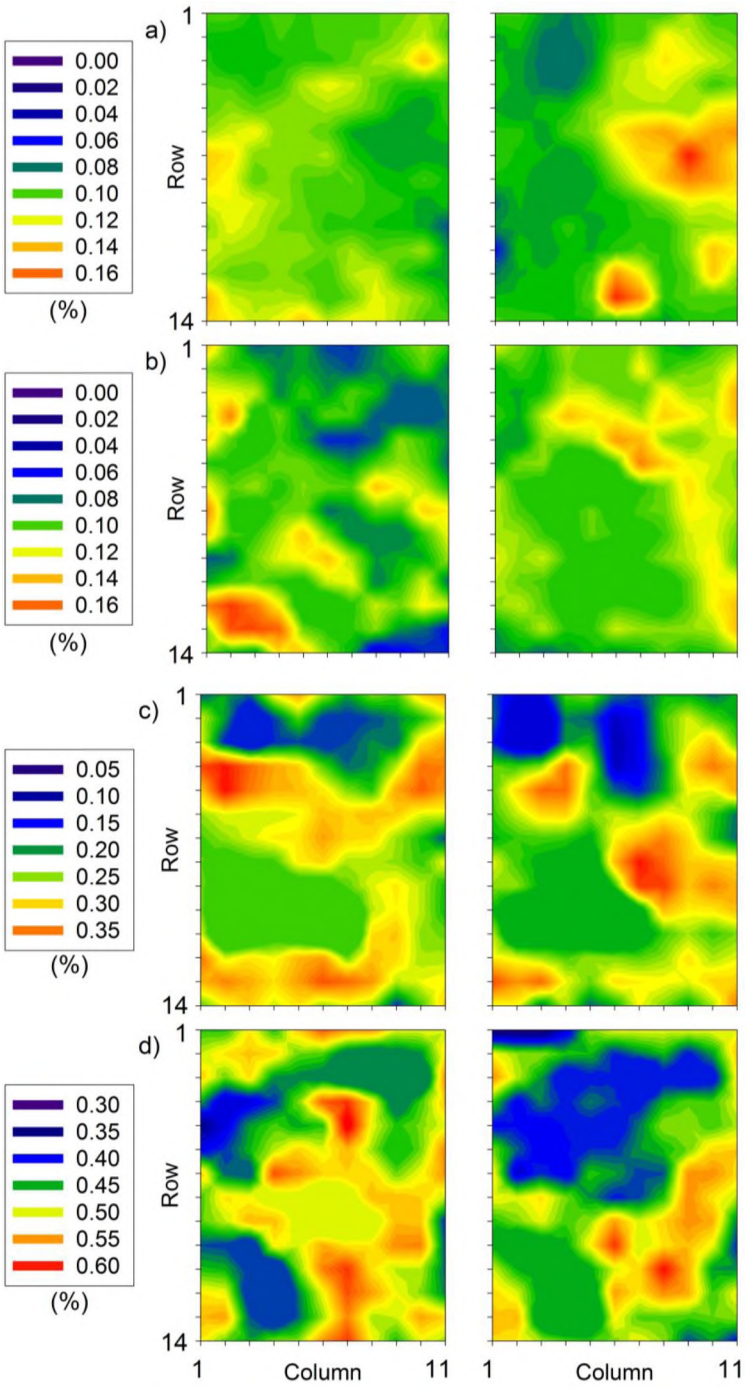

Figure 6.8. Portable XRF-determined K distribution maps for a) SP2, b) SP5, c) Layer 8 and d) Layer 5B using individual scales to display the range of concentrations ***within*** a sample. In each example, the bottom slab is given on the left and the top is on the right.

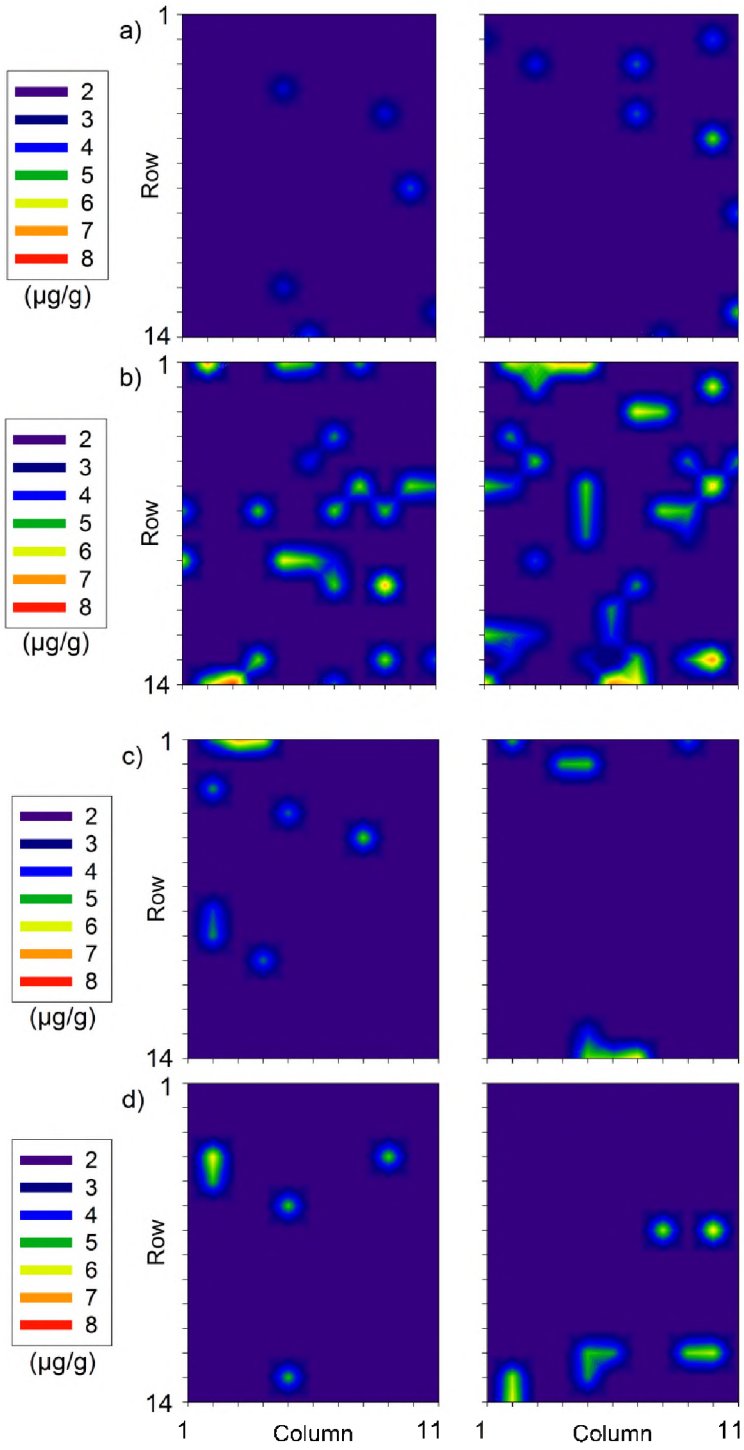

Figure 6.9. Portable XRF-determined U distribution maps for a) SP2, b) SP5, c) Layer 8 and d) Layer 5B. In each example the same U scale (2–8 µg/g) has been used to facilitate comparison ***between*** samples. The bottom slab is given on the left and the top is on the right.

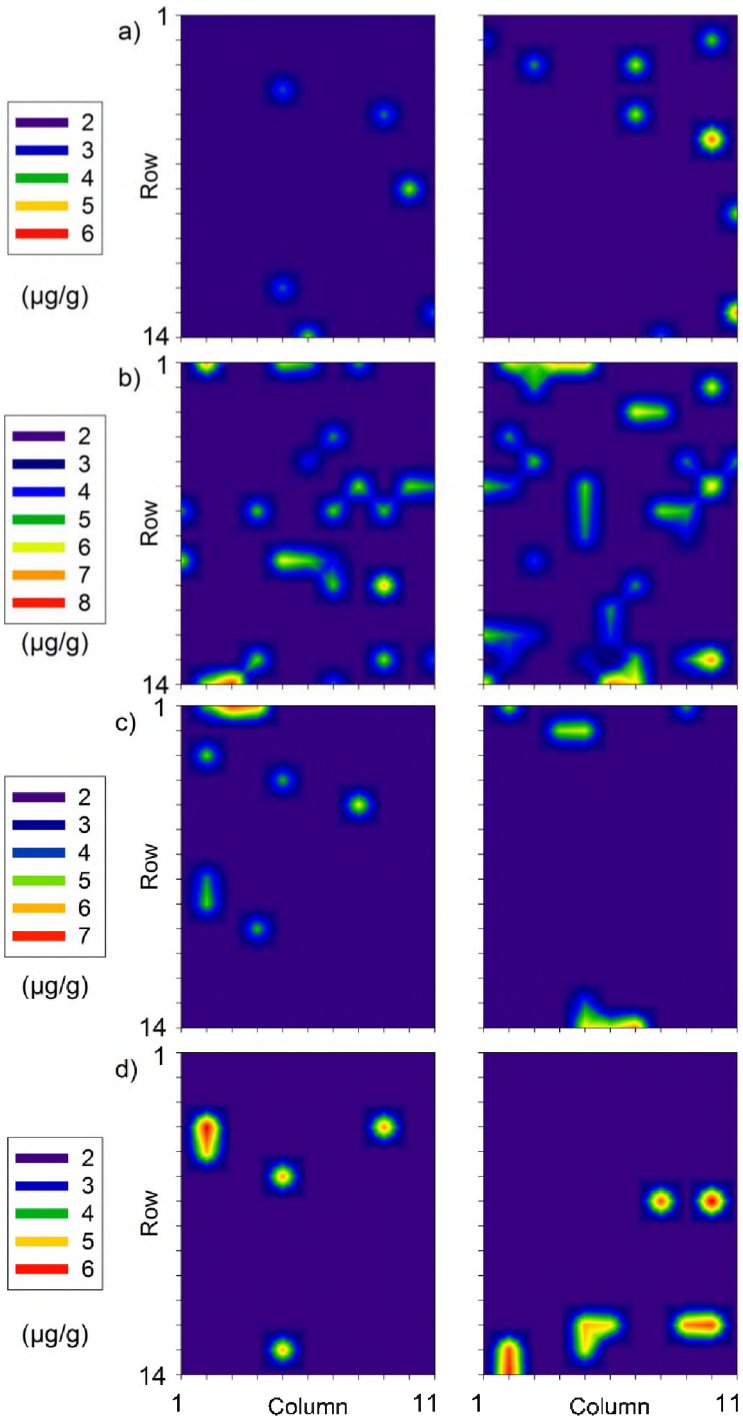

Figure 6.10. Portable XRF-determined U distribution maps for a) SP2, b) SP5, c) Layer 8 and d) Layer 5B using individual scales to display the range of concentrations ***within*** a sample. In each example, the bottom slab is given on the left and the top is on the right.

blue to green in Figure 6.9a and dark blue to red in Figure 6.10a. In contrast, the range of concentrations for detectable U in SP5 is substantially greater than that for SP2, ranging between 3.58 ± 1.11 and 7.86 ± 2.41 μg/g (dark blue to red in both Figure 6.9b and Figure 6.10b). The spatial distribution U is heterogeneous, occurring as discrete 'hotspots' unlike the interconnected and broad regions of high K presented in Figure 6.7 and 6.8. Given this punctuated distribution pattern, the component concentrations for these two samples provided in Tables 6.3 and 6.4 and analysis of the associated thin sections, suggests that it is most likely that these U 'hotspot' regions are associated with the inhomogeneous distribution of heavy minerals throughout these sediment samples.

At Pech IV, the Layer 8 above detection level U concentrations range from 4.07 ± 1.40 to 6.75 ± 2.08 μg/g and between 4.80 ± 2.26 and 6.23 ± 2.33 μg/g for Layer 5B (Figures 6.9 and 6.10c and d). An inhomogeneous, and punctuated, U 'hotspot' distribution is observed for both samples. Using thin sections made from the same resin-impregnated slabs, these hotspots can be correlated to regions containing bone fragments rather than sedimentary matrix.

The Th distribution maps determined using the pXRF are displayed in Figures 6.11 and 6.12 at standardised (former) and variable (latter) scales. Inhomogeneous Th distribution patterns were observed in each of the four samples. For SP2, the calibrated Th concentrations range from 2.78 ± 0.92 to 10.65 ± 1.22 μg/g (dark blue to green in Figure 6.9a), whereas SP5 Th concentrations range from 2.94 ± 0.92 to 18.03 ± 1.57 μg/g (dark blue to red in Figure 6.9b). The variability in SP2 is further highlighted in Figure 6.12a, where the lower end of this range (2.78 ± 0.92 μg/g) is shown as dark blue and the upper end (10.65 ± 1.22 μg/g) as red. The distribution patterns for these two samples are slightly more interconnected than their U counterparts. While the punctuated Th 'hotspots' are again considered to be due to the same heavy mineral component that gave rise to the U distribution, the interconnections are more likely the result of Th being found within the interstitial silt and clay matrix. This position is supported by SP2 silt and clay components (Table 6.3) have higher Th concentrations than any other component measured, with the exceptions of the CS and FS heavy mineral components.

At Pech IV, similar interconnected distributions of detectable Th are observed (shown in dark blue in Figures 6.11c and d). The detectable Th concentrations range from 2.51 ± 1.44 to 5.80 ± 2.30 µg/g for Layer 8 and between 2.64 ± 1.80 and 7.96 ± 2.33 µg/g for Layer 5B. This variability is better observed in Figures 6.12c and d where these ranges are shown by dark blue to red. A comparison of the distribution of detectable Th for Layer 8 (in Figure 6.9c) and the thin sections shown in Figure 6.5 shows that these regions are often associated with bone fragments. This apparent high-concentration of Th also present in bone fragments is not echoed in the ICP-MS burnt or unburnt bone concentrations of 0.04 ± 0.00 or 0.18 ± 0.01 µg/g, respectively, presented Table 6.5. Presumably, the Th is taken up by the bone fragments in localised regions rather than uniformly throughout the entire bone fragment. In this scenario, the pXRF would be able to resolve the elevated Th regions, whereas (by pulverising an entire bone fragment) the ICP-MS would be measuring the average Th concentration for the entire fragment.

6.4.1.7.3 Beta dose rate maps for MacCauley's Beach and Pech IV

The ultimate goal of this experiment was to construct a β-D_r map for both internal faces of the four samples investigated and to compare these values with the D_e distributions in an attempt to explain the measured OD. This goal requires that the concentrations of U, Th and K measured at each analysis position be converted into dose rate. Yet, is it not possible to do this when U and Th concentrations were below the detection limit of the pXRF. It was assumed that those positions with no detectable U and Th have mean concentration that are less than that of the 4 µg/g detection limit for these elements. These positions were, therefore, assigned U and Th concentrations of 2 ± 1 (1σ) µg/g, making them consistent with both the 4 µg/g detection limit of the pXRF and 0 at 2σ. The value of constructing a β-D_r map using the pXRF, therefore, is to spatially resolve the distribution of β-D_r 'hotspots' alone, as only the upper tail end members of the true β-D_r distribution could be accurately determined with this instrument.

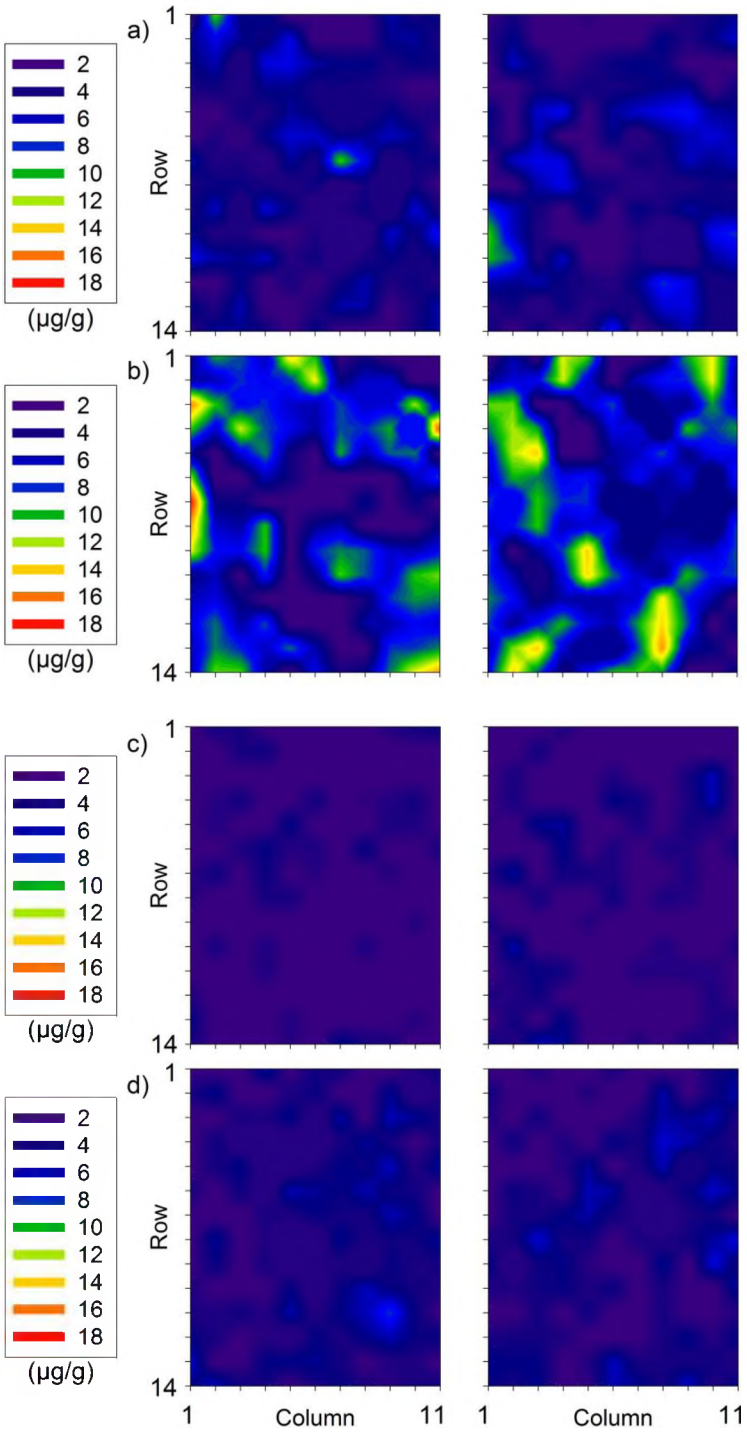

Figure 6.11. Portable XRF-determined Th distribution maps for a) SP2, b) SP5, c) Layer 8 and d) Layer 5B. In each example the same Th scale (2–18 µg/g) has been used to facilitate comparison *between* samples. The bottom slab is given on the left and the top is on the right.

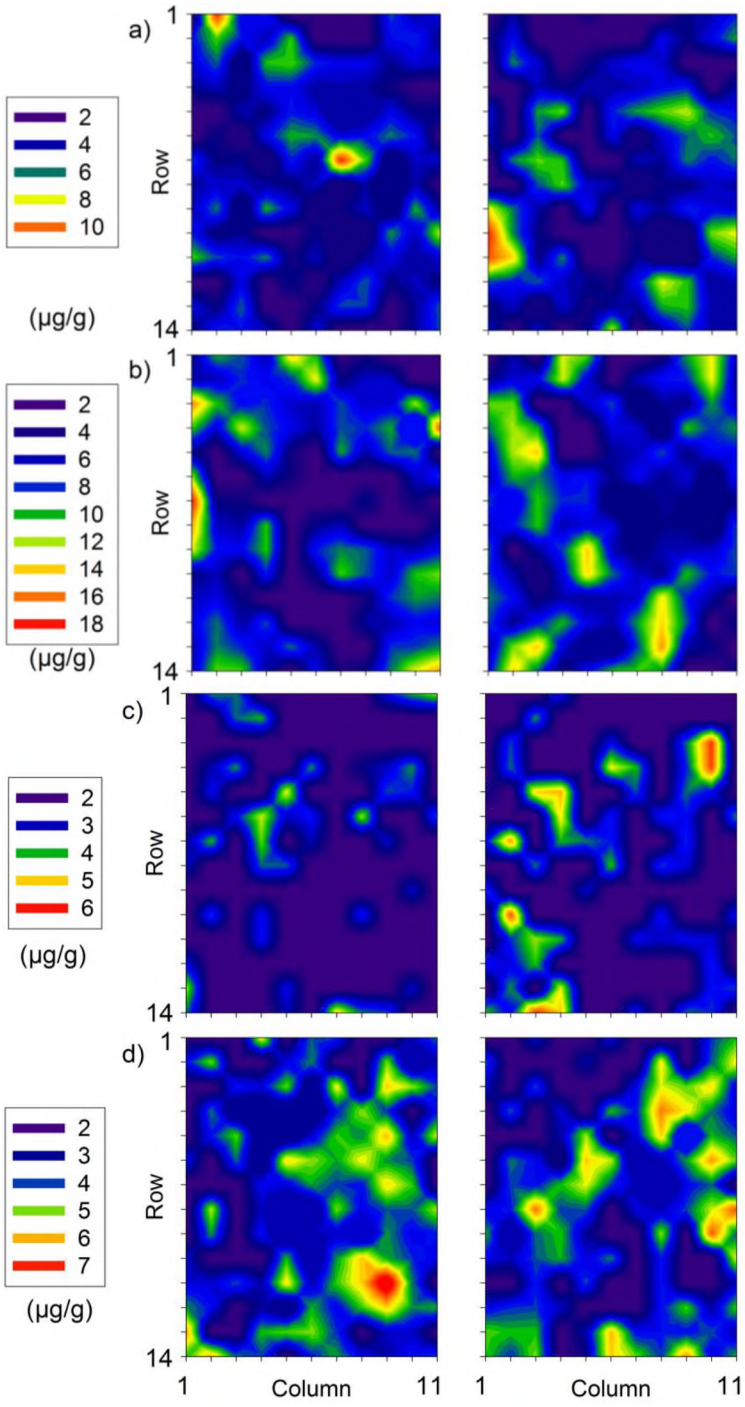

Figure 6.12. Portable XRF-determined Th distribution maps for a) SP2, b) SP5, c) Layer 8 and d) Layer 5B using individual scales to display the range of concentrations *within* a sample. In each example, the bottom slab is given on the left and the top is on the right.

6.4.1.7.3.1 β-D_r calculations from pXRF-determined concentrations of U, Th and K

To calculate the β-D_r for a given analysis position, the calibrated elemental concentrations of U, Th and K (Step 1; Table 6.9) were converted into beta dose rate (Step 3; Gy/ka) using the respective conversion factors of Guérin *et al.* (2011) (Step 2). Because these β-D_r values are to be compared to their respective D_e distributions, the converted β-D_r (Step 3) are required to account for water content of their respective samples (Step 4). This was achieved using the water correction factor equation (equation 4.6) in Aitken (1985) (Step 5) and multiplying the converted β-D_r by this factor (Step 6). The 'wet' β-D_r values need to be attenuated to account for the 180–212 μm HF-acid etched quartz grains used in D_e determinations. The 'wet' β-D_r were then multiplied by their respective attenuation coefficients (Step 8) presented in Brennan (2003) (Step 7). The 'wet' and attenuated β-D_r values for U, Th and K were then summed (Step 9).

The associated uncertainty is the quadratic sum of the individual uncertainties on the U, Th and K concentration measurements with a systematic 3% error added to account for the uncertainty on the β-D_r attenuation factors. The relative standard error on each elemental concentration measurement was calculated (Step 10) and this value multiplied by the converted β-D_r values for the respective element (Step 11). The 3% systematic error was estimated by multiplying the 'wet' and attenuated β-D_r by 0.03 and then by 1/water content correction factor (Step 12). The individual standard errors on the converted β-D_r and the 3% systematic error were then added in quadrature (Step 13). By completing these steps for each individual analysis position, a 'wet' and attenuated β-D_r and an associated uncertainty (Step 14) were calculated for each sample. It should be noted that the β-D_r provided here are effectively averages of the 6 mm diameter of the pXRF detection window and represent only the true upper-tail members of the β-D_r distribution. Regardless, the β-D_r maps are an improvement on the disturbed sample β-D_r measurements as they show the distribution of 'true' β-D_r 'hotspots' in space.

Table 6.9. Steps taken to convert concentrations of U, Th and K determined using the pXRF into β-D_r.

Step	Description	Calculation
1	Calibrated concentrations of U, Th and K	U = 6.13 ± 2.23 µg/g Th = 4.12 ± 2.24 µg/g K = 0.37 ± 0.01%
2	Dose rate conversion factors for full U and Th series, and K, from Guérin *et al.* (2011)	U_{con} = 0.1457 Th_{con} =0.0277 K_{cov} = 0.7982
3	Convert U, Th and K concentrations into dry β-D_r using respective conversion factors in Step 2	U_{dry} β-D_r = 6.13 × 0.1457 U_{dry} β-D_r = 0.89 Gy/ka Th_{dry} β-D_r = 4.12 × 0.0277 Th_{dry} β-D_r = 0.11 Gy/ka K_{dry} β-D_r = 0.37 × 0.7982 K_{dry} β-D_r = 0.29 Gy/ka
4	Water content (WC) for Layer 5B	WC = 6.6 ± 1.7%
5	WC correction factor using equation 4.6 of Aitken (1985)	Correction factor = 1/[1+1.25×(0.066)] Correction factor = 0.924
6	Adjust dry β-D_r for WC by multiplying by the correction factor in Step 5	U_{wet} β-D_r = 0.89 × 0.924 U_{wet} β-D_r = 0.83 Gy/ka Th_{wet} β-D_r = 0.11 × 0.924 Th_{wet} β-D_r = 0.11 Gy/ka K_{wet} β-D_r = 0.29 × 0.924 K_{wet} β-D_r = 0.27 Gy/ka
7	Attenuation factors for U, Th and K delivered to 180–212 HF-acid etched quartz grains from Brennan (2003)	U_{atten} = 0.839 Th_{atten} = 0.782 K_{atten} = 0.918
8	Attenuate the 'wet' U, Th and K β-D_r using the attenuation factors in Step 7	$U_{wet+atten}$ β-D_r = 0.83 × 0.839 $U_{wet+atten}$ β-D_r = 0.69 Gy/ka $Th_{wet+atten}$ β-D_r = 0.11 × 0.782 $Th_{wet+atten}$ β-D_r = 0.08 Gy/ka $K_{wet+atten}$ β-D_r = 0.27 × 0.918 $K_{wet+atten}$ β-D_r = 0.25 Gy/ka
9	Sum 'wet' and attenuated β-D_r for U, Th and K	Total β-D_r = 0.69 + 0.08 + 0.25 Total β-D_r = 1.02 Gy/ka

10	Find the relative standard error (RSE) on U, Th and K concentrations in Step 1	U_{RSE} = 2.23/6.13 U_{RSE} = 0.36 Th_{RSE} = 2.24/4.12 Th_{RSE} = 0.54 K_{RSE} = 0.01/0.37 K_{RSE} = 0.04
11	Find the standard error by multiply the wet and attenuated U, Th and K β-D_r in Step 9 by their respective RSE from Step 10	U_{se} = 0.69 × 0.36 U_{se} = 0.25 Th_{se} = 0.08 × 0.54 Th_{se} = 0.04 K_{se} =0.25 × 0.04 K_{se} = 0.01
12	Determine the 3% systematic uncertainty to account for uncertainty in the attenuation factors. Multiply the total 'wet' and attenuated β-D_r (Step 9) by 0.03 and then multiply by 1/WC correction factor (Step 5)	3% systematic uncertainty = 0.03 × 1.02 × (1/0.924) = 0.03
13	Sum in quadrature the standard errors for U, Th and K in Step 11 and the 3% systematic error in Step 12.	se = SQRT(0.25^2 + 0.04^2 + 0.01^2 + 0.03^2) se = 0.26
14	Wet and attenuated β-D_r (± 1σ)	1.02 ± 0.26 Gy/ka

6.4.1.7.4 β-D_r maps

The β-Dr maps constructed using the pXRF-determined concentrations of U, Th and K are shown in Figures 6.13 and 6.14. From Figure 6.14 it is evident that SP5 and layer 5B contain the highest β-D_r values (shown as red and yellow; Figure 6.13b and d), whereas SP2 and Layer 8 are substantially lower (shown as mainly blues and greens; Figures 6.13a and c). For the SP2 sample (Figure 6.14a), the β-Dr ranges between 0.30 ± 0.11 (dark blue) and 0.80 ± 0.14 Gy/ka (red). This is in contrast to the SP5 sample where β-Dr of between 0.32 ± 0.12 (medium blue) and 1.20 ± 0.29 Gy/ka (red) were obtained (Figure 6.14b). The pXRF β-Dr values for Layer 8 range

from 0.31 ± 0.12 to 0.98 ± 0.24 Gy/ka (shown in purple to red in Figure 6.14c), whereas that for Layer 5B is slightly larger, ranging from 0.49 ± 0.12 to 1.17 ± 0.27 Gy/ka (Figure 6.14d). The large errors associated with the lower most β-Dr values are the result of the 50% relative uncertainties on the arbitrarily assigned U concentrations of U and Th that were below the pXRF detection levels. In contrast, the errors on the highest β-Drs are due to the large errors associated with the detection of U by the pXRF.

It is interesting to compare the weighted mean pXRF-determined β-D_r with those obtained for the 'bulk' samples using the GMBC. The weighted mean pXRF β-D_r for SP2 (0.38 ± 0.01 Gy/ka) falls higher than that of the GMBC (0.31 ± 0.03 Gy/ka), but is consistent at 2σ. For Layers 8 and 5B from Pech IV the GMBC β-D_r values of 0.29 ± 0.03 and 0.49 ± 0.03 Gy/ka, respectively, are significantly less that the weighted mean pXRF β-D_r values of 0.47 ± 0.01 (Layer 8) and 0.63 ± 0.01 (Layer 5B). The reverse situation is true for SP5. The SP5 GMBC β-D_r (0.92 ± 0.07 Gy/ka) is significantly higher than (and almost double) that of the pXRF (0.51 ± 0.01 Gy/ka). Disequilibrium in the SP5 U-series has been shown to exist (Chapter 5. Table S5.3). HRGS results estimate the β-D_r to be 0.74 ± 0.03 Gy/ka. This β-D_r value is still much greater than the weighted mean pXRF β-D_r. β-D_r values of 0.29 ± 0.03 using the GMBC. It is clear that for SP2, Layer 8 and Layer 5B, the 2 ± 1 μg/g assigned to both U and Th are resulting in overestimation of the β-D_r, whereas in SP5, these same values are underestimating the β-D_r.

The spatial distribution of these β-Dr 'hotspots' is quite inhomogeneous across each of the eight 11.7 cm^2 areas investigated, with the exception of SP2. In each of the remaining three samples investigated, the positions of high β-D_r (that is the β-D_r 'hotspots') are primarily dictated by the presence of detectable U. The influence of K and Th, however, is interchangeable. At MacCauley's Beach, the presence of Th is of secondary importance producing a number of discrete β-D_r 'hotspots.' In contrast, the distribution of K at Pech IV effectively negates any spatially heterogeneous β-D_r effects that arise from variability in the Th concentrations.

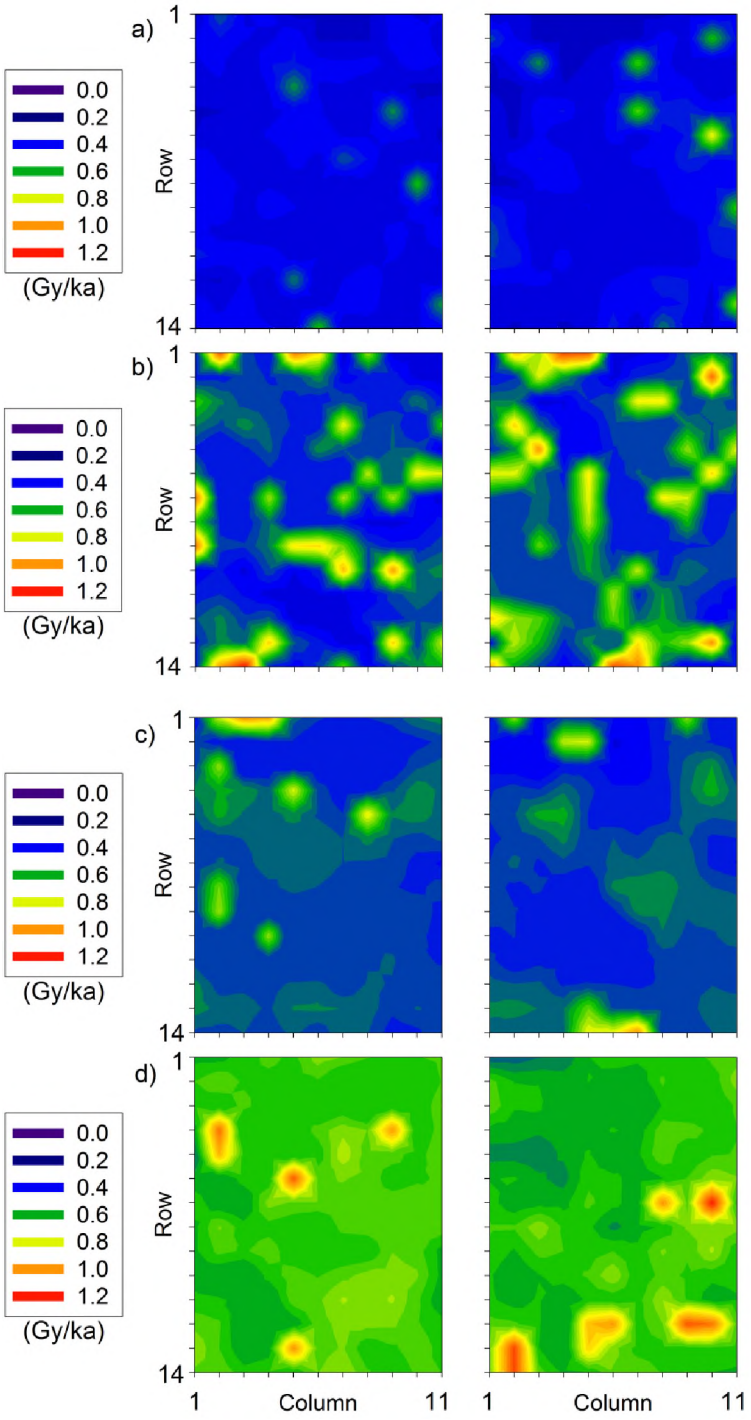

Figure 6.13. Portable XRF-determined β-D_r distribution maps for a) SP2, b) SP5, c) Layer 8 and d) Layer 5B. In each example the same β-D_r scale (0–1.2 Gy/ka) has been used to facilitate comparison *between* samples. The bottom slab is given on the left and the top is on the right.

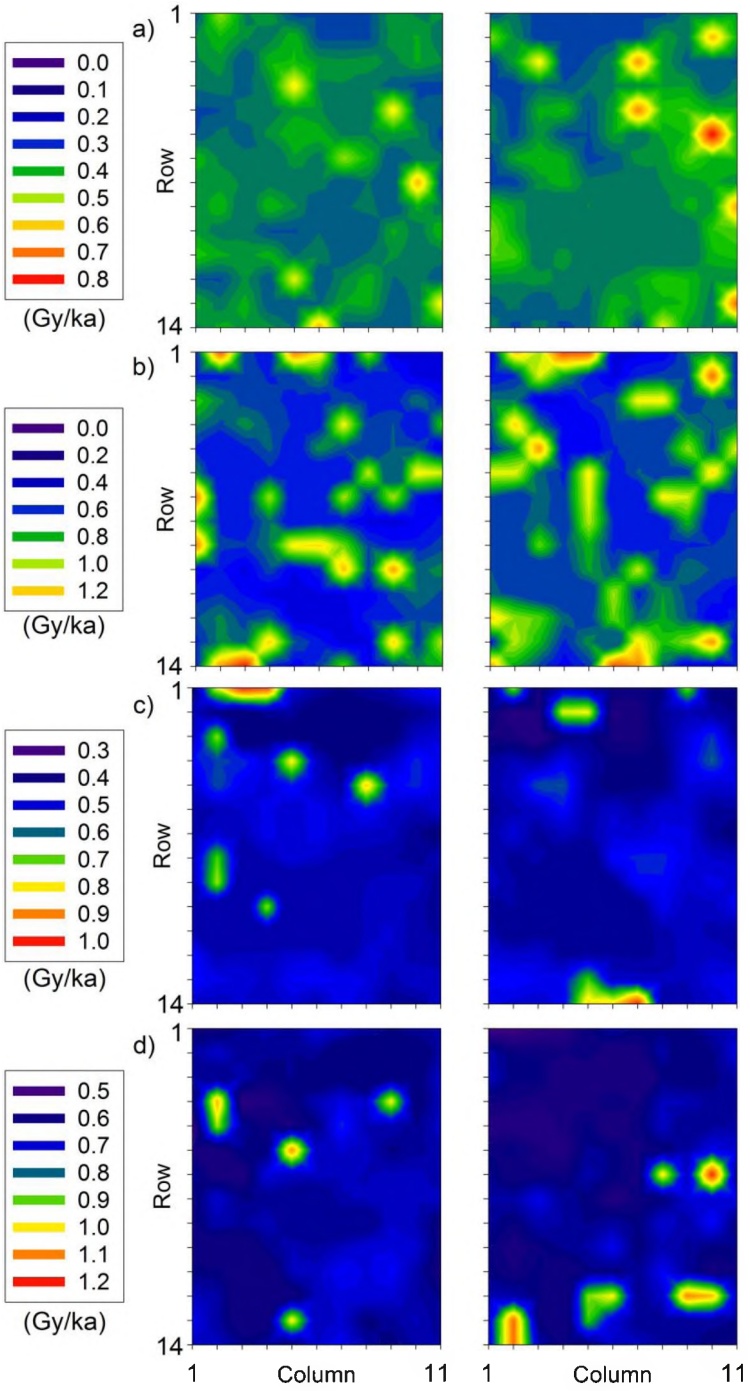

Figure 6.14. Portable XRF-determined β-D_r distribution maps for a) SP2, b) SP5, c) Layer 8 and d) Layer 5B using individual scales to display the range of concentrations *within* a sample. In each example, the bottom slab is given on the left and the top is on the right.

6.4.1.8 Relationship between D_e distribution, pXRF and beta dose rate

It was assumed that the majority of the observed OD in the D_e distributions for all four samples was due to BM (Chapter 2 and 8). Using the pXRF-determined β-D_r values this assumption can now be tested. It was first assumed that the lowest D_e values in each of the four single-grain D_e OSL distribution to be those exposed to the least amount of beta radiation over burial time. Conversely, the highest D_e values represent those grains that have experienced the highest beta flux over the period of burial. If BM is solely responsible for the observed OD in a given D_e distribution then central, minimum and maximum sample D_e ought to produce statistically consistent ages with each using their respective β-D_r values.

The central, minimum and maximum D_e values for each of the four samples investigated in this study were calculated with the central, minimum (MAM) and maximum age (MAX) models (Galbraith *et al.* 1999, Olley *et al.* 2006). These values are presented in Table 6.10 and displayed in Figure 6.15. The MAM and MAX were also used to determine the lowest and highest pXRF-determined β-D_r for each sample. These values are also presented in Table 6.10 and displayed as radial plots in Figure 6.15.

Inspection of the radial plots in Figure 6.15 reveals that the MAM and MAX models converge on different values for one sample (SP5), only. The SP5 sample had a higher number of β-D_r values where the concentrations of U and Th were above the ~4 μg/g detection level. Thus, the MAM and MAX β-D_r values were determined to be 0.46 ± 0.01 Gy/ka and 0.64 ± 0.03 Gy/ka, respectively. In each of the remaining samples, the MAM and MAX converge at the same β-D_r values. A β-D_r value of 0.37 ± 0.01 Gy/ka was determined for SP2, 0.47 ± 0.01 Gy/ka for Layer 8 and 0.63 ± 0.01 Gy/ka for Layer 5B. In each of these three samples, the radial plots are typified by a cluster of β-D_r values that are consistent with those analysis points assigned U and Th concentrations of 2 ± 1 μg/g because the U and Th concentrations were not present above detection levels (Figure 6.15e to h). These clusters are

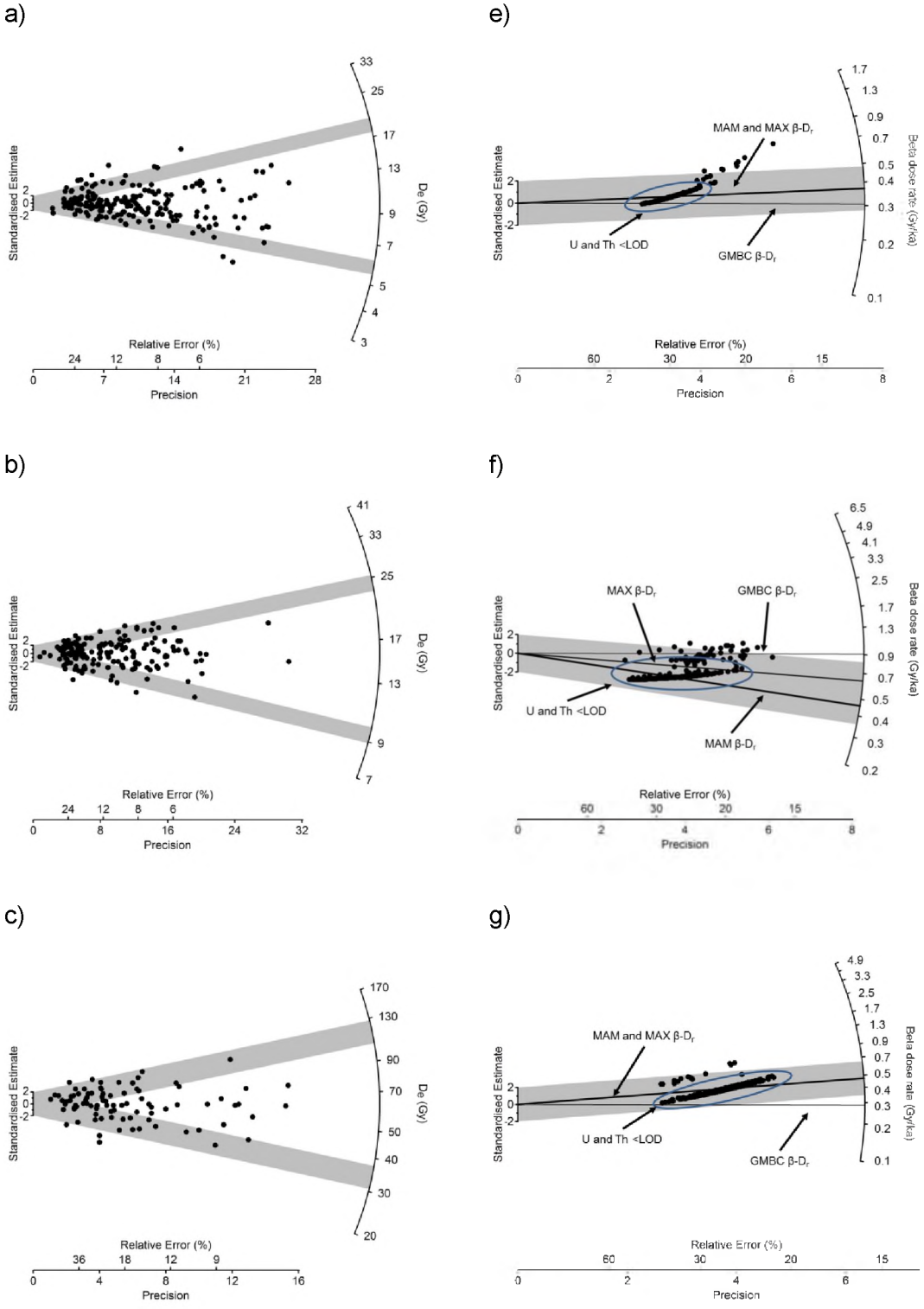
a)
Standardised Estimate
De (Gy)
Relative Error (%)
Precision
b)
Standardised Estimate
De (Gy)
Relative Error (%)
Precision
c)
Standardised Estimate
De (Gy)
Relative Error (%)
Precision
e)
MAM and MAX β-Dr
U and Th <LOD
GMBC β-Dr
Standardised Estimate
Beta dose rate (Gy/ka)
Relative Error (%)
Precision
f)
MAX β-Dr
GMBC β-Dr
U and Th <LOD
MAM β-Dr
Standardised Estimate
Beta dose rate (Gy/ka)
Relative Error (%)
Precision
g)
MAM and MAX β-Dr
U and Th <LOD
GMBC β-Dr
Standardised Estimate
Beta dose rate (Gy/ka)
Relative Error (%)
Precision

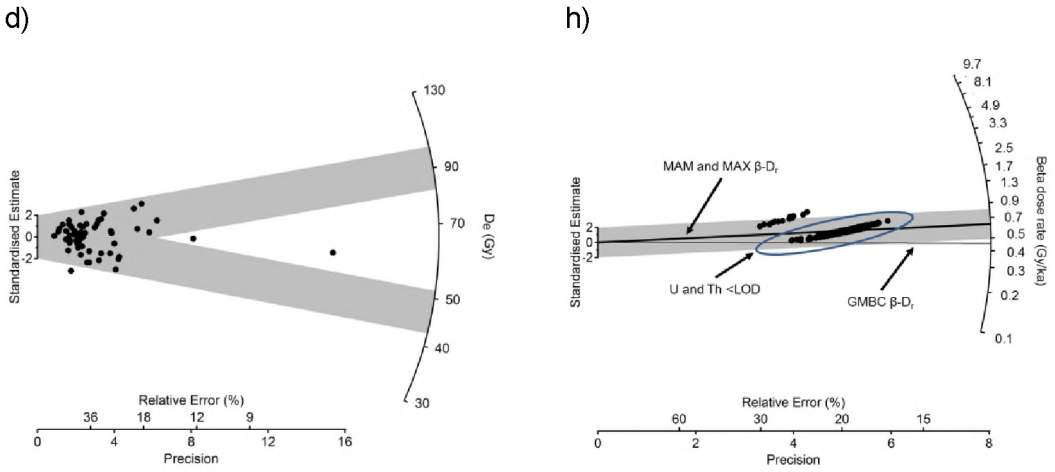

Figure 6.15. D_e distributions for a) SP2, b) SP5, c) Layer 8 and d) Layer 5B showing the MAM and MAX D_e values for each sample. The grey bands are centred on the MAM- and MAX-determined D_e values presented in Table 6.10.
The pXRF-determined β-D_r values for e) SP2, f) SP5, g) Layer 8 and h) Layer 5B are also displayed. In each case the distribution is centred on the GMBC-determined β-D_r which is indicated by the thin black 'pale' line. The MAM and MAX β-D_r values determined with the pXRF are indicated by the thicker black lines surrounded by grey bands. Also indicated in each β-D_r distribution are those measurement points where U, Th or both, were present at levels lower than the detection limit (<LOD).

---

indicated by a blue circle in Figures 6.15e to h). The variability in the slope and position of these clusters is the result of the variable contribution of the pXRF-determined K to the associated β-D_r values. In each case, the distribution of β-D_r values does not resemble the distribution of the associated D_e values.

The spread within each of the four samples investigated cannot be accounted for using the pXRF-determined β-D_r values. Only the MAX OSL age of the Layer 5B sample is consistent with the CAM OSL age (Table 6.10). The consistency of the Layer 5B MAX age is considered to be a function of the large uncertainty on the MAX D_e (17%) rather than the determined β-D_r value. The pXRF β-D_r estimates for

the remaining samples, as well as the MAM OSL age for Layer 5B, were not able to achieve MAM or MAX OSL ages that are consistent with the reported CAM OSL ages. The issue then is, are the pXRF-determined β-D_r meaningful in terms of representing 'true' end members of the β-D_r distribution. It is clear from the radial plots in Figures 6.15e, g and h, that the MAM-determined β-D_r are not representative of the 'true' β-D_r distribution. In each of these distributions, the MAM-determined β-D_r (i.e., the beta dose rate that was determined by running the minimum age model using the pXRF β-D_r data set) falls higher than that determined using the GMBC. It is apparent that the assignation of a 2 ± 1 µg/g for both U and Th, for positions where these concentrations could not be resolved, is an overestimate of the 'true' lower-tail arm of the β-D_r distribution. In contrast, it appears as though the 2 ± 1 µg/g for SP5 (Figure 6.15f) is an underestimate as the MAX-determined β-D_r for this sample (0.64 ± 0.03 Gy/ka) is less than that of the GMBC (0.92 ± 0.07 Gy/ka). However, these observation may simple be a function of the large relative errors (between 20 and 40%) on the pXRF-determined β-D_r values. In reducing these errors it may be possible to better resolve the MAM and MAX β-D_r for each analysis position, and hence, the associated OSL ages.

Table 6.10. OSL age estimates for the four samples investigated using the pXRF-determined β-D_r values.

Sample	Method	Age model[1]	D_e (Gy)[2]	Total environmental dose rate (Gy/ka)[3]	β-D_r (Gy/ka)[4]	Age (ka)[5]
SP2	GMBC	CAM	9.84 ± 0.30	0.99 ± 0.06	0.31 ± 0.03	9.99 ± 0.71
	pXRF	MAM	5.82 ± 0.28	1.04 ± 0.05	0.37 ± 0.01	5.59 ± 0.40
	pXRF	MAX	18.75 ± 0.95	1.04 ± 0.05	0.37 ± 0.01	17.96 ± 1.27
SP5	GMBC	CAM	15.62 ± 0.46	2.37 ± 0.13	0.92 ± 0.07	6.60 ± 0.42
	pXRF	MAM	9.38 ± 0.57	1.90 ± 0.08	0.46 ± 0.01	4.93 ± 0.38
	pXRF	MAX	24.13 ± 2.34	2.09 ± 0.09	0.64 ± 0.03	11.57 ± 1.26
Layer 8	GMBC	CAM	63 ± 4	0.69 ± 0.05	0.29 ± 0.03	92 ± 9
	pXRF	MAM	34 ± 3	0.87 ± 0.04	0.47 ± 0.01	39 ± 4
	pXRF	MAX	115 ± 12	0.87 ± 0.04	0.47 ± 0.01	132 ± 15
Layer 5B	GMBC	CAM	66 ± 4	0.97 ± 0.05	0.46 ± 0.03	69 ± 6
	pXRF	MAM	47 ± 11	1.13 ± 0.04	0.63 ± 0.01	42 ± 10
	pXRF	MAX	90 ± 15	1.13 ± 0.04	0.63 ± 0.01	79 ± 14

6.4.1.9 SUMMARY

In this section it has been demonstrated that the pXRF method of determining spatially-resolved β-D_r values is only of value where all three radionuclides (U, Th and K) are present above the detection limits at the same measurement position. Approximately 91% and 36% of the measurement positions had concentrations of U and Th, respectively, below the pXRF detection level (~4 μg/g). It is considered, therefore, that no reliable quantitative β-D_r map that encompasses the entire β-D_r distribution was able to be constructed.

6.4.2 IMAGE ANALYSIS MODELLING USING JMICROVISION

6.4.2.1 OBJECTIVE

To overcome the limitations of the pXRF experiments, and also attempt to produce a β-D_r map that captures a more complete range of values, the β-D_r information gained from the 'disturbed' sediment samples (from Tables 6.3, 6.4 and 6.5) was considered. The average concentrations of U, Th and K for the various mineralogical fractions and grain-size components were combined with thin section analysis and image processing of the same sample. The aim was to generate a β-D_r map that provided a more complete picture of the β-D_r environment than could be gained from pXRF analysis alone.

6.4.2.2 THIN SECTIONS, MICROPHOTOGRAPHS AND JMICROVISION

6.4.2.2.1 Thin section production

Using the same polyester resin-impregnated slabs that were used in Section 6.4.1 (Figures 6.4 and 6.5) for pXRF analysis, thin sections were made at Spectrum

Petrographics (Washington State, USA). The resulting thin sections measured ~7.5×5 cm, an area significantly larger than that investigated using the pXRF (3×3.9 cm). It should be noted that the thin section surface is not the exact equivalent of the one analysed using the pXRF due to the grinding of the slabs to an optically smooth surface prior to attachment to the glass slide. Thus, an exact 1:1 relationship between the image analysis modelling and the pXRF β-D_r maps is not expected. This is particularly the case for the MacCauley's Beach samples where it is thought that the β-D_r 'hotspots' are housed in individual mineral grains rather than the matrix (as is the case for the Pech IV samples).

6.4.2.2.2 Microphotograph procedures

Each thin section was placed into a graduated slide holder. This holder could be moved in both the X and Y planes with millimetre precision. The slide holder was mounted onto an Olympus SZ61 polarising binocular microscope. Using location marks cut into the resin slabs prior to thin sectioning, the slides were aligned to match the position of the pXRF analysis as closely as possible. A cross-polarised light microphotograph was taken at each pXRF analysis position (N=154) using an Infinity-1 1.3 megapixel camera. Each image was taken so that the centre of the microphotograph aligned with the centre of the pXRF analysis point and that the image incorporated a 6 mm diameter sphere from this centre point. The slide was then systematically moved in 3 mm increments (both along the X and Y axes) using the graduated slide holder.

6.4.2.2.3 Image categorisation and analysis with the JMicroVision program

Image analysis was conducted using JMicroVision (v.1.2.7) software package (Roduit 2013). The freely downloadable JMicroVision program was used to measure, extract and quantify image components according to their size, as well as pixel colour and grey scale intensity (other parameters can also be defined by the user). A simplified Table of the steps taken during the extraction and analysis of

objects using the JMicroVision program is given in Table 6.11. A more in-depth methodological outline, featuring screenshots from JMicroVision is given in Appendix 3.

Table 6.11. Steps taken in the classification and extraction of objects from thin section microphotographs using the JMicroVision program.

Step	Description	Appendix 3 Figure numbers
1	Set 6 mm diameter circle for all analyses using a calibration image	1–4.
2	Determine the calibration width of an individual pixel	5
3	Extract objects with uniform optical properties (quartz, calcite, bone, black heavy minerals, voids etc) using the 'Color or gray scale intensity threshold' option from the 'Object Extraction' menu.	6–11
4	Extract objects with non-uniform optical properties (birefringent heavy minerals) using the 'Magic Wand' function under the 'Object Extraction' menu.	12–14

A calibration image was taken prior to thin section analysis (Step 1, Table 6.11). A 3×3 mm grid was printed onto a plastic transparency and placed under the microscope and the central vertex of the grid aligned with the centre of the microphotograph (Appendix 3 Figure 12.1). Using this calibration image, a 6 mm diameter circle was drawn and saved as the region of analysis in all subsequent image processing.

6.4.2.2.3.1 MacCauley's Beach object extraction procedures

For the MacCauley's Beach samples, quartz, heavy mineral, silt and clay fractions were extracted during image analysis. The JMicroVision program, however, cannot distinguish between quartz and feldspar grains as a result of their overlapping interference colours. These two components, therefore, were categorised together.

The quartz and feldspar fraction were digitally extracted using the methods outlined in Table 6.11 and shown in Appendix 3 Figure 12.1 using the user-defined *'Color and gray scale intensity threshold'* function. The interference colours of this fraction however ranged from dark grey to bright white, so these two different coloured components (dark and light grey) were extracted separately (Step 3, Table 6.11). The dark and light components were also separated according to grain size to give a CS and FS components. Here, surface area values of between 1018 and 125,663 $pixel^2$ (equating to grains size diameters of 180 μm and 2 mm, respectively) were used as threshold values for the CS fraction. These surface area were based upon the area of a circle with diameters of 180 μm and 2 mm and a pixel width of 5 μm. Surface area values of between 120 and 1018 $pixel^2$ (or 62 and 180 μm diameter spherical grains) were used to define the FS component range. The respective dark grey and bright white CS and FS fractions were then summed.

The silt fraction was also extracted using the same methods as for the CS and FS quartz fractions. However, grain size threshold values of 10 and 120 $pixel^2$ were used. This lower limit (10 $pixel^2$ or ~15 μm diameter grain) is the limit of the JMicroVision program to recognise individual clasts. Although this 10 $pixel^2$ limit is larger than the sedimentological silt/clay grain size boundary (2 μm), this is the best means of estimating this fraction at the moment. It is, therefore, likely that the clay fraction contains a small contribution from the silt fraction.

Void space was extracted based on its dark grey colour. However, it is possible that a small proportion of the area classified as 'void' may, in fact, be mineral grains that were photographed at their extinction angle (dark grey colour). Yet, comparison with the point counting data presented for the two MacCauley's Beach samples in Chapter 5 provides proportions consistent with those digitally extracted here.

The clay component could only be extracted from SP2 using the same method as in Step 3 of Table 6.11. For SP5, the clay component could not be identified at the resolution of the microphotograph; clays are only present as thin clay coatings surrounding the grains. Here, a constant 1.7% clay proportion was assumed for each microphotograph based on Malvern Mastersizer grain size analysis (Chapter 5).

The FG component was extracted using a minimum pixel area threshold value of 125,663 pixel^2 (equivalent to 2 mm diameter grain). The majority of these FG components were dark black in colour and quite simple to categorise and extract.

The heavy mineral component was slightly more difficult to extract due to the significant variation in both their interference and birefringence colours. The black heavy mineral grains were extracted according to grain size (CS and FS) using the same method as in Step 3 of Table 6.11. A number of heavy minerals species (such as: zircon, rutile and tourmaline) have a range of inference colours (e.g., yellow, red, blue, pink) that were not able to be adequately categorised using this method. Instead, these grains were individually classified using the *'Magic Wand'* function of the *'Object Extraction'* menu (Step 4 in Table 6.11).

6.4.2.2.3.2 Pech IV object extraction procedures

The extraction procedures for the Pech IV samples were not as difficult as the MacCauley's Beach samples as they were only required to be extracted according to grain size ranges, rather than mineral species. As such grains size fractions of >2 mm, 180 µm to 2 mm and <180 µm were extracted. The >2 mm categories of flint, bone and limestone, were categorised and extracted using the same procedures outlined in Step 3 of Table 6.11. A minimum surface area of 125,663 µm^2 was used as the lowermost grain size threshold value.

The data output of the extracted object components was a Table of component proportions for the total area of each 6 mm in diameter circle – equivalent to the 6

mm in diameter analysis field of the pXRF. Examples of extracted object maps are shown in Figure 6.16a and b for SP5 and Layer 8, respectively.

6.4.2.3 BETA DOSE RATE MODELLING USING THE JMICROVISION EXTRACTED COMPONENTS

The concentrations of U, Th and K for each measurement position were estimated using the JMicroVision-determined proportions of each component and their respective concentration information presented in Tables 6.3, 6.4 and 6.5. For the Pech IV samples, the ICP-OES/MS concentrations were used (Table 6.5), whereas only the ICP-OES/MS concentrations of Th and K were used for the MacCauley's Beach samples. Here the TSAC determined U concentration was used.

6.4.2.3.1 Modelling considerations with regards to the quartz and feldspar components from MacCauley's Beach

Consideration was made for the U, Th and K concentrations of the JMicroVision extracted quartz and feldspar component for SP samples due to inability of these components to be resolved. Composite radionuclide concentrations, weighted according to the proportions presented in Table 6.1, were calculated for both the CS and FS quartz and feldspar component of SP2 and SP5. An example of the steps taken to calculate the composite radionuclide concentrations is presented in Table 6.12. The composite U, Th and K concentrations for both samples are given in Table 6.13.

6.4.2.3.2 *Modelling radionuclide concentrations using JMicroVision extracted components and 'disturbed' sample radionuclide concentrations*

At each measurement point, the proportion of each component and its respective U, Th and K concentrations have been estimated. It is therefore possible to model distribution maps for these radionuclide concentrations and, ultimately, the β-D_r for each sample.

The steps taken to estimate the average U, Th and K concentration at each measurement point are shown graphically in Figure 6.17. Here, only the Th determination is used – however the process for U and K estimation are identical. First, it was assumed that the concentration of Th for each component at any given measurement position was derived from a normal distribution, with a mean and standard error equivalent to those values determined using TSAC (U) and ICP-OES/MS (Th and K) in Tables 6.3, 6.4 and 6.5 – Figure 6.17; part 1.

From each component distribution, a random number (read concentration) was generated using a Microsoft Excel macro for each of the extracted sedimentary components (c_1, c_2, … c_7) – Figure 6.17 part 2. These concentrations were then proportionally adjusted using the associated component proportion that was determined from the JMicroVision extraction for the given measurement point (Figure 6.17; part 3) to give proportionally adjusted concentrations of Th (y_1, y_2 … y_7). Each of the y values were then summed (Figure 6.17; part 4) to given an estimate of Th (Z_x) for the given measurement point. This process was repeated 25 times, subsampling the original component distributions each time. A mean Th concentration and standard deviations were calculated for each measurement point from these 25 replicates. The standard error was then calculated by dividing the standard deviation by 5 (the square root of 25). The estimate for U and K were calculated in exactly the same way as that used for the Th (Figure 6.17) and carried out for each of the 154 measurement points per slab.

a)

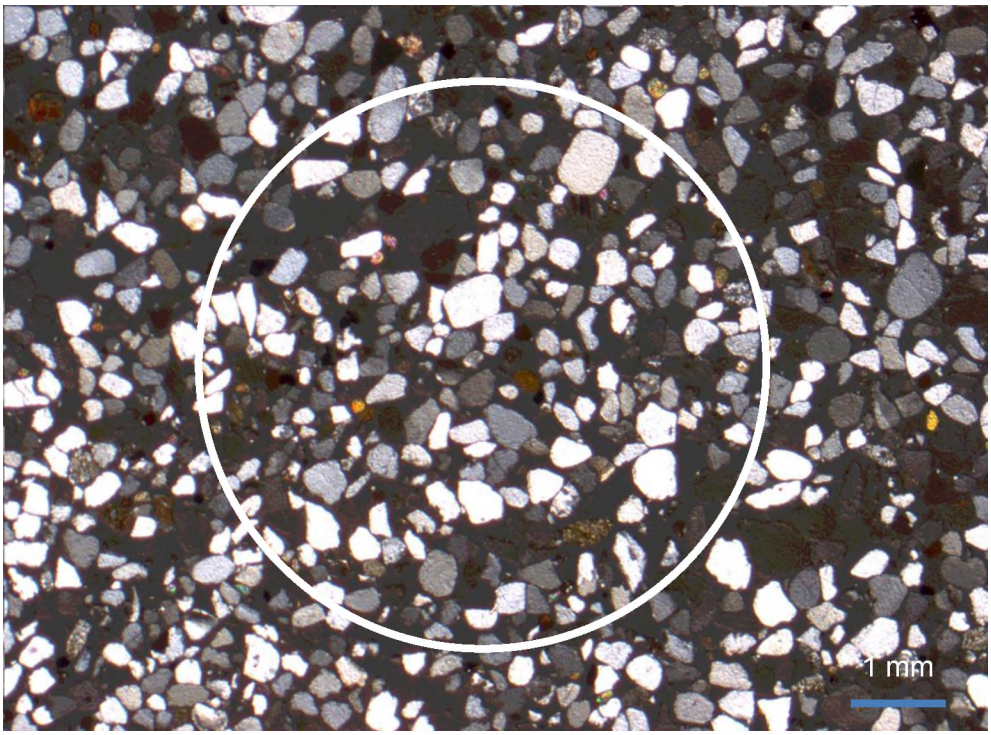
1 mm

b)

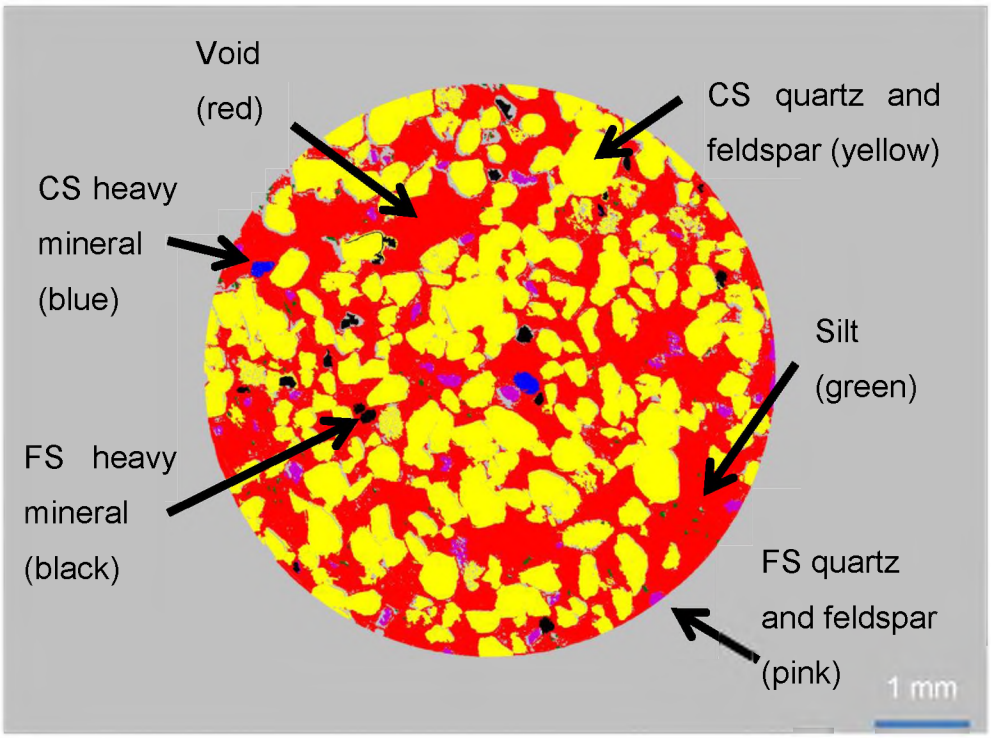
Void
(red)
CS quartz and
feldspar (yellow)
CS heavy
mineral
(blue)
Silt
(green)
FS heavy
mineral
(black)
FS quartz
and feldspar
(pink)
1 mm

c)

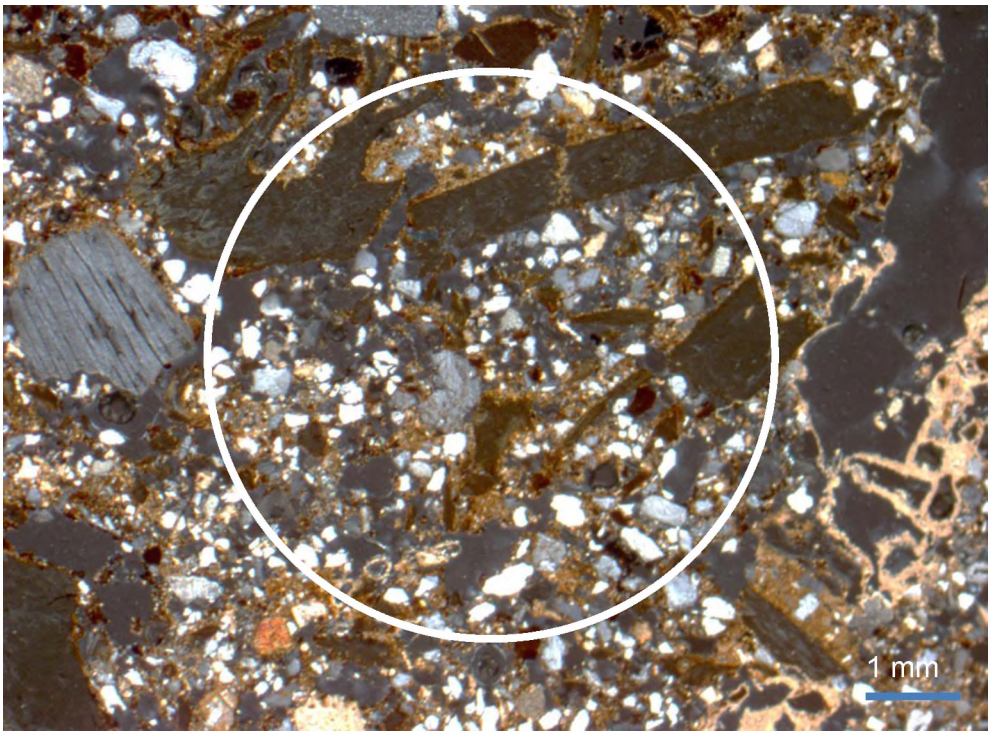

d)

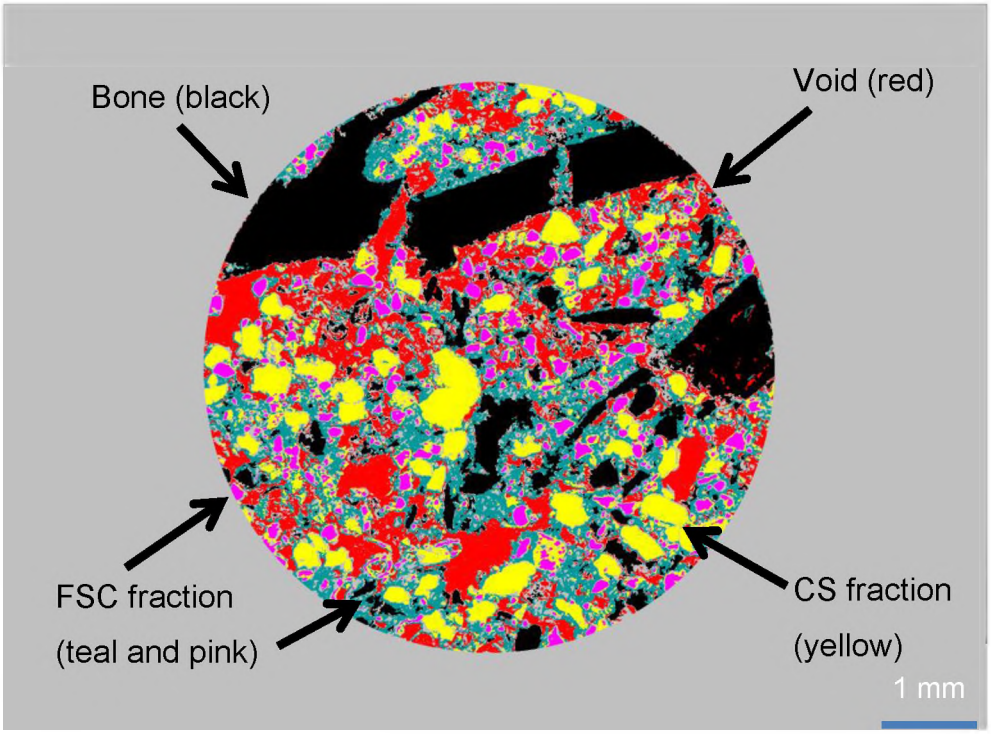

Figure 6.16. Examples of microphotographs of thin sections and their associated JMicroVision object extracted images for SP5 (Top, Row 2, Column 4; a and b) and Layer 8 (Top, Row 2, Column 10; c and d).

Table 6.12. Steps taken in the calculation of the composite U, Th and K concentrations for the quartz and feldspar component extracted using JMicroVision.

Step	Description	Calculation
1	CS quartz and CS feldspar Th concentrations (μg/g ± 1σ)	CS quartz = 0.51 ± 0.02 CS feldspar = 0.71 ± 0.03
2	FS quartz and FS feldspar proportions from Table 6.1	CS quartz = 0.846 CS feldspar = 0.055
3	Find the relative proportion of the CS quartz and CS feldspar components as a function of the total CS proportion of these two components	CS quartz = (0.846/[0.846 + 0.055]) = 0.939 CS feldspar = (0.055/[0.846 + 0.055]) = 0.061
4	Multiply the Th concentrations in Step 1 by respective proportions in Step 3.	CS quartz = 0.51 × 0.939 = 0.479 CS feldspar = 0.71 × 0.061 = 0.043
5	Sum proportionally adjusted Th concentrations (in μg/g) in Step 4	Composite CS quartz and feldspar Th concentration = 0.479 + 0.043 = 0.522
6	Proportionally adjust the respective 1σ errors in Step 1 by the respective proportions in Step 3	CS quartz Th error = 0.02 × 0.939 = 0.019 Cs feldspar Th error = 0.03 × 0.061 = 0.002

7	Sum the proportionally adjusted 1σ error in Step 6 in quadrature	Combined Th error = SQRT(0.019^2 + 0.002^2) =0.019
8	Composite CS quartz and feldspar Th concentration (μg/g)	0.52 ± 0.02

Table 6.13. Composite U, Th and K concentrations for the CS and FS quartz and feldspar components for SP2 and SP5.

Sample	Fraction	U	Th	K
SP2	CS quartz	0.20 ± 0.01	0.54 ± 0.02	0.01 ± 0.00
	CS feldspar	0.34 ± 0.01	0.56 ± 0.02	0.07 ± 0.00
	CS composite	**0.21 ± 0.01**	**0.54 ± 0.02**	**0.02 ± 0.00**
	FS quartz	0.40 ± 0.01	1.01 ± 0.04	0.06 ± 0.00
	FS feldspar	1.03 ± 0.04	1.74 ± 0.07	0.81 ± 0.02
	FS composite	**0.60 ± 0.01**	**1.24 ± 0.04**	**0.30 ± 0.01**
SP5	CS quartz	0.29 ± 0.01	0.51 ± 0.02	0.02 ± 0.00
	CS feldspar	0.21 ± 0.01	0.71 ± 0.03	0.28 ± 0.01
	CS composite	**0.29 ± 0.01**	**0.52 ± 0.02**	**0.04 ± 0.00**
	FS quartz	0.45 ± 0.01	1.02 ± 0.04	0.06 ± 0.00
	FS feldspar	0.28 ± 0.01	0.83 ± 0.03	1.17 ± 0.03
	FS composite	**0.42 ± 0.01**	**0.99 ± 0.03**	**0.25 ± 0.01**

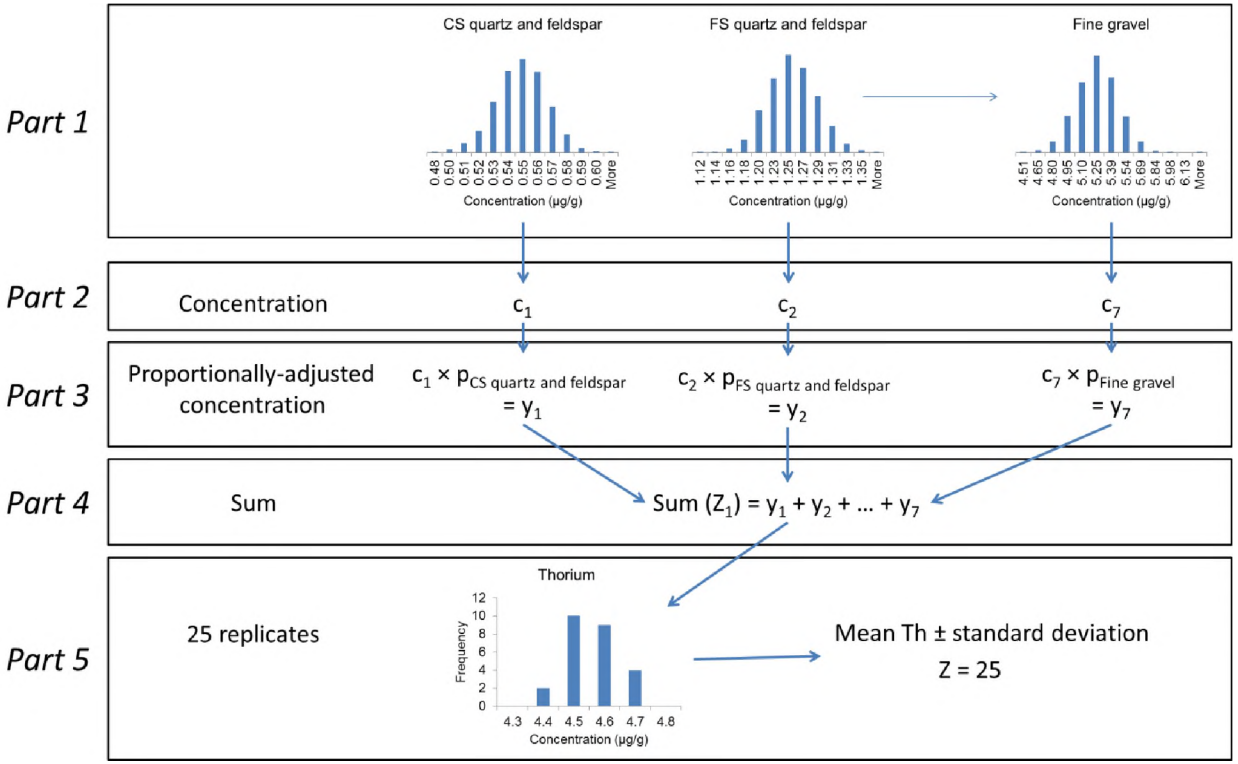

Figure 6.17. A schematic of the steps taken to calculate the average Th concentration for a given point for sample SP2. Concentration is represented by *c*, proportion by *p*, proportionally-adjusted concentration by *y*, and the summed Th concentration for a given measurement point by *z*. This process was also conducted for both U and K at each measurement position for each sample.

The modelled concentrations of U, Th and K were then converted to β-D_r using the same method and assumptions (including water content estimates and attenuation) that are presented in Section 6.4.1.7.3.1 and Table 6.8.

6.4.2.4 RESULTS

The proportions of components and the estimates of average U, Th and K and β-D_r for the second row of samples SP5 and Layer 8 are given in Tables 6.14 and 15.

6.4.2.4.1 Unclassified object extraction proportions

At each measurement point the summed total proportion of extracted objects fell short of 100%, typically between 92 and 100%. This maximum 8% unclassified area was found surrounding the CS fraction grains where the boundary colours took on a blue or yellow hue that was not selected during extraction. If this area was included a >100% proportion was calculated as a proportion of the 'white' CS grains was included in this extraction also. To test whether this unclassified region had substantial influence on the calculated β-D_r, the second row of data from SP5 in Table 6.14 was recalculated. The unclassified proportion of the data was included in the CS fraction and the model was run again and β-D_r values determined using the same procedures as before. The results are presented in Table 6.16. It is clear that the inclusion of this small unclassified proportion to the CS fraction makes no significant contribution to the modelled β-D_r. Rather, each β-D_r estimate with this region included in the CS fraction is statistically similar to the β-D_r if this region was ignored. In light of this, the unclassified region was not included in the final proportion sum as it makes no difference if it is included or not.

6.4.2.4.2 *Modelled K distribution maps*

The K distributions are shown in Figures 6.18 and 6.19 for all four samples. The SP samples have similar distributions, rather homogeneous distributions of K. In terms of abundance, the SP samples have lower concentration of K compared with those from Pech IV (Figure 6.18). For sample SP2, the lowest modelled K concentration was 0.1020 ± 0.0003%, and 0.1668 ± 0.0006% was the highest K concentration. This range is shown as dark blue to orange/red in Figure 6.19a. Regions of higher modelled K correlate to thin section positions associated with higher silt and clay contents. The modelled K concentration range for SP5 is much lower than that of SP2 (Figure 6.18b). The K concentrations for this sample range between 0.0545 ± 0.0001 and 0.0793 ± 0.0002% – these values are shown as dark blue to red in Figure 6.19b.

The modelled K concentrations for the Pech IV samples reveal greater variability than those from MacCauley's Beach (Figure 6.18c and d). The modelled K concentrations in Layer 8 range from 0.0459 ± 0.0002 to 0.303 ± 0.001%. In Figure 6.19c, this range is represented by dark blue through to orange/red. It is interesting to note that the regions that have the highest K concentrations (those regions coloured yellow to red; Figure 6.19c) are those that are mainly comprised of FSC component materials and are free from bone and flint fragments. In contrast, the lowest modelled K concentrations (coloured dark to mid blue; Figure 6.19c) are associated with regions that entirely encompass bone.

The modelled K concentrations for Layer 5B attain the highest values of any sample investigated in this manner (Figure 6.18d). The range of modelled K, here, ranges from 0.1524 ± 0.0004 to 0.5128 ± 0.0013% and are shown as dark blue through to orange in Figures 6.18d and 6.19d. The majority of the orange regions (Figure 6.19d) in the modelled K distributions for this sample are associated with areas that have higher contributions from the CS and FSC components. Where limestone gravel is present the K content decreases and appears as both light green and yellow (Figure 6.19d). Where the limestone pebbles encompass the entire

Table 6.14. Estimates of β-D_r, U, Th and K determined from JMicroVision extractions component for the second row of sample SP5.

Position (row:column)	Component proportions (%)							Total	U (μg/g)	Th (μg/g)	K (%)	β-D_r (Gy/ka)[a]
	1	2	3	4	5	6	7					
2:1	18.7	68.1	4.1	0.5	2.2	0.4	1.7	95.7	3.90 ± 0.01	12.00 ± 0.11	0.067 ± 0.001	0.74 ± 0.02
2:2	21.7	64.6	4.1	0.7	1.7	0.2	1.7	94.7	2.98 ± 0.01	9.11 ± 0.07	0.064 ± 0.001	0.57 ± 0.02
2:3	23.8	65.3	3.7	0.4	1.5	0.4	1.7	96.8	2.75 ± 0.01	8.29 ± 0.06	0.062 ± 0.001	0.53 ± 0.02
2:4	20.0	66.5	4.5	0.7	1.8	0.4	1.7	95.6	3.17 ± 0.01	9.71 ± 0.08	0.067 ± 0.001	0.61 ± 0.02
2:5	24.0	65.5	4.7	0.2	2.1	0.5	1.7	98.7	3.77 ± 0.01	11.47 ± 0.09	0.066 ± 0.001	0.71 ± 0.02
2:6	18.8	66.0	4.4	0.4	1.9	0.4	1.7	93.6	3.39 ± 0.01	10.19 ± 0.07	0.065 ± 0.001	0.64 ± 0.02
2:7	16.5	68.4	4.1	0.1	1.8	0.4	1.7	93.0	3.25 ± 0.01	9.75 ± 0.09	0.063 ± 0.001	0.62 ± 0.02
2:8	15.8	68.4	4.8	0.9	2.1	0.3	1.7	94.0	3.67 ± 0.01	11.06 ± 0.08	0.070 ± 0.001	0.70 ± 0.02
2:9	19.3	68.0	4.2	0.1	1.9	0.5	1.7	95.7	3.36 ± 0.01	10.27 ± 0.07	0.064 ± 0.001	0.64 ± 0.02
2:10	20.6	68.2	4.5	0.1	2.0	0.4	1.7	97.5	3.64 ± 0.01	11.07 ± 0.09	0.065 ± 0.001	0.69 ± 0.02
2:11	20.4	63.2	7.0	0.3	2.3	0.5	1.7	95.4	4.09 ± 0.01	12.42 ± 0.11	0.072 ± 0.001	0.77 ± 0.02

1. Void space
2. CS quartz and feldspar
3. FS quartz and feldspar
4.CS heavy minerals
5. FS heavy minerals
6. Silt
7. Clay

[a] The β-D_r values were converted from elemental concentrations of U, Th and K to β-D_r using the conversion factors set out in Guérin *et al.* (2011) and adjusted to account for a water content of 5 ± 1% (Aitken 1985) and attenuated for 180–212 μm grains of quartz (Brennan 2003).

Table 6.15. Estimates of β-D_r, U, Th and K determined from JMicroVision extractions component for the second row of sample Layer 8.

Position (row:column)	Fraction proportions (%)				Total	U (μg/g)	Th (μg/g)	K (%)	β-D_r (Gy/ka)[a]
	1	2	3	4					
2:1	35.7	6.2	27.8	26.9	96.6	0.66 ± 0.02	1.08 ± 0.04	0.163 ± 0.003	0.21 ± 0.01
2:2	31.0	5.5	20.4	43.1	100.0	0.90 ± 0.02	0.81 ± 0.03	0.128 ± 0.002	0.21 ± 0.01
2:3	36.8	3.1	13.8	42.5	96.2	0.85 ± 0002	0.55 ± 0.02	0.087 ± 0.001	0.17 ± 0.01
2:4	43.0	4.8	18.0	29.6	95.4	0.65 ± 0.02	0.72 ± 0.02	0.111 ± 0.002	0.16 ± 0.01
2:5	64.3	4.3	20.0	6.9	95.5	0.25 ± 0.01	0.75 ± 0.03	0.114 ± 0.002	0.12 ± 0.01
2:6	76.6	1.0	10.6	7.8	96.0	0.20 ± 0.00	0.37 ± 0.01	0.057 ± 0.001	0.07 ± 0.01
2:7	69.2	2.8	15.1	8.1	95.2	0.24 ± 0.01	0.57 ± 0.02	0.085 ± 0.001	0.10 ± 0.01
2:8	50.2	8.2	29.1	8.0	95.5	0.34 ± 0.01	1.16 ± 0.04	0.171 ± 0.002	0.18 ± 0.01
2:9	29.7	15.0	44.4	6.8	95.9	0.43 ± 0.01	1.84 ± 0.05	0.270 ± 0.005	0.27 ± 0.01
2:10	29.5	16.5	42.0	8.2	96.2	0.45 ± 0.01	1.80 ± 0.05	0.265 ± 0.005	0.27 ± 0.01
2:11	37.0	10.1	35.2	14.0	96.3	0.49 ± 0.01	1.38 ± 0.05	0.209 ± 0.003	0.23 ± 0.01

1. Void
2. CS fraction
3. FSC fraction
4. Bone

[a] The β-D_r values were converted from elemental concentrations of U, Th and K to β-D_r using the conversion factors set out in Guérin *et al.* (2011) and adjusted to account for a water content of 6.9 ± 1.7% (Aitken 1985) and attenuated for 180–212 μm grains of quartz (Brennan 2003).

Table 6.16. Estimates of β-D_r, U, Th and K determined from JMicroVision extractions component for the second row of sample SP5.

Position (row:column)	Component proportions (%)							Total	U (μg/g)	Th (μg/g)	K (%)	β-D_r (Gy/ka)[a]	Ratio
	1	2	3	4	5	6	7						
2:1	18.7	72.4	4.1	0.5	2.2	0.4	1.7	100	3.91 ± 0.01	12.02 ± 0.07	0.069 ± 0.001	0.74 ± 0.02	1.00 ± 0.05
2:2	21.7	69.9	4.1	0.7	1.7	0.2	1.7	100	3.00 ± 0.01	9.14 ± 0.07	0.066 ± 0.001	0.58 ± 0.02	1.01 ± 0.05
2:3	23.8	68.5	3.7	0.4	1.5	0.4	1.7	100	2.76 ± 0.01	8.31 ± 0.06	0.063 ± 0.001	0.53 ± 0.02	1.00 ± 0.05
2:4	20.0	70.9	4.5	0.7	1.8	0.4	1.7	100	3.18 ± 0.01	9.73 ± 0.07	0.069 ± 0.001	0.61 ± 0.02	1.00 ± 0.05
2:5	24.0	66.8	4.7	0.2	2.1	0.5	1.7	100	3.77 ± 0.01	11.47 ± 0.07	0.066 ± 0.001	0.71 ± 0.02	1.00 ± 0.05
2:6	18.8	72.4	4.4	0.4	1.9	0.4	1.7	100	3.41 ± 0.01	10.22 ± 0.07	0.067 ± 0.001	0.65 ± 0.02	1.01 ± 0.05
2:7	16.5	75.4	4.1	0.1	1.8	0.4	1.7	100	3.27 ± 0.01	9.79 ± 0.07	0.066 ± 0.001	0.62 ± 0.02	1.01 ± 0.05
2:8	15.8	74.4	4.8	0.9	2.1	0.3	1.7	100	3.69 ± 0.01	11.10 ± 0.07	0.072 ± 0.001	0.70 ± 0.02	1.01 ± 0.05
2:9	19.3	72.3	4.2	0.1	1.9	0.5	1.7	100	3.37 ± 0.01	10.29 ± 0.07	0.066 ± 0.001	0.64 ± 0.02	1.00 ± 0.05
2:10	20.6	70.7	4.5	0.1	2.0	0.4	1.7	100	3.64 ± 0.01	11.09 ± 0.07	0.066 ± 0.001	0.69 ± 0.02	1.00 ± 0.05
2:11	20.4	67.8	7.0	0.3	2.3	0.5	1.7	100	4.11 ± 0.01	12.44 ± 0.07	0.074 ± 0.001	0.78 ± 0.02	1.00 ± 0.05

1. Void space
2. CS quartz and feldspar
3. FS quartz and feldspar
4.CS heavy minerals
5. FS heavy minerals
6. Silt
7. Clay

[a] The β-D_r values were converted from elemental concentrations of U, Th and K to β-D_r using the conversion factors set out in Guérin *et al.* (2011) and adjusted to account for a water content of 5 ± 1% (Aitken 1985) and 3% uncertainty associated with the attenuation for 180–212 μm grains of quartz (Brennan 2003).

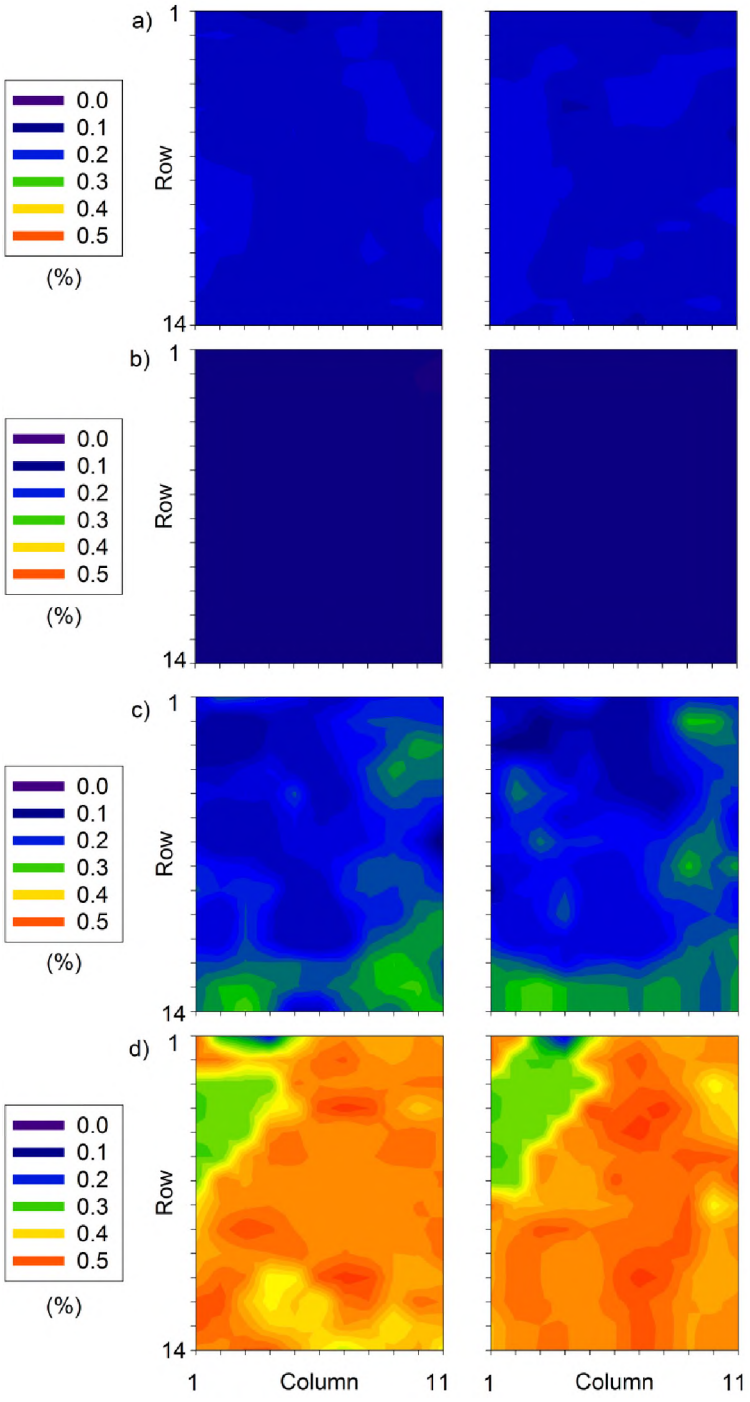

Figure 6.18. Image analysis-determined K distribution maps for a) SP2, b) SP5, c) Layer 8 and d) Layer 5B. In each example the same K scale (0–0.5%) has been used to facilitate comparison *between* samples. The bottom slab is given on the left and the top is on the right.

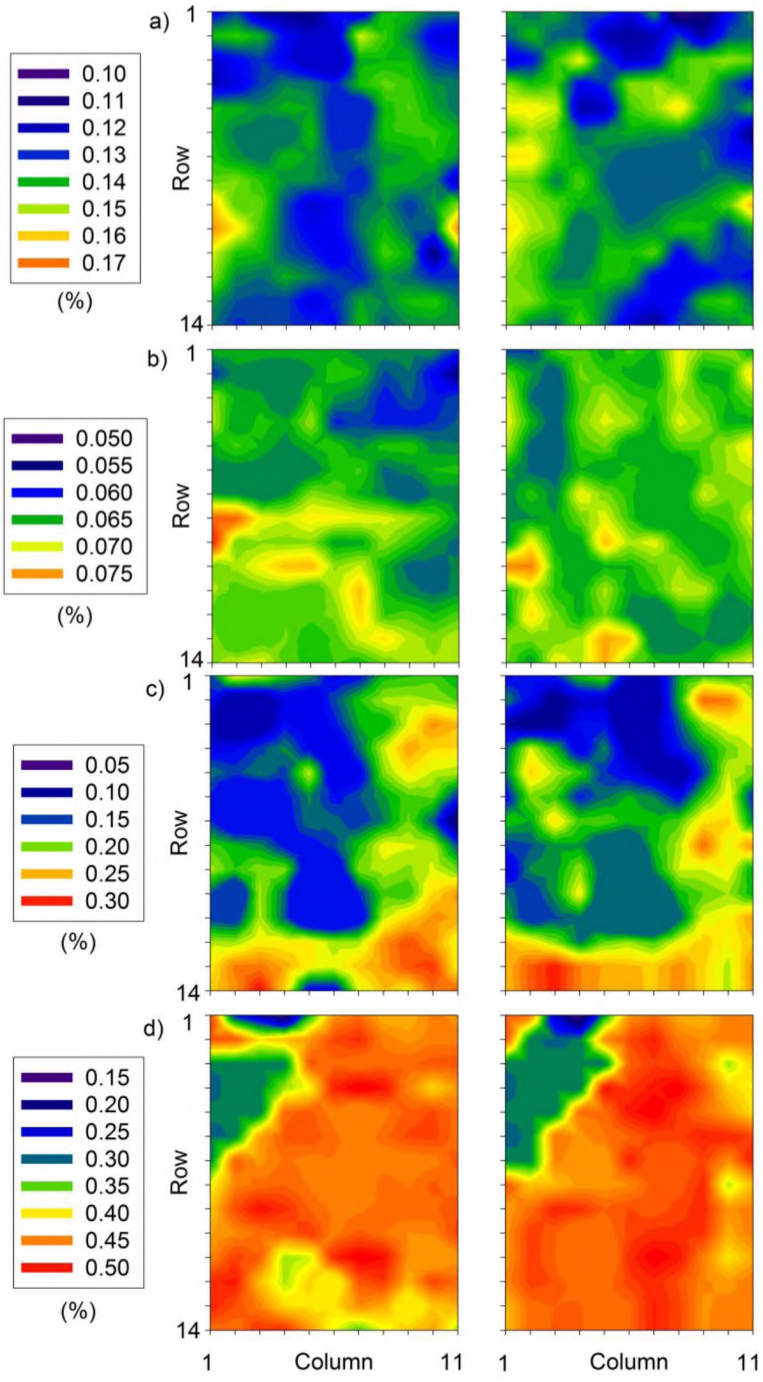

Figure 6.19. Image analysis-determined K distribution maps for a) SP2, b) SP5, c) Layer 8 and d) Layer 5B using individual scales to display the range of concentrations *within* a sample. In each example, the bottom slab is given on the left and the top is on the right.

modelled area, the K content is ~0.3%, equivalent to the 'pure' limestone K content given in Table 6.5 and shown in dark green (Figure 6.19d). Where bone fragments are present, the K content is at its lowest values (top left hand corner of Figure 6.19d) and are shown as blue.

6.4.2.4.3 Modelled U distribution maps

The modelled U distributions are shown in Figures 6.20 and 21a-d for the four samples investigated in this study. Due to the higher amounts of U measured in the disturbed samples for the MacCauley's Beach samples, the U distribution maps for these two samples show relatively higher concentrations of U than those coming from Pech IV (Figure 6.20). The modelled U values for SP2 range between 0.96 ± 0.01 and 1.99 ± 0.02 μg/g. In Figure 6.21a, this range is shown by regions of dark blue to red. The orange/red regions (those with relatively higher modelled U concentrations) are associated with higher proportions of silt and clay (much like the modelled K concentrations in Figure 6.19a). The modelled U distribution for this sample is rather homogeneous (ranging over ~1 μg/g). The proportions for the heavy mineral fraction here are all <1% of the total 6 mm diameter area at each of the measurement positions. This is not to say that their influence is negligible but rather their contribution to the modelled U distributions is swamped by those of the silt and clay fraction given their much greater proportions; 20–30% for silt and 18–25% for clay.

The U distribution for SP5 contains the highest U concentrations of any of the four samples modelled in this study (Figure 6.20b). The distribution of modelled U concentrations ranges from 1.719 ± 0.004 to 5.09 ± 0.01 μg/g. This range is represented by light green to red in Figure 6.20b and 6.21b. Unlike SP2, here the influence of the FS and CS heavy minerals are solely responsible for the heterogeneous distribution of U throughout the sample due to the significantly smaller proportions of silt and clay. The CS heavy mineral component proportions range between 0.09 and 1.91%, the FS heavy mineral component from 0.89 to 2.82%, whereas the silt component proportions are all <0.6%.

The Pech IV samples are relatively U poor based upon the U distribution maps and have similar distributions (Figure 6.20c and d). The Layer 8 modelled U concentrations range between 0.199 ± 0.001 to 1.21 ± 0.01 μg/g, and Layer 5B from 0.237 ± 0.002 to 0.764 ± 0.004 μg/g. These are shown as purple and dark blue regions of Figures 6.20c and d. In Layer 5B the regions of low U are associated with limestone inclusions (purple colour; Figure 6.21d). In Layer 8 those regions with bone fragments produced U concentrations (yellow and red; Figure 6.21c) that are higher than the surrounding matrix – a situation that is opposite to that for the K concentration, i.e., low K equates to regions of bone.

6.4.2.4.4 Modelled Th distribution maps

Figures 6.22 and 6.23 show the modelled Th distribution maps for the four samples investigated in this study. The relative magnitude of the Th values follow similar pattern to that of the U, i.e., the MacCauley's Beach samples are relatively higher in Th (Figure 6.22a and b) than those from Pech IV (Figure 6.22c and d). Sample SP2 has a distribution of modelled Th concentrations that range from 3.34 ± 0.01 to 6.99 ± 0.03 μg/g and are shown as dark blue to red in Figure 6.23a. Again, the measurement positions with relatively high Th concentrations are associated with higher proportions of silt and clay. Sample SP5, again, have the highest modelled concentrations of Th (Figure 6.22b). These values range between 5.03 ± 0.03 and 15.62 ± 0.12 μg/g and are shown as regions of dark blue through to orange and red in Figure 6.23b. These high Th concentration regions are again associated with heavy mineral components for the same reasons as outlined in Section 6.4.2.4.2 for the image analysis β-D_r modelled SP5 U distribution.

The Layer 8 Pech IV sample has a distribution of modelled Th concentrations that ranges from 0.265 ± 0.002 to 2.11 ± 0.01 μg/g. In Figure 6.23c, these are shown as mainly orange/red (where the matrix dominates) and dark blue (where bone material is present). Slightly higher Th concentrations were modelled for Layer 5B with a range of values distributed between 1.15 ± 0.01 and 3.97 ± 0.03 μg/g. The low modelled Th regions (shown in dark blue, Figure 6.23d) are associated with

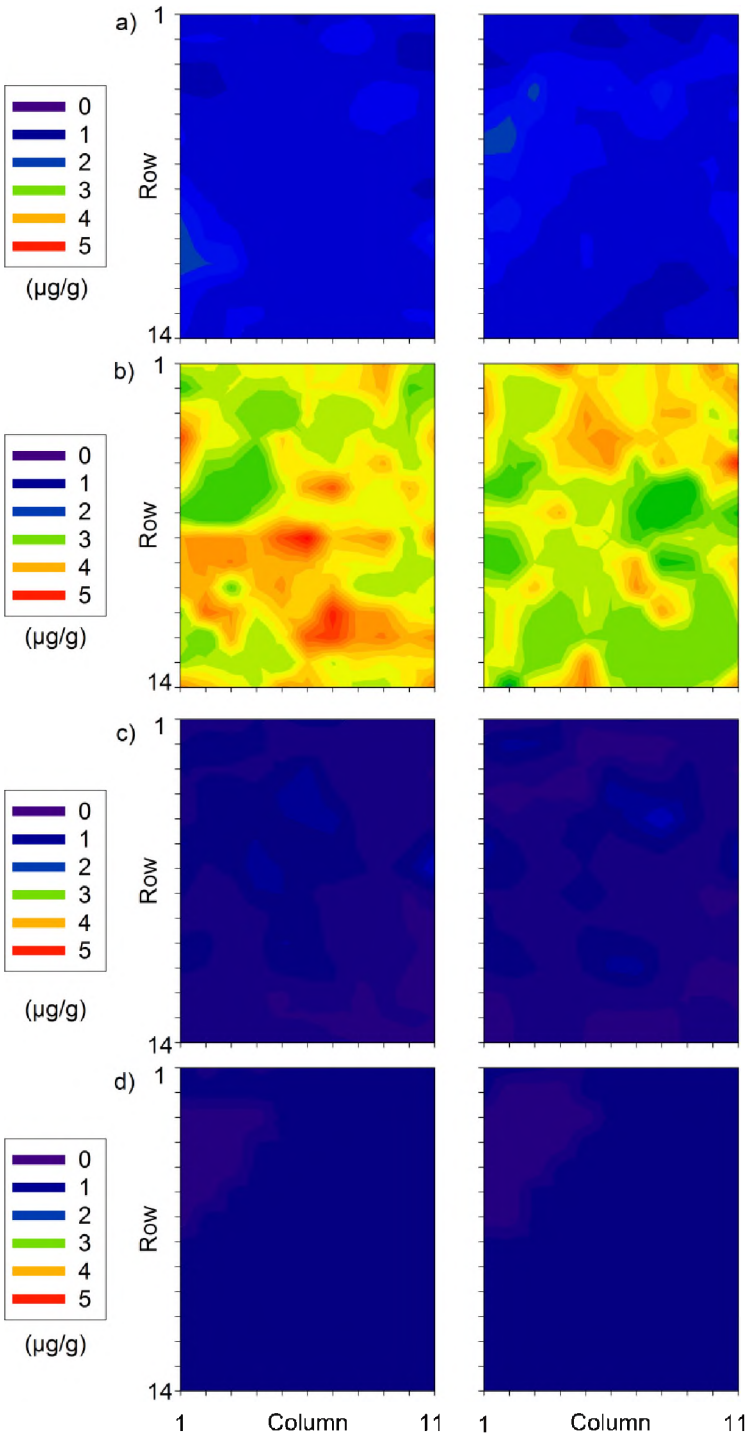

Figure 6.20. Image analysis-determined U distribution maps for a) SP2, b) SP5, c) Layer 8 and d) Layer 5B. In each example the same U scale (0–5 µg/g) has been used to facilitate comparison *between* samples. The bottom slab is given on the left and the top is on the right.

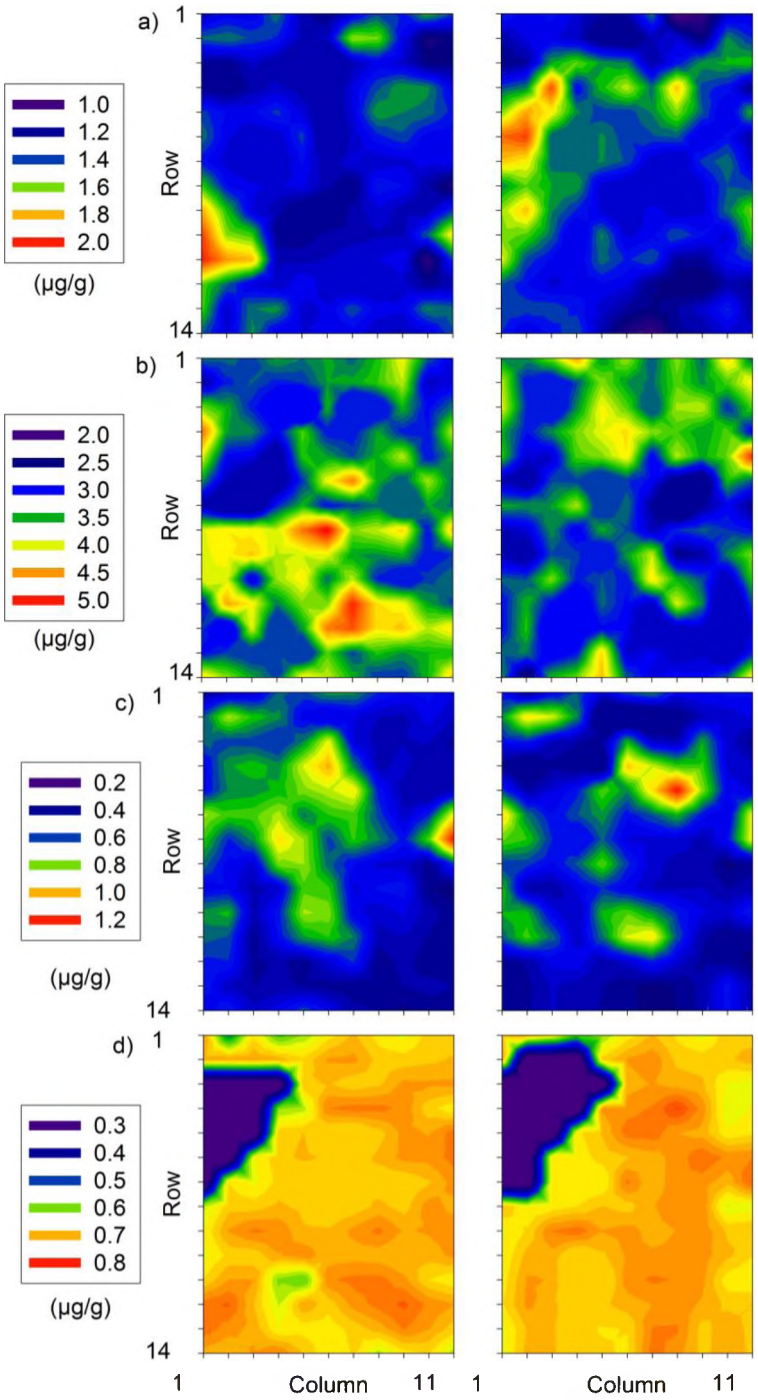

Figure 6.21. Image analysis-determined U distribution maps for a) SP2, b) SP5, c) Layer 8 and d) Layer 5B using individual scales to display the range of concentrations *within* a sample. In each example, the bottom slab is given on the left and the top is on the right.

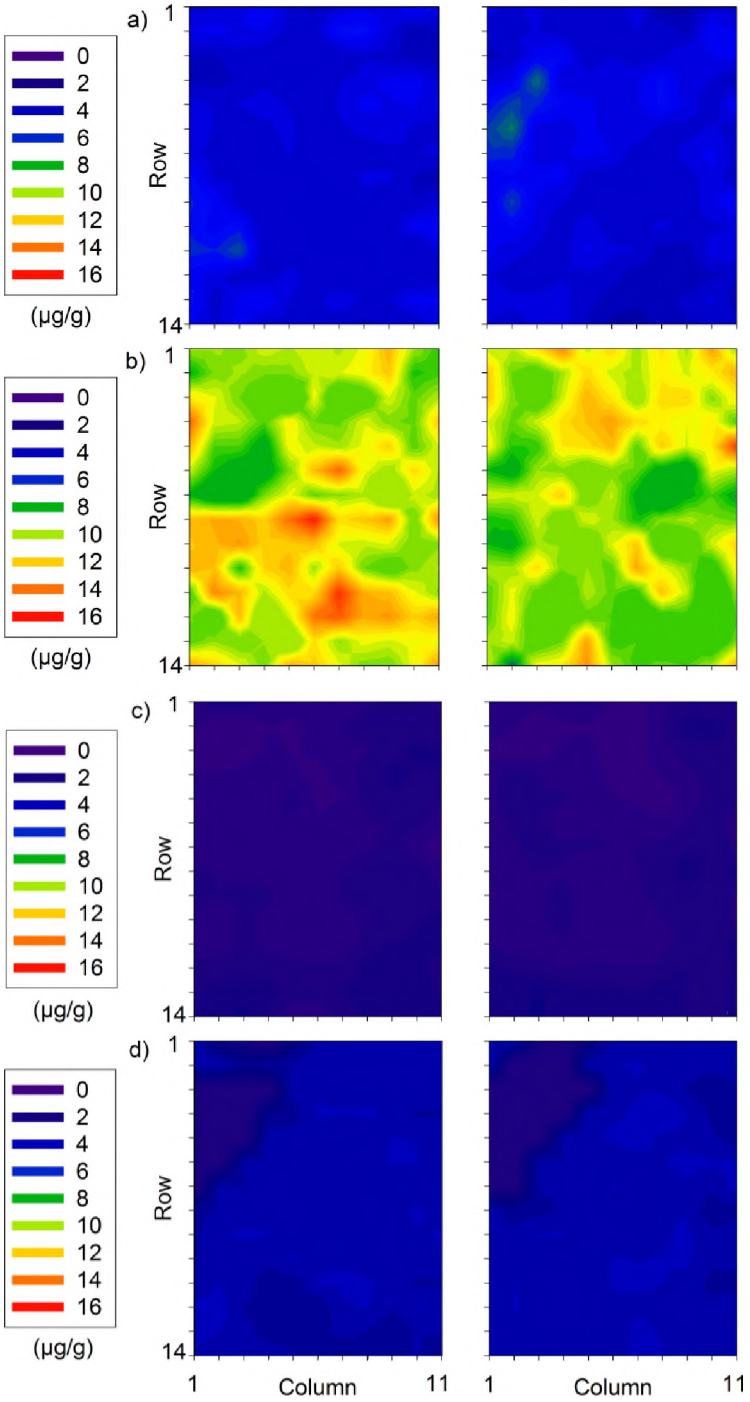

Figure 6.22. Image analysis-determined Th distribution maps for a) SP2, b) SP5, c) Layer 8 and d) Layer 5B. In each example the same Th scale (0–16 µg/g) has been used to facilitate comparison between samples. The bottom slab is given on the left and the top is on the right.

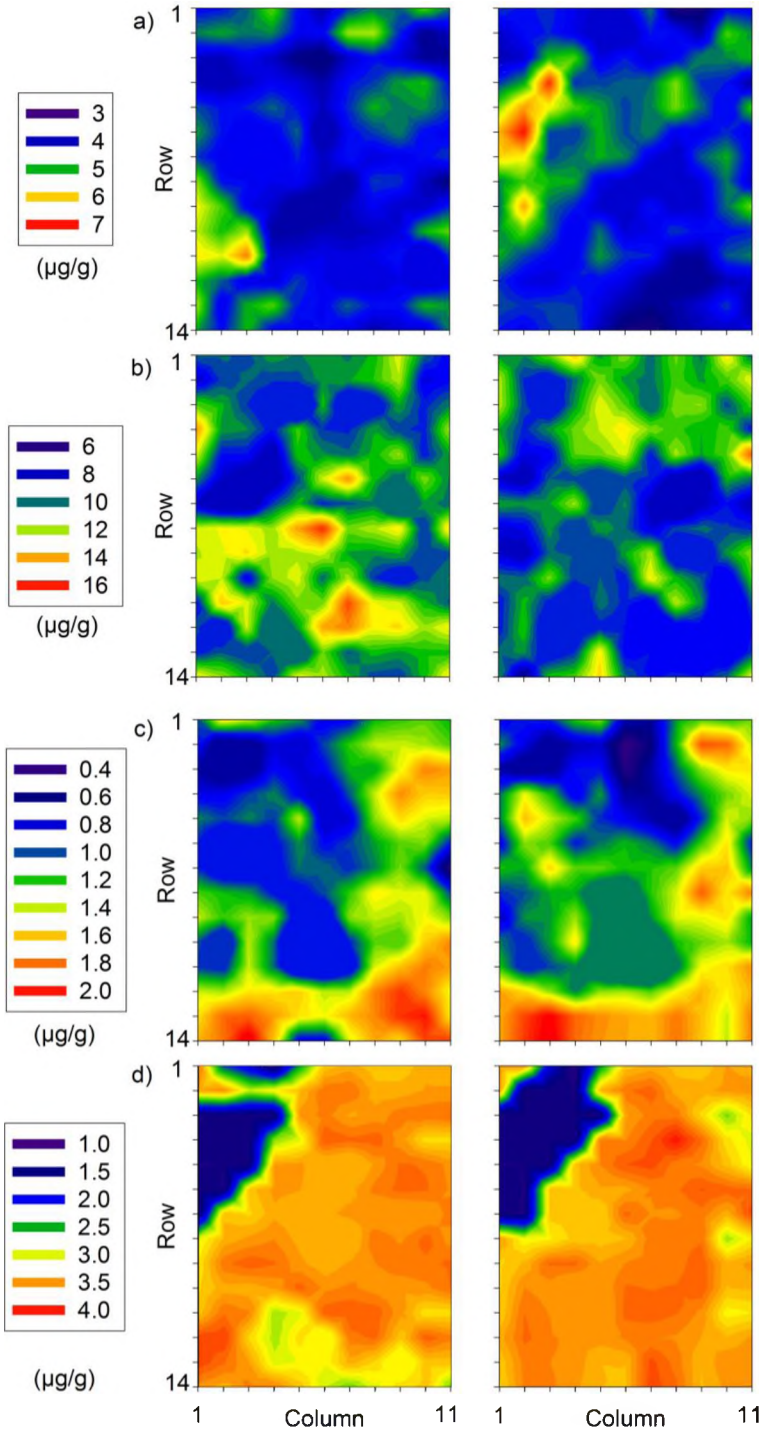

Figure 6.23. Image analysis-determined Th distribution maps for a) SP2, b) SP5, c) Layer 8 and d) Layer 5B using individual scales to display the range of concentrations *within* a sample. In each example, the bottom slab is given on the left and the top is on the right.

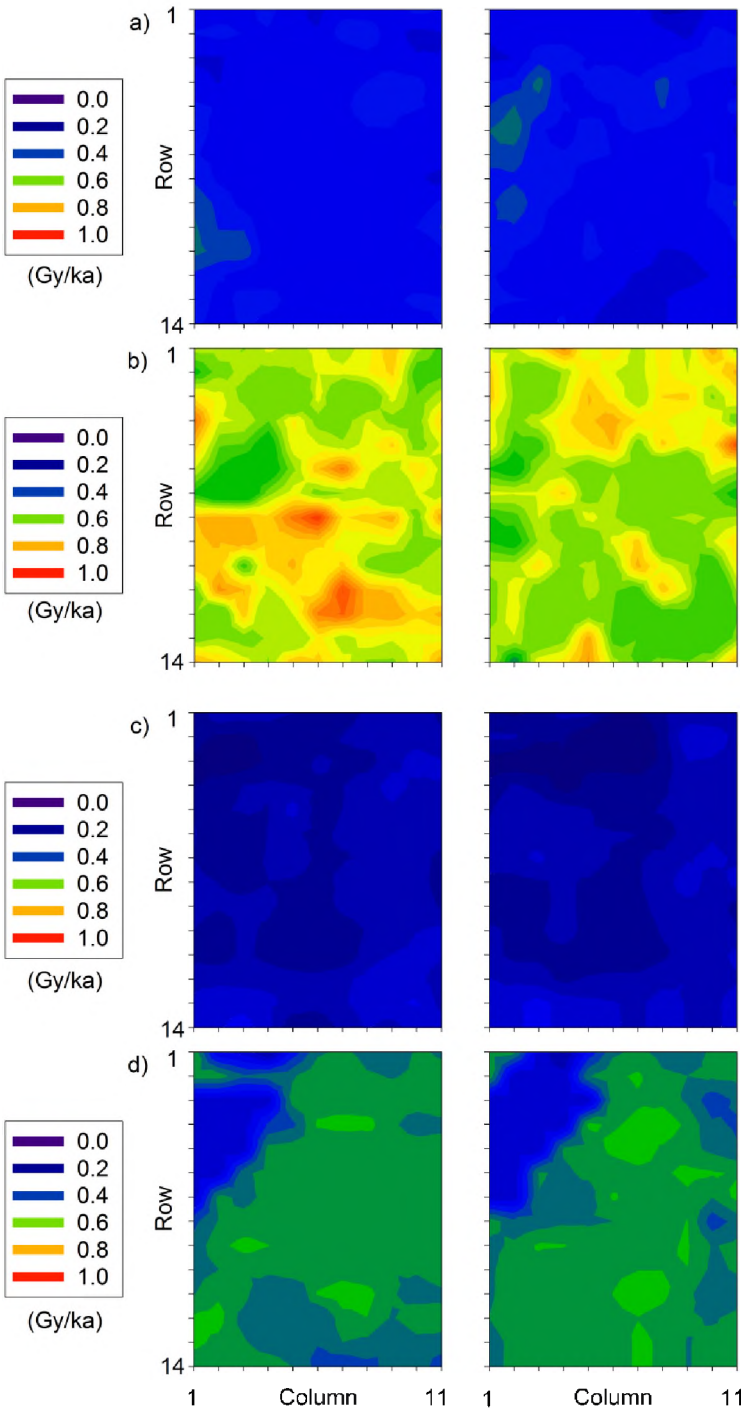

Figure 6.24. Image analysis-determined β-D_r distribution maps for a) SP2, b) SP5, c) Layer 8 and d) Layer 5B. In each example the same β-Dr scale (0–1 Gy/ka) has been used to facilitate comparison between samples. The bottom slab is given on the left and the top is on the right.

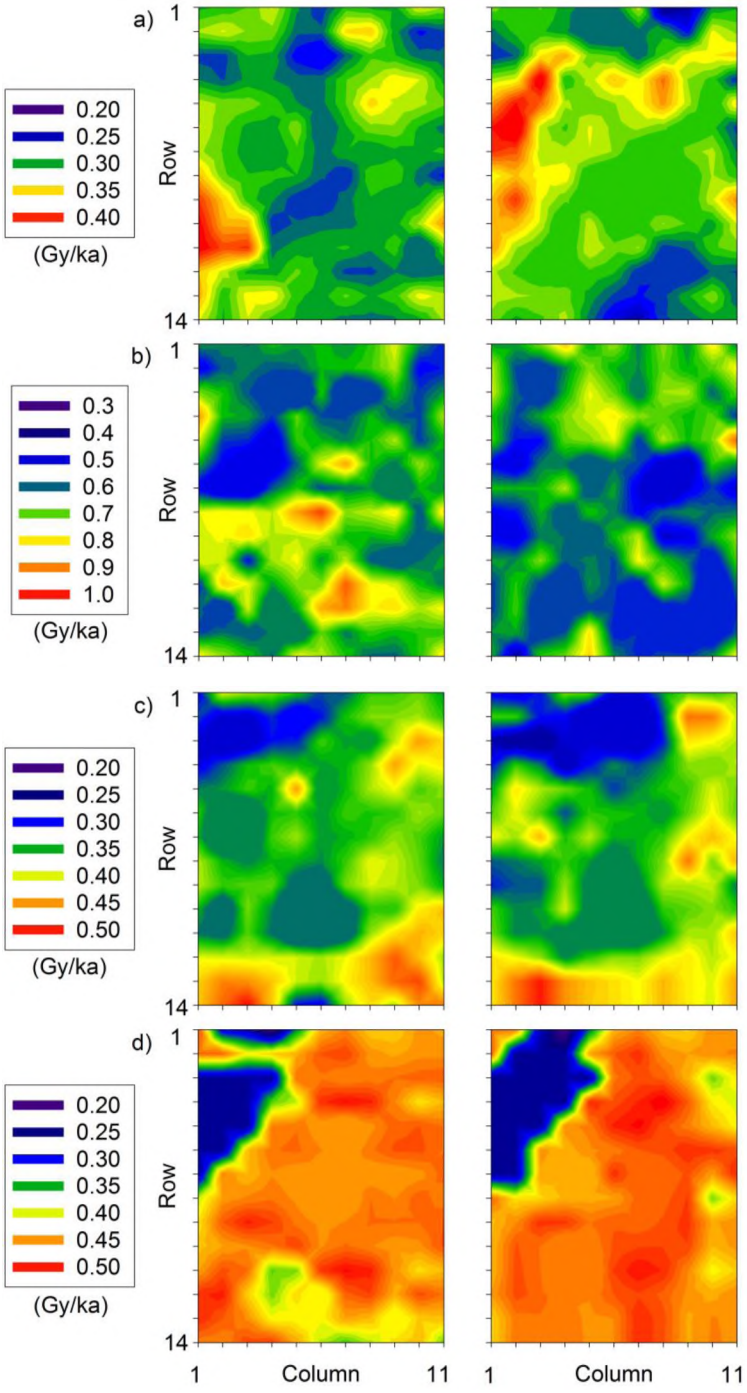

Figure 6.25. Image analysis-determined β-D_r distribution maps for a) SP2, b) SP5, c) Layer 8 and d) Layer 5B using individual scales to display the range of concentrations *within* a sample. In each example, the bottom slab is given on the left and the top is on the right.

limestone and bone, whereas the higher regions (shown in ornage/red, Figure 6.23d) are associated with the matrix.

6.4.2.4.5 Modelled beta dose rate maps

The β-Dr maps constructed using the modelled concentrations of U, Th and K are shown in Figures 6.24 and 6.25. The modelled β-D_r values for samples SP5 and Layer 5B (Figures 6.24b and d) are, on average, higher than those for SP2 and Layer 8 (Figures 6.24a and c). For the SP2 sample (Figure 6.25a), the β-Dr ranges between 0.23 ± 0.01 and 0.43 ± 0.01 Gy/ka. This is in contrast to the SP5 sample where β-Dr of between 0.34 ± 0.01 and 0.95 ± 0.03 Gy/ka were obtained, and represented by light green to orange in Figure 6.25b. The modelled β-Dr values for Layer 8 range from 0.070 ± 0.003 to 0.30 ± 0.01 Gy/ka (Figure 6.25c). The Layer 5B modelled β-D_r is slightly larger, ranging from 0.19 ± 0.01 to 0.51 ± 0.02 Gy/ka (Figure 6.25d). These β-Dr distributions are considerably tighter than their pXRF β-D_r counterparts (Section 6.4.1.7.4). This difference is most probably due to the application of two different techniques and analysis of slightly different surfaces (for the points outlined in Section 6.4.2.2.1).

The distribution of β-D_r values for each sample is displayed as radial plots in Figure 6.26. The most striking features of these plots is the uniformity in the associated relative errors on each β-D_r estimate. In each sample, the relative errors all fall between 3 and 4%, suggesting that the total uncertainty is dominated by the 3% error associated with the attenuation of the β-D_r for 180–212 μm quartz grains. There is potential, then, that the errors associated with the modelling of the U, Th and K concentrations are underestimated.

The distributions of β-D_r values in Figure 6.26 show a smooth continuum of values from low to high, with the exception of Layer 5B. Within the Layer 5B sample, three clusters of β-D_r values can be observed. When these values are spatially referenced to their positions on the associated thin sections, the lowest cluster of β-D_r values (indicated in Figure 6.26g) are associated with the bone

fragment found at the top of the thin sections, whereas the middle cluster of β-D_r values are found in association with the limestone pebbles (also indicated in Figure 6.26g). The remaining samples (SP2, SP5 and Layer 8) do not display this clustering of β-D_r values, apart from two β-D_r values in SP5 and Layer 8 that fall below the main spread of values.

The MAM and MAX β-D_r values determined for each sample are also indicated on the radial plots in Figure 6.26. SP2 is the only sample where the MAM- (0.27 ± 0.01 Gy/ka) and MAX- (0.36 ± 0.01 Gy/ka) determined β-D_r values bracket the 'bulk' GMBC β-D_r (0.31 ± 0.03 Gy/ka) (Figure 6.26e). In every other sample, the MAM- and MAX-determined β-D_r values fall below or are consistent with the 'bulk' GMBC β-D_r (Figures 6.26f,g and h; Table 6.17).

The weighted mean modelled β-D_r values were compared with their associated 'bulk' GMBC β-D_r. Of the four samples only the SP5 had modelled and bulk β-D_r values that were not consistent, being 0.62 ± 0.01 and 0.92 ± 0.07 Gy/ka, respectively. The remaining three samples, SP5, Layer 8 and Layer 5B, all have modelled β-D_r values that are significantly less than their GMBC β-D_r counterparts. The remaining samples had modelled and 'bulk' β-D_r values that were either consistent, or almost consistent, at 2σ. For SP2, the modelled β-D_r of 0.307 ± 0.002 Gy/ka was consistent with the GMBC 'bulk' β-D_r of 0.31 ± 0.03 Gy/ka. Layer 8 has a weighted mean modelled β-D_r of 0.203 ± 0.002 Gy/ka falls short of the GMBC β-D_r of 0.29 ± 0.03 Gy/ka. The weighted mean modelled β-D_r for Layer 5B of 0.417 ± 0.005 Gy/ka also falls just short of the GMBC β-D_r of 0.49 ± 0.03 Gy/ka.

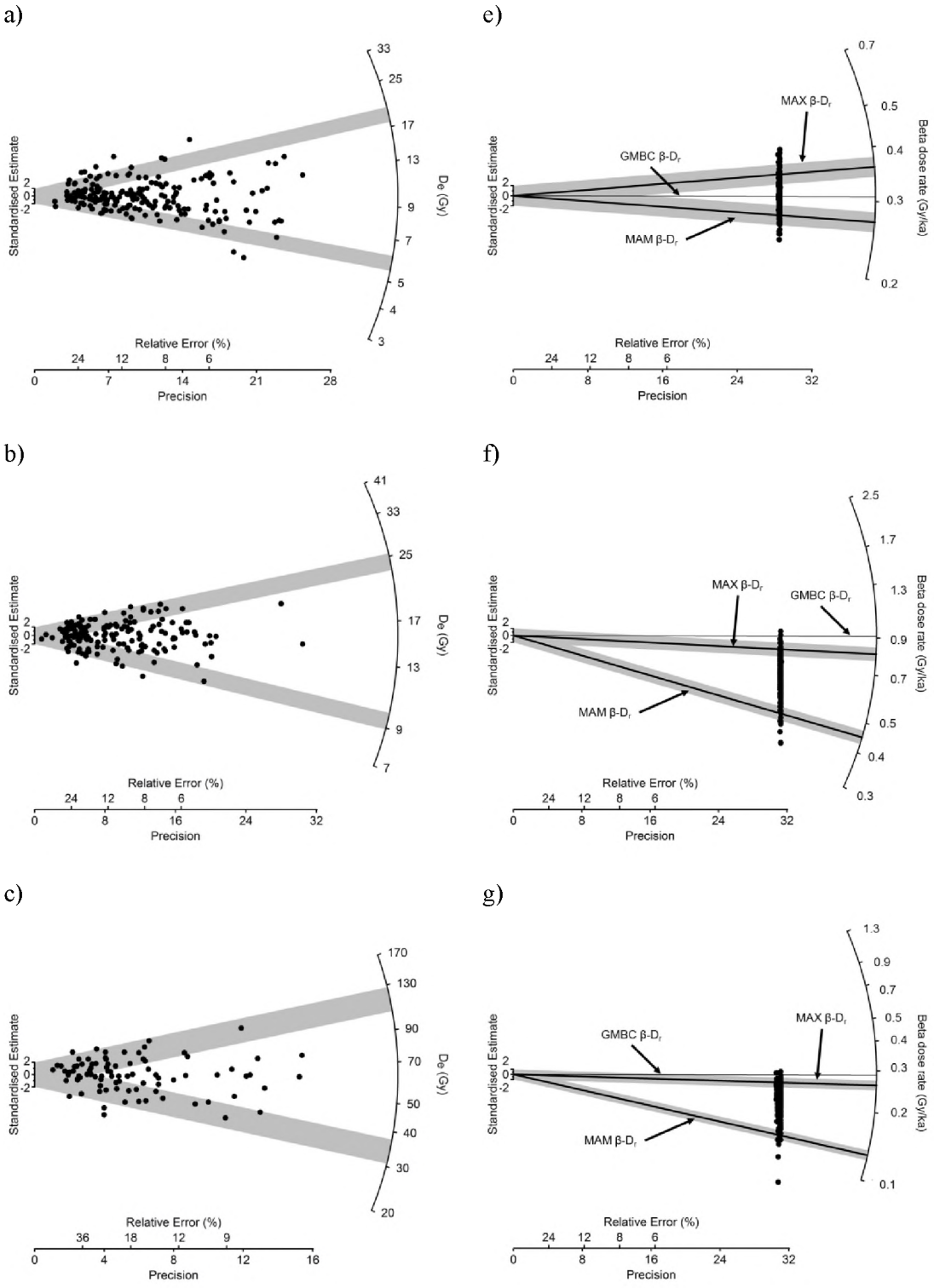
a)
Standardised Estimate
De (Gy)
Relative Error (%)
Precision
b)
Standardised Estimate
De (Gy)
Relative Error (%)
Precision
c)
Standardised Estimate
De (Gy)
Relative Error (%)
Precision
e)
MAX β-Dr
GMBC β-Dr
MAM β-Dr
Standardised Estimate
Beta dose rate (Gy/ka)
Relative Error (%)
Precision
f)
MAX β-Dr
GMBC β-Dr
MAM β-Dr
Standardised Estimate
Beta dose rate (Gy/ka)
Relative Error (%)
Precision
g)
GMBC β-Dr
MAX β-Dr
MAM β-Dr
Standardised Estimate
Beta dose rate (Gy/ka)
Relative Error (%)
Precision

d) h)

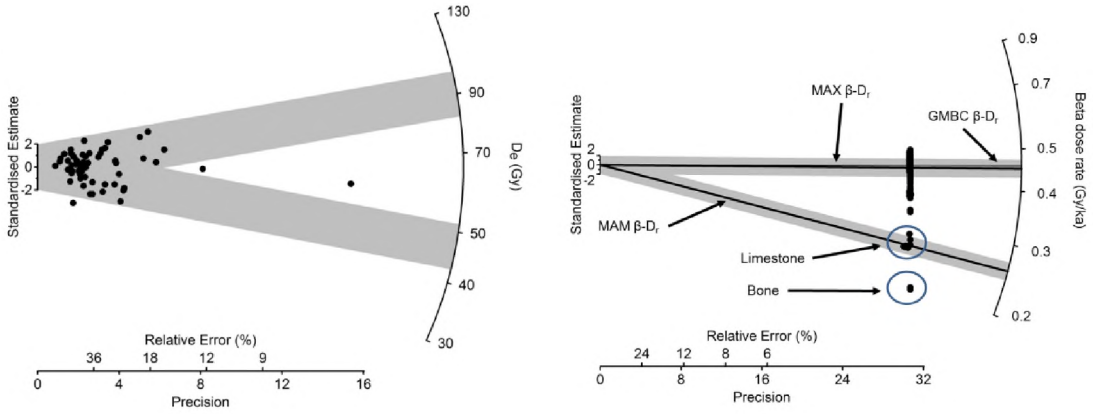

Figure 6.26. D_e distributions for a) SP2, b) SP5, c) Layer 8 and d) Layer 5B showing the MAM and MAX D_e values for each sample. The grey bands are centred on the MAM- and MAX-determined D_e values presented in Table 6.10. The image analysis modelled β-D_r values for e) SP2, f) SP5, g) Layer 8 and h) Layer 5B are also displayed. The β-D_r distributions are centred on the GMBC-determined β-D_r which is indicated by the thin black line. The MAM and MAX β-D_r values are indicated by the thicker black lines and grey bands.

6.4.2.5 Relationship between D_e distribution and modelled beta dose rate

In a similar fashion as was done with the pXRF β-D_r results, the D_e distributions of the four samples are addressed using the minimum and maximum modelled β-D_r determined using the image analysis method. As was the case for the pXRF data (Section 6.4.1.7.4.), it is assumed that if the MAX, MAM and CAM OSL ages using the MAM, MAX and 'bulk' GMBC β-D_r values, respectively, are equivalent then the spread in the D_e distribution can be explained as the result of β-D_r variability within the sample. The results of this examination are given in Table 6.17.

Table 6.17. OSL age estimates for the four samples investigated using the image analysis-determined β-D_r values.

Sample	Method	Age model[1]	D_e (Gy)	Total environmental dose rate (Gy/ka)[3]	β-D_r (Gy/ka)	Age (ka)
SP2	GMBC	CAM	9.84 ± 0.30	0.99 ± 0.06	0.31 ± 0.03	9.99 ± 0.71
	Image analysis	MAM	5.82 ± 0.28	0.94 ± 0.05	0.27 ± 0.01	5.71 ± 0.43
	Image analysis	MAX	18.75 ± 0.95	1.03 ± 0.05	0.36 ± 0.01	18.17 ± 1.32
SP5	GMBC	CAM	15.62 ± 0.46	2.37 ± 0.13	0.92 ± 0.07	6.60 ± 0.42
	Image analysis	MAM	9.38 ± 0.57	1.89 ± 0.08	0.45 ± 0.01	4.95 ± 0.38
	Image analysis	MAX	24.13 ± 2.34	2.25 ± 0.08	0.81 ± 0.01	10.70 ± 1.13
Layer 8	GMBC	CAM	63 ± 4	0.69 ± 0.05	0.29 ± 0.03	92 ± 9
	Image analysis	MAM	34 ± 3	0.53 ± 0.04	0.13 ± 0.01	64 ± 7
	Image analysis	MAX	115 ± 12	0.66 ± 0.04	0.26 ± 0.01	175 ± 21
Layer 5B	GMBC	CAM	66 ± 4	0.97 ± 0.05	0.46 ± 0.03	69 ± 6
	Image analysis	MAM	47 ± 11	0.76 ± 0.03	0.26 ± 0.01	62 ± 15
	Image analysis	MAX	90 ± 15	0.95 ± 0.04	0.45 ± 0.01	95 ± 16

The MAM (5.71 ± 0.43 ka, SP2; 4.95 ± 0.38 ka, SP5) and MAX ages (18.17 ± 1.32 ka, SP2; 10.70 ± 1.13 ka, SP5) for both MacCauley's Beach samples are not consistent with the reported CAM ages (9.99 ± 0.71 ka, SP2; 6.60 ± 0.42 ka, SP5). This is also true for the Layer 8 sample from Pech IV, where the MAM (64 ± 7 ka) and MAX age (175 ± 21 ka) are inconsistent with the reported CAM age (92 ± 9 ka). However, both the MAX (95 ± 16 ka) and MAM (62 ± 15 ka) for Layer 5B are concordant with the reported CAM age of 69 ± 6 ka. again, this is considered to be due to the larger uncertainties on the D_e estimates, rather than the MAM and MAX β-D_r values determined using image analysis modelling for this sample.

6.4.3 APPLICABILITY OF PXRF AND IMAGE ANALYSIS MODELLING IN THE RECONSTRUCTION OF THE BETA DOSE RATE ENVIRONMENT

6.4.3.1 OBJECTIVE

The methods described thus far have investigated the β-D_r environment of paired resin-impregnated sediment slabs. From these flat, 2π surfaces, estimates of

three dimensional, 4π β-D_r values have been constructed. The question arises whether the β-D_r estimates using pXRF and image analysis modelling are good approximations of the 'true' β-D_r environment. This section aims to address this question.

6.4.3.2 EXPERIMENTAL DESIGN

To address this question requires that the geometry of the resin-impregnated slabs first be considered. As shown in Figure 6.4, each sample investigated consisted of a 'top' and 'bottom' sediment slab, the internal faces of which was measured using the pXRF and modelled using the image analysis methods in Section 6.4.1 and 6.4.2, respectively. It was assumed that each of the measured or modelled elemental concentrations, and hence calculated β-D_r values, for the bottom measurement position and the corresponding position found on the top slab (e.g., Row 1, column 1 on the bottom slab correlates with Row 1, Column 1 on the top slab; each pair of corresponding point is hereafter termed a *spatially-equivalent point*) were representative of the same infinite dose matrix. In saying this, it was assumed that the loss of ~0.8 mm of material due to the width of the cutting blade used for bisection of the slab did not change the beta-dose geometry from which the radioactivity is measured. If both these assumptions are correct then the β-D_rs for these spatially-equivalent positions ought to be equivalent.

To test these assumptions, U, Th, K and β-D_r ratios for each spatially-equivalent point on the 'top' and 'bottom' sediment slabs were calculated for each of the four samples using the values obtained from the image analysis results. The pXRF values were not used as these were considered to be incomplete due to the significant number of measurement positions that had levels of U and Th below the level of detection. The spatially-equivalent point β-D_r and radionuclide ratios were then arbitrarily ranked in ascending order and displayed graphically in Figure 6.27 and Figure 6.28, respectively. Using the CAM, a qualitative understanding of the spread in the spatially-equivalent point β-D_r ratios for each of the four data sets was also obtained and the results are shown in Table 6.18.

6.4.3.3 RESULTS

6.4.3.3.1 Beta dose rate ratios

All samples, except SP5, have a weighted mean spatially-equivalent point β-D_r ratio that is consistent with unity (Figure 6.27). It should be noted that, for the Layer 8 distribution curve, two additional ratios at 2 and 2.4 were excluded for ease of comparison with the remaining samples. Each of the four data sets has a significant amount of spread beyond the mean of the population as shown by the OD values in Table 6.18. SP2 and Layer 5B record the lowest OD values of 11 ± 1%, Layer 8 somewhat higher at 17 ± 1%, while SP5 records the highest OD value at 23 ± 2%. These OD values are also reflected in the β-D_r ratio distribution curves of Figure 6.27. The variation within each of these datasets is significantly less that their corresponding D_e values, it is therefore likely that BM is only partially responsible for the variation within the D_e distributions for these 4 samples.

Table 6.18. Weighted mean β-D_r ratios for spatially-equivalent points for each of the four samples investigated in this study. Also shown is the overdispersion for each data set.

Sample Name	CAM Ratio	OD (%)
SP2	1.02 ± 0.01	11 ± 1
SP5	0.94 ± 0.02	23 ± 2
Layer 8	1.02 ± 0.01	17 ± 1
Layer 5B	1.00 ± 0.01	11 ± 1

6.4.3.3.2 Radionuclide ratios

There is also variability in the U, Th and K ratios for the four samples (Figure 6.28). The K ratios (stippled black) of the MacCauley's Beach samples are the most consistent with unity, with the U (black) and Th (dark grey) ratios more widely

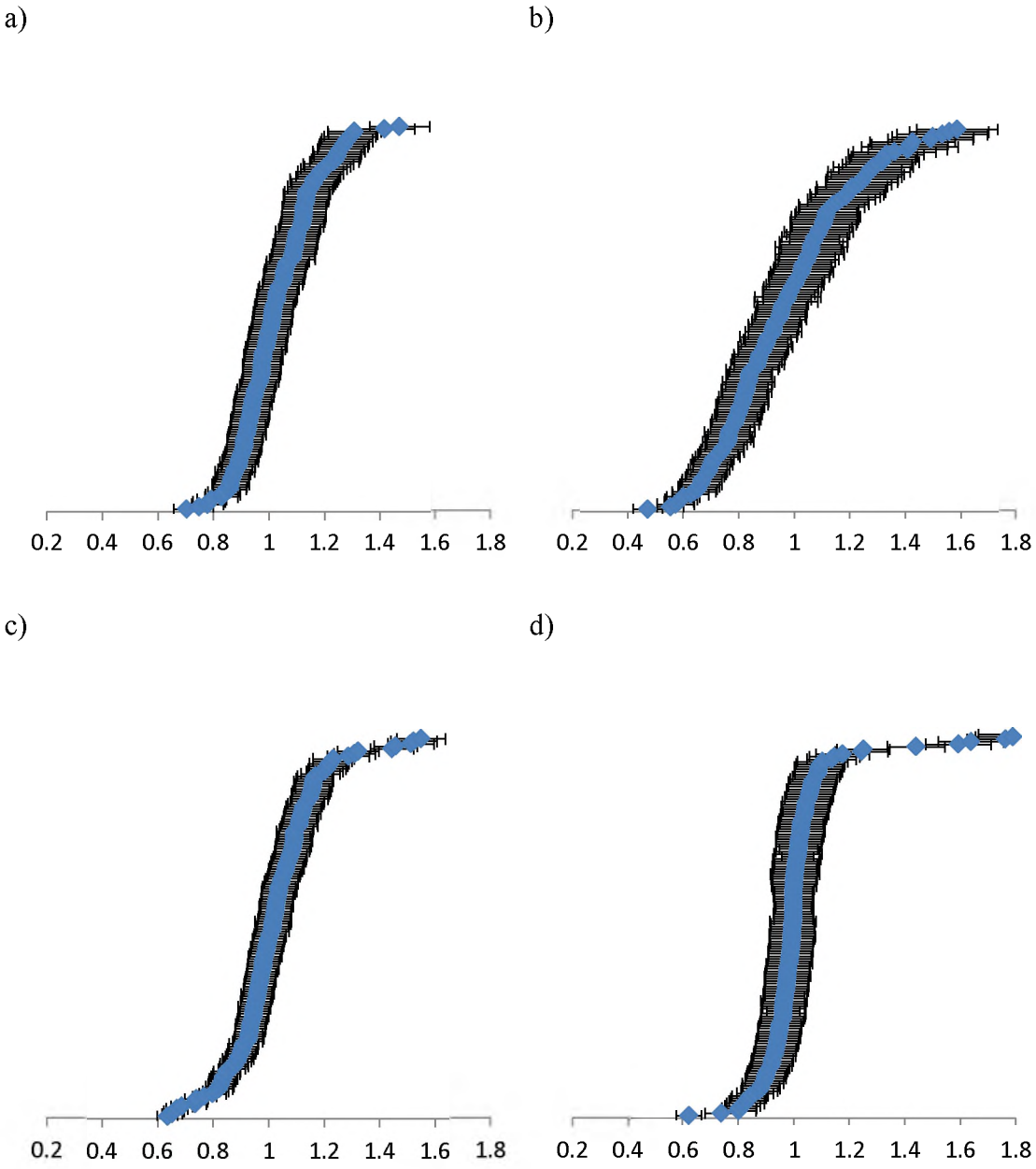

Figure 6.27. β-D_r ratios for image analysis modelled spatially-equivalent points (N = 154) for a) SP2; b) SP5; c) Layer 8; and d) Layer 5B. These values are arbitrarily ranked in ascending order and shown with 1σ error bars. Two additional points for Layer 8, at 2.0 and 2.4, not shown due to the truncation of the x-axis

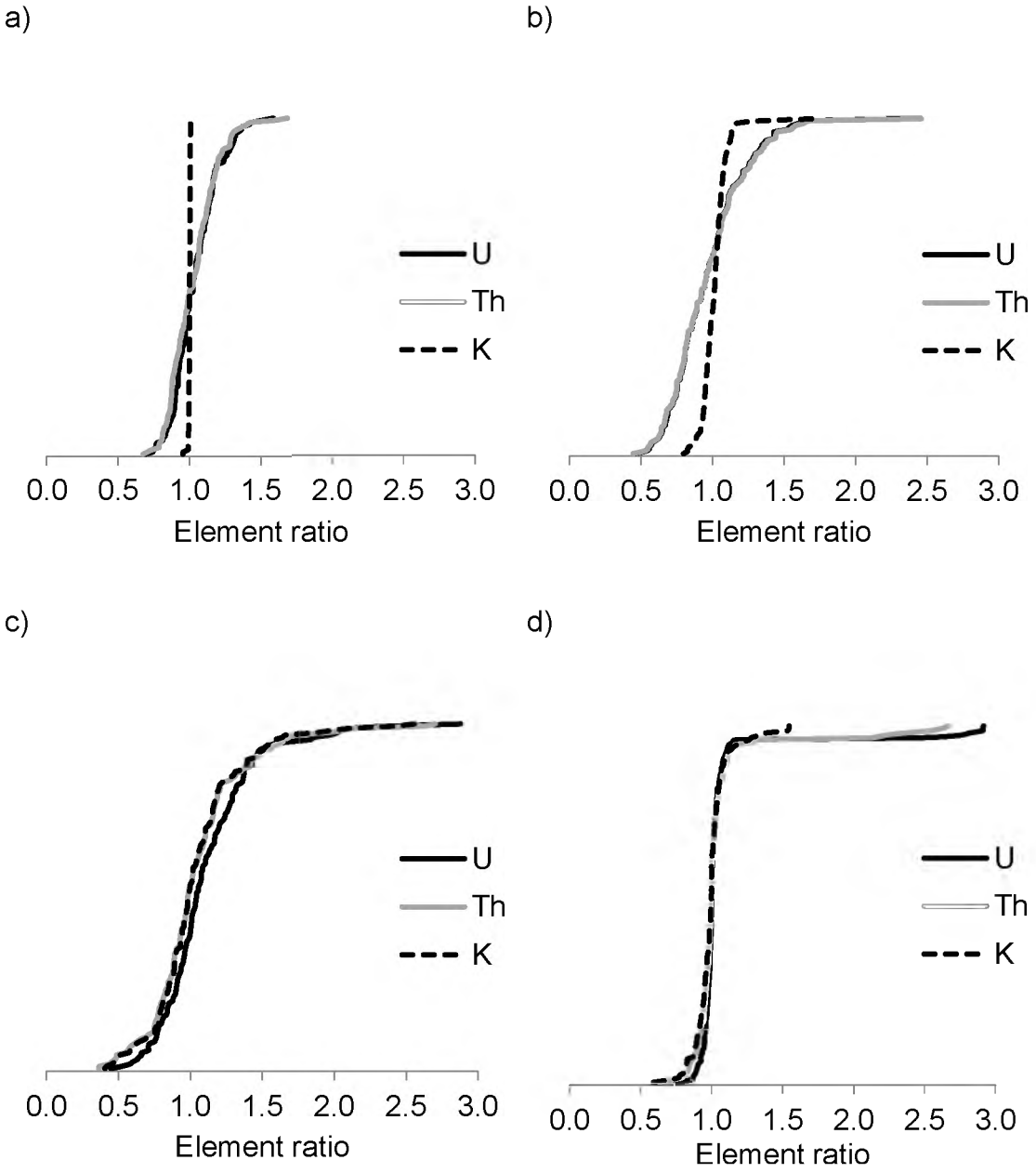

Figure 6.28. Ratios of U, Th and K for image analysis modelled spatially equivalent points (N=154) for a) SP2; b) SP5; c) Layer 8; and d) Layer5B. These values are arbitrarily ranked in ascending order.

distributed (Figure 6.28a and b). It is interesting to note that the U and Th ratio distribution curves are more similar than they are to that of the K ratio curve. The U, Th and K ratios for the Pech IV samples show a similar deviation from unity for all elements (Figure 6.28c and d). However, unlike the MacCauley's Beach samples, the U, Th and K ratio distribution curves are substantially less divergent.

6.4.3.4 DISCUSSION

The significant deviation from unity for a substantial proportion of spatially-equivalent β-D_r ratios (e.g., the ratio of the β-D_rs modelled for Row 1, Column 1 on the bottom slab and Row 1, Column 1 on the top slab) in each sample suggests that our original assumption (that the modelled β-D_rs from spatially-equivalent points are sampling equivalent β-D_r spheres) is not supported. The variability in the modelled β-D_rs is considered to be underlain by the variability in the concentrations of U, Th and K. The spread in the MacCauley's Beach U and Th ratios is much greater than that of K. Yet, this same pattern is not observed in the Pech IV samples.

The question then is why such a deviation exists at spatially-equivalent measurement positions. Soil micromorphological analysis, presented for MacCauley's Beach samples in Chapter 5, as well as the image analysis modelling carried out in this study reveals that heavy mineral grains such as zircon and rutile (having known affinities with U and Th) are distributed heterogeneously throughout these sediments. In contrast, the presence of clay (containing K) as interstitial matrix, infillings or void coatings in SP2 or as thin coatings around grains in SP5 are more homogeneously distributed. The variability in the U and Th is, therefore, going to be more pronounced as these elements are 'housed' in individual heavy mineral grains whereas the K is found predominantly in the matrix.

There is little variation in the any of the three elements in either of the Pech IV samples. There is slightly more variation in the U ratios, as this radionuclide is associated with randomly distributed burnt bone. The large ratios for Th and U in

Layer 5B are associated with spatially-equivalent points where one side is totally covered by limestone pebbles, whereas the other is situated in the CS and FSC matrix.

Of all the samples investigated in this manner, it is the Layer 5B sample that shows the least variation in the U, Th and K ratios. However, this result may be an artefact of the image analysis experimental design. In the image modelling for the Pech IV samples, only the FG (>2 mm) fraction was comprised of 'individual' components. Both the CS and FSC fractions were composite samples of various mineralogies. This would mean that any variability in the U, Th and K concentrations within these fractions would, effectively, be drawn towards the average of all those mineralogies present.

6.4.3.5 IMPLICATIONS

The above findings provide two points of discussion with regards to the applicability of the 2π pXRF and image analysis modelling of the β-D_r environment. First, it would appear that in samples where radioactively 'hot' minerals grains are the source of β-D_r variability that these techniques do not provide representative estimates of the same β-D_r sphere. The second point is that, where the radioactivity is concentrated in the matrix of the sample, these techniques appear to be able to provide representative estimates of the same β-D_r sphere. In either case, it is clear that the presentation of both 'top' and 'bottom' radionuclide and β-D_r maps (as has been done in Sections 6.4.1. and 6.4.2.) is more appropriate rather than one map that combines both the 'top' and 'bottom' concentrations or β-D_r values.

6.4.4 ALUMINIUM OXIDE DOSIMETRY TO SPATIALLY RESOLVE THE BETA DOSE RATE ENVIRONMENT

6.4.4.1 OBJECTIVE

The objective of this experiment was to build upon the 2π geometry studies presented in Sections 6.4.1 and 6.4.2, by investigating the 4π geometry of the β-D_r environment using grains of carbon-doped aluminium oxide (Al_2O_3:C). Unlike the pXRF and image analysis methods where the average concentrations for U, Th and K are determined over a 6 mm diameter surface, the use of Al_2O_3:C provides an estimate of the actual β-D_r that is emitted from the sediment. Previous investigations using Al_2O_3:C have mainly dealt with the use of environmental dosimetry using the OSL (Burbidge & Duller 2003) or TL (Kalchgruber & Wagner 2006) signal from Al_2O_3:C discs (commonly referred to in the literature as 'chips') or the TL signal from individual grains (Kalchgruber *et al.* 2003). In this study, the β-D_r determination was attempted using the OSL signal from individual grains and 4-grain aliquots of Al_2O_3:C.

6.4.4.2 ALUMINIUM OXIDE GRAINS

This experiment was completed using Al_2O_3:C grains grown by Landauer Inc., Crystal Growth Division, Stillwater, Oklahoma, USA (Akselrod *et al.* 1990, Akselrod *et al.* 1993, Akselrod & Akselrod 2002). The 180–212 μm in diameter size fraction was isolated from a bulk 'powder' sample of Al_2O_3:C and annealed at 900°C for 15 min to evict any trapped charge from deep traps (Yukihara *et al.* 2003, Yukihara *et al.* 2004). This grain size fraction was used as the quartz grains used for D_e determinations were also of this size. The assumptions used to calculate the β-D_r dosimetry for the Al_2O_3:C grains are therefore directly comparable to those of the quartz grains.

6.4.4.3 EXPERIMENTAL DESIGN

The 3×3 mm grid (Figures 6.5) used previously in the pXRF analysis was also used here. A number of Al_2O_3:C grains were placed at each of the vertices of this grid using a pin. The grains were held in place with a small amount of silicon spray oil. The corresponding slab was then replaced and both the top and bottom slabs of each sample were wrapped together in a double layer of 150 μm thick black plastic and a 2 mm thick lead jacket prior to storage in a wooden cabinet.

Storage time before measurement varied. SP5 was stored for a total of 233 days, SP2 for 364 days; Layer 8 for 399 days and Layer 5B for 411 days. By embedding the Al_3O_2:C grains between the two sediment slabs, it is ensured that these grains measured the β-D_r directly from the real 4π geometry of the sample. This is in contrast to the pXRF measurements where it was required to assume an infinite dose matrix from measurement of a 2π slab. It was, however, assumed that the removal of ~0.8 mm by the saw blade between the two slabs did not alter the composition or geometry of the original beta dose sphere.

6.4.4.4 MEASUREMENT PROCEDURES, TESTS AND SIGNAL CHARACTERISATION

6.4.4.4.1 Measurement instrumentation

All OSL measurements of the Al_3O_2:C grains were conducted using a Risø TL/OSL-DA-20 reader (Bøtter-Jensen *et al.* 2000, Bøtter-Jensen *et al.* 2003) – see Chapter 2.3.3.2. The D_e of the Al_2O_3:C grains was measured in two ways. Initially, single grains from SP5, SP2 and Layer 8 were measured. Later small aliquots were measured, again, from Layer 8 and also Layer 5B. Optical stimulation of individual grains was carried out using the green laser at a constant power (90%) for 60 s at 50°C. The aliquots were stimulated using blue LEDs at a constant power (90%) for a duration of 120 s at 50°C. The OSL signal was taken from the first 2 s of optical

stimulation, with the background calculated as the average OSL counts during the last 15 s of stimulation. These parameters were used for both the single grain and single aliquot measurements. Examples of OSL decay curves from single grains and multi-grain aliquots of Al_2O_3:C are shown in Figure 6.29.

a)

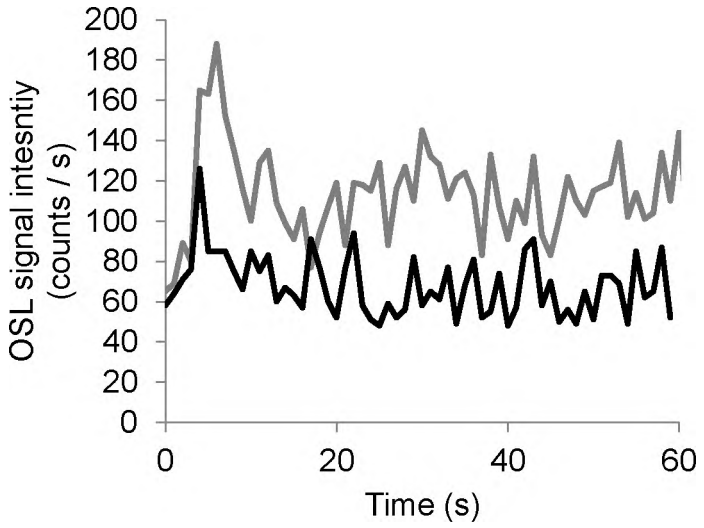

b)

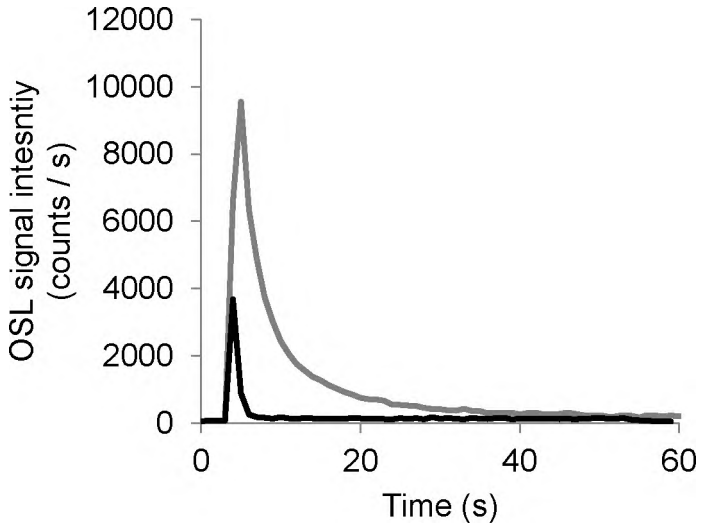

Figure 6.29. OSL decay curves for a) environmentally and b) laboratory dosed single grain (black) and small (4 grain) aliquot (grey) of Al_2O_3:C. Both single grain and single aliquot were from the same measurement position from Layer 8.

6.4.4.4.2 Aluminium oxide SAR procedure

The Al_2O_3:C D_e values were measured using a single-aliquot regenerative-dose (SAR) procedure (Murray & Wintle 2000, 2003), outlined in Table 6.19. Following environmental and regenerative dose irradiations, the Al_2O_3:C grains were preheated to 80°C for 10 s prior to OSL measurement for 60 s using the green laser at a temperature of 50°C. The power of the green laser was set at a 90%, a power density of about 45 mW/cm^2. The grains were then given a test dose to correct for any sensitivity changes that may occur throughout the repeated cycles of irradiation, heating and annealing. Following test dose irradiation, the grains where preheated to 80°C for 5 s and the OSL signal measured using the same parameters used for the environmental and regenerative doses.

Table 6.19. SAR procedure used in the measurement of Al_2O_3:C single grains.

Step	Treatment	Comments
1	Dose	
2	TL to 80 °C for 10 s	Preheat to empty 80 °C TL trap
3	OSL at 50 °C using green laser at 90% power	L_N or L_X
4	OSL at 30 °C using blue LED for 250 s	Optical bleach to reduce OSL signal to stable background
5	Test dose	T_D
6	TL to 80 °C for 10 s	Preheat to empty 80 °C TL trap
7	OSL at 50 °C using green laser at 90% power	T_N or T_X
8	OSL at 30 °C using blue LED for 250 s	Optical bleach to reduce OSL signal to stable background level

6.4.4.4.2.1 OSL background signal build-up

It was noticed during SAR measurements that the OSL signal background increased as a function of SAR cycle. To test this further, a single Al_2O_3:C grain was given four identical regenerative doses (about 0.11 Gy), preheated to 80°C for 10 s and the OSL signal measured using the green laser at 90% power for 60 s. The decay curves shown in Figure 6.30a revealed an increasing OSL signal background with successive irradiations. Using a separate, annealed grain, the experiment was repeated with the application of an 'optical wash' – 250 s blue LED stimulation at 30°C – after each OSL measurement to determine if this background signal build-up could be removed. The results, in Figure 6.30b, show that this procedure effectively prevented the build-up of the OSL background signal. Thus, in the SAR procedure used in this study, a 250 s blue LED stimulation at 30°C was inserted after each L_X and T_X measurement.

6.4.4.4.3 Establishing aluminium oxide measurement procedures using dose recovery experiments

Dose recovery tests (Murray & Roberts 1997) were also conducted to determine the most appropriate measurement conditions for the Al_2O_3:C grains. Single-grains of annealed Al_2O_3:C were loaded into an aluminium single-grain disc (Bøtter-Jensen *et al.* 2000) and a 'surrogate natural' laboratory beta dose of ~0.11 Gy was administered. Four different preheat temperatures were investigated (60, 80, 100 and 120°C) and these were held for 10 s following regenerative doses, or 5 s following a test dose.

Dose response curves were constructed using regeneration doses of 0, 0.11 and 0.22 Gy, followed by another 0 Gy dose to check for signal build-up from cycle-to-cycle. A test dose of 0.11 Gy was also used to monitor for sensitivity change from cycle-to-cycle. The OSL signal was then measured using the green laser for a period of 60 s holding the sample at 50°C. To prevent the build-up of the slowly bleaching background over repeated SAR cycles, an optical bleach of 250 s was applied at the

a)

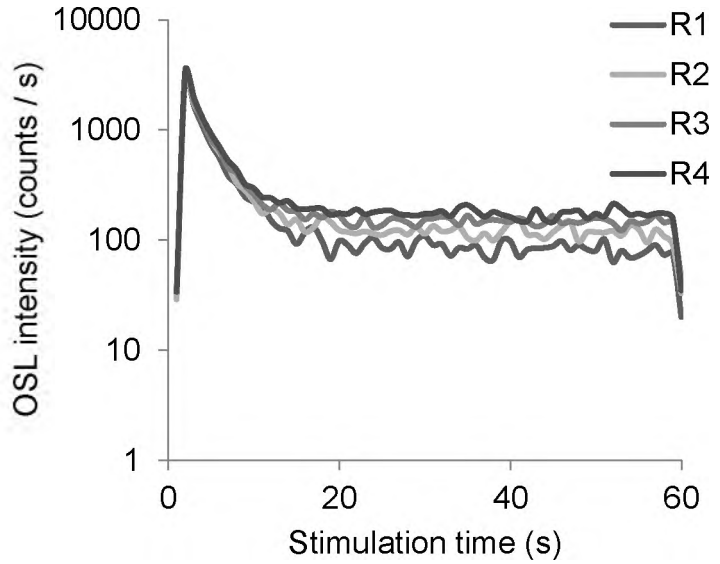

b)

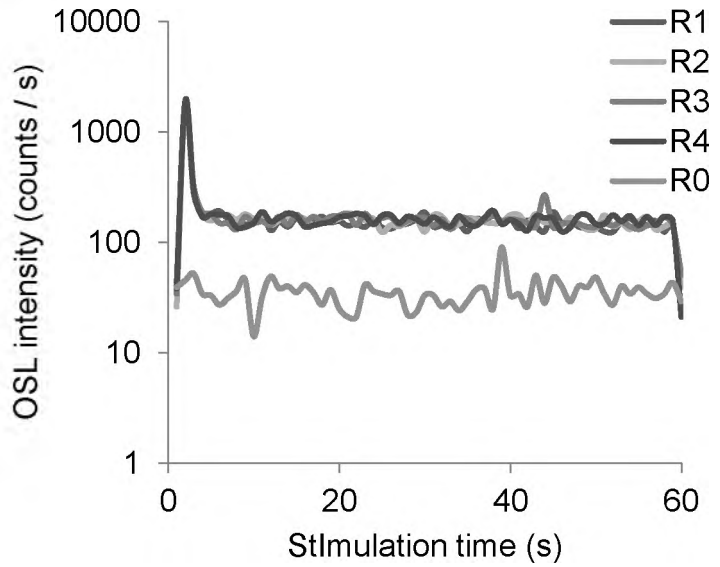

Figure 6.30. OSL decay curves for two separate Al_2O_3:C grains. Each grain was given four repeat 0.11 Gy beta irradiations and measured for 60 s using the green laser. Grain a) received no optical wash between irradiations. Grain b) received an optical wash using the blue LEDs for 250 s between each successive irradiation. R refers to regenerative dose and R0 the OSL response from no additional beta irradiation. The grain in a) shows a much slower decay rate compared to the grain in b).

end of each regenerative and test dose measurement using blue LEDs to reduce the OSL signal to a stable background level prior to giving it a new regeneration or test dose.

The results are summarised in Table 6.20. The recovered dose and OD were determined using the central age model of Galbraith *et al.* (1999). Only the 80°C preheat combination resulted in a measured/given dose ratio (0.96 ± 0.02) that was consistent with unity at 2σ (Table 6.20). Therefore, these preheat parameters were used throughout this study for β-D_r determination using Al_2O_3:C grains.

Table 6.20. Results of the dose recovery tests showing the recovered dose and overdispersion values for each thermal pre-treatment procedure following a 0.109 ± 0.002 Gy laboratory beta irradiation.

Thermal treatment	Recovered dose (Gy) (± 1σ)	Overdispersion (%) (±1σ)	Measured/given dose ratio (±1σ)
60°C /10 s + 60°C / 5 s	0.096 ± 0.001	8 ± 1	0.88 ± 0.02
80°C /10 s + 80°C / 5 s	0.104 ± 0.001	7 ± 1	0.96 ± 0.02
100°C /10 s + 100°C / 5 s	0.097 ± 0.001	7 ± 1	0.88 ± 0.02
120°C /10 s + 120°C / 5 s	0.101 ± 0.001	7 ± 1	0.92 ± 0.02

6.4.4.4.4 Standardised growth curve construction

To reduce the amount of machine time, and also the likelihood of filling up deep, hard-to-bleach traps (Yukihara *et al.* 2003, Yukihara *et al.* 2004), the D_e for each Al_2O_3:C grain was determined using the standardised growth curve (SGC) approach of Roberts & Duller (2004). This work was carried out on a separate Risø reader (Risø 5) to that used above for the dose recovery and signal characterisation tests (Risø 3). Risø 5 was used as the substantially smaller instrument background

signal of this machine allowed for better OSL signal-to-noise ratios. The lowest beta dose able to be delivered on Risø 5 was 0.13 Gy, rather than 0.11 Gy as used previously on Risø 3.

The single-grain SGC (Figure 6.31a) was constructed using the SAR procedure outlined in Table 6.19. Forty two annealed Al_2O_3:C grains were given regenerative doses of 0, 0.13 and 0.26 Gy and a test dose of 0.13 Gy. The single-aliquot SGC (Figure 6.31b) was constructed using 12 single aliquots of Al_2O_3:C and the a modified version of the SAR procedure presented in Table 6.19. Here, L_X and T_X were measured using the blue LEDs for 120 s duration at 50°C, rather than the green laser. To create the aliquots, four annealed grains were picked using a pin and deposited onto the centre of a stainless steel disc using a small amount of silicon spray oil to hold them in place. Each aliquot was given the same test and regenerative dose irradiations as the single-grains, with an additional 0.39 Gy regenerative dose added to ensure linear growth of the dose response curve. The L_X/T_X ratios for each single-grain and single-aliquot were multiplied by the T_D (0.13 Gy) to obtain a standardised OSL response and could be fitted with a linear equation that was forced through the origin.

A similar SGC is produced regardless of whether aliquots or single grains are used. In the small aliquot SGC, the standardised luminescence signal for one aliquot is substantially higher than the remaining points. The OSL sensitivity of this aliquot shows a sharp decrease by about 20% following the first SAR cycle that is not observed in any of the other aliquots (Figure 6.32). The sensitivity changes in the remaining aliquots are contained within about 10% of the initial value and change gradually with SAR cycle number (Figure 6.32). The removal of all the data points associated with the 'outlying' aliquot results in no significant change in either the slope of the line (m = 1.04) or the R^2 value (R^2 = 0.996). For this study, the data associated with this aliquot was removed from the SGC. Using the equations set out in Duller (2007), the curve fitting errors for the single grain SGC were calculated to be 0.60%, whereas the small grain SGC fitting error was slightly larger at 0.98%.

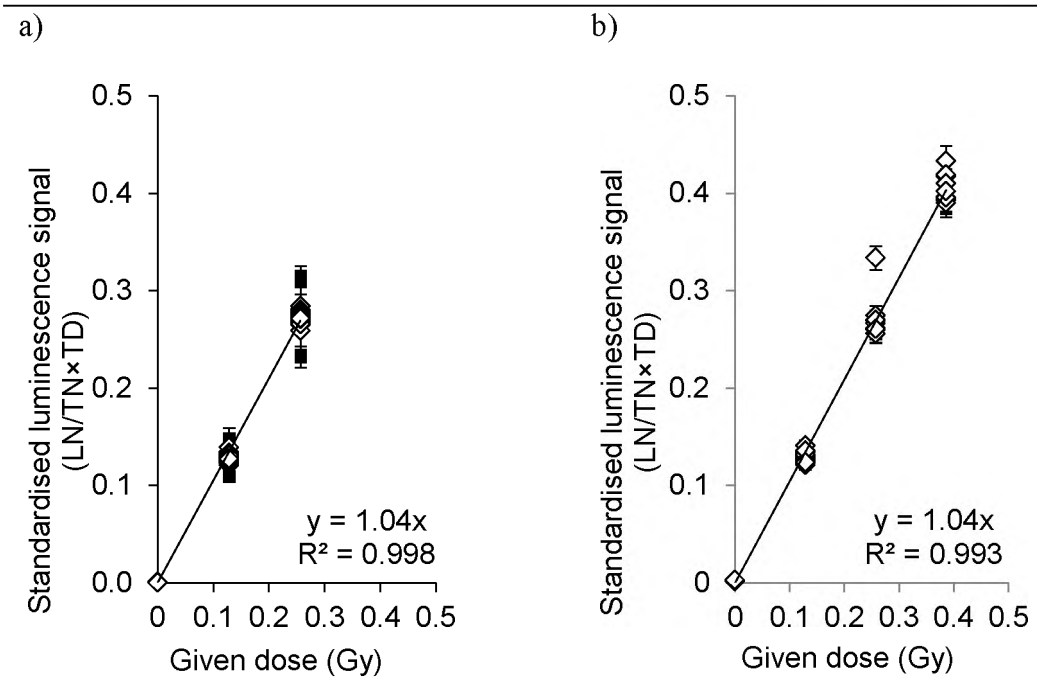

Figure 6.31. Standardised growth curve used throughout this study for D_e determination using a) single-grains and b) single-aliquots of Al_2O_3:C. Each given dose point is comprised of 42 individual grains or 12 aliquots. Error bars are shown at 1σ.

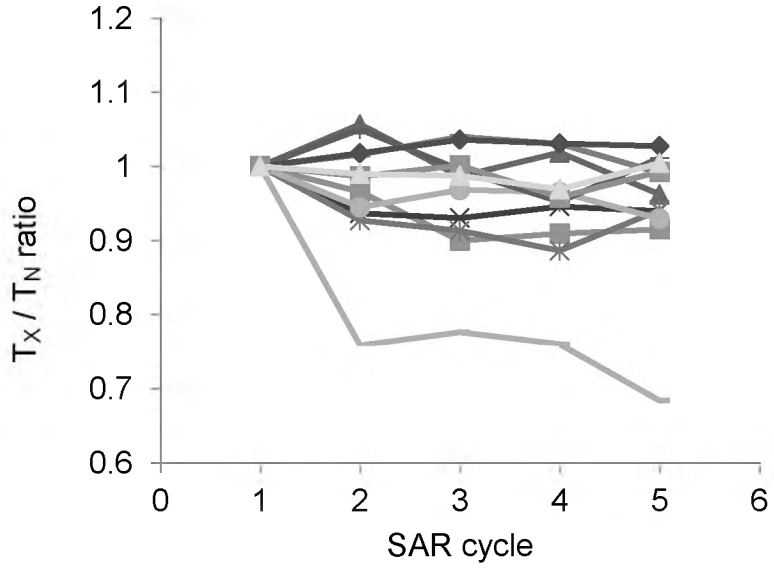

Figure 6.32. Sensitivity changes for the 12 small aliquots of Al_2O_3:C used to construct the single aliquot SGC shown in Figure 6.31b.

6.4.4.4.5 Environmentally dosed aluminium oxide measurement procedure

Measurement of the OSL signal the Al_2O_3:C grains embedded between the resin-impregnated sediment slabs was carried out in two ways: 1) as single grains, and 2) as small aliquots. For the single-grain method individual grains were hand-picked using a pin from the SP2, SP5 and Layer 8 sediment slabs. These grains were removed from their position on the resin slab and placed into the single-grain aluminium discs one-by-one. The position of each grain on the slab and the hole it was deposited into on the single-grain disc were noted so that the results could be spatially resolved following measurement.

The small aliquot method was used for the Pech IV samples of Layer 8 and Layer 5B only. Four single grains from the same measurement position were, again, hand-picked using a pin and deposited onto the centre of a stainless steel disc. The grains were adhered using a small amount of silicon spray oil. The measurement position of the Al_2O_3:C grains was noted and recorded against the position of the aliquot once placed into the Risø reader carousel, to allow for spatial resolution of the resulting D_e and β-D_r values.

6.4.4.4.6 Aluminium oxide OSL decay curve shapes

6.4.4.4.6.1 Laboratory irradiation

Examples of a laboratory-irradiated single grain and single aliquot of Al_2O_3:C are shown in Figure 6.33. Both figures show the L_X and the corresponding T_X signal for a 0.26 Gy regenerative dose (black) and a 0.13 Gy test dose (grey). These curves have been normalised to their initial OSL signal intensity. For the single grain measurements, the OSL signal reaches ~25% of the initial signal intensity after 6 s of blue LED stimulation. In contrast, this ~30% intensity is achieved after only 1 s of green laser stimulation.

a)

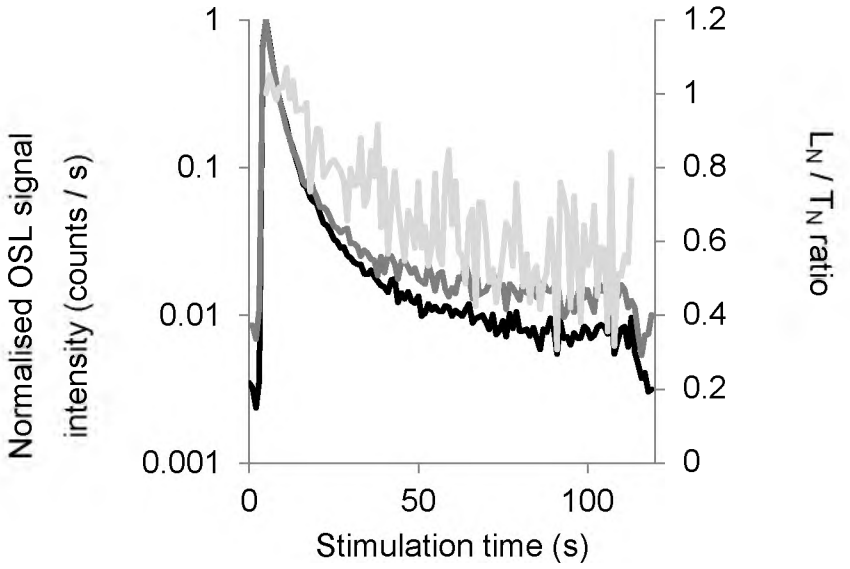

b)

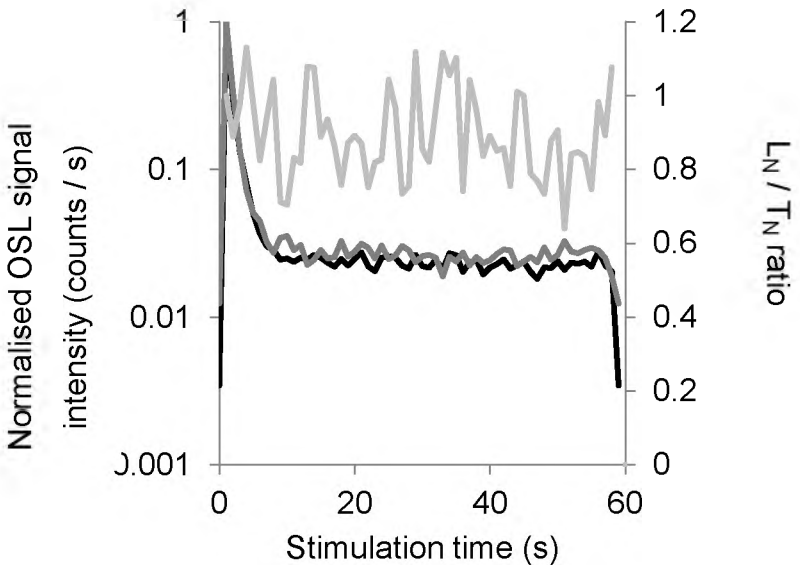

Figure 6.33. Normalised OSL decay curves for a) a small 4 grain aliquot, and b) single-grain of Al_2O_3:C. In both cases the L_X curve was measured after a 0.26 Gy beta irradiation (black line) and the T_X curve after a 0.13 Gy test dose irradiation (mid-grey line). These decay curves use the logarithmic left hand y-axis. The ratio (light grey line; right hand y-axis) of the two curves is also given.

Also shown in Figure 6.33, on the right hand axis, is the ratio (L_X/T_X) of the two normalised signals. In both cases, the L_X/T_X ratio displays a plateau region in the first 2 data channels (2 s) of OSL stimulation. Beyond this point, the L_X/T_X ratios become more variable as the OSL count achieve a stable background level. The L_X/T_X single-aliquot ratio appears to diverge with time, decreasing to a value of ~0.6. It should be noted that the L_X decay curve represents the OSL response for an irradiation double that of the T_X. It is considered that this divergence is due to the filling of a 'slow' component, with the signal build-up removed during the optical bleach between the L_X and T_X measurements. In contrast, the L_X/T_X single grain ratio remains relatively stable, presumably due to the greater power density of the laser in comparison to the blue LEDs.

6.4.4.4.6.2 Environmental irradiation

6.4.4.4.6.2.1 Single grain OSL decay curves

Single grain Al_2O_3:C OSL decay curves for the environmental dose absorbed during storage, and their associated test dose (0.13 Gy) OSL decay curves, are shown in Figure 6.29. The OSL response to the environmental dose is significantly smaller, by between 1 and 2 orders of magnitude, than the associated test dose OSL response. The background signal levels for the individual Al_2O_3:C grains stimulated using the green laser are rather high with average 'stable background' OSL counts in the vicinity of between 60 to 100 counts per second. As such, the signal-to-noise ratios for the individual Al_2O_3:C grains fall roughly between 0.85 and 3.02.

In an attempt to increase the signal-to-noise ratio for each measurement position, the L_N and T_N from an additional grain from the same grid location was measured. This could be achieved as a number of grains ($n<10$) were placed at the vertices of the 3×3 mm grid (as shown in Figure6.5). The L_N and T_N decay curves from the two grains were then summed, with the signal-to noise ratio values falling within a range of about 0.90 and 2.18. Histograms for the single-grain Al_2O_3:C signal-to-noise ratio distributions are shown in Figure 6.34. Only 2 points from SP5,

a)

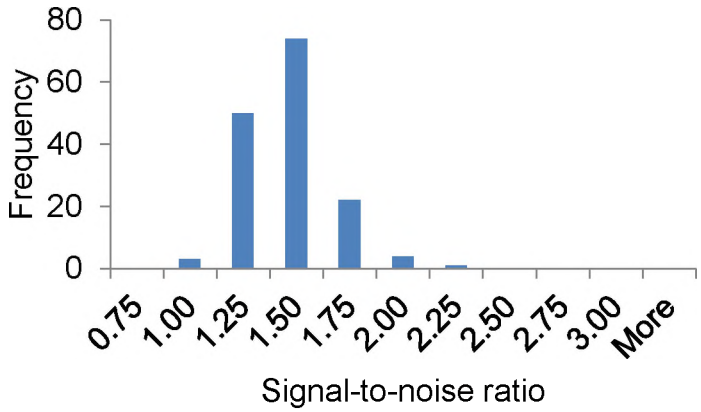

b)

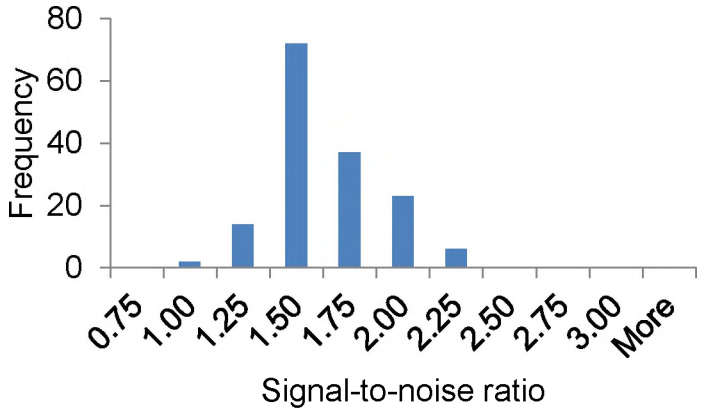

c)

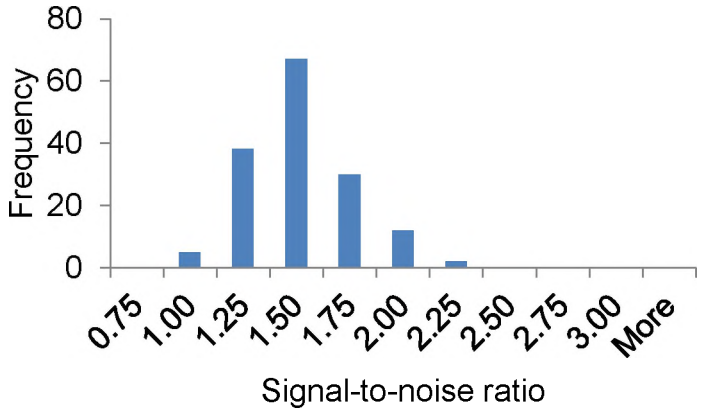

Figure 6.34. Histograms of the signal-to-noise ratios for the summed single grain Al_2O_3:C OSL decay curves for a) SP2, b) SP5 and c) Layer 8.

3 points from SP2 and 5 points from Layer 8 had signal-to-noise ratios of <1. Throughout the remainder of this investigation, therefore, the summed single-grain OSL decay curves were used. Although now constituting an aliquot, they will continue to be termed the 'single grain' data to avoid confusion with the small 4-grain aliquots.

Normalising both the summed L_N and T_N signals, as was done for the laboratory irradiated decay curves (Section 6.4.4.4.6.1), shows that, for the L_N, the OSL signal returns to background after about 2 s of optical stimulation (Figure 6.35a). In contrast, the T_N signals require up to 6 s to reach a steady background. The resulting L_N/T_N ratios, therefore, show a small stable region (with a ratio between 1 and 1.4) during the first 2 s of optical stimulation before significantly increasing (to between 20 and 30).

6.4.4.4.6.2.2 Small aliquot OSL decay curves

Small, 4-grain aliquots were used to try and improve the signal-to-noise ratios of the environmentally dosed Al_2O_3:C. Only the Pech IV samples were investigated in this manner. The use of small aliquots appears to have had the desired effect, with signal-to-noise ratios ranging between 0.96 and 15.5 – the distribution of signal-to-noise ratios for all the single aliquot measurements is given as histograms in Figure 6.36. Only the one measurement from Layer 5B had a signal-to-noise ratio of <1 – and was not used in further analysis. The initial OSL intensity of the aliquot with the 15.5 ratio was an order of magnitude brighter than any other aliquot measured.

a)

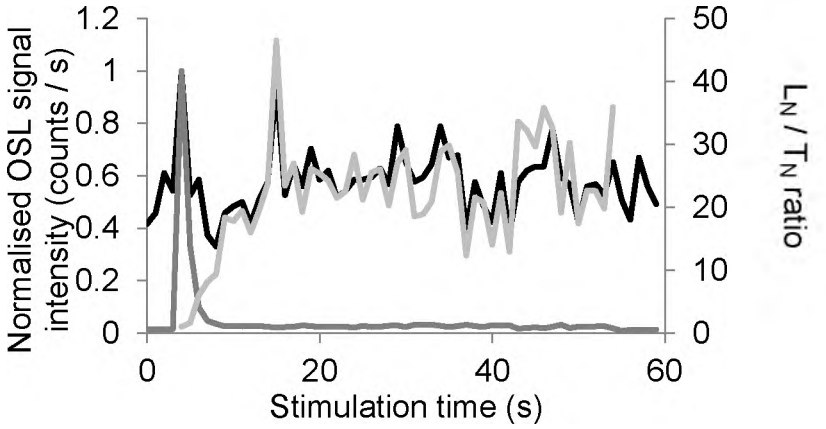

b)

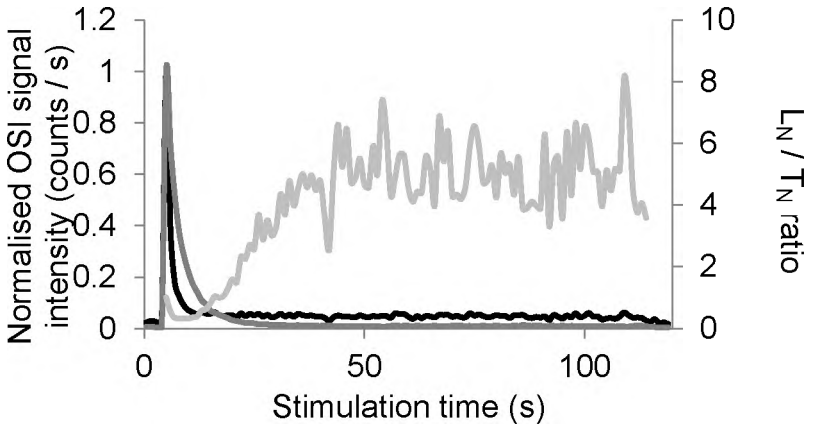

c)

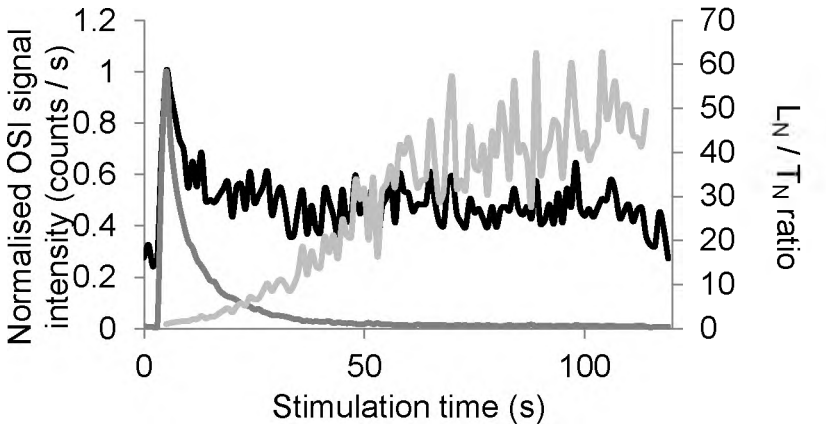

Figure 6.35. Normalised L_N and T_N OSL decay curves for a) summed single-grain, and b,c) small 4-grain aliquot of Al_2O_3:C for the environmental dose (black line) and laboratory test dose (mid-grey line). The OSL decay curves use the left hand y-axis. The ratio of the L_N and T_N decay curves is also given (light-grey) and is plotted against the right hand y-axis.

a)

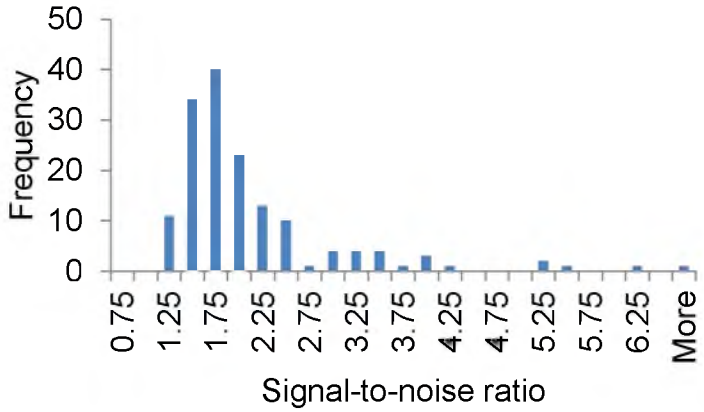

b)

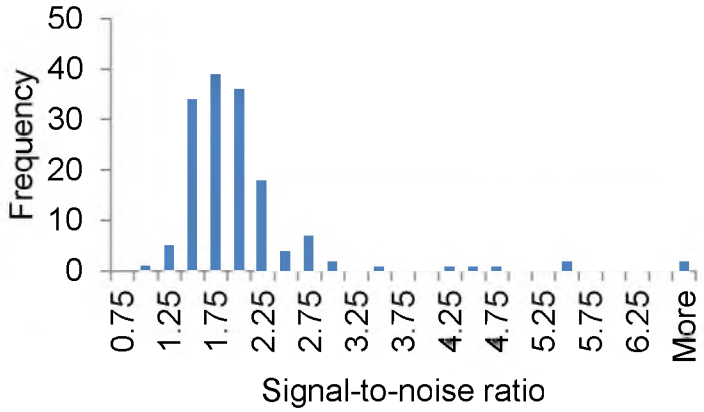

Figure 6.36. Histograms of the signal-to-noise ratios for the small, 4 grain aliquots of Al_2O_3:C for a) Layer 8 and b) Layer 5B.

For small aliquots that have signal-to-noise ratios of >4, a difference in the decay curve shape is observed between L_N and T_N. In general, the T_N curve appears to decay faster than the L_N (Figure 6.35b). Taking the ratio of the L_N and T_N counts at each channel reveals that for these aliquots, there is an initial decrease in this ratio to ~0.7 over the first 3 s of stimulation before increasing back up towards a steady background level. In contrast, those grains that have signal-to-noise ratios of <4 (Figure 6.35c) have L_N/T_N ratios that are similar to those of the single grain data (Figure 6.35a). A more stable region in the L_N/T_N ratio can be observed over the first 2 s of stimulation time before increasing towards a stable background level.

Investigation of the OSL decay curve shapes for those aliquots with large signal-to-noise ratios (typically >4) show a substantial difference between the L_N and T_N decay curve shapes. In general, the L_N decays at a faster rate than the T_N. Taking the ratio of the L_N and T_N curves (as is shown in Figure 6.35), a substantial decrease, to about 0.7, is observed over the first 3 s of optical stimulation before increasing back up towards a steady background level (Figure 6.35b). In contrast, those small aliquots that have signal-to-noise ratios <4 show a similar L_N and T_N decay curve shapes (and ratios) as the single-grain measurements (compare Figure 6.35a and c). The ratio between the L_N and T_N curves for these aliquots show a relatively stable region over the first 3 s of optical stimulation (similar to the single-grain counterpart) before increasing to a background level.

The underlying mechanism responsible for the disparity between the L_N and T_N OSL decay curves for some of the aliquots is unknown. Potentially, this disparity may be the result of an unsuitably large test dose being administered (Kalchgruber *et al.* 2003), or perhaps the laboratory irradiation of the Al_2O_3:C grains may be depositing charge into more slowly decaying electron traps than natural irradiation (Yukihara *et al.* 2003, Yukihara *et al.* 2004). The degree of variability within the OSL decay curves remains uncertain at the present, pending further investigation.

The differences between the L_N and T_N decay curves shapes can be circumvented, to some extent, by using a short signal integration period. In this study, the signal integration limits (for both the small aliquot and single grain data) was set to the first 2 data channels (the first 2 seconds of optical stimulation). This practice takes advantage of the short initial plateau region where the L_N and T_N decay curve shapes are most conformable. Thus, the effect of the non-conformable signal shapes would be minimised.

6.4.4.5 EQUIVALENT DOSE RESULTS AND CONVERSION TO BETA DOSE RATE

6.4.4.5.1 Conversion procedures

To obtain an estimate of β-D_r at a given measurement point required that the L_N/T_N ratio for the single grain or single aliquot first be converted into a D_e. This was carried out using the steps outlined in Table 6.21 that shows an example of single-grain data from SP5. The L_N and T_N signal and background counts (Step 1) were normalised to an equivalent channel width (Step 2) and the background count subtracted from their respective L_N and T_N signals (Step 3). The L_N/T_N ratio was then calculated (Step 4) and its associated error (Step 5) using equation 4 in Duller (2007).

Table 6.21. Steps taken to convert the L_N and T_N signals measured from the sum of two single-grain Al_2O_3:C OSL decay curves into β-D_r.

Step	Description	Calculation
1	Natural and test dose signal and background counts	L_N signal = 477 over 2 channels L_N background = 2061 over 15 channels T_N signal = 13714 over 2 channels T_N background = 4376 over 15 channels
2	Normalise the background to the same channel width as the signal	L_N signal = 477 L_N background = 275 T_N signal = 13714 T_N background = 583
3	Subtract the background counts from the signal	L_N = 202 T_N = 13131
4	Determine L_N over T_N ratio	L_N/T_N = 0.015

5	Propagate the counting statistics errors on the L_N and T_N ratios in quadrature using equation 4 in Duller (2007) $S_{\frac{L_N}{T_N}} = \frac{L_N}{T_N}\sqrt{\left[\frac{L_{Signal}+L_{BG}}{\left(L_{Signal}-L_{BG}\right)^2}\right]+\left[\frac{T_{Signal}+L_{BG}}{\left(T_{Signal}-L_{BG}\right)^2}\right]}$	L_N/T_N error = 0.002
6	Sensitivity corrected Al_2O_3:C luminescence signal for the given pair of grains	L_N/T_N = 0.015 ± 0.002
7	Determine the standardised luminescence signal by multiplying the L_N/T_N by the test dose (T_D = 0.128 Gy) and proportionally adjust the associated error	$(L_N/T_N)\times T_D$ = 0.0020 ± 0.0003
8	Using the SGC in Figure 6.31a (y = 1.04x), determine the D_e of the given pair of grains and proportionally adjust the associated error	D_e = 1.04/0.0020 D_e = 0.0019 ± 0.0003
9	Convert D_e into total environmental dose rate in Gy/ka by dividing by storage time (here 233 days) multiply by 365 days and 1000 years. Proportionally adjust associated error	Total environmental dose rate (Gy/ka) = 0.0019/233 × 365 × 1000 = 2.95 ± 0.40 Gy/ka
10	Subtract the gamma+cosmic dose rate (0.82 ± 0.03 Gy/ka) component from the total environmental dose rate to obtain β-D_r (Gy/ka) Proportionally adjust the associated error.	β-D_r (Gy/ka) = 2.95 – 0.82 = 2.13 ± 0.29 Gy/ka

11	Adjust the β-D_r to account for resin-saturated pore space using equation 4.6 in Aitken (1985) to determine a 'dry' β-D_r. A resin-saturated content of 30% was used to determine a weighting factor of 0.727. The errors were proportionally adjusted.	Dry β-D_r (Gy/ka) = 2.13 × 0.727 = 2.93 ± 0.40 Gy/ka
12	Using the field measured water content (5 ±1%; weighting coefficient of 0.941) and an average beta attenuation coefficient of 0.857 (Brennan 2003), the 'dry' β-D_r were then adjusted to represent wet and attenuated β-D_r being delivered to 180–212 µm quartz grains used in D_e determination. The associated errors were proportionally adjusted.	Wet and attenuated β-D_r (Gy/ka) = 2.93 × 0.941 ×0.863 = 2.38 ± 0.32 Gy/ka

---

This series of steps gives the sensitivity-corrected OSL signal (L_N/T_N) and its associated error (Step 6).

The L_N/T_N signal then needs to be converted to D_e using the SGC. The L_N/T_N signal is multiplied by its respective test dose (Step 7) to give the standardised L_N/T_N signal. The standardised L_N/T_N signal is then substituted into the appropriate SGC equation (for the y variable) and solved for x (Step 8) to give the D_e for the specific grain or aliquot.

The D_e must then be converted into a dose rate. This is achieved by dividing the D_e by the period of storage (to give Gy/day), before multiplying by 365000 (to give Gy/ka) (Step 9). The error here is proportionally adjusted. This dose rate estimate represents the sum of the alpha, beta, gamma and cosmic radiation experienced throughout the storage period. As only the β-D_r is of interest, the alpha, gamma and cosmic contributions were needed to be removed. No allowance was

made for the alpha contribution because the α-value of Al_2O_3:C is <0.01 and, therefore, can be disregarded (Nathan *et al.* 2003). The summed gamma and cosmic dose rate was estimated to be 0.82 ± 0.03 Gy/ka and was subtracted from the total environmental dose rate (Step 10) to give just the β-D_r (Gy/ka) contribution.

The β-D_r estimated in Step 10 represents that delivered to the Al_2O_3:C grains in a resin-saturated sediment matrix, and was needed to be accounted for. The density of the resin that filled the void space had a similar density to water (~1.09 g/cm^3). To correct for the resin-filled void space required that the maximum moisture saturation content be determined for each sample studied. This was done empirically with maximum water saturation values of 17% (SP2), 30% (SP5), 6.9% (Layer 8) and 6.6% (Layer 5B).

The 'resin-saturated' β-D_r was then adjusted to account for the proportion of radioactivity absorbed by the resin by multiplying this value by the associated moisture content weighting factor calculated using equation 4.6 in Aitken (1985) (Step 11). This procedure provided a 'dry' β-D_r (Gy/ka). For this value to be meaningful, in terms of being used in comparison with the quartz D_e distributions, required that these β-D_r values first be adjusted to the determined field moisture content for each of the respective samples (Step 12) using equation 4.6 of Aitken (1985). The moisture contents of 13 ± 2% (SP2), 5 ± 1% (SP5), 6.9 ± 1.7% (Layer 8) and 6.6 ± 1.7% (Layer 5B) were used. Finally, the 'wet' β-D_r values were multiplied by the average 200 μm grain beta attenuation factor (0.863) using the values presented in Brennan (2003). This final step provided a β-D_r (Gy/ka) value for the given grain/aliquot that was both 'wet' and 'attenuated.'

All random errors were propagated through systematically, but no systematic errors were included since these are consistent among all measurements and grains in this study. This means that the distributions of β-D_r between samples can be compared but not with other methods of β-D_r determination. To compare the Al_2O_3:C β-D_r values to the reported β-D_r (e.g., pXRF, image analysis or GMBC) requires that the systematic errors be added. A 5.4% systematic uncertainty was added in quadrature to each individual β-D_r value. This 5.4% was calculated by

summing in quadrature the errors associated with the beta dose irradiation (2%), cosmic and gamma dose rate (4%) and beta attenuation uncertainty (3%).

6.4.4.5.2 Beta dose rate distributions

The above procedure was carried out for each of the single grain and small aliquot measurement position. A number measurement positions (for both single-grain and small aliquot measurements) had β-D_r values that were <0 Gy/ka. It should be noted that these grains/aliquots that had β-D_r values of <0 Gy/ka showed a substantial luminescence response from the laboratory beta irradiation but a much smaller response for the natural irradiation. It is only once the gamma and cosmic contribution to the total dose rate is subtracted (to obtain the β-D_r) that these values are less than 0 Gy/ka. For the single-grain data series, the proportion of <0 Gy/ka values were calculated to be 46% for SP2 (41 measurement positions), 3% for SP5 (4 measurement positions); and 45% for Layer 8 (69 measurement positions). The small aliquot series was also found to have a number of points with β-D_r less than 0 Gy/ka. For Layer 8, 30 measurement positions (19%) had a β-D_r <0 Gy/ka, whereas only 17 measurement points (11%) were less than 0 Gy/ka for Layer 5B.

The distribution of β-D_r values that are >0 Gy/ka are shown for each sample for the single-grain β-D_r as radial plots in Figure 6.37. The distribution of β-D_r values for sample SP2 ranges from 0 to 1.57 ± 0.43 Gy/ka (Figure 6.37b); for SP5 from 0 to 3.23 ± 0.80 Gy/ka (Figure 6.37d); and for Layer 8 from 0 to 1.42 ± 0.33 Gy/ka (Figure 6.37f). In each instance, the associated total uncertainty term is dominated by the random uncertainty that arises from the luminescence counting statistics. In each of these cases, the β-D_r distribution show similar patterns as their D_e value counterparts, although the spread in the β-D_r distributions is significantly greater.

The weighted mean Al_2O_3:C β-D_r were calculated to be 0.20 ± 0.02 (SP2), 1.06 ± 0.05 (SP5) and 0.14 ± 0.02 Gy/ka (Layer 8) using only those β-D_r values that are >0 Gy/ka. Arithmetic means of 0.17 (SP2), 1.15 (SP5) and 0.13 (Layer 8) were also calculated including those measurement positions that were calculated to be <0

Gy/ka, and are consistent with their respective weighted mean β-D_r values. For the MacCauley's Beach samples, these weighted mean values are consistent with those reported for these two samples in Table 6.22 of 0.31 ± 0.03 (SP2) and 0.92 ± 0.07 Gy/ka (SP5). The Layer 8 sample from Pech IV, in comparison, is significantly less than that reported, having a weighted mean Al_2O_3:C β-D_r of 0.14 ± 0.02 Gy/ka and a reported β-D_r of 0.29 ± 0.03 Gy/ka in Table 6.22.

The small aliquot distributions of β-D_r are shown as radial plots in Figure 6.38. The distributions in these figures have a much greater range than those of the single-grain counterparts, regardless of the sample investigated. The β-D_r values for Layer 8 range between 0 and 21.25 ± 1.96 Gy/ka (Figure 6.38b) and Layer 5B between 0 and 15.78 ± 1.57 Gy/ka (Figure 6.38d). Weighted mean β-D_r values of 0.59 ± 0.08 (Layer 8) and 0.44 ± 0.05 Gy/ka (Layer 5B) were calculated from the small aliquot β-D_r values of >0 Gy/ka, i.e., those aliquots with a β-D_r value of <0 were not included in this calculation. The weighted mean for the Layer 5B sample is consistent with that of the GMBC-determined β-D_r (0.46 ± 0.03 Gy/ka), whereas the Layer 8 sample is significantly higher than that of the GMBC β-D_r of 0.29 ± 0.03 Gy/ka.

a)

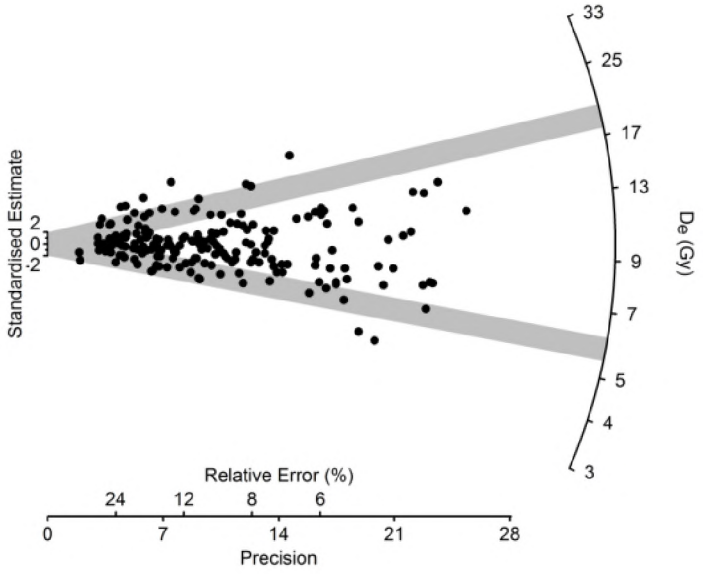

d)

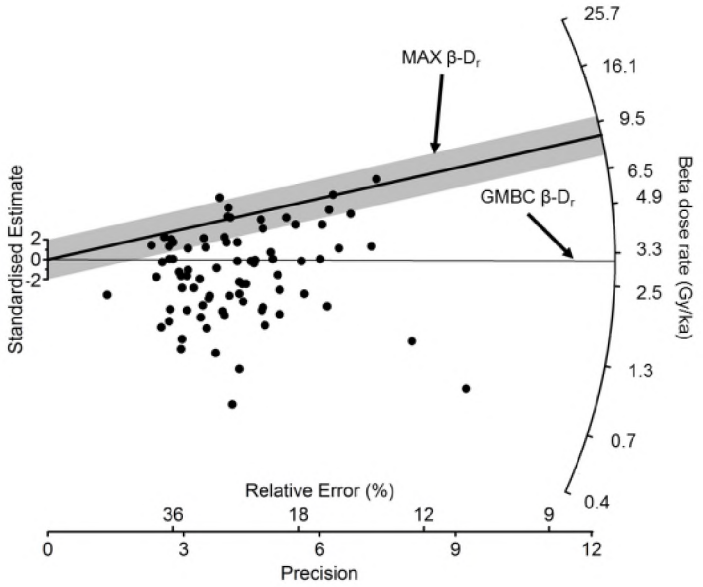

Figure 6.37 (part A). Single-grain quartz OSL D_e and single-grain Al_2O_3:C-determined β-D_r values. The D_e distributions for quartz single grains of a) SP2 is displayed with the MAM and MAX D_e value (indicated by the grey bands) and b) the single-grain Al_2O_3:C-determined β-D_r values for the same sample. The β-D_r distribution is centred on the GMBC-determined β-D_r which is indicated by the thin black line. Only the MAX β-D_r value is indicated by the thicker black lines and grey bands.

c)

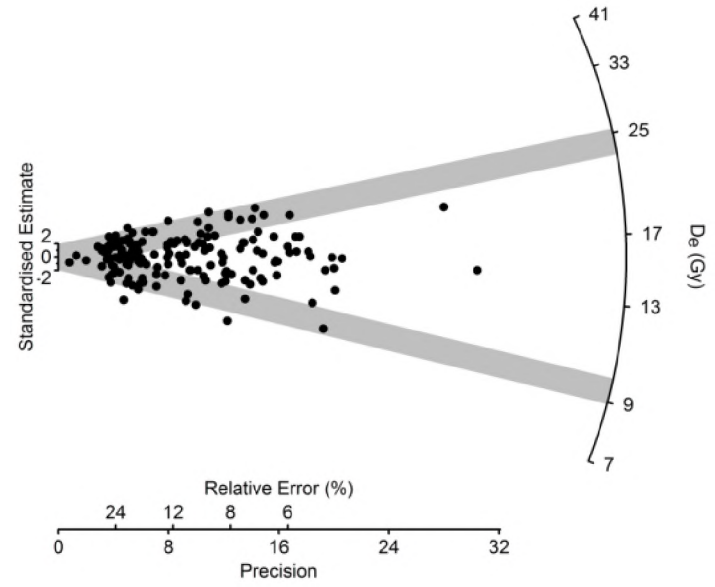

d)

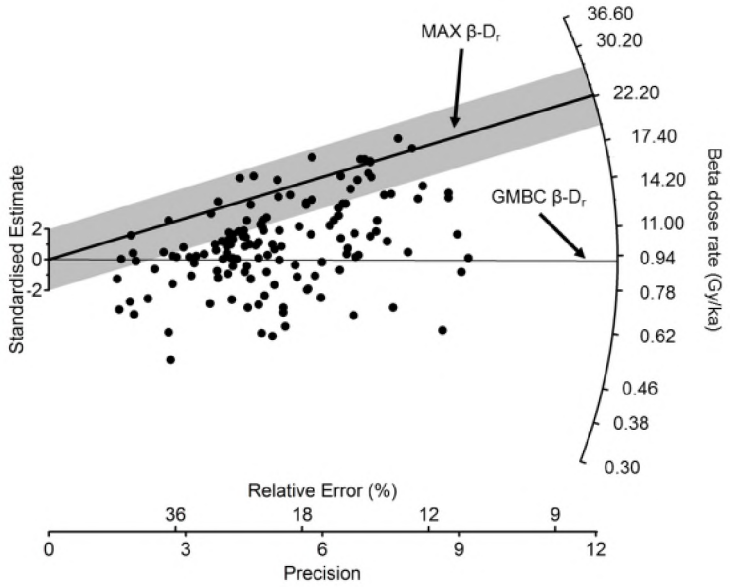

Figure 6.37 (part B). Single-grain quartz OSL D_e and single-grain Al_2O_3:C-determined β-D_r values. The D_e distributions for quartz single grains of c) SP5 is displayed with the MAM and MAX D_e value (indicated by the grey bands) and d) the single-grain Al_2O_3:C-determined β-D_r values for the same sample. The β-D_r distribution is centred on the GMBC-determined β-D_r which is indicated by the thin black line. Only the MAX β-D_r value is indicated by the thicker black lines and grey bands.

e)

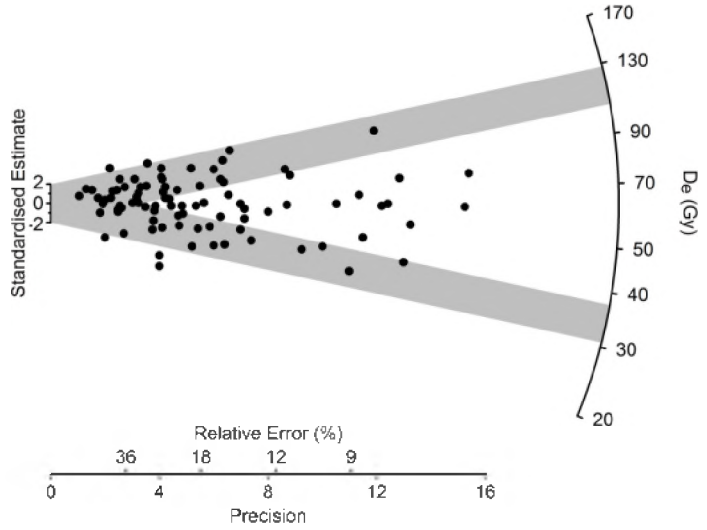

f)

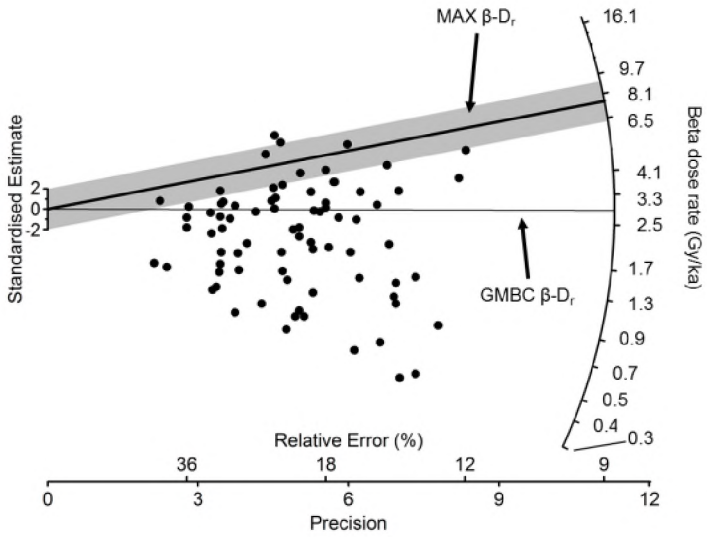

Figure 6.37 (part C). Single-grain quartz OSL D_e and single-grain Al_2O_3:C-determined β-D_r values. The D_e distributions for quartz single grains of e) Layer 8 is displayed with the MAM and MAX D_e value (indicated by the grey bands) and f) the single-grain Al_2O_3:C-determined β-D_r values for the same sample. The β-D_r distribution is centred on the GMBC-determined β-D_r which is indicated by the thin black line. Only the MAX β-D_r value is indicated by the thicker black lines and grey bands.

a)

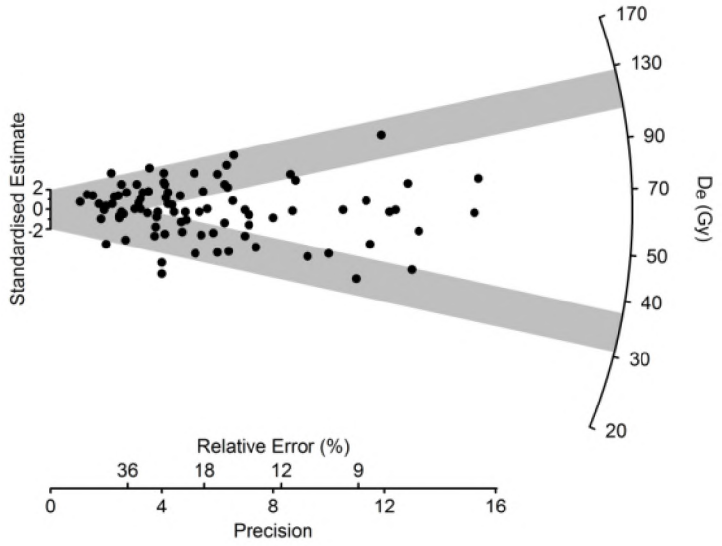

b)

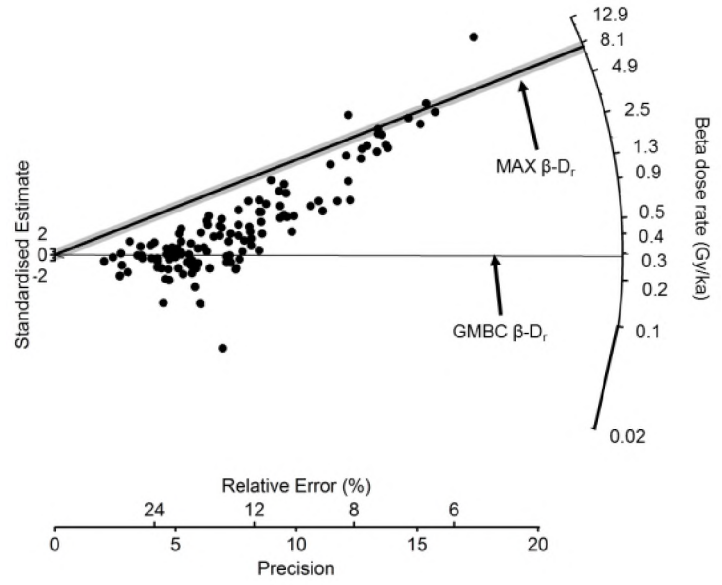

Figure 6.38 (part A). Single-grain quartz OSL D_e (a) and small aliquot Al_2O_3:C- determined β-D_r values (b) for Layer 8. The MAM and MAX D_e value are indicated by the grey bands for each sample. The small aliquot Al_2O_3:C-determined β-D_r values is centred on the GMBC-determined β-D_r which is indicated by the thin black line. Only the MAX β-D_r value is indicated by the thicker black lines and grey band.

c)

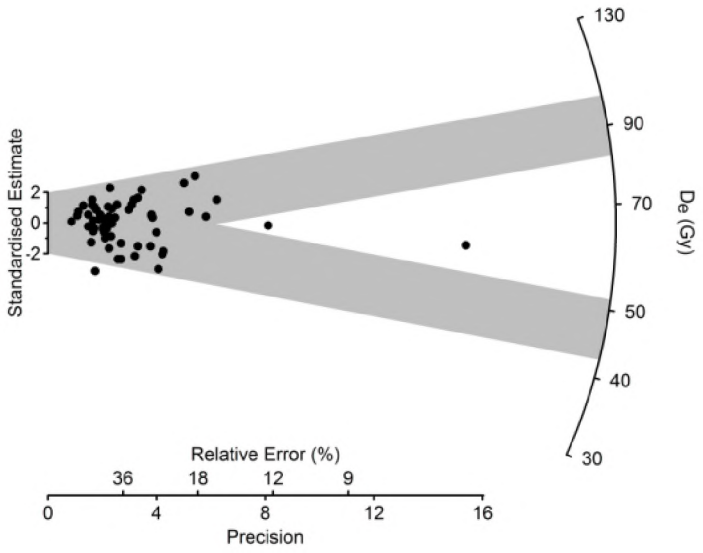

d)

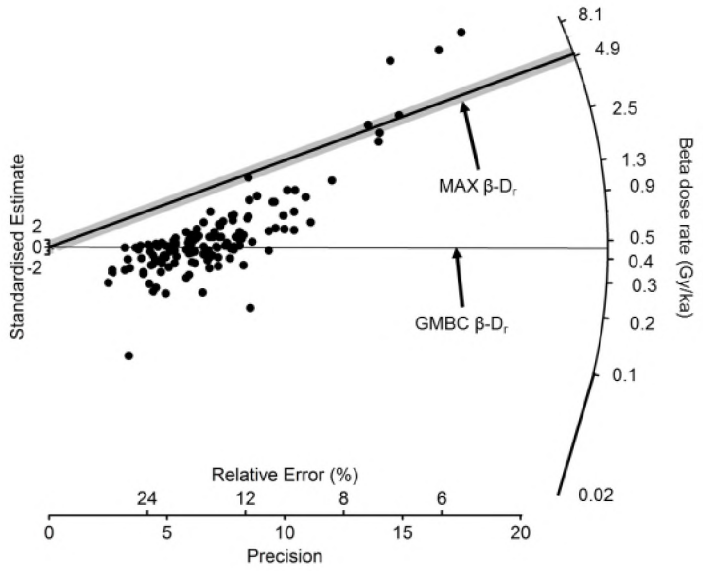

Figure 6.38 (part B). Single-grain quartz OSL D_e (c) and small aliquot Al_2O_3:C- determined β-D_r values (d) for Layer 5B. The MAM and MAX D_e value are indicated by the grey bands for each sample. The small aliquot Al_2O_3:C-determined β-D_r values is centred on the GMBC-determined β-D_r which is indicated by the thin black line. Only the MAX β-D_r value is indicated by the thicker black lines and grey band.

6.4.4.5.3 Aluminium oxide beta dose-rate map

The distribution of β-D_r values were spatially resolved to produce a β-D_r map. Unlike the pXRF (Figures 6.11 and 6.12) or image analysis maps (Figure 6.22 and 6.23), the Al_2O_3:C maps do not represent an average of the 6 mm diameter sphere, but rather measure the β-D_r delivered to the grains at this point (Figure 6.4). It should be noted, therefore, that this is not a 1:1 comparison and some differences are expected to be present.

6.4.4.5.3.1 Single-grain β-D_r distribution maps

The single-grain Al_2O_3:C β-D_r maps are shown in Figure 6.39 for SP2, SP5 and Layer 8. In each case the distribution of β-D_r 'hotspots' appears to be heterogeneous and SP5 having (on average) a higher β-D_r than either of the other samples (Figure 6.39). The single-grain Al_2O_3:C maps are also presented in Figure 6.40 using different scales to elucidate the variability in β-D_r values within each sample. For SP2 and Layer 8, the majority of points have β-D_r values <1 Gy/ka (shown as purple; Figures 6.40a and c) with comparatively few points were the β-D_r is greater than 1 Gy/ka (shown as yellow to red). In contrast, the SP5 sample has a significantly higher proportion of measurement positions where the β-D_r is >1 Gy/ka (shown as blue, green, yellow and orange; Figure 6.40b).

The punctuated nature of the β-D_r 'hotspots' suggests that the source of the beta dose is, firstly, non-uniform, and secondly, smaller than the 6 mm diameter sphere of influence. For the MacCauley's Beach samples, given the more uniform distribution of silts and clays at this 6 mm field of investigation, the random distribution of heavy mineral species is the most probable source for the β-D_r 'hotspots.' The Pech IV Layer 8 sample is much more complex. From thin section analyses, the regions having higher β-D_r values appear to be associated with the matrix, rather than large bone or flint fragments. Given the relatively homogeneous distribution of silts and clays and the paucity of K-feldspars, these β-D_r 'hotspots' are

considered to be attributable to either small bone fragments with high U and Th concentrations, or mica flakes that contain K.

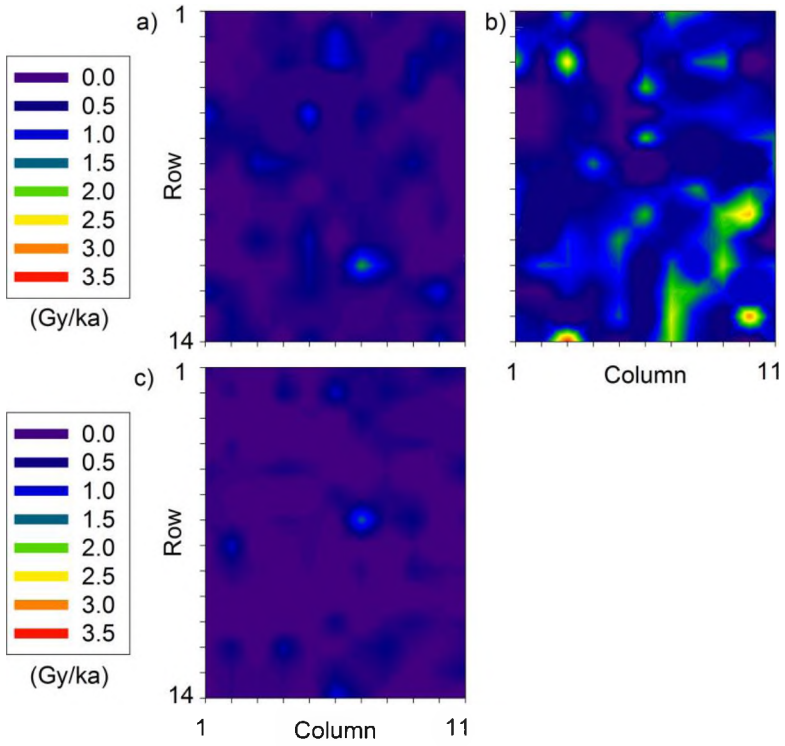

Figure 6.39. Summed single-grain Al_2O_3:C β-D_r distribution maps for a) SP2, b) SP5 and c) Layer 8. In each example the same β-D_r scale (0–1 Gy/ka) has been used to facilitate comparison between samples.

6.4.4.5.3.2 Small aliquot β-D_r distribution maps

The β-D_r distribution maps for the small aliquots from Layer 8 and Layer 5B are shown in Figure 6.41a and b. In both cases, the β-D_r maps are dominated by one individual point that is significantly larger than the remaining measurements. To better interpret the β-D_r maps, therefore, these points were removed. The revised β-D_r distribution maps are shown in Figure 6.41c and d. In a similar way as the single-grain Al_2O_3:C β-D_r maps, the small aliquot counterparts show a relatively uniform

distribution of β-D_r values between 0 and 2 Gy/ka (shown as purple and dark blue) that is then intermittently punctuated with regions of higher β-D_r (shown as mid blue, green and yellow).

A comparison of the relative positions of the β-D_r 'hotspots' in Layer 8 for the single-grain (Figure 6.40c) and small aliquot (Figure 6.41c) data shows a similar distribution pattern. Again, the 'hotspot' regions appear to align with the matrix rather than discrete large bone fragments. However, the magnitude of the β-D_r values is significantly different, with the β-D_r 'hotspots' of the small aliquots attaining about 6 Gy/ka (Figure 6.41c) (and higher, up to ~21 Gy/ka; Figure 6.41a) in comparison to the roughly 1.5 Gy/ka for the single-grain distribution (Figure 6.40c). This discrepancy can be drawn back to the difference in the L_N and T_N OSL decay curves and the reasons outlined in Section 6.1.4.4.6.2. However, as explained, the underlying cause of this phenomenon is currently uncertain. In this light, the β-D_r maps constructed using small aliquots should be viewed as qualitative until further examination is conducted.

The Layer 5B distribution is now considered in terms of the qualitative insights it can provide in terms of β-D_r distribution. The β-D_r map for the Layer 5B sample (Figures 6.41b and d) shows a similar punctuated distribution. A comparison of these 'hotspot' positions with the respective thin sections (Figure 6.5) reveals that these hotspots are found in both the matrix and in limestone pebble inclusions. The presence of these discrete regions of higher-than-average β-D_r values are considered to be attributable to K-bearing mica flakes which can be found both within the limestone pebbles and matrix. This proposition fits well with the disturbed sediment samples for this sample where the β-D_r for the FSC and limestone components is dominated by K.

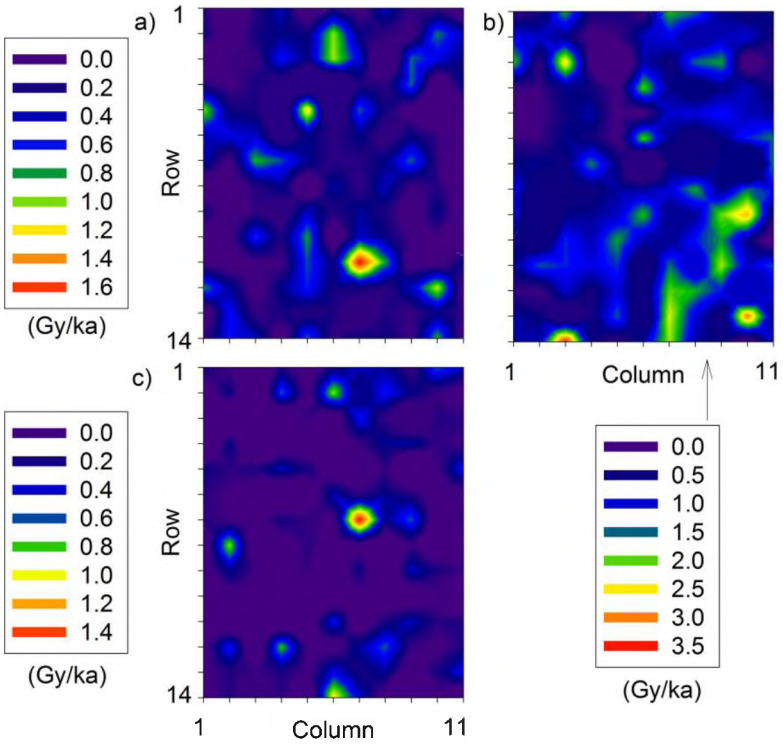

Figure 6.40. Summed single-grain Al_2O_3:C β-D_r distribution maps for a) SP2, b) SP5 and c) Layer 8 using individual scales to display the range of concentrations *within* a sample.

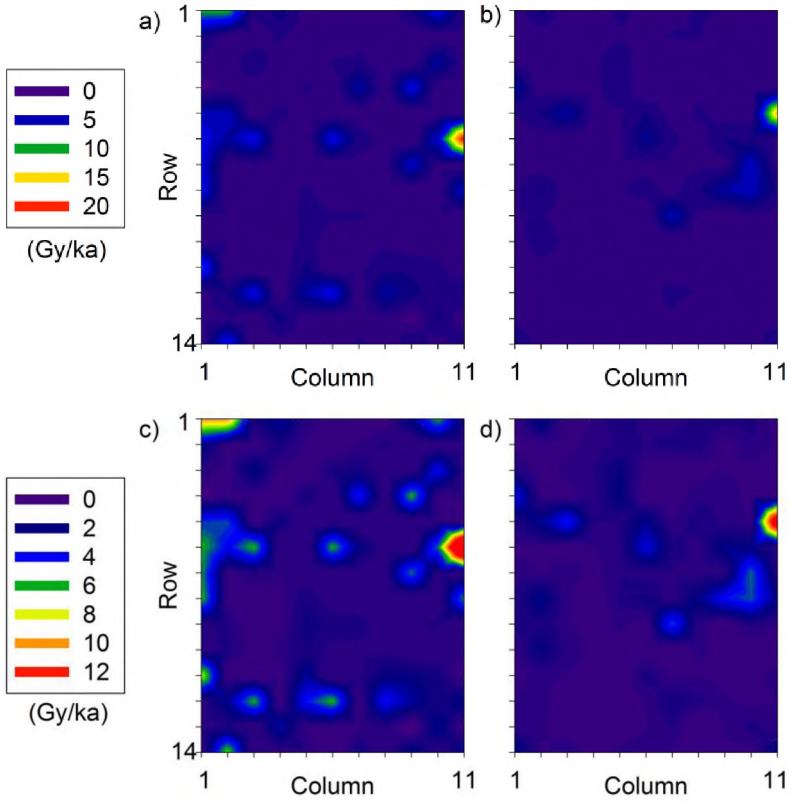

Figure 6.41. Small 4 grain aliquots of Al_2O_3:C β-D_r distribution maps for a) Layer 8, b) Layer 5B showing the complete distribution of β-D_r. Also shown are the same distributions for Layer 8 (c) and Layer 5B (d) removing the highest β-D_r to show the distribution pattern with greater resolution.

6.4.4.6 Relationship between equivalent dose distribution and aluminium oxide beta dose rate

As was done for the pXRF and image analysis β-D_r data, the D_e distributions of the four samples are now addressed using the modelled β-D_r determined using the Al_2O_3:C method. The minimum β-D_r in each case was set to 0 Gy/ka for each sample as estimate that were less that (but consistent with) 0 Gy/ka were achieved in every experiment. The maximum β-D_r value was determined using the MAX age model. The results of this examination are presented in Table 6.22.

Table 6.22. OSL age estimates for the four samples investigated using the summed single-grain (SG) and small aliquot (SA) Al_2O_3:C-determined β-D_r values.

Sample	Method	Age model[1]	D_e (Gy)	Total environmental dose rate (Gy/ka)[3]	β-D_r (Gy/ka)	Age (ka)
SP2	GMBC	CAM	9.84 ± 0.30	0.99 ± 0.06	0.31 ± 0.03	9.99 ± 0.71
(SG)	Al_2O_3:C	MAM	5.82 ± 0.28	0.64 ± 0.04	0.00 ± 0.00	8.66 ± 0.66
	Al_2O_3:C	MAX	18.75 ± 0.95	1.53 ± 0.15	0.86 ± 0.12	12.26 ± 1.37
SP5	GMBC	CAM	15.62 ± 0.46	2.37 ± 0.13	0.92 ± 0.07	6.60 ± 0.42
(SG)	Al_2O_3:C	MAM	9.38 ± 0.57	1.44 ± 0.07	0.00 ± 0.00	6.49 ± 0.51
	Al_2O_3:C	MAX	24.13 ± 2.34	3.68 ± 0.21	2.24 ± 0.15	6.55 ± 0.75
Layer 8	GMBC	CAM	63 ± 4	0.69 ± 0.05	0.29 ± 0.03	92 ± 9
(SG)	Al_2O_3:C	MAM	34 ± 3	0.40 ± 0.03	0.00 ± 0.00	85 ± 10
	Al_2O_3:C	MAX	115 ± 12	1.15 ± 0.12	0.75 ± 0.10	100 ± 15
Layer 8	GMBC	CAM	63 ± 4	0.69 ± 0.05	0.29 ± 0.03	92 ± 9
(SA)	Al_2O_3:C	MAM	34 ± 3	0.40 ± 0.03	0.00 ± 0.00	85 ± 10
	Al_2O_3:C	MAX	115 ± 12	8.40 ± 0.34	7.81 ± 0.33	14 ± 2
Layer 5B	GMBC	CAM	66 ± 4	0.97 ± 0.05	0.46 ± 0.03	69 ± 6
(SA)	Al_2O_3:C	MAM	47 ± 11	0.50 ± 0.03	0.00 ± 0.00	94 ± 23
	Al_2O_3:C	MAX	90 ± 15	5.52 ± 0.22	5.02 ± 0.18	16 ± 3

In each of the three samples examined using the single-grain Al_2O_3:C-determined β-D_r, both the MAM and the MAX ages were consistent with that of the reported CAM age (Table 6.22). For SP2, the MAM and MAX ages of 8.66 ± 0.66 and 12.26 ± 1.37 ka, respectively, were consistent with the 9.99 ± 0.71 ka reported (Table 6.22) CAM age at 2σ. The MAM and MAX ages of 6.49 ± 0.51 and 6.55 ± 0.75 ka, respectively, for SP5 were both consistent at 1σ with the reported CAM age (Table 6.22) of 6.60 ± 0.42 ka. The Layer 8 sample from Pech IV was also shown to have MAM (85 ± 10 ka) and MAX (100 ± 15 ka) ages consistent with that of the reported CAM age (92 ± 9 ka; Table 6.22), at 1σ.

The small aliquot Al_2O_3:C results for Layer 8 and 5B are also presented in Table 6.22. Here, only the MAM ages (using a β-D_r of 0 Gy/ka) for these samples are consistent with the CAM ages reported in Table 6.22. In contrast, the MAX ages are significantly smaller than the CAM ages. Layer 8 MAX age was calculated to be 14 ± 2 ka almost seven times less than the CAM age (92 ± 9 ka) presented in Table

6.22. The Layer 5B MAX age of 16 ± 3 ka is also significantly less than the CAM age (69 ± 6 ka; Table 6.22) for this sample.

6.5 DISCUSSION

The occurrence of BM in single-grain OSL dating studies is often inferred rather than empirically shown. For BM to be ascribed to a certain D_e distribution requires; 1) that there is variability in the β-Dr present in the sample being analysed and 2) that the distribution of β-Dr 'hotspots' be spatially heterogeneous. These requirements are now to be discussed in relation to the four samples analysed in this present study.

6.5.1 BETA DOSE RATE VARIABILITY

The existence of β-D_r variability is imperative if BM is going to be cited as affecting D_e distributions. For the four samples investigated in this study, variability between the samples, and their components, is recognised. The range of the β-D_r values determined for both SP2 and SP5 is greater than two orders of magnitude; ~0.06 to ~16 Gy/ka for SP2, and ~0.07 to ~38 Gy/ka for SP5 using the 'combined' β-D_r values in Tables 6.3 and 6.4. In both samples from MacCauley's Beach, the lowest β-D_r was measured from the CS quartz component, while the highest was recorded for the FS heavy mineral component. It is also interesting to note, that where a complement of a FS and CS fraction were measured (i.e., quartz, feldspar and heavy mineral components) the β-D_r of the FS was consistently higher than the CS fraction.

The range of β-D_r measured using the GMBC for the Pech IV (Table 6.5) samples is not as large, with the range of Layer 8 moving between 0.18 ± 0.04 (FG) and 0.53 ± 0.03 Gy/ka (FSC). Although significantly higher, the range of β-D_r values for Layer 5B show a similar three-fold increase moving from 0.37 ± 0.02 Gy/ka for the FG fraction to 1.12 ± 0.04 Gy/ka for the FSC fraction. Presumably, these ranges

could be extended if further mineralogical fractionation was carried out on the Pech IV samples as was done for the MacCauley's Beach samples. In this study, it has been shown that there is significant variability in the β-D_r values present, both within and between samples, regardless of being fractionated according to grain size and mineralogical components, or grain size alone (Tables 6.3, 6.4 and 6.5).

^{40}K found in individual K-feldspar grains is considered by the literature to be the most important radionuclide with regards to the occurrence of BM (Mayya *et al.* 2006, Cunningham *et al.* 2012, Guérin *et al.* 2012b). This scenario for BM does not appear to be the case for the MacCauley's Beach samples presented in this investigation. From the ternary diagram presented in Figure 6.3, it is only the feldspar fractions of both SP2 and SP5, and the silt and clay fraction in SP5 alone, that have a β-D_r values dominated (>50%) by K. Yet, the β-D_r for these components are all more than one order of magnitude less than that of the FS heavy mineral component (Tables 6.3 and 6.4). The FS heavy mineral component of SP5 is dominated by U (~62%), and also for SP2 (~52%).

With respect to the Pech IV sample, there is certainly a dominance (>60%) of ^{40}K in the β-D_r values measured in both samples (Figure 6.3c). It is clear that the K does not come from the burnt and unburnt bone or the flint fragments found throughout the sediment (Figure 6.3c) but most likely from the clays. Soil micromorphological analysis revealed a paucity of K-feldspars in the sedimentary matrix of these sediments. In the CS fraction, the presence of limestone roof spall which contains K-bearing mica flakes could be responsible for the ^{40}K contribution (Figure 6.3c), whereas the increased clay content in the FSC fraction, as well as the same mica component could account for the ^{40}K contribution.

The importance of ^{40}K to the total β-D_r, and hence the occurrence of BM, is shown to be highly variable for each sample. To hold fast to the notion that ^{40}K, and only ^{40}K, is responsible for BM in sediments is strongly ill-advised by these data. BM ought to be assessed on a per sample basis.

6.5.2 SPATIAL DISTRIBUTION MAPS OF U, TH, K AND BETA DOSE RATE

The empirical investigations carried out in this study reveal that the beta dosimetric environments in all four samples show some degree of variability. The β-D_r distributions presented in Figures 6.10, 6.16 and 6.29, give similar, although not equivalent, β-D_r distribution patterns. It needs to be remembered that the three methods used in this study have been measuring the β-D_r at different scales. The image analysis modelling method (Figures 6.22 and 6.23) is based on a two-dimensional slice through three-dimensional sediment and average elemental concentrations of constituent sediment fractions within a 6 mm diameter sphere. The pXRF (Figures 6.11 and 6.12), although also providing surficial information, is able to probe slightly deeper than the standard 32 μm thickness of the thin sections. However, it too is a two dimensional representation of a three dimensional sediment and still only provides average elemental concentrations within a 6 mm sphere. Perhaps the most realistic of the β-D_r mapping experiments carried out in this study is that of the Al_2O_3:C investigations (Figure 6.39, 6.40 and 6.41). Unlike the other two methods, this technique measures the β-D_r delivered to individual grains from the three dimensional geometry surrounding the grains. This is not to say that the image analysis and pXRF β-D_r maps are redundant or uninformative, as these still provide information about β-D_r distributions using relatively simplistic analytical tools.

The spatial distribution of U, Th and K is an important factor to consider as this dictates the positioning of β-D_r 'hotspots'. The use of the pXRF in this study has enabled the mapping of U and Th, along with K, across the resin-impregnated sediment slabs (Figures 6.7 to 6.12). However, the detection limit of the pXRF plays a critical role in the mapping of these elements. A significant number of points in both samples had no detectable U or Th, and were set to 2 ± 1 μg/g. Image analysis modelling was carried out with an aim to obtain a more complete distribution of β-D_r values, particularly at the bottom range of the distribution.

In all four samples, the pXRF and image analysis modelling gave distributions of U and Th that are heterogeneous (Figures 6.10, 6.12, 6.21 and 6.23). At MacCauley's Beach, this inhomogeneity in U and Th suggests that, rather than being present within the fine-grained matrix, these elements are housed within individual heavy mineral grains. In Chapter 3 it has been shown using thin sections that the presence of heavy mineral grains, such as rutile and zircons, occur heterogeneously throughout these samples. Conversely, the distribution of K is more homogeneous (Figure 6.8 and 6.19), providing evidence that K is associated with the more homogeneously dispersed silt and clay fractions. That is not to say that coarser K-bearing minerals are not present as a number of K 'hotspots' can be discerned and are attributed to feldspar-bearing lithic fragments and K-feldspars. However, a comparison of the elemental maps with their corresponding β-D_r maps (Figure 6.13 and 6.24) reveals that for SP2 and SP5 the importance of K in producing regions of significantly greater β-D_r is negligible with U being most influential.

The Pech IV samples, in contrast, show a much greater importance of K in relation to U and Th. For both the Layer 8 and Layer 5B samples, K dominates in the sedimentary matrix (Figures 6.8 and 6.19) where it is relatively uniformly distributed and associated with clay material. This uniform distribution is interrupted by the presence of bone fragments, flint and limestone pebbles (in the case of Layer 5B). In the case of Layer 8, these regions of bone can be associated with regions of greater U concentrations (Figure 6.21c), whereas the flint fragments are relatively poor in U, Th and K. The corresponding β-D_r maps (Figures 6.13 and 6.24), show higher β-D_r across the matrix compared to areas of discrete bone and flint nodules. The same pattern holds for Layer 5B with respect to the bone and limestone pebbles, both having low concentrations of U, Th and K, resulting in regions of lower β-D_r. However, as was the case with the MacCauley's Beach samples, the importance of K-feldspars does not appear to be a driving process for the distribution of K throughout the sediments, with the clay fraction dictating the K distribution.

A number of aspects with regards to the Al_2O_3:C β-D_r distribution maps are yet to be resolved. Perhaps the two most obvious are: 1) the need for improvement in the signal-to-noise ratios in the single grain measurements, and 2) a means of resolving

the divergent L_N and T_N decay curve shapes. With respect to the former point, this problem may potentially be overcome through longer periods of storage or, indeed, simply using samples with a higher β-D_r than those investigated in this study. In either case, the result will be more dose delivered to the grains producing a stronger L_N response. With regards to the second point, one possibility would be to deliver a much smaller normalising test dose. Kalchgruber *et al.* (2003) dosed their Al_2O_3:C grains by irradiating the carousel position directly next to the position holding the grains. The dose delivered was calibrated against a sample of gamma irradiated Al_2O_3:C. The test doses used in this study were the smallest that could be delivered using the Risø readers available in our laboratory. The outcome of using a smaller test dose is expected to be a smaller deviation of L_N and T_N signals. Alternatively, assuming that the sensitivity of the Al_2O_3:C grains remains constant (as demonstrated in Figure 6.32) the T_N measurement can be omitted and β-D_r determined using a sensitivity 'uncorrected' standardised growth curve. At present the single-grain Al_2O_3:C β-D_r maps appear to be more reliable than those of the small aliquots based upon the results presented in Table 6.22 where the small aliquot MAX β-D_r values produced significantly smaller ages in comparison to the CAM and 'bulk' GMBC ages for both Layers 8 and 5B. Although further development of this technique is required, this method does show promise in being able to resolve the β-D_r environment.

6.5.3 BETA DOSE RATES, OVERDISPERSION AND OSL CONSIDERATIONS

Of the samples investigated here, the D_e distributions measured from individual grains of quartz revealed typical amounts of OD. The OD values were calculated to be: 40 ± 2% (SP2), 35 ± 2% (SP5), 48 ± 4% (Layer 8), and 30 ± 6% (Layer 5B). In each case, this OD was considered the result, as least in part, of micro-scale variations in the beta dose rate environment. This conclusion was explicitly tested in this study using the β-D_r determined using pXRF, image analysis modelling and Al_2O_3:C dosimetry. The results for these studies are presented in Table 6.10 for the

pXRF data, Table 6.17 for the image analysis data, and Table 6.22 for the Al_2O_3:C data.

- Large uncertainties on the pXRF β-D_r values resulted the MAM and MAX obtaining the same β-D_r values for three out of the four samples
- Portable XRF can measure the upper-tail of the β-D_r distribution, when U, Th and K are present at the one analysis position (i.e., one grid position, for example, Row 1, Column 1 is one measurement position), but not the lower-tail range

For one out of the four samples (Layer 5B), the pXRF β-D_r estimates are able to achieve an equivalent age for the MAX, only. For the remaining three samples (SP2, SP5 and Layer 8), the pXRF did not give consistent ages for either the MAM and MAX estimates. This inability to obtain consistent MAM, MAX and CAM ages is thought to be due to the large errors associated with the pXRF β-D_r values, thus leading to the MAM and MAX converging at the same point rather than resolving the top and bottom of the β-D_r distribution.

- Image analysis modelling β-D_r values could not explain the spread in the D_e values for three of the four samples
- The underpinning assumptions of this method do not allow for the upper- and lower-tail ranges of the β-D_r distribution to be modelled fully

The image analysis modelling MAM and MAX OSL ages for SP2, SP5 and Layer 8 (Table 6.17) failed to achieve ages equivalent to those calculated using the CAM and 'bulk' GMBC β-D_r. The constancy of the MAX age for Layer 5B from Pech IV with the CAM age (Table 6.17) is thought to be due to the large uncertainty on the MAX D_e rather than a reflection of an appropriate image analysis modelled β-D_r. The inability of this method to achieve consistency between the MAM, MAX and CAM ages is thought to be due to the assumptions underpinning the modelling. Taking the FS heavy mineral fraction of SP5 as an example, the use of the average U

concentration (163 ± 2 μg/g; Table 6.4) for this fraction assumes that the U concentration for 95% of the grains falls between ~159 and 167 μg/g. Yet, given that this fraction is comprised of a suite of mineral species (e.g., rutile, ilmenite, zircon, hematite, etc) this 'average' U concentration range is not going to be applicable for every individual mineral grains that was ground and homogenised to measure this U concentration. This argument could be used for each of the various fractions measured. The image modelling β-D_r are the sum total of these average concentrations and are not be able to span the 'true' range of β-D_r values.

- Single-grain Al_2O_3:C dosimetry could be used to explain the spread in the D_e distribution when using single-grain but not small aliquots

In all three samples were single-grain Al_2O_3:C estimates were made (SP2, SP5 and Layer 8); both the MAM and MAX estimates give consistent ages to those previously reported (Table 6.22). However, it should be noted that the uncertainties on the single-grain Al_2O_3:C β-D_r estimates are quite large (20 to 40%). It is possible that the consistent ages produced are simply a result of these large uncertainties. Future work would benefit from better control of the storage dosimetric environment and longer periods of storage to increase the OSL signal-to-noise ratio. A comparison with the single-aliquot Al_2O_3:C estimates reveal that, while the MAM estimates have equivalent ages to those reported previously (Table 6.22), the ages calculated using the MAX are significantly too young suggesting that MAX β-D_r values obtained are overestimates (Table 6.22).

- BM plays a role in the OD observed in the D_e distributions of the four samples

In terms of OD, BM can explain some of the spread observed in the D_e distribution values for each of the four samples investigated in this study. Only the Al_2O_3:C study using individual grains was able to explain all the spread in the D_e distributions as entirely the result of micro-variations in the β-D_r environment. It is most likely that a number of factors, including intrinsic and post-depositional mixing

(for the Pech IV samples more than those from MacCauley's Beach) also contribute to the observed OD.

6.6 CONCLUSIONS

The variations present in the β-D_r environment at MacCauley's Beach and Pech IV are complex, both within and between sites. The use of empirical investigations, although destructive, has been able to inform about both the magnitude, and spatial distribution of β-D_r values and their associated 'hotspots'. The assessment of β-D_rs of mineralogical components within four sediment samples (SP2, SP5, Layer 8 and Layer 5B) has elucidated two important issues. First, the range of β-D_r values within the one sample varies significantly. Second, that U and Th are just as important, in not more so, as K when it comes to the β-D_r of the samples investigated here. Both MacCauley's Beach samples U and Th were present in the fine sand heavy mineral components of these sediments and dominate the 'bulk' β-D_r. In contrast, ^{40}K certainly dominates the β-D_r for both samples at Pech IV.

The spatial distribution of β-D_r 'hotspots' were estimated using the results of the pXRF measurements, image analysis modelling and Al_2O_3:C dosimetry analysis. Each of these three techniques revealed that the spatial distribution of β-D_r 'hotspots' was heterogeneous. At MacCauley's Beach 'hotspots' are associated with the heavy mineral fractions, while at Pech IV β-D_r are more homogeneous but with 'coldspots' produced by the presence of flint and limestone. The β-D_r distribution maps generated from these results suggested that the OD present in the single-grain OSL D_e distributions for all four samples, at least in part, could be attributed to BM.

CHAPTER SUMMARY

In this chapter I have shown that the ß-D_r for two MacCauley's Beach and two Pech IV samples are highly variable. This variability is evident using both 'disturbed' and 'undisturbed' methods of assessment.

It should be noted that each of the 'undisturbed' methods have their own merits and shortcomings.

- *pXRF – although this technique allows for the rapid assessment of sedimentary composition, due to the 4 µg/g detection limit for both U and Th, this technique is only sampling the high tail end members of the ß-D_r distribution. That is to say, it can only provide an understanding of the true ß-D_r where U, Th and K are present concurrently at the same analysis point. Future work requires that techniques more sensitive to the detection of U and Th be used to resolve the entire ß-D_r distribution, e.g., laser ablation ICP-MS.*

- *Al_2O_3:C – although able to assess the entire range of the ß-D_r distribution, the dim signals of individual Al_2O_3:C grains means that the determined ß-D_r*

are not as accurate as they could be. The measured ß-D_r distribution using single grains, however, is acceptable but contains a number of measurements that are larger than those of the pXRF high-tail end members. This dim signal in the L_N also manifests as a proportion of measurements positions having ß-D_r that are equivalent to 0 Gy/ka. To overcome both of these problems require that the storage time of the sediment slabs be increased to allow for more dose to accrue and thereby have brighter signals. The use of small, 4-grain aliquots of Al_2O_3:C resulted in much better OSL signal-to-noise ratios, however, produced unrealistically large ß-D_r values and a deviation in decay curve shape between the L_N and T_N measurement. This occurrence requires further investigation in the future.

- *Image analysis modelling – the use of microphotograph analysis in tandem with the measured 'disturbed' ß-D_r values for the corresponding sedimentary components provided a sophisticated and readily accessible means of examining the magnitude and distribution of ß-D_r throughout the sediment samples. However, like all model, the output is only as good as the assumptions that it is based upon. By using average ß-D_r of the sediment components, only an average distribution of ß-D_r values was obtained.*

Taken individually, the methods develop to assess both ß-D_r variability and spatial distribution are, in truth, lacking. Yet, as a whole they provide complementary views into the complexity of the ß-D_r in sediments. Using these data sets, the OD in the four investigated samples could effectively be explained as the result of beta microdosimetry using one, or more, of these developed methods. The testing of these methods on samples with known higher ß-D_r is suggested for future work to overcome some of the issues associated with the detection levels of the pXRF and dim L_N signals of the Al_2O_3:C grains.

Chapter 7

Micro-computer tomography (μ-CT) of sediments and its applicability to optically stimulated luminescence studies

The effect of beta microdosimetry has been both qualitatively and quantitatively determined for two samples from MacCauley's Beach. However, both the studies carried out thus far, with the exception of the Al_2O_3:C dosimetry, have focused upon the use of two-dimensional surfaces to reconstruct three-dimensional radiation geometries. For the Al_2O_3:C dosimetry maps, the three dimensional depth investigated was only the thickness of one beta sphere in diameter (~6mm). Here, building upon the information I have gathered over the past two chapters, I investigated the sediments as three-dimensional volumes using micro-computer tomography.

Aims of this chapter:

- *Investigate the three-dimensional distribution of heavy minerals throughout resin-impregnated sediment core samples from MacCauley's Beach.*
- *Link the distribution of the radioactively 'hot' heavy minerals to the OD from D_e distribution measured from within the same sediment core.*

ABSTRACT

Localised variations in the beta dose flux in sediments (termed beta microdosimetry; BM) can result in greater than expected spread in single-grain OSL equivalent dose (D_e) values. Previously, the heavy mineral fraction of samples from MacCauley's Beach have been shown, both qualitatively (soil micromorphology) and quantitatively (portable x-ray fluorescence (pXRF) and aluminium oxide (Al2O3:C) dosimetry, to contribute substantially to the spread in D_e due to BM. Micro-computer tomography (μ-CT) was employed to assess the distribution and proportion of heavy minerals in two sediments samples (SP2 and SP5) from MacCauley's Beach, and to determine if these properties could be correlated with the spread in the corresponding D_e distributions. The results of the μ-CT analysis reveal that the heavy mineral fraction in both a clay-rich (SP2) and 'clean' sand (SP5) sample could be digitally identified. The distribution and proportion of heavy minerals in three successive 3 mm slices of a core digitally extracted from sample SP5 using μ-CT were shown to be homogeneous and consistent (1.4 to 1.8%). Portable XRF analysis of physically sectioned, and corresponding, slices revealed significant variability in the beta dose rate (between 0.31 ± 0.12 to 0.97 ± 0.19 Gy/ka), assuming a concentration of 2 ± 1 μg/g for U and Th where present below the pXRF detection limits. The consistency of the heavy mineral proportions and the variability in the beta dose rate is attributed to the inability of the μ-CT to distinguish radioactively 'hot' heavy minerals species (such as zircons) from those that are 'cold' (such as ilmenite). The corresponding D_e distributions of the SP5 core slices are all significantly larger than the 16 ± 1 Gy weighted mean D_e presented for SP5 in Chapter 5. This increase in D_e is assigned to the deposition of dose during μ-CT (between ~35 and 106 Gy) and pXRF (~2 Gy) analysis. The significant overprinting of the natural D_e distributions by the μ-CT irradiation means that no conclusions could be formed to relate the heavy mineral proportions to the corresponding D_e distribution patterns.

7.1 INTRODUCTION

The effect of BM in the field of optically stimulated luminescence (OSL) dating has become an increasingly important area of research. This growth in activity and importance has been spurred on by the advent of single-grain OSL dating (Murray & Roberts 1997, Roberts *et al.* 1999, Jacobs *et al.* 2003b, Duller 2004, Lian & Roberts 2006, Jacobs *et al.* 2006c), which has a number of advantages over the antecedent multi-grain OSL method. One limitation, however, is that the determination of the radiation flux (termed the dose rate) of beta particles delivered to individual mineral grains remains an unresolved problem at a grain-by-grain level. For multi-grain OSL that measures the average accumulation of trapped electron charge (or equivalent dose, D_e) since burial, the average beta dose rate (β-D_r) could simply be used in age determinations. In contrast, the average β-D_r is not applicable to every grain, with each receiving its own β-D_r due to the heterogeneous distribution of beta particle-emitting radionuclides throughout the sediments (Murray & Roberts 1997, Olley *et al.* 1997, Nathan *et al.* 2003, Mayya *et al.* 2006). This spatial heterogeneity of the β-D_r is due to the localised penetrating power of the beta particle, which travels between 2–3 mm in sediments (Aitken 1998). The outcome of this is that the scatter in the D_e values for single-grain OSL samples tend to be larger than expected once all other quantifiable analytical uncertainties and variability in OSL characteristics have been accounted for and sufficiently explained; this is termed overdispersion (OD; Galbraith *et al.* 1999).

Previously, I have shown that the highest β-D_r for the samples collected from MacCauley's Beach is derived from the heavy mineral fraction (Chapter 6). This study is a continuation of that investigation paying particular attention to samples SP2 and SP5. Micromorphological analysis of thin sections and β-D_r modelling revealed that the spatial distribution of heavy minerals in thin section was inhomogeneous; similar results were also shown in the spatial distributions of β-D_r 'hotspots' determined using Al_2O_3:C dosimetry and pXRF analysis of the resin-impregnated slabs. It was concluded that the amount of OD in the D_e distributions for SP2 and SP5, above that obtained from a ~12 Gy dose recovery test (9 ± 2%), was

the result of the heterogeneous distribution of radioactive heavy minerals in the sediment (Chapter 5). Further testing of the heavy mineral separates from SP2 and SP5 showed that they contributed ~13 and ~69% to the total beta dose of their respective samples. To further understand the spatial distribution of highly radioactive heavy mineral grains requires that a non-invasive and non-destructive means of determining their three dimensional spatial position be employed. It was considered that the use of μ-CT was one possible method of achieving this.

The μ-CT technique relies on the variability in the x-ray attenuation coefficients of the objects being investigated to create a digital three-dimensional reconstruction (Ketcham & Carlson 2001). The x-ray attenuation coefficients relate closely to the density of the materials being examined (e.g., hematite has a greater density than quartz and, therefore, a greater x-ray attenuation coefficient, resulting in a higher grey-scale value in the final μ-CT reconstruction). This method provides a means of determining the spatial distribution, and volume, of the mineral grains in the samples under investigation, and has been used previously, with great effect, in determining three-dimensional sedimentary textures and fabrics in glacial tills (Tarplee *et al.* 2011) and archaeological sediments (Adderley *et al.* 2001). It is fortunate, in this study, that the fraction of interest (the heavy mineral fraction) is also the fraction with the greatest collective density and also the highest collective β-D_r.

The current study has an overarching aim to investigate the efficacy of the μ-CT technique in determining the three-dimensional distribution of heavy mineral grains in sediment core samples prior to single-grain OSL analysis. In particular, to: 1) determine the applicability of the μ-CT technique in the differentiation of heavy mineral grains in clay-rich (SP2) and 'clean' sand (SP5) sediments, 2) investigate the spatial distribution pattern and volume of heavy minerals throughout a 'clean' sand (SP5) sediment core, and 3) to relate the spatial distribution of heavy minerals to the OD present by measuring the D_e values of μ-CT-analysed sediment cores using single-grain OSL. It is considered that by undertaking this investigation, the amount of OD, both within and between consecutive core sections, could be accounted for by

the volume and spatial distribution of the heavy mineral fraction residing within them.

7.2 METHODS

7.2.1 STUDY SAMPLES, COLLECTION AND μ-CT PREPARATION

The samples used in this study were collected from MacCauley's Beach, a receded barrier beach deposit located ~12 km north of Wollongong City, on the New South Wales coast of Australia (Figure 7.1a). The study was carried out primarily on SP5, a clast-supported sediment dominated by sand-sized grains of quartz and a small amount of heavy minerals (3.4% of total mass; Figure 7.1b). Single-grain OSL investigations carried out on this sample in Chapter 5 show D_e values that are distributed symmetrically around a central mean D_e value. This pattern is displayed graphically as a radial plot in Figure 7.1c. The central age model (CAM) of Galbraith *et al.* (1999) gave a weighted mean sample D_e value of 16 ± 1 Gy, with an OD value of 35 ± 2%. An age of 6.6 ± 0.4 ka was produced using a total environmental dose rate of 2.37 ± 0.13 Gy/ka, assuming that the present dose rate (which shows disequilibrium within the U-series) has existed throughout the period of burial (Chapter 5). If the disequilibrium in the decay chain is taken into account and assumed to have prevailed throughout the burial history of SP5, then an age of 7.9 ± 0.4 ka is obtained using a total environmental dose rate of 1.98 ± 0.6 Gy/ka.

Sample SP2, a matrix supported, clay-rich sediment (Figure 7.1b), was also used in this investigation. This sample has an OD value of 40 ± 2% and has D_e values ranging between ~4 and ~34 Gy (Figure 7.1d). Visual assessment of the D_e distribution for SP2 reveals that the majority of grains are spread symmetrically around a central D_e value, with the exception of a few higher D_e values >25 Gy. It should be noted, however, that this sample was only used as a contrast to SP5 to determine the ability of the μ-CT technique to distinguish heavy mineral grains in clay-rich sediment.

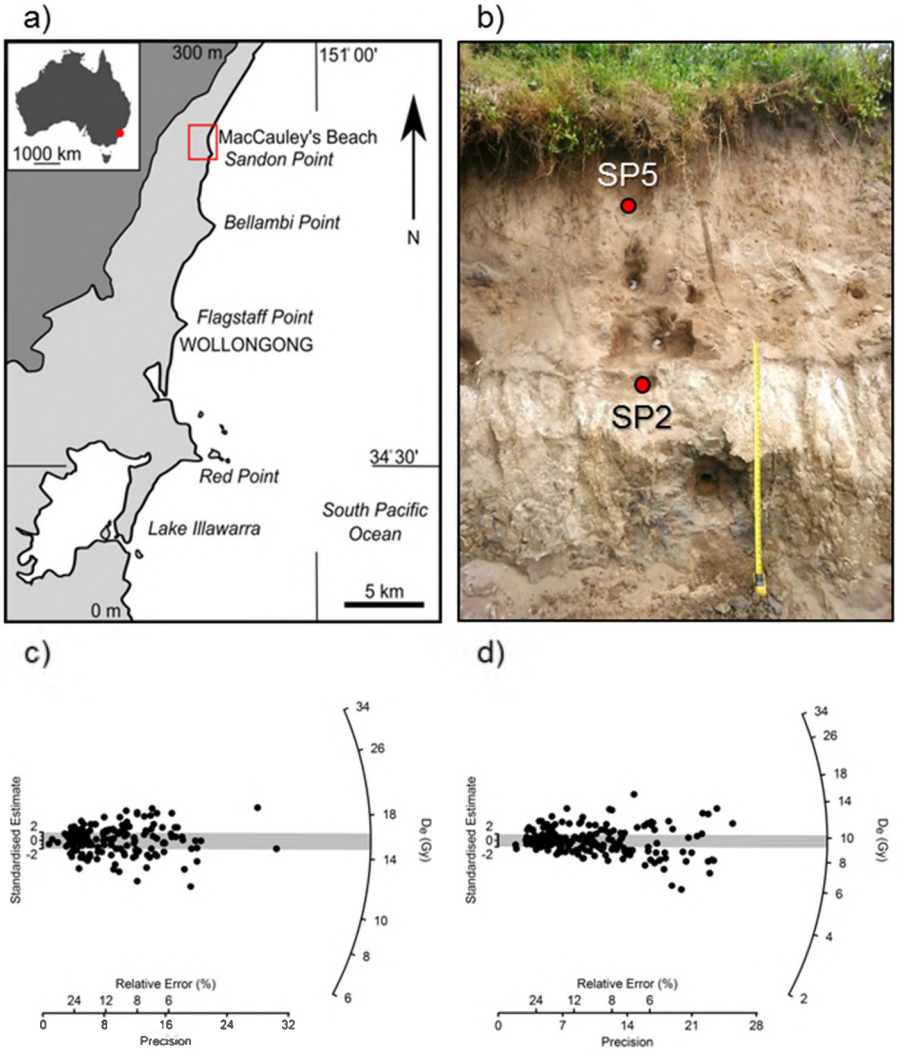

Figure 7.1. a) Location of MacCauley's Beach in relation to Wollongong. b) the sedimentary profile examined in this study with the locations of SP2 and SP5 marked with red dots. c) D_e distribution of SP5 and d) SP2. Grey bands are centred on the central age model determined weighted mean for the sample as determined in Chapter 5.

These two samples were collected from MacCauley's Beach as part of the soil micromorphological and chronological investigation presented in Chapter 5. A more detailed review of the sample collection processes can be found in Chapters 3 and 5. Sediment block samples were collected from the exposed sediment profile using 10

by 5 cm aluminium pipe cut into 10 cm lengths inserted into the section. The pipe, and the contained sediments, were then excised from the section before being wrapped in tissue paper and packing tape – to prevent sediment disturbance – and transported to the University of Wollongong for resin-impregnation. The sediment block samples were prepared using techniques outlined in Courty *et al.* (1989). The blocks were oven dried at 60°C for several days and then impregnated with polyester resin (Dalchem; Clear Casting Resin), diluted with styrene in a ratio of 7:3, with 2-butanone peroxide ($C_8H_{16}O_4$) catalyst. They were then returned to the oven to cure fully. The blocks were then cored using a 'Delta Diamond Tools' diamond core drill bit with an internal diameter of 28 mm, producing sediment cores of 24 mm diameter.

7.3 EFFICACY OF THE μ-CT TECHNIQUE

7.3.1 μ-CT MEASUREMENT, ANALYSIS AND RECONSTRUCTION OF SP2 AND SP5

All μ-CT measurements were carried out at the University of Sydney's Australian Centre for Microscopy and Microanalysis (ACMM). Both cores were scanned at a low (29.64 μm pixel width) and high (15.05 μm pixel width) resolution using the ACMM's Xradia MicroXCT-400 μ-CT scanning unit. For the low resolution scan the core was rotated 210°, captured 1051 images with an x-ray exposure time of 0.3 s. The high resolution scan, in contrast, rotated the core 196°, collecting 981 images with an x-ray exposure time of 1 s. The energy of the x-ray beam was kept constant throughout both scans at a voltage of 120 kV. The images collected for both the high and low resolution scans were then reconstructed to produce a series of ordered, 64-bit greyscale tomographic images stored as .tiff files – each file equivalent to a cross-section slice through the core. The vertical distance between each tomographic image is equivalent to the pixel size resolution of the scan, either 29.64 or 15.05 μm.

7.3.2 RESULTS

Examples of both high and low resolution μ-CT images of SP2 and SP5 are shown in Figure 7.2. It should be noted that the images shown are not from the same cross sectional position through the sediment cores (i.e., they cannot be directly compared to one another) but are of equivalent area (12×12 mm). In both samples, three broad density phases are present, comprised of: 1) bright white, 2) mid-grey, and 3) dark-grey/black constituents. Bright white density phases are comprised of a number of discrete objects and, from previous soil micromorphological analysis of thin sections, are considered to be the heavy mineral fraction. It can be seen that in the high resolution images (Figures 7.2a and 7.2c), the boundaries of the heavy minerals are significantly clearer than those in the low resolution (Figures 7.2b and 7.2d) images. Additionally, the number of heavy minerals is about two times greater in SP5 than in SP2 by visual assessment, consistent with the point counting of thin sections presented in Chapter 5.

The mid-grey density phase, in both samples, dominates the μ-CT images. This phase is considered to be comprised of quartz, feldspars and clays. In SP2, it is possible to visually differentiate discrete, lighter-coloured objects (presumably quartz grains) from a darker coloured background (clay) in the high resolution image only (Figure 7.2a). The dark-grey/black component, representing void space, can be seen as linear features and irregular shaped objects in SP2 (Figure 7.2a), but only as packing voids and vughs in SP5 (Figure 7.2c); this morphology is also consistent with thin section analysis of these two samples (Chapter 5, Figures 5.4e, g and p).

From the μ-CT results, it is apparent that the heavy mineral fraction can be distinctly recognised, with respect to the remaining density phases (i.e., quartz, void, etc.) present in both SP2 and SP5. However, is the distribution of the heavy mineral grains present homogeneous throughout the length of the sediment cores or is this distribution more heterogeneous? It could be argued that the result in either case would still give rise to BM however, the corresponding D_e distribution patterns these scenarios would show subtle differences. We propose that, a homogeneous

distribution of heavy minerals may give rise to a D_e distribution that is dispersed, whereas a heterogeneous distribution of heavy minerals may result in a distribution of D_e values that may also contain some discrete D_e components that make up a small proportion of the overall D_e distribution.

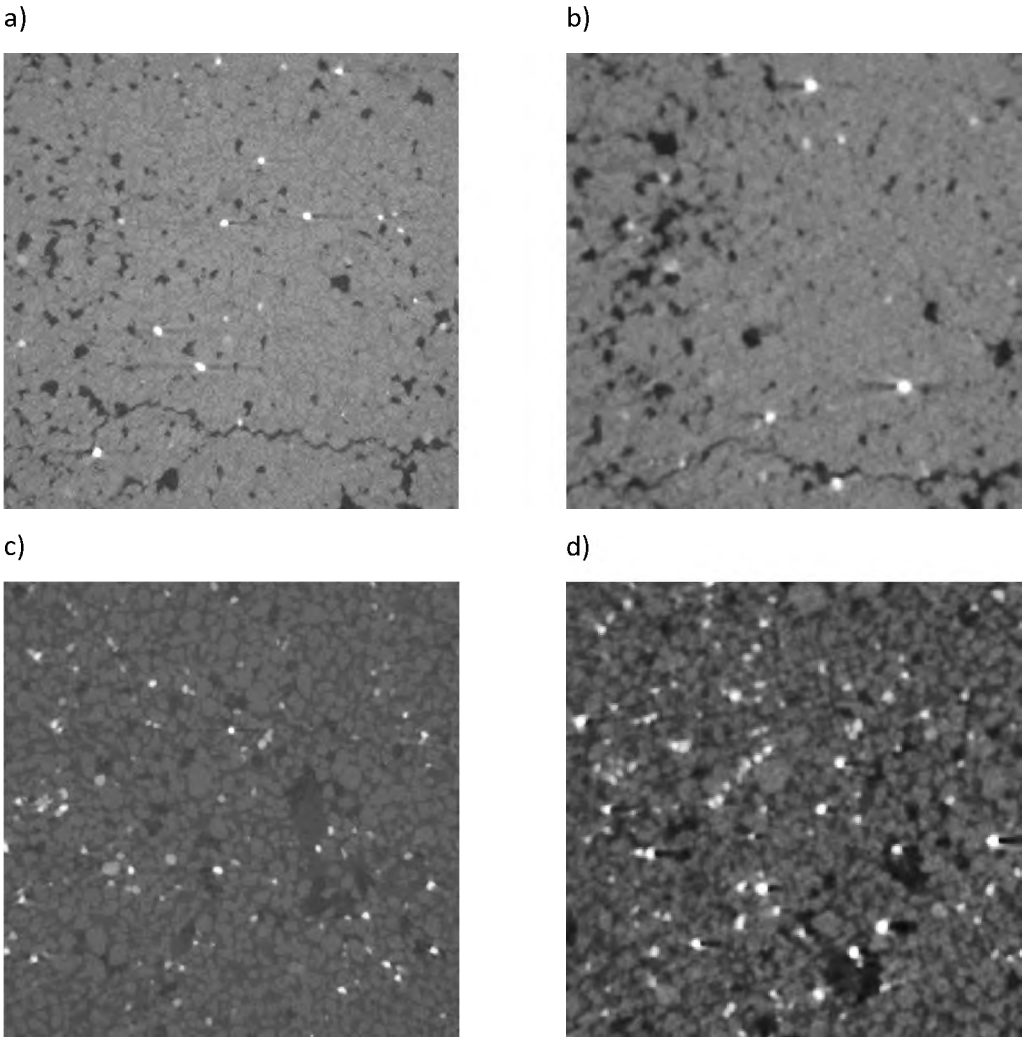

Figure 7.2. µ-CT images of the SP2 (a and b) and SP5 (c and d) sediment cores at both a high (15.05 µm pixel width; a and c) and low resolution (29.64 µm pixel width; b and d). These images are at right angles to the long axis of the core samples collected. The core samples, themselves, taken horizontally into the section, at right angles to the bedding planes of the sediment. The slices presented here are a 2D slice through the sediments and therefore have no thickness.

7.4 SP5 HEAVY MINERAL PROPORTION AND DISTRIBUTION USING μ-CT

7.4.1 μ-CT IMAGE PROCESSING AND HEAVY MINERAL EXTRACTION

To assess the spatial distribution and proportion of heavy mineral grains, the low resolution (29.64 μm) μ-CT scan was used. While the high resolution scan provides greater image quality (in terms of delimiting object boundaries), the low resolution scan captured the entire length of the SP5 sediment core as opposed to the partial volume captured in the high resolution counterpart. Visualisation and basic quantitative analyses of the low resolution scan series of the SP5 core was carried out using the freely downloadable ImageJ software program (Abramoff *et al.* 2004, Schneider *et al.* 2012).

The ordered series of greyscale SP5 tomographic images was imported into the ImageJ program as an 'image stack' and converted into binary (black and white) images using a threshold value of 11 000 to isolate the heavy mineral fraction. The binary image stack was filtered to include only those heavy mineral grains that had a diameter of 63–180 μm using the 3D object counter (Bolte & Cordelières 2006) – a freeware 'plug-in.' This choice of grain size fraction was based upon the results of the β-D_r experiments conducted in Chapter 3 which showed that this fine-sand heavy mineral fraction was responsible for ~69% of the total SP5 β-D_r. The SP5 low resolution image stack was then digitally 'sectioned' into three 3 mm-thick slices with a 0.8 mm space separating each slice – hereafter termed Slices 1, 2 and 3. The percentage of 63–180 μm heavy mineral grains was then calculated for each 3 mm slice using the 3D object counter 'plug-in' and visually rendered using the 3D Viewer 'plug-in' (Schmid *et al.* 2010).

7.4.2 RESULTS

The percentage volume of heavy minerals in digital Slices 1, 2 and 3 of the SP5 sediment cores is shown in Table 7.1. Although no errors could be calculated using the 3D object counter plug-in, it is apparent that the amount of heavy minerals between each slice remains consistent, ranging between 1.4 and 1.8%. It should be noted that the ImageJ-determined percentage volume of heavy minerals is significantly less than that presented previously by weight for this particular fraction (2.9%; Chapter 6), or the entire heavy mineral fraction by point counting (3.4%; Chapter 5). This discrepancy, at the present, cannot be fully explained. One potential cause for this underestimation is that the boundaries of the heavy minerals may have been removed during the threshold processes due to the partial volume effect (Adderley *et al.* 2001). This effect would have been more substantial for those grains that had diameters closer to the 63 µm of the 63–180 µm range. It is also likely given the range of heavy mineral species present in the sample, that some of these are not as dense as others making them difficult to distinguish from the 'quartz' fraction.

A visual rendering of the heavy mineral distribution of each slice is shown in Figure 7.3. Also provided on the accompanying Compact Disc (CD) to this thesis are 3D rotational movies of each of these slices, generated using the 3D viewer in ImageJ. At face value, the static images presented in Figure 7.3 appear, to a greater or lesser extent, to be uniform throughout the 3 mm thick sediment slices. However, the heavy mineral fraction is not comprised of a single heavy mineral species (e.g., rutile only) but is a conglomerate of many different mineral species including rutile, zircon, tourmaline-group minerals, hematite, ilmenite, etc. This apparent homogeneity requires further investigation to determine if the distribution of radionuclides throughout the slices is as uniform as their equivalent heavy mineral distributions.

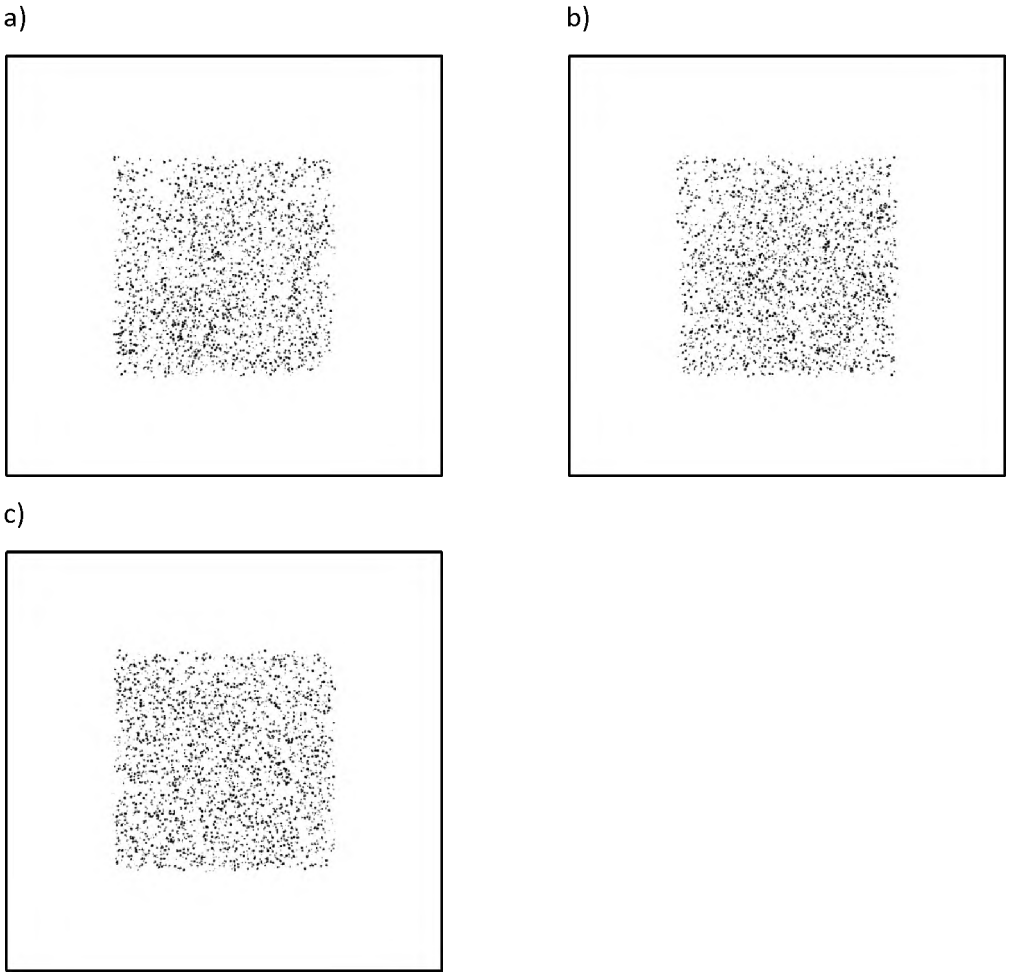

Figure 7.3. Three-dimensional visualisations for 63-180µm heavy mineral grain fractions of the SP5 core Slices a) 1, b) 2, and c) 3. The views are shown looking through the 3 mm thick µ-CT slices from the front, which covers an area of 15 × 15 mm.

Table 7.1. Table showing the percentage heavy mineral grains with a diameter of < 180 µm in each of the three SP5 sediment core slices.

Slice number	Heavy mineral proportion (%)
Slice 1	1.4
Slice 2	1.7
Slice 3	1.8

7.5 RADIONUCLIDE ANALYSIS OF SP5 SEDIMENT CORE SLICES

7.5.1 SP5 SEDIMENT CORE SECTIONING PROCEDURES

To confirm whether the radionuclide concentrations (in particular U, Th and K) in the SP5 core slices were uniform with respect to their μ-CT-determined distributions of heavy minerals, required that the SP5 core be sectioned. The physical sectioning of the SP5 core was carried out using a Buehler IsoMet® 1000 precision saw, fitted with a 0.8 mm cutting blade. The water-cooled cutting blade of this bench-top precision saw could be accurately positioned at precise intervals along the SP5 core. Slices were made as close as possible to those made 'digitally' in ImageJ. All sectioning was carried out under subdued red light in the OSL laboratory, with minimal force applied during cutting and using the lowest possible blade rotational speed of 100 revolutions per minute. These measures were taken to preserve the OSL signal at the centre of each of the slices for future analysis (described below). Three slices were cut from the SP5 core and labelled according to their 'digital' counterparts.

7.5.2 PORTABLE XRF PROCEDURES AND MEASUREMENT

Following sectioning, portable x-ray fluorescence (pXRF) analysis was carried out on each slice to determine the distribution of U, Th and K using the methods outlined in Chapter 3. Using the same instrument (a Thermo Scientific Niton XL3t GOLDD+ handheld pXRF), the concentrations of U, Th and K across the top and bottom sides of the sediment slices were measured. Unlike the previous pXRF investigations, the 'range-finder' function of the pXRF (giving a real time image of the sample surface that was previously used to locate the analysis positions) was required to be turned off in the dark room as it uses a white LED light source.

Another means of determining the position of the detection window was, therefore, required.

A simple sample holder was made using printer paper with a cavity cut into the sheets that was the same diameter and height as the sediment core slices (24 mm diameter and 3 mm deep), with a 3×3 mm grid printed on the uppermost page. With the slice placed into the sample position, and using the external grid as a reference, the pXRF was then systematically shifted across the surface of each slice covering an area 12×12 mm on both the top and bottom faces of each SP5 core slice. This area is delimited by the black square in the Figure 7.4 schematic, and constitutes 25 separate points of analysis. It was considered that any additional pXRF analysis beyond this 12×12 mm area at the centre of each core slice would be impinged upon by the sample holder. To ensure that the detector was positioned above each point of analysis, positioning marks located on all four sides of the pXRF detector where aligned with the corresponding grid lines printed onto the sample holder (Figure 7.4).

Analyses were conducted using the 'Test all Geo' function, which measures the concentrations of all elements from Na to U for 2 min at each point. As was the case in Chapter 5, a number of measurement positions had U and Th concentrations below the level of detection (~4 μg/g for U and Th). For these points a value of 2 ± 1 μg/g U and Th was assigned as this value is consistent with both 0 and 4 μg/g at 2σ. The raw pXRF values for U, and Th (where detected) and K were then calibrated using the calibration curves presented in Chapter 6, and converted into β-D_r using the conversion factors of Guérin *et al.* (2011), taking into account water content (5 ± 2%, Chapter 5) following the equations of Aitken (1985) and beta dose attenuation factors for 200 μm in diameter grains (Brennan 2003).

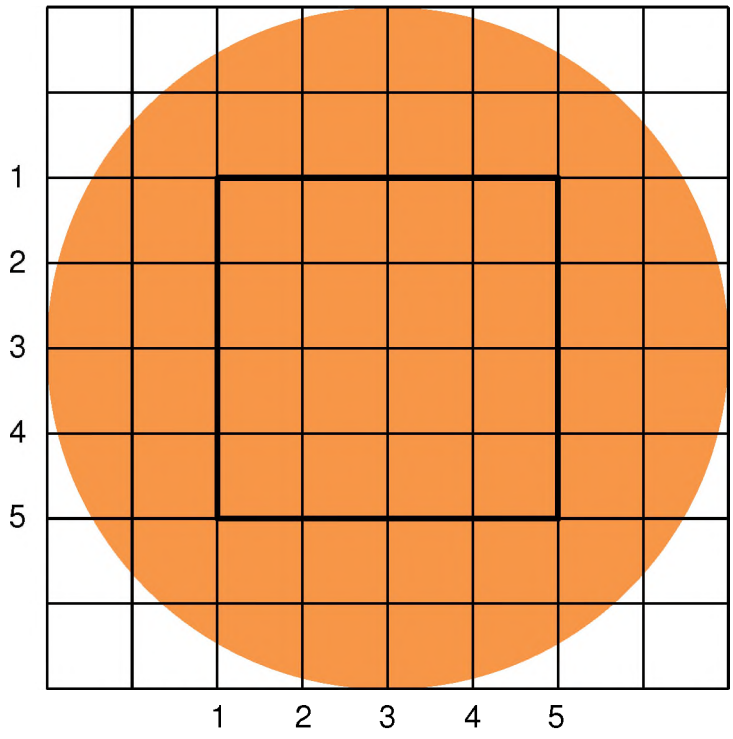

Figure 7.4. Schematic of the 3×3 mm grid system used in the analysis of SP5 core slices (orange circle) using pXRF. The black square in the centre represents the boundary of the 5×5 vertices used in this study and are labelled according to row and column. pXRF analysis was carried out moving the instrument left to right, and top to bottom, over the vertices contained in the central black square.

7.5.3 SP5 RADIONUCLIDE DISTRIBUTION MAP RESULTS

The β-D_r distribution maps for the top and bottom of each slice (1 to 3) are shown in Figure 7.5. Each of the images uses the same scale (Gy/ka), given on the right hand side of the Figure. It should be noted that in each of the minimum β-D_r values presented, the concentrations of U and Th were assumed to be 2 ± 1 µg/g due to the detection limit of the pXRF (4 µg/g).

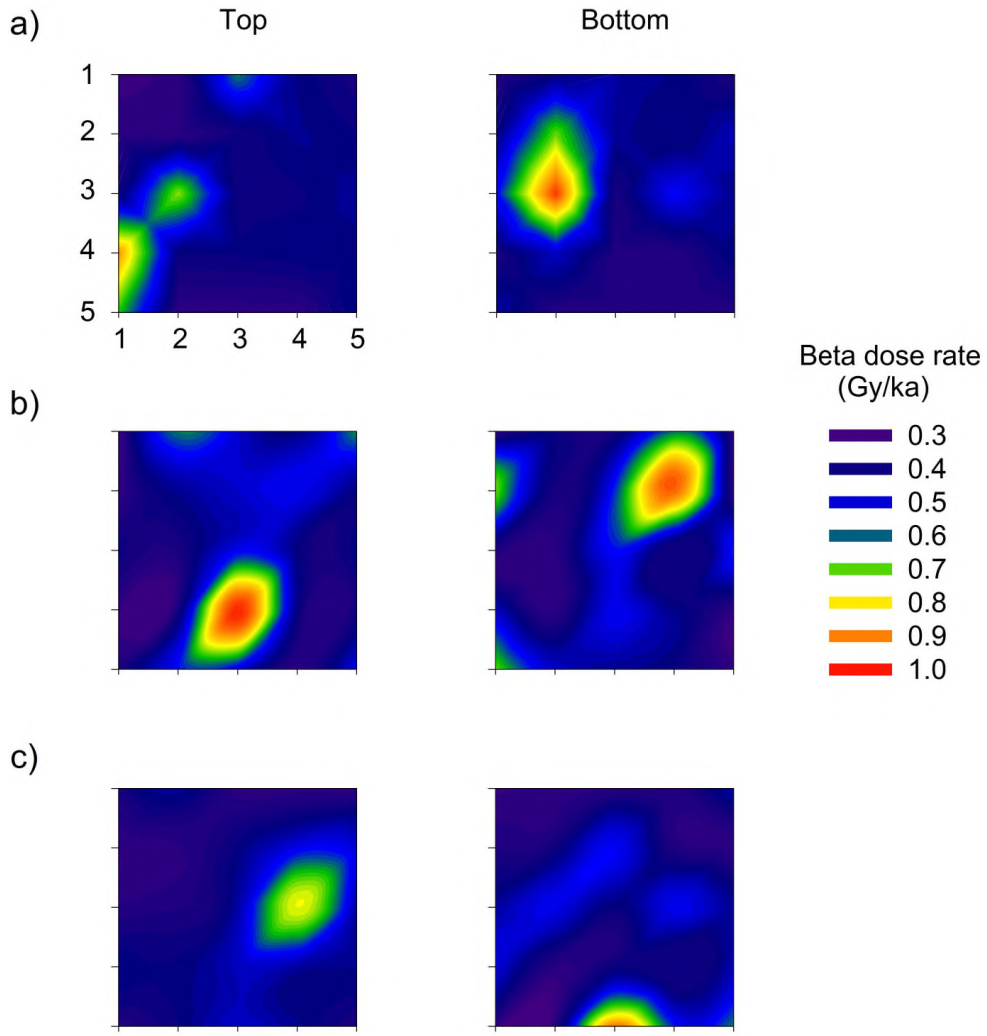

Figure 7.5. pXRF β-Dr maps for a) Slice 1; b) 2; and c) 3 from the SP5 sediment core. In each case the 'top' surface is the image on the left and the 'bottom' surface the image on the right. The total area covered by each map is 15×15 mm. All maps use the same scale (right of maps) which gives the moisture-corrected β-D_r for each point of analysis (Gy/ka).

Each of the β-D_r maps show at least one area of higher dose rate across the 12×12 mm surface area analysed using the pXRF. The maximum β-D_r value estimated for Slice 1 (Figure 7.5a) was 0.96 ± 0.18 Gy/ka and a minimum β-D_r value of 0.31 ± 0.12 Gy/ka. The elemental contributions to the maximum β-D_r for U, Th and K were 79, 10 and 11%, respectively. Slice 2 and 3 (Figures 5.5b and c,

respectively) have maximum β-D_r values consistent with Slice 1 (0.97 ± 0.19 and 0.90 ± 0.20 Gy/ka, respectively). U, Th and K contribute 78, 15 and 7%, respectively to the Slice 2 maximum β-D_r, whereas values 65, 28 and 7%, respectively, contribute to the maximum β-D_r for Slice 3. The minimum β-D_r values for Slices 2 and 3 were both estimated to be 0.32 ± 0.12 Gy/ka.

The results of the pXRF investigation are similar to those obtained in Chapter 6 for the SP5 sediment slab samples, with consistent β-D_r range (ranging from 0.32 ± 0.12 to 1.20 ± 0.29 Gy/ka). It should be remembered that the pXRF is only 'truly' measuring the upper end of the β-D_r range for the sample (i.e., only where detectable concentrations of U, Th and K are all obtained at an individual point of analysis, and that the lower end of the β-D_r distribution is defined through the arbitrary assignation of concentrations for U and Th (2 ± 1 μg/g)). It could be concluded, then, that the β-D_r distributions presented in Figure 7.5 are 'user manipulated' and that the distributions shown, therein, are not appropriate representations of the true β-D_r distribution. For example, the steep gradient between the ~1 Gy/ka point at in the centre of the top surface of Slice 2 (Figure 7.5 middle) and the point directly to the left of it at ~0.3 Gy/ka, may simply be an artefact of the former point having a detectable amount of U (>4 μg/g) and the later having no detectable U (and arbitrarily assigned 2 ± μg/g).

While this may be the case for the pXRF data, the microphotograph modelling using the JMicroVision analysis toolkit (Roduit 2013; and Chapter 4 for further details about this freeware package) of this sample in Chapter 6 reveals that, while the gradient between high and low β-D_r points of analysis is much gentler, the same range of β-D_r values exists and display the same heterogeneous in β-D_rs as the pXRF technique used in this investigation. For the purposes of this study (to determine if the homogeneous distribution of heavy minerals revealed during the μ-CT analysis (Figure 7.3) equates to a homogenous β-D_r distribution) the magnitude of difference in the β-D_r values obtained is not important. More important is that there exists a spatial variability in β-D_r. Importantly, the inhomogeneity in the β-D_r distribution maps presented in Figure 7.5 does not correspond with the homogeneous distribution of heavy minerals shown in the μ-CT data.

I have shown the β-D_r to be heterogeneous on a coarse-scale (Figure 7.5). It can be hypothesised that, as the heavy mineral content increases, the likelihood of a uniform β-D_r throughout the sediments would also increase as a result of reduction in the distance between radioactively 'hot' minerals to less than the size of the beta sphere of influence (~2–3 mm diameter). Following on from this, one could expect that the OD in the single-grain OSL D_e values would decrease as the effect of BM is reduced with an increase in heavy minerals. This hypothesis assumes that BM, alone, is responsible for the OD present in the SP5 sample (35 ± 2%) beyond that obtained for the ~12 Gy beta dose recovery test (9 ± 2%) that is thought to be an indication of inherent variability.

7.6 SINGLE-GRAIN OSL DISTRIBUTIONS FROM SP5 CORE SLICES

7.6.1 SINGLE-GRAIN OSL SAMPLE PREPARATION AND MEASUREMENT PROCEDURES

The three slices from the SP5 sediment core were prepared for single-grain OSL measurement. First, using a pair of wire cutters, approximately 1 mm was removed from the circumference of each of the core slices. This step was carried out to remove those grains on the outside of the polyester resin-impregnated core that were exposed to light during coring, and μ-CT measurement. The trimmed core slices were then placed in an acetone bath for at least one week, to dissolve the polyester resin and liberate the sediment grains. The sediments from each slice were then chemically pre-treated using standard OSL sample preparation procedures as outlined in Wintle (1997) (Chapter 3). The measurement of the samples was carried out using the same equipment, techniques and single-aliquot regenerative-dose (SAR) procedure outlined in Chapter 5.

7.6.2 SINGLE-GRAIN OSL RESULTS FOR SLICES 1, 2 AND 3

The individual D_e values obtained for each of the three slices, analysed with μ-CT and pXRF, are shown as radial plots in Figure 7.6. The D_e distribution patterns for the three slices are broadly similar, with D_e values ranging between ~40 and 140 Gy. In each case there are a small number of D_e values that fall below this range (<10 Gy). Weighted mean D_e and OD values were calculated using the CAM of Galbraith *et al.* (1999) (Table 7.2) The CAM D_e values are consistent amongst the three slices (83 ± 3, 77 ± 4 and 72 ± 5 Gy for Slices 1, 2 and 3, respectively) (Figure 7.6). The OD values for Slices 2 and 3 are significantly higher at 51 ± 4% and 65 ± 5%, respectively, compared to that obtained for Slice 1 (29 ± 3%). These D_e and OD values are at odds with those presented in Chapter 5 (Figure 7.1c) for sample SP5 that shows a range of D_e values between ~6 and 30 Gy, with a weighted mean D_e value of 16 ± 1 Gy and an OD of 35 ± 2%. This inconsistency between the SP5 D_e distribution presented in Chapter 5 and those of the SP5 core samples requires further investigation.

7.6.3 THE EFFECT OF PXRF ON SINGLE-GRAIN OSL D_e DISTRIBUTIONS

To assess whether the disparity between the D_e values of the SP5 core samples and that of the SP5 sample presented in Chapter 5 was the result of pXRF analysis of the sample, a polyester resin 'button' – termed the pXRF button – was created as a control sample. The pXRF button was made by mixing a portion of SP5 grains with a quantity of polyester resin. The grains used had previously been sun-bleached for a number of days, hydrofluoric-acid etched, and stored in the dark room prior to usage. The pXRF button was equivalent in both diameter and depth to that of the SP5 core samples and was measured using the same pXRF instrument and the same method as for the SP5 core sample. The pXRF button was then disaggregated, chemically pre-treated and measured on the same Risø TL/OSL-DA-20 reader using the same procedures as above for the SP5 core samples.

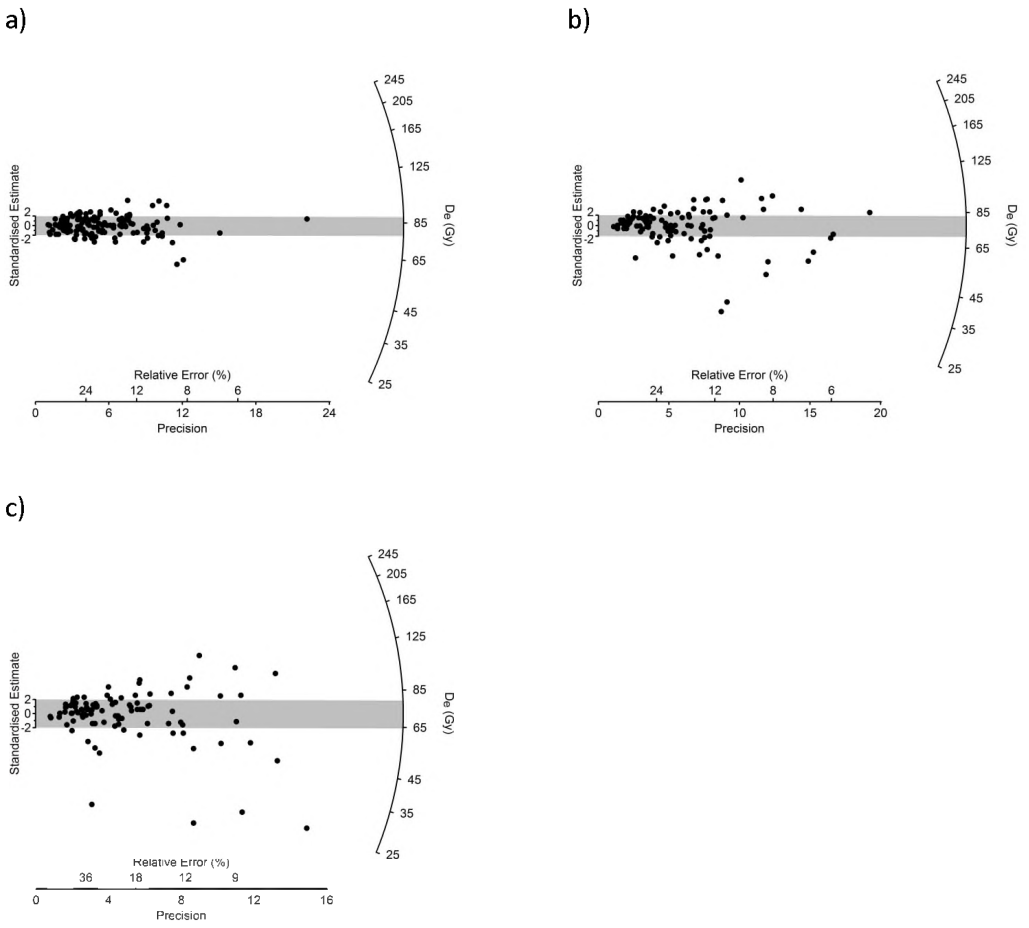

Figure 7.6. Single-grain OSL D_e distributions for: a) Slice 1, b) Slice 2, and c) Slice 3. Grey bands in each radial plot are centred on the weighted mean D_e value as determined by the central age model (Galbraith *et al.* 1999)

The individual D_e values of the grains extracted from the pXRF analysed button is shown graphically in Figure 7.7a and relevant data are provided in Table 7.2. The D_e distribution shows a thick cluster of D_e values centred at ~2 Gy, with a small number (<10%) producing a scattering of values between ~7 and 35 Gy. The weighted mean sample D_e was estimated to be 2.4 ± 0.2 Gy using the CAM and has an OD value of 68 ± 5%. It is apparent that, although the pXRF certainly does deliver a small dose (2.4 Gy) to the sediments during analysis, this dose is not

sufficient to increase the weighted mean D_e of the SP5 core samples from ~16 Gy to ~75–85 Gy.

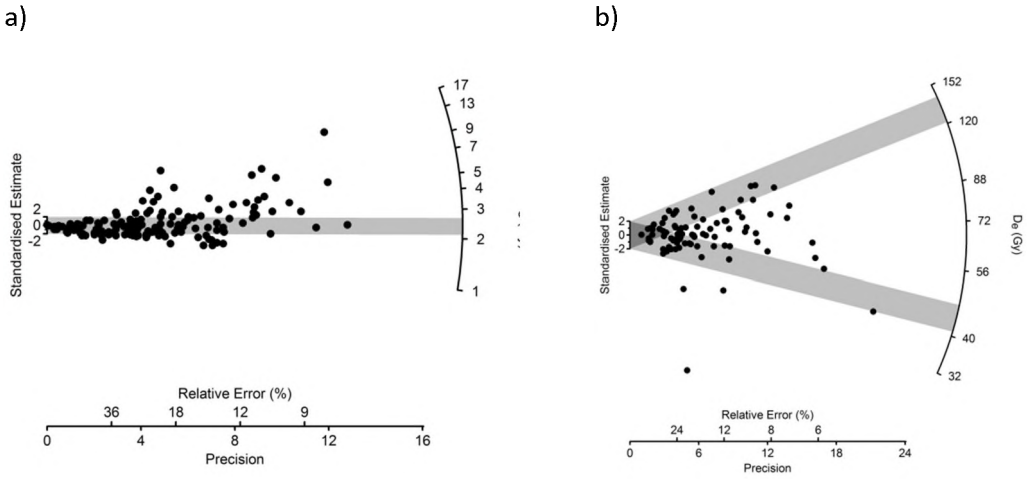

Figure 7.7. Single-grain OSL D_e values shown as radial plots for the pXRF button (a) and SP5 μ-CT only core slice (Slice 4). Grey bands are centred on 1) the weighted mean D_e for the pXRF button, and 2) the maximum and minimum D_e values for SP5 Slice 4.

Table 7.2. Single-grain OSL weighted mean D_e and OD values for three SP5 core slices that underwent μ-CT and pXRF analysis, the pXRF button and SP5 core slice 4 that was only analysed using μ-CT. The number of grains rejected, number of grains measured and percentage of accepted grains are shown for each sample.

Sample name	D_e (Gy)	OD (%)	Grains rejected/grains measured (N)	Percentage accepted grains (%)
Slice 1	83 ± 3	29 ± 3	657/800	18
Slice 2	77 ± 4	51 ± 4	595/700	15
Slice 3	72 ± 5	65 ± 5	499/600	17
pXRF button	2.4 ± 0.2	68 ± 5	857/1000	14
Slice 4	67 ± 4	57 ± 5	509/600	15

7.6.4 THE EFFECT OF μ-CT ON SINGLE-GRAIN OSL D_e VALUES AND THEIR DISTRIBUTIONS

To assess the effect that μ-CT analysis alone may have on D_e of the SP5 core sample, an additional slice was removed from the end of the SP5 core that was previously exposed to the μ-CT scanner. This slice (Slice 4) was not analysed using the pXRF, but did receive both a high- and low-resolution μ-CT scan at the ACMM facility at the University of Sydney. Once the slice had been removed, it was prepared using the same sample preparation and chemical pre-treatment procedures and measured on the same Risø TL/OSL-DA-20 reader using the same SAR procedure.

The individual D_e values for grains extracted from Slice 4 are shown in Figure 7.7b, and is very different from either the natural SP5 sample (Figure 7.1c) or the pXRF button (Figure 7.7a), but similar to that of the three SP5 slices (Figures 7.6a to c). The majority of the D_e values for this sample fall between ~40 to 140 Gy, three grains have much lower D_e values. The weighted mean D_e value of 67 ± 4 Gy was obtained and the OD value estimated to be 57 ± 5%. If we remove the three lowest D_e grains, then the weighted mean increases to 72 ± 3 Gy and the OD decreases to 32 ± 3%; The D_e and OD values are consistent with those obtained from the three slices.

It is apparent that the increase in the D_e values must be the result of x-ray irradiation during μ-CT scanning. To gain a better understanding of the range of D_e values present, the minimum (MAM) and maximum (MAX) age models of Galbraith *et al.* (1999) and Olley *et al.* (2006), respectively, were applied to the D_e values of Slice 4 (Figure 7.7b). Prior to running both models an additional 10% systematic uncertainty was added, in quadrature, to each individual D_e value to account for any intrinsic OD in a well-bleached population of SP5 quartz (based on the OD value of 9 ± 2% obtained from the beta dose recovery experiment; (see Chapter 3). The results of these models provide minimum and maximum D_e values of 44 ± 2 and 130 ± 9 Gy, respectively. This modelling was also carried out for the SP5 sample

presented in Chapter 6 and gave D_e values of 9 ± 1 (MAM) and 24 ± 2 Gy (MAX), respectively.

From these results, it is evident that the increase in the D_e values of the SP5 core samples is not uniform. The minimum D_e value increased by 35 ± 2 Gy compared to an increase of 106 ± 9 Gy for the maximum $D_e$value. We hypothesise that the skewness evident in the MAM and MAX D_e values is due to the way in which the SP5 core was measured. First, the core was not fully rotated 360° during analysis: a routine practice at the ACMM to reduce instrument time. Second, the x-rays that penetrate the core effectively attenuate as they pass through the sediments; it is this attenuation that allows for the μ-CT reconstruction of the core. The outcome of both these points is the deposition of higher doses at the edges of the core in comparison to that deposited at the centre, at least for part of the core that was exposed during radiation. It is not, therefore, possible to take into account the effects of μ-CT-induced irradiation on the sample.

7.7 DISCUSSION

7.7.1 μ-CT SCANNING AND ITS APPLICABILITY TO RESIN-IMPREGNATED SEDIMENTS

In the context of BM, it is fortunate that, for this study, those grains with the highest β-D_r were also those with the highest density. In situations such as this, it is clear that the μ-CT technique is exceptionally powerful in its ability to detect and resolve the three-dimensional position of these heavy mineral grains, regardless of the resolution used. However, the resolution of the scanned sediments places constraints on the appropriateness of the results for further use in different areas. For example, in this study the low resolution scan was sufficient to categorise and extract the heavy mineral grains over a relatively large volume of sediment, in comparison to that produced by the high resolution scan. Yet, the use of the low resolution μ-CT scan would be an inappropriate scaffold on which to develop digital Monte Carlo

simulations of β-D_r due to the poor clarity of grain boundaries and increased partial volume effects (Ketcham & Carlson 2001, p 391). Thus, the choice of resolution for future studies will depend upon the aims specific to the investigation.

The ability to separate heavy minerals that may produce a higher than average β-D_r from the surrounding sedimentary matrix would not have been achieved had K-feldspars been the mineralogy under investigation here. The close x-ray attenuation coefficients of K-feldspar and quartz (and clay if present) results in considerable overlap in the greyscale values and the inability to separate or indeed distinguish one mineralogy from the other (Figure 7.2). However, one possibility for future investigations would be to adjust the energy level of the x-ray beam during μ-CT scanning (120 KeV was used in this study) to take advantage of the regions where the x-ray attenuation coefficients of K-feldspar and quartz are most dissimilar; such as between 40 and 60 KeV (Ketcham & Carlson 2001, Ketcham 2005b), thereby optimising the ability to digitally resolve these mineral species.

7.7.2 3D DISTRIBUTION OF HEAVY MINERALS

The central premise of BM rests upon the spatial distribution of beta particle-emitting mineral species having a non-uniform, heterogeneous distribution (Nathan *et al.* 2003, Mayya *et al.* 2006, Guérin *et al.* 2012b). For each of the SP5 core slices (i.e., Slices 1 to 3) the distribution of heavy minerals was broadly homogeneous with consistent proportions (1.4 to 1.8%; Table 7.1). Although the μ-CT analysis is apt at differentiating heavy mineral grains from the surrounding sediment matrix, it cannot, however, quantitatively differentiate between the mineral species that constitute the heavy mineral class. It is plausible that the vast majority of the heavy minerals may be comprised of relatively radioactively inert mineral species.

Heavy mineral species found within Slices 1 to 3 (Figure 7.3) contain an unknown quantity of radioactively 'hot' heavy minerals (e.g., zircon) as well as those that are relatively 'cold' in terms of their radioactivity (e.g., hematite) as determined by pXRF analysis. The β-D_r maps produced for Slices 1 to 3 revealed regions with

significant variations in the β-D_r even within the small (6.25 mm^2) area of each slice investigated, and range from 0.32 ± 0.12 to 0.97 ± 0.19 Gy/ka. We conclude that while the μ-CT can differentiate the heavy mineral fraction from the surrounding matrix, without additional investigation into the distribution of radionuclides important to OSL dose rates (i.e., U, Th and K), in conjunction with μ-CT, the μ-CT results, standing alone, are meaningless with respect to identifying BM.

7.7.3 THE APPLICABILITY OF μ-CT AND PXRF TO SEDIMENTS UNDERGOING OSL

It is apparent that, although generally quoted as being a 'non-destructive' analytical technique, the μ-CT method, at least for samples undergoing OSL analysis, is severely detrimental in terms of the D_e being recorded in the mineral grains of the core samples. Having undergone two rounds of μ-CT scanning (one high and one low resolution), the effect of this x-ray irradiation is clearly seen in the distribution of D_e values obtained for Slice 4 (Figure 7.7b). A comparison with the D_e values for SP5 presented in Chapter 5 (i.e. grains with a natural dose not exposed to μ-CT) reveals a greater than four-fold increase in weighted mean D_e; 16 ± 1 compared to 67 ± 4 Gy. Additionally, the x-ray irradiation is non-uniform which we consider to be the result of the attenuation of the x-ray beam as it passes through the sediment core, as well as the incomplete rotation of the core sample during μ-CT scanning.

The results of the pXRF button D_e distribution are also worth mentioning here. Given that the 180-212 μm sand grains used in the making of the resin button were sun-bleached for a number of days, it is clear that the pXRF also deposits a measurable radiation dose (2.4 ± 0.2 Gy) during analysis and that this dose, is itself, not uniform. The presence of ~10 grains that have D_e values of >7 Gy can be considered to be the result of multiple irradiations/measurements of the grains located at positions of overlap between pXRF measurement positions. These findings are supported by the work of Davids *et al.* (2010) that found that a dose of >2 Gy could be measured in Al_2O_3:C grains embedded in a sediment core following

analysis using an ITRAX XRF core scanner. In a similar fashion to the μ-CT, then, the pXRF can also be considered destructive, but to a much lesser extent, in terms of depositing additional dose to the sediments being investigated.

7.8 CONCLUSION

This study aimed to investigate the distribution of beta particle-emitting heavy mineral grains in three-dimensional space, and its relationship with OD in the resulting distribution of single-grain OSL D_e values. This was to be carried out using the μ-CT technique as a means of determining the spatial positioning of heavy mineral grains within undisturbed sediment core samples. The ability of the μ-CT method to distinguish heavy mineral species from the remaining sediments (i.e., quartz, clay, feldspar, voids and pores) was successfully demonstrated at both low (29.64 μm per pixel) and high resolution (15.05 μm per pixel) in a clay-rich (SP2) and 'clean' sand (SP5) resin-impregnated core sample.

Quantitative analysis of the μ-CT low resolution scan of the SP5 core was carried out using ImageJ software to extract the 63–180 μm grain size of the heavy mineral fraction from the remaining sediment. Visualisation of the three successive 3 mm thick slices coming from the SP5 core revealed a homogenous distribution, and consistent proportions (between 1.4 and 1.8%), of heavy minerals in each slice. Further investigation using pXRF, however, revealed that this distribution of heavy minerals (determined using μ-CT) resulted in heterogeneous β-D_r distribution. We concluded that this discrepancy was the result of the inability of the μ-CT technique to differentiate between heavy mineral grain species. Thus, a proportion of the heavy mineral grains in each of the SP5 slices is considered to be composed of relatively radioactively 'inert' minerals such as ilmenite and/or hematite.

The ultimate goal of this study was to link the proportion of heavy mineral grains within each sediment core slice to the amount of OD present within each. We hypothesised that as the heavy mineral proportion increases, the amount of OD would decrease and the β-D_r will become closer to that of the infinite dose matrix

assumption. However, this hypothesis could not be tested due to the deposition of dose into the quartz grains during both μ-CT (67 ± 4 Gy) and pXRF (2.4 ± 0.2 Gy) measurements.

The aims of the current investigation were only partially achieved. It is clear that the μ-CT technique does, indeed, have the ability to resolve the heavy mineral fraction, and through the use of ImageJ software, to visualise the data as a three-dimensional model. However, the irradiation of the sample with x-rays during the μ-CT analysis, as well as the pXRF study, has been 'destructive,' in terms of the deposition and absorption of dose in the quartz grains. Thus, although suitable for the investigation of three-dimensional geometries and the inter-relationship of the sediment grains, the μ-CT technique is not suitable for those sediments that are then to be measured using OSL.

7.9 ACKNOWLEDGEMENTS

I would like to acknowledge the facilities as well as the scientific and technical assistance from the staff in the ACMM (Australian Centre for Microscopy and Microanalysis) at the Electron Microscope Unit, The University of Sydney.

SECTION SUMMARY

In this chapter I have assessed the applicability of μ-CT to: 1) detect three dimensional distribution of heavy minerals in resin-impregnated core samples, and 2) use this information to account for OD in D_e values measured from sediments taken from the same core following μ-CT analysis. While the first outcome has been realised, the second outcome has not.

The μ-CT method can clearly resolve the distribution of heavy minerals within the MacCauley's Beach sedimentary cores, regardless of overall sedimentology of the sample. However, it cannot distinguish between the various heavy mineral species. More frustratingly, the effect that μ-CT x-ray beam was not realised until after the D_e distributions were measured from the core samples. While this method can be used to investigate sedimentary composition, once scanned this D_e recorded within the sedimentary grains are effectively corrupted by the deposition of x-ray radiation dose.

The three dimensional reconstructions do have potential use in future work. The increasing attractive method of computer simulations and Monte Carlo modelling of β-D_r distributions currently suffers from the use of unrealistic and over simplistic sedimentary geometries. The digital reconstructions of the sedimentary geometries, however, could be imported into these computer programs and used as a realistic scaffold over which to develop and conduct β-D_r modelling studies.

Chapter 8

Shedding light on a burning question: luminescence characteristics, dosimetry and OSL ages from Pech de l'Azé IV, France

OSL dating of sedimentary quartz grains remains largely unexplored in south-western France, although more studies are being conducted in the present time. The nearby site of Roc de Marsal, containing sediments derived from the same source geology as Pech IV, is one of the few OSL studies conducted in this region but presents little information in the way of the intrinsic OSL behaviour of quartz. This paucity in our understanding requires that the range of intrinsic behaviours of Pech IV quartz grains first be investigated. The extensive and dichotomous site formation history of Pech IV details a period of intensive anthropogenic burning in Layer 8 and a contrasting period of predominantly geogenic processes, thereafter. The influence of these two different modes of site formation, with respect to the intrinsic and extrinsic factors, also needs to be addressed. Finally, with no previous OSL work conducted at Pech IV, applicability of this method in the systematic dating of the sediments is also to be investigated.

Aims of this chapter:

- *determine the variability in quartz OSL behaviour at Pech IV*
- *assess the influence of site formation processes on the intrinsic and extrinsic factors that can potentially influence the De distribution of single grains of quartz*
- *determine the feasibility of single-grain OSL to produce a chronological framework for Pech IV*

ABSTRACT

The feasibility of single-grain OSL dating was investigated at the Mousterian site of Pech de l'Azé IV (Pech IV), located in the southwest of France. Pech IV preserves a long record of Mousterian Industries that proved to be critical in the arguments put forward by François Bordes to explain Middle Palaeolithic culture. Here, the intrinsic luminescence characteristics of six sediment samples were examined and characterised with particular attention paid to the effect of extensive anthropogenic burning practices in the basal unit (Layer 8) compared to the remaining unburnt sedimentary strata. A 'low' preheat treatment of 180°C prior to measurement of the OSL signals was determined to be capable of recovering a known laboratory-administered beta dose, and was used in the single-aliquot regenerative dose procedure used to determine the equivalent dose (D_e) for our six samples. Comparison of the luminescence characteristics of the burnt and unburnt sediments reveals marked differences in their intrinsic behaviours, which were considered to be the result of the sensitisation of the burnt grains due to intensive and extensive heating during antiquity. The single-grain OSL ages of 95 ± 4 ka for Layer 8 (weighted mean of four sub-samples), 69 ± 6 ka for Layer 5B and 65 ± 5 ka for Layer 4A, are consistent with previously published TL ages from these, and bounding, units. The procedures developed and results presented herein imply that the sediments preserved at Pech IV are well suited to the OSL method and can be applied for age determination of all sedimentary layers preserved at the site.

8.1 INTRODUCTION

Over the past few decades, numerous dating studies have been undertaken in the south-west of France to provide a chronological framework for the cultural development, and variability, of the Mousterian technocomplex – the stone tool industries associated with western European Neanderthals. The overarching goal of these studies was to differentiate if the variability in the Mousterian Industries was due to cultural development over time, or the result of contemporaneous cultural groups. By far the most frequently used techniques were radiocarbon (^{14}C) dating of bone and charcoal (e.g., Vogel and Walterbolk 1967, Soressi et al. 2007, McPherron et al. 2012), thermoluminescence (TL) dating of burnt flint (e.g., Bowman and Sieveking 1983, Valladas et al. 1986, Valladas et al. 2008, Valladas et al. 1999, Valladas et al. 2003, Guérin et al. 2012a), and electron spin resonance (ESR) dating of tooth enamel (e.g., Grün et al. 1991, Grün et al. 1999, Mellars and Grün 1991, Soressi et al. 2007). Yet, each of these methods of age determination requires that specific material be present in the deposit, and, for ^{14}C dating only, is no older than ~45–50 ka. The outcome of these studies is a 'hazy' understanding of the Mousterian chrono-stratigraphic record. Optically stimulated luminescence (OSL) dating of sedimentary grains remains largely unexplored in south-western France, although more studies are being conducted in the present time (e.g., Guérin *et al.* 2012a, Soressi *et al.* 2013, Jacobs et al. submitted). This radiometric technique has been previously used to clear the 'haze' surrounding the timing and transition of important stone tool industries at archaeological sites in southern Africa (Jacobs and Roberts 2008, Jacobs et al. 2008b).

In 2011, an OSL dating project was launched at the three closely-located archaeological sites of Pech de l'Azé (Pech I, II and IV). These three sites, and the Mousterian artefacts recovered from them, played a key role in the arguments proposed by Françoise Bordes in the renowned Bordes-Binford debate. The aim of this study was to construct reliable OSL chronologies for the sediment sequences exposed at all three sites that will enable us to link the sites using a common chronological yardstick. As the OSL method uses mineral grains for age

determination, there is potential to provide radiometric ages for each sedimentary layer preserved at the Pech sites. Since little is known about the applicability of OSL dating to the sediment found in this region, it was deemed fundamentally important to systematically investigate the luminescence properties of the sediment to inform how best to measure and interpret the results obtained from dating these sediments. The complications experienced by Guérin *et al.* (2012a) in their OSL dating study at the nearby site of Roc de Marsal (~25 km west) supports this assertion.

The aim of this paper is, therefore, to provide the necessary data to support all OSL ages that will be reported for Pech IV in this study, and elsewhere for Pech I, II and IV. The intrinsic luminescence characteristics and behaviour (both TL and OSL) of quartz grains collected from two different types of sediment found at Pech IV will be explored. The first type of sediment is broadly representative of the sediment found at all three sites and is mainly geogenic in origin, whereas, the second type experienced extensive burning during antiquity and is dominated by an anthropogenic signature. The effect that this burning may have had on the luminescence characteristics of the sediment are of particular interest. The possible extrinsic factors (both syn- and post-depositional) that may influence estimation of the burial dose and environmental dose rate of our samples is also explored. A complete explanation of how the age estimates were derived and why these specific methods were used is also given.

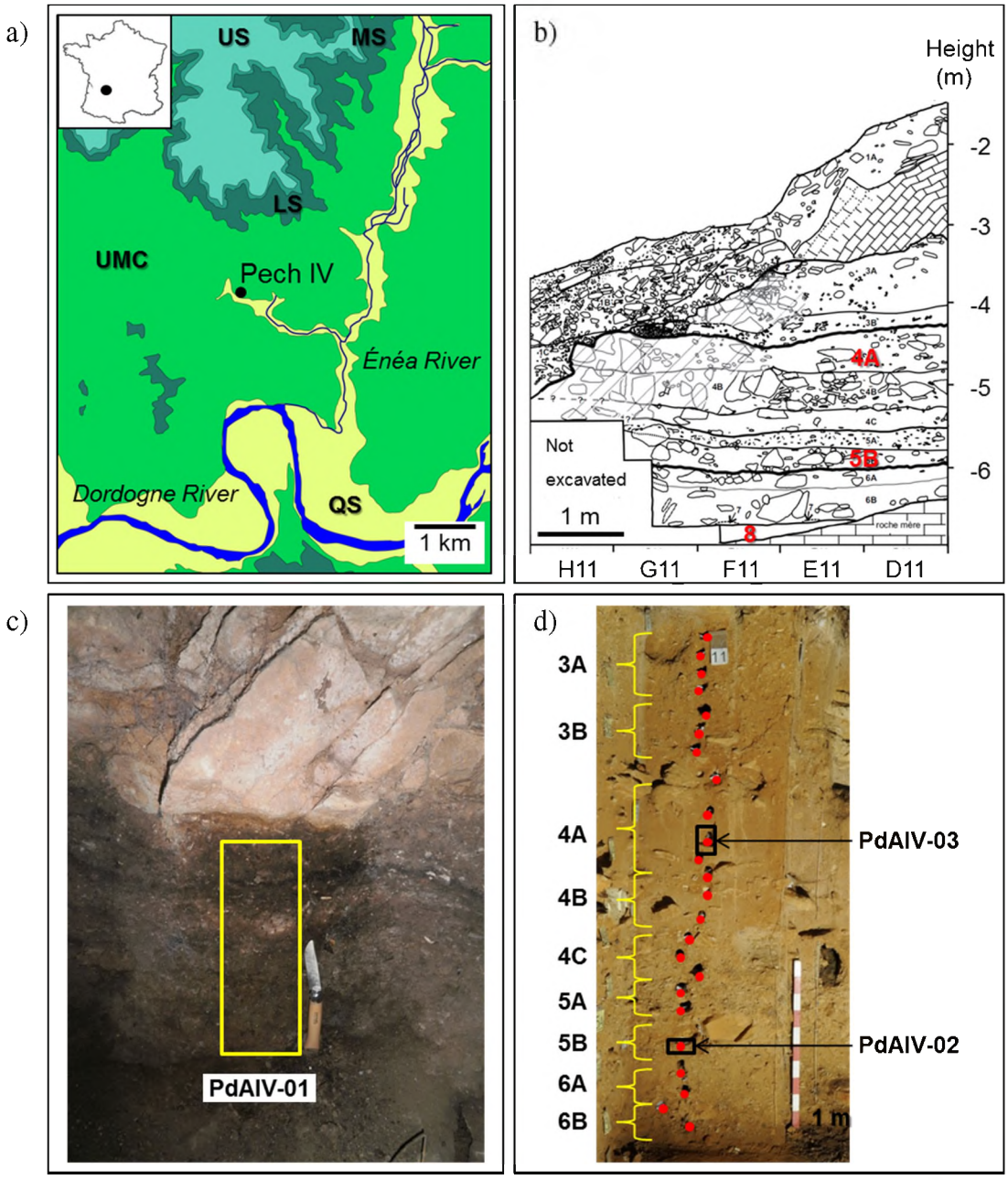

Figure 8.1. A) Geological map of the region surrounding the Pech de l'Azé IV site. US – Upper Santonien limestone; MS – Middle Santonien limestone; LS – Lower Santonian limestone; UMC – Upper and Middle Coniacien limestone; QS – Quaternary sediments. Inset: French map and relative location of Pech IV (black circle). B) Site stratigraphy of Pech IV presented in Turq *et al.* (2011). C) Location photograph of PdAIV-01 sediment column with knife for scale (15 cm). D) Location photograph of northern wall sample column showing positions of PdAIV-02 and PdAIV-03 block samples in relation to the stratigraphy and OSL sample locations (red circles) presented in Jacobs *et al.* (submitted).

8.2 OSL SAMPLE COLLECTION AND DETAILS

A total of 27 sediment samples were collected for OSL dating from Layer 8 through to Layer 3A in an almost continuous sediment column (Figure 8.1c and d) in 2011. The context and results obtained for these samples are reported in Jacobs *et al.* (submitted). Three intact and orientated sediment blocks from Layer 8 (PdAIV-01), 5B (PdAIV-02) and 4A (PdAIV-03) (Figure 8.1c and d) were also collected for more detailed methodological investigations and to explicitly examine the effect that various site formation processes may have had on the sediment. These samples are the focus of this study.

The sediments were cut from the exposed sedimentary profiles using a sharp knife. Prior to removal, two of the block samples (PdAIV-01 and PdAIV-02) were coated in plaster bandages to provide structural support during removal and transportation. The block samples were then removed from the section, wrapped in tissue paper, secured with packing tape and transported back to the laboratory.

Sample PDAIV-01 was collected as a column ~30 cm long and 12 cm wide, and sampled the entire height of Layer 8 in square H14 (Figure 8.1c). The dark brown/black colour of the sediment in Layer 8 suggests that anthropogenic processes (in particular burning) were involved in its formation. Micromorphological analysis of the sediments show that, in addition to geogenic sands, silts and clays, a significant amount of anthropogenically derived material is also found throughout Layer 8 (Dibble *et al.* 2009). These include the presence of burnt and unburnt bone, charcoal, flint and ash. Goldberg *et al.* (2012) suggest that this layer is the result of intensive and continuous construction of fireplaces and the redistribution of hearth ash across the cave floor.

Samples PdAIV-02 and PdAIV-03 were collected from square C11 and sampled Layer 5B and 4A, respectively (Figure 8.1d). The processes responsible for the formation of these two layers are predominantly geogenic and provide an

interesting contrast to Layer 8. The sediment in all three layers is derived from the disintegration of the host limestone that is found throughout the region (Figure 8.1a), the weathering of exotic minerals in the limestone to form clays, and/or in-washing of materials from the 'siderolitique' soil profile formed on top of the limestone above the cave (Goldberg et al. 2012, Turq et al. 2011). The juxtaposition of anthropogenic and geogenic formation processes in sediment derived from the same source means that the effect that these processes have on the luminescence and dosimetric characteristics of the sediments can be investigated.

Additional, and stratigraphically analogous samples, were also used as part of this study. This includes a small bag of light-exposed sediment collected from Layer 8 (PDL10-01) during the active excavation seasons between 2000–2003, and two OSL samples (PdLIV-1 and PdLIV-8) collected in 2011 from Layers 8 and 5B, respectively.

8.3 LABORATORY SUB-SAMPLING PROCEDURES AND SAMPLE PREPARATION

PdAIV-02 (Layer 5B) and PdAIV-03 (Layer 4A) was sub-sampled in the laboratory by removing a small portion of sediment from each under dim, red light conditions. These portions were then split: one half to be used for OSL measurements, the other to determine the β-D_r. These two samples are equivalent to PdLIV-8 and PdLIV-18, respectively, presented in Jacobs *et al.* (submitted). The remaining undisturbed parts of the two blocks were then impregnated with polyester resin for spatially-resolved β-D_r investigations.

PdAIV-01 covered the entire height of Layer 8 (~30 cm) (Figure 8.1c and 8.2). We collected four sub-samples from this block to gain a better understanding of the age profile of the sediment and to further investigate the coarse- and finer-scale spatial variation in the β-D_r. Before sub-sampling, the entire block was first

impregnated with polyester resin and cured, and then transversely sectioned using a rock saw. Under dim red light conditions, one half of the block was sectioned using a Beuhler Isomet 1000 precision saw to obtain 4 sub-samples, each 14 mm in height and labelled A (top) to D (bottom) (Figure 8.2).

The choice of sub-sample location was based on macroscopically visible changes in sedimentary characteristics (Figure 8.2). Sub-sample A was taken from a dark-brown unit rich in charcoal material; sub-sample B from a layer that was lighter brown in colour and contained ash-coloured material; sub-sample C from a dark brown layer similar to sub-sample A; and sub-sample D from the massive basal, light brown layer (Figure 8.2). Sub-samples PdAIV-01-D and PdAIV-01-B are roughly equivalent to samples PdLIV-1 and PdLIV-2, respectively, presented in Jacobs *et al.* (submitted); these samples extend horizontally further into the sampled section as these samples were collected using opaque plastic tubes after the block samples were removed.

From each of the ~14 mm thick sub-samples (A-D), two 3 mm-thick slices were then cut with the Isomet saw from the top and bottom surfaces (labelled Upper and Lower) of each sub-sample. These 3 mm slices were used in the radionuclide distribution study presented in Section 8.8.2.1. The remaining ~6 mm thick sub-samples sandwiched between the two ~3 mm thick slabs were then bisected (Figure 8.2); one half was used for single grain OSL measurements and the other half for β-D_r determination. Both these sub-samples were then placed in toluene, and then acetone, to disaggregate the sample and to remove the mineral grains from the polyester resin. All six OSL samples, as well as sediment from PdL10-01, PdLIV-1 and PdLIV-8, as well as a limestone pebble from Layer 5B, were prepared for OSL measurement using standard laboratory techniques and procedures (Wintle 1997). See Chapter 3, Section 3.2 for further details.

D_e values were estimated for individual 180–212 μm in diameter sand-sized grains for all the samples. We used the standard Risø single grain aluminium discs (Bøtter-Jensen *et al.* 2000) for measurement of all individual grains. All single aliquots were made using stainless steel discs and 'Silkospray' oil to adhere grains to

the surface of the disc in a monolayer. All D_e measurements were made using automated Risø TL/OSL readers, either TL/OSL-DA-15 or TL/OSL-DA-20 models (Bøtter-Jensen *et al.* 2000, Bøtter-Jensen *et al.* 2003). See Chapter 3, Section 3.2.2 for further details. The D_e of single grains of quartz were determined using the single aliquot regenerative-dose (SAR) procedure described in Table 8.1, Chapter 3, Section 3.2.4 and elsewhere (e.g., Murray & Wintle 2000, 2003). The D_e and associated uncertainty associated were determined using Analyst 3.24.

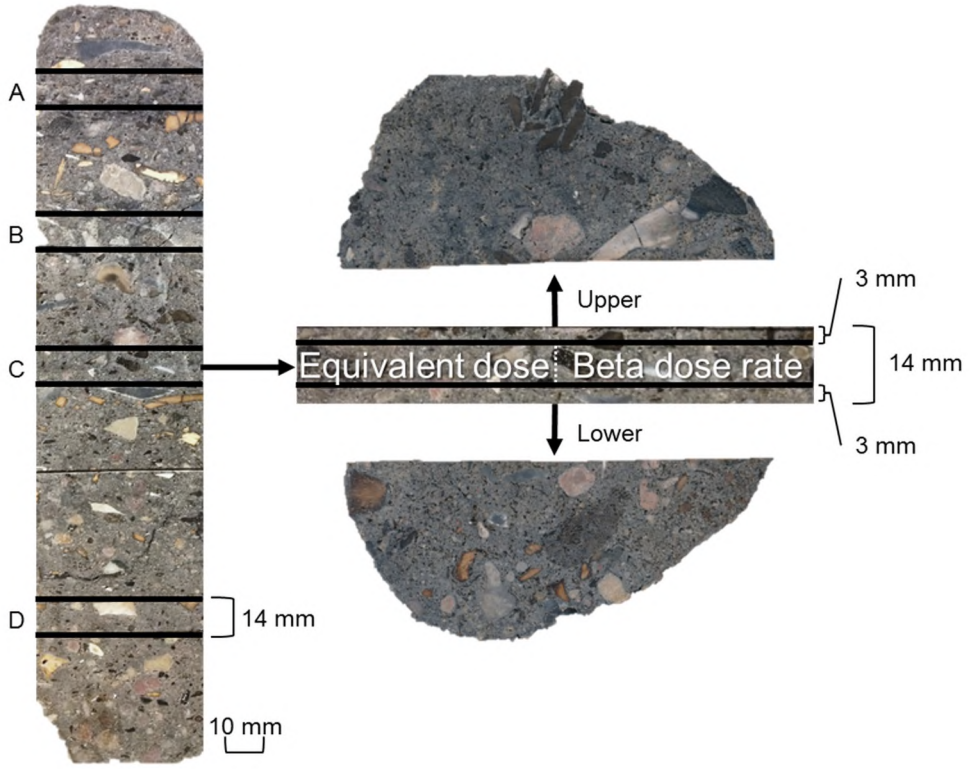

Figure 8.2. Layer 8 sediment column and sampling strategy. Four 14 mm sub-sample slabs were cut from the resin-impregnated column (A–D). The slabs were sectioned under dim red light conditions using a water-cooled, high precision saw with a blade width of 0.8 mm. A 3 mm slice was removed from the top and bottom of each 14 mm thick slab. The remaining 6 mm thick slab was then bisected with one half being used for D_e determination and the other for beta dose rate measurements.

Table 8.1. SAR procedure used throughout this study for dose recovery experiments and the determination of D_e values for naturally-irradiated quartz grains.

Step	Treatment	Purpose
1	Preheat (PH1) to T1 ˚C for 10 s	–
2	Stimulate using focussed green laser for 2 s at 125 ˚C	Induce OSL from natural or regenerative dose
3	Test dose	–
4	Preheat (PH2) to T2 ˚C for 5 s	–
5	Stimulate using focussed green laser for 2 s at 125 ˚C	Induce OSL from test dose
6	Regenerative dose	–
7	Return to step 1 and repeat at least 3 times altering the size of the regenerative dose	–
8	Give 0 Gy dose and repeat steps 1–5	Check for recuperation
9	Repeat first regenerative dose and steps 1–5	Check recycling ratio
10	Repeat first regenerative point	–
11	Stimulate using infrared diodes for 40 s at 50 ˚C	–
12	Repeat steps 1–5	Check for feldspar contamination

8.4 LUMINESCENCE CHARACTERISTICS OF MULTI-GRAIN ALIQUOTS

8.4.1 LINEARLY MODULATED OSL SIGNAL COMPOSITION

The contribution of the various OSL components was investigated using linearly modulated OSL (LM-OSL). Rather than using a constant stimulation power, here the power output of the blue LEDs was ramped from 0 to 90% (0–30 mW/cm^2) to resolve the OSL signal components as a function of optical sensitivity – this is termed linearly modulated (LM-) OSL (Bulur 1996, Bulur *et al.* 2000, Choi *et al.* 2006). The LM-OSL signal provides a series of peaks that relate to the various OSL signal components each termed according to their rate of decay, including: ultrafast (UFC), fast, medium, slow 1 (S1), slow 2 (S2), slow 3 (S3) and slow 4 (S4) (Singarayer and Bailey 2003, Jain et al. 2003). The contribution of each component to the total LM-OSL signal can be determined through mathematically deconvolution of the meauresed signal. Throughout this paper the terminology of Jain *et al.* (2003) is use in the categorisation of LM-OSL components (Table 8.2).

The LM-OSL measurments were made using a single 5 mm aliquot of 180–212 μm in diameter quartz grains from the burnt (PdAIV-01-C) and both unburnt (PdAIV-02 and -03) samples. Three measurements were made and each LM-OSL measurement was preceeded by either a natural or laboratory beta dose that was preheated to 180°C for 10 s. First, the natural-dose LM-OSL curve was measured for 1 hr (3600 s) while holding the aliquot at 125°C. Each aliquot was then given a regenerative dose of ~105 Gy, preheated to 180°C before the LM-OSL signal was measured again as above. This was then repeated but with a preheat tof 260°C for 10 s. Between each LM-OSL measurement a blue LED bleach for 1000 s at 125°C was used to bleach the OSL signal back to a stable background level.

The resulting natural-dose LM-OSL curves, corrected for background contribution, are presented in Figure 8.3a. The LM-OSL background count rate was measured

from a blank stainless steel disc coated with a 5 mm layer of 'silkospray.' The LM-OSL signal was measured over 3600 s while ramping the blue LEDs from 0 to 90%. The resulting LM-OSL signal could be fit using a quadratic equation ($y = 0.0000007x^2 + 0.0116x + 106.79$) and is shown in Figure 8.4. This curve is similar to that measured by Choi *et al.* (2006), which was explained as the slight variation is the stimulating wavelength as the power of the LEDs is increased. The resulting quadratic function was subtracted from each of the LM-OSL measurements, as a measure of background signal, for all samples investigated in this study. This was carried out prior to the mathematical deconvolution of the LM-OSL signals.

Table 8.2. Table of LM-OSL resolved components presented in Jain *et al.* (2003) showing *b* value and relative PIC values (with respect to the Fast component) for each LM-OSL signal component.

Component	*b* value (s^{-1})	Relative PIC
Ultrafast	32	13
Fast	2.5 ± 0.2	1
Medium	0.62 ± 0.05	0.2
Slow 1	0.15 ± 0.03	0.06
Slow 2	0.023 ± .005	0.01
Slow 3	0.0022 ± 0.0002	0.001
Slow 4	0.00030 ± 0.00001	0.0001

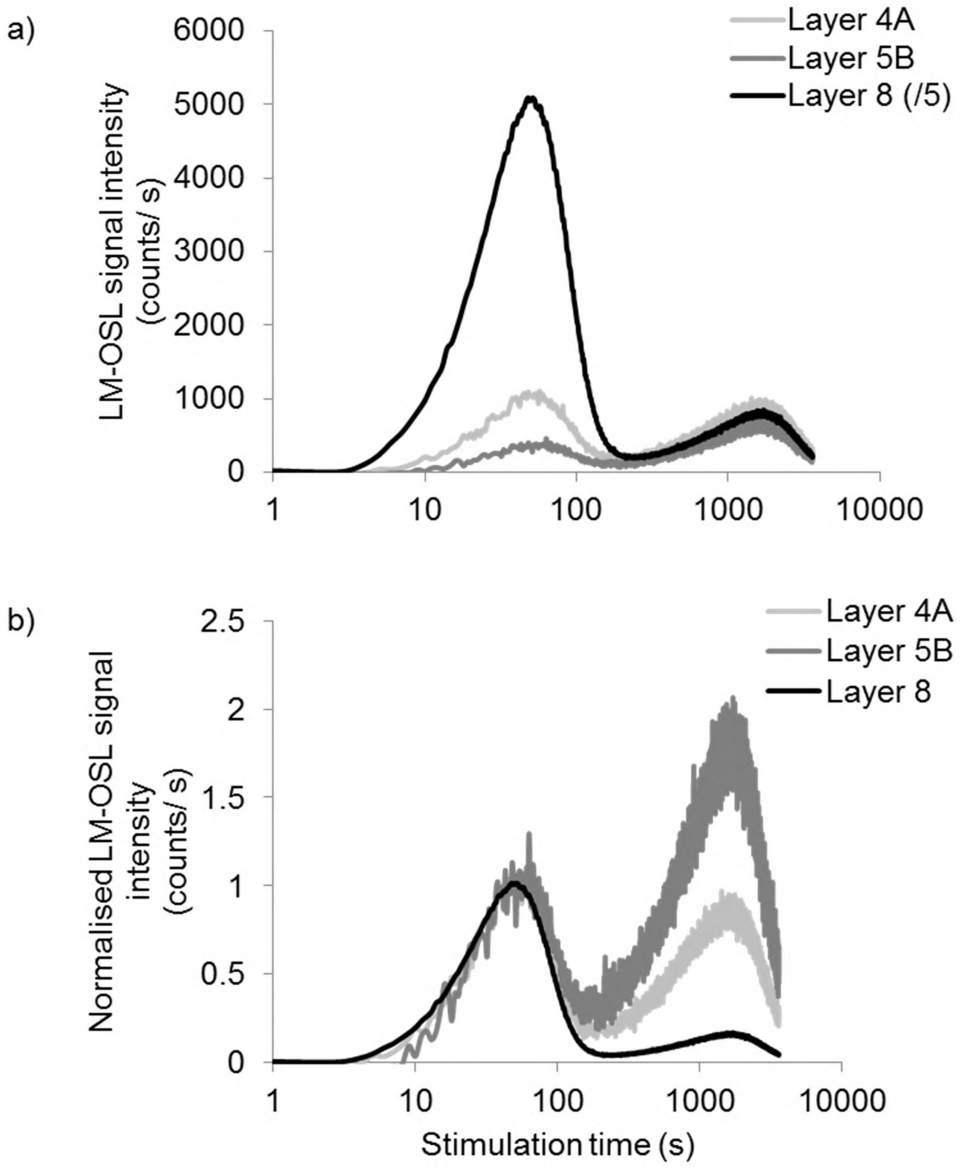

Figure 8.3. a) Background-corrected LM-OSL curves for a 5 mm aliquot of 180–212 µm grains from Layers 8 (PdAIV-01-C), 5B (PdAIV-02) and 4A (PdAIV-03). The LM-OSL curve for the Layer 8 sample is one fifth of the measured LM-OSL signal and presented as such for clarity and comparison with the other curves. b) Same as in a) except the fast component peak has been normalised to show the proportional contribution of the slow component peak.

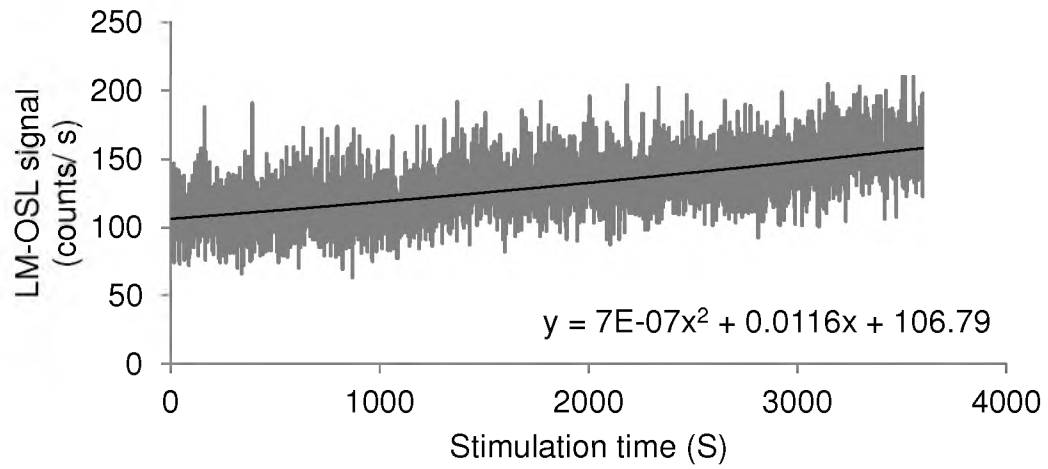

Figure 8.4. a) Background LM-OSL signal for Risø 5 (and quadratic line-of-best-fit equation) for one blank stainless steel disc covered with 5 mm diameter circle of 'silkospray' oil.

Figure 8.3a reveals two distinct peaks that indicate the presence of both 'Fast' and 'Slow' components in each sample. To get a better sense of the relative contribution of the 'Slow' components compared to the 'Fast' component, the same data is presented Figure 8.3b but, this time, the data was normalised to the maximum height of the 'Fast' component peak. From these data it is observed that the Layer 5B (PdAIV-02) sample has the highest contribution of 'Slow' component LM-OSL relative to the fast component of the sample; Layer 8 (PdAIV-01-C) has the smallest; and Layer 4A (PdAIV-03) falls in between.

To further investigate the thermal stability of the LM-OSL signal components, mathematical devolution of the regenerative-dose LM-OSL curves following both the 180 and 260°C preheats was carried out using the equations of Bulur *et al.* (2000) and the procedures outlined in Choi *et al.* (2006). The fitted LM-OSL components are shown in Figure 8.5 alongside their measured LM-OSL curves. Here, a maximum of three components could be fitted (Fast, S1 and S3); with only two components

(Fast and S3) fitting the LM-OSL curves for the Layer 8 and Layer 5B samples. For the samples investigated here, the detrapping probabilities of the Fast, S1 and S3 components are given by the *b* value (s^{-1}). These values were determined to be 1.1–1.5 for the Fast, 0.15 for the S1 and, between 0.0014–0.0015 for the S3 component.

Previous investigations into the thermal stability of the S3 component of Jain *et al.* (2003) (or the S_2 component of Singarayer & Bailey 2003) have shown that a reduction of 50% in the LM-OSL intensity can be achieved by preheating the sample to 260°C prior to LM-OSL measurement (Arnold et al. 2008, Jain et al. 2003, Singarayer and Bailey 2003). A similar reduction in the S3 components is evident in the three sample investigated following the same preheat. To quantify this the difference in the LM-OSL intensities, the fitted S3 components following the 260°C preheat was subtracted from the equivalent S3 component following 180°C, before dividing this difference by the latter. As such, the S3 component reduced by 66, 56 and 55% for Layer 8, 5B and 4A, respectively, following a 260°C preheat.

The presence of the S3 component in all the samples investigated here presents a number of important points to consider. First, given the thermal instability of the S3 component, it is important that this OSL component is removed prior to OSL measurement (for dating purposes) to reduce the likelihood of producing erroneous D_e values. This could be achieved using a hot optical 'wash' (i.e., a 40 s blue LED stimulation at ~280°C) at the end of each SAR cycle (Murray & Wintle 2003, Jacobs *et al.* 2006a, Gliganic *et al.* 2012a) or a higher preheat temperature prior to OSL measurements. As shown in Figure 8.5, heating to 260°C does not entirely deplete the source traps of the S3 component. An alternative means of circumventing the contribution of the S3 component would be to use single grains of quartz, as opposed to multi-grain aliquots. In this case, those grains with no S3 component can be readily distinguished and actively selected for D_e calculations.

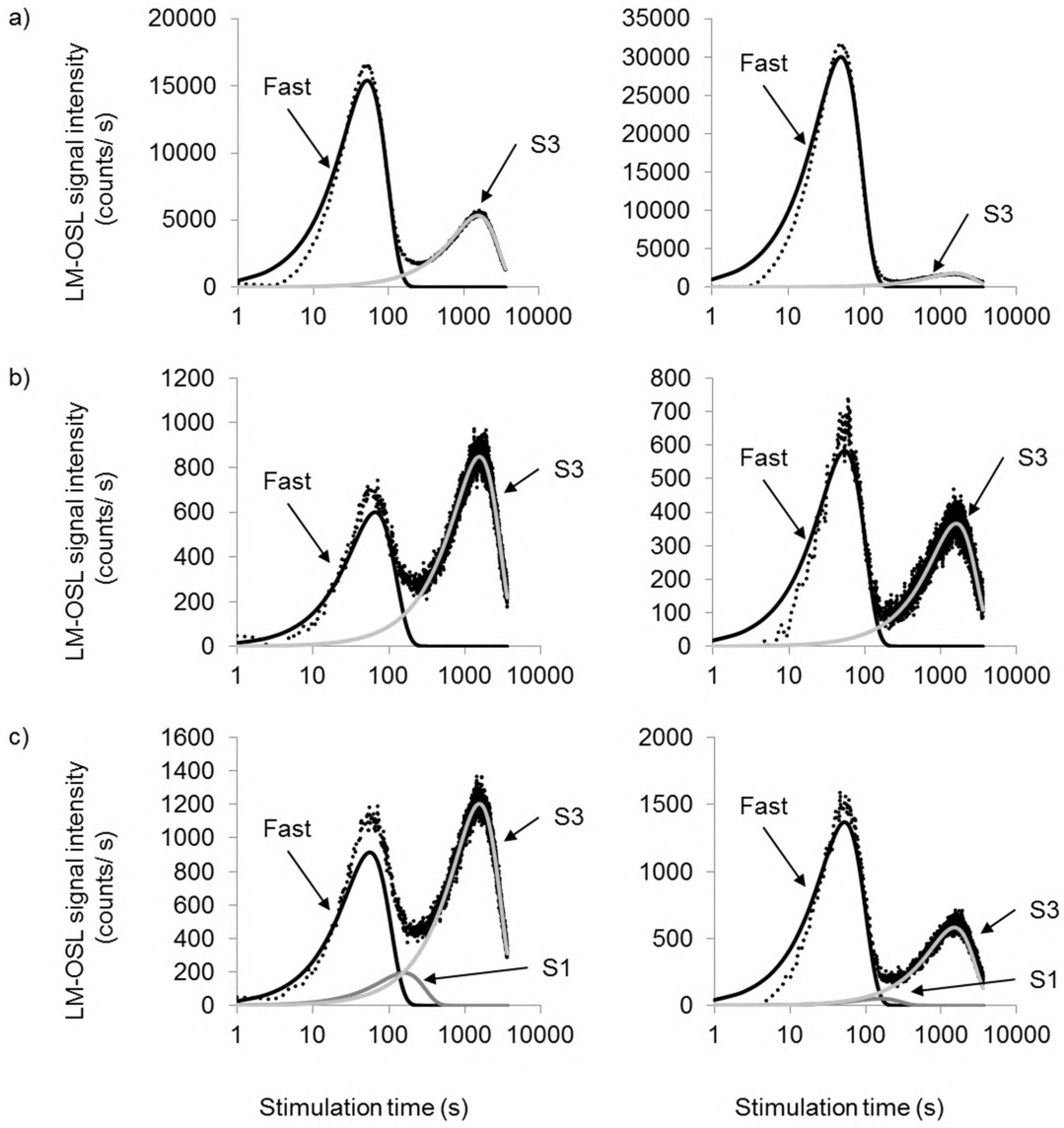

Figure 8.5. Background-corrected LM-OSL curves and fitted components for a) Layer 8; b) Layer 5B; and c) Layer 4A for the same samples as in Figure 8.3. Each aliquot was given a ~102 Gy regenerative dose and were preheated to 180 (left image) or 260˚C (right image) for 10 s, prior to LM-OSL measurement.

8.4.2 THERMOLUMINESCENCE CHARACTERISTICS

We have demonstrated thus far that unburnt sediment have a substantially greater proportion of the thermally unstable S3 LM-OSL component of Jain *et al.* (2003). To determine the potential source trap for this component the following points were investigated: 1) the response of the natural-dose TL glow curve to preheating; and 2) the response of a regenerative-dose TL glow curve to optical stimulation using the same three samples from Layers 8, 5B and 4A (PdAIV-01-C, -02 and -03).

8.4.2.1 TL CHARACTERISTICS OF THE NATURAL SIGNAL

The effect of preheating on the TL glow curves of naturally-irradiated quartz was first examined. Four groups of three 5 mm in diameter mask-size aliquots of 90–125 μm quartz, each containing ~2000 grains, for each sample had their TL glow curves measured following either a 180, 220 or 260°C preheat for 10 s or no preheat. TL curves were measured by heating the aliquots to 500°C at 2°C/s and a background signal was subtracted. This background signal was measured for each individual stainless steel disc by repeating the TL measurement to 500°C at 2°C/s, directly after the initial TL signal was measured (i.e., no laboratory dose was given). The average TL glow curve for the 3 aliquots following treatment was calculated and normalised using the integrated TL signal between 295 and 304°C. By normalising the natural TL signals, the differences due to preheating are highlighted, while those related to TL signal variability due to intrinsic/extrinsic complications are rendered negligible. The results of this experiment are shown in Figure 8.6.

The natural TL glow curves shown in black stippled lines in each sample are comprised of the 280 and 325°C TL peaks. In Figure 8.6 these occur at ~265 and ~300°C, respectively, due to the slower heating rate (2°C/s) used here. The 280°C TL peak is more intense in the unburnt samples, when measured using U-340 filters and,

therefore, more likely to give rise to a more slowly decaying OSL signal. The 280˚C TL peak is the largest in sample PdAIV-02 from Layer 5B. This is also the sample

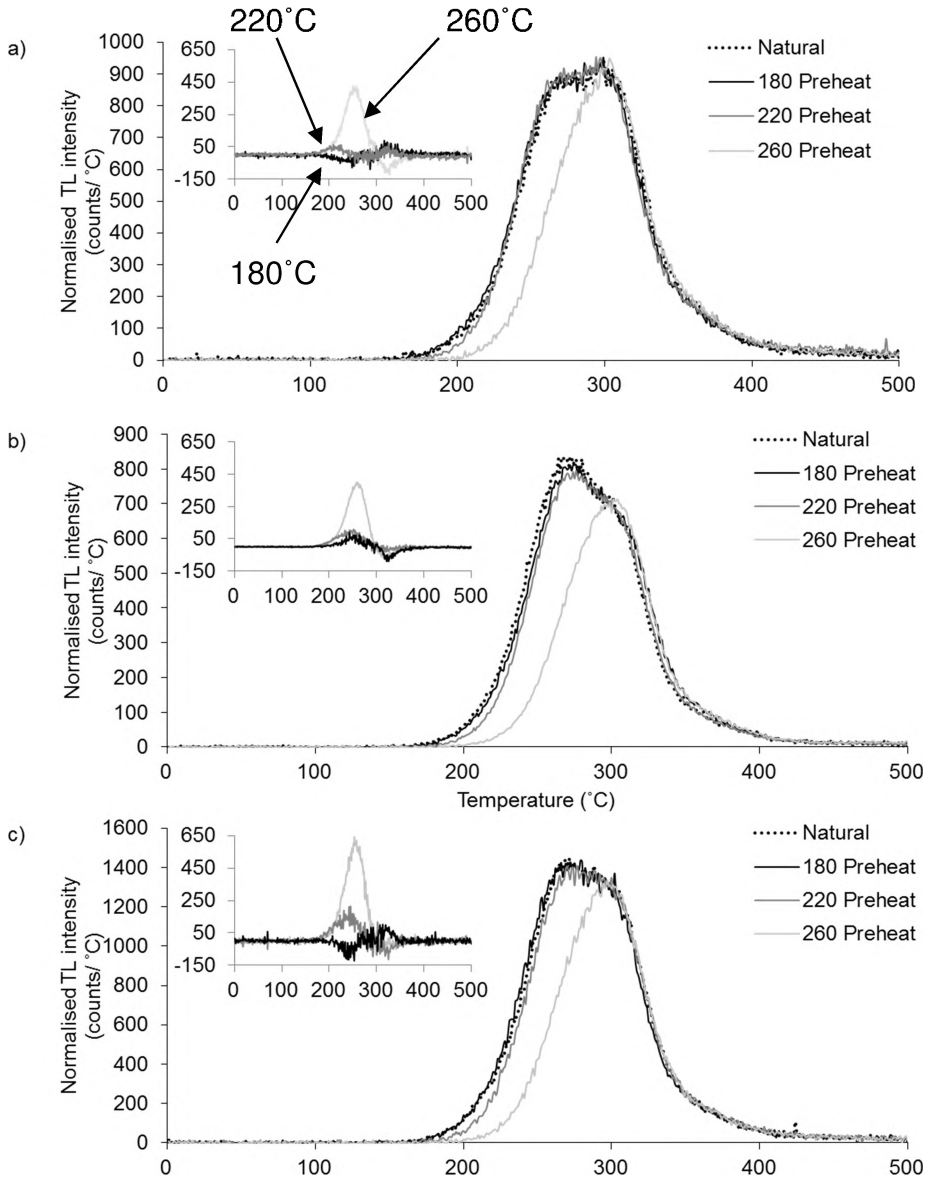

Figure 8.6. Naturally-irradiated TL curves from a) Layer 8 (PdAIV-01-C), b) Layer 5B (PdAIV-02) and c) Layer 4A (PDAIV-03). Samples were heated at a rate of 2˚C/s and normalised to the peak height between 295 and 304˚C. The inset images in each case are the difference between the natural 180 (black line), 220 (mid-grey line) and 260˚C (light grey line) preheat curves. The difference between these various preheating treatments is thought to be caused by the thermal erosion of charge form the 325 °C TL peak.

with the highest proportional contribution of the S3 component (Figure 8.3). The 325°C TL peak is more pronounced in PdAIV-01-C from Layer 8 and is commonly referred to as the 'rapidly-bleaching peak' (Wintle and Murray 1997, Spooner et al. 1988, Spooner and Questiaux 2000). It should be noted, however, that only a portion of this peak is bleached during light exposure.

Also shown in Figure 8.6 are aliquots that were measured in the same way except that one of the three preheat temperatures preceded the measurement of the TL glow curve. The differences between the natural TL glow curves and those following the three preheat treatments are shown as insets in Figure 8.6. In each sample, there is little difference between the TL glow curves with no preheat and a preheat of 180°C; a small loss can be seen at ~260°C in PdAIV-03, but this is transferred into the 325°C TL trap. Following a 220°C preheat, however, there appears to be a greater loss of signal in the unburnt compared to the burnt samples, particularly in PdAIV-03 (Figure 8.6 insets). This result is considered to be due to the relatively greater contribution of the 280°C TL peaks in the unburnt samples. Singarayer & Bailey (2003) found that preheat temperatures as low as 220°C could start to thermally erode the S3 component. By increasing the preheat to 260°C for 10 s a much greater decrease in the TL signal can be seen (Figure 8.6 insets). The 280°C TL peak height is reduced by 30–40% in all samples and mimics the behaviour seen in the LM-OSL signals (Figure 8.5) and serves as evidence that the 280°C TL trap is likely the source trap of the S3 component.

8.4.2.2 TL SIGNALS FOLLOWING LABORATORY IRRADIATION AND LIGHT EXPOSURE

The response of the 280°C TL peak was further investigated using laboratory-irradiated aliquots of 90–125 μm quartz from the same three samples. Here, a single 5 mm in diameter aliquot of material was given a repeated ~105 Gy laboratory beta dose, preheated to 180°C for 10 s and then optically stimulated for either 0, 40, 100 or 1000 s using the blue LEDs while holding the sample at 125°C. The TL glow

curve was then measured ramping the temperature from room temperature to 500°C at 5 °C/s. As such, the 280 and 325°C TL peaks occur roughly at these positions. The results, shown in Figure 8.7, reveal that there is a substantial reduction in peak height (200, 280 and 325°C) after any given period of optical stimulation.

This result is both in line and at odds with the literature. Franklin *et al.* (1995) presented findings that the 280°C TL peak was optically insensitive for their Australian quartz samples, a result supported by the work of Wintle & Murray (1997) for their WIDG8 sample (also Australian), and noted in Packman *et al.* (2007). In contrast, Roberts *et al.* (1993) found that the 280°C TL peak was optically sensitive following a 20 hr bleach from a UV-deficient lamp, a position that was supported by the work of Arnold *et al.* (2008) who showed that the 280°C TL peak was sensitive to blue light stimulation for their Siberian quartz samples.

It is considered that the S3 slow component in the Pech IV sediments is sourced from the trap visible as the 280°C TL peak. The 30–40% decrease in the 280°C TL peak height after a 260°C preheat for 10 s mirrors the corresponding decrease in the S3 component following the same preheat treatment. The complication for the 280°C TL peak is similar, therefore, to the S3 component. For meaningful D_e estimates to be made, this peak needs to be entirely removed or remain untouched. Packman *et al.* (2007) suggested that a preheat of up to 300°C would be required to remove the 280°C TL peak from their samples. The authors noted that such a high temperature preheat would also cause the thermal erosion of the 325 °C TL peak and the associated D_e values, by extension. It has been shown in this study that a 260 °C preheat severely impinges upon the 325°C region of the naturally-irradiated samples. As was the case with the S3 component, the use of single-grain OSL measurements is an alternative means of selecting those grains with favourable OSL decay characteristics as well as circumventing problems associated with the optically sensitive and thermally unstable S3 component.

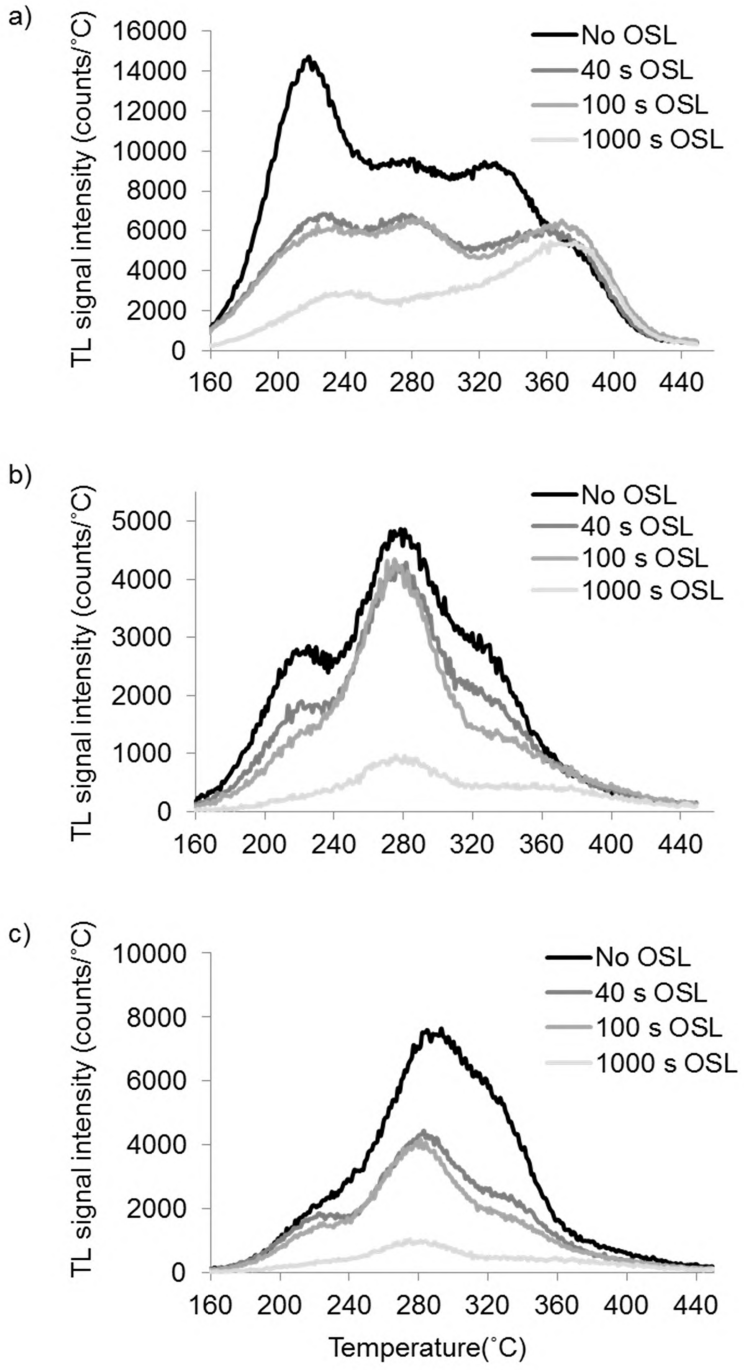

Figure 8.7. TL glow curves following a laboratory beta dose of ~105 Gy for a) Layer 8 (PdAIV-01-C); b) Layer 5B (PdAIV-02); and c) Layer 4A (PdAIV-03). The four different glow curves were measured following a preheat of 180 ˚C and a blue LED exposure of 0, 40, 100 and 1000 s blue LED stimulation at 125 ˚C. TL curves were measured at a heating rate of 5 ˚C/ s to 450 ˚C

8.5 SUITABILITY OF THE SAR PROCEDURE AND LUMINESCENCE CHARACTERISTICS OF QUARTZ GRAINS

Numerous studies have documented the grain-to-grain variability in the OSL signal of individual grains of quartz in both anthropogenic and geogenic settings (e.g., Murray and Roberts 1997, Roberts et al. 1999, Jacobs et al. 2006c, Jacobs et al. 2012, Arnold and Roberts 2011, Guérin et al. 2012a, Medialdea et al. 2014, Reimann et al. 2012, Thomsen et al. 2005). This variability manifests itself as differences in the inherent brightness of the OSL signal, and the shapes of the OSL signal decay and sensitivity-corrected dose-response curves. Thus, not every grain within a sample responds in a similar or suitable manner to the same measurement conditions. This means that not every grain that is measured will provide a reliable estimate of the D_e. The challenge is, therefore, to identify and discard those grains with aberrant luminescence characteristics before calculation of D_e and age. A standard set of rejection criteria exists that was routinely applied to screen our data sets from aberrant grains, but this does not get rid of all aberrant grains (e.g., Jacobs *et al.* 2006c). Those grains that are accepted are, therefore, further scrutinised for their OSL behaviour before being accepted for age determination. In the following sections, the following points are addressed: 1) determine the optimum measurement conditions for samples from Pech IV through a series of dose recovery tests, 2) assess the stability of the OSL signal and 3) analyse the reasons for data rejection and scrutinise the OSL behaviour of the accepted grains.

8.5.1 SINGLE-GRAIN OSL DOSE-RECOVERY TESTS

To determine the most appropriate measurement conditions for the Pech IV samples, and to validate the methods used to analyse the resulting OSL data, dose recovery tests were conducted (Murray & Roberts 1997, Roberts *et al.* 1999, Murray & Wintle 2003) on two of the samples: PDL10-01 from Layer 8 (burnt) and PdLIV-8

(equivalent to PdAIV-02) from Layer 5B (unburnt) (Figure 8.2c and d). Quartz grains (180–212 μm in diameter) from each sample were exposed to natural sunlight for at least 5 days to empty the OSL traps. A surrogate natural dose of ~41 Gy was then given to each grain using the laboratory beta source, and the individual grains measured using the SAR procedure (Murray & Wintle 2000) to determine if the known dose could be measured accurately.

In the first set of tests, six groups of 500 grains each were measured from sample PDL10-01 and the preheats applied before measurement of the natural and regenerative (PH_1) and test doses (PH_2) were co-varied (e.g., $PH_1 = PH_2$). These temperatures were systematically increased in 20°C intervals between 160 and 260°C where PH_1 was held at maximum temperature for 10 s and PH_2 for 5 s. We followed the same procedure for PdLIV-8, but only conducted three sets of measurements of >900 grains each at the same PH_1 and PH_2 temperatures (180, 200 and 260°C).

All grains were analysed using standard rejection criteria (Chapter 3, Section 3.2.4). The measured doses of all accepted grains at each preheat combination were combined using the central age model (CAM) to obtain a weighted mean measured/given dose ratio. The detailed results, including the number of accepted grains, weighted mean measured dose and overdispersion values for each preheat combination are provided in Table 8.3 and the measured/given dose ratios are shown in Figure 8.8a.

There is an inverse relationship between preheat temperature and measured-to-given dose ratio for the grains measured from PDL10-01 (Layer 8). As shown by the filled circles in Figure 8.8a, as preheat is increased the ability to measure a known dose decreases. Preheat temperatures of 160 and 180°C gave results most consistent with unity at 1σ: 1.06 ± 0.06 and 0.97 ± 0.03, respectively. Higher preheat combinations resulted in underestimation of the given dose by up to ~30% (Table 8.3). This pattern was, however, not observed for PdLIV-8 (Layer 5B). For this sample, all three preheat combinations gave measured/given dose ratios consistent with unity at 2σ (102 ± 0.05, 0.90 ± 0.05 and 1.00 ± 0.04; Table 8.3), shown as open circles in Figure 8.8a. The OD values for those combinations that have consistent

measured/given dose ratios range between 11 ± 3% (180/180°C; PDL10-01) and 20 ± 4% (160/160°C; PDL10-01). Note that the omission of the one precisely measured value at ~20 Gy result in a decrease in OD to 8 ± 5%. These values are similar to those previously reported from individual quartz grains from a range of different depositional and geographical areas (e.g., Arnold & Roberts 2009, Duller 2012b).

Table 8.3. Results for the dose recovery tests conducted using the SAR procedure outlined in Table 8.1. The measured dose and overdispersion (OD) values were calculated using the central age model of Galbraith *et al.* (1999). Those measured/given dose ratios marked with an (*) are consistent with unity at either 1 or 2σ.

Sample name	PH_1 (°C/ 10 s)	PH_2 (°C/ 5 s)	Given dose (Gy)	Measured dose (Gy)	OD (%)	Grains measured (N)	Accepted grains (N)	Measured-to-given-dose ratio
PDL10-01 (burnt; Layer 8)	160	160	40.8 ± 0.8	43.2 ± 2.2	19.7 ± 4.1	500	24	1.06 ± 0.06*
	180	180	40.8 ± 0.8	39.6 ± 1.1	10.7 ± 2.6	500	39	0.97 ± 0.03*
	200	200	40.8 ± 0.8	35.4 ± 0.7	4.8 ± 2.6	500	50	0.87 ± 0.02
	220	220	40.8 ± 0.8	34.7 ± 1.1	20.8 ± 2.5	500	50	0.85 ± 0.03
	240	240	40.8 ± 0.8	31.7 ± 0.8	14.1 ± 2.2	400	52	0.78 ± 0.03
	260	260	40.8 ± 0.8	27.9 ± 1.0	29.5 ± 2.8	500	80	0.68 ± 0.03
	260	160	40.8 ± 0.8	37.5 ± 0.8	5.1 ± 2.6	400	31	0.92 ± 0.03
	260	180	40.8 ± 0.8	40.7 ± 0.7	2.8 ± 2.9	300	36	1.00 ± 0.03*
	260	200	40.8 ± 0.8	42.4 ± 0.7	-	300	35	1.04 ± 0.03*
	260	220	40.8 ± 0.8	37.8 ± 0.7	8.5 ± 1.8	400	51	0.93 ± 0.03
	260	240	40.8 ± 0.8	34.4 ± 0.8	13.8 ± 2.0	400	59	0.84 ± 0.03
PdLIV-08 (unburnt; Layer 5B)	180	180	41.2 ± 0.8	41.9 ± 1.8	19.2 ± 4.4	1000	53	1.02 ± 0.05*
	220	220	41.2 ± 0.8	36.9 ± 1.7	13.8 ± 5.8	900	52	0.90 ± 0.05*
	260	260	41.2 ± 0.8	41.1 ± 1.5	12.5 ± 4.6	1400	68	1.00 ± 0.04*
	260	180	41.2 ± 0.8	42.5 ± 1.1	5.4 ± 3.9	1000	57	1.03 ± 0.03*
	260	200	41.2 ± 0.8	43.0 ± 1.5	-	600	43	1.05 ± 0.04*

In a second set of dose recovery tests of sample PDL10-01, the PH_1 temperature was fixed at 260°C for 10 s and the PH_2 temperature was systematically increased from 160 to 240°C for 5 s in 20°C intervals. The results are provided in Table 8.3 and shown in Figure 8.8b as filled circles. A different, but still preheat-sensitive trend can be observed, where the increase in PH_2 after 200°C results in a significant decrease in our ability to measure a known dose. Only two PH_1 and PH_2 combinations gave ratios consistent with unity: 260/180°C (1.00 ± 0.03) and 260/200°C (1.04 ± 0.03).

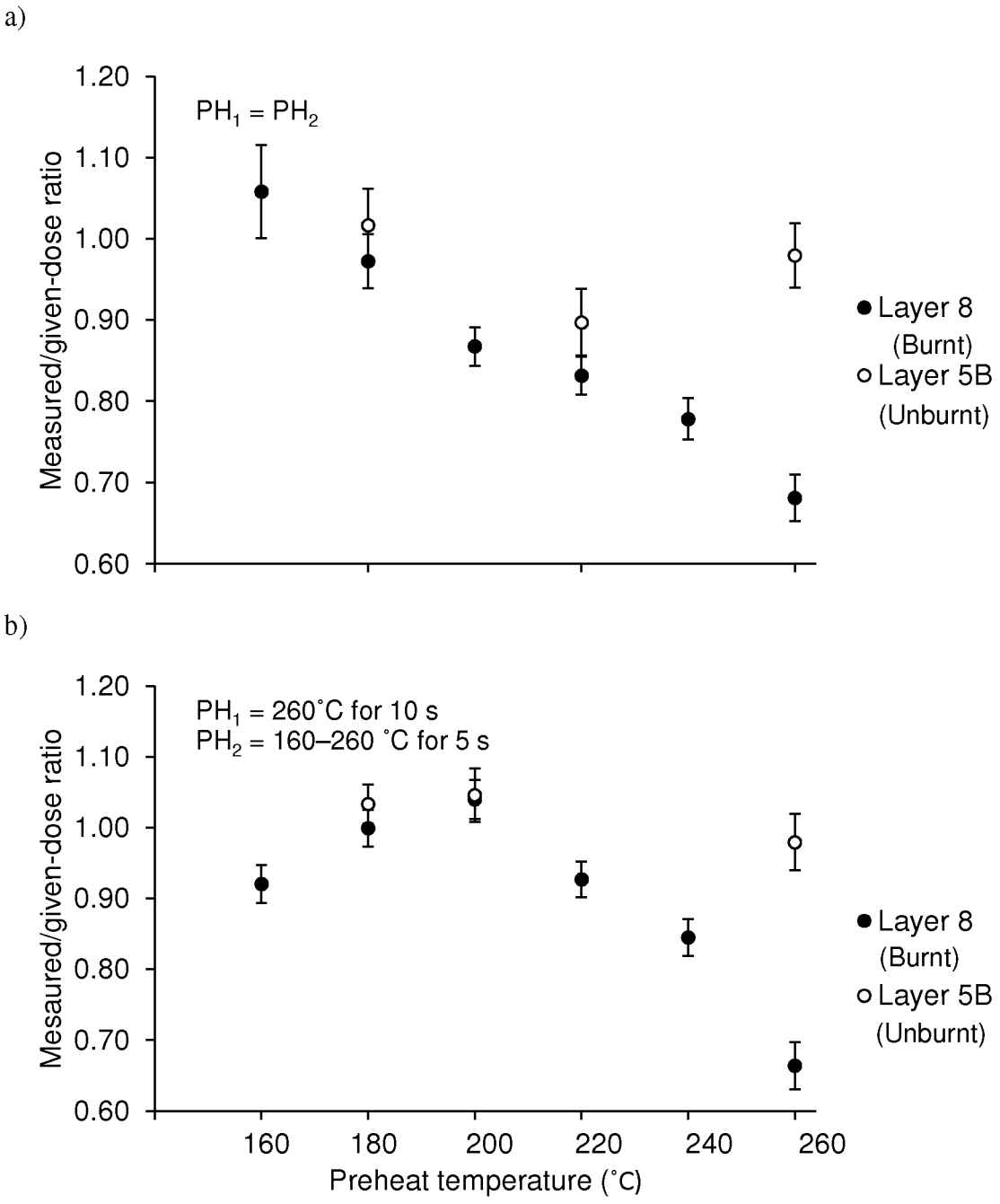

Figure 8.8. Measured/given-dose ratios obtained from dose recovery tests for burnt (PDL10-01; Layer 8) and unburnt sediments (PdLIV-08; Layer 5B), with a) equivalent PH_1 and PH_2 temperatures, and b) a fixed PH_1 temperature at 260 ˚C and a PH_2 temperature that was increased in 20˚C intervals from 160˚C to 260˚C for 5 s.

Grains of PdLIV-8 were not measured over the full range of PH temperatures, but only measured for those two PH combinations that gave positive results for PDL10-01. The results for PdLIV-8 are presented in Table 8.3 and shown in Figure 8.8b as open circles. In both cases the measured/given dose ratios are consistent with unity at 1σ (1.03 ± 0.03 for 260/180°C and 1.05 ± 0.04 for 260/200°C). In this set of tests, the OD values were also reduced to range between 0% and 5.4 ± 3.9% (PdLIV-8; 260/200°C).

The range of dose recovery tests clearly demonstrates the sensitivity of the OSL signal to changes in PH temperature. This is particularly true for the sample from Layer 8, the burnt (anthropogenic) layer. The questions that emerge from this difference in the behaviour between the anthropogenic and geogenic sediments are: 1) whether the heating of these sediment grains by humans in the past (e.g., fireplaces) have altered the luminescence properties of the grains, and 2) where and how these differences might manifest itself.

8.5.2 SINGLE-GRAIN OSL PREHEAT PLATEAU TESTS

A preheat plateau test was conducted to determine if naturally-irradiated grains from Layer 8 behave in a similar way to those that were irradiated in the laboratory. In this test, the PH_1 and PH_2 temperatures were, again, co-varied from 180°C to 260°C in 20°C intervals, i.e., the same as Figure 8.9a. Between 400 and 500 grains were measured for each of the five preheat temperature combinations. The accepted grains where combined using the CAM. The results are shown in Figure 8.9 and in Table 8.4.

A dependence of determined D_e with preheat temperature is observed. The D_e values for the 180, 200 and 220°C temperatures are consistent with each other and form a 'D_e plateau,' with a weighted mean value of 72 ± 2 Gy (shown in Figure 8.8a as the solid [mean] and dashed [± 1σ] lines). The 240°C D_e is only just consistent with this plateau region at 2σ. However the OSL signal appears to have been

substantially depleted at this PH_1 temperature. The 260˚C PH_1 temperature again resulted in D_e values underestimates by ~30% compared to that of the plateau area and similar to that obtained by both dose recovery tests (Figure 8.8).

Table 8.4. Results for the preheat plateau test. The PH_1 and PH_2 temperatures were co-varied in 20˚C increments and held for 10 and 5 s, respectively. The weighted mean D_e values for each preheat condition were calculated using the central age model of Galbraith *et al.* (1999). The ratio of the each preheat temperature condition over the 180 ˚C response is also shown.

PH_1 and PH_2 temperatures	Grains measured	Accepted Grains	CAM D_e (Gy)	OD (%)	Ratio
180/1800	500	50	69 ± 5	44 ± 6	1.00 ± 0.10*
200/200	500	56	70 ± 4	42 ± 5	1.02 ± 0.10*
220/220	400	74	76 ± 4	40 ± 4	1.10 ± 0.10*
240/240	500	62	62 ± 3	38 ± 4	0.90 ± 0.08*
260/260	500	71	51 ± 3	39 ± 4	0.74 ± 0.06

There is a significant difference in the patterns observed between the dose recovery and preheat plateau tests. Both of these tests co-varied the PH_1 and PH_2 temperatures. Yet, for the dose recovery tests, the data almost follow a step-wise linear decrease with an increase in preheat temperatures (Figure 8.8a), whereas for the preheat plateau tests, there is a distinct plateau in the data between the preheat temperatures of 180 and 220°C, before starting to decrease (Figure 8.9b). It is considered that these differing results reflect the difference between natural- and laboratory-dosed quartz grains.

The findings of these tests have two important conclusions. The first is that PH_1 treatments used for determination of D_e values for the six samples investigated in this study (i.e., PH_1 of 180˚C for 10 s and PH_2 of 180˚C for 5 s) are appropriate and able to recover the given laboratory doses. This PH temperature combination also gave D_e values that fall within the plateau region. The second is that, for OSL studies conducted in the local region, investigations are required to experimentally check the appropriateness of the preheat treatments used for samples collected from

within the same site; where measurement conditions may be appropriate for one sample, these may underestimate the D_e for another. Without the supporting experimental data, the confidence in the final sample D_e values, and OSL ages, may be undermined.

a)

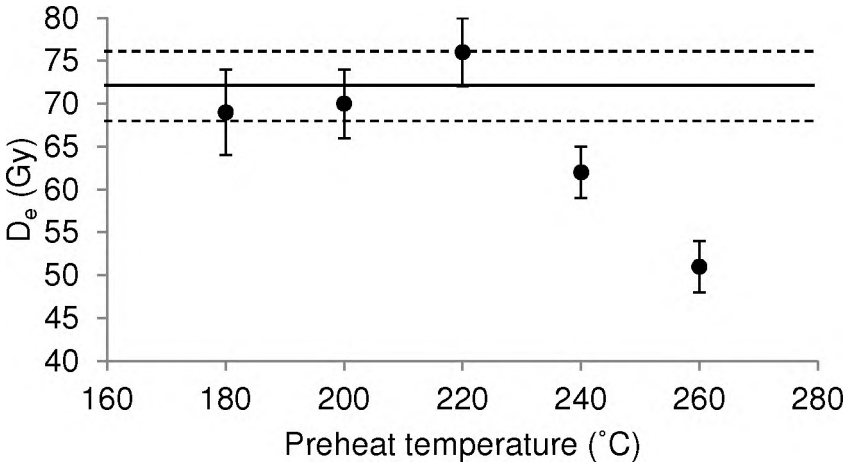

b)

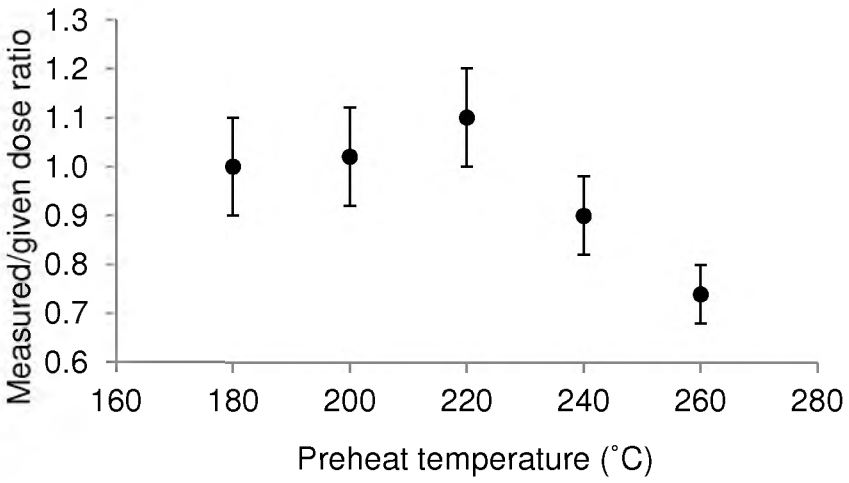

Figure 8.9. a) Preheat plateau results for sample PdLIV-1. Here, PH1 and PH2 temperatures were increased concurrently from 180 ˚C to 260 ˚C in 20 ˚C intervals. b) Same as in a) but normalised to the initial 180˚C preheat combination result.

8.5.3 SINGLE-GRAIN OSL CHARACTERISTICS

8.5.3.1 APPLICATION OF REJECTION CRITERIA

The four burnt sub-samples from Layer 8 (Figure 8.2), along with each sample from the unburnt sediments of Layers 5B and 4A (Figure 8.1d), were measured using the SAR procedure outlined in Table 8.1. A total number of 9100 individual grains of quartz were measured between the six samples investigated here. Of these grains, only 470 (5.2%) were deemed to provide meaningful D_e values, with the remaining 8630 (94.8%) failing to pass one or more of the rejection criteria.

Table 8.5. Distribution of rejected grains for each of the six Pech IV samples investigated in this study based upon the rejection criteria outlined in Jacobs *et al.* (2003, 2006a, 2006b).

Sample Name	Number of grains	Number of grains rejected on the basis of:					Total number of rejected grains	Total number of usable grains
		Brightness[a]	Recycling ratio[b]	IR-depletion ratio[c]	Recuperation[d]	Failed to intersect dose response curve[e]		
PdAIV-03	2600	2400	23	75	5	26	2528	72
PdAIV-02	2000	1866	9	36	10	18	1938	62
PdAIV-01-A	1000	743	75	40	41	11	910	90
PdAIV-01-B	1500	1180	103	50	58	29	1420	80
PdAIV-01-C	1000	740	83	42	38	8	911	89
PdAIV-01-D	1000	790	57	35	33	8	923	77

[a] The OSL signal determined for the test dose given directly after measurement of the natural OSL signal was less than 3 times the respective background count or the error on the T_N signal was >20%.

[b] The 'recycling ratio' (the ratio of sensitivity-corrected OSL signals produced by 2 identical regenerative dose points) differed from unity by more than 2σ.

[c] The OSL signal resulting from an identical dose to that given in the recycling ratio following a 40 s infrared stimulation at room temperature was less than 2σ from unity.

[d] The sensitivity-corrected OSL signal measured after preheating a regenerative dose of 0 Gy was greater than 5% of the sensitivity-corrected natural OSL signal.

[e] The sensitivity-corrected natural OSL signal failed to intercept the dose-response because it had reached saturation or was a Class 3 grain of Yoshida *et al.* (2000).

Table 8.5 shows the number of grains measured for each of the six samples, the number of grains rejected and the reasons for rejection. Grains where rejected if they failed one, or more, of the following criteria: 1) the OSL signal determined for the test dose given directly after measurement of the natural OSL signal was less than 3 times the respective background count or the error on the T_N signal was >20% (Figure 8.10a), 2) the 'recycling ratio' (the ratio of sensitivity-corrected OSL signals produced by 2 identical regenerative dose points given at the start and the end of the measurement cycles) differed from unity by more than 2σ (Figure 8.10b), 3) the OSL signal resulting from an identical dose to that given in the recycling ratio following a 40 s infrared stimulation at room temperature, the 'OSL-IR-depletion ratio test,' was less than 2σ from unity (Figure 8.10b), 4) the sensitivity-corrected OSL signal measured after preheating a regenerative dose of 0 Gy was greater than 5% of the sensitivity-corrected natural OSL signal (Figure 8.10c), and 5) the sensitivity-corrected natural OSL signal either failed to intercept the dose-response, termed a Class 3 grain of Yoshida *et al.* (2000) (Figure 8.10d), or the L_N/T_N were in saturation and did not intercept the dose-response curve (Figure 8.10e). No D_e values could be calculated for these grains.

The majority of grains that were rejected from the total six samples investigated (~85%, N=7719) were done so on the basis of having poor or no luminescence signal or a T_N error that was >20% (Figure 8.10a). A further ~1% (N=99) failed to provide any D_e value as they were either saturated or failed to intersect the dose-response curve completely (Figure 8.10 d and e). An additional 2% (N=185) displayed a recuperated signal following a 0 Gy regenerative dose.

Of the remaining 'rejected' grains a number of patterns were observed and could be subdivided into four groups. The diagnostic features of these grain subdivisions are given in Table 8.6. Group 1 grains (Figure 8.11a) have reproducible T_X decay curves over the SAR cycles, failed the recycling ratio test, but passed the OSL-IR-depletion ratio test. Group 2 grains (Figure 8.11b) have reproducible T_X decay curves, pass the recycling ratio test, but fail the IR-depletion ratio test. Group 3 grains (Figure 8.11c) present similar characteristics to Group 1, in that they pass the

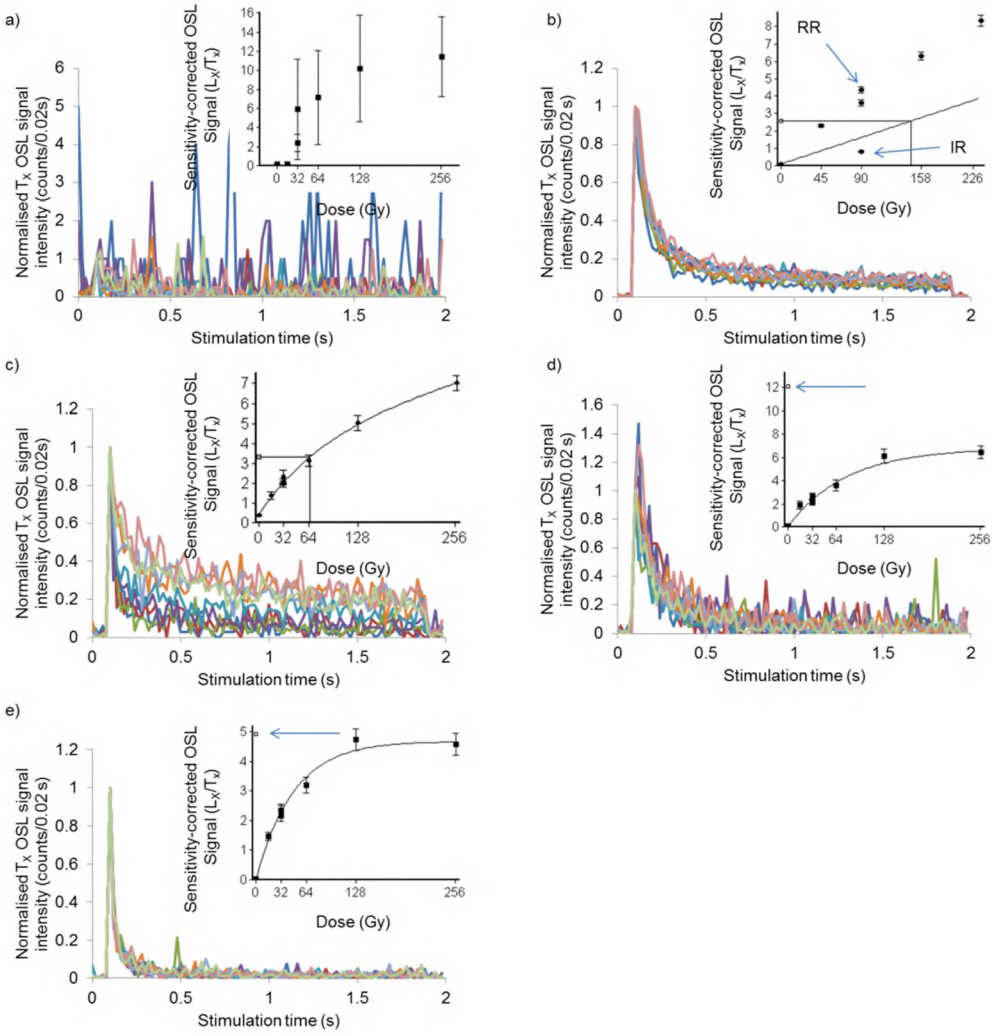

Figure 8.10. A series of OSL decay and dose-response curves for grains that failed one or more rejection criteria. a) Quartz grain with poor luminescence signal (PdAIV-01-B), b) Quartz grain that failed both the recycling ratio test (RR) and IR-depletion ratio test (IR) (PdAIV-03). c) Quartz grain that displays a recuperated OSL signal that is >5% that of the sensitivity-corrected natural OSL signal (PdAIV-02). d) A 'Class 3' quartz grain where the sensitivity-corrected natural OSL signal (indicated with an arrow) fails to intersect the dose response curve (PdAIV-02). e) Saturated quartz grain (PdAIV-02) where the sensitivity-corrected natural OSL signal (indicated with an arrow) falls within the saturated portion of the dose-response curve.

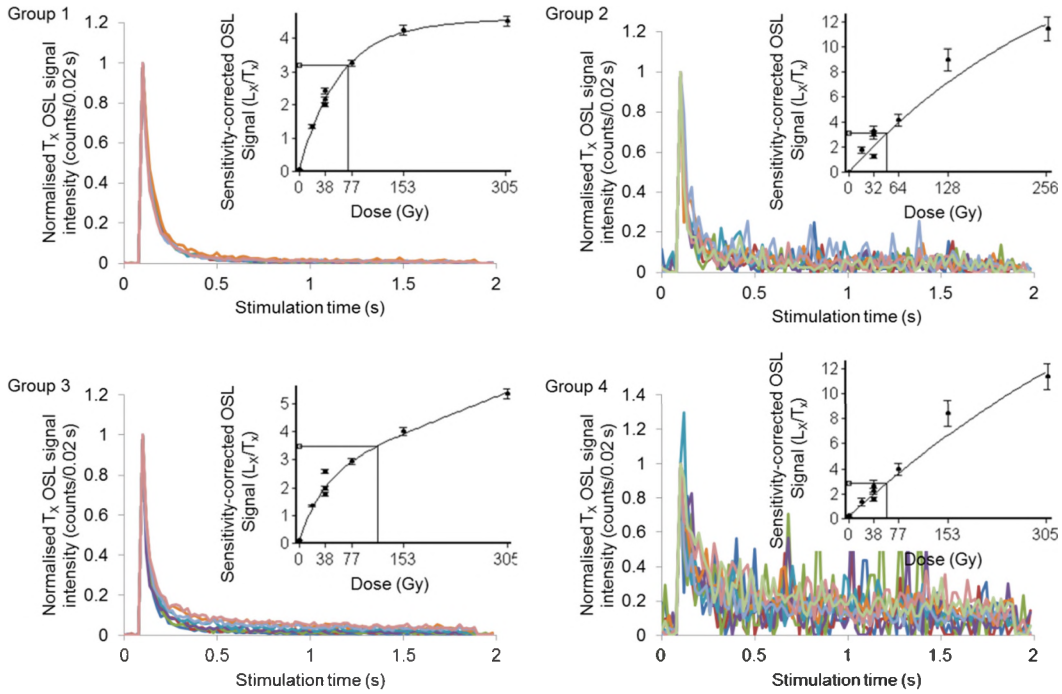

Figure 8.11. The T_X decay and dose-response curves for grains typical of the four subdivisions outlined in Table 8.6. These include an example of Group 1 (PdAIV-01-A), Group 2 (PdAIV-02), Group 3 (PdAIV-01-B) and Group 4 (PdAIV-01-C) grains.

Table 8.6. Diagnostic characteristics for rejected grain subdivisions.

Group number	Reproducible T_X curves	Passes the recycling ratio test	Passes the OSL-IR-depletion ratio test
Group 1	Yes	No	Yes
Group 2	Yes	Yes	No
Group 3	No	No	Yes
Group 4	No	Yes	No

OSL-IR-depletion ratio test and fail the recycling ratio test but have T_X signals that are not reproducible (i.e., the OSL signal appears to increase with SAR cycle). Group 4 grains (Figure 8.11d) have non-reproducible T_X curves, fail the IR-depletion ratio test but pass the recycling ratio test. Grains with recuperated and non-recuperated

OSL signals are present in each of the four subdivisions. The significant variability in the dose-response and decay curve characteristics of the rejected grains reinforces the case for their removal from the data set prior to D_e determination, and hence, age estimation.

8.5.3.2 SIGNAL BRIGHTNESS

During sample analysis it was noticed that there was substantial variability in the intrinsic luminescence brightness of the constituent grains. It has previously been shown that only a small proportion of grains within a sample (generally <30%) give rise to the majority (90–95%) of the luminescence signal (Duller et al. 2000, Duller and Murray 2000, Jacobs et al. 2003b). To investigate the intrinsic brightness for the Pech IV samples, cumulative light sum plots (Duller and Murray 2000) were constructed for each of our six samples shown in Figure 8.16.

However, not all samples investigated received the same size test dose as they were measured using different Risø readers. The burnt Layer 8 samples (PdAIV-01-A to D) were run using one machine, whereas the unburnt samples from Layer 5B (PdAIV-02) and Layer 5B (PdAIV-03) were both measured on two separate machines. The four Layer 8 sub-samples can be directly compared to one another, but these cannot be directly compared to the remaining two sample run on separate Risø readers (i.e., PdAIV-02 and -03). The T_N signal was corrected for the size of the test dose given to each sample to normalise between the different samples. While this procedure overcomes the difference in the size of the tests doses used, it does not overcome the variability in the detection of the OSL signals by the three different photomultiplier tubes. The cumulative light sum plots are, therefore, more appropriately considered to be qualitative rather than quantitative.

The grains in each sub-sample were ranked in order of descending T_N brightness. The test-dose corrected cumulative light sum for each sample was then plotted as a function of the cumulative contribution of each grain to the total number of grains measured. The cumulative light sum plots for Layer 8 sub-samples are

shown in Figure 8.16a, and Layers 5B and 4A in Figure 8.16b. From Figure 8.16a, the Layer 8 sub-sample show some degree of variability, with 90% of the light coming from 11 (PdAIV-01-B and D), 14 (PdAIV-01-C) and 18% (PdAIV-01-A) of the measured grains. From Figure 8.16b, 90% of the light comes from 23% of the grains for the Layer 5B sample (PdAIV-02), and 14% of the grains measured for Layer 4A (PdAIV-03).

The luminescence sensitivities of the grains within each sample reveal significant variability. To compare the sensitivities of the grains within each sample, the background-corrected T_N OSL signal was divided by the administered test dose to give OSL sensitivity (counts/Gy). The results are plotted in Figure 8.17 and presented in Table 8.8. We have arbitrarily categorised grain sensitivities into three groups; high (>100 counts/Gy), moderate (100–10 counts/Gy) and poor (<10 counts/Gy). From Figure 8.17, it can be seen that the burnt samples from Layer 8 (PdAIV-01-A to D) all have, across all grains, a higher sensitivity than those from the geogenic layers. Between 11 and 14 grains from the Layer 8 samples fall into the 'high' category, whereas only 6 grains from Layer 4A, and none from Layer 5B, are categorised as 'high.' The grains from Layer 5B (PdAIV-02) are dominated by 'poorly' sensitive grains (N=49). It is proposed that the higher proportion of highly sensitive grains in Layer 8 is due to the heating of these sediments during antiquity. However, it is also likely that these differences may be a result of measuring the geogenic samples on a different Risø machines.

Table 8.7. Distribution of grain sensitivities using the background-corrected T_N signal of all accepted grains. High, >100 counts/ Gy; Moderate, 100–10 counts/ Gy; Poor <10 counts/ Gy. Ranges chosen are arbitrary.

Sample name	Number of accepted grains	Sensitivity (counts/Gy)		
		High	Moderate	Poor
PdAIV-01-A	90	13	43	34
PdAIV-01-B	80	16	41	23
PdAIV-01-C	89	11	49	29
PdAIV-01-D	77	14	39	24
PdAIV-02	62	0	13	49
PdAIV-03	72	6	37	29

a)

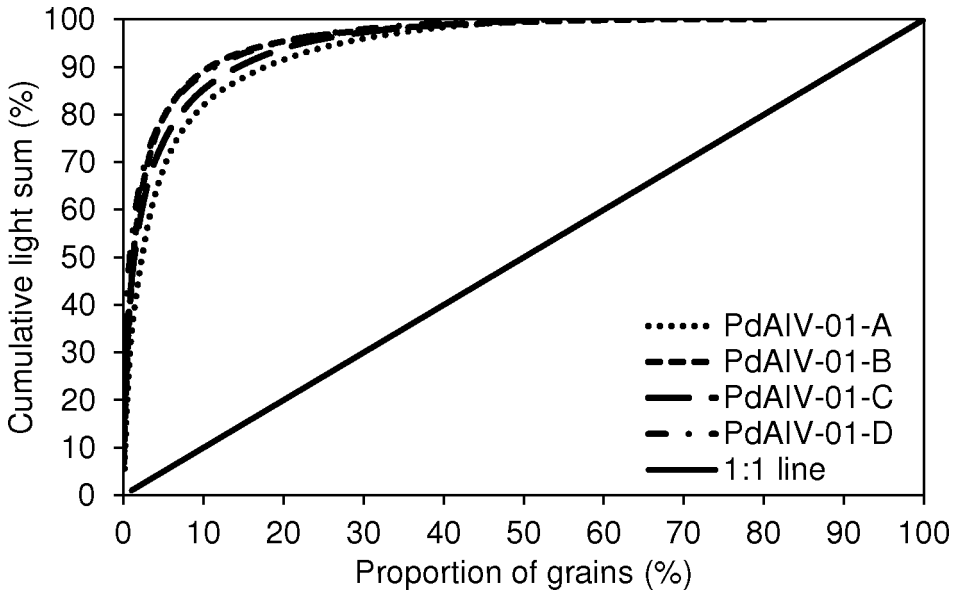

b)

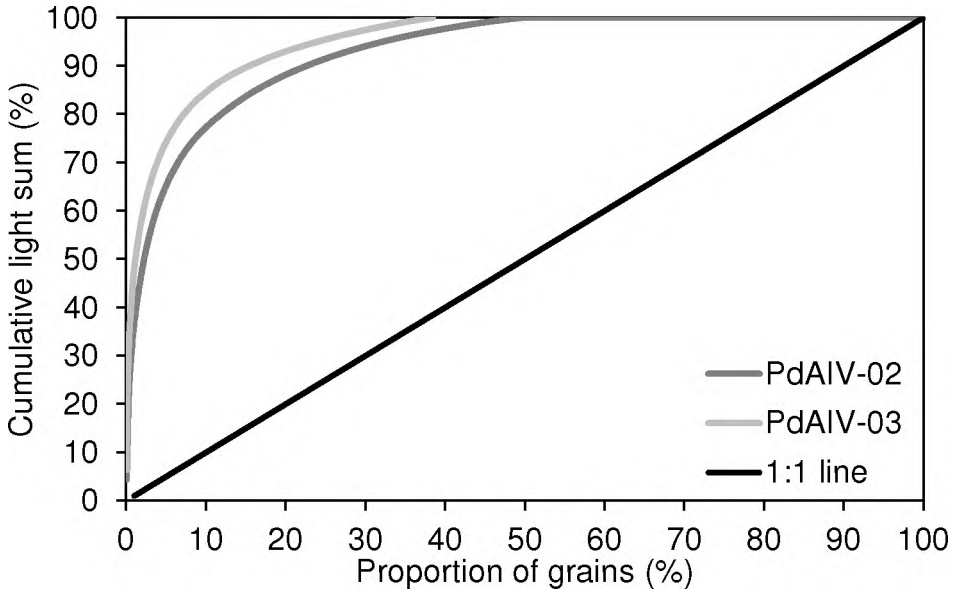

Figure 8.12. Cumulative light sum plots for back-ground corrected T_N signals for a) Layer 8 subsamples and b) Layers 5B and 4A. If all grains measured contributed the same proportion to the total luminescence signal then the resulting curve would be a straight one-to-one line (shown in solid black)

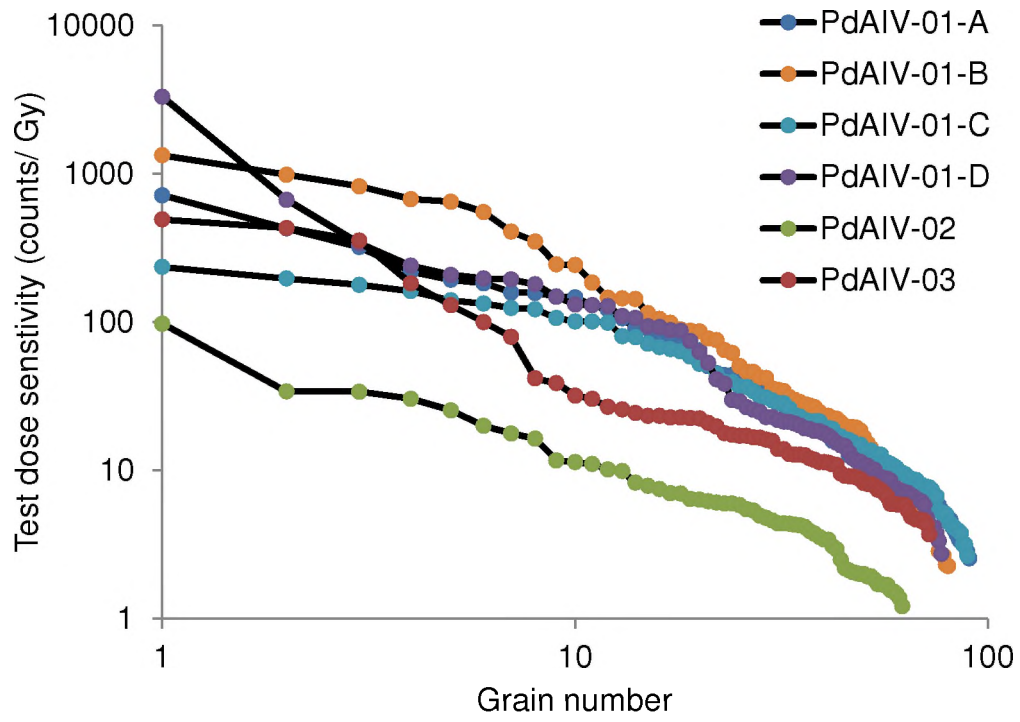

Figure 8.13 Plot of the T_N OSL sensitivities (counts/Gy) of all accepted grains as a function of the number of accepted grains for each of the six Pech IV samples investigated. The grains were ranked in descending order of sensitivity. Please note the logarithmic x and y axes.

8.5.3.3 OSL DECAY CURVE SHAPES

The OSL signal is considered to be the result of the release of photons from different OSL component (Bailey et al. 1997, Bulur 1996, Jain et al. 2003, Singarayer and Bailey 2003). Bailey *et al.* (1997) were able to describe three separate OSL components that contributed to their OSL decay curves, namely fast, medium and slow according to their rate of decay. The variability in the proportion of each of these decay components is considered to give rise to the variability in the decay curve shapes presented by the 470 accepted grains coming from the different Pech IV samples.

An examination of the decay curve shapes of the grains that were accepted reveals substantial variation both within and between samples. The L_N OSL decay curves for each of the accepted grains in samples PdAIV-01-C, -02 and -03 are

shown in Figure 8.18. The majority of these grains display decay curves that rapidly reach background levels within the first 0.2 s of optical stimulation. A number of grains exhibit much slower rate of decay, requiring up to 0.5 s of stimulation before background levels are attained: this can be observed more clearly in the insets in Figure 8.18 which show the same decay curves but on a logarithmic y-axis. It is observed that a substantially higher proportion of 'slowly' decaying grains are present in the unburnt samples (Figure 8.18b and c). It is likely that such variability is due to variable proportional contributions from the different OSL components (i.e., fast, medium and slow) to the total OSL signal.

8.5.3.3.1 The 'fast ratio' and OSL signal decay

The 'fast ratio' (FR) was initially developed by Madsen *et al.* (2009) as a method to identify multi-grain aliquots that were dominated by the OSL fast component. This was achieved by taking the initial OSL signal dominated by the fast component (minus the background) and dividing it by the photon count rate contribution of the medium component (taken from further down the optical decay curve again minus the background). This technique was later built upon by Durcan & Duller (2011) by defining the integration limits of the 'fast' and 'medium' components using their respective photo-ionisation cross-sections as a result of blue LED stimulation and applied it exclusively to multi-grain aliquots of quartz. The higher the FR, the more the fast OSL component dominates the total OSL signal. Duller & Durcan (2011) proposed that a FR threshold value of 20 be used as in these cases the total OSL signal of the multi-grain aliquots would be comprised of ~90% fast component. Duller (2012) developed a similar FR procedure for single grains of quartz measured using the green laser at 25% power and over a stimulation period of 4 s.

a)

b)

c)

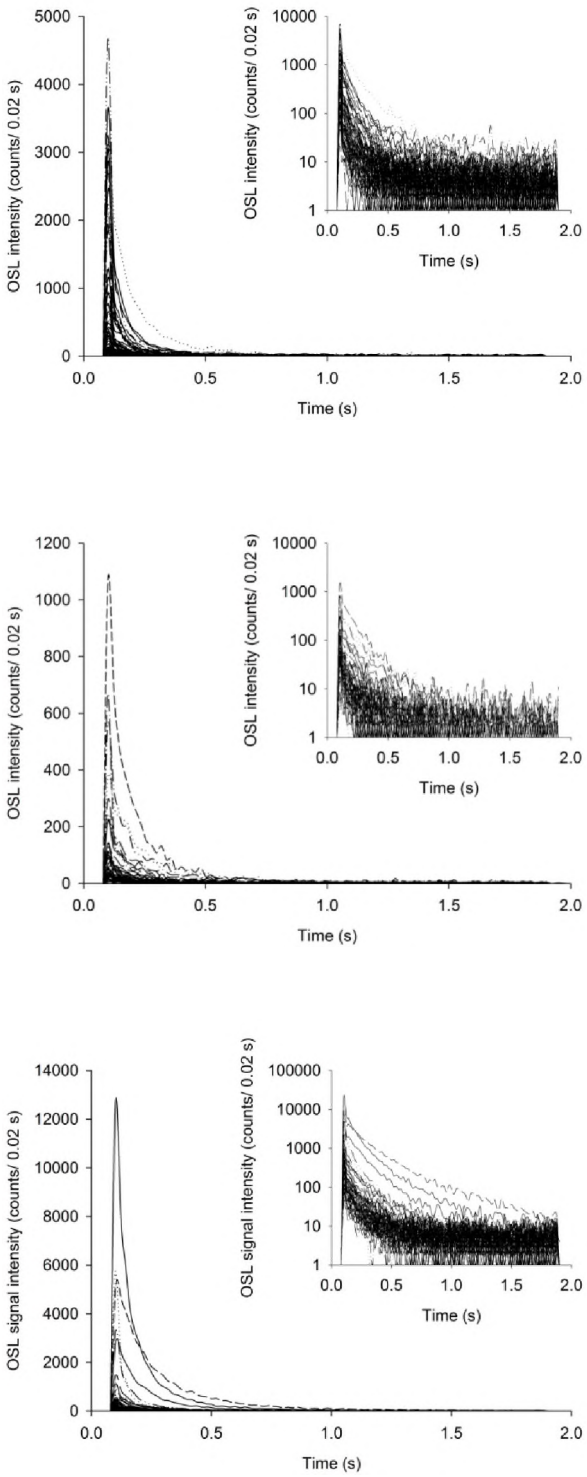

Figure 8.14. OSL decay curves for: a) 89 accepted grains from PdAIV-01-C, Layer 8; b) 62 accepted grains from PdAIV-02, Layer 5B; and c) 72 accepted grains from PdAIV-03, Layer 4A. Inset in each are the same data but with a logarithmic y-axis.

A modified version of the FR of Durcan & Duller (2011) was applied to the one burnt (PdAIV-01-C) and the two unburnt (PdAIV-02 and -03) samples. Three separate integration limits were used. The current study measured the quartz grains for 2 s using the green laser at 90% power. In this instance, even the initial 0.02 s of stimulation time contains a portion of the medium component. The first 0.02 s of optical stimulation was taken to represent the 'fast' component, the 'medium and slow' component as the integral between 0.18 and 0.22 s of optical stimulation. A 'background' component was measured from the final 0.3 s of optical stimulation and proportionally subtracted from both the 'fast' and 'medium and slow' components. The modified FR was then calculated by dividing the background-subtracted 'fast' component by the background-subtracted 'medium and slow' components.

The FR results are shown in Table 8.9, the number of grains with FRs greater than 20 is substantially higher for the burnt sample (52%; PdAIV-01-C) than for the unburnt (19%; PdAIV-02 and -03) samples. It appears, therefore, that the quartz grains coming from the burnt sample (PdAIV-01-C) have faster rates of decay than either of the unburnt sample counterparts and/or have brighter initial signals that result in a better signal-to-noise ratio.

Table 8.8. Distribution of fast ratio values for accepted grains from the six Pech IV samples. Also shown is the proportion of grains in each range as a percentage of the total number of accepted grains.

Sample Name	Fast Ratio range:				
	0 – 5	6 – 10	11 – 15	15 – 20	>20
PdAIV-03 (unburnt)	21 (31%)	20 (29%)	8 (12%)	6 (9%)	13 (19%)
PdAIV-02 (unburnt)	24 (39%)	19 (31%)	3 (5%)	4 (6%)	12 (19%)
PdAIV-01-C (burnt)	9 (10%)	11 (12%)	11 (12%)	12 (13%)	46 (52%)

8.5.3.4 EARLY LIGHT SUBTRACTION VS LATE LIGHT SUBTRACTION

Although the possibility of OSL signal carry over is negligible (as demonstrated in Figure 8.18) it is imperative that the presence of medium and slowly decaying components in the OSL signal does not influence the D_e for the grain. As the SAR procedure was developed to measure grains dominated by the fast component (Murray & Wintle 2000, 2003), where the medium and slow components dominate the OSL signal, the SAR procedure can produce erroneous D_e values. To minimise the possibility, the 'early' background (EBG) subtraction of Cunningham & Wallinga (2010) was applied for D_e determination of two samples: PdAIV-01-C and PdAIV-02. These samples were chosen as they represent extreme examples of fast component dominance (Figure 8.3b); the former sample having a significantly larger proportion of 'fast' dominated grains. Here, an EBG contribution was calculated from the 0.3 s (0.18–0.38 s) of optical stimulation following directly after the integration limits of the OSL signal. By using an EBG, the contribution of the medium and slow OSL components will be more completely removed from the OSL signal.

For both samples, the weighted mean D_e values were calculated using the CAM and gave statistically consistent results with the 'late' background weighted mean D_e values. For PdAIV-01-C a weighted mean D_e of 71 ± 4 Gy was determined compared to 63 ± 4 Gy for the 'late' light subtraction. For Layer 5B a D_e of 68 ± 7 Gy was calculated using the EBG method, whereas a 'late' light background subtraction D_e of 66 ± 4 Gy was determined.

The systematic use of the 'late' background method is preferred for calculation of the D_e values for the six samples investigated in this study for two reasons. First, the EBG did not appear to have a significant effect on the final D_e. Second, in the case of PdAIV-02 (unburnt), the number of accepted grains used in the final EBG D_e calculation (N = 28) was about half of that used in the 'late' light background approach (N = 62), resulting in a much larger uncertainty. For the PdAIV-01-C (burnt) sample, there was only a slight reduction in the number of accepted grains, from 89 ('late' light) to 77 (EBG).

8.5.3.5 DOSE-RESPONSE CURVE FITTING: SINGLE SATURATING EXPONENTIAL PLUS AN ADDITIONAL LINEAR TERM VS DOUBLE SATURATING EXPONENTIAL

Selected OSL decay and dose-response curves for three of the six Pech IV samples are shown in Figure 8.19. These curves were selected to illustrate the variations apparent in L_N and T_N decay and dose-response curve shapes for grains with high (Figures 8.19a,d and g), medium (Figures 8.19b, e and h) and low (Figures 8.19c, f, and i) FR values. In the majority of cases, the response of the OSL signal with increasing laboratory dose could be best explained by a saturating exponential function with an additional linear term, as is the case for all those curves shown in Figure 8.19. For the remaining grains, a single exponential function (without the additional linear term) proves to be a better fit to the dose-response data.

Figure 8.19 also demonstrates the grain-to-grain variability in the onset of dose saturation. Some grains show little increase in OSL signal beyond ~60 Gy (Figure 8.19d) while others have almost linear growth up to ~100 Gy before beginning to plateau off (Figure 8.19i). For some grains (Figure 8.19a and b), there appears to be a rapid increase in OSL signal with dose to ~60 Gy after which point the dose-response curve continues to grow in a linear fashion. Lowick *et al.* (2010) suggested that such dose-response curves (i.e., those curves taking on a saturating plus an additional linear term) are not representative of naturally-irradiated samples due to the finite number of electron traps in each grain. Rather, they choose to fit these grains with a double saturating exponential function (i.e., the sum of two exponential curves). To determine the effect that this may have on our datasets, a double saturating exponential curve was applied to the PdAIV-01-C data set. No significant difference between using the (preferred) exponential plus linear or double saturating exponential curve functions was found. The ratio of the CAM D_e for double saturating exponential to exponential plus linear fit was 1.04 ± 0.08 and consistent with unity. With no significant difference apparent between the dose-response curve fits, the exponential plus linear fit was used for all samples analysed in this study.

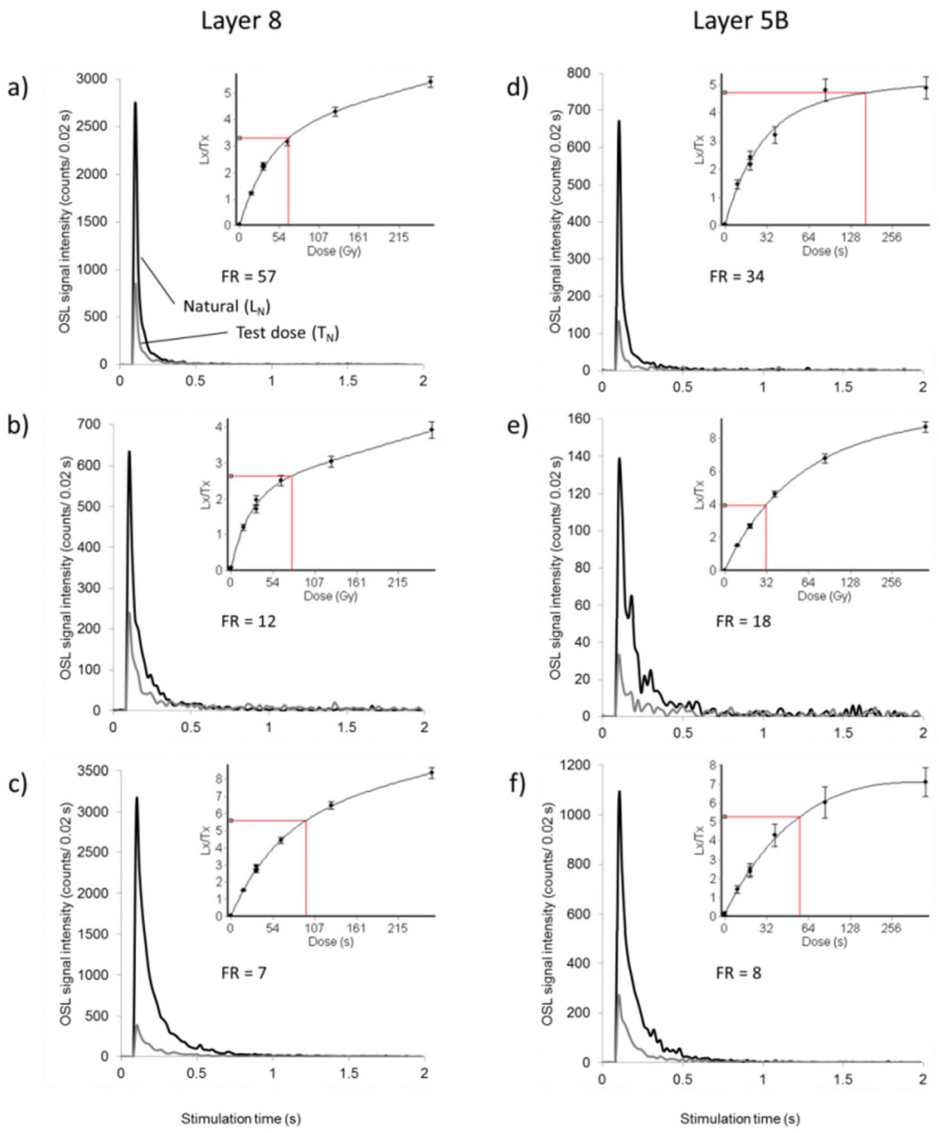

Figure 8.15 L_N (black) and T_N (grey) OSL decay curves for selected accepted grains from Layer 8 (a–c) and Layer 5B (d–f). The inset in each figure is the corresponding dose-response curve with errors shown at 1σ. Also shown is the fast ratio (FR) value for the L_N OSL decay curves in each example.

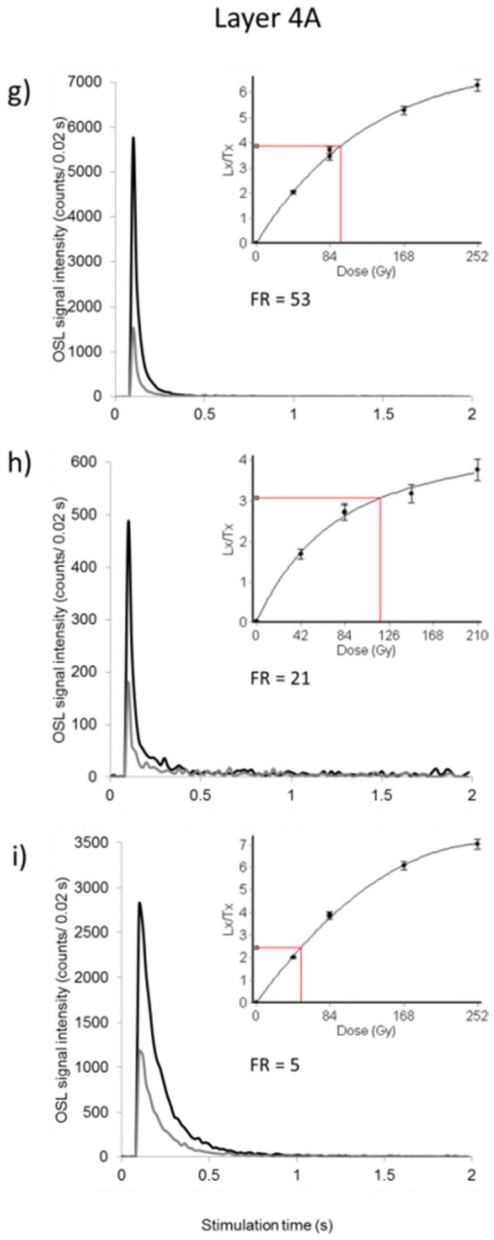

Figure 8.15 (continued) L_N (black) and T_N (grey) OSL decay curves for selected accepted grains from Layer 4A (g–i). The inset in each figure is the corresponding dose-response curve with errors shown at 1σ. Also shown is the fast ratio (FR) value for the L_N OSL decay curves in each example.

8.5.3.6 SUMMARY

The intrinsic OSL characteristics for the Pech IV samples are highly variable. Not only is there significant variation in the rate of decay for OSL decay curves within the same sample (Figures 8.18 and 8.19) but the decay curves for the burnt samples have a faster decay rate than those for the unburnt (Table 8.9). Regardless of the rate of OSL decay, however, the majority of grains reach a stable background OSL count that is less than 10% of the initial OSL signal after only 2 s of green laser stimulation (Figure 8.18). Additionally, an EBG subtraction was used as a means of testing the potential influence of the medium and slow components on D_e determination using the SAR procedure, with no significant difference observed (Section 8.7.3.5). The dose-response of the OSL signal was best described using a saturating exponential plus linear function. The fitting of a double saturating exponential curve (as suggested by Lowick *et al.* 2010) made no significant difference to the D_e values obtained (Section 8.7.3.6). In terms of saturation, there is no observed relationship between burnt and unburnt samples and the onset of dose-response curve saturation (Figure 8.18 insets), with saturation generally occurring between 60 and 100 Gy.

8.6 D_e DISTRIBUTION ANALYSIS

The accepted D_e estimates from individual grains of quartz measured for each of the six Pech IV samples are displayed graphically as radial plots in Figure 8.20 (Galbraith 1990). There is substantially more scatter in the D_e estimates than what measurement uncertainties will allow for – this additional scatter is termed overdispersion (OD) (Galbraith *et al.* 1999). For the burnt Layer 8 samples the OD values range from 39 ± 4 to 72 ± 6%, whereas the OD values for the unburnt sediments from Layers 5B and 4A are somewhat less at 30 ± 6 and 30 ± 4%, respectively. In the following sections, the additional sources of scatter present in the D_e distributions will be considered.

a)

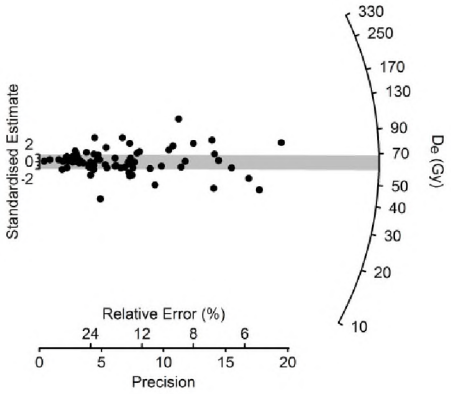
Standardised Estimate
2
0
-2
De (Gy)
330
250
170
130
90
70
50
40
30
20
10
Relative Error (%)
24
12
8
6
0
5
10
15
20
Precision

b)

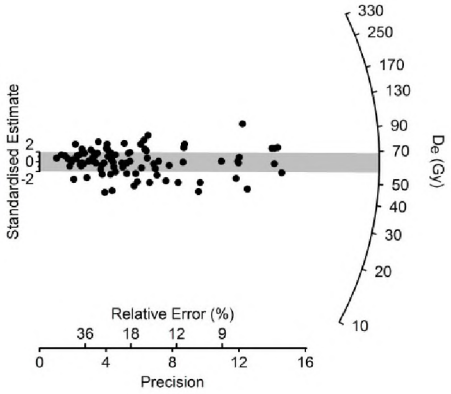
Standardised Estimate
2
0
-2
De (Gy)
330
250
170
130
90
70
50
40
30
20
10
Relative Error (%)
36
18
12
9
0
4
8
12
16
Precision

c)

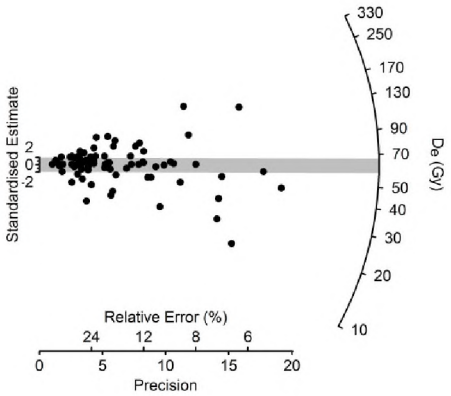
Standardised Estimate
2
0
-2
De (Gy)
330
250
170
130
90
70
50
40
30
20
10
Relative Error (%)
24
12
8
6
0
5
10
15
20
Precision

d)

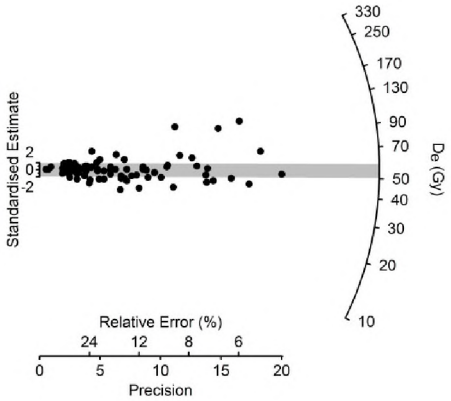
Standardised Estimate
2
0
-2
De (Gy)
330
250
170
130
90
70
50
40
30
20
10
Relative Error (%)
24
12
8
6
0
5
10
15
20
Precision

e)

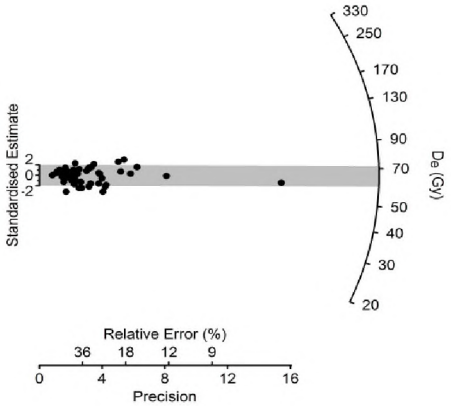
Standardised Estimate
2
0
-2
De (Gy)
330
250
170
130
90
70
50
40
30
20
Relative Error (%)
36
18
12
9
0
4
8
12
16
Precision

f)

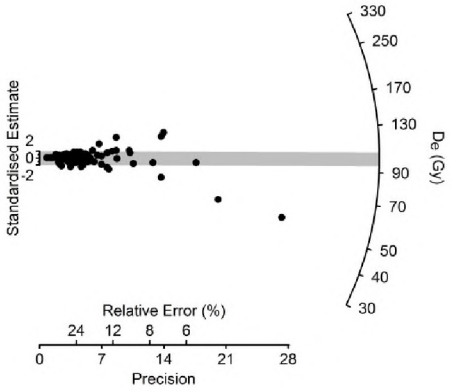
Standardised Estimate
2
0
-2
De (Gy)
330
250
170
130
90
70
50
40
30
Relative Error (%)
24
12
8
6
0
7
14
21
28
Precision

Figure 8.16. (opposite) Single-grain D_e values plotted as radial plots for each of the Pech IV samples measured in this study a) PdaIV-01-D; b) PdAIV-01-C; c) PdAIV-01-B; d) PdAIV-01-A; e) PdAIV-02 and f) PdAIV-03. The grey band (± 2σ of standardised estimate) is centred on the weighted mean value for each distribution as determined by the central age model (Galbraith *et al.* 1999). If each distribution conformed to the statistical expectation that 95% of the data falls within 2σ of the sample mean then the majority of the D_e value would fall within the grey band, which is not the case. Each distribution investigated shows evidence of overdispersion.

It is appreciated that the beta dose recovery tests that were conducted provide only a *minimum* estimate of the OD due to intrinsic grain-to-grain variability. This minimum value for the samples from Pech IV was determined to be 11 ± 3%, for Layer 8, and 19 ± 4%, for the unburnt Layers 4A and 5B sediment samples. The additional OD obtained for the natural samples of between ~30 and 72% (Figure 8.20) may be the result of unexplained intrinsic variability and a number of extrinsic influences. The latter may include, but are not limited to: 1) the incomplete eviction of trapped electrons during the previous zeroing event ('partial bleaching') (Olley *et al.* 1999); 2) mixing of different age sediments due to bioturbation, pedoturbation or other such processes (Bateman et al. 2007a, David et al. 2007, Jankowski et al. submitted); and 3) localised variations in the β-D_r due to heterogeneous distribution of radioactive materials in the surrounding sediments (beta microdosimetry; BM) (Guérin et al. 2012b, Murray and Roberts 1997, Olley et al. 1997, Nathan et al. 2003).

To this end, an investigation into the sedimentary and dosimetric composition for the Layer 8 samples, the most complex of any samples investigated in this study, is presented below. In Chapter 5 it was argued that a detailed understanding of the sedimentology and depositional histories of the samples under investigation would allow for informed interpretations of whether the D_e values could be combined and, if so, ways in which this can be achieved.

8.6.1 EXTRINSIC FACTORS CONTRIBUTING TO OBSERVED OVERDISPERSION

8.6.1.1 BETA MICRODOSIMETRY

The work presented in Chapter 6 conducted a number of different studies into the beta particle dosimetric environments of samples PdAIV-01-C (Layer 8) and PdAIV-02 (Layer 5B) using portable x-ray fluorescence (pXRF), Al_2O_3:C mapping and image analysis modelling. In particular, the use of the pXRF was considered to be a rapid means of assessing the distribution of K throughout the resin impregnated sediment slabs. Due to the detection limits of the device, concentrations of U and Th were only detected when present at concentrations of >4 μg/g. Following the work presented there, I have investigated the distributions of these three radionuclides in the four burnt sediment sub-samples of Layer 8. It is appreciated that the detection of U and Th will be restricted to those regions where concentrations are greater than the pXRF detection limit. The distributions of P, Si and Ca were also investigated and are indicators for the presence of bone, flint and calcite/limestone, respectively.

8.6.1.1.1 Experimental approach

The spatial distribution of the U, Th and K radionuclides, as well as P, Si and Ca, were made using the 'Upper' and 'Lower' 3 mm thick resin-impregnated slabs taken from directly above and below the Layer 8 sub-sample slabs (Section 8.4 and Figure 8.2). Regions of interest (ROI) were selected on the internal faces of each of the 'Upper' and 'Lower' slabs (i.e., the side facing towards the OSL sub-sample; Figure 8.2). These ROI were inscribed with a 3×3 mm grid using pencil and covered an area 25×25 mm, equating to 25 individual pXRF analyses per region. Portable XRF measurements were made using a Thermo Scientific Niton XL3t GOLDD+ instrument and the procedures outlined in Chapter 6. The raw concentrations of U, Th and K were calibrated using the curves presented therein (Figure 6.6) and in

Figure 8.21 the calibration curves for Ca, P and Si are presented. Selected distributions of the six elements of interest (U, Th, K, Ca, P and Si) are shown in Figure 8.22, with the distribution maps for all six elements for each ROI also found in the Supplementary Materials section of this Chapter (Section 8.13). Allowances had to be made for the ~4 µg/g detection limit of the pXRF for both U and Th. In each of the distribution maps shown, points of analysis with no detectable U or Th were arbitrarily assigned a value of 2 ± 1 µg/g which is consistent both with 0 and the 4 µg/g detection limit.

8.6.1.1.2 Spatial distribution results for U, Th and K

The presence of Th was detected in all but two of the 15 ROI analysed using the pXRF. The presence of Th appears to be associated with bone material – in particular those that remained relatively unburnt (Figure 8.22 in A-Upper-01, C-Lower-01). Th also appears in a number of instances associated with sedimentary matrix where a significant proportion of the sediments comprise of bone fragments. U was only present at detectable levels in one ROI (Figure 8.22; A-Lower-01), and is associated with three separate burnt bone fragments. There is a clear gradient in the abundance of K, increasing with depth. For example, the K content of sample A-Lower-02 is between 2000 and 2500 µg/g (Figure 8.22), while in C-Upper-02 and D-Lower-02 are significantly higher at levels greater than 5000 µg/g.

8.6.1.1.3 Spatial distribution of Ca, P and Si

The presence of Ca is highly variable, with high Ca concentrations associated with limestone nodules, such as that found in B-Lower-02 (Figure 8.22). Interestingly, there are regions within the same slab (B-Upper, Figure 8.22) where the concentration of Ca ranges from ~14% on one side of the slab to greater than 24% on the other and are most associated with ash clasts or calcite cementation. It should be noted that PdAIV-01-B was collected from an ash-coloured layer, probably explaining the high proportion of Ca here. P is found throughout each of the Layer 8

sub-sample slabs and is associated with the presence of bone fragments (such as those shown in C-Upper-01; Figure 8.22). Both burnt and unburnt bone fragments have similar P concentrations of ~25%. Si is found throughout the Layer 8 sediments. Typical concentrations for Si in the matrix range between 5 and 15%. Concentrations of greater than 20% are only found in association with flint fragments.

8.6.1.1.4 Summary

The study clearly depicts a sedimentary matrix where the distribution of radioactive elements is far from homogenous. This heterogeneity can still be seen even with the inability to determine U and Th concentrations below 4 µg/g. As was the position taken in Chapter 6, it is considered that the pXRF is only detecting the upper tail-end members of the U and Th distributions. Given that concentrations of Th were present from detection levels (4 µg/g) up to 10 µg/g suggests that the central portions of the Th concentration distribution might also show similar variability. This same argument is not as strong for the U distribution, using the pXRF data here, as only 7 measurement positions in one ROI had detectable U. However, the modelled radionuclide distribution studies conducted in Chapter 6 support this assertion, that spatial distributions of both Th and U are inhomogeneous at lower than detection level concentrations. In Figures 6.13, 6.14 and 6.15, the distribution pattern modelled for U and Th for a sample from Layer 8 (sub-sample PdAIV-01-C) was shown to be heterogeneous. The distribution of K was also heterogeneous with relatively high concentrations found in the matrix and considerably lower concentrations in bone, flints or calcite nodules. It is this heterogeneity of U, Th and K that would give rise to variability in the β-D_r within the sediments of Layer 8. In each of the sub-samples investigated here, a case for β-D_r heterogeneity can be made as a possible extrinsic factor affecting and contributing to the spread in their respective D_e distributions.

a)

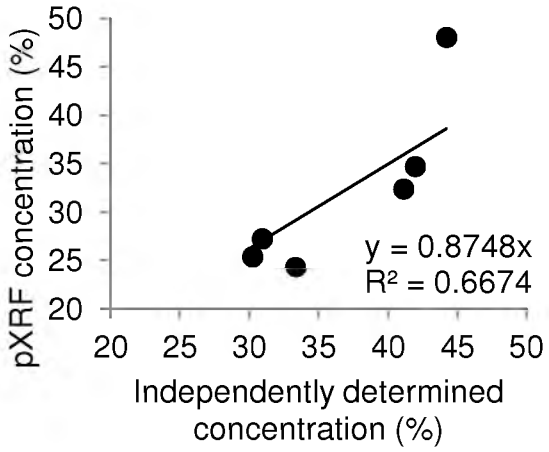

b)

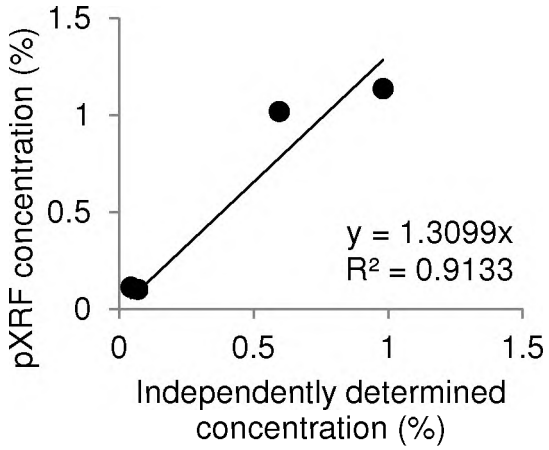

c)

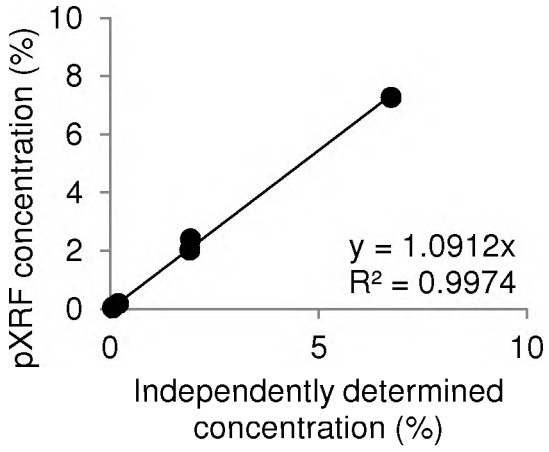

Figure 8.17. Portable XRF calibration curves for a) P, b) Ca and c) Si.

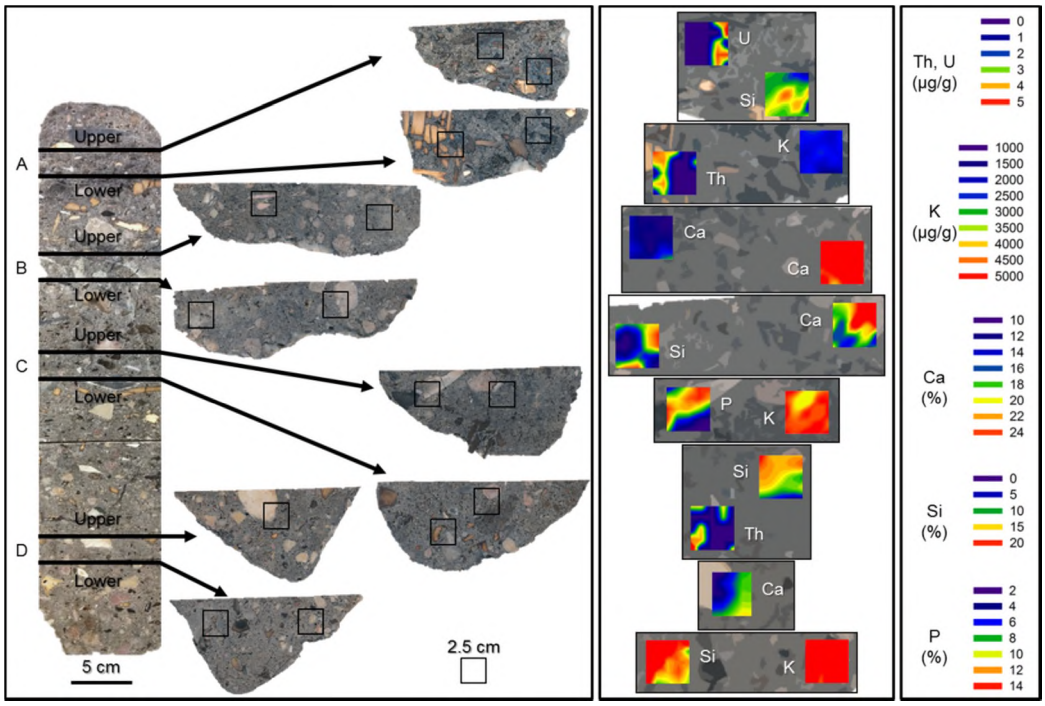

Figure 8.18. **Left panel**: PdAIV-01 sample column showing the positions of the Upper and Lower slabs for each of the four Layer 8 sub-samples. It should be noted that the OSL sample for these samples comes from the sediments between these surfaces. Features investigated with pXRF are delimited by the 2.5 cm squares. Where more than one feature was analysed per slab, the square to the left is labelled feature 01 and that on the right 02. **Centre panel**: pXRF distribution maps for selected elements for each of the features analysed in this study displayed upon stylised drawings of each slab for reference. Element being shown is noted adjacent to each distribution map. **Right panel**: legend for the various elements shown in centre panel.

8.7 D_e DETERMINATION FOR SAMPLES FROM PECH IV

In this section, each of the D_e distributions will be assessed in turn to determine the most appropriate means of combining the values. To aid in the interpretation, I have integrated the Layer 8 pXRF results from Section 8.8.2, the beta microdosimetry results presented for samples PdAIV-01-C and -02 presented in Chapter 6 and the soil micromorphological work undertaken by a co-supervisor (Paul Goldberg) as part of the recent re-excavation of Pech IV presented in Turq *et al.* (2011).

With respect to the last point, the integration of soil micromorphology with single-grain OSL dating has previously been shown to be mutually beneficial (Chapter 5). Not only can the use of soil micromorphology inform about sedimentary composition (i.e. grain size fractions and mineralogies) but also offer qualitative insights into the processes involved in site formation, both syn- and post-depositionally (Courty et al. 1989, Goldberg and Macphail 2006). Throughout this section the terminology presented in Stoops (2003) was used to describe the sedimentary characteristics of thin sections (Figure 8.23, 8.24 and 8.25) taken from the same stratigraphic layers as the OSL samples. We present the samples in ascending stratigraphic order.

8.7.1 PdAIV-01-D – 26 CM FROM THE TOP OF THE LAYER 8 COLUMN – FIGURE 8.20A

The D_e values measured for the basal sample in Layer 8 shows a broad distribution. The majority of the grains fall within a 160 Gy range between 26 ± 6 and 182 ± 16 Gy; one grain has a significantly smaller D_e value of 8 ± 2 Gy. The D_e values show more scatter than is statistically expected with an OD value of 49 ± 5% calculated using the CAM (Galbraith *et al.* 1999). As this OD value is significantly

greater than that measured during the dose-recovery tests (~10%; Section 8.7.1), further investigation is required to explain this additional spread.

The sediments in Layer 8 are chaotic and heterogeneous (Figure 8.23a), but this sub-sample has a number of unique features. Apart from the random scattering of burnt and unburnt bones and flint tools (Figure 8.23a and b: representative of all Layer 8 samples), soil micromorphological investigation of thin section from the base of Layer 8 revealed an abundance of calcite hypocoatings within the large void spaces in the sediments (Figure 8.23f) (Goldberg *et al.* 2012). The presence of calcite, in terms of radiation dosimetry, is often associated with regions of relatively low β-D_r – commonly termed 'coldspots' (Jacobs et al. 2008c, Nathan et al. 2003, Olley et al. 1997, Murray and Roberts 1997). Given the millimetre size of the voids that are coated with calcite, it is proposed that the grains closest to, or embedded in, the calcite precipitates may receive a β-D_r that was substantially less than one that was, say, surrounded in matrix alone.

Thin section analysis suggests that Pech IV was intensively occupied during the deposition of Layer 8 (Dibble *et al.* 2009, Goldberg *et al.* 2012). The chaotic sedimentary nature of the Layer 8 sediments (Figure 8.23b) suggests that this layer was extensively reworked over the period of occupation. The reworking of this layer would not only result in the physical mixing of the sediment but also serve to bleach the OSL signal of the quartz grains as well. Concurrently, bone fragments have been observed in thin section complete with refitting fractures (Figure 8.23c). Goldberg *et al.* (2012) hypothesise that such features provide evidence of anthropogenic trampling of the sediment, however, the fact that these refitting bone fragments have remained '*in situ*' (Figure 8.23c) suggests that the sediments had not been significantly reworked following the trampling.

It is considered, therefore, that the additional spread evident in the D_e distribution for this sample consists of a degree of unexplained inherent variability and also variations in the β-D_r environment and (to a lesser extent) mixing during antiquity. The CAM was used to calculate the weighted mean D_e value of 64 ± 4 Gy for this sample and was considered to be the most appropriate method for doing so.

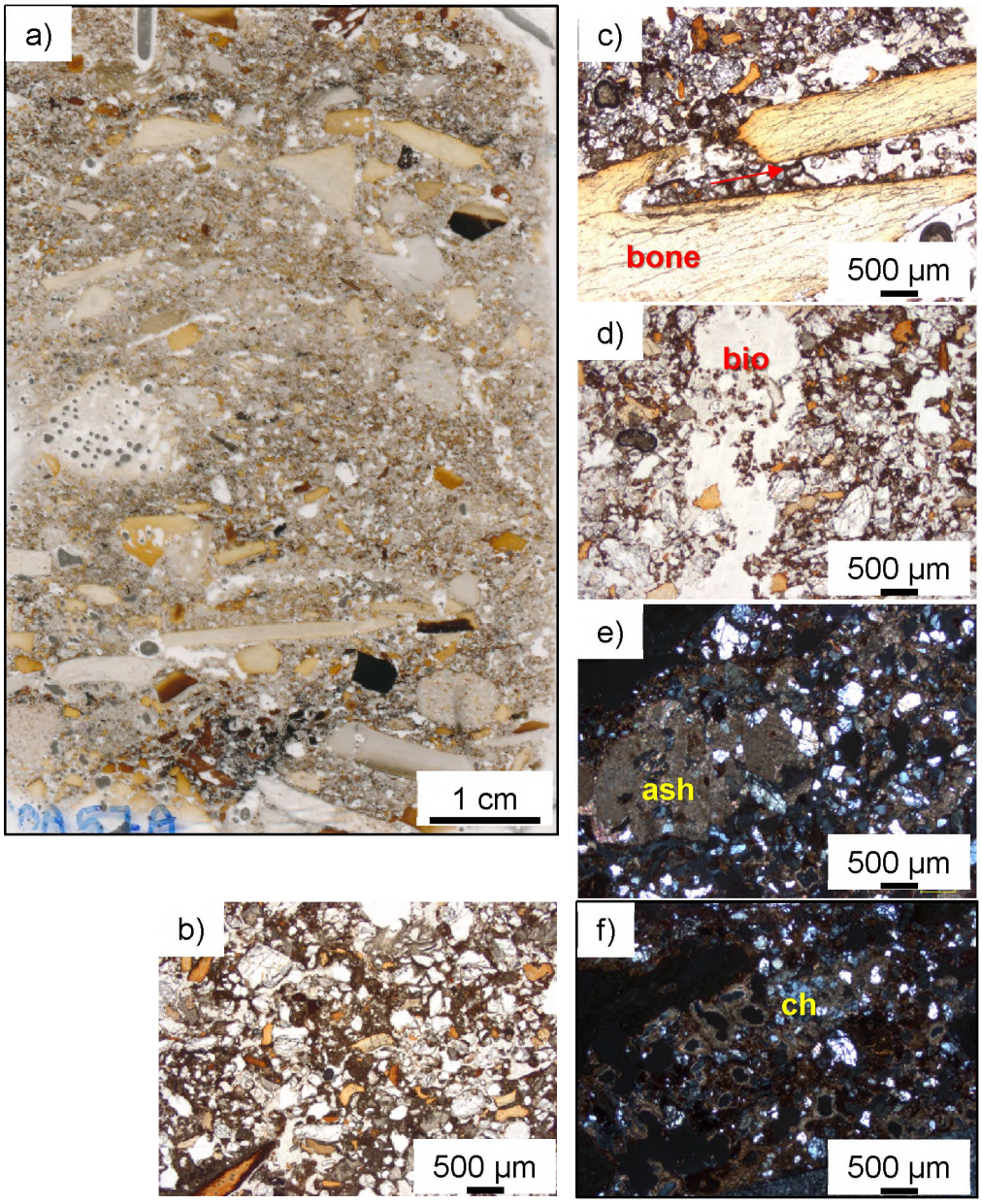

Figure 8.19. Typical thin section and microphotographs from Layer 8 sediments of Pech IV. a) Representative thin section for Layer 8. Microphotographs of b) Layer 8 sedimentary matrix typified by dark brown/black colour, the presence of burnt and unburnt bone fragments, flint tool, ash and limestone spall (plane polarised light; ppl). c) Accommodating bone fracture pattern (indicated by the arrow) indicative of anthropogenic trampling (ppl). d) Channel void and disrupted sedimentary matrix suggestive of bioturbation (indicated) (ppl). e) Redistributed ash material (indicated) (cross polarised light; xpl). f) Calcite hypocoatings (ch) within void space at the base of Layer 8 (xpl).

8.7.2 PdAIV-01-C – 15 CM FROM THE TOP OF THE LAYER 8 COLUMN – FIGURE 8.20B

The range of D_e values measured for sub-sample C are consistent with those measured for the underlying sub-sample D. Here, the D_e values, once again, fall almost symmetrically around a central value and range from 10 ± 5 to 200 ± 56 Gy. The OD for this distribution was estimated to be 48 ± 4% using the CAM.

This sample was studied extensively in Chapter 6. The dry and unattenuated β-D_rs of the three grain size fractions of >2 mm, 2 mm–180 μm and <180 μm fractions were measured to be 0.18 ± 0.04, 0.40 ± 0.03 and 0.53 ± 0.03 Gy/ka, respectively, using a GM-25-5 low-level beta counter (Bøtter-Jensen and Mejdahl 1988). This variability in β-D_r was also found to be distributed heterogeneously throughout the sediment. It was concluded that the spread in D_e values could be entirely explained by variations in the β-D_r for the sample. The most appropriate means of combining the individual D_e values for this sample is also to use the CAM. Here, a weighted mean D_e value of 63 ± 4 Gy was estimated.

8.7.3 PdAIV-01-B – 9 CM FROM THE TOP OF THE LAYER 8 COLUMN – FIGURE 8.20C

The spread in the D_e values for this sample is not only the largest for any of the Layer 8 samples at 72 ± 6%, but also the largest of any of the samples investigated in this study. Like the previous two samples, the D_e values fall symmetrically around a central point and range from 4 ± 1 to 311 ± 68 Gy. Based on this D_e distribution pattern, and the extensive geoarchaeological investigations carried out by Turq *et al.* (2011), it is unlikely that the quartz sands currently found in the cave and dated using the single-grain OSL method are incompletely bleached prior to burial.

Soil micromorphology shows that, in conjunction with fragmentary bone and flint, ash clasts are also prevalent (Figure 8.23e). The presence of indurated ash clasts

are a clastic feature unique to this sample. It should be noted that this sub-sample was taken from within a layer that appeared to be lighter in colour than the bounding layers and contained ash-coloured material (Figure 8.2). The presence of the ash is also evident in the pXRF ROI analysis for this sample shown in Figure 8.22 B-Upper. Here, regions of substantially greater Ca are positioned in close proximity to those with much less (Figure 8.22 B-Upper). The same argument for β-D_r 'coldspots' with regards to calcite infilling in sub-sample D can again be used here. The chaotic nature of the sedimentary fabric for this portion of Layer 8, and indeed all of Layer 8, has been suggested to be the result of continuous hearth maintenance and rake out activities (Goldberg *et al.* 2012, Turq *et al.* 2011), therefore the likelihood of post-depositional mixing can't be ruled out. However, the D_e distribution for this sub-sample does not show the tell-tale discrete D_e 'bands' that represent singular mixing events (c.f., David *et al.* 2007). It is likely that the mixing that took place would have been so intense that the reworked grains would have been bleached prior to reburial or that it happened at the same time as the occupation of the cave, but has remained undisturbed since.

The spread (OD) within this sample could therefore be the result of the intrinsic variability in the quartz grains, an artefact of the reworking of the sediments, and beta microdosimetric differences. The CAM was used to estimate the weighted mean D_e for the sample of 64 ± 5 Gy.

8.7.4 PdAIV-01-A – 3 CM FROM THE TOP OF THE LAYER 8 COLUMN – FIGURE 8.20D

The D_e distribution for this sample is the most constrained in terms of the range of measured D_e values and OD value of 39 ± 4%. Here, the majority of the grains fall within a 160 Gy range from 20 ± 5 to 182 ± 42 Gy, with a few grains with D_e values up to ~180 Gy.

The pXRF investigation carried out on the 'Upper' and 'Lower' slabs of this sub-sample are perhaps the most variable of any investigated here (Figure 8.22). The presence of bone fragments is associated with substantially higher Th concentrations than the surrounding matrix, which is hosting the majority of the K in the fine fraction. This sub-sample also has the only recorded U concentrations that were greater than the detection limit of the pXRF. Therefore, the same argument for beta microdosimetry can again be used here. So, too, can the argument for post-depositional mixing by human agents. Soil micromorphological analysis also reveals a number of channel voids in this sub-sample suggesting either earth worm or rootlet activity (Figure 8.23d).

The spread within this sample could again be the result of inherent variability, beta dose heterogeneity, post-depositional reworking, or any combination of these. To meaningfully combine these D_e values, the CAM was once again used to provide a weighted mean D_e value of 55 ± 3 Gy for the sample.

8.7.5 PdAIV-02 – Layer 5B – Figure 8.20e

The D_e values measured for the sample from Layer 5B have the poorest precision of any of the samples investigated in this study. The OD of this sample was calculated to be 30 ± 6%. Of the 62 acceptable grains, only 7 have a relative uncertainty that is <20%. This large relative uncertainty is the result of the low sensitivity of the grains that comprise this sample (Figure 8.17). The range of D_e values is spread between about 26 ± 10 and 178 ± 77 Gy and fall symmetrically around a central value. The dose-recovery experiments for this layer were conducted on the stratigraphically equivalent PdLIV-8 sample of Jacobs *et al.* (submitted) and gave a OD value of 19 ± 4%, a value consistent with the OD of this sample (30 ± 6%). It is therefore possible to explain the additional scatter in the D_e values for this sample purely as a result of intrinsic grain variability.

However, the Layer 5B sediments (Figure 8.20e) were investigated in Chapter 6. In that chapter, it was established that the variability in the β-D_r for the sample was

dependent on the grain size fractions measured. Here the >2 mm, 2 mm–180 μm and <180 μm fractions were measured as having dry and unattenuated β-D_rs of 0.37 ± 0.02, 0.52 ± 0.03 and 1.12 ± 0.04 Gy/ka using a GM-25-5 beta counter (Bøtter-Jensen and Mejdahl 1988). Using pXRF, Al_2O_3:C grains and image analysis modelling, it was also shown that the distribution of β-D_r across the sediments was heterogeneous.

Soil micromorphological analysis supports this finding (Figure 8.24a). Typical sedimentary matrix from this unit is comprised of large limestone clasts and heterogeneously distributed clay coatings surrounding the coarser grains and clasts (Figure 8.24b). Thus, the clay coatings are likely to provide regions of higher than average β-D_rs. In contrast, the presence of large calcite hypocoatings (Figure 8.24c) with diameters of >2 mm are likely to provide regions of lower than average β-D_r. Although already explained as intrinsic variability, the case for BM as an extrinsic agent leading to the spread in the D_e values for this sample could be made but the uncertainties associated with the D_e values overshadows the differences in β-D_r. In either case, the most appropriate means of combining the D_e values for age determination is the CAM. As such, a weighted mean D_e of 64 ± 4 Gy was estimated for this sample.

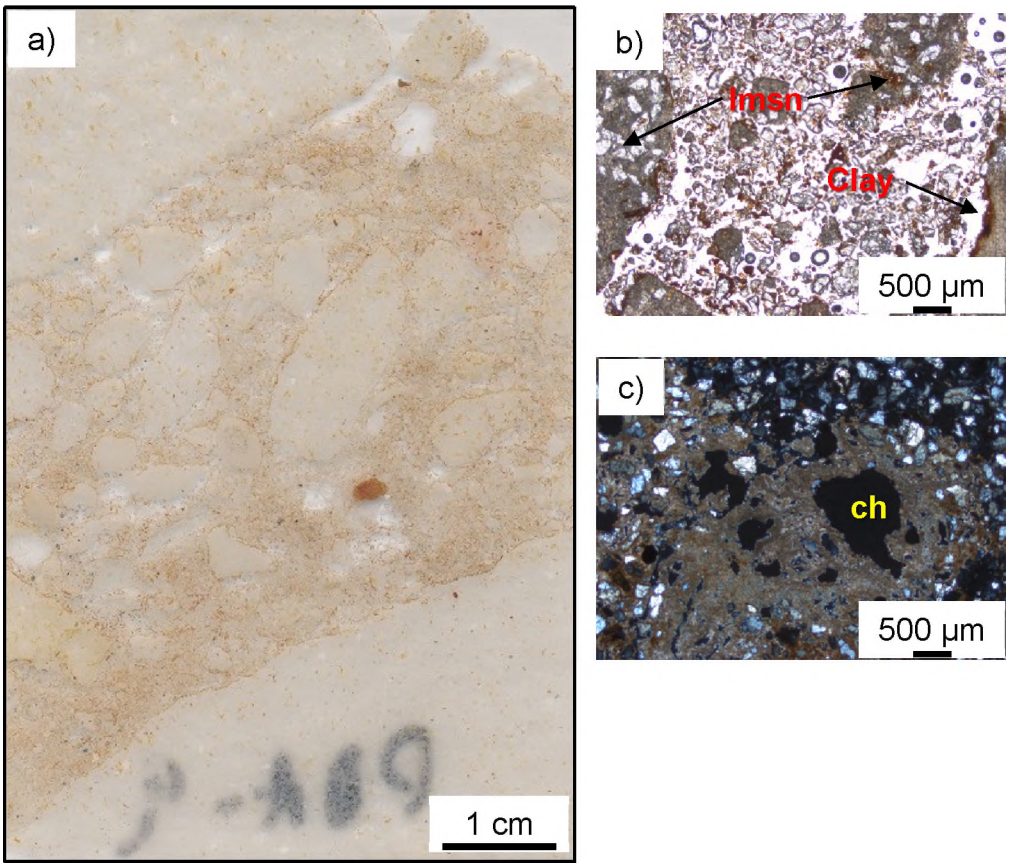

Figure 8.19. Typical thin section and microphotographs from Layer 5B sediments of Pech IV. a) Representative thin section for Layer 5B. Microphotographs of: b) Layer 5B sedimentary matrix comprising of mainly quartz grains, limestone clasts (lmstn) and clay (ppl), and c) calcite hypocoatings (ch in the central void) of >2 mm diameter (xpl).

8.7.6 PdAIV-03 – Layer 4A – Figure 8.20f

Unlike the unburnt sediments of Layer 5B, here the relative uncertainties for the majority of grains are better than 25%. These grains have slightly brighter luminescence signals and sensitivities (Figure 8.17). The D_e values measured for this sample range from 38 ± 15 to 198 ± 23 Gy and appear to cluster around a central value. The OD for this sample was estimated to be 30 ± 4%.

Beta microdosimetry could also be considered as a likely process to induce spread within the D_e distributions. The sediments of this layer are composed of roughly equal proportions of quartz sand and clays (Figure 8.25a and b). The dry and unattenuated β-D_r for two grain size fractions of 0.48 ± 0.03 (180 μm–2 mm) and 1.23 ± 0.04 (<180 μm) were measured using a GM-25-5 low-level beta counter. The higher β-D_r of the <180 μm is considered to be the result of the K-bearing mica (probably muscovite) flakes and clays within this grain size fraction (Figure 8.25d). In contrast, the lower β-D_r for the 180 μm–2 mm fraction is thought to be due to calcite hypocoatings filling void space (Figure 8.25c).

The most reliable means of combining the individual D_e values for this sample was through the application of the CAM. The resulting weighted mean D_e for this sample was calculated to be 101 ± 4 Gy.

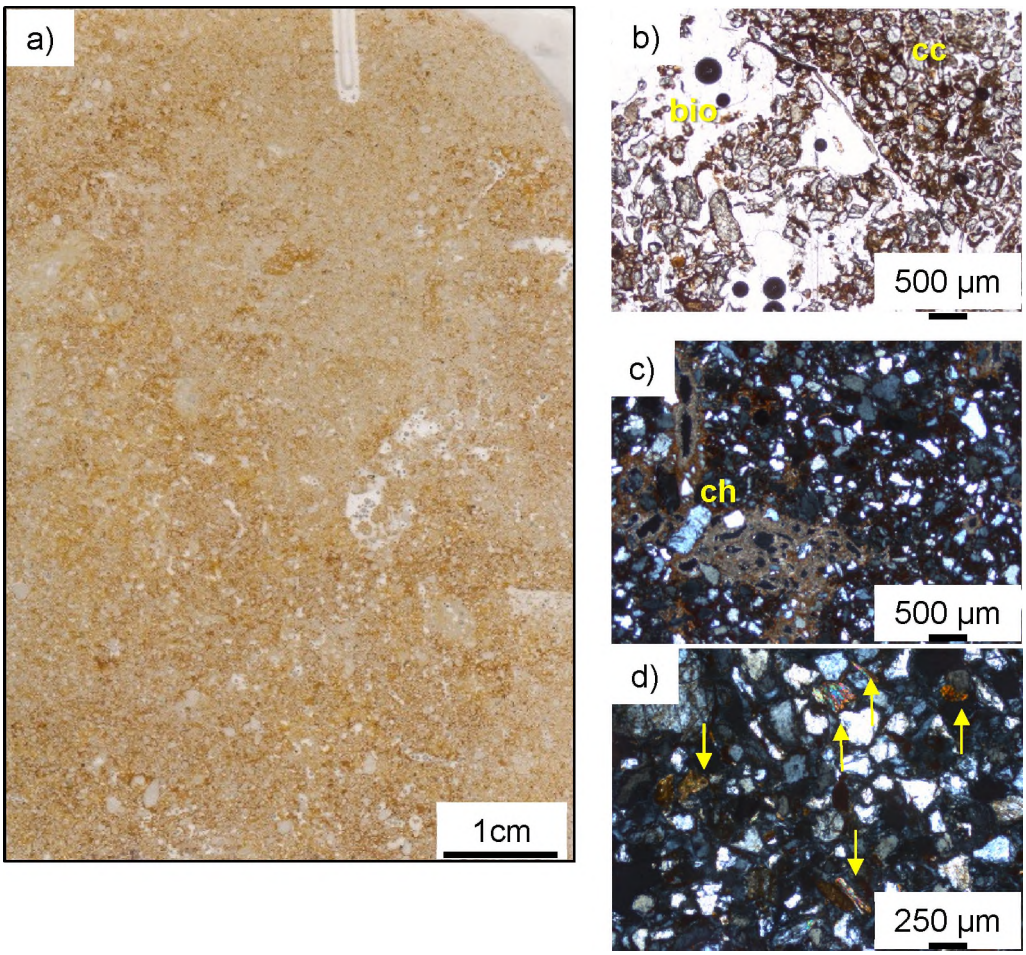

Figure 8.21. Typical thin section and microphotographs from Layer 4A sediments of Pech IV. a) Representative thin section for Layer 4A. Microphotographs of: b) Layer 4A sedimentary matrix comprising of mainly quartz grains and clay. Also shown is evidence of bioturbation in the lower left hand corner of the image (ppl). c) A complex of calcite hypocoatings (ch) (xpl), and d) abundant mica (muscovite) flakes (indicated by the yellow arrows) found within the fine fraction of Layer 4A (xpl).

8.8 ENVIRONMENTAL DOSE RATE MEASUREMENTS

The environmental dose rate delivered to the quartz grains of the Pech IV samples is the sum of: 1) beta and gamma radiation from the surrounding sediments produced by the radioactive decay of ^{238}U, ^{235}U and ^{232}Th (and their daughter products) and ^{40}K; 2) an alpha particle dose rate coming from inside each of the grains produced by the radioactive decay of ^{238}U, ^{235}U and ^{232}Th; and 3) a contribution made by intergalactic cosmic rays. Soil moisture plays an important role in environmental dose rate estimation as it effectively attenuates the incoming radiation flux. As a general rule, for every 1% increase in soil moisture a concomitant decrease of ~1% is observed in the total environmental dose rate and a corresponding ~1% increase in OSL age.

8.8.1 BETA DOSE RATE

The β-D_r for each sample was measured using a GM-25-5 low-level beta counter (Bøtter-Jensen and Mejdahl 1988). The sediment samples used for β-D_r determination for Layer 8 were the resin-impregnated portions indicated in Figure 8.2, whereas the 'loose' light-exposed sediments were used for the Layer 5B and 4A samples. Following disaggregation of the Layer 8 samples in the toluene/acetone bath, the sediments were separated using graduated sieves into three fractions: >2 mm, 2 mm–180 µm and <180 µm. No sediments in the >2 mm fraction were recovered for Layer 4A. Each fraction was then dried and weighted, and the proportional contribution of each to the total weight of the sample calculated (Table 8.10). The fractions were then pulverised to a fine powder using a ball mill. Each fraction was then placed into beta 'pots' for measurement that were partially-filled with polyethylene glycol wax (PEG), following the procedures outlined in Chapter 6 (Section 6.3.2). All 'pots' were filled to the brim with powder and scraped level to ensure a homogeneous presentation to the detectors. Once each grain-size fraction for each sample had been measured, a proportional mixture of each grain size

fraction was made to represent the mean β-D_r for the sample – this value was used in the determination of OSL ages for each of the sediments.

The results for each grain size fraction and the 'average' β-D_rs are displayed in Table 8.11. Allowances in the β-D_rs reported in Table 8.11 were made for β-D_r attenuation and HF-acid etching (Brennan 2003). It should be noted that both the grain size fraction and mean β-D_rs for samples PdAIV-01-C and PdAIV-02 are those presented in Chapter 6. In each sample there is an increase in β-D_r with decreasing grain size. The higher β-D_r in the <180 µm grain size fraction is considered to be the result of the greater abundance of silt, clay and (in the case of Layer 4A) mica flakes in this fraction which have higher K concentrations (Figures 8.24b and 8.25b). In contrast, the >2 mm grain size fraction are composed of mostly limestone, flint and bone fragments, each having low total β-D_r values as was shown in Table 6.5 in Chapter 6.

There is some variation between the grain-size and mean β-D_rs for the Layer 8 sub-samples. PdAIV-01-B in all but the >2 mm fraction has the lowest values recorded for any Pech IV sample measured in this study. This is presumable due to the significant proportion of calcite ash found throughout this sub-sample (Figures 2.23e and 2.22-B-Upper). The mean β-D_rs for Layer 5B (0.46 ± 0.03 Gy/ka) and 4A (0.84 ± 0.03 Gy/ka) are significantly higher than those for the sub-samples from Layer 8 (0.23 ± 0.03 to 0.31 ± 0.02 Gy/ka). These values were used in the age estimates provided in Table 8.12.

Table 8.9. Grain size proportions (% total weight) for the six Pech IV samples investigated in the beta dose rate study.

Layer	Sample name	Grain size fraction proportions (%)		
		>2 mm	2 mm–180 µm	<180 µm
8	PdAIV-01-A	31	62	8
	PdAIV-01-B	42	54	5
	PdAIV-01-C	22	66	11
	PdAIV-01-D	25	62	14
5B	PdAIV-02	40	41	19
4A	PdAIV-03	-	42	58

Table 8.10. Beta dose rates for the six Pech IV samples studied. Here, the three different grain size fractions of sample is shown. The average beta dose rate was found by mixing proportions of each grains size fraction according to the values displayed in Table 8.10.

Layer	Sample name	Water content (%)	Grain size fraction beta dose rates (Gy/ka)[a]			
			>2 mm	2 mm–180 µm	<180 µm	Average
8	PdAIV-01-A	5.6	0.21 ± 0.01	0.26 ± 0.02	0.39 ± 0.02	0.27 ± 0.02
	PdAIV-01-B	5.6	0.16 ± 0.03	0.22 ± 0.03	0.30 ± 0.03	0.23 ± 0.03
	PdAIV-01-C	6.9	0.14 ± 0.05	0.32 ± 0.02	0.44 ± 0.04	0.29 ± 0.03
	PdAIV-01-D	8.1	0.22 ± 0.01	0.31 ± 0.03	0.42 ± 0.02	0.31 ± 0.02
5B	PdAIV-02	6.6	0.30 ± 0.02	0.41 ± 0.03	0.88 ± 0.04	0.46 ± 0.03
4A	PdAIV-03	4.0	-	0.40 ± 0.03	1.00 ± 0.04	0.84 ± 0.03

[a] All beta dose rates were measured using a GM-25-5 beta counter and beta pots that were half filled with polyethylene glycol wax. Each measurement was then adjusted to account for their respective field water content and attenuation for 200 µm grains.

8.8.2 GAMMA DOSE RATE

The gamma dose rates are those reported in Jacobs *et al.* (submitted) and are presented in Table 8.12. Here, an *in situ* 1-inch in diameter NaI(TI) gamma detector was used to determine the gamma dose rate at the time of sampling. This technique accounts for any inhomogeneity in the gamma sphere surrounding the point of sample collection. We were able to directly use the gamma dose rate measurements reported for Jacobs and others' samples PdLIV-1, -2, -8 and -18 as these were taken at the same sampling locations as PdAIV-01-D, -01-B, -02 and -03, respectively. The gamma dose rates for the remaining two samples (PdAIV-01-A and PdAIV-01-C) had to be calculated separately.

The Layer 8 sub-sample C (PdAIV-1-C) is located roughly half way between sub-samples B (above) and D (below). The gamma dose rate for this sample was taken as the average of the gamma dose rates from these two bounding samples, with the uncertainties on each propagated accordingly. The gamma dose rate for sub-sample A, at the top of the Layer 8 sediment block, is considered to have received half its gamma dose rate from the underlying sediments, with the other half derived from the overlying limestone slabs. It was considered that an average of the gamma dose rates came from: 1) the *in situ* measurement made for sub-sample B; and 2) that of the overlying limestone slab, and that this would provide the most appropriate estimate of gamma flux for this sample. The gamma dose rate of the limestone was determined by pulverising a number of limestone cobbles that had been collected from the site and washed of any external sediment. Using this powdered sample, a gamma dose rate of 0.15 ± 0.01 Gy/ka was determined using a combination of GM-25-5 beta counting and thick-source alpha counting. Therefore, the gamma dose rate for sub-sample A was determined to be 0.24 ± 0.01 Gy/ka.

Table 8.11. Dose rate values, D_e values and single-grain OSL ages for the six Pech IV samples investigated in this study

Sample code	Layer	Moisture content (%)[a]	Dose rates (Gy/ka)[b]			Total dose rate (Gy/ka)[c]	D_e (Gy)[d]	Number of grains[e]	Over dispersion (%)	OSL age (ka)[f]
			Beta	Gamma	Cosmic					
PdAIV-03	4A	4.0 ± 1.0	0.84 ± 0.03	0.58 ± 0.03	0.10	1.56 ± 0.08	100.7 ± 4.4	72 / 2600	30 ± 4	64.6 ± 4.6
PdAIV-02	5B	6.6 ± 1.7	0.46 ± 0.03	0.39 ± 0.03	0.08	0.97 ± 0.05	66.4 ± 4.1	62 / 2000	30 ± 6	68.8 ± 5.9
PdAIV-01-A	8	5.6 ± 1.4	0.27 ± 0.03	0.24 ± 0.01	0.05	0.60 ± 0.04	55.1 ± 2.7	90 / 1000	39 ± 4	91.5 ± 7.6
PdAIV-01-B	8	5.6 ± 1.4	0.23 ± 0.03	0.33 ± 0.02	0.05	0.64 ± 0.05	63.5 ± 5.4	80 / 1500	72 ± 6	98.6 ± 11.1
PdAIV-01-C	8	6.9 ± 1.7	0.29 ± 0.03	0.31 ± 0.02	0.05	0.69 ± 0.05	62.9 ± 3.6	89 / 1000	48 ± 4	91.6 ± 8.8
PdAIV-01-D	8	8.1 ± 2.0	0.31 ± 0.02	0.29 ± 0.02	0.05	0.68 ± 0.04	63.7 ± 3.9	77 / 1000	49 ± 5	93.1 ± 8.4

a. Moisture contents are based on those presented in Jacobs *et al.* (submitted) where stratigraphically-equivalent samples was collected. These values were calculated as the % mass of water per unit of dried sediment and a random relative uncertainty of ± 25% (1σ) was assigned to each value.

b. Measured and calculated dose rates ± (1σ). All beta dose rates were measured using GM-25-5 beta counter using dried, powdered and homogenised sediment samples. Gamma dose rates for all samples, except PdIV-01-A and -C, were measured using a 1-inch gamma detector. The cosmic dose rates were calculated using the equations of Prescott & Hutton (1994) and the cos2-Φ zenith angle dependence (Smith *et al.* 1997). The cosmic dose rates were assigned relative uncertainty of ± 10%.

c. Mean ± total (1σ) uncertainty and includes an assumed internal alpha dose rate value of 0.03 ± 0.01 Gy/ka for all samples.

d. Mean CAM D_e ± total (1σ) uncertainty.

e. The number of accepted grains used in the calculation of the sample D_e.

f. Mean ± total (1σ) uncertainty.

8.8.3 ALPHA DOSE RATE

The internal alpha dose rate contribution comes from the radioactive decay of U and Th within the crystal lattice of the each quartz grains. For the Pech IV samples, an internal alpha dose of 0.03 ± 0.01 Gy/ka was assumed.

8.8.4 COSMIC DOSE RATE

The cosmic dose rate for each sample is based on those presented in Jacobs *et al.* (submitted) and are presented in Table 8.12. The cosmic dose rates were adjusted for an average site elevation above sea level (~165 m), geomagnetic latitude (47.3°), the density and thickness of rock (2 g/cm^3) and sediment (1.8 g/cm^3) overburden, using the equations presented in Prescott & Hutton (1994). Allowances in the cosmic dose rate were made for the cos2-Φ zenith angle dependence of cosmic rays (Smith *et al.* 1997) and also the evolution of the Pech IV cave morphology (Turq *et al.* 2011). An uncertainty of 10% was assigned to each estimate to account for the uncertainty in the primary cosmic-ray intensity (Prescott & Hutton 1994).

8.8.5 SOIL MOISTURE CONTENT

The measurement of soil moisture was made on sediments collected at the time of sampling and based on those reported in Jacobs *et al.* (submitted) and presented in Table 8.12. Again, a one-to-one usage of the moisture contents for the Layer 8 sub-sample D (8.1%) and B (5.6%), and Layer 5B (6.6%) and 4A (4.0%) samples could be made. The moisture content for Layer 8 sub-sample A was assumed to be the same as that for sub-sample B (5.6%), while the average moisture content for sub-samples D and B was considered to be an appropriate estimate of soil moisture for Layer 8 sub-sample C (6.9%).

The variation in the soil moisture contents for the Layer 8 sub-samples was deliberately chosen to reflect the apparent variation in the water regime for the site. Soil micromorphological analysis has observed that the abundance of calcite hypocoatings is greatest at the base of Layer 8 (Figure 8.23f). Goldberg *et al.* (2012) suggested that this variation was the result of interstitial pore water 'ponding' above the impermeable limestone floor. It was considered, therefore, that, moving down through the Layer 8 sub-samples, the soil moisture content experienced by the sediments over the period of burial was also likely to increase. Thus, the stratigraphically highest sub-sample (PdAIV-01-A) would have been relatively drier than the lowest sub-samples (PdAIV-01-D) from Layer 8.

A relative uncertainty of ±25% at 1σ was assigned to each soil moisture estimate to account for any long term fluctuations for each of the samples. Allowances in the external beta, gamma and cosmic dose rates were made to account for the respective soil moisture contents for each of the six Pech IV samples (Aitken 1985, Aitken and Xie 1990, Nathan and Mauz 2008).

8.8.6 TOTAL ENVIRONMENTAL DOSE RATES

The total environmental dose rates, presented in Table 8.12, represent the sum of each of the dose rate contributions outlined above. The associated uncertainty (1σ) on each estimate represents the quadratic sum of all known random and systematic errors. There is a distinct shift in the total environmental dose rates with depth, decreasing down profile (Table 8.12). The Layer 4A sample (PdAIV-03) has the largest total environmental dose rate (1.56 ± 0.08 Gy/ka) of any sample investigated in this study. The significantly higher proportion of the <180 µm fraction (58% Table 8.10), which contained mainly clay-size material, is considered to be responsible for the higher dose rate measured for this sample. Furthermore, the abundance of mica (Figure 2.25d) is also considered to contribute to this result.

The total environmental dose rate for the Layer 5B sample (PdAIV-02) was determined to be 0.97 ± 0.05, roughly two thirds that of the stratigraphically higher Layer 4A sample. In this instance, the decrease in the proportion of the <180 µm

fraction (19%, Table 8.10) and the relative proportion of clay within this grain size fraction, coupled with the concomitant increase in limestone cobbles is thought to be responsible for this significantly lower total environmental dose rate.

The total environmental dose rates determined for each of the four Layer 8 sub-samples are all internally consistent (Table 8.10). A total environmental dose rate of 0.60 ± 0.04 Gy/ka was determined for sub-sample PdAIV-01-A (at the top of the Layer 8 column), 0.64 ± 0.05 Gy/ka for sub-sample PdAIV-01-B, 0.69 ± 0.05 Gy/ka for sub-sample PdAIV-01-C and 0.68 ± 0.04 Gy/ka for sub-sample PdAIV-01-D (at the bottom of the Layer 8 column). These total environmental dose rates are the lowest of the 6 samples investigated here, with the increase in the amount of flint, bone and calcite (as limestone, hypocoatings or ash) and relatively reduced proportions of clay (5–14%; Table 8.10) considered responsible for the reduction in total radiation flux for these samples.

8.9 DISCUSSION

8.9.1 PECH IV SINGLE-GRAIN OSL AGES AND COMPARISON WITH EXISTING CHRONOLOGY

The single-grain OSL ages for the six samples collected from Pech IV were determined by dividing the D_e of each sample (Section 8.9) with their corresponding total environmental dose rates (Section 8.10). The uncertainty on each age estimate (reported at 1σ) was calculated as the quadratic sum of the uncertainties associated with both the D_e and dose rate estimates as well as a 2% systematic uncertainty to account for uncertainty in the calibration of the laboratory beta source (refer to Chapter 3, Sections 3.4 and 3.5 for further details of error estimation and propagation). These ages are presented in Table 8.12. A age-depth profile of these ages, along with those calculated by Jacobs et al. (submitted) and other forms of independent age control published previously for Pech IV, is given in Figure 8.22.

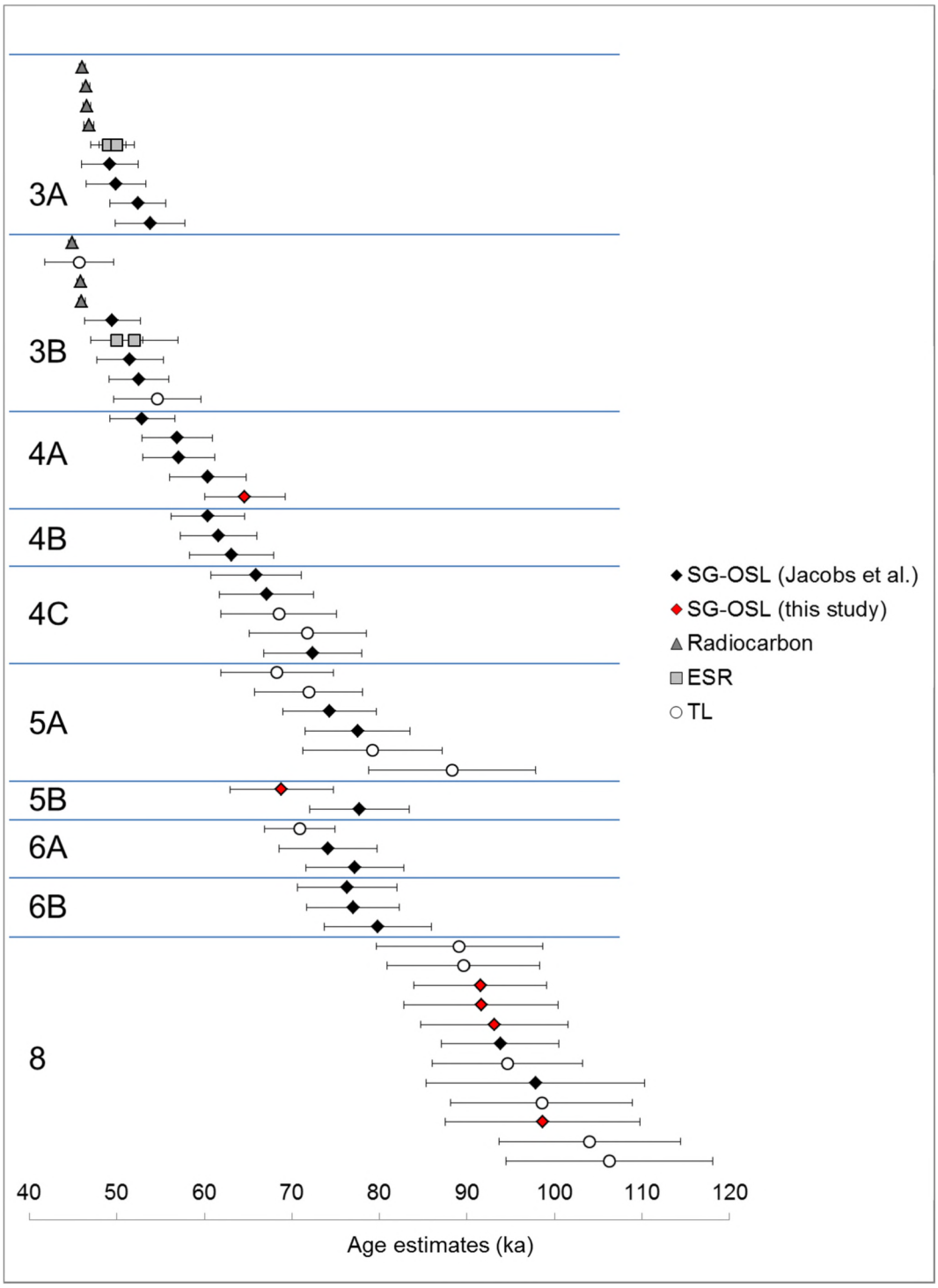

Figure 8.22. Pech IV age estimates ranked according to layer. The single-grain quartz OSL ages determined in this study are shown as red diamonds. The remaining SG-OSL ages are those of Jacobs *et al.* (submitted). The radiocarbon, ESR and TL ages can be found in McPherron *et al.* (2012), Turq *et al.* (2011), and Richter *et al.* (2013), respectively.

The single-grain OSL ages of Jacobs *et al.* were produced in conjunction with those presented in this study. Thus, the analytical and measurement procedures are analogous to those outlined here for the PdA samples. Furthermore, the D_e distribution patterns of all samples measured by Jacobs and colleagues are distributed around a central mean value. This pattern, according to the authors, is the unlikely to have been produced had the quartz grains been partially-bleached prior to burial within Pech IV. If this were the case the application of the minimum age model to these samples would have resulted in a vast underestimate of the single-grain OSL ages in comparison with the multitude of independent age controls available for the Pech IV deposit (see Figure 8.22). Turq *et al.* (2011) point out that the carse fraction (including the 180–212 μm quartz used for single-grain OSL) is the product of the local dissolution of the hsot limestone. These grains would have either fallen from the roof of the cave or have been transported into the cave as material was washed in from the talus cone that would have been present under the cave opening. In either case, it is likely that the quartz grains would have been closer to fully-bleached, than partially-bleached, at the time of deposition.

The four Layer 8 sub-samples have statistically consistent single-grain OSL ages, in ascending stratigraphic order, of: 93 ± 8 (PdAIV-1-D), 92 ± 9 (PdAIV-1-C), 99 ± 11 (PdAIV-1-B) and 92 ± 8 ka (PdAIV-1-A; Table 8.12). At the resolution that the single-grain OSL dating provides, it is clear that no time sequence can be resolved between the base and the top of Layer 8. Rather, it is likely that the deposition of Layer 8 was either continuous between ~100 and 90 ka ago, or occurred as distinct sedimentary events. Goldberg *et al.* (2012) favour the hypothesis that Layer 8 is composed of two separate subunits but this could not be temporally resolved using these ages given the 8–11 ka uncertainties at 1σ. As such, a weighted mean of 95 ± 5 ka was calculated using the four Layer 8 single-grain OSL ages, having remove all common systematic uncertainties prior to calculation.

The individual OSL ages from this study agree well with those presented in Jacobs *et al.* (submitted). In their investigation, Jacobs and colleagues estimated the burial age for the basal portion of Layer 8 (PdLIV-1) to be 94 ± 7 ka, with a consistent age of 97 ± 8 ka (PdLIV-2) reported for the top of the unit. They also

provide a weighted mean of 94 ± 4 ka for all six single-grain OSL ages from Layer 8 collected during the 2011 field season. The six Layer 8 samples included two independent samples in their study and the four Layer 8 samples from this study. Only TL dating of burnt flints have previously been reported from Layer 8 and a weighted mean age of 96 ± 5 ka was calculated from 11 separate burnt flint samples (Richter et al. 2013, Dibble et al. 2009, Turq et al. 2011). The concordance of our single-grain OSL ages with those of Jacobs *et al.* (submitted), and also both of these with the independent TL ages gives confidence in procedures and assumptions made in the age calculations presented in this study.

A single-grain OSL age of 69 ± 6 ka was obtained for the unburnt sediment sample collected from Layer 5B. This age is consistent with that of Jacobs *et al.* (submitted) further sample from Layer 5B/A (PdLIV-8) of 78 ± 6 ka, as well as the 70 ± 5 (PdLIV-9) and 76 ± 6 (PdLIV-10) ka ages from the overlying Layer 5A. Jacobs *et al.* (submitted) calculated a weighted mean OSL age of 75 ± 4 ka for the deposition of Layer 5, as a whole (i.e., disregarding the subdivisions). While no absolute dating other than those presented in these two studies have been conducted for Layer 5B, TL ages have been calculated for the Layer 5A (Richter *et al.* 2013) and provide a weighted mean age for this layer of 74 ± 5 ka, again concordant with the single-grain OSL age determinations.

Finally, the 65 ± 5 ka age of the Layer 4A (PdAIV-03) sample is slightly older than, but consistent with those, presented in Jacobs *et al.* (submitted). The Layer 4A ages of Jacobs and colleagues range from 62 ± 4 ka at the base to 53 ± 4 ka at the top. A weighted mean of 58 ± 2 ka was calculated from the six individual samples taken from Layer 4A. No further independent absolute dating techniques have been used in the age determination of Layer 4A. However, weighted mean TL ages of 70 ± 5 and 50 ± 3 ka for bounding Layers 4C and 3B, respectively, have been reported (Richter *et al.* 2013). Additionally, ESR (Turq *et al.* 2011) and ^{14}C (McPherron *et al.* 2012) ages of 47–57 ka and 51–45 ka cal BP, respectively, for Unit 3, constrain and provide support for the single-grain OSL chronologies constructed in this study.

8.9.2 THE SUITABILITY OF OSL DATING TO THE PECH IV SEDIMENTS

The results presented in the previous sections indicate that a portion of quartz grains from both the burnt and unburnt sediments at Pech IV have luminescence characteristics that make them suitable for OSL dating. Analysis of the cumulative light sum plots (Figure 8.16) revealed that a reasonable proportion of grains within each sample were luminescent, with between 10 and 18% of grains in each sample producing roughly 90% of the luminescence signal. Furthermore, the corresponding OSL decay signals tend to have a fast rate of decay with background level generally reached within 0.2–0.5 s of stimulation time with the green laser (Figures 8.18 and 8.19). The dose-recovery experiments carried out in this study indicated that low PH_1 and PH_2 temperatures of 180°C for 10 and 5 s, respectively, are adept at recovering a given laboratory beta dose (Figure 8.3). The presence of IR-sensitive quartz grains in all of our samples requires further investigation to understand why this is the case. Although these are present in each sample, the application of the rejection criteria means that they are removed prior to combining the D_e values for age determination, having failed the IR-depletion ratio test. In terms of the response of the OSL signal to laboratory beta irradiation, the onset of saturation varied substantially, occurring between ~60 and ~100 Gy (Figure 8.19).

It was considered that the D_e values determined for these samples are true representations of the D_e population (i.e., they are not truncated due to dose saturation or insufficient laboratory regeneration). It is fortunate that the total environmental dose rates measured at the site increase with decreasing age; from ~0.64 ± 0.05 Gy/ka in Layer 8 to 1.56 ± 0.08 Gy/ka in Layer 4A (Table 8.12). When this is taken into account with respect to the dose-response curve saturation characteristics, it is possible to obtain reliable and accurate single-grain OSL ages for all sedimentary units found within the Pech IV deposit.

The D_e distributions for all six Pech IV samples show similar patterns. These distributions, when displayed as radial plots (Galbraith 1990), reveal a roughly symmetrical spread of values around a central mean, and a variable amount of OD

(between 30 ± 4 and 72 ± 6%; Table 8.12). The assessment of the Layer 8 sediment slabs using the pXRF in combination with soil micromorphological investigations of contiguous sediment samples, as well as the in depth investigations using Al_2O_3:C grains and image analysis modelling carried out in Chapter 6, provide support for the hypothesis that these D_e distributions could result from microscale variations in the β-D_r delivered to individual grains, post-depositional mixing, inherent OSL variability, or some combination of these.

In this case the most appropriate means of combining these D_e values for age determination was to use the CAM (Galbraith *et al.* 1999). In using the CAM, weighted mean D_e for each sample were calculated, with the resulting OSL age estimates being consistent with previously published absolute dating methods (McPherron et al. 2012, Richter et al. 2013, Turq et al. 2011).

It is concluded that the sediments preserved at Pech IV are suitable for OSL dating and the procedures outlined in this study are appropriate for determining the ages of stratigraphic layers that have not yet been dated with independent methods. Furthermore, the fact that the nearby locations of Pech de l'Azé I and II contain sediments also derived from the Coniacien Limestone, these procedures would also be applicable to those deposits by extension.

8.9.3 THE BURNING QUESTION: THE EFFECT OF HEATING ON THE LUMINESCENCE CHARACTERISTICS

The aim of this study, beyond investigating the suitability of the quartz grains at Pech IV for OSL dating, was to explore the effect of anthropogenic burning on the quartz grains. This investigation could be carried out at Pech IV because the primary, and possibly only, source of quartz grains found within the deposit is the Upper and Middle Coniacien Limestone. Before drawing any conclusion it is important to first outline the burning processes conducted, during antiquity, at Pech IV. The soil micromorphological investigations carried out to investigate the use of fire at Pech

IV was the subject of a study by Goldberg *et al.* (2012). Here, the authors indicated that combustion temperatures of hearths reached at least 500°C, determined using Fourier-transform infrared spectrometry of burnt bone fragments found throughout Layer 8. Goldberg and colleagues noted that these hearth features and associated material were spread across the cave floor as part of hearth maintenance practice, which involved the mixing, and redistribution, of both the hearth and the underlying heated sediments. Goldberg *et al.* (2012) concluded that not only was the heating intense but also repeated over time to generate the black, organic-rich Layer 8 sediments. One further outcome of this process is that the sediments would have been thermally reset due to the repeated heating and is supported by the single age estimates for each of the Layer 8 sub-samples.

The effect of heating is immediately noticeable by the differences between the TL peaks, LM-OSL curves, OSL decay curves and grain sensitivities of the burnt and unburnt samples. In both the natural-dose (Figure 8.6) and laboratory-irradiated TL curves (Figure 8.7) the relative proportion of the 280°C TL peak between the burnt and unburnt samples are in stark contrast. In the unburnt samples the 280°C TL peak is prominent, whereas the 220, 325 and 375°C peaks are substantially more pronounced in the burnt samples. This reconfiguration of TL peak proportions has knock-on effects in terms of the luminescence characteristics of burnt vs. unburnt sediments, including both the thermal stability and the rate of OSL decay.

It has been shown that the 280°C TL can be linked to the S3 component in the LM-OSL signal (Arnold et al. 2008, Arnold and Roberts 2011, Roberts et al. 1993, Packman et al. 2007, Singarayer and Bailey 2004, Jain et al. 2003). While this LM-OSL component is present in the burnt sediment, it is proportionally greater in the unburnt examples (Figure 8.3) – mirroring the relative magnitude of the 280°C TL peak in their respective samples (Figure 8.7). A link between the S3 component and the 280°C TL peak has previously been made by Arnold *et al.* (2008) in their investigations of Siberian sediments. The authors considered the variability in the 280°C TL peak to be responsible for the inter-aliquot variation in their D_e estimates both within and between samples.

Perhaps the most obvious effect of the anthropogenic burning is the sensitisation of the OSL signal (Table 8.8). The use of prolonged preheating has often been used in experimental OSL work as a means of sensitising grains (Thomsen *et al.* 2005). At Pech IV, unlike the 12–14% of 'highly' sensitive grains (>100 counts/Gy) (Table 8.8) from the burnt samples of Layer 8, only 8% of Layer 4A grains were 'highly' sensitive, while the Layer 5B sample had none. This increase in sensitivity with heating, however, is not unexpected.

8.10 CONCLUSIONS

All the cultural layers preserved at Pech IV have now been systematically dated using one absolute dating technique. This study aimed to determine the feasibility of using these sediments for OSL dating and to form the basis of a large-scale dating study of all three Pech sites – Pech I, II and IV – using the OSL dating technique (Jacobs *et al* submitted). Six OSL samples were collected from the site during the 2011 sampling season as three separate sediment blocks. Four samples came from the anthropogenically burnt Layer 8, and the remaining two from the overlying unburnt sediments in Layers 5B and 4A.

The anthropogenic burning of the Layer 8 sediments by the cave occupants has resulted in the sensitisation of the luminescence signal of these quartz grains. The burnt samples show a dominance of the 325°C TL peak over the 280°C peak – the latter dominates the TL glow curve measured for the unburnt sediments. The OSL decay curves are typically faster in the Layer 8 samples (Figure 8.18 and Table 8.9), with respect to those that remain unburnt.

Using dose-recovery tests, it has been demonstrated that the low PH_1 and PH_2 temperatures of 180°C for 10 s and 5 s, respectively, were appropriate at recovering the given laboratory dose. We also demonstrate that a reasonable proportion of the grains in each sample are bright in terms of their measured OSL signal (Figure 8.16), and have a fast rate of decay (Figure 8.18 and Table 8.9) and produced sensible dose-response curves (Figure 8.19), with the onset of dose saturation occurring between

about 60 and 100 Gy for the majority of grains. These luminescence characteristics are typical of grains that passed the rejection criteria (N=470; Table 8.5) and suggests that these accepted quartz grains are suitable for D_e measurement using a SAR procedure.

For the six samples dated in this study the CAM was used to combine the individual D_e values for age determination. This age model was considered the most appropriate means of doing so, as the OD in these samples was thought to be a combination of natural variability between grains, beta microdosimetry and to a much lesser extent post-depositional mixing. This conclusion was arrived at through the use of pXRF assessment of sediment slabs and soil micromorphological investigations of analogous sediment thin sections. The weighted mean single-grain OSL age of 95 ± 4 ka, and individual OSL ages of 69 ± 6 and 65 ± 5 ka for Layers 5B and 4A, respectively, are consistent with previously published ages for these, or bounding, layers. It can, therefore, be concluded that the procedures outlined in this chapter for the single-grain OSL method are applicable and suitable to obtain accurate and reliable age estimates for all stratigraphic units preserved at the Neanderthal occupation site of Pech IV, and potentially those in the surrounding vicinity hosted within the Coniacien Limestone.

CHAPTER SUMMARY

In this chapter I have demonstrated the significant variability in the intrinsic OSL behaviours of individual quartz grains collected from Pech IV. This variability is further compounded by the dichotomous site formation processes palpable between the anthropogenic Layer 8 and the overlying geogenic sediments. The intensive burning during and after the deposition of Layer 8 has led to the sensitisation of the electron trap associated with the 325˚C TL peak in the constituent quartz grains resulting in significantly greater proportions of bright, sensitive and rapidly decaying grains compared to the unburnt sediments and, overall, a higher proportion of 'acceptable' grains to use in final age determinations.

A number of points remain to be explained more fully, in particular the cause of the IR-sensitive grains. Thus far, I have shown that the underestimation of D_e by these grains is the result on an underlying unstable ultrafast OSL signal component. However, the reason as to why a significant portion of the grains behave in such a fashion remains to be explained.

Perhaps the most important point to take from this investigation is that the site formation history influences the intrinsic characteristics of the grains and thereby the appropriateness of the measurement procedures used. For example, the use of the 260 PH_1 and PH_2 combination was appropriate for the geogenic sediments but not appropriate for the anthropogenic Layer 8 sediments, thus reinforcing the importance of conducting appropriate characterisation tests prior to the measurement of naturally-irradiated grains to be used in age determinations.

In terms of the viability of using the single-grain OSL technique at Pech IV, the general OSL characteristics of the sedimentary quartz grains are acceptable and the presence of a (apparently) decreasing total environmental dose rate with age make it likely that the entire sequence of Pech IV sediments could be sampled and dated using this method.

PART C

Chapter 9

Synthesis

This chapter draws together the main conclusions of this thesis. In section one, the implications for the single-grain OSL method are considered with respect to the studies carried out in the Chapters 5–8 of this thesis. Section 2 presents future research questions are then considered in light of the findings of this study as a whole. Section three revisits the specific, broad and overarching aims proposed in Chapter 1 and comments on whether these have been achieved or not. Finally, section four provides some concluding remarks.

9.1 RECONCILING CONTEXT

The motivation of this thesis was founded upon the requirement that further study be dedicated to the placing single-grain OSL D_e distributions into the sedimentary context in which they were found. By doing so, the presence of overdispersion (OD) can be more clearly defined and scrutinised in terms of the extrinsic processes at play during the depositional histories of the samples. The majority of this thesis is devoted to the development of novel and alternative methods of investigating the sedimentary context of OSL samples. These methods form a linear progression from the qualitative to the quantitative and were designed to be readily accessible using standard equipment found in the OSL laboratory or geological sciences department. The main outcome of this methodological development was to be able to answer such questions as "does (extrinsic factor) influence the amount of OD in the D_e distribution of this sample and, if so, to what extent?" without the need to resort to assumptions based upon macroscopic observations or past literature. It is also worth noting that the methods developed rely heavily upon empiric observation to explain and understand the OD, rather than computer modelling of simplistic geometries, as the former is inextricably linked to the D_e distribution of the OSL sample.

9.1.1 CHRONOLOGIES IN CONTEXT: SOIL MICROMORPHOLOGY

The sedimentary context of the OSL sample dictates the likelihood of the extrinsic factors experienced over the period of burial. Therefore, an understanding of the sedimentary composition at the fundamental level is imperative. By the term 'fundamental,' I refer to basic sedimentary principals of grain size and sorting, mineralogy, sedimentary geometry and fabric analysis. Presently, sedimentological investigation apparently ceases at the point of sampling, with board macroscopic observations used to explain the microscopic sedimentary context. This practice is not ideal considering: 1) the size of the grains being dated (180–212 μm), and 2) the range over which localised variations in the beta dose rate occur (2–3 mm).

To overcome this issue, soil micromorphological analysis was carried out in Chapters 5 and 8. Here, thin sections were produced from resin-impregnated sedimentary blocks collected from either directly in front of the OSL sampling positions or the sediments from the same stratigraphic unit. Using these thin sections, broad questions (e.g. is this sediment mixed? Does bioturbation play a role in the formation of this sediment? Are K-feldspars abundant and heterogeneously distributed?) can be asked and either confirmed or refuted. The answers to questions such as these fundamentally influence the way in which the single-grain D_e values are combined, and hence the accuracy of the resultant OSL age.

9.1.2 BLAME IT ON THE BETA: β-D_r VARIATION AND EVALUATION

The extent of β-D_r variability throughout the sediments and the effect that it has on the sample OD is at the forefront of OSL research. While the influence of ^{40}K has been repeatedly discussed (Murray & Roberts 1997, Jacobs *et al.* 2008c, Guérin *et al.* 2012a) and modelled in computer simulations (Nathan *et al.* 2003, Cunningham *et al.* 2012, Guérin *et al.* 2012b), the 1:1 spatial mapping of β-D_r in natural sediments is yet to be achieved. A series of methods were proposed in this thesis specifically to establish first, if a β-D_r gradient was present in the sample; second, if the radionuclides responsible for the β-D_r were heterogeneously distributed through space; and, ultimately, to determine a β-D_r map for the sediments under investigation. This continuum of BM evaluation methods were formulated and tested in Chapter 6 and employed at Pech IV in Chapter 8.

The fractionation of dosimetry samples according to grain size and mineralogy provides a qualitative understanding of the β-D_r environment, in particular the presence of a β-D_r gradient and the dominance of a particular radionuclide (U, Th or K) in BM production. The fact that this procedure can be measured using standard *in house* OSL laboratory equipment makes it readily assessable to the majority of OSL practitioners. Further to this, the use of portable x-ray fluorescence (pXRF) was carried out to provide a spatial understanding of the distribution of β-D_r producing

radionuclides. Not only is the pXRF able to detect differences in radionuclides concentrations but also provides an insight into how the elements are 'housed;' i.e. if they are present within the clay fraction or as singular grains. Despite the limitations posed by the 4 μg/g detection level for U, and Th, this method proved to be a powerful tool in the rapid assessment of the dosimetric environment in terms of spatial distributions of radioactive elements.

To be able to accurately determine the spatial variability in β-D_r was also examined in this thesis. The use of pXRF, microphotograph β-D_r modelling and Al_2O_3:C dosimetry in conjunction with resin impregnated slabs was employed to generate spatially-resolved β-D_r maps. These methods and procedures are outlined in detail in Chapter 6. By mapping the radionuclide concentrations of both internal faces of a bisected resin-impregnated slab, it was possible to reconstruct the β-D_r environment for each slab. A complementary map was made using Al_2O_3:C grains that were then placed between the internal face of the slabs and allowed to accumulate dose. By measuring the D_e of Al_2O_3:C grains taken systematically across the resin-slab faces, a direct measure of β-D_r can be determined. Presently, it appears as though the use of single-grain OSL method of measuring Al_2O_3:C grains provides a more accurate and reliable estimate of β-D_r (as was carried out in Chapter 6), with a number of issues (such as the divergent nature of the L_N and T_N signals) associated with the use of aliquots identified (also in Chapter 6). Both pXRF and Al_2O_3:C mapping are by no means infallible methods of spatial resolving β-D_r variability across sediments; they do, however, represent a step toward the goal of spatially resolving β-D_r values.

9.2 DIRECTIONS FOR FUTURE RESEARCH

This thesis provides a variety of different methods that can be used to investigate the sedimentary context from which OSL samples are collected. These have focused mainly on the presence of OD as a result of localised variations in the β-D_r stemming from the inhomogeneous distribution of radionuclides throughout the

sediment. I maintain that for the OSL dating method to progress, the ability to accurately and reliably determine the spatial distribution of beta dose ought to be a goal that the OSL community endeavours to achieve. The studies carried out in this thesis provide a solid foundation upon which further developments towards this goal can be based and these are outlined below.

Al_2O_3:C as a β-D_r dosimeter

Investigation into the ability of Al_2O_3:C to record and accurately determine special variations in the β-D_r has shown promising results. Further investigation using similar techniques as those presented in Chapter 6 is required. One major shortfall of the investigation carried out here was the poor luminescence signal obtained from individual grains of Al_2O_3:C. This poor signal was most probably a result of insufficient storage time (particularly for the Pech IV samples) to provide a strong luminescence response due to the low β-D_r of the samples. In future, longer storage periods should be considered to help alleviate the issue of dim luminescence response.

To circumvent the dim luminescence response problem, 4-grain aliquots of Al_2O_3:C were also used for both Pech IV samples to determine the spatial distribution of β-D_r. However, this method produced a number of erroneously (and unrealistic) β-D_r values. Investigation of the OSL decay curves from the 4-grain aliquots was disturbingly dissimilar between natural and laboratory irradiation. Future work here would include a more detailed investigation of the luminescence characteristics of Al_2O_3:C particularly its response to laboratory irradiation. For instance, reducing the size of the regenerative dose and test doses (given the mGy doses being recorded) may help overcome these issues.

Furthermore, it is considered that the external dose rate to the Al_2O_3:C grains within the resin slabs during the period of storage could be better constrained. This could be done by housing the slabs in a storage container filled with sediment of a known gamma dose rate.

Monte Carlo simulations and computer modelling

In this thesis, I often critique the use of computer modelling and simulations of the β-D_r environment. This criticism stems from the inability of the models to accurately represent natural sediment context due to their over-simplistic geometries. Although, the μ-CT investigation (Chapter 7) failed to demonstrate the correlation between OD, heavy mineral fraction and β-D_r, it could clearly differentiate between heavy minerals, quartz and pore space (particularly in SP5) with remarkable resolution in three-dimensions. Thus, this digital μ-CT geometry, in future, could be imported into various Monte Carlo modelling programs (such as Geant4) to provide an accurate representation of sedimentary geometry. Within the computer simulation, dosimetric attributes can be given to the heavy mineral fraction, the pore space filled with water and 180–212 μm quartz grains digitally selected to act as dosimeters. The resulting Monte Carlo simulation D_e distribution is therefore inextricably linked to that derived from the single-grain OSL investigation of the corresponding sediment sample. In carrying out a procedure such as this, the issues associated with an over-simplistic geometry would be overcome.

9.3 AIMS REVISITED

The motivation for this thesis was bought about by the little investigative work that has been carried out in terms understanding the intricacies and nuances of

sedimentary contexts from which OSL samples have been collected. Effectively, it seems as though the line of inquiry into the sedimentological realm stops at the point of sample collection. This lack of enthusiasm for sedimentological investigation appears to stem from the standard procedure of removing only the grains of interest to be dated (180–212 μm quartz) and disregarding the remaining sediment. As such, nothing more than the broad macroscopic observations of site stratigraphy are used in the speculation as to why certain D_e distribution patterns (and spread; OD) are present to such an extent in some samples and yet is not nearly pronounced in others. The rhetorical question posed by Rainer Grün at LED 2011 conference of "Why don't you guys simply look at the sediment?" could not sum up the current situation in OSL dating more succinctly.

This thesis set out five specific aims that were nested within a broad and an overarching aim. These were presented in Chapter 1.2. The remainder of this chapter will present the aims again and state whether or not they have been met.

1. *Develop novel sampling techniques that allow the investigation and assessment of sedimentary characteristics from which the single-grain OSL samples have been collected*

To assess the sedimentary geometry of OSL samples, a sampling strategy was developed, outlined in Chapter 5, based on the methods described in Courty *et al.* (1989) for the collection of soil micromorphological samples. In Chapters 5 and 8, intact and orientated sediment block samples were collected from the study sites to provide important sedimentary context for the corresponding OSL samples. The OSL samples were then collected from either directly behind the block in the field, or the blocks themselves can be subsampled back in the laboratory. This tandem approach opens up a wide variety of techniques that can be used to examine the sedimentary context. For example, soil micromorphological analysis of thin sections made for these sediment blocks can be used to provide qualitative insights about site formation processes and post-depositional histories of the sample. This I have shown to be a

useful and, indeed, mutually beneficial, practice. I consider, therefore, that this aim has been achieved.

2. *Develop a method of evaluating the spatial variability of the beta dose rate throughout the sediments*

A number of procedures were developed throughout the course of this body of work in an effort to evaluate the variability in the β-D_r from naturally occurring sediments. These methods have had variable levels of success. The fractionation of sediment samples and the independent measurement of these fractions proved to be the most reliable method of observing β-D_r variability within a sample. Yet, this method destroys the sedimentary geometry and fabric relationships. The use of the pXRF was partially successful where the concentrations of U and Th were greater than the 4 μg/g detection limit. No difficulty was encounter in the measurement of K given the higher natural abundances of this element. Taken as a whole, only the upper end of the β-D_r flux was able to be detected using this technique. It was also used rather successfully in the rapid assessment of the sedimentary context for Layer 8 samples at Pech IV. The shortcomings of the Al_2O_3:C have already been discussed at the end of Chapter 6 and above in Section 9.2. The single-grain Al_2O_3:C β-D_r values are considerably more reliable the 4-grain counterparts. Further work is required to develop this method further before it can become routinely used. Finally, the modelling of the spatial β-D_r distribution using the fractionated β-D_r values and JMicroVision proved only be as good as the assumptions upon which it was built. The use of average β-D_r in the modelling exercise gave rise to an 'average' β-D_r distribution pattern with the extreme tail end members of the distributions removed. Although each of these methods has their own successes and limitations, with respect to the specific aim above, this has been achieved to a certain degree.

3. *Investigate the association between the distribution of radioactive mineral species in 3-dimensions and the amount of spread (OD) in a single-grain OSL D_e distribution*

The use of μ-CT was conducted on resin-impregnated core samples coming from MacCauley's Beach to determine both the proportion and distribution of heavy minerals throughout the sediment. This study and the procedures used are outlined in Chapter 7. It was envisaged that by subdividing the cores following μ-CT scanning and measuring the OSL of each slice that OD present could be correlated to the proportion of heavy minerals in each slice. While the micro-CT method was certainly able to distinguish heavy minerals for both the quartz and void space fractions, conclusions as to the correlation between OD and heavy mineral fraction could not be drawn. This result was due to the deposition of dose in the quartz grains during μ-CT scanning; a visible miscalculation in hindsight. The results of this investigation, however, provide a promising foundation for future research in computer modelling of β-D_r. In terms of this specific aim, however, it has not been achieved.

4. *Investigate how the site formation processes influence the intrinsic OSL signal behaviour of quartz*

This aim was specifically addressed in the characterisation of the luminescence behaviour of single grains of quartz recovered from Pech IV. This site provides an ideal laboratory to test the impact that site formation processes, in particular the extensive heating of the sediments, has had on the luminescence behaviours. Here, the black Layer 8 sediments show irrefutable evidence of prehistoric anthropogenic heating, whereas the remaining layers are effectively geogenic in nature. The effect that this heating had on the Layer 8 quartz sediment was to effective provide multiple preheats during antiquity that produced a sensitisation of the OSL traps relating to the 325 °C TL peak. This underlying sensitisation is clearly evidenced in the high OSL sensitivities and faster decaying OSL signal of the grains from this layer in comparison with any of the other geogenic layers investigated in Chapter 8. These changes in OSL sensitivity and TL trap configuration also appear to influence the selection of appropriate preheating treatments to be used during D_e measurement. This aim, therefore, has been achieved.

5. *Investigate the sediments preserved at MacCauley's Beach and Pech IV to evaluate the extent and causes of the OD present in the single-grain D_e distributions.*

The use of soil micromorphology has been shown to be invaluable in aiding the understanding of the extent that extrinsic influences can have on single-grain OSL D_e distributions and the amount of OD recorded within them. When used in combination with the analysis of spatial variability in β-D_r flux, these findings are further strengthened. At MacCauley's Beach, two distinctive D_e distributions were observed. The first distribution type displayed a continuous smear of D_e values ranging from ~6 to ~400 Gy and had an OD of 87 ± 5% (SP1). Without any further investigation, it is possible that this distribution type was either: 1) be rejected out of hand or 2) be described as the result of partially-bleached grains. Soil micromorphology however was able to definitively determine that post-depositional mixing brought about by pedoturbation was the result of this distribution pattern type. The second D_e distribution showed a much smaller, but symmetrical, spread of D_e values of typically no more than 20 Gy and OD in the region of 30% (SP2–SP5). Using soil micromorphology, the heterogeneous distribution of heavy minerals could be discerned. Fractionation of the samples and dose rate evaluation of the constituents showed that these same heavy minerals gave off significantly higher β-D_r that was dominated by U and Th, not K. Quantitative, spatially-resolved measurements of these radionuclides for two of the MacCauley's Beach samples (SP2 and SP5) suggested that this they was heterogeneously distributed throughout the sediments. Thus, the assignation that BM was the responsible for the OD in these samples could be empirically shown, rather than supposed. Only one type of distribution was evident at Pech IV and was similar in shape to the BM-influenced distributions at MacCauley's Beach. Using the same techniques developed throughout this thesis, the spread in these also considered to be the result of BM, post-depositional mixing or grain-to-grain intrinsic variability. This aim, I believe, has been met.

Broad aim: assess the site formation processes, sedimentary geometry and chronology of the two stratigraphic profiles preserved at MacCauley's Beach and Pech IV.

The integration of soil micromorphology and single-grain OSL dating has provided the opportunity to construct robust chronologies for the sites of MacCauley's Beach and Pech IV. The interpretations made from the D_e distributions are based on empiric observation of the sedimentary context rather than assumptions based on either previous studies or macroscopic observations. Thus, at MacCauley's Beach, I have been able to discern four different periods of site formation and their associated processes. Furthermore, investigation of the sediments using thin sections and the analysis of spatial distribution of radionuclides and β-D_r 'hotpots' has allowed for substantially greater knowledge to be gleaned with respect to the influence of extrinsic factors on the D_e distributions of the samples collected form the site.

A similar outcome was also arrived to at Pech IV. Here, the extensive thin section library compiled by Paul Goldberg (co-supervisor) was able to be analysed for qualitative interpretations of the how site formation processes and sedimentary context impact upon the D_e distributions of the samples. Here, also, this influence is evident in the differences between the OSL characteristics of the burnt (Layer 8) and unburnt layers (Layers 5B and 4A). In both cases, the chronologies produced are considered to be improvements upon those previously reported (Bryant *et al.* 1992b, Turq *et al.* 2011). This consideration is either because the new chronologies are more completely cover the entire span of the deposit or that sedimentary context has been more clearly reported.

Overarching aim: to contribute towards the advancement of the OSL method by integrating sedimentological studies with the standard OSL practice and procedures.

The body of work presented in this thesis has presented a number of important developments that can be easily reconciled into current OSL practice and procedure.

To borrow the arguments present by both Stoops (2003) and Goldberg & Macphail (2006), the results produced as part of any OSL dating program ought to represent a continuum of observation from the macroscopic to the microscopic as the grains being used to determine the burial age are not simply collected from within a sedimentary vacuum. The present practice of using the macroscopic stratigraphy is inadequate when dealing with grains that are orders of magnitude smaller than the field of observation. Thus, I move that more detailed sedimentary examination become part of standard OSL procedure – be this through soil micromorphology or some other means.

In terms of more quantitative approaches, the methods outlined in this thesis were devised with the non-specialist in mind. Thus, the majority of these techniques and methods can be performed using standard OSL laboratory equipment or common facilities available within an Earth Sciences department. The ability to fractionate dosimetry samples into either constituent minerals or even simply grain sizes (as was conducted in Chapter 6) is a simple, but effective, means of determining the potential variability in the β-D_r for a sample. If this is carried out in tandem with thin section analysis then the potential to model both the β-D_r magnitude and spatial distribution becomes an option and, potentially, more informative assessment of β-D_r within a sample. This β-D_r modelling process does not need to be as exhaustive as that conducted in this thesis; a transect across a thin section would be just as informative. With respect to the pXRF the detection limit of for U and Th make this technique appropriate only for the rapid assessment of the upper tail of the β-D_r distribution. Whereas the Al_2O_3:C dosimetry methods require substantially more work.

I am satisfied that the procedures present in this thesis will make some contribution, however small, to the advancement of the OSL method.

9.4 CONCLUDING REMARKS

Single-grain OSL dating provides a means of providing depositional ages for late Quaternary-aged sedimentary deposits. The fact that this method utilises

ubiquitous minerals make this dating technique widely applicable. However, the apparent unease of many OSL practitioners to delve deeper into the sedimentary environment, beyond the macroscopic, to help explain the D_e distributions for their samples provided the motivation for this thesis. Further insights, using the procedures presented in this thesis, allow additional and vital information to be gleaned about site formation processes, sedimentary context and their influence on OSL dating results. The methods presented, herein, are not set in stone, but remain with future developments and improvements to be made. Further research into the sedimentary and, specifically, the beta dose rate environment remains at the cutting edge of the OSL technique. It is only through investigations into these areas that the method can move forward. In short, the grains used for OSL dating are not collected from within a sedimentary vacuum, but are surrounded by (more-or-less) random assortment of terrigenous material. To understand the OSL results requires them to be assessed within the context in which they were formed and remained over the period of burial.

References

ABRAMOFF M. D., MAGALHAES P. J. & RAM S. J. 2004. Image processing with ImageJ. *Biophotonics International* **11**, 36-42.

ADAMIEC G., DULLER G. A. T., ROBERTS H. M. & WINTLE A. G. 2010. Improving the TT-OSL SAR protocol through source trap characterisation. *Radiation Measurements* **45**, 768-777.

ADDERLEY W. P., SIMPSON I. A. & MACLEOD G. W. 2001. Testing high-resolution X-ray computed tomography for the micromorphological analyses of archaeological soils and sediments. *Archaeological Prospection* **8**, 107-112.

AITKEN M. J. 1985. *Thermoluminescence dating*. Academic Press, London.

AITKEN M. J. 1990. Pairs precision required in alpha counting. *Ancient TL* **8**, 12 - 14.

AITKEN M. J. 1998. *An introduction to optical dating: the dating of Quaternary sediments by the use of photon-stimulated luminescence*. Oxford University Press, Oxford.

AITKEN M. J. & XIE J. 1990. Moisture correction for annual gamma dose. *Ancient TL* **8**, 6-9.

AKSELROD A. E. & AKSELROD M. S. 2002. Correlation Between OSL and the Distribution of TL Traps in Al2O3:C. *Radiation Protection Dosimetry* **100**, 217-220.

AKSELROD M. S., KORTOV V. S. & GORELOVA E. A. 1993. Preparation and Properties of α-Al_2O_3:C. *Radiation Protection Dosimetry* **47**, 159-164.

AKSELROD M. S., KORTOV V. S., KRAVETSKY D. J. & GOTLIB V. I. 1990. Highly Sensitive Thermoluminescent Anion-Defective α-Al_2O_3:C Single Crystal Detectors. *Radiation Protection Dosimetry* **32**, 15-20.

ALLEN M. J., GODDEN D. & MATTHEWS C. 2002. Mesolithic, Late Bronze Age and Medieval activity at Katherine Farm, Avonmouth, 1998. *In*, *Archaeology in the Severn Estuary 2002*, pp 85-105, Severn Estuary Levels Research Committee, Bath.

ARNOLD L. J., BAILEY R. M. & TUCKER G. E. 2007. Statistical treatment of fluvial dose distributions from southern Colorado arroyo deposits. *Quaternary Geochronology* **2**, 162-167.

ARNOLD L. J. & ROBERTS R. G. 2009. Stochastic modelling of multi-grain equivalent dose (D_e) distributions: Implications for OSL dating of sediment mixtures. *Quaternary Geochronology* **4**, 204-230.

ARNOLD L. J. & ROBERTS R. G. 2011. Paper I – Optically stimulated luminescence (OSL) dating of perennially frozen deposits in north-central Siberia: OSL characteristics of quartz grains and methodological considerations regarding their suitability for dating. *Boreas* **40**, 389-416.

ARNOLD L. J., ROBERTS R. G., GALBRAITH R. F. & DELONG S. B. 2009. A revised burial dose estimation procedure for optical dating of young and modern-age sediments. *Quaternary Geochronology* **4**, 306-325.

ARNOLD L. J., ROBERTS R. G., MACPHEE R. D. E., WILLERSLEV E., TIKHONOV A. N. & BROCK F. 2008. Optical dating of perennially frozen deposits associated with preserved ancient plant and animal DNA in north-central Siberia. *Quaternary Geochronology* **3**, 114-136.

BAILEY R. M. 2001. Towards a general kinetic model for optically and thermally stimulated luminescence of quartz. *Radiation Measurements* **33**, 17-45.

BAILEY R. M., SMITH B. W. & RHODES E. J. 1997. Partial bleaching and the decay form characteristics of quartz OSL. *Radiation Measurements* **27**, 123-136.

BALLARINI M., WINTLE A. G. & WALLINGA J. 2006. Spatial variation of dose rate from beta sources as measured using single-grains. *Ancient TL* **24**, 1-8.

BANERJEE D., HILDEBRAND A. N., MURRAY-WALLACE C. V., BOURMAN R. P., BROOKE B. P. & BLAIR M. 2003. New quartz SAR-OSL ages from the stranded beach dune sequence in south-east South Australia. *Quaternary Science Reviews* **22**, 1019-1025.

BATEMAN M. D., BOULTER C. H., CARR A. S., FREDERICK C. D., PETER D. & WILDER M. 2007a. Detecting post-depositional sediment disturbance in sandy deposits using optical luminescence. *Quaternary Geochronology* **2**, 57-64.

BATEMAN M. D., BOULTER C. H., CARR A. S., FREDERICK C. D., PETER D. & WILDER M. 2007b. Preserving the palaeoenvironmental record in Drylands: Bioturbation and its significance for luminescence-derived chronologies. *Sedimentary Geology* **195**, 5-19.

BATEMAN M. D., HOLMES P. J., CARR A. S., HORTON B. P. & JAISWAL M. K. 2004. Aeolianite and barrier dune construction spanning the last two glacial–interglacial cycles from the southern Cape coast, South Africa. *Quaternary Science Reviews* **23**, 1681-1698.

BELL W. T. 1979a. Attenuation factors for the absorbed radiation dose in quartz grains for thermoluminescence dating. *Ancient TL* **8**, 2-13.

BELL W. T. & ZIMMERMAN D. W. 1978. The effect of HF acid etching on morphology of quartz inclusions for thermoluminescence dating. *Archaeometry* **20**, 63 - 65.

BERGER G. W. 1990. Effectiveness of natural zeroing of the thermoluminescence in sediments. *Journal of Geophysical Research: Solid Earth* **95**, 12375-12397.

BERGER G. W. & LUTERNAUER J. J. 1987. Preliminary fieldwork for thermoluminescence dating studies at the Fraser River delta, British Columbia. *Current Research, Part A, Geological Survey of Canada Paper* **87-1A**, 901-904.

BINFORD L. R. 1962. Archaeology as Anthropology. *American Antiquity* **28**, 217-225.

BINFORD L. R. 1965. Archaeological Systematics and the Study of Culture Process. *American Antiquity* **31**, 203-210.

BINFORD L. R. & BINFORD S. R. 1966. A Preliminary Analysis of Functional Variability in the Mousterian of Levallois Facies. *American Anthropologist* **68**, 238-295.

BLACKWELL B. & SCHWARCZ H. P. 1995. The uranium series disequilibrium dating methods. *In:* Rutter N. W. & Catto N. R. eds., *Dating Methods for Quaternary Deposits*, Vol. GEOtext 2, pp 167-208, Geological Association of Canada, St John's.

BOLTE S. & CORDELIÈRES P. 2006. A guided tour into subcellular colocalization analysis in light microscopy. *Journal of Microscopy* **224**, 213-232.
BORDES F. 1961. Mousterian Cultures in France: Artifacts from recent excavation dispel some popular misconceptions about Neanderthal man. *Science* **134**, 803-810.
BORDES F. 1975. Le gisement de Pech de l'Azé IV: Note préliminaire. *Bulletin de la Société Préhistorique Française* **72**, 293–308.
BORDES F. 1978. Typological variability in the Mousterian layers at Pech de l'Azé I, II, and IV. *Journal of Anthropological Research* **34**, 181-193.
BØTTER-JENSEN L., ANDERSEN C. E., DULLER G. A. T. & MURRAY A. S. 2003. Developments in radiation, stimulation and observation facilities in luminescence measurements. *Radiation Measurements* **37**, 535-541.
BØTTER-JENSEN L., BULUR E., DULLER G. A. T. & MURRAY A. S. 2000. Advances in luminescence instrument systems. *Radiation Measurements* **32**, 523-528.
BØTTER-JENSEN L. & MEJDAHL V. 1988. Assessment of beta dose-rate using a GM multicounter system. *International Journal of Radiation Applications and Instrumentation. Part D. Nuclear Tracks and Radiation Measurements* **14**, 187-191.
BOWLER J. M. 1976. Aridity in Australia: Age, origins and expression in aeolian landforms and sediments. *Earth-Science Reviews* **12**, 279-310.
BOWLER J. M., JOHNSTON H., OLLEY J. M., PRESCOTT J. R., ROBERTS R. G., SHAWCROSS W. & SPOONER N. A. 2003. New ages for human occupation and climatic change at Lake Mungo, Australia. *Nature* **421**, 837-840.
BOWMAN H. N. 1974. *Geology of the Wollongong, Kiama and Robertson 1 : 50 000 sheets*. Geological Survey of New South Wales.
BOWMAN S. G. E. & SIEVEKING G. D. G. 1983. Thermoluminescence dating of burnt flint from Combe Grenal. *PACT* **9**, 253-268.
BOYD R., DALRYMPLE R. & ZAITLIN B. A. 1992. Classification of clastic coastal depositional environments. *Sedimentary Geology* **80**, 139-150.
BRAY H. E., BAILEY R. M. & STOKES S. 2002. Quantification of cross-irradiation and cross-illumination using a Risø TL/OSL DA-15 reader. *Radiation Measurements* **35**, 275-280.
BRENNAN B. J. 2003. Beta doses to spherical grains. *Radiation Measurements* **37**, 299-303.
BREWER R. 1964. *Fabric and mineral analysis of soils*. John Wiley & Sons, New York.
BREWER R. & SLEEMAN J. R. 1960. Soil structure and fabric: Their definition and description. *Journal of Soil Science* **11**, 172-185.
BRUNNABEND S. E., SCHRÖTER J., TIMMERMANN R., RIETBROEK R. & KUSCHE J. 2012. Modeled steric and mass-driven sea level change caused by Greenland Ice Sheet melting. *Journal of Geodynamics* **59–60**, 219-225.
BRYANT E. A. 1992a. Last interglacial and Holocene trends in sea-level maxima around Australia: Implications for modern rates. *Marine Geology* **108**, 209-217.

BRYANT E. A., YOUNG R. W., PRICE D. M. & SHORT S. A. 1990. Thermoluminescence and Uranium-Thorium chronologies of Pleistocene coastal landforms of the Illawarra region, New South Wales. *Australian Geographer* **21**, 101-112.

BRYANT E. A., YOUNG R. W., PRICE D. M. & SHORT S. A. 1992b. Evidence for Pleistocene and Holocene raised marine deposits, Sandon Point, New South Wales. *Australian Journal of Earth Sciences* **39**, 481-493.

BRYANT E. A., YOUNG R. W., PRICE D. M. & SHORT S. A. 1994. Late Pleistocene dune chronology: Near-coastal New South Wales and eastern Australia. *Quaternary Science Reviews* **13**, 209-223.

BULLOCK P., FEDOROFF N., JONGERIUS A., STOOPS G., TURSINA T. & BABEL U. 1985. *Handbook for soil thin section description*. Waine Research Publications, Wolverhampton.

BULUR E. 1996. An alternative technique for optically stimulated luminescence (OSL) experiment. *Radiation Measurements* **26**, 701-709.

BULUR E., BØTTER-JENSEN L. & MURRAY A. S. 2000. Optically stimulated luminescence from quartz measured using the linear modulation technique. *Radiation Measurements* **32**, 407-411.

BULUR E., DULLER G. A. T., SOLONGO S., BØTTER-JENSEN L. & MURRAY A. S. 2002. LM-OSL from single grains of quartz: a preliminary study. *Radiation Measurements* **35**, 79-85.

BURBIDGE C. I. & DULLER G. A. T. 2003. Combined gamma and beta dosimetry, using Al_2O_3:C, for in situ measurements on a sequence of archaeological deposits. *Radiation Measurements* **37**, 285-291.

BURBIDGE C. I., DULLER G. A. T. & ROBERTS H. M. 2006. Determination for young samples using the standardised OSL response of coarse-grain quartz. *Radiation Measurements* **41**, 278-288.

CHAPMAN D. M., GEATY M., ROY P. S. & THOM B. G. 1982. *Coastal evolution and coastal erosion in New South Wales*. Coastal Council of New South Wales.

CHOI J. H., DULLER G. A. T. & WINTLE A. G. 2006. Analysis of quartz LM-OSL curves. *Ancient TL* **24**, 9-20.

CONSTANTIN D., TIMAR-GABOR A., VERES D., BEGY R. & COSMA C. 2012. SAR-OSL dating of different grain-sized quartz from a sedimentary section in southern Romania interbedding the Campanian Ignimbrite/Y5 ash layer. *Quaternary Geochronology* **10**, 81-86.

COURTY M.-A., GOLDBERG P. & MACPHAIL R. 1989. *Soils and micromorphology in archaeology*. Cambridge University Press, Cambridge.

COWELL P. J., ROY P. S. & JONES R. A. 1992. Shoreface translation model: Computer simulation of coastal-sand-body response to sea level rise. *Mathematics and Computers in Simulation* **33**, 603-608.

CUNNINGHAM A. C., DEVRIES D. J. & SCHAART D. R. 2012. Experimental and computational simulation of beta-dose heterogeneity in sediment. *Radiation Measurements* **47**, 1060-1067.

CUNNINGHAM A. C. & WALLINGA J. 2010. Selection of integration time intervals for quartz OSL decay curves. *Quaternary Geochronology* **5**, 657-666.

DALRYMPLE R. W., ZAITLIN B. A. & BOYD R. 1992. Estuarine facies models: conceptual basis and stratigraphic implications. *Journal of Sedimentary Petrology* **62**, 1130-1146.

DAVID B., ROBERTS R. G., MAGEE J., MIALANES J., TURNEY C., BIRD M., WHITE C., FIFIELD L. K. & TIBBY J. 2007. Sediment mixing at Nonda Rock: investigations of stratigraphic integrity at an early archaeological site in northern Australia and implications for the human colonisation of the continent. *Journal of Quaternary Science* **22**, 449-479.

DAVIDS F., ROBERTS H. M. & DULLER G. A. T. 2010. Is X-ray core scanning non-destructive? Assessing the implications for optically stimulated luminescence (OSL) dating of sediments. *Journal of Quaternary Science* **25**, 348-353.

DEMURO M., ARNOLD L. J., FROESE D. G. & ROBERTS R. G. 2013. OSL dating of loess deposits bracketing Sheep Creek tephra beds, northwest Canada: Dim and problematic single-grain OSL characteristics and their effect on multi-grain age estimates. *Quaternary Geochronology* **15**, 67-87.

DEMURO M., ROBERTS R. G., FROESE D. G., ARNOLD L. J., BROCK F. & RAMSEY C. B. 2008. Optically stimulated luminescence dating of single and multiple grains of quartz from perennially frozen loess in western Yukon Territory, Canada: Comparison with radiocarbon chronologies for the late Pleistocene Dawson tephra. *Quaternary Geochronology* **3**, 346-364.

DIBBLE H. L., BERNA F., GOLDBERG P., MCPHERRON S. P., MENTZER S., NIVEN L., RICHTER D., SANDGATHE D., THÉRY-PARISOT I. & TURQ A. 2009. A preliminary report on Pech de l'Azé IV, Layer 8 (Middle Paleolithic, France). *PaleoAnthropology* **2009**, 182-219.

DIBBLE H. L., MAREAN C. W. & MCPHERRON S. P. 2007. On the use of barcodes in excavtion projects with examples from Mossel bay (South Africa) and Roc de Marsal (France). *The SAA Archaeological Record* **71**, 33-38.

DULLER G. A. T. 2003. Distinguishing quartz and feldspar in single grain luminescence measurements. *Radiation Measurements* **37**, 161-165.

DULLER G. A. T. 2004. Luminescence dating of quaternary sediments: recent advances. *Journal of Quaternary Science* **19**, 183-192.

DULLER G. A. T. 2007. Assessing the error on equivalent dose estimates derived from single aliquot regenerative dose measurements. *Ancient TL* **25**, 15-24.

DULLER G. A. T. 2012a. Cross-talk during single grain optically stimulated luminescence measurements of quartz and feldspar. *Radiation Measurements* **47**, 219-224.

DULLER G. A. T. 2012b. Improving the accuracy and precision of equivalent doses determined using the optically stimulated luminescence signal from single grains of quartz. *Radiation Measurements* **47**, 770-777.

DULLER G. A. T., BØTTER-JENSEN L. & MURRAY A. S. 2000. Optical dating of single sand-sized grains of quartz: sources of variability. *Radiation Measurements* **32**, 453-457.

DULLER G. A. T. & MURRAY A. S. 2000. Luminescence dating of sediments using individual mineral grains. *Geologos* **5**, 87-106.

DURCAN J. A. & DULLER G. A. T. 2011. The fast ratio: A rapid measure for testing the dominance of the fast component in the initial OSL signal from quartz. *Radiation Measurements* **46**, 1065-1072.

EPICA COMMUNITY MEMBERS 2004. Eight glacial cycles from an Antarctic ice core. *Nature* **429**, 623-628.

FAN A., LI S.-H. & LI B. 2011. Observation of unstable fast component in OSL of quartz. *Radiation Measurements* **46**, 21-28.

FEATHERS J. K. 2003. Single-grain OSL dating of sediments from the Southern High Plains, USA. *Quaternary Science Reviews* **22**, 1035-1042.

FEATHERS J. K., RHODES E. J., HUOT S. & MCAVOY J. M. 2006. Luminescence dating of sand deposits related to late Pleistocene human occupation at the Cactus Hill Site, Virginia, USA. *Quaternary Geochronology* **1**, 167-187.

FEDOROFF N., BRESSON L. M. & COURTY M. A. (Editors) 1987. *Micromorphologie des Sols - Soil Micromorphology.* . Association Française pour l'Étude du Sol, Plaisir.

FITZPATRICK E. A. 1993. *Soil Microscopy and Micromorphology*. John Wiley & Sons, Chichester.

FITZSIMMONS K. E., RHODES E. J. & BARROWS T. T. 2010. OSL dating of southeast Australian quartz: A preliminary assessment of luminescence characteristics and behaviour. *Quaternary Geochronology* **5**, 91-95.

FLEMING K. & LAMBECK K. 2004. Constraints on the Greenland Ice Sheet since the Last Glacial Maximum from sea-level observations and glacial-rebound models. *Quaternary Science Reviews* **23**, 1053-1077.

FORNÓS J. J., CLEMMENSEN L. B., GÓMEZ-PUJOL L. & MURRAY A. S. 2009. Late Pleistocene carbonate aeolianites on Mallorca, Western Mediterranean: a luminescence chronology. *Quaternary Science Reviews* **28**, 2697-2709.

FRANKLIN A. D., PRESCOTT J. R. & SCHOLEFIELD R. B. 1995. The mechanism of thermoluminescence in an Australian sedimentary quartz. *Journal of Luminescence* **63**, 317-326.

FUCHS M. & LANG A. 2001. OSL dating of coarse-grain fluvial quartz using single-aliquot protocols on sediments from NE Peloponnese, Greece. *Quaternary Science Reviews* **20**, 783-787.

GALBRAITH R. 2005. *Statistics for Fission Track Analysis*. Chapman & Hall, Boca Raton, Florida.

GALBRAITH R. F. 1990. The radial plot: Graphical assessment of spread in ages. *International Journal of Radiation Applications and Instrumentation. Part D. Nuclear Tracks and Radiation Measurements* **17**, 207-214.

GALBRAITH R. F. 2010. On plotting OSL equivalent doses. *Ancient TL* **28**, 1-9.

GALBRAITH R. F. & ROBERTS R. G. 2012. Statistical aspects of equivalent dose and error calculation and display in OSL dating: An overview and some recommendations. *Quaternary Geochronology* **11**, 1-27.

GALBRAITH R. F., ROBERTS R. G., LASLETT G. M., YOSHIDA H. & OLLEY J. M. 1999. Optical dating of single and multiple grains of quartz from

Jinmium rock shelter, Northern Australia: Part I, experimental design and statistical models. *Archaeometry* **41**, 339-364.

GALBRAITH R. F., ROBERTS R. G. & YOSHIDA H. 2005. Error variation in OSL palaeodose estimates from single aliquots of quartz: a factorial experiment. *Radiation Measurements* **39**, 289-307.

GLIGANIC L. A., JACOBS Z. & ROBERTS R. G. 2012a. Luminescence characteristics and dose distributions for quartz and feldspar grains from Mumba rockshelter, Tanzania. *Journal of archaeological and anthropological science*.

GLIGANIC L. A., JACOBS Z., ROBERTS R. G., DOMÍNGUEZ-RODRIGO M. & MABULLA A. Z. P. 2012b. New ages for Middle and Later Stone Age deposits at Mumba rockshelter, Tanzania: Optically stimulated luminescence dating of quartz and feldspar grains. *Journal of Human Evolution* **62**, 533-547.

GODFREY-SMITH D. I., HUNTLEY D. J. & CHEN W. H. 1988. Optical dating studies of quartz and feldspar sediment extracts. *Quaternary Science Reviews* **7**, 373-380.

GOLDBERG P. & BERNA F. 2010. Micromorphology and context. *Quaternary International* **214**, 56-62.

GOLDBERG P., DIBBLE H., BERNA F., SANDGATHE D., MCPHERRON S. J. P. & TURQ A. 2012. New evidence on Neandertal use of fire: Examples from Roc de Marsal and Pech de l'Azé IV. *Quaternary International* **247**, 325-340.

GOLDBERG P. & MACPHAIL R. 2006. *Practical and Theoretical Geoarchaeology*. Blackwell Publishing, Oxford.

GOLDBERG P., MILLER C., SCHIEGL S., LIGOUIS B., BERNA F., CONARD N. & WADLEY L. 2009. Bedding, hearths, and site maintenance in the Middle Stone Age of Sibudu Cave, KwaZulu-Natal, South Africa. *Archaeological and Anthropological Sciences* **1**, 95-122.

GRIFFIN J. D., HEMER M. A. & JONES B. G. 2008. Mobility of sediment grain size distributions on a wave dominated continental shelf, southeastern Australia. *Marine Geology* **252**, 13-23.

GRÜN R., MELLARS P. & LAVILLE H. 1991. ESR chronology of a 100,000-year archaeological sequence at Pech de l'Aze II, France. *Antiquity* **65**, 544-551.

GRÜN R., YAN G., MCCULLOCH M. T. & MORTIMER G. 1999. Detailed Mass Spectrometric U-series Analyses of Two Teeth from the Archaeological Site of Pech de l'Aze II: Implications for Uranium Migration and Dating. *Journal of Archaeological Science* **26**, 1301-1310.

GUÉRIN G., DISCAMPS E., LAHAYE C., MERCIER N., GUIBERT P., TURQ A., DIBBLE H. L., MCPHERRON S. P., SANDGATHE D., GOLDBERG P., JAIN M., THOMSEN K., PATOU-MATHIS M., CASTEL J.-C. & SOULIER M.-C. 2012a. Multi-method (TL and OSL), multi-material (quartz and flint) dating of the Mousterian site of Roc de Marsal (Dordogne, France): correlating Neanderthal occupations with the climatic variability of MIS 5–3. *Journal of Archaeological Science*.

GUÉRIN G., MERCIER N. & ADAMIEC G. 2011. Dose-rate conversion factors: update. *Ancient TL* **29**, 5-8.

GUÉRIN G., MERCIER N., NATHAN R., ADAMIEC G. & LEFRAIS Y. 2012b. On the use of the infinite matrix assumption and associated concepts: A critical review. *Radiation Measurements* **47**, 778-785.

HAY C., MITROVICA J. X., GOMEZ N., CREVELING J. R., AUSTERMANN J. & E. KOPP R. 2014. The sea-level fingerprints of ice-sheet collapse during interglacial periods. *Quaternary Science Reviews* **87**, 60-69.

HAYNES D. E. & RINGIS J. 1973. Seafloor spreading in the Tasman Sea. *Nature* **243**, 454-458.

HENSHILWOOD C. S., D'ERRICO F., YATES R., JACOBS Z., TRIBOLO C., DULLER G. A. T., MERCIER N., SEALY J. C., VALLADAS H., WATTS I. & WINTLE A. G. 2002. Emergence of modern human behavior: Middle Stone Age engravings from South Africa. *Science* **295**, 1278-1280.

HUNTLEY D. J., GODFREY-SMITH D. I. & THEWALT M. L. W. 1985. Optical dating of sediments. *Nature* **313**, 105-107.

IMBRIE J., BOYLE E. A., CLEMENS S. C., DUFFY A., HOWARD W. R., KUKLA G., KUTZBACH J., MARTINSON D. G., MCINTYRE A., MIX A. C., MOLFINO B., MORLEY J. J., PETERSON L. C., PISIAS N. G., PRELL W. L., RAYMO M. E., SHACKLETON N. J. & TOGGWEILER J. R. 1992. On the Structure and Origin of Major Glaciation Cycles 1. Linear Responses to Milankovitch Forcing. *Paleoceanography* **7**, 701-738.

JACOBS Z. 2004. Development of luminescence techniques for dating Middle Stone Age sites in South Africa. Aberystwyth University, Aberystwyth (unpubl.).

JACOBS Z., DULLER G. A. T. & WINTLE A. G. 2003b. Optical dating of dune sand from Blombos Cave, South Africa: II--single grain data. *Journal of Human Evolution* **44**, 613-625.

JACOBS Z., DULLER G. A. T. & WINTLE A. G. 2006c. Interpretation of single grain D_e distributions and calculation of D_e. *Radiation Measurements* **41**, 264-277.

JACOBS Z., DULLER G. A. T., WINTLE A. G. & HENSHILWOOD C. S. 2006a. Extending the chronology of deposits at Blombos Cave, South Africa, back to 140 ka using optical dating of single and multiple grains of quartz. *Journal of Human Evolution* **51**, 255-273.

JACOBS Z., HAYES E. H., ROBERTS R. G., GALBRAITH R. F. & HENSHILWOOD C. S. 2013. An improved OSL chronology for the Still Bay layers at Blombos Cave, South Africa: further tests of single-grain dating procedures and a re-evaluation of the timing of the Still Bay industry across southern Africa. *Journal of Archaeological Science* **40**, 579-594.

JACOBS Z. & ROBERTS R. G. 2007. Advances in optically stimulated luminescence dating of individual grains of quartz from archeological deposits. *Evolutionary Anthropology* **16**, 210-223.

JACOBS Z. & ROBERTS R. G. 2008. Testing times: old and new chronologies for the Howieson's Poort and Still Bay industries in environmental context. *South African Archaeological Society Goodwin Series* **10**, 9 - 34.

JACOBS Z., ROBERTS R. G., NESPOULET R., EL HAJRAOUI M. A. & DEBÉNATH A. 2012. Single-grain OSL chronologies for Middle Palaeolithic deposits at El Mnasra and El Harhoura 2, Morocco: Implications for Late

Pleistocene human–environment interactions along the Atlantic coast of northwest Africa. *Journal of Human Evolution* **62**, 377-394.

JACOBS Z., WINTLE A. G. & DULLER G. A. T. 2003a. Optical dating of dune sand from Blombos Cave, South Africa: I--multiple grain data. *Journal of Human Evolution* **44**, 599-612.

JACOBS Z., WINTLE A. G. & DULLER G. A. T. 2006b. Evaluation of SAR procedures for D_e determination using single aliquots of quartz from two archaeological sites in South Africa. *Radiation Measurements* **41**, 520-533.

JACOBS Z., WINTLE A. G., DULLER G. A. T., ROBERTS R. G. & WADLEY L. 2008b. New ages for the post-Howiesons Poort, late and final Middle Stone Age at Sibudu, South Africa. *Journal of Archaeological Science* **35**, 1790-1807.

JACOBS Z., WINTLE A. G., ROBERTS R. G. & DULLER G. A. T. 2008c. Equivalent dose distributions from single grains of quartz at Sibudu, South Africa: context, causes and consequences for optical dating of archaeological deposits. *Journal of Archaeological Science* **35**, 1808-1820.

JAIN M., CHOI J. H. & THOMAS P. J. 2008. The ultrafast OSL component in quartz: Origins and implications. *Radiation Measurements* **43**, 709-714.

JAIN M., MURRAY A. S. & BØTTER-JENSEN L. 2003. Characterisation of blue-light stimulated luminescence components in different quartz samples: implications for dose measurement. *Radiation Measurements* **37**, 441-449.

JONES B. G., YOUNG R. W. & ELIOT I. G. 1979. Stratigraphy and chronology of receding barrier-beach deposits on the northern Illawarra coast of New South Wales. *Journal of the Geological Society of Australia* **26**, 255 - 264.

KALCHGRUBER R., FUCHS M., MURRAY A. S. & WAGNER G. A. 2003. Evaluating dose-rate distributions in natural sediments using α-Al_2O_3:C grains. *Radiation Measurements* **37**, 293-297.

KALCHGRUBER R., GÖKSU H. Y., HOCHHÄUSER E. & WAGNER G. A. 2002. Monitoring environmental dose rate using Risø TL/OSL readers with built-in sources: recommendations for users. *Radiation Measurements* **35**, 585-590.

KALCHGRUBER R. & WAGNER G. A. 2006. Separate assessment of natural beta and gamma dose-rates with TL from α-Al_2O_3:Csingle-crystal chips. *Radiation Measurements* **41**, 154-162.

KETCHAM R. A. 2005b. Computational methods for quantitative analysis of three-dimentional features in geological specimens. *Geosphere* **1**, 32-41.

KETCHAM R. A. & CARLSON W. D. 2001. Acquisition, optimization and interpretation of X-ray computed tomographic imagery: applications to the geosciences. *Computers & Geosciences* **27**, 381-400.

KOVDA I. & MERMUT A. R. 2010. Vertic Features. *In:* Stoops G., Marcelino V. & Mees F. eds., *Interpretation of Micromorphological Features of Soils and Regoliths*, pp 109-127, Elsevier, Amsterdam.

KREUTZER S., FUCHS M., MESZNER S. & FAUST D. 2012. OSL chronostratigraphy of a loess-palaeosol sequence in Saxony/Germany

using quartz of different grain sizes. *Quaternary Geochronology* **10**, 102-109.

KUBIËNA W. L. 1938. *Micropedology*. Collegiate Press, Ames, Iowa.

KUBIËNA W. L. 1970. *Micromorphological features of soil geography*. Rutgers University Press, New Brunswick.

KÜHN P., AGUILAR J. & MIEDEMA R. 2010. Textural pedofeatures and related horizons. *In:* Stoops G., Marcelino V. & Mees F. eds., *Interpretation of Micromorphological Features of Soils and Regoliths*, pp 217-250, Elsevier, Amsterdam.

LAMBECK K. 1993. Glacial rebound and sea-level change: An example of a relationship between mantle and surface processes. *Tectonophysics* **223**, 15-37.

LAMBECK K. 2001. Glacial Crustal Rebound, Sea Levels and Shorelines. *In:* Steele J. H. ed., *Encyclopedia of Ocean Sciences*, pp 1157-1167, Academic Press, Oxford.

LAMBECK K. 2004. Sea-level change through the last glacial cycle: geophysical, glaciological and palaeogeographic consequences. *Comptes Rendus Geoscience* **336**, 677-689.

LAMBECK K. & CHAPPELL J. 2001. Sea Level Change Through the Last Glacial Cycle. *Science* **292**, 679-686.

LAMBECK K. & NAKADA M. 1990. Late Pleistocene and Holocene sea-level change along the Australian coast. *Global and Planetary Change* **3**, 143-176.

LEES B. 2006. Timing and formation of coastal dunes in northern and eastern Australia. *Journal of Coastal Research*, 78-89.

LEPPER K., LARSEN N. A. & MCKEEVER S. W. S. 2000. Equivalent dose distribution analysis of Holocene eolian and fluvial quartz sands from Central Oklahoma. *Radiation Measurements* **32**, 603-608.

LEVY G. J. 2011. Sodicity. *In:* Huang P. M., Li Y. & Sumner M. E. eds., *Handbook of Soil Sciences. Resource management and environmental impacts*, pp 1-28, CRC Press.

LEWIS S. E., SLOSS C. R., MURRAY-WALLACE C. V., WOODROFFE C. D. & SMITHERS S. G. 2013. Post-glacial sea-level changes around the Australian margin: a review. *Quaternary Science Reviews* **74**, 115-138.

LIAN O. B. & ROBERTS R. G. 2006. Dating the Quaternary: progress in luminescence dating of sediments. *Quaternary Science Reviews* **25**, 2449-2468.

LOMAX J., HILGERS A., TWIDALE C. R., BOURNE J. A. & RADTKE U. 2007. Treatment of broad palaeodose distributions in OSL dating of dune sands from the western Murray Basin, South Australia. *Quaternary Geochronology* **2**, 51-56.

LØVBORG L. & KIRKEGAARD P. 1974. Response of 3″ × 3″ NaI(Tl) detectors to terrestrial gamma radiation. *Nuclear Instruments and Methods* **121**, 239-251.

LOWICK S. E., PREUSSER F. & WINTLE A. G. 2010. Investigating quartz optically stimulated luminescence dose–response curves at high doses. *Radiation Measurements* **45**, 975-984.

MACPHAIL R. I., ALLEN M. J., CROWTHER J., CRUISE G. M. & WHITTAKER J. E. 2010. Marine inundation: Effects on archaeological features, materials, sediments and soils. *Quaternary International* **214**, 44-55.

MADSEN A. T., DULLER G. A. T., DONNELLY J. P., ROBERTS H. M. & WINTLE A. G. 2009. A chronology of hurricane landfalls at Little Sippewissett Marsh, Massachusetts, USA, using optical dating. *Geomorphology* **109**, 36-45.

MARSHALL J. F. 1983. Geochemistry of iron-rich sediments on the outer continental shelf off northern New South Wales. *Marine Geology* **51**, 163-175.

MARSHALL J. F. & THOM B. G. 1976. The sea level in the last interglacial. *Nature* **263**, 120-121.

MAYYA Y. S., MORTHEKAI P., MURARI M. K. & SINGHVI A. K. 2006. Towards quantifying beta microdosimetric effects in single-grain quartz dose distribution. *Radiation Measurements* **41**, 1032-1039.

MCPHERRON S. P. & DIBBLE H. L. 2000. The lithic assemblages of Pech de l'Azé IV (Dordogne, France). *Préhistoire Européenne* **15**, 9-43.

MCPHERRON S. P. & DIBBLE H. L. (Editors) 2007. *Artefact orientations from total station proveniences*. (The World is in your eyes, Vol. 161-166). CAA Portugal, Tomar.

MCPHERRON S. P., TALAMO S., GOLDBERG P., NIVEN L., SANDGATHE D., RICHARDS M. P., RICHTER D., TURQ A. & DIBBLE H. L. 2012. Radiocarbon dates for the late Middle Palaeolithic at Pech de l'Azé IV, France. *Journal of Archaeological Science* **39**, 3436-3442.

MEDIALDEA A., THOMSEN K. J., MURRAY A. S. & BENITO G. 2014. Reliability of equivalent-dose determination and age-models in the OSL dating of historical and modern palaeoflood sediments. *Quaternary Geochronology* **22**, 11-24.

MEJDAHL V. 1979. Thermoluminescence dating: beta-dose attenuation in quartz grains. *Archaeometry* **21**, 61-72.

MELLARS P. 1970. Some Comments on the Notion of 'Functional Variability' in Stone-Tool Assemblages. *World Archaeology* **2**, 74-89.

MELLARS P. 1996. *The Neanderthal legacy: an archaeological perspective from western Europe*. Princeton University Press, Princeton, New Jersey.

MELLARS P. & GRÜN R. 1991. A Comparison of the Electron Spin Resonance and Thermoluminescence Dating Methods: The Results of ESR Dating at Le Moustier (France). *Cambridge Archaeological Journal* **1**, 269-276.

MERCIER N. & FALGUÈRES C. 2007. Field gamma dose-rate measurement with a NaI(Tl) detector: re-evaluation of the "threshold" technique. *Ancient TL* **25**, 1-4.

MERMUT A. R., SEHGAL J. L. & STOOPS G. 1988. Micromorphology of swell-shrink soils. *In, Classification, management and Use Potential of Swell-Shrink Soils.*, pp 127-144, Bureau of Soil Servey and Land Use Planning, Nagpur, India.

MILANKOVITCH M. 1930. *Mathematische Klimalehre und Astronomische Theorie der Klimaschwankungen, Handbuch der Klimalogie Band 1, Teil A Borntrager*. Berlin.

MILOSHEVSKY G. & HASSANEIN A. 2014. Time correlation of cosmic-ray-induced neutrons and gamma rays at sea level. *Nuclear Instruments and Methods in Physics Research Section A: Accelerators, Spectrometers, Detectors and Associated Equipment* **737**, 33-41.

MUNYIKWA K., FEATHERS J. K., RITTENOUR T. M. & SHRIMPTON H. K. 2011. Constraining the Late Wisconsinan retreat of the Laurentide ice sheet from western Canada using luminescence ages from postglacial aeolian dunes. *Quaternary Geochronology* **6**, 407-422.

MURRAY A. S. 1981. Environmental radioactivity studies relevent to Thermoluminescence dating. PhD thesis, University of Oxford, Oxford (unpubl.).

MURRAY A. S. 1987. Analysis for naturally occurring radionuclides at environmental concentrations by gamma spectrometry. *Journal of radioanalytical and nuclear chemistry* **115**, 263-288.

MURRAY A. S., BOWMAN S. G. E. & AITKEN M. J. 1978. Evaluation of the gamma dose-rate contribution. *PACT* **2**, 84-96.

MURRAY A. S. & OLLEY J. M. 2002. Precision and accuracy in the optically stimulated luminescence dating of sedimentary quartz: a status review. *Geochronometria* **21**, 1 - 16.

MURRAY A. S. & ROBERTS R. G. 1997. Determining the burial time of single grains of quartz using optically stimulated luminescence. *Earth and Planetary Science Letters* **152**, 163-180.

MURRAY A. S. & ROBERTS R. G. 1998. Measurement of the equivalent dose in quartz using a regenerative-dose single-aliquot protocol. *Radiation Measurements* **29**, 503-515.

MURRAY A. S. & WINTLE A. G. 2000. Luminescence dating of quartz using an improved single-aliquot regenerative-dose protocol. *Radiation Measurements* **32**, 57-73.

MURRAY A. S. & WINTLE A. G. 2003. The single aliquot regenerative dose protocol: potential for improvements in reliability. *Radiation Measurements* **37**, 377-381.

MURRAY-WALLACE C. V. & BELPERIO A. P. 1991. The last interglacial shoreline in Australia — A review. *Quaternary Science Reviews* **10**, 441-461.

MURRAY-WALLACE C. V., FERLAND M. A. & ROY P. S. 2005. Further amino acid racemisation evidence for glacial age, multiple lowstand deposition on the New South Wales outer continental shelf, southeastern Australia. *Marine Geology* **214**, 235-250.

MURRAY-WALLACE C. V., FERLAND M. A., ROY P. S. & SOLLAR A. 1996. Unravelling patterns of reworking in lowstand shelf deposits using amino acid racemisation and radiocarbon dating. *Quaternary Science Reviews* **15**, 685-697.

MURRAY-WALLACE C. V., KIMBER R. W. L., BELPERIO A. P. & GOSTIN V. A. 1988. Aminostratigraphy of the last interglacial in southern Australia. *Search* **19**, 33-36.

NAKADA M., KIMURA R., OKUNO J., MORIWAKI K., MIURA H. & MAEMOKU H. 2000. Late Pleistocene and Holocene melting history of the Antarctic ice sheet derived from sea-level variations. *Marine Geology* **167**, 85-103.

NATHAN R. P. & MAUZ B. 2008. On the dose-rate estimate of carbonate-rich sediments for trapped charge dating. *Radiation Measurements* **43**, 14-25.

NATHAN R. P., THOMAS P. J., JAIN M., MURRAY A. S. & RHODES E. J. 2003. Environmental dose rate heterogeneity of beta radiation and its implications for luminescence dating: Monte Carlo modelling and experimental validation. *Radiation Measurements* **37**, 305-313.

NICHOL S. L. & MURRAY-WALLACE C. V. 1992. A partially preserved last interglacial estuarine fill: Narrawallee Inlet, New South Wales. *Australian Journal of Earth Sciences* **39**.

NOTT J., YOUNG R., BRYANT E. & PRICE D. 1994. Stratigraphy vs. pedogenesis; problems of their correlation within coastal sedimentary facies. *Catena* **23**, 199-212.

OLLEY J. M., CAITCHEON G. G. & ROBERTS R. G. 1999. The origin of dose distributions in fluvial sediments, and the prospect of dating single grains from fluvial deposits using optically stimulated luminescence. *Radiation Measurements* **30**, 207-217.

OLLEY J. M., DE DECKKER P., ROBERTS R. G., FIFIELD L. K., YOSHIDA H. & HANCOCK G. 2004a. Optical dating of deep-sea sediments using single grains of quartz: a comparison with radiocarbon. *Sedimentary Geology* **169**, 175-189.

OLLEY J. M., MURRAY A. & ROBERTS R. G. 1996. The effects of disequilibria in the uranium and thorium decay chains on burial dose rates in fluvial sediments. *Quaternary Science Reviews* **15**, 751-760.

OLLEY J. M., PIETSCH T. & ROBERTS R. G. 2004b. Optical dating of Holocene sediments from a variety of geomorphic settings using single grains of quartz. *Geomorphology* **60**, 337-358.

OLLEY J. M., ROBERTS R. G. & MURRAY A. S. 1997. Disequilibria in the uranium decay series in sedimentary deposits at Allen's Cave, Nullarbor Plain, Australia: Implications for dose rate determinations. *Radiation Measurements* **27**, 433-443.

OLLEY J. M., ROBERTS R. G., YOSHIDA H. & BOWLER J. M. 2006. Single-grain optical dating of grave-infill associated with human burials at Lake Mungo, Australia. *Quaternary Science Reviews* **25**, 2469-2474.

OU X., XU L., LAI Z., LONG H., HE Z., FAN Q. & ZHOU S. 2010. Potential of quartz OSL dating on moraine deposits from eastern Tibetan Plateau using SAR protocol. *Quaternary Geochronology* **5**, 257-262.

PACKMAN S. C., MAUZ B., ROUSSEAU D. D., ANTOINE P., ROSSIGNOL J. & LANG A. 2007. Implications of broad dose distributions obtained with the single-aliquot regenerative-dose method on quartz fine-grains from loess. *Quaternary Geochronology* **2**, 39-44.

PANAYOTOU K., WOODROFFE C. D., JONES B. G., CHENHALL B. E., MCLEAN E. J. & HEIJNIS H. 2007. Patterns and rates of sedimentary infilling in the Minnumurra River Estuary, South-Eastern Australia. *Journal of Coastal Research* **Special Issue 50**, 688-692.

PICKETT J. 1981. A Late Pleistocene coral fauna from Evans Head, N.S.W. *Alcheringa: An Australasian Journal of Palaeontology* **5**, 71-83.

PICKETT J. W., KU T. L., THOMPSON C. H., ROMAN F. D., KELLEY R. A. & HUANG Y. P. 1989. A review of age determination on Pleistocene corals in Eastern Australia. *Quaternary Research* **31**.

PIETSCH T. J., OLLEY J. M. & NANSON G. C. 2008. Fluvial transport as a natural luminescence sensitiser of quartz. *Quaternary Geochronology* **3**, 365-376.

PORAT N., DULLER G. A. T., ROBERTS H. M., PIASETZKY E. & FINKELSTEIN I. 2012. OSL dating in multi-strata Tel: Megiddo (Israel) as a case study. *Quaternary Geochronology* **10**, 359-366.

PRESCOTT J. R. & HUTTON J. T. 1994. Cosmic ray contributions to dose rates for luminescence and ESR dating: large depths and long-term time variations. *Radiation Measurements* **23**, 497-500.

PREUSSER F., CHITHAMBO M. L., GÖTTE T., MARTINI M., RAMSEYER K., SENDEZERA E. J., SUSINO G. J. & WINTLE A. G. 2009. Quartz as a natural luminescence dosimeter. *Earth-Science Reviews* **97**, 184-214.

PRICE D. M., BRYANT E. A. & YOUNG R. W. 1999. Thermoluminescence evidence for the deposition of coastal sediments by tsunami wave action. *Quaternary International* **56**, 123-128.

PRIDEAUX G. J., GULLY G. A., COUZENS A. M. C., AYLIFFE L. K., JANKOWSKI N. R., JACOBS Z., ROBERTS R. G., HELLSTROM J. C., GAGAN M. K. & HATCHER L. M. 2010. Timing and dynamics of Late Pleistocene mammal extinctions in southwestern Australia. *Proceedings of the National Academy of Sciences* **107**, 22157-22162.

PRITCHARD D. W. 1967. What is an estuary: physical viewpoint. *In:* Lauff G. H. ed., *Estuaries*, pp 3-5, American Association for the Advancement of Science, Washington DC.

REIMANN T., LINDHORST S., THOMSEN K. J., MURRAY A. S. & FRECHEN M. 2012. OSL dating of mixed coastal sediment (Sylt, German Bight, North Sea). *Quaternary Geochronology* **11**, 52-67.

RHODES E. J. & SCHWENNINGER J.-L. 2007. Dose rates and radioisotope concentrations in the concrete calibration blocks at Oxford. *Ancient TL* **25**, 5-8.

RHODES E. J., SINGARAYER J. S., RAYNAL J. P., WESTAWAY K. E. & SBIHI-ALAOUI F. Z. 2006. New age estimates for the Palaeolithic assemblages and Pleistocene succession of Casablanca, Morocco. *Quaternary Science Reviews* **25**, 2569-2585.

RICHTER D., DIBBLE H., GOLDBERG P., MCPHERRON S. P., NIVEN L., SANDGATHE D., TALAMO S. & TURQ A. 2013. The late Middle Palaeolithic in Southwest France: New TL dates for the sequence of Pech de l'Azé IV. *Quaternary International* **294**, 160-167.

ROBERTS D. L., KARKANAS P., JACOBS Z., MAREAN C. W. & ROBERTS R. G. 2012. Melting ice sheets 400,000 yr ago raised sea level by 13 m: Past analogue for future trends. *Earth and Planetary Science Letters* **357–358**, 226-237.

ROBERTS H. M. & DULLER G. A. T. 2004. Standardised growth curves for optical dating of sediment using multiple-grain aliquots. *Radiation Measurements* **38**, 241-252.

ROBERTS R. G., GALBRAITH R. F., OLLEY J. M., YOSHIDA H. & LASLETT G. M. 1999. Optical dating of single and multiple grains of quartz from

Jinmium rock shelter, Northern Australia: Part II, results and implications. *Archaeometry* **41**, 365-395.

ROBERTS R. G., GALBRAITH R. F., YOSHIDA H., LASLETT G. M. & OLLEY J. M. 2000. Distinguishing dose populations in sediment mixtures: a test of single-grain optical dating procedures using mixtures of laboratory-dosed quartz. *Radiation Measurements* **32**, 459-465.

ROBERTS R. G., SPOONER N. A. & QUESTIAUX D. G. 1993. Cautions on the use of extended duration preheats in the optical dating of quartz. *Ancient TL* **11**, 47-54.

ROBERTS R. G., YOSHIDA H., GALBRAITH R. F., LASLETT G., JONES R. & SMITH M. 1998. Single-aliquot and single-grain optical dating confirms thermoluminescence age estimates at Malakunanja II rock shelter in northern Australia. *Ancient TL* **16**, 19 - 24.

RODUIT N. 2013. *JMicroVision: Image analysis toolbox for measuring and quantifying components of high-definition images*.

ROLLAND N. & DIBBLE H. 1990. A new synthesis of Middle Palaeolithic variability. *American Antiquity* **55**, 480-499.

ROY P. & CRAWFORD E. 1977. Significance of Sediment Distribution in Major Coastal Rivers, Northern N.S.W. Australian Conference on Coastal and Ocean Engineering (3rd : 1977 : Melbourne, Vic.), Barton, A.C.T. (unpubl.).

ROY P. S. 1984. New South Wales estuaries: their origin and evolution. *In:* Thom B. G. ed., *Coastal Geomorphology in Australia*, pp 99-121, Academic Press, Sydney.

ROY P. S., COWELL P. J., FERLAND M. A. & THOM B. G. 1994. Wave-dominated coasts. *In:* Carter R. W. G. & Woodroffe C. D. eds., *Coastal Evolution: Late Quaternary shoreline morphodynamics*, Cambridge University Press, Cambridge.

ROY P. S. & THOM B. G. 1981. Late Quaternary marine deposition in New South Wales and southern Queensland — An evolutionary model. *Journal of the Geological Society of Australia* **28**, 471-489.

ROY P. S., THOM B. G. & WRIGHT L. D. 1980. Holocene sequences on an embayed high-energy coast: an evolutionary model. *Sedimentary Geology* **26**, 1-19.

SCHMID B., SCHINDELIN J., CARDONA A., LONGAIR M. & HEISENBERG M. 2010. A high-level 3D visualization API for Java and ImageJ. *BMC Bioinformatics* **11**, 274.

SCHNEIDER C. A., RASBAND W. S. & ELICEIRI K. W. 2012. NIH Image to ImageJ: 25 years of image analysis. *Nat Meth* **9**, 671-675.

SCHWARCZ H. P. 1989. Uranium series dating of Quaternary deposits. *Quaternary International* **1**, 7-17.

SINGARAYER J. S. 2003. Linearly modulated optically stimulated luminescence of sedimentary quartz: physical mechanisms and implications for dating. University of Oxford, Oxford (unpubl.).

SINGARAYER J. S. & BAILEY R. M. 2003. Further investigations of the quartz optically stimulated luminescence components using linear modulation. *Radiation Measurements* **37**, 451-458.

SINGARAYER J. S. & BAILEY R. M. 2004. Component-resolved bleaching spectra of quartz optically stimulated luminescence: preliminary results and implications for dating. *Radiation Measurements* **38**, 111-118.

SLOSS C. R., JONES B. G., MCCLENNEN C. E., DE CARLI J. & PRICE D. M. 2006b. The geomorphological evolution of a wave-dominated barrier estuary: Burrill Lake, New South Wales, Australia. *Sedimentary Geology* **187**, 229-249.

SLOSS C. R., JONES B. G., MURRAY-WALLACE C. V. & MCCLENNEN C. E. 2005. Holocene Sea Level Fluctuations and the Sedimentary Evolution of a Barrier Estuary: Lake Illawarra, New South Wales, Australia. *Journal of Coastal Research* **21**, 943-959.

SLOSS C. R., JONES B. G., SWITZER A. D., NICHOL S., CLEMENT A. J. H. & NICHOLAS A. W. 2010. The Holocene infill of Lake Conjola, a narrow incised valley system on the southeast coast of Australia. *Quaternary International* **221**, 23-35.

SLOSS C. R., MURRAY-WALLACE C. V. & JONES B. G. 2006a. Aminostratigraphy of two Holocene wave-dominated barrier estuaries in southeastern Australia. *Journal of Coastal Research* **22**, 113+.

SLOSS C. R., MURRAY-WALLACE C. V. & JONES B. G. 2007. Holocene sea-level change on the southeast coast of Australia: a review. *The Holocene* **17**, 999-1014.

SLOSS C. R., MURRAY-WALLACE C. V., JONES B. G. & WALLIN T. 2004. Aspartic acid racemisation dating of mid-Holocene to recent estuarine sedimentation in New South Wales, Australia: a pilot study. *Marine Geology* **212**, 45-59.

SMITH B. W. & RHODES E. J. 1994. Charge movements in quartz and their relevance to optical dating. *Radiation Measurements* **23**, 329-333.

SMITH M. A., PRESCOTT J. R. & HEAD M. J. 1997. Comparison of ^{14}C and luminescence chronologies at Puritjarra rock shelter, central Australia. *Quaternary Science Reviews* **16**, 299-320.

SORESSI M., JONES H. L., RINK W. J., MAUREILLE B. & TILLIER A. M. 2007. The Pech-de-l'Azé I Neandertal child: ESR, uranium-series, and AMS ^{14}C dating of its MTA type B context. *Journal of Human Evolution* **52**, 455-466.

SORESSI M., MCPHERRON S. P., LENOIR M., DOGANDŽIĆ T., GOLDBERG P., JACOBS Z., MAIGROT Y., MARTISIUS N. L., MILLER C. E., RENDU W., RICHARDS M., SKINNER M. M., STEELE T. E., TALAMO S. & TEXIER J.-P. 2013. Neandertals made the first specialized bone tools in Europe. *Proceedings of the National Academy of Sciences* **110**, 14186-14190.

SPOONER N. A., PRESCOTT J. R. & HUTTON J. T. 1988. The effect of illumination wavelength on the bleaching of the thermoluminescence (TL) of quartz. *Quaternary Science Reviews* **7**, 325-329.

SPOONER N. A. & QUESTIAUX D. G. 2000. Kinetics of red, blue and UV thermoluminescence and optically-stimulated luminescence from quartz. *Radiation Measurements* **32**, 659-666.

STONEHAM D. & STOKES S. 1991. An investigation of the relationship between the 110°C TL peak and optically stimulated luminescence in sedimentary quartz. *Nuclear tracks and radiation measurements* **18**, 119-123.

STOOPS G. 2003. *Guidelines for the Analysis and Description of Soil and Regolith Thin Sections*. Soil Science Society of America, Madison, Wisconsin.

STOOPS G. & ESWARAN H. 1985. Morphological characteristics of wet soils. *In*, *Wetland soils: Characterization, Classification and Utilization*, pp 177-190, International Rice Research Institute, Manila.

STOOPS G., MARCELINO V. & MEES F. 2010. *Interpretation of Micromorphological Features in Soils and Regoliths*. Elsevier, Amsterdam.

SWITZER A. D., PUCILLO K., HAREDY R. A., JONES B. G. & BRYANT E. A. 2005. Sea level, storm, or tsunami: enigmatic sand sheet deposits in a sheltered coastal embayment from southeastern New South Wales, Australia. *Journal of Coastal Research* **21**, 655+.

TARPLEE M. F. V., VAN DER MEER J. J. M. & DAVIS G. R. 2011. The 3D microscopic 'signature' of strain within glacial sediments revealed using X-ray computed microtomography. *Quaternary Science Reviews* **30**, 3501-3532.

TEXIER J. P. 2009. *Histoire Géologique de Sites Préhistoriques Classiques du Périgord: une Vision Actualisée*. Editions du Comité des Travaux Historiques et Scientifiques, Paris.

THOM B. G. 1978. Coastal sand deposition in southeast Australia during the Holocene. *In:* Davies J. L. & Williams M. A. F. eds., *Landofrom Evolution in Australasia*, pp 3-17, Australian National University press, Canberra.

THOM B. G. 1984a. Sand barriers of earstern Austrlaia: Gippsland - a case study. *In:* Thom B. G. ed., *Coastal Geomorphology in Australia*, pp 233-261, Academic Press, Sydney.

THOM B. G. 1984b. Transgressive and regressive stratigraphies of coastal sand barriers in eastern Australia. *Marine Geology* **56**, 137-158.

THOM B. G., BOWMAN G. M., GILLESPIE R., TEMPLE R. & BARBETTI M. 1981. *Radiocarbon dating of Holocene Beach-ridge Sequences in Southeast Australia.* Geography Department, Faculty of Military Studies, University of NSW, Duntroon, Canberra.

THOM B. G. & CHAPPELL J. 1975. Holocene sea levels realtive to Australia. *Search* **6**, 90-93.

THOM B. G., MCLEAN R. F., LANGFORD-SMITH T. & ELLIOT I. 1973. Seasonal beach change, central and south coast, N.S.W. *In*, *Engineering dynamics of the coastal zone*, Vol. 73, pp 35-42, Institution of Engineers, Australia.

THOM B. G. & MURRAY-WALLACE C. V. 1988. Geological note: last Interglacial (Stage 5e) estuarine sediments at Largs, New South Wales. *Australian Journal of Earth Sciences* **35**, 571-574.

THOM B. G., POLACH H. A. & BOWMAN G. M. 1978. *Holocene-age structure of coastal sand barriers in New South Wales, Australia*. Department of Geography, Faculty of Military Studies, University of N.S.W., Duntroon, Canberra.

THOM B. G. & ROY P. S. 1985. Relative sea levels and coastal sedimentation in Southeast Australia in the Holocene. *JOURNAL OF SEDIMENTARY RESEARCH* **55**, 257-264.

THOM B. G., SHEPHERD M., LY C. K., ROY P. S., G.M. B. & HESP P. A. 1992. *Coastal Geomorphology and Quaternary Geology of the Port Stephens-Myall Lakes Area*. Australian National University Press, Canberra.

THOMAS P. J., JAIN M., JUYAL N. & SINGHVI A. K. 2005. Comparison of single-grain and small-aliquot OSL dose estimates in years old river sediments from South India. *Radiation Measurements* **39**, 457-469.

THOMSEN K. J., MURRAY A. & JAIN M. 2012. The dose dependency of the over-dispersion of quartz OSL single grain dose distributions. *Radiation Measurements* **47**, 732-739.

THOMSEN K. J., MURRAY A. S. & BØTTER-JENSEN L. 2005. Sources of variability in OSL dose measurements using single grains of quartz. *Radiation Measurements* **39**, 47-61.

THORNE A., GRÜN R., MORTIMER G., SPOONER N. A., SIMPSON J. J., MCCULLOCH M., TAYLOR L. & CURNOE D. 1999. Australia's oldest human remains: age of the Lake Mungo 3 skeleton. *Journal of Human Evolution* **36**, 591-612.

TIMAR-GABOR A., VASILINIUC Ş., VANDENBERGHE D. A. G., COSMA C. & WINTLE A. G. 2012. Investigations into the reliability of SAR-OSL equivalent doses obtained for quartz samples displaying dose response curves with more than one component. *Radiation Measurements* **47**, 740-745.

TURNEY C. S. M., BIRD M. I., FIFIELD L. K., ROBERTS R. G., SMITH M., DORTCH C. E., GRÜN R., LAWSON E., AYLIFFE L. K., MILLER G. H., DORTCH J. & CRESSWELL R. G. 2001. Early human occupation at Devil's Lair, southwestern Australia 50,000 years ago. *Quaternary Research* **55**, 3-13.

TURNEY C. S. M., FLANNERY T. F., ROBERTS R. G., REID C., FIFIELD L. K., HIGHAM T. F. G., JACOBS Z., KEMP N., COLHOUN E. A., KALIN R. M. & OGLE N. 2008. Late-surviving megafauna in Tasmania, Australia, implicate human involvement in their extinction. *Proceedings of the National Academy of Sciences* **105**, 12150-12153.

TURQ A., DIBBLE H. L., GOLDBERG P., MCPHERRON S. P., SANDGATHE D., JONES H., MADDISON K., MAUREILLE B., MENTZER S., RINK J. & STEENHUYSE A. 2011. Les fouilles récentes du Pech de l'Azé IV (Dorgodne). *Gallia Préhistoire* **53**, 1-58.

VALLADAS H., GENESTE J. M., JORON J. L. & CHADELLE J. P. 1986. Thermoluminescence dating of Le Moustier (Dordogne, France). *Nature* **322**, 452-454.

VALLADAS H., MERCIER N., AYLIFFE L. K., FALGUÈRES C., BAHAIN J. J., DOLO J. M., FROGET L., JORON J. L., MASAOUDI H., REYSS J. L. & MONCEL M. H. 2008. Radiometric dates for the Middle Palaeolithic sequence of Payre (Ardèche, France). *Quaternary Geochronology* **3**, 377-389.

VALLADAS H., MERCIER N., FROGET L., HOVERS E., JORON J. L., KIMBEL W. H. & RAK Y. 1999. TL Dates for the Neanderthal Site of the Amud Cave, Israel. *Journal of Archaeological Science* **26**, 259-268.

VALLADAS H., MERCIER N., JORON J. L., MCPHERRON S. P., DIBBLE H. L. & LENOIR M. 2003. TL dates for the Middle Paleolithic site of Combe-

Capelle Bas, France. *Journal of Archaeological Science* **30**, 1443-1450.

VOGEL J. C. & WALTERBOLK H. T. 1967. Groningen Radiocarbon Dates VII. *Radiocarbon* **9**, 107-155.

WESTAWAY K. E. 2010. The red, white and blue of quartz luminescence: A comparison of D_e values derived for sediments from Australia and Indonesia using thermoluminescence and optically stimulated luminescence emissions. *Radiation Measurements* **44**, 462-466.

WINTLE A. G. 1997. Luminescence dating: laboratory procedures and protocols. *Radiation Measurements* **27**, 769-817.

WINTLE A. G. & MURRAY A. S. 1997. The relationship between quartz thermoluminescence, photo-transferred thermoluminescence, and optically stimulated luminescence. *Radiation Measurements* **27**, 611-624.

WINTLE A. G. & MURRAY A. S. 2006. A review of quartz optically stimulated luminescence characteristics and their relevance in single-aliquot regeneration dating protocols. *Radiation Measurements* **41**, 369-391.

WODA C. & FUCHS M. 2008. On the applicability of the leading edge method to obtain equivalent doses in OSL dating and dosimetry. *Radiation Measurements* **43**, 26-37.

WOODROFFE C. D. 2002. *Coasts: form, process, and evolution*. Cambridge University Press, New York.

WRIGHT L. D. 1976. Nearshore wave-power dissipation and the coastal energy regime of the Sydney-Jervis Bay region, New South Wales: a comparison. *Marine and Freshwater Research* **27**, 633-640.

YAALON D. H. & KALMAR D. 1978. Dynamics of cracking and swelling clay soils: Displacement of skeletal grains, optimum depth of slickensides, and rate of intra-pedonic turbation. *Earth Surface Processes* **3**, 31-42.

YASSINI I. & JONES B. G. 1995. *Recent Foraminifera and Ostracoda from Estuarine and Shelf Environments on the Southeastern Coast of Australia*. University of Wollongong Press, Wollongong.

YASSINI I. & JONES B. G. 1995. *Recent Foraminifera and Ostracoda from Estuarine and Shelf Environments on the Southeastern Coast of Australia*. University of Wollongong Press, Wollongong.

YOSHIDA H., ROBERTS R. G. & OLLEY J. M. 2003. Progress towards single-grain optical dating of fossil mud-wasp nests and associated rock art in northern Australia. *Quaternary Science Reviews* **22**, 1273-1278.

YOSHIDA H., ROBERTS R. G., OLLEY J. M., LASLETT G. M. & GALBRAITH R. F. 2000. Extending the age range of optical dating using single `supergrains' of quartz. *Radiation Measurements* **32**, 439-446.

YOUNG R. W., BRYANT E. A., PRICE D. M., WIRTH L. M. & PEASE M. 1993. Theoretical constraints and chronological evidence of Holocene coastal development in central and southern New South Wales, Australia. *Geomorphology* **7**, 317-329.

YUKIHARA E. G., WHITLEY V. H., MCKEEVER S. W. S., AKSELROD A. E. & AKSELROD M. S. 2004. Effect of high-dose irradiation on the optically stimulated luminescence of Al_2O_3:C. *Radiation Measurements* **38**, 317-330.

YUKIHARA E. G., WHITLEY V. H., POLF J. C., KLEIN D. M., MCKEEVER S. W. S., AKSELROD A. E. & AKSELROD M. S. 2003. The effects of deep trap population on the thermoluminescence of Al_2O_3:C. *Radiation Measurements* **37**, 627-638.

PART D

Appendix I

OSL dating supplementary information

10.1.1 REJECTION CRITERIA

10.1.1.1 RECYCLING RATIO TEST

The power behind the SAR procedure, unlike its predecessors, is that the changes in luminescence sensitivity that occurs over the cycles of irradiation, heating and stimulation are corrected for by a fixed T_D administered directly after measurement of the L_N or L_X (Murray & Wintle 2000). The assumption built into the SAR procedure is that the OSL response to the T_D adequately represents the changes in sensitivity that has occurred during the last regenerative cycle. The determination of sensitivity changes is paramount to the accuracy of the D_e measurement, as it is the L_x/T_X ratios that produce the sensitivity-corrected dose response curve from which the D_e is calculated.

To this end, the application of a T_D was specifically incorporated in the SAR procedure to account for sensitivity changes (Murray & Wintle 2000). By measuring the T_X response to a fixed T_D the sensitivity changes that occurred during the previous SAR cycle could not only be monitored but corrected for. By dividing each L_X by their respective T_X responses, a series of sensitivity-corrected OSL signals is generated to produce a dose-response curve and ultimately, to determine the D_e. Yet, in some instances, the sensitivity correction does not satisfactorily account for the changes in sensitivity that occurs throughout the SAR procedure. The adequacy of the sensitivity correction is tested by delivering an identical regenerative dose at both the start and end of the SAR procedure. As outlined in Section 3.2.4.2, if the

recycling ratio fails to be consistent with unity at 2σ, the sensitivity-correction procedure for that grain, or aliquot, is considered to be inappropriate and the D_e rejected.

10.1.1.2 THERMAL TRANSFER TEST

The SAR procedure, as outlined by Murray & Wintle (2000), rests upon the assumption that the OSL signal induced by laboratory irradiation (L_X) is derived from the same source traps as those sampled during stimulation of the natural dose (L_N). However, this is not necessarily the case with both thermally and optically unstable traps being filled during laboratory irradiations. To ensure that the same traps are being sourced for each successive measurement of L_X and T_X requires that the samples be preheated to remove the charge form the thermally unstable traps centred at 110 and 160 °C (when a heating rate of 5 °C/ s is used). Typical preheat temperatures range between ~160 and 280 °C, with choice of preheat temperature and duration not universally applicable to all samples. This outcome reiterates the importance of the dose recovery test (see Section 3.2.5.1.5) in determining the correct preheat parameters to accurately determine the D_e.

One notable consequence of the preheat procedure, however, is the transfer of electron charge from light-insensitive to light-sensitive traps resulting in a 'recuperated' OSL signal (Smith & Rhodes 1994, Aitken 1998). These light insensitive traps are thought to be sourced from TL peaks at temperatures greater than 300 °C (Adamiec *et al.* 2010). If accurate measures of D_e are to be obtained by using the SAR procedure, the recuperation of the OSL signal is required to be monitored. This can be achieved using a 0 Gy regenerative dose (as outlined above; Murray & Wintle 2000). Thus, those grains where the L_X/T_X for the 0 Gy R_X is >5% of the corresponding L_N/T_N are rejected on the basis of containing a recuperated OSL signal, which is also assumed to contribute similar proportions to all other L_X and T_X OSL signals leading to the inaccurate estimation of the D_e. It should be noted, however, that the origin of charge is important and that the 0 Gy dose procedure outlined here does not detect the main, underlying source of thermal transfer disruption in many cases.

10.1.1.3 OSL IR-DEPLETION RATIO TEST

The SAR procedure was originally developed for the use of quartz grains, as opposed to feldspars or mixed mineral samples. Given that the OSL signal decay and dose response characteristics of feldspars are significantly different to quartz, they are required to be removed.

Duller (2003) proposed the incorporation of an OSL IR depletion ratio into the SAR procedure to identify and reject feldspar grains. Exploiting the relative sensitivities of quartz and feldspar to IR-stimulation, Duller (2003) suggests that the final cycle of the SAR procedure should deliver a regenerative dose of the same magnitude as that used during the recycling ratio test. This is then followed by a period of IR stimulation at 50 °C, before continuing on with the SAR procedure as normal. Where the OSL IR-depletion ratio falls more than 2σ below unity, it can be assumed that the grain measured is highly likely a feldspar contaminant grain, rather than quartz, and rejected.

10.1.2 SAMPLE PREPARATION METHODS

Due to the light-sensitive nature of the OSL signal, sample collection is typically conducted in a manner that exposes the sediments to no natural light. Although it is preferable to carry out sampling at night, this may not be always possible. In this instance, samples can be collected using opaque plastic or metal tubes that are hammered into the stratigraphic section and sealed at both ends to prevent light exposure. This method works particularly well in homogeneous sedimentary layers (e.g., aeolian dune or fluviatile sands). Here, the light-exposed ends of the tubes are removed and used for sediment water content and dosimetry measurements.

An alternative method, however, is used in situations where tubes cannot be used or it is impractical to do so (e.g., the sediments are mainly comprised of cobbles or limestone rubble). If this is carried out during daylight hours, the sedimentary

section (and the researcher) is required to be covered by a thick black plastic tarpaulin to prevent light exposure. Sediments are scraped from the section using a trowel or spoon and placed into a sample bag that is then wrapped in black plastic to prevent light-exposure. Alternatively, this method can also be carried out at night, without the use of the tarpaulin. An additional bag of sediments is also collected from the back of the OSL hole after OSL sampling and is used for sediment water content and dose rate evaluation.

The OSL samples are prepared under dim red light conditions in the laboratory using the procedures outlined in Wintle (1997) to produce a 'purified' quartz subsample for D_e measurement. Carbonate grains and cements are removed using a 10% hydrochloric acid wash for a period of at least 24 hr or until the dissolution reaction has ceased. Organic matter, such as charcoal and humic acids, is then oxidised using hydrogen peroxide (H_2O_2) solution for 24 hr (10%), or until completely digested, before the sample is washed in distilled water. The samples were allowed to dry and then sieved to obtain the 180–212 μm in diameter grain size fraction. Density separations using sodium polytungstate (SPT) solutions with specific gravities of 2.62 and 2.70 are used to separate the quartz grains from the feldspar and heavy minerals fractions, respectively. Finally, each sample was then etched in 48% HF acid for 40 min to remove the outer alpha-irradiated 'rinds' and dissolve any residual feldspar grains. The grains are then washed in hydrochloric acid (32%) to dissolve any fluoride precipitates that may have formed during the etching processes. As the HF-acid etching preferentially targets the feldspar grains, the samples were again sieved to remove the now much smaller feldspar grains and leave behind the 'purified' >180 μm in diameter quartz grains that are used for D_e determination.

10.1.3 DOSE RATE DETERMINATION PROCEDURES

10.1.3.1 INTERNAL DOSE RATE

10.1.3.1.1 Alpha dose rate

Although the majority of the total environmental dose rate received by quartz grains is produced externally to the grain, a small internal dose rate contribution is made by the presence of U, Th and K within the quartz crystal lattice (Aitken 1985, 1998). The radioactive decay of these radionuclides results in alpha, beta and gamma radiation. It is only the alpha component, however, that is of importance due to its short range of influence (effectively 'self-dosing' the grain). In contrast, both beta particles and gamma rays have a negligible contribution to the internal dose rate. The internal alpha contribution is generally small as a result of the low alpha efficiency of quartz (Aitken 1985, 1998, Thorne *et al.* 1999) and the low concentrations of U, Th and K radionuclides (Thorne *et al.* 1999).

It is often not practical to measure the internal dose rate for each OSL sample. As such, a common internal alpha value for all samples measured is assumed or not stated explicitly (Olley *et al.* 2004a - 0.03 Gy/ka, Lomax *et al.* 2007 - not stated, Fornós *et al.* 2009 - not stated, Constantin *et al.* 2012 - 0.01 Gy/ka, Reimann *et al.* 2012 - 0.06 Gy/ka, Medialdea *et al.* 2014 - 0.06 Gy/ka). At the University of Wollongong laboratory, it is common practice to assume an internal alpha dose rate value of ~0.03 Gy/ka based on the calculations of Bowler *et al.* (2003) for Australian quartz grains.

10.1.3.2 EXTERNAL DOSE RATES

10.1.3.2.1 Alpha dose rate

In addition to an internal alpha dose rate, an external contribution of alpha particles is also made to the total environmental dose rate. Yet, this external alpha dose rate contribution is routinely made negligible during sample preparation procedures (Wintle 1997). As the efficiency of the alpha particle of quartz is low (Thorne *et al.* 1999), only a ~10 µm 'rind' on the quartz grain becomes alpha-irradiated. By hydrofluoric (HF-) acid etching the quartz grains prior to measurement, this 'rind' is removed along with the contribution of the external alpha dose (Bell & Zimmerman 1978, Brennan 2003), leaving behind only the beta and gamma irradiated quartz grain 'cores.' This practice removes the need to assess the uncertainties in the external alpha dose rate resulting from partial penetration of the quartz grain (Aitken 1985).

10.1.3.2.2 Cosmic dose rate

The total contribution of the cosmic-ray dose rate to the total environmental dose rate is typically small, but is not always insignificant. The interaction and collision of intergalactic particles with molecules in the upper atmosphere of Earth produces a 'shower' of lighter particles. This 'shower' is composed of a 'soft' and a 'hard' component (Prescott & Hutton 1994). The former is comprised mainly of electrons and penetrate only the upper ~0.6 m of sediment, whereas the latter (comprised of muons) has the ability to penetrate through meters of sediment and rock material before ionisation begins (Miloshevsky & Hassanein 2014). However, the cosmic-ray dose rate fluctuates according to geomagnetic latitude, height above sea level and the sample burial depth and (if present) rock overburden (Prescott & Hutton 1994).

Typically, the cosmic-dose rate is not measured but rather estimated using the published equations of Prescott & Hutton (1994). Using these equations, the geomagnetic latitude, sample altitude and sediment/rock overburden can be accounted for. Additionally, the $\cos^2$ ø-zenith angular distribution of cosmic-rays (Smith *et al.* 1997) can be used to account for the partial shielding effects (for instance, if the sample was shielded on one side by a rock cliff but open to the sky on the other). The calculated cosmic-ray dose rates were assigned a systematic relative uncertainty of 10% (Prescott & Hutton 1994). This uncertainty is built upon the assumption that the cosmic ray flux has not varied by more than 10% over the period of the past 500 ka.

10.1.3.2.3 Beta and gamma dose rates

The contribution of beta and gamma radiation can be measured using a variety of different laboratory and field techniques. A further distinction can be made between methods that directly measure the elemental concentrations of U, Th and K (e.g., inductively coupled plasma optical emission or mass spectrometry) compared to emission counting methods that measure the alpha, beta and gamma emissions coming from the sediments over a given time (e.g., thick source alpha counting, GM-25-5 beta counting, high-resolution gamma-spectrometry, field gamma spectrometry and aluminium oxide dosimetry).

Laboratory-based measurements can be used to obtain both the beta and the gamma dose rate from a sample. Such methods require that the sediment samples be oven dried, pulverised and homogenised (e.g., using a Retsch ball-mill) to produce a fine powder and allowed to rest for at least two weeks prior to measurement to allow the ingrowth of post-Rn radioactive daughters. However, the measurement of the beta and gamma dose rate using laboratory-based techniques implicitly assumes that the samples being measured are representative of homogeneous spheres of beta or

gamma influence in the field. This assumption may not always be true, since heterogeneity is also possible at both the scale of the beta particle (2–3 mm) (Murray & Roberts 1998, Jacobs *et al.* 2008c) and gamma ray (~30 cm).

This heterogeneity is particularly problematic where materials such as carbonate nodules, bone fragments, carbonaceous material, flint tools, rock slabs, flowstone complexes, etc., are present in the sediment section and each component having different radioactivities. While solutions to account for the beta dose rate delivered to individual grains are still being developed, a common solution for the gamma dose rate is to measure the contribution of the gamma radiation to the external dose rate in the field at the point of sampling, using a portable gamma detector.

Many of the dose rate evaluation techniques used in luminescence applications, specifically those that measure the parent activity, assume that the ^{235}U, ^{238}U and ^{232}Th decay chains have always been in secular equilibrium. For secular equilibrium to occur requires that daughter radionuclides have a much shorter half-life than their respective parents, e.g., the ratio of the half-life of ^{238}U to that of its daughter ^{234}Th is $\sim 6.8 \times 10^{10}$. Thus, after ~10 half-lives of the daughter, the rate of daughter production is equal to the rate of daughter decay and the total activity of the daughter (Bq/Kg) that is equivalent to the activity of the parent. The emission counting methods, however, assume that the dose rate at the time of sampling has prevailed throughout the period of burial, but does not necessarily imply secular equilibrium (Olley *et al.* 1996). Below, I outline the techniques used in the determination of the external beta and gamma dose rates used in this thesis.

10.1.3.3 LABORATORY-BASED MEASUREMENTS

10.1.3.3.1 Thick-source alpha counting (TSAC)

As a standalone technique, TSAC can provide an estimate of the beta and gamma contributions coming from U and Th only (Aitken 1985, 1990). However, when used in combination with an independent measurement for K, the total beta and gamma dose rates can be determined. TSAC is an inexpensive, and accurate, means

of determining U and Th concentrations in a given sample using alpha particle emissions given off by these radionuclides and, more importantly, their radioactive daughters. In fact, the 'pairs' counting technique (Aitken 1990) is used to measure the proportion of alpha decays coming from the ^{220}Rn and ^{216}Po daughters of the ^{232}Th chain in relation to the overall alpha counts for the sample. Given the short half-life of 0.15 s for the ^{216}Po radionuclide, the rapid decay of ^{220} Rn to ^{216}Po, and ^{216}Po to ^{212}Pb results in a 'pair' of alpha particles being generated within 0.2 s of each other that can be exclusively attributed to the ^{232}Th decay chain. When the number of 'pairs' from the Th decay chain are compared to the total number of alpha decays over a given period of time, concentrations of U and Th (in µg/g) can be established, and dose rates determined using the conversion factors of Guérin *et al.* (2011).

The TSAC measurements carried out in this thesis were conducted on a calibrated Daybreak 583 thick source alpha counter (Figure 10.1). Prior to measuring dried and powdered sediments, a background check was conducted on the zinc sulphide screens. Two screens, 14.70 cm^2, were placed face-to-face into the custom made Perspex sample-holder, with a stainless steel retaining ring holding them in place and lid sealed with a rubber 'O' ring. Of the total background counts recorded, half were used as an estimate of background for each of the screens measured. With a zinc sulphide screen (powder side up) and the stainless steel retaining ring holding it in place, the powdered sediments were placed on top of the screen in an 'alpha-thick' (> 1 mm) layer. The lid and 'O' ring were then replaced but the holder was left unsealed using spacers between the holder and the lid. The sample was then counted for a period of time until the total alpha counts reached at least 2000. As beta counting was carried out alongside TSAC, the concentrations of U, Th (from the TSAC, exclusively) and K (only when TSAC is used in conjunction with beta counting; there is no K measured by TSAC alone) were calculated using the equations and methods outlined in Appendix J in Aitken (1985) and in Appendix C in Jacobs (2004) and converted into dose rate (Gy/ka) using the conversion factors of Guérin *et al* .(2011). In this thesis, TSAC in combination with beta counting (see below) was used to determine gamma dose rate exclusively, with typical uncertainties ranging between 3 and 5% for those samples measured here.

10.1.3.3.2 Geiger-Müller beta counter (GMBC)

The beta dose rate contribution to the total environmental dose rate can be obtained by directly measuring the emission of beta particles from pulverised and homogenised sediment samples using a low-level GM-25-5 beta counter (Bøtter-Jensen & Mejdahl 1988). The apparatus consists of a gas flow counter, five individual Geiger-Müller detectors mounted in a row, a common guard counter and lead brick housing (Figure 10.2). Within the lead brick housing each of the five detectors are mounted with their Mylar windows facing down to record the emission of beta particles from five sample containers (termed 'pots') loaded underneath. Each pot measures 25 mm in diameter and 6 mm in depth. The pots are loaded into the GMBC using a purpose made sample holder to ensure accurate and reproducible positioning of the samples below the detectors.

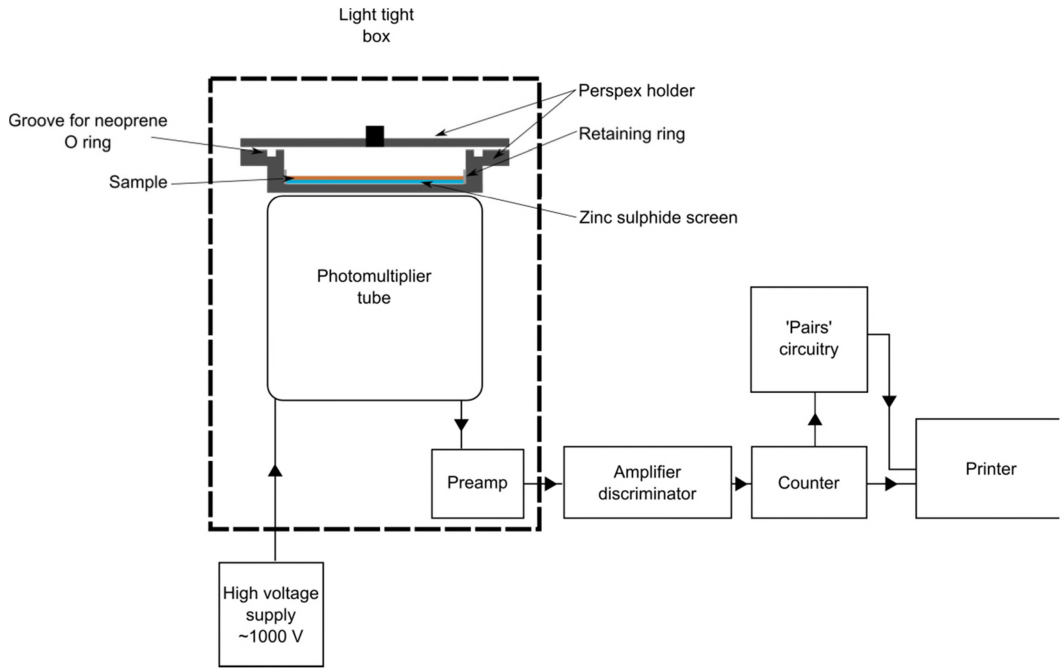

Figure 10.1 Daybreak 583 thick-source alpha counter system set-up. Image based upon Figures 4.7 and 4.8 in Aitken (1985).

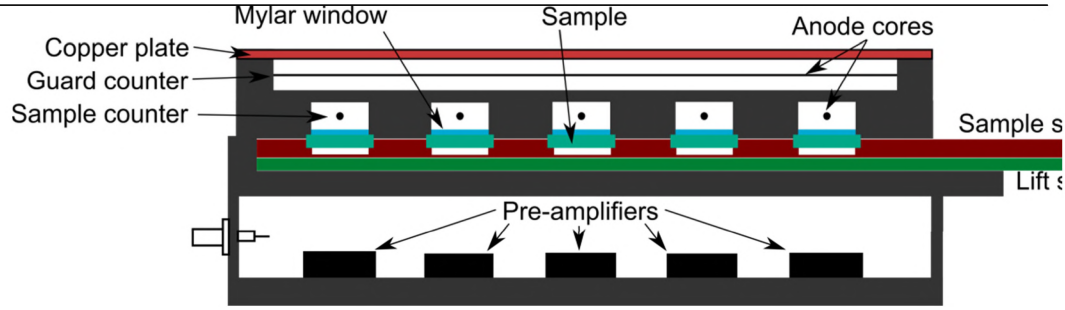

Figure 10.2 The five-sample low-level GM beta counter developed by Risø. Image based upon Figure 1 of Bøtter-Jensen & Mejdahl (1988).

Bulk dried pulverised and homogenised sediment samples are loaded into each individual pot. The packing of the sediments into each pot is crucial to obtain reliable beta dose rate estimates. Here, sediments are tightly packed so as to entirely fill the pot before the upper surface is levelled flat to ensure a uniform surface is presented to the Geiger-Müller detectors. The sample pots are covered with a thin plastic film to prevent contamination of the detectors. Three of the five sample positions are then filled with powdered sediment requiring beta dose rate evaluation. The two vacant positions are filled with one pot that contains magnesium oxide and another with a standard of known beta dose rate. The former pot provides an estimate of measurement background: magnesium oxide being non-radioactive. The standard used in all measurements was a dried and pulverised sample of Nussloch Loess (termed 'Nussi') and determined to have a beta dose rate of 1.49 Gy/ka (Kalchgruber *et al.* 2002). Each of the five measurement positions are counted simultaneously for a period of 24 hr, providing 24 measurements per pot each 1 hr in duration.

The beta dose rate for the sample was then calculated by subtracting the sum of the background counter over the 24 cycles from the corresponding sum of the sediment and Nussi samples. The background-corrected count rate for each sediment sample was then divided by the background-corrected Nussi count rate and multiplied by the beta dose rate of the Nussi standard (1.49 Gy/ka). The average of the three replicate sediment samples was taken to obtain a dry and uncorrected, bulk beta dose rate for the sample. The uncertainty on this beta dose rate was calculated from the quadratic sum of the relative errors arising both between and within the

three replicate sample beta count rates. It is important to consider here the variation between each of the three replicate samples due to the inherent variation in the sensitivity of each of the three measurement position sample counters. An additional systematic 3% uncertainty is also added to account for the uncertainty in the beta dose rate estimate for the Nussi standard. Typical total uncertainties on the beta dose rate determined using this piece of equipment is in the order of 5 to 10%.

10.1.3.3.3 High-resolution gamma spectrometry (HRGS)

Unlike the previously discussed methods of emission counting, HRGS not only provides an estimate of the beta and gamma dose rates coming from U, Th and K, but also has the ability to determine if, and the extent of, any disequilibrium in either the ^{238}U or ^{232}Th chains. The HRGS measurements for only two samples reported in this thesis were analysed at the Jabiru Facility of the Australian Federal Government's Department of Environment, in Australia's Northern Territory. Using 200 g of ground and homogenised sample, HRGS samples were pressed and measured for radionuclides after a minimum ingrowth period of three weeks was reached. This latter step was used to allow for the ingrowth of post-Rn progeny to allow the measurement of ^{226}Ra concentrations from the ingrowth of ^{214}Pb and ^{214}Bi. The samples were measured for a period of 2 days, using in-house methods. Further information can be found at the following web address:

http://www.environment.gov.au/system/files/resources/8a5d8b68-8070-4d12-970f-d2437ef01b6f/files/tm47.pdf

10.1.3.3.4 Inductively coupled plasma-optical emission and mass spectrometry (ICP-OES/MS)

The only direct measurements of the U, Th and K parents made in this thesis were the ICP-OES/MS carried out at the Intertek Genalysis commercial facility in Perth, Western Australia. Caution is required in the usage of 'head-of-the-chain' estimates of U and Th, as the resulting beta and gamma dose rate can be significantly over- or underestimated if any parent radionuclide enrichment or leaching has

occurred over the period of burial. ICP-OES/MS measurements were made on ~0.25 g of powdered sample material that underwent a four-acid digest prior to either OES (for K) or MS (for U and Th) measurement. The multi-acid digest consisted of hydrofluoric acid, nitric acid, perchloric acid and hydrochloric acid treatments in Teflon tubes. The resulting concentrations of U, Th and K were assigned relative errors of 3, 4 and 2.5% based on reproducibility measurements and counting errors and converted into beta and gamma dose rates using the conversion factors of Guérin *et al.* (2011).

10.1.3.3.5 Carbon-doped aluminium oxide (Al_2O_3:C) dosimetry

Al_2O_3:C was developed as a highly sensitive dosimeter mainly to be used for radiation therapy dosimetry (Akselrod *et al.* 1990). However, this laboratory-grown phosphor is equally reliable at detecting and measuring the cosmic, gamma and beta dose rates in natural sediments (Burbidge & Duller 2003, Kalchgruber *et al.* 2003, Kalchgruber & Wagner 2006). Numerous testing of the Al_2O_3:C material show that it has deep electron traps that are thermally stable over long periods and that these same traps are optically accessible, both favourable characteristics in terms of its application as a dosimeter (Yukihara *et al.* 2003, Yukihara *et al.* 2004). The combination of high sensitivity to environmental doses, linear growth of the dose response curve to ~10 Gy, negligible sensitivity change, acceptable photoionisation cross-section of traps and the reusability of this material have all contributed to the popularity of this material which has been used by a variety of authors in the evaluation of natural environmental dose rates (Burbidge & Duller 2003, Kalchgruber *et al.* 2003, Kalchgruber & Wagner 2006, Porat *et al.* 2012).

Al_2O_3:C crystals grown at Landauer Inc., Crystal Growth Division, Stillwater, Oklahoma, USA (Akselrod *et al.* 1990, Akselrod *et al.* 1993, Akselrod & Akselrod 2002) were used to determine the beta dose rate emitted directly from the resin-impregnated sediment blocks. The 180–212 μm fraction was sieved from a sample of Al_2O_3:C powder and annealed at 900 °C for 15 min to bleach any charge trapped in deep traps (Yukihara *et al.* 2003, Yukihara *et al.* 2004). The Al_2O_3:C grains were

then spread between the two corresponding halves of a resin impregnated sediment slab and stored for a period of time (~1 yr) to allow dose to accumulate. In this instance the dose received would be the sum of beta, gamma and cosmic radiation. The beta dose rate could then be estimated by subtracting the independently estimated contribution of the gamma and cosmic dose rates. No account for alpha particles is required given the poor alpha efficiency of Al_2O_3:C (<0.01) (Nathan *et al.* 2003).

To determine the radiation dose absorbed by the Al_2O_3:C grains, and to reduce the amount of machine time, and also the likelihood of filling up deep, hard-to-bleach traps (Yukihara *et al.* 2003, Yukihara *et al.* 2004), the standardised growth curve (SGC) approach of Roberts & Duller (2004) was adopted. The SCG was constructed using the SAR procedure, and used 42 annealed Al_2O_3:C grains. Regenerative doses of 0, 0.13 and 0.26 Gy were delivered to each grain, and a test dose of 0.13 Gy. The optical signal was measured after preheating the Al_2O_3:C grains to 80 °C for 10 s and stimulating with the green laser for 60 s at 50 °C. The OSL signal was integrated over the first 2 s of the optical decay curve (Figure 10.3a) and a background count was taken as the average OSL signal over the last 15 s of stimulation. The L_X/T_X ratios were multiplied by the T_D (Gy) to obtain a standardised OSL response (Figure 10.3b). The standardised OSL values for all grains could be fitted with a linear equation that was forced through the origin; linear growth of the Al_2O_3:C dose response curve has previously been established by Yukihara *et al.* (2003) for doses up to ~10 Gy. The curve fitting error was calculated using the equations outlined in Duller (2007).

The D_e of the naturally-irradiated Al_2O_3:C grain could, therefore, be determined by measuring the L_X and T_X of each grains using a T_D of 0.13 Gy. By calculating the standardised OSL response ($L_X/T_X \times T_D$), the equation of the linear SGC could be solved to determine the D_e. Only the random uncertainties on each D_e were propagated through and consisted of a counting statistics error and curve fitting error; no systematic errors were carried through since these are consistent among all measurements and grains in this study.

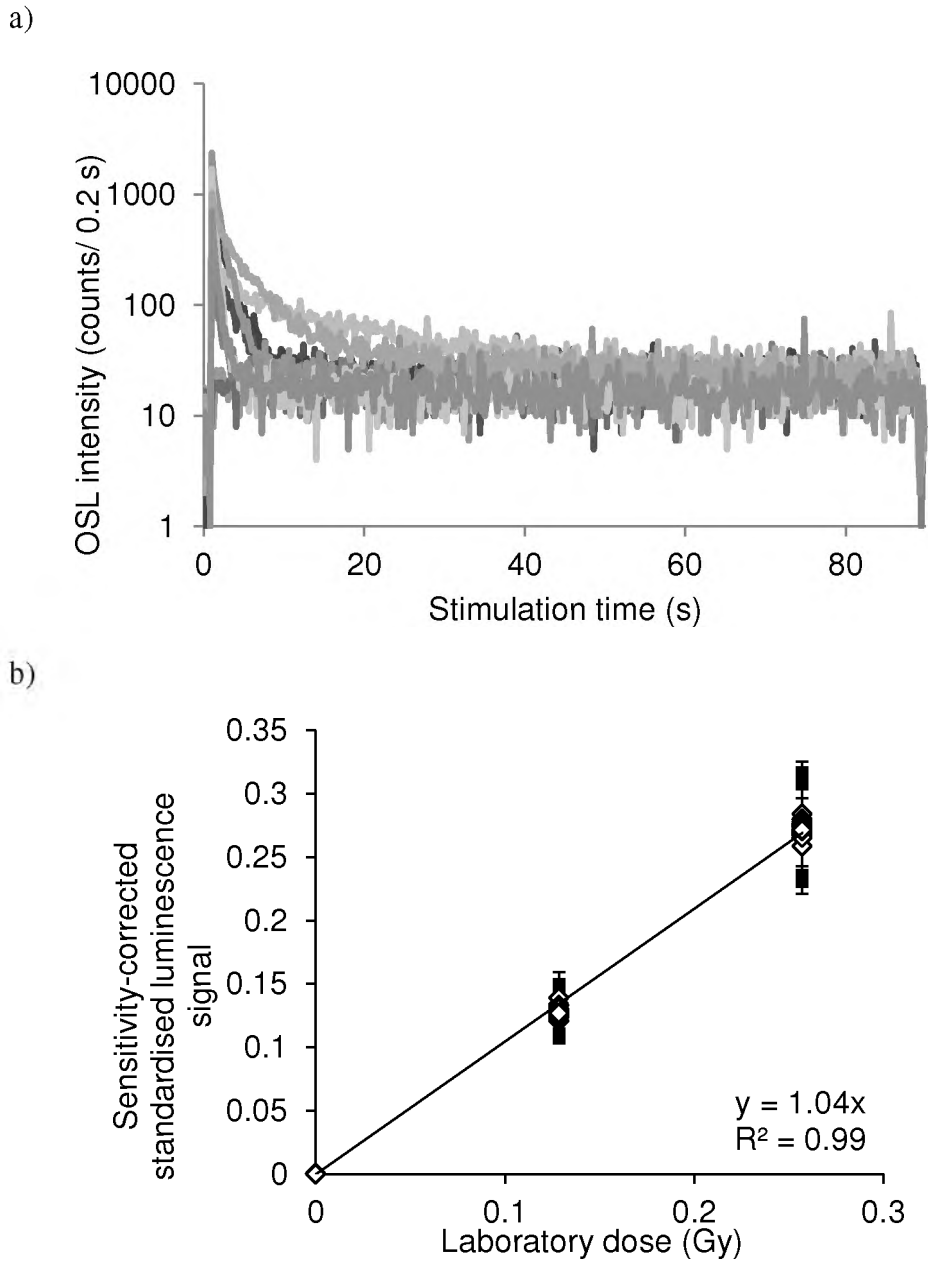

Figure 10.3 a) OSL decay curves for 10 separate 180–212 µm in diameter Al_2O_3:C grains shown on a semi-log scale. The initial OSL signal intensity varies over two orders of magnitude and the rate of decay varies with some grains achieving background intensity after ~5 s of optical stimulation, whereas others require ~40 s before background levels of luminescence are reached. b) Sensitivity-corrected standardised growth curve constructed using 42 individual 180–212 µm in diameter Al_2O_3:C grains. Errors bars are shown at 1σ.

10.1.3.4 FIELD-BASED MEASUREMENTS

10.1.3.4.1 Field gamma spectrometry

The external gamma dose rate, as it currently exists, is most accurately determined using a field gamma detector at the time of sampling. This technique, unlike the HRGS or ICP-OES/MS measurements takes into account the heterogeneity of the surrounding gamma sphere with respect to the sample position (Murray *et al.* 1978, Murray 1981, 1987). The total gamma flux emitted from the sediments is an admixture coming from ^{238}U, ^{232}Th (and their radioactive progeny) and ^{40}K. Here, specific high-energy gamma peaks from the measured gamma emission spectrum are used to ascertain the contribution of each of these radionuclides to the total gamma dose rate.

In this thesis two different gamma detectors were used in the determination of gamma dose rates; a 2-inch NaI(Tl) crystal detector and a 3-inch diameter GR-320 Exploranium NaI(Tl) detector. The 2-inch detector was calibrated by Z. Jacobs using the 'Oxford Blocks' (Rhodes & Schwenninger 2007) located at the Research Laboratory for Archaeology and History of Art, Oxford University, whereas the 3-inch Exploranium was calibrated at the Fugro Instruments flatpad calibration facility in Sydney.

The measurement of the gamma dose rate was conducted by first enlarging the sample hole to the appropriate size to allow the detector/s to be fully inserted into the sediment. For the 3-inch detector, five separate readings of 5 min duration each were made at each sample location. For the 2-inch detector, the gamma spectrum was measured for a duration of 30 min to 1 hr.

Gamma dose rate measurement of the 3-inch detector used the 'windows' technique as outlined in Aitken (1985). Here, three separate peaks of interest are selectively targeted to determine the contribution of U, Th and K to the total environmental gamma dose rate. The contribution of U is determined by the ^{214}Bi

peak (1.76 MeV) with a window between ~1.69 and 1.84 MeV. The contribution for Th is calculated from the ^{208}Tl peak (2.61 MeV) with a window between ~2.46 and 2.76 MeV. The contribution of K is evaluated from the ^{40}K peak (1.46 MeV) with a window between ~1.38 and 1.53 MeV.

The results of each measurement provides concentrations of U and Th (in μg/g) and K (in %). Each of the radionuclide concentrations are required to be corrected to account for the difference between the 2π flatpad calibration geometry and the 4π measurement geometry. All concentrations of U, Th and K made using the 3-inch detector were therefore divided by 2.11 for all measurements made in this study. The geometry-corrected radionuclide concentrations were then converted into dose rate (Gy/ka) using the dose rate conversion factors of Guérin *et al.* (2011). The mean gamma dose rate for U, Th and K was calculated, and all three summed to provide an estimate of the total environmental gamma dose rate. The uncertainty on the total gamma dose rate was taken as the quadratic sum of the standard errors on each of the 5 replicate measurements of U, Th and K.

For the 2-inch detector, the total gamma dose rate is determined using the threshold technique (Løvborg & Kirkegaard 1974, Murray *et al.* 1978, Aitken 1985, Mercier & Falguères 2007). Using this method, the count-rate measured by the portable detector above the calibrated threshold for the instrument is considered directly proportional to the incident gamma-dose rate (Gy/ka). A relative uncertainty of 5% was always applied to each of the 2-inch detector measurements throughout this study. This estimate of uncertainty is based upon: 1) counting statistics, 2) instrument drift, 3) instrument reproducibility, and 4) uncertainty in the calibration brick housing used at the University of Wollongong.

Appendix II

Soil micromorphology: Further information

11.1.1 HISTORICAL DEVELOPMENT

The major difficulty of pioneering soil micromorphology studies - apart from recognising and interpreting the basic features and components within a sample - was related to the terminology used to describe the sections. Direct comparison of samples described using different terminologies proved to be difficult without a common terminological yardstick. To this end, the early work of Kubiëna (1938) sought to provide such a framework for the systematic and objective description of thin sections of soils. In *Micropedology*, Kubiëna outlined, and defined, not only a hierarchy of soil fabrics (see section 2.4.2.1 for definition), but also the spatial and geometric relationships between the *stable* coarse and the *mobile* fine fractions. These definitions were presented using an admixture of newly coined terms but also those borrowed heavily from the field of petrography. The terminological framework outlined by Kubiëna (1938) would be built upon over the next thirty years, with the culmination of this work published in *Micromorphological Features in Soil Geography* (Kubiëna 1970). Yet, the dominating focus of this text centred upon the samples Kubiëna, himself, had collected over his academic career. It was difficult to apply his scheme for any soil/sediment thin section beyond which Kubiëna had studied.

The descriptive scheme proposed by Brewer & Sleeman (1960) was developed as a means of overcoming the shortfalls in the work of Kubiëna (1938, 1970). Brewer (1964) furthered this initial proposal with the publication of *Fabric and Mineral Analysis of Soils.* Yet, in a similar style as Kubiëna, the new framework of Brewer (1964) focussed primarily on the inorganic soil/sediment components (e.g.,

quartz, clays, etc) and gave little regard to the organic (bone, charcoal, rootlet, etc) components, or anything related to archaeology. His system was not entirely objective in its descriptions with a strong genetic theme underlying much of the terminology, thereby presupposing specific processes. Again, this shortcoming made the widespread application of Brewer's nomenclature – and micromorphology in general - a difficult task, especially where organic components were common.

The publication of the *Handbook for Soil and Thin Section Descriptions* by Bullock *et al.* (1985) represents the first international attempt at providing a comprehensive and objective working terminological framework for soil micromorphological studies. Rather than being the result of an individual's work, Bullock *et al.* (1985) was the outcome of a collaborative, decade-long effort of prominent members of the International Soil Sciences Society. This simple and easy to understand nomenclature allowed for both the organic and inorganic components of the soil to be described, and used terminology and approaches similar to those in sedimentary petrography. As such, it was intensively and extensively used by researchers and as a teaching aid. However, the calls for a second edition of Bullock *et al.* (1985) were met with little enthusiasm by the original publisher.

The most recent incarnation of Bullock *et al.* (1985) framework was published by Stoops (2003) in *Guidelines for Analysis and Description of Soil and Regolith Thin Sections.* This work not only provided an update of the original Bullock *et al.* handbook but also gave clarification of a number of terms and concepts that were not as explicitly defined previously, such as the c/f-related distribution types and the subdivision of pedofeatures into matrix and intrusive varieties. Stoops' terminology and nomenclature is heavily relied upon throughout this thesis.

The application of soil micromorphology has become a foundational tool in geological and geoarchaeological investigations. This technique, however, is more commonly used throughout Europe and Northern America, with where regular conference and workshops are conducted. The most recent product of the soil micromorphological community is the publication of *Interpretation of Micromorphological Features of Soils and Regoliths* by Stoops *et al.* (2010), a full-

colour volume that covers a wide range of topics that were written by field experts (e.g., Redoximorphic Features, Frost Action, Calcium Carbonate Features, etc.). It is unfortunate, however, that the field of micromorphology has not experienced the same widespread application in Australia that it has received throughout Europe and Northern America.

11.1.2 TERMINOLOGICAL FRAMEWORK OF STOOPS (2003)

In this section I provide a basic overview of the main concepts and terminological framework presented in Stoops (2003). These can be classified under four headings: soil fabric, soil microstructure, groundmass and pedofeatures.

11.1.2.1 FABRIC AND RELATED DISTRIBUTIONS

The fundamental concepts of micromorphology rest upon the understanding of soil fabrics. The term fabric was originally defined by Kubiëna (1938) as 'the arrangement of constituents in the soil in relation to each other.' Stoops (2003) borrows his definition of soil fabric from Bullock *et al.* (1985) defining it as 'the total organisation of a soil, expressed by the spatial arrangement of soil constituents (solid, liquid and gaseous), their shape, size and frequency, considered from a configurational, functional and genetic viewpoint.'

Fabrics are required to be considered as infinite entities and are described on the basis of heterogeneity. That is to say that a homogeneous body has no fabric, although this must be qualified by the fact that this homogeneity depends upon the scale at which it is viewed. For example, a beach viewed from a headland may appear to be homogeneous, and yet, standing on the beach, the sand can be seen to comprise of quartz, heavy mineral and shell fragments that can be mixed, bedded, or arranged in a number of ways. Thus, the degree of heterogeneity can be measured by reducing the field of view until homogeneity of the constituent(s) is attained. As such, homogeneity can be total if *all* fabric units are considered; or partial if only one

aspect is under study. Fabric units are the basic building blocks of the soil/sediments. Thus a fabric unit could comprise exclusively of sand-sized quartz grains, clay material, iron oxide nodules or gas (void space). The overall description of the fabric units is based upon basic sedimentological principals. These include: size, sorting, abundance, shape, roundness, sphericity of coarse fraction, as well as the boundary pattern between one fabric with another, and colour.

11.1.2.2 SOIL MICROSTRUCTURE

The structure of the soil/sediment sample is comprised of aggregated or non-aggregated sedimentary material, as well as the associated void space. The term soil structure in a micromorphological context was developed by Bullock *et al.* (1985) and is 'concerned with the size, shape and arrangement of primary particles and voids in both aggregated and non-aggregated material and the size, shape and arrangement of any aggregates present.'

Soil structure is refers to the relationship between the solid particles and the pore space. Stoops (2003) argues that the use of the term aggregates inherently assumes that an interpretation has already been made with respect to their formation. As such, the term aggregate (used by Bullock *et al.*, 1985) is replaced by the term ped.

The description of peds can be categories into four broad types of spheroidal, blocky, plates and prisms, with examples shown in Figure 11.1. It follows that the soil/sediments under investigation may have developed more than one type of ped resulting in a hierarchy of nested ped types. In all cases, the completeness of separation between adjacent peds can be described according to Stoops (2003) by the degree of ped separation; being either highly, moderately or weakly separated depending on the connectedness of the interstitial ped void space. The sharpness of the boundaries between adjacent peds can be described in terms of accommodation. Accommodation is defined as 'the degree to which opposing ped boundaries have complementary shapes.' Thus, accommodated peds would be able to be

(hypothetically) translated next to each other with little overlap or void space occurring; a partially-accommodated ped has some overlap or void space; whereas unaccommodating peds have little complementary ped face boundary.

Void space – the portion of the soil/sediment not occupied by solid matter (p. 63) – between the peds can also be described according to their morphology. Six broad categories are listed by Stoops (2003). These are shown in Figure 11.2 and include: packing voids, vesicles, vughs, channels, chambers and planes.

The aim of both fabric and soil structural analysis and descriptions is to assign a microstructure facies type to the soil/sediment samples. It is from these microstructures that interpretation of the (post)depostional history of the sample can be made (Goldberg & Macphail, 2006). The range and variability of such microstructures is too great to detail here. A number of these can be found in Appendix 4 of Stoops (2003), along with descriptions of each.

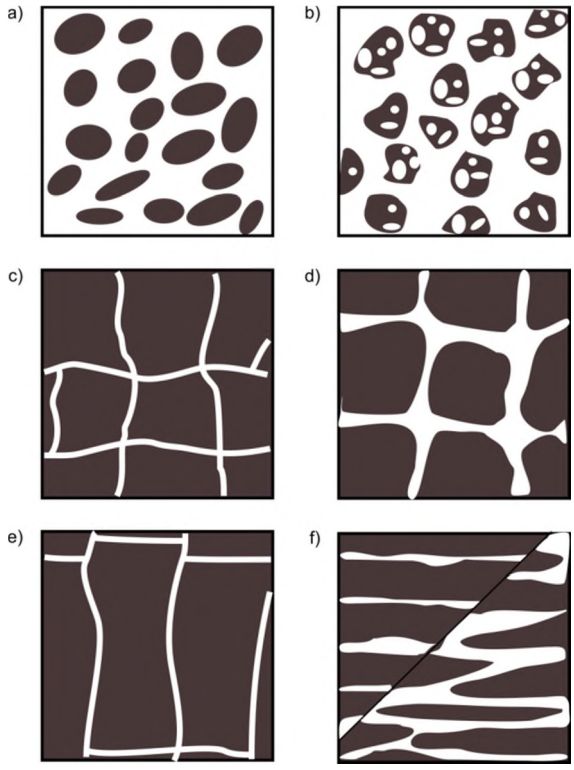

Figure 11.1. Soil microstructures presented in Stoops (2003). a) spheroidal granules; b) spheroidal crumb; c) angular blocky peds; d) sub-angular blocky peds; e) prisms; and f) straight and lenticular plates.

Figure 11.2. Void descriptions based on Stoops (2003). a) simple packing voids; b) complex packing voids; c) compound packing voids; d) vesicles; e) vughs; f) channels; g) chamber; and h) plane. Here, coarse grains are represented in orange, porous crumb as dark brown and micromass as light brown.

11.1.2.3 GROUNDMASS

Due to the complexity of the soils and the fabric(s) that they contain, it is not possible to use one single approach in the description of each fabric unit. Rather, Bullock *et al.* (1985) proposed dividing these descriptions into two classes. The first group refers to the fabric units that form the base of the soil/sediment, whereas the second group deals with those features that formed during soil formation processes. The terms groundmass and pedofeatures were coined, respectively, to differentiate these two categories. In this section I will focus on the former, with the latter the subject of a later section.

As outlined in Stoops (2003), Bullock *et al.* (1985) defined groundmass as a general term used for the coarse and fine material and packing voids which forms the base material of the soil in thin section, other that in pedofeatures. Stoops (2003) recommended that the description of the groundmass be separated into the coarse and

fine fractions. The coarse fraction is described using basic terminology (size, shape, mineralogy, etc.) and includes not only geogenic mineral grains (e.g., quartz, feldspar, heavy minerals, etc.), but also the organic components (such as charcoal). In the case of archaeological contexts, flint and bone are also included in the coarse groundmass descriptions.

The basic components of the fine fraction (clays, iron oxides, organic matter and finely crystalline material) are typically too fine to be resolved using an optical microscope; these components cannot be observed directly. They can, however, be indirectly observed by describing their associated birefringence- or *b-fabric*. The b-fabric describes the origin and the patterns of orientation and distribution of interference colours in the fine fraction and is produced as a result of individual clay particles aligning themselves roughly parallel to each other. Under such conditions, the optical properties of the groups of orientated clays act as if comprised on one 'large' anisotropic grain. It needs to be recognised that b-fabrics are not pedofeatures. Five main types of b-fabric are outlined and defined in Stoops (2003). These include; undifferentiated, crystallic, speckled, striated and strial (Figure 11.3).

11.1.2.4 PEDOFEATURES

The concept of pedofeatures, presented in Bullock *et al.* (1985), is built upon the previous understanding of pedological features presented by Brewer & Sleeman (1960). The original authors introduced the term to differentiate between features formed during soil formation and those of the original sedimentary material. *Pedofeatures* are defined by Bullock *et al.* (1985) as discrete fabric units present in soil materials that are recognisable from an adjacent material by difference in concentration in one or more components or by a difference in internal fabric. In short, pedofeatures reflect the past and current pedogenic processes operating within the sedimentary deposit.

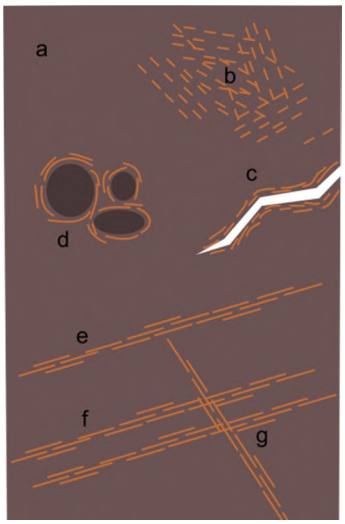

Figure 11.3. Some examples of b-fabric patterns as described in Stoops (2003). a) undifferentiated; b) speckled; c) poro-striated; d) grano-striated; e) mono-striated; f) parallel-striated and g) cross-striated b-fabrics. Here, the b-fabric is represented by the orange stripes and the micromass by the light brown colour.

Stoops (2003) further subdivides pedofeatures into two categories of *matrix* and *intrusive* pedofeatures based on their relationship with the groundmass. Thus, *matrix pedofeatures* result from the change in composition or fabric of the groundmass. This definition implies that several characteristics of the groundmass remain visible in the pedofeatures. Most commonly the nature and distribution pattern of the coarse fraction are preserved. The matrix pedofeatures can be subdivided into three further classes of impregnative (e.g., iron and manganese impregnation), depletion (e.g., iron-depletion hypocoatings) and fabric (e.g., worm burrows and excrement) pedofeatures. Intrusive pedofeatures, in contrast to matrix pedofeatures, are those features that do not enclose groundmass materials. Intrusive pedofeatures can be comprised of pedogenic crystals (such as calcite, gypsum and iron oxide), and nodules that form in pre-existing void space or within the groundmass either through displacement or replacement of the original soil/sediment constituents.

Two common and important pedofeatures are coatings and nodules. Coatings can be subdivided into three separate categories that can be classified as matrix and

intrusive pedofeatures. *Coatings* are intrusive, textual pedofeatures that cover a natural surface in the soil/sediment and occupy <90% of the original void space (Figure 11.4a). These coating are often formed by the fine fraction (i.e., silt grains and clay particles). The fine fraction coatings can be described in terms of their limpidity. This property is associated with the abundance of other materials found within the clay that are smaller than the thickness of the thin section itself, e.g., silts, organic residues, calcite crystallites, etc. Thus, a sliding scale of limpidity is described in Stoops (2003). The finest clay with no additional material is termed *limpid*, clay with clay-sized opaque mineral is termed *speckled*, while *dotted* is used to describe clay with the inclusion of silt-sized material. Dotted limpidity is also referred to as *dusty* by some authors. In contrast, *hypocoatings* and *quasicoatings* are considered matrix pedofeatures. Where hypocoatings are referred to a natural surface (e.g., a void) and immediately adjoining to it (Figure 11.4b), quasicoatings do not adjoin the surface that they are referred to (Figure 11.4c).

Nodules are typically formed by the concentration of iron, manganese and calcite within the soil. *Nodules* are defined roughly equidimensional pedofeatures that are not related to surfaces or voids, which do not consist of single crystal or crystal ingrowths as described above and are intrusive pedofeatures (Stoops 2003). A distinction, however, is required to be made between those nodules that have been inherited from the original parent material and those that have formed *in situ* as a pedofeatures. Three categories are described by Stoops (2003); anorthic, orthic and disorthic and are shown in Figure 11.5. Orthic nodules are those nodules that have formed in situ and has an internal groundmass that is equivalent to that which it is currently located (Figure 11.5a). Disorthic nodules have been displaced from their original position in the groundmass due to soil formation processes (Figure 11.5b).Anorthic nodules are not formed *in situ* by are derived from the parent material (Figure 11.5c). As such, anorthic nodules are not considered by Stoops (2003) to be pedofeatures, but rather are classified as part of the coarse fraction.

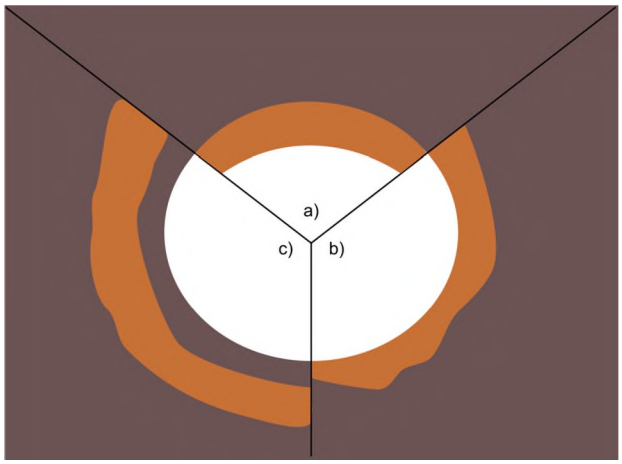

Figure 11.4. Coating types as described by Stoops (2003). a) Coatings cover the surface of the void (white area); b) hypocoatings impregnate into the matrix surrounding the void but remains attached to it; whereas c) quasicoatings are separated from the associated void.

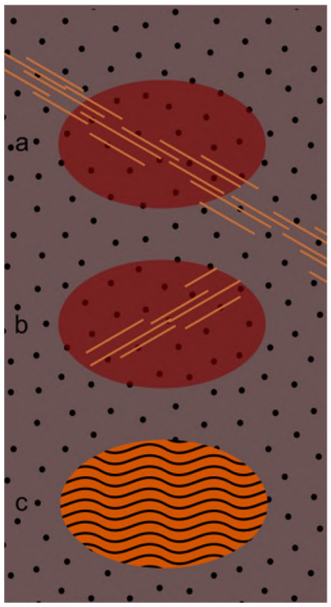

Figure 11.5. Nodule types following Stoops (2003). a) orthic nodules have formed in situ; b) disorthic nodules formed in situ but subsequently mobilised; and c) anorthic nodules are formed from different parent material entirely.

11.1.3 THIN SECTION ANALYSIS AND REPORTING

Once the thin sections have been made, the detailed, and systematic, analysis of each thin section can begin. Prior to beginning any analysis of thin sections, Stoops (2003) recommends looking at each of the thin sections from the same layer, in turn. By doing so, the features that may be difficult to observe in one may be more readily observable in another – therefore saving both time and energy. Stoops also recommends that each thin section be carefully cleaned prior to analysis to remove any fingerprints and dust that may obscure the microscopic analysis (particularly at higher magnifications).

A framework for analysing thin sections using optical microscopy is presented in Goldberg & Macphail (2006). The authors, following the opinion outlined in Stoops (2003), encourage a continuum of observation be made from the lowest magnification (i.e., naked eye ×1) through to the highest magnification available (generally ×400) and is proposed for three reasons. First, by doing this the micromorphological analysis is effectively a continuation of the sedimentological observations made in the field – there is no observation break between field and thin section description. Second, coarser fabric feature and boundaries can be observed more readily at lower magnifications that would otherwise be overlooked at higher magnifications. Third, this approach allows analysis to stop once further data collection becomes redundant for the purposes of the study being conducted.

Goldberg & Macphail (2006) outline a six stage framework for the analysis of thin sections. These stages include: 1) Preliminary examination; 2) Thin section scanning; 3) Detailed observation and description; 4) Presentation of data; 5) Interpretation; and 6) Testing of interpretations. Each of these stages is outlined below.

11.1.3.1 STAGE 1: PRELIMINARY EXAMINATION

At this stage the thin section is observed by eye or low magnifications using a binocular microscope (×4–×20) in either PPL or XPL. Stoops (2003) urges soil

micromorphologists not to fall into the mind-set that a higher the magnification used provides a better observation of sediment constituents. This is not the case, as it becomes a situation of being unable to see the forest for the trees. The aim here, however, is to relate the observation made in the field with those found in the thin section. For example, if a sample was collected between two discrete layers, these ought to be recognised in the thin section also. The macrostructure and textural differences should be identified, along with any regions or features of interest, and noted for further examination in later stages. Additionally, it is beneficial to make a digital scan of the thin section at this stage. The use of software packages (such as Adobe Photoshop® or JMicroVision - Roduit 2013) can be used to digitally manipulate the images to enhance features that are not readily obvious, or to quantify the proportions of certain components within the thin sections, e.g., bone fragments as a proportion of the total thin section area. High-resolution scans (e.g., 2400 dpi) permit detailed observations of the thin section components and organization from the computer, permitting a large but detailed view of all the components.

11.1.3.2 STAGE 2: THIN SECTION OVERVIEW

This stage is carried out using a polarising binocular microscope at magnifications between ×25 to ×40. Here the regions and feature of interest identified in Stage 1 can be further examined, and the composition of these features, again, linked back with the observations made in the field. Here, the thin section should be viewed using PPL, XPL, and also oblique light sources. For example, humic stained clay coatings surrounding sand grains can be easily distinguished using PPL; calcium carbonate coatings and hypocoatings are more readily observable using XPL due to their high interference colours. Oblique light sources are useful for observing components that are opaque using PPL or XPL – burnt or 'rubified' soils appear red under oblique lighting, whereas charcoal remains black. If available the use of UV or blue light can also aid revealing bone and other phosphates (such as guano and coprolites). Important or interesting features can be noted by drawing on the back of the glass slide with a permanent marker or, if scanned in Stage 1, on the digital scanned image.

11.1.3.3 STAGE 3: DETAILED OBSERVATION AND DESCRIPTION

This stage requires the objective description of the thin sections as a whole but also the regions and features of interest investigated in Stage 2. By 'objective,' no *interpretation* of the features being described is meant. Goldberg & Macphail (2006) argue that the inclusion of interpretation at this stage weakens the systematic and objective gathering of soil micromorphological data with preconceived notions. They also urge that the terminological framework of Stoops (2003; see Section 2.4) be employed in conjunction with Courty *et al.* (1989) to provide detailed descriptions of the thin sections. Goldberg & Macphail (2006; p 396) provide a scheme for making basic descriptions of thin sections, this scheme is presented below in Table 11.1.

Stoops (2003) also recommends that the term 'absent' not be used as it implies that it is not present at all, when in fact it may be present in another thin section from the same layer. Rather, he suggests terms such as 'not detected' or 'not observed' be used instead. These systematic descriptions should then be transferred into a table to allow rapid accessibility to other soil micromorphologists as well as the non-specialist.

11.1.3.4 STAGE 4: PRESENTATION OF DATA

The way in which the data are then presented is a reflection of the intended audience. Detailed and lengthy descriptions will be considered by readers to be off-putting (or, more likely, tedious), when a graphic or table summarising the data would be just as appropriate. We should remember that good photographs serve as the principal means for illustrating the basic and significant features or aspects present in thin sections. They are to be encouraged, rather than tables, which show relative abundances with different number of symbols, ranging from few (*) to abundant (***). Such tables are difficult to read and do not permit the reader to fully understand what is actually present in the thin sections as photographs do. However, it is required that the information presented is done in a way that provides a balance between the relevant and the informative. For example, point counting data can be

used to summarise the various proportions of mineral species allowing rapid assessment of sedimentological changes throughout the section.

Table 11.1 Scheme presented by Goldberg & Macphail (2006) for the description of soils and sediments in thin section

Heterogeneity

Structure and Voids

- Type(s) of structure, size and shape of aggregates (if present) and the proportion if more than one type occurs
- Intra- and transpedal voids, abundance, size, pattern and shape

Groundmass

- Coarse Mineral: size, frequency, pattern, sorting, coarse-to-fine ratio and size limit of said ratio
- Coarse Organic:
- Coarse Anthropogenic: (where present)
- Fine fabric: colour, limpidity, interference colours (if present) and b-fabric.

Pedofeatures

- In order of textural, depletion, crystalline, amorphous, cryptocrystalline, fabric and excrement pedofeatures.

11.1.3.5 STAGE 5: INTERPRETATION

Goldberg & Macphail (2006) emphasise the identification of soil/sediment microfabric types, inclusions and features, either sedimentological or pedological, to achieve the first level of interpretation. The second level of interpretation requires the identification of a specific type of deposit by defining a series of microfacies types. Finally, the third level of interpretation requires that these microfacies be placed in the wider context of the site and landscape. For example, a homogeneous sandy sediment with clay coatings (level one) can be interpreted as an albic (Ae) horizon

(level two) that formed as a result of coastal dune stabilisation in the Holocene (level three). The work conducted by Goldberg et al. (2009) at Sibudu Cave, South Africa, provides an extensive, and in depth, working example of how these three levels of interpretation can be applied. Goldberg & Macphail (2006) warn against 'leaping' to conclusions too early in thin section investigations as this undermines the objective descriptions made due to the preconceived notions of the investigator. Also, one needs to continuously 'revisit' previously viewed thin sections to make more complete and accurate interpretations.

11.1.3.6 STAGE 6: TESTING THE INTERPRETATIONS

The interpretations made as part of Stage 5 are then tested by reviewing them against the findings presented in Stages 1–4. It is also meaningful to test the validity of these findings against independent results and other lines of evidence gathered from the site either as field observations or independent analyses (sedimentological, geochemical or botanical data sets). It is also beneficial to compare the final interpretations with similar contexts in the surrounding landscape and/or analogous contexts in more distant locations.

Appendix III

Chapter 6: Supplementary Information

12.1.1 SAMPLE DESCRIPTIONS

SP2 was collected from a layer of greyish brown, indurated and clay-rich sediment at a depth of 1.4 m below the current ground surface. Grain size analysis of this sample showed a composition of 54% angular to subangular sand, 26% silt and 20% clay (Chapter 5). The D_e distribution of this sample is shown in Figure 6.2a as a radial plot where it can be seen that the D_e values range from ~4 to 34 Gy. An OD value of 40 ± 2% was calculated. OD is the amount of spread in D_e values left after all measurement uncertainties have been taken into account (Galbraith *et al.* 1999).

Micromorphological analysis of the sediment sample showed the presence of several different types of heavy mineral and lithic fragments is small (1.2%), but significant (Chapter 5, Table 5.2). More importantly, these grains were shown to be distributed heterogeneously throughout the sample. Micromorphology also revealed that the interstitial space between the sand-sized grains was filled with clay resulting in a matrix-supported fabric. Micromorphology, thus, sheds light onto the possible contributors to the spread in D_e values, in this case BM, but does not provide information on the possible extent of this effect. In the absence of any other evidence (e.g., mixing) that could explain the spread in D_e, it was assumed that the spread in D_e was mainly a result of BM. As a result, a weighted mean D_e value of 9.84 ± 0.30 Gy (N = 193; Figure 6.2a) was calculated using the central age model (CAM) of Galbraith *et al.* (1999) for final age determination (Chapter 5). This resulted in an OSL age of 10.0 ± 0.7 ka, using a total dose rate of 0.99 ± 0.06 Gy/ka, of which the average β-D_r was measured to be 0.31 ± 0.03 Gy/ka.

SP5 was collected from a layer of greyish brown, 'clean' sand, 0.4 m below the current ground surface. Grain size analysis of this sample showed that the sediment is dominated by sand (94%), with little silt (4%) or clay (2%). The D_e distribution is shown in Figure 6.2b as a radial plot. The D_e values show a similar range to that obtained for SP2 ranging from ~8 to 30 Gy and has an OD value of 35 ± 2%. Like SP2, heavy minerals (3.4%) are randomly distributed throughout the sample, but, due to the clast-supported fabric of this sample, the clay coatings are much thinner and will likely have a lesser effect. The sample showed a broad, but symmetrical, D_e distribution around a central D_e value that was also interpreted to be the result of BM. A sample weighted mean D_e value of 15.6 ± 0.5 Gy (N = 170) was determined using the CAM, resulting in an OSL age of 6.6 ± 0.4 ka, obtained using a total environmental dose rate of 2.37 ± 0.13 Gy/ka, with the average β-D_r contribution measured as 0.92 ± 0.07 Gy/ka. There is a considerable difference (2.5–3 times) in the measured beta and total dose rates of the two samples.

The second study location is a Neanderthal occupation site positioned in the Périgord of southwestern France. The stratigraphy and archaeological assemblages for this site have been reported previously in Turq *et al.* (2011), and single-grain OSL investigation reported in Jacobs *et al.* (submitted). For this study, two samples (PdAIV-01-C and PdAIV-02) where chosen for further investigation due to their contrasting and complex sedimentological characteristics.

PdAIV-01-C is one of four sub-samples collected from an intact and orientated sediment block that sampled the entire 30 cm height of Layer 8 (Figure 6.1b). This sample was taken from the middle of the block sample and is referred to, hereon, as Layer 8. Thin section analysis of Layer 8 sediments, carried out by Goldberg *et al.* (2012) showed a complex of poorly sorted sediments of mainly anthropogenic origin. The anthropogenic components comprise of randomly-distributed burnt and unburnt bone, flint, ashes and charcoal aligned along poorly developed, sub-horizontal bedding planes. The geogenic material is dominated by poorly-sorted, sand-sized grains of quartz with small amounts of mica, glauconite and dark brown/black clay material impregnated with micritic calcite. Goldberg *et al.* (2012) stated that post-depositional modification, by both anthropogenic reworking and soil mesofauna

bioturbation, was a significant process in the formation of this sedimentary layer. The D_e distribution for this sample is shown in Figure 6.2c, and reveals D_e values that range from ~10 to 170 Gy. The CAM was considered to be the most appropriate method of combining the individual D_e values of this sample; giving a weighted mean D_e of 63 ± 4 Gy and an OD value of 48 ± 4%. The OSL age for this sample was calculated to be 92 ± 9 ka using a total dose rate of 0.69 ± 0.05 Gy/ka to which the β-D_r contributed 0.29 ± 0.03 Gy/ka.

The final sample, PdAIV-02, was taken from a sediment block collected from Layer 5B –this sample is referred to as Layer 5B. Unlike the chaotic sedimentary environment of the Layer 8 sample, here the red-brown sediments are typified by limestone pebbles and very rare pieces of bone, flint and charcoal fragments. Although dominated by poorly-sorted quartz sand and limestone clasts, thin section analysis shows these latter components to be present as <2 mm fragments. The clay is found mainly as thick coatings surrounding the larger limestone clasts and quartz grains. The post-depositional modifications are similar in kind to those of Layer 8. Bioturbation was an active process as shown by the elongate channel voids, while the presence of calcite hypocoatings provides regions of potentially low β-D_r values (Chapter 8).

The D_e distribution for Layer 5B is shown in Figure 6.2d. The majority of the D_e values for this sample are considerably less precise than those for Layer 8 or indeed SP2 or SP5; typical relative errors >20%. The D_e values range between about 20 and 120 Gy and an OD value of 30 ± 6% was calculated. The CAM was used to calculate a weighted mean D_e of 66 ± 4 Gy which, when using a total dose rate of 0.97 ± 0.05 Gy/ka (β-D_r contribution of 0.49 ± 0.03 Gy/ka), an age of 69 ± 6 ka was obtained.

Although the use of soil micromorphology was certainly helpful in terms of providing a general understanding of the dosimetric composition of the sediments, quantification is still required to determine the magnitude and spatial variation present in any sample and what effect that will have on the D_e distributions.The four samples chosen for this study represent extreme contrasts both within and between

sites. The MacCauley's Beach sediments were formed under geogenic processes in a coastal estuarine depositional setting. Conversely, the colluvial deposits of Pech IV show a significant anthropogenic signature in Layer 8 and limestone-rich sediment in Layer 5B. Thus the four samples selected represent: 1) clay-rich sediment (SP2); 2) quartz dominated sand (SP5); 3) anthropogenic sediment (Layer 8); and 4) carbonate-rich quartz sand.

12.1.2 JMICROVISION CALIBRATION PROCEDURES

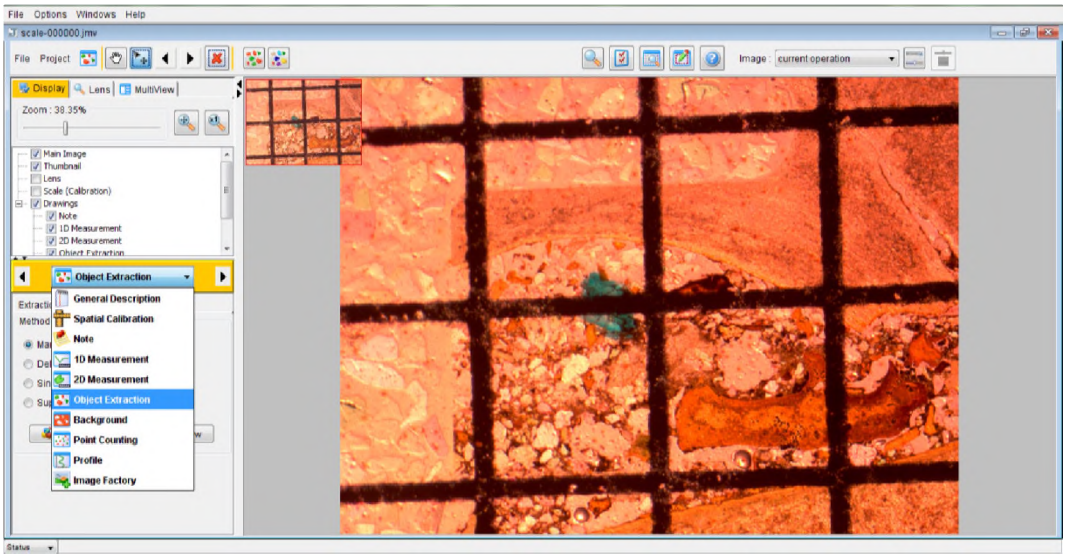

Figure 12.1. Open calibration image in JMicroVision program. From the drop down menu, select *'Object Extraction.'*

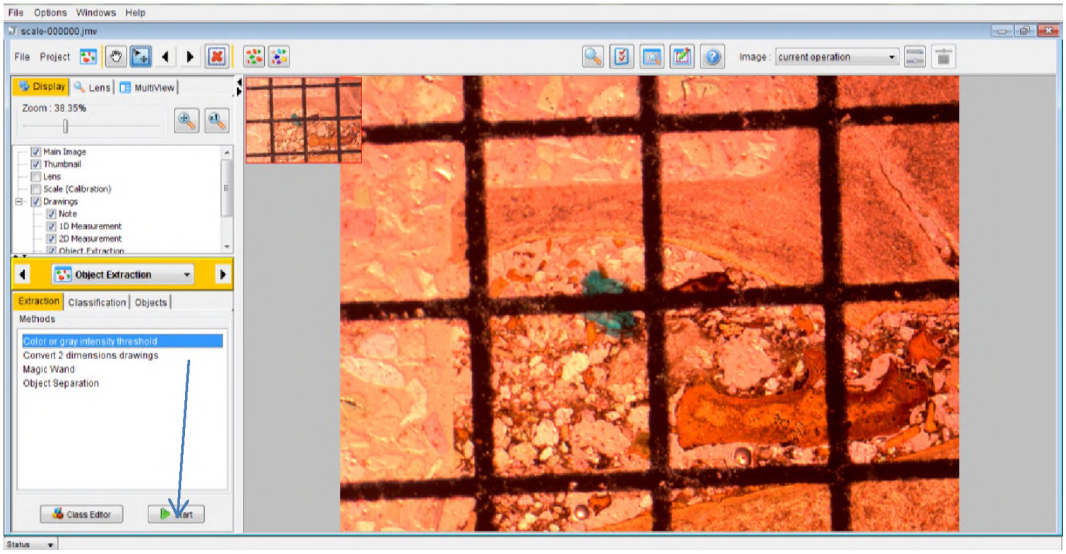

Figure 12.2. Under the *'Extraction'* header tab, select the *'Color or gray intensity threshold'* option then select *'Start.'*

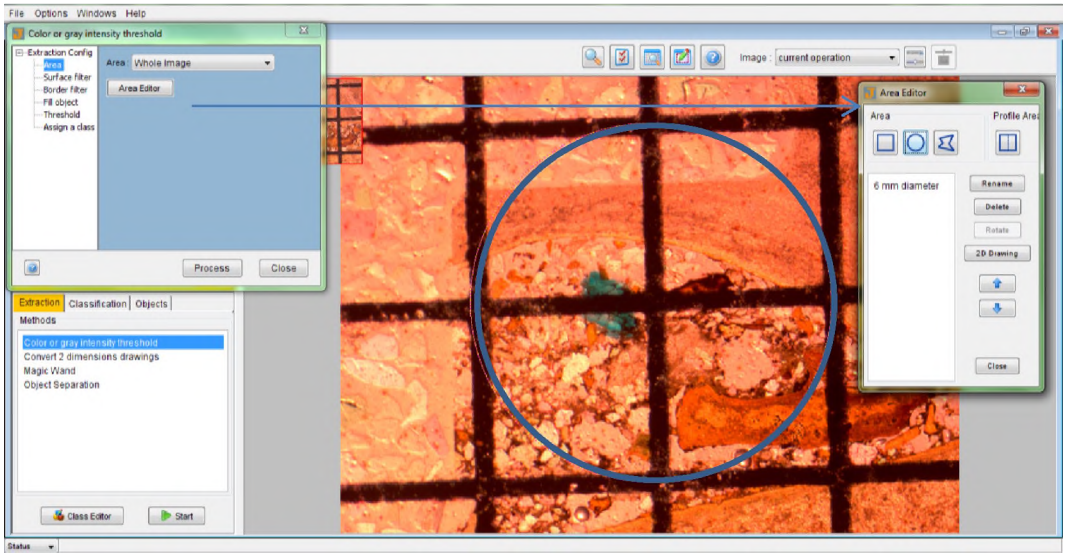

Figure 12.3. In the pop-up window, select the *'Area'* tab and click on the *'Area Editor'* button. This will open up another pop-up window. Select the circle option under the *'Area'* heading and draw a circle that is of equal dimensions as the calibration image. It is possible to give this circle a name (such as 6 mm diameter) using the *'Rename'* option in the *'Area Editor'* window.

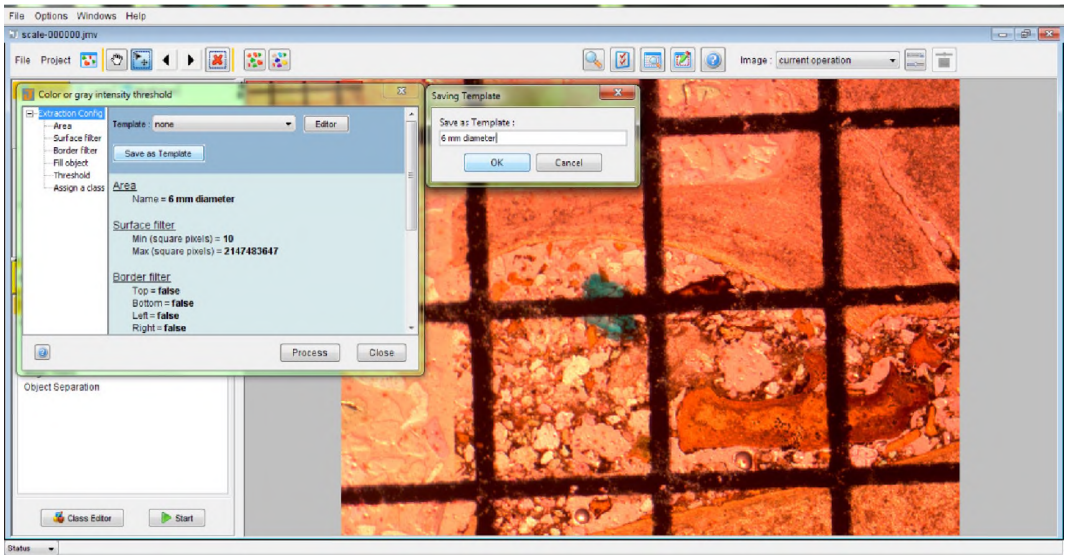

Figure 12.4. With the '6 mm diameter' area selected under the *'Area'* drop-down menu of the '*Color or grey scale intensity threshold'* pop-up window, click on the *'Extraction Config'* tab and the *'Save as Template'* button to save the area as the region of interest to be analysed in all subsequent analyses.

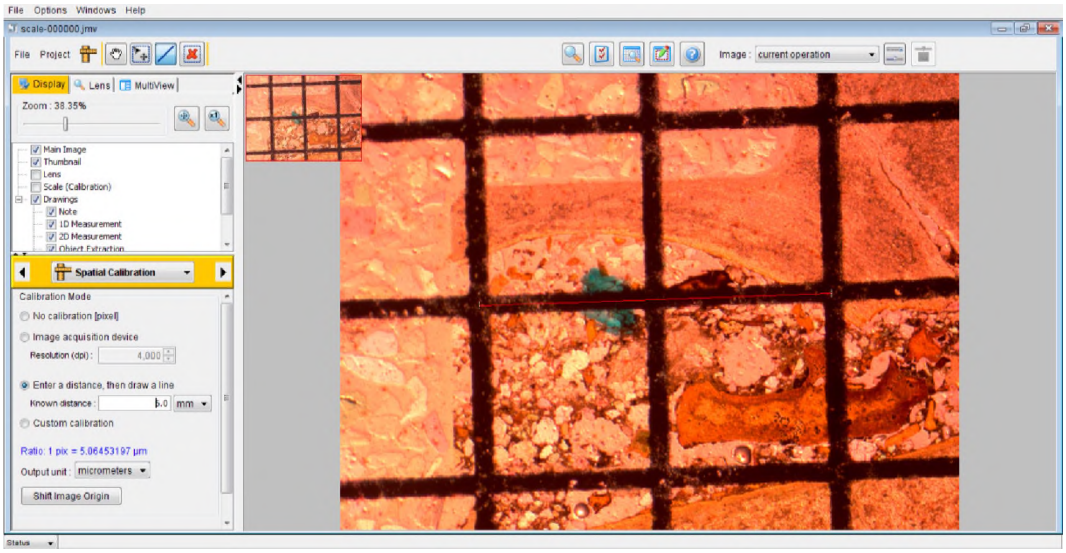

Figure 12.5. From the drop down menu used in Figure 1, select the '*Spatial Calibration'* menu. Then select the *'Enter a distance, then draw a line'* option. Click on the line icon from the top menu bar and draw a line across the 6 mm width of the calibration image. Fill in the *'Known distance'* box with 6.0 and select the 'mm' option from the associated drop-down menu. Record the ratio of 1 pixel to distance once 'micrometers' has been chosen from the *'Output unit'* drop-down menu. This ratio is then used when determining grain size classes in later steps. In this study, 1 pixel has a width of ~5 µm.

12.1.2.1 EXTRACTING OBJECT WITH UNIFORM OPTICAL PROPERTIES

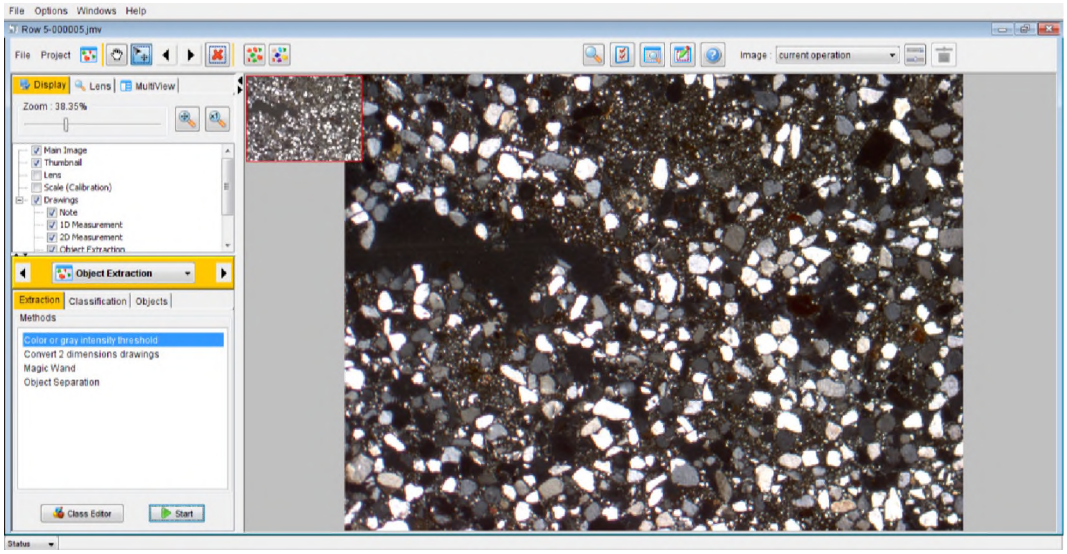

Figure 12.6. Open image of measurement position in JMicroVision. Open *'Colour or gray intensity threshold'* option under as per Figure 12.2.

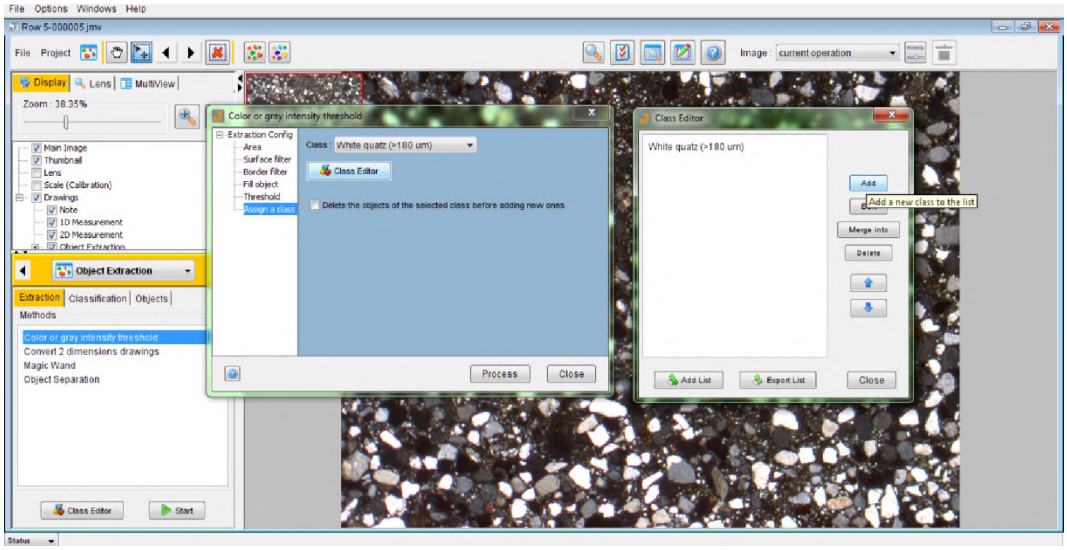

Figure 12.7. Click on the *'Assign a class'* tab and the *'Class Editor'* button to open up the *'Class Editor'* pop-up window. Select *'Add'* from the right hand column of buttons to add a class name. Here, 'White quartz (>180 µm)' was used. Click on close and select 'White quartz (>180 µm) from the drop down menu of the *'Assign a class'* tab in the *'Color or gray scale intensity threshold'* window. Next, click on the *'Area'* tab and select the '6 mm diameter' option from under the *'Area'* drop down menu (see Figure 12.3).

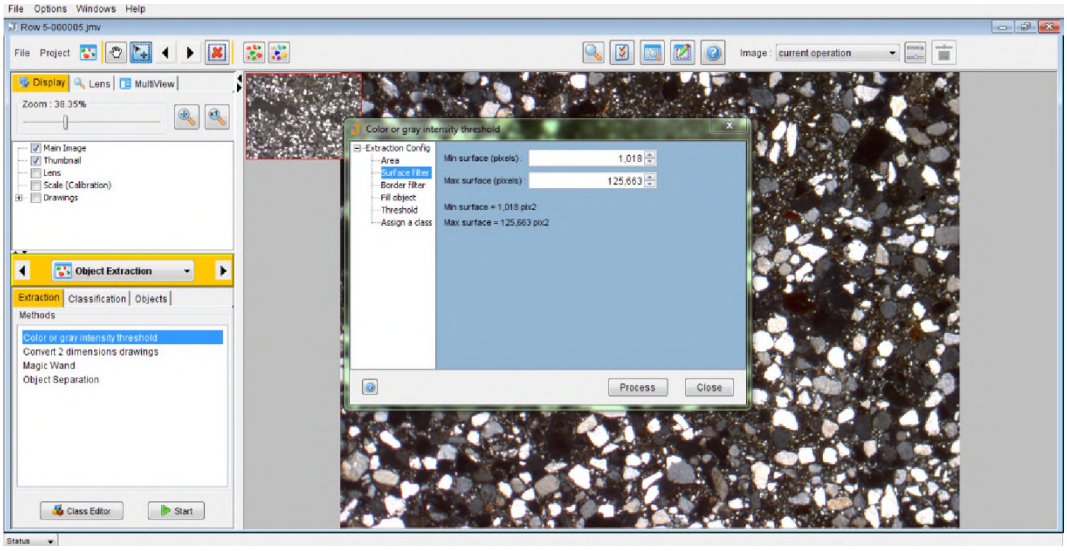

Figure 12.8. In this example, the 180 µm – 2 mm fraction is going to be extracted based upon the pixel area estimates. Using the pixel length established in Figure 6S.5, an estimate of pixel area that brackets this range was calculated based on the assumption of spherical grains and the formula for the area of a circle. 180 µm and 2 mm diameter grains would have a pixel areas of 1018 and 125663 pixel^2, respectively. In the *'Surface filter'* tab of the *'Color or grey scale intensity threshold'* pop-up window, these two pixel areas were entered into the *'Min surface'* and *'Max surface'* dialogue boxes.

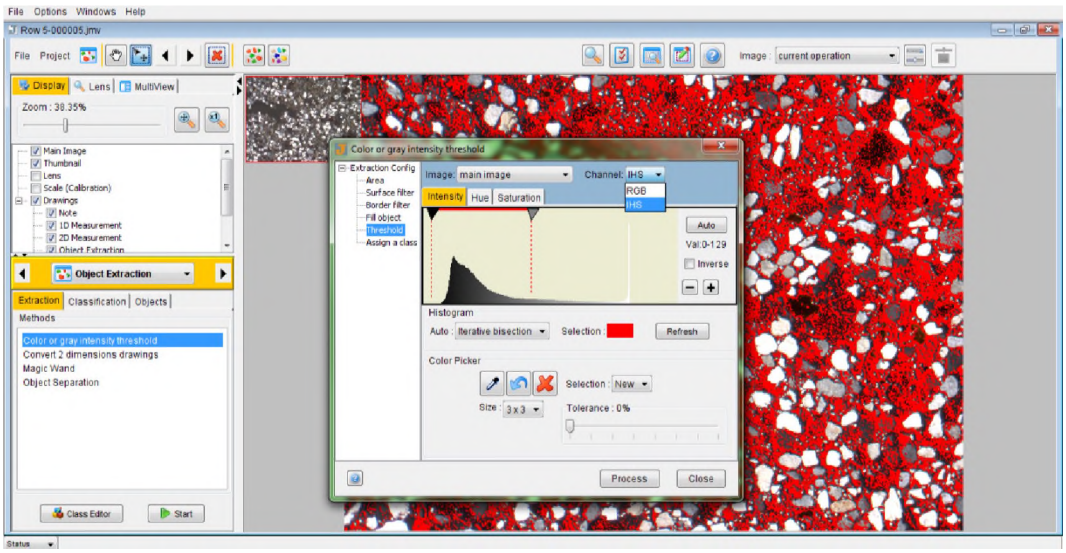

Figure 12.9. The *'Threshold'* tab is then selected from the *'Colour or gray scale intensity threshold'* pop-up window. With *'main image'* and *'IHS'* selected in the top two drop down menus, the JMicroVision program automatically selects a random interval for each of the three parameters of IHS (intensity, hue and saturation,

respectively). To clear these auto-selected values, select the large red cross below the *'Color Picker'* heading.

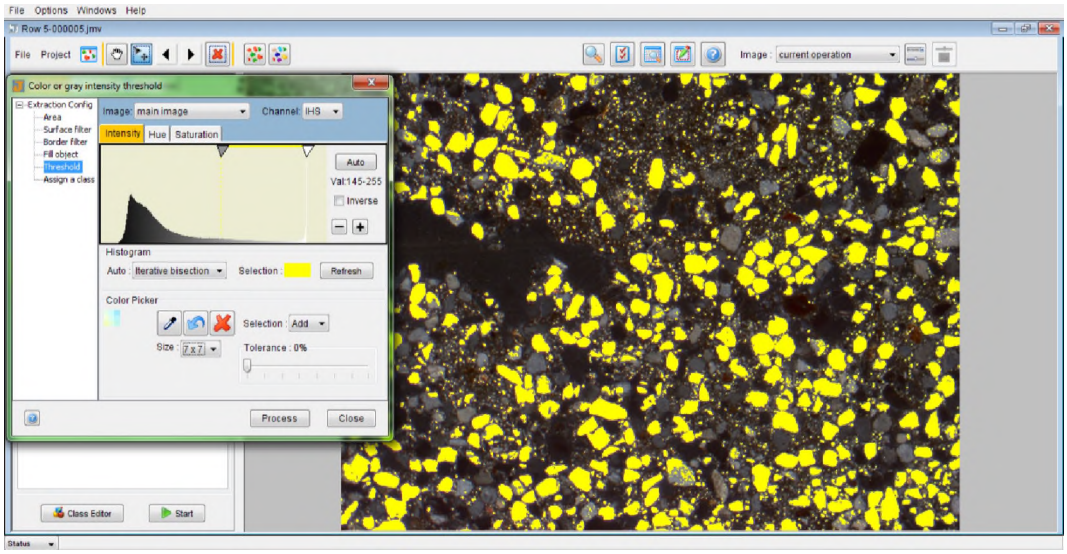

Figure 12.10. With all parameters of IHS cleared, the desired parameters can then be chosen. Here, the white quartz fraction is to be selected and extracted. Under the *'Colour Picker'* heading, ensure that the *'Selection'* drop down menu is on *'Add'* rather than *'New.'* With this function selected, the IHS parameters will be compiled over multiple selections to build up the desired range of values. With the *'Tolerance'* set at 0%, the eyedropper button can be used to select the desired pixel parameters. Once the eyedropper button is selected, the user then clicks the main image on a region that contains the wanted pixel characteristics. A small viewing screen appears below the *'Colour Picker'* heading to aid in this process. The size of the screen (and hence the area sampled) can be altered from a 3×3, 5×5, 7×7 or 9×9 pixel area under the *'Size'* drop-down menu.

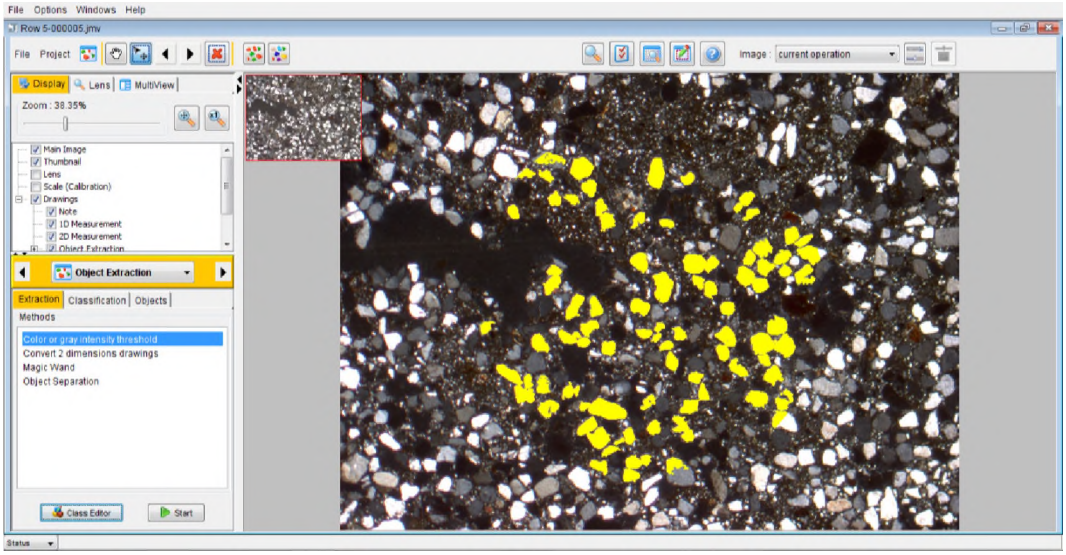

Figure 12.11. Once the desired region of IHS characteristics has been selected the *'Process'* button can be pressed. The JMicroVision program extracts only those objects according to the parameters that have been specified, i.e. fall within the 6 mm diameter, have a pixel area between 1018 and 125663 pixel^2 and the IHS-selected characteristics. These are then displayed as an overlay over the original microphotograph.

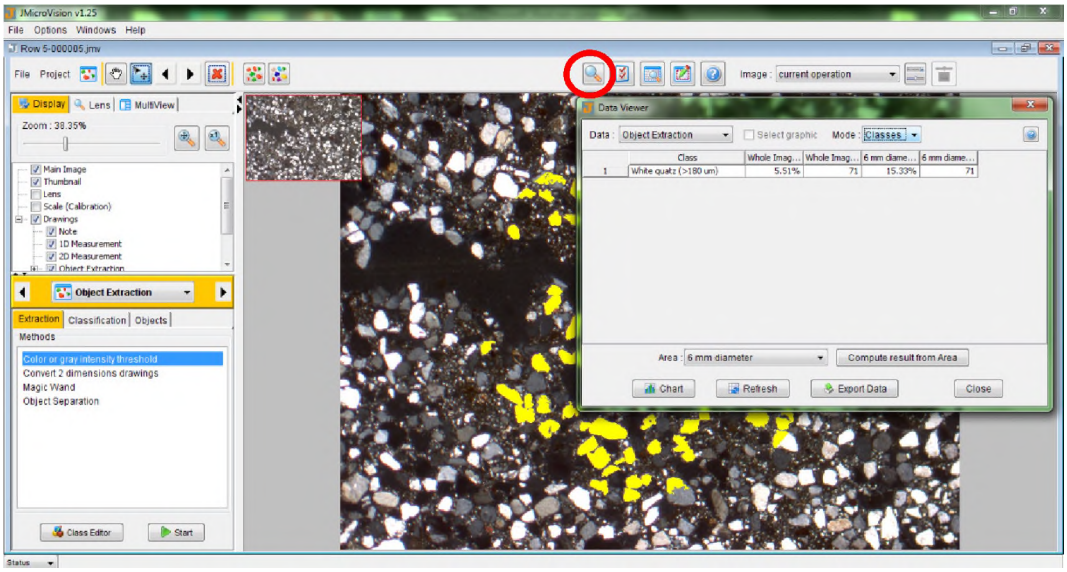

Figure 12.12. The proportion of area that is covered by this object class, i.e. the White quartz (>180 µm), can be found by clicking on the *'Data Viewer'* button highlighted by the red circle. This opens the *'Data Viewer'* pop-up window. With the *'Object Extraction'* and *'Classes'* options selected from the *'Data'* and *'Mode'* drop-down menus, respectively, the proportion of the image occupied by this object class is presented. To determine the amount of area occupied just within the 6 mm

diameter region, the '6 mm diameter' option from the *'Area'* drop-down menu at the bottom of the *'Data Viewer'* window needs to be selected and the *'Compute results from Area'* button selected. The *'Data Viewer'* Table will list the classes extracted, the proportion of the entire image, the number of objects extracted, the proportion of the 6 mm diameter area and the number of objects within the 6 mm diameter area.

12.1.3 EXTRACTING OBJECT WITH NON-UNIFORM OPTICAL PROPERTIES

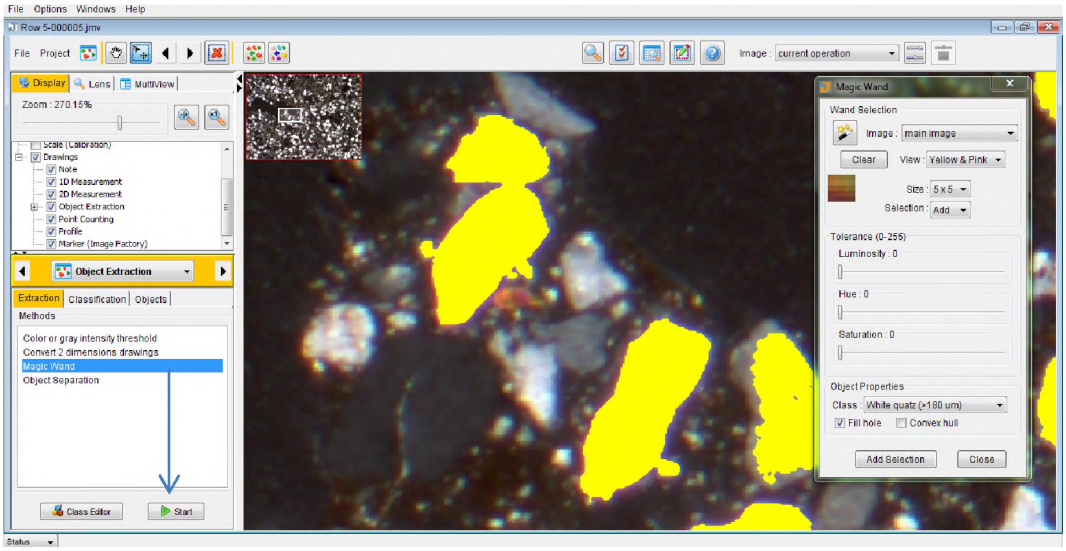

Figure 12.13. In cases where the optical properties are not uniform across the extracted object (such as the case of birefringent heavy mineral species) it may be more appropriate to extract these images individually using the *'Magic Wand'* function under the *'Object Extraction'* drop-down menu (see Figure 6S.1). Before starting, however, a new or pre-existing class is required – this can be done in the same way as in Figure 6S.7. To begin, the *'Magic Wand'* option is selected and the *'Start'* button clicked. This opens the *'Magic Wand'* pop-up menu.

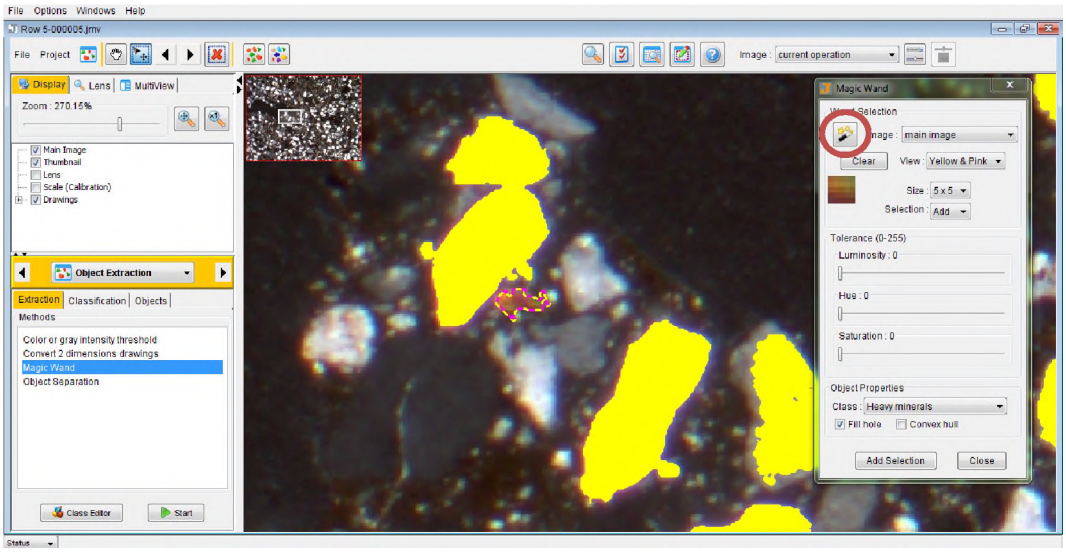

Figure 12.14. The process of individually selecting the grains is very similar to that

of choosing the desired HIS characteristics in Figure 12.10 using the eyedropper. Here, however, the *'Magic Wand'* button is used and the region of desired colour selected. In the same way as described in Figure 12.10, the size of the area selected can be altered using the drop-down *'Size'* menu, and the *'Add'* (rather than *'New'*) option selected from the *'Selection'* menu. It is beneficial to set the three *'Tolerance'* parameters of Luminosity, Hue and Saturation to 0, otherwise large area of unwanted colour generally is selected also. The area selected can then be extracted by clicking the *'Add Selection'* button. This process add the area selected using the *'Magic Wand'* to the chosen object class in the *'Class'* drop-down menu.

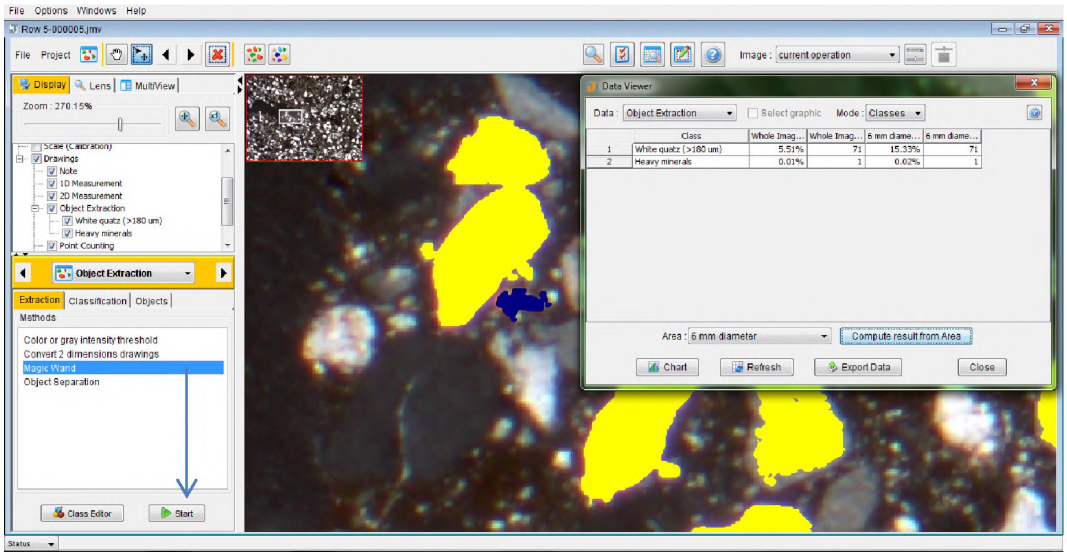

Figure 12.15. Once the desired region has been selected, it is filled with plain colour and the data added to the chosen object class. This can be viewed in the same way as in Figure 12.11 by selecting the *'Data Viewer'* button along the top menu button bar. This Table can then be exported simply by highlighting the wanted cells and copying them (Ctrl+c) and pasting them (Ctrl+v) into an excel spreadsheet or selecting the *'Export Data'* button at the bottom of the *'Data Viewer'* window.

Appendix IV

Chapter 8: Supplementary Information

13.1.1 Luminescence characteristics of IR-sensitive grains from Pech IV

A point of interest among the grains examined from each of the six samples investigated is the presence of IR-sensitive grains. These grains, like those described in Section 8.7.3.1, display substantial variability in terms of their luminescence and dose-response characteristics. Examples of three different IR-sensitive grains are shown in Figure 8.12. From this figure it is can be observed that the ability for a grain to: 1) recycle, 2) not to recuperate, 3) give reproducible T_X decay curves, and 4) generate sensible dose-response curves are all variable from grain-to-grain. For the remainder of this section, only those IR-sensitive grains that passed all rejection criteria, expect the OSL-IR depletion ratio, are considered.

The OSL-IR depletion ratio test conducted during the SAR procedure, outlined in Section 8.7.3.1, was found to reject a substantial proportion of grains from each sample. From Table 8.5, these IR-sensitive grains, when expressed as a percentage of 'usable' grains (i.e., grains that are not dim) for a given sample, have an abundance that ranges from 16% (PdAIV-01-A) to 38% (PdAIV-03) to those grains accepted for D_e determination. Furthermore, the D_e values for these IR-sensitive grains typically underestimate the D_e value calculated from those grains that show no sensitivity to IR stimulation. For example, the D_e values of the 38 IR-sensitive grains from PdAIV-01-C gave a weighted mean D_e of 37 ± 4 Gy, and an OD of 44 ± 9% using the CAM. This D_e is roughly 58% that of the weighted mean of 63 ± 4 Gy and OD value of 48 ± 4% determined for the 89 'accepted' grains for the same sample.

One explanation for the abundance of IR-sensitive grains is that these are either feldspar grains or are quartz grains with feldspar inclusions. It should be kept in mind that, prior to OSL signal measurement, the samples of 180–212 μm quartz grains were etched in 48% HF-acid for 40 min, a procedure used to not only etch the alpha-irradiated rind of the quartz grains but dissolve (at least partially) any feldspar contaminant grains. The samples were then re-sieved to 180–212 μm to remove any, now much smaller, feldspar grains. Additionally, intensive soil micromorphological investigations of thin sections from Pech IV has revealed that feldspar grains have failed to be observed – suggesting that their abundance is significantly less than that of the ubiquitous quartz grains. The IR-sensitive grains are, therefore, not likely to be the result of a feldspar grain surviving the etching process and being measured.

The IR-sensitivity of such grains was further examined using: 1) pulse-anneal tests, and 2) LM-OSL measurements. The procedures and findings for these two tests are outlined in the following two sections.

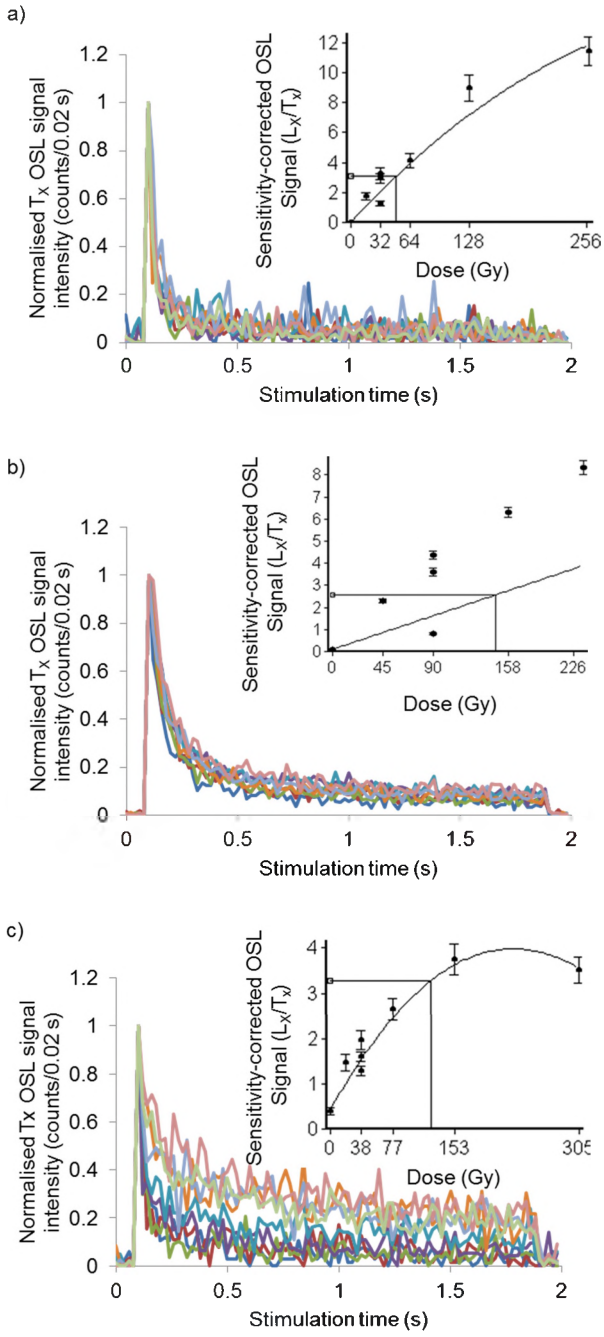

Figure 8.12. A series of OSL decay and dose-response curves for IR-sensitive grains. a) An IR-sensitive grain that recycles well, has a small recuperated signal and reproducible T_X OSL decay curves. b) An IR-sensitive grain that fails to recycle, has a small recuperated signal and quite reproducible T_X OSL decay curves. c) An IR-sensitive grain that fails both the recycling ratio and IR-depletion ratio tests, has a high recuperated OSL signal, and non-reproducible T_X OSL decay curves.

13.1.1.1 PULSE ANNEAL TESTS

To test whether the grains sensitive to IR stimulation may contain thermally unstable OSL components, five single-grain discs were loaded with natural 180–212 μm in diameter quartz grains from sample PdLIV-1 (Layer 8). To identify the grains that failed the OSL-IR depletion ratio test, the D_e values were determined in the same way as in Section 6.3. At the end of the usual SAR measurement cycles, the grains were subjected to a pulse anneal test following the approach of Fan *et al.* (2011). First, each single-grain disc was given a hot optical wash using the blue LEDs for a period of 40 s holding the sample at a temperature of 280°C. The samples were then given a fixed regenerative dose of ~64 Gy. The PH_1 treatment was given to T°C for 10 s and the OSL signal measured using the green laser for 2 s holding the sample at 125°C. A fixed test dose of ~11 Gy and PH_2 of 180°C for 5 s were given prior to the measurement of the test dose OSL signal. This cycle was then repeated, with the PH_1 increased in 20°C intervals from 180 to 280°C. The hot optical wash of Fan *et al.* (2011), however, was not repeated at the beginning of each cycle.

Of the 500 grains measured 14 grains (2.8%) failed only the OSL-IR depletion ratio test. Figure 8.13 shows a selection of pulse anneal curves for those grains that: 1) did not fail any rejection criteria (black circles), 2) that failed the RR rejection criteria only (grey circles) and 3) that only failed the OSL-IR depletion ratio test (white circles). In general, the IR-sensitive grains show a decrease in the OSL single with increasing PH_1 temperature beyond 180°C, whereas those grains that were accepted, or that failed only the RR test do not show any significant deviation from unity until a preheat of >280°C is used, and the OSL trap is starting to be thermally eroded. The same pulse anneal test was also conducted using a hot optical wash after each successive measurement cycle with similar patterns observed.

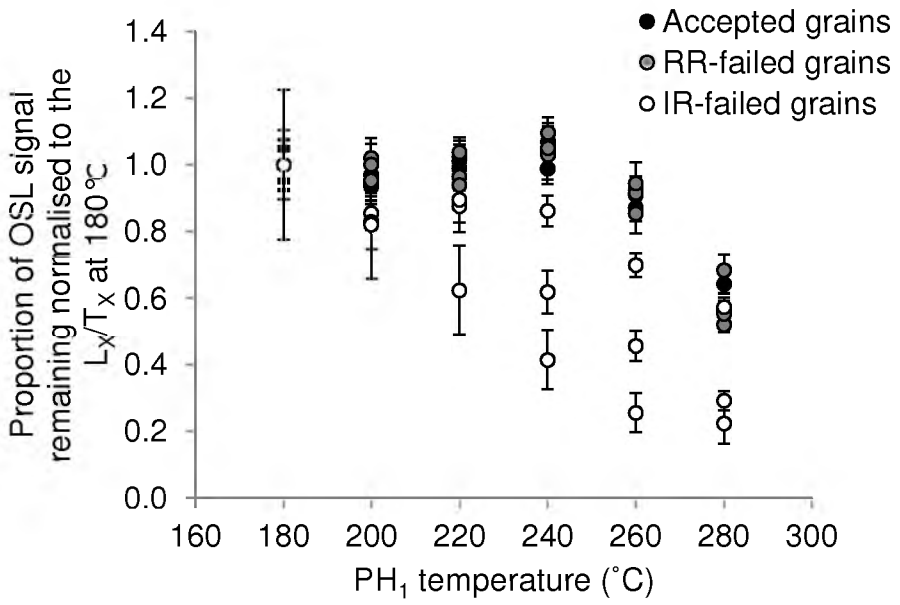

Figure 8.13. Pulse anneal results for grains that: 1) passed the rejection criteria and were considered acceptable for D_e determination (black); 2) only failed the RR test (grey); and 3) only failed the OSL-IR depletion ratio test of Duller (2003). Three grains of each group are shown. The uncertainties shown are at 1σ.

13.1.1.2 LM-OSL OF IR-SENSITIVE GRAINS

Given that the OSL signal of these IR-sensitive grains is depleted with increasing preheat temperature, it is clear that a thermally unstable OSL component is at play here. To further test this, LM-OSL measurements were made on 7 of the 14 grains that were only rejected due to their IR sensitivity. A pin was used to transfer the IR-sensitive grains from their original position within the single-grain discs onto 3 stainless steel discs. Disc 1 and 2 contained 2 grains each, with Disc 3 contained 3 grains. These grains were held in place with a small amount of silicon spray oil. The three stainless steel discs were then given a ~320 Gy dose before being preheated to 180°C for 10 s. The LM-OSL signal was then measured using the same procedure as outlined in Section 8.6.1. The aliquot was given a repeat ~320 Gy irradiation and optically stimulated using the IR LEDs for 40 s at a temperature of 50°C. The sample was again preheated and the LM-OSL measured as previously. The results of both

the LM-OSL and post-IR LM-OSL measurements for all 3 discs are displayed in Figure 8.14.

It should be noted that the LM-OSL curves here have not been corrected for background contribution as no background measurement was made on this Risø machine (Risø 4). It was also considered that the use of the background signal displayed in Figure 8.4 and applied to those LM-OSL curves displayed in Figure 8.5 is not appropriate for were measured on a different reader (Risø 5) with a different PM tube sensitivity. The measurement of the background signal will need to be made on Risø 4 in future to account for the contribution of the background to total LM-OSL signal. It is assumed, at present, that the contribution of the background will have no great effect on the result presented below.

From visual inspection of the 'Fast' component peak position it is clear that there is significant variability in the response of the LM-OSL grains to IR stimulation. For Disc 1 (Figure 8.14a) the peak height for the 'Fast' component remains at the same position (~47 s) before and after IR stimulation. However, for the remaining two discs, Discs 2 and 3, following IR stimulation, this 'Fast' component peak has shifted slightly to the right from ~47 s to 58 s (Figure 8.14b). For comparison, the 'Fast' component peak height for PdAIV-01-C from Layer 8 (see Figure 8.3a) is situated at ~ 50 s, falling within the range of this IR-induced shift in peak heights. To further investigate the LM-OSL response to IR stimulation, mathematical deconvolution of the LM-OSL decay curves was conducted.

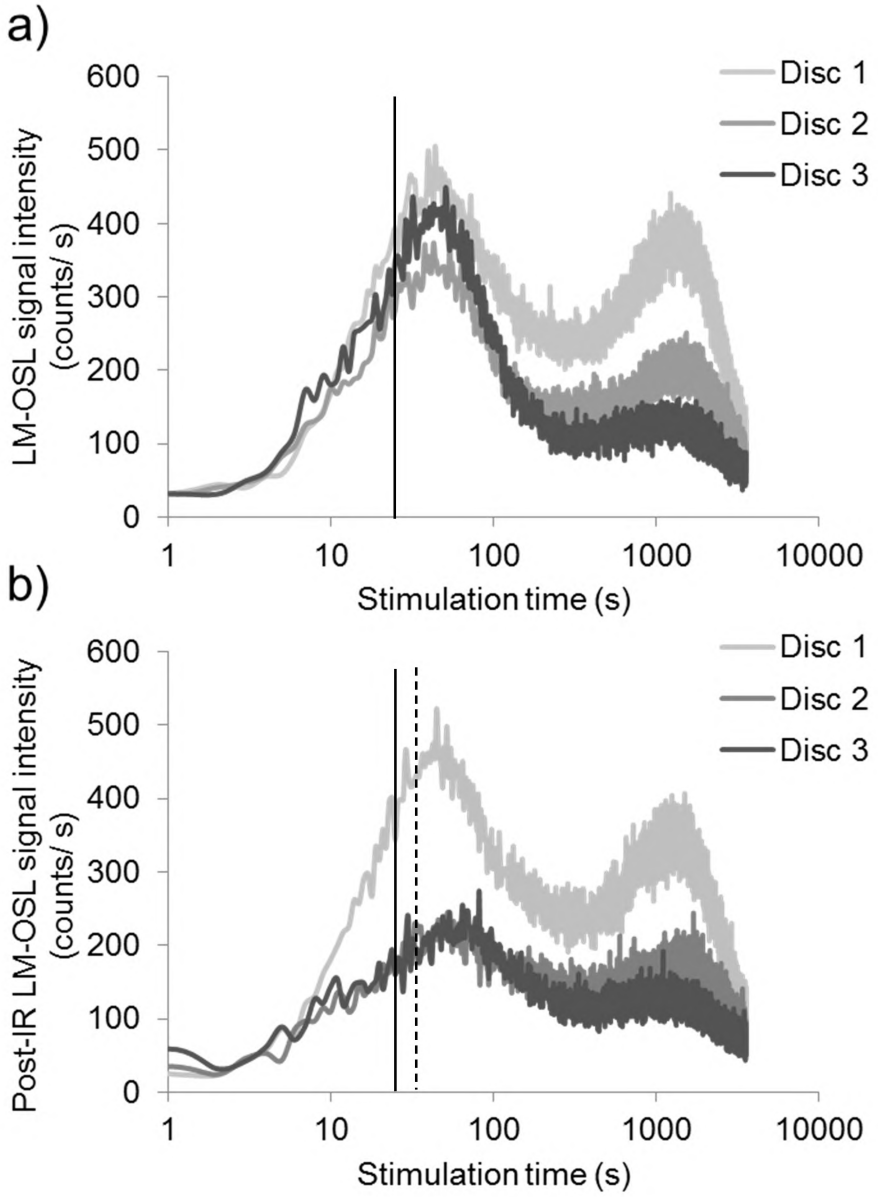

Figure 8.14. a) LM-OSL and b) post-IR LM-OSL signals for the three discs containing IR-sensitive grains. In figure a), each disc was given a ~320 Gy beta dose, before being preheated to 180˚C for 10 s. The LM-OSL signal was then measured for a duration of 3600 s at 125˚C. This was then repeated for b) with a 40 s IR-stimulation at 50˚C made prior to preheating. The 47 s stimulation time is indicated by a solid black vertical line in both a) and b). The 58 s stimulation time is shown as a broken vertical black line in b) only.

The deconvoluted LM-OSL decay curves for all three discs of IR-sensitive grains are shown in Figure 8.15. It is clear that in each case the proportion and type of LM-OSL components present differ from sample to sample. Such variability has previously been described at both the multi-grain (Arnold *et al.* 2009) and the single-grain level (Bulur *et al.* 2002, Singarayer 2003, Jacobs *et al.* 2008c). For Disc 1, a 5 component fit was determined by be the most appropriate for both the LM-OSL and post-IR LM-OSL signals. This response is in contrast to those of Discs 2 and 3. For Disc 2, 4 components (Fast, S1, S3 and S4) could be fitted to the regenerative LM-OSL signal, whereas, following IR-stimulation, two additional components (an ultra-fast (UFC) and a S2) were required to explain the post-IR LM-OSL decay curve. A similar situation exists for Disc 3, where the UFC component is also evident in the post-IR LM-OSL response in addition to the 5 components (Fast, S1, S2, S3 and S4) used to explain the associated LM-OSL decay curve.

An UFC is present in two of the three discs measured. For Discs 2 and 3, the application of IR-stimulation has removed more than 50% of what appears to be the Fast component and enabled the UFC to be revealed. In naturally-irradiated samples, the presence of the UFC can lead to the underestimation of D_e values. This underestimation is due to the short lifetime of this trap: a few hours to a few days (Jain *et al.* 2008). The UFC is therefore not present in naturally-irradiated decay curves but can be found in laboratory-irradiated curves. The UFC is also considered to be present in the laboratory-irradiated LM-OSL decay curves but is swamped by the fast component and not visible. Jain *et al.* (2008) suggested the use of preheat temperatures of >200°C to remove the UFC from the OSL decay curves.

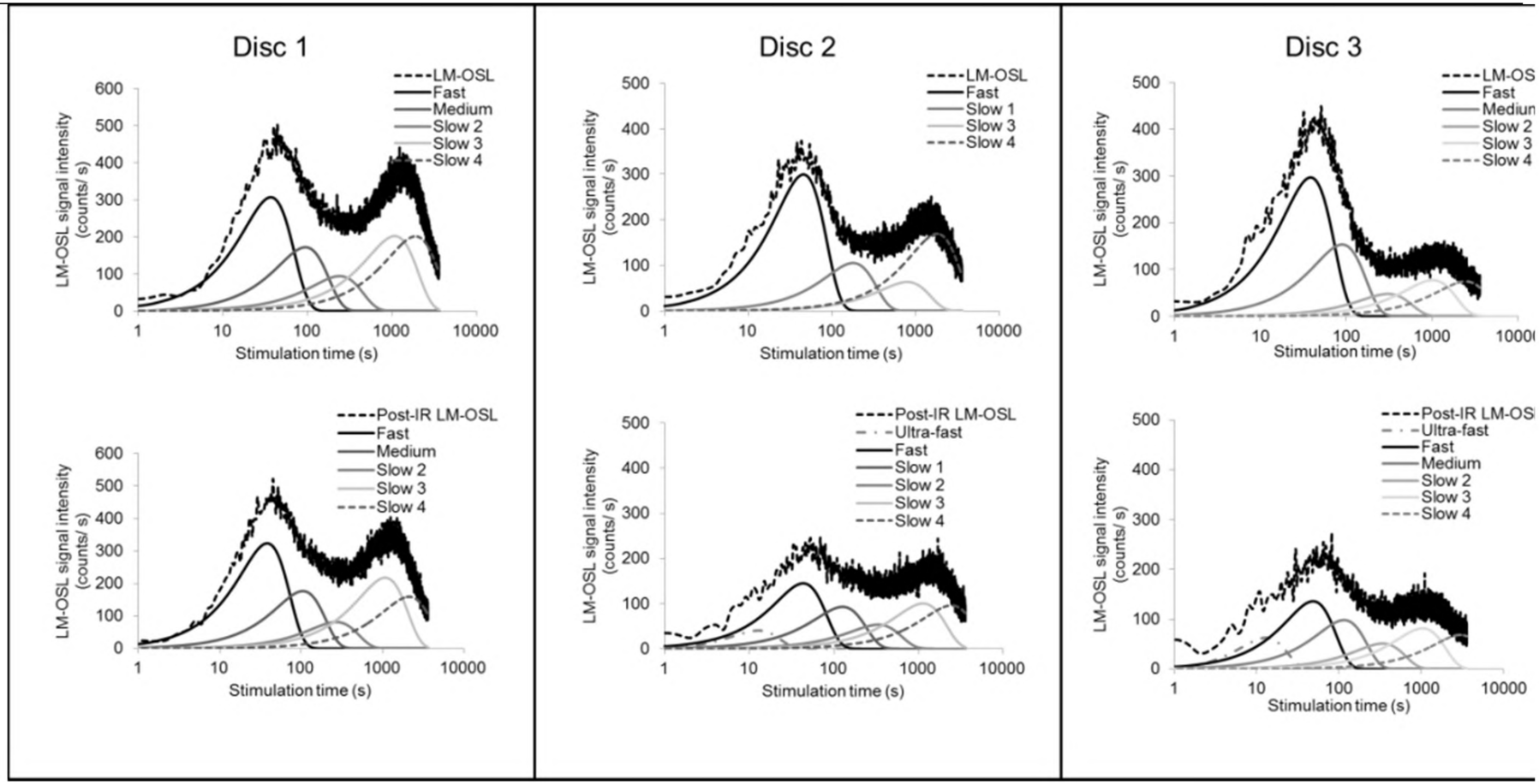

Figure 8.15. LM-OSL (top) and post-IR LM-OSL (bottom) fitted components for the same three discs of IR-sensitive grains as in Figure 8.14, for (from left to right) Disc 1, 2 and 3.

13.1.1.3 TESTING UFC IR-SENSITIVITY USING THE PREHEAT PLATEAU DATA SET

If the UFC component in the Pech IV quartz grains is the result of the 'low' preheat temperature used (180°C) during D_e determination, then an increase in preheat temperature will, presumably, deplete the thermally unstable UFC and result in a reduced number of IR-sensitive grains. To test this, the preheat plateau data set (used in Section 8.7.2) was re-analysed for the changes in the proportion of IR-sensitive grains as a function of increasing preheat temperature. It should be noted that Layer 8 (PdLIV-1) 180–212 μm quartz grains used that contained their natural dose and both the PH_1 and PH_2 temperatures were co-varied. If the UFC is responsible for the IR-sensitivity of some of the Pech IV quartz grains, then as preheat temperatures increase, the number of IR-sensitive grains ought to decrease. Displayed in Table 8.7 are the total number of grains that displayed IR-sensitivity (regardless of whether they passed or failed the recycling ratio and recuperation rejection criteria), those grains that passed all rejection criteria (except the IR-depletion ratio test) and the proportion of IR-sensitive grains with respect to the total number of accepted quartz grains.

The results, presented in Table 8.7, reveal an apparent decrease in the proportion of IR-sensitive grains with increasing preheat temperatures. The total number of IR-sensitive grains reduced from a proportion that is 112% with respect to the associated accepted grains at a preheat combination of 180°C/180°C, to 41% using the 260°C/260°C combination. If those grains that only failed the IR-depletion ratio test are considered, then a similar situation exists with the proportion decreasing from 40% at 180°C/180°C to 10% following the 260°C/260°C preheat treatments.

The results of this study are not, however, considered meaningful in terms of assessing purely the removal of the UFC. First, the increase in preheat temperature has previously been shown to result in the depletion of the thermally unstable S3 component. This is apparent in both the LM-OSL decay curves in Figure 8.5 and the pulse anneal experiments in Figure 8.13. Second, the increase in preheat temperature

also results in the inability to recover a known laboratory dose (as is shown in the dose recovery tests of Figure 8.8) and also decreases the apparent D_e of naturally-irradiated quartz (preheat plateau tests in Figure 8.9). The effect of the increased preheat on the UFC alone, therefore, most probably is evident in the 13% difference between the 180˚C and 200˚C preheat treatments (Table 8.7) if just those grains that failed only the IR-depletion ratio test are considered. It is evident that the cause of the IR-sensitive response of these grains is more complex than simply the interplay between thermally unstable source traps.

Table 8.7. Proportion of IR-sensitive grains with respect to the number of accepted grains for the preheat plateau data for sample PdLIV-1 presented in Table 8.3. Also given are the results for a limestone pebble collected from Layer 5B using a PH_1/PH_2 combination of 180˚C.

Preheat combination	Total number of grains measured	Total number of accepted grains	Total number of IR-sensitive grains	Number of IR-sensitive grains that pass all rejection criteria except the IR-depletion ratio test
180/180	500	50	56 (112%)	20 (40%)
200/200	400	56	40 (71%)	15 (27%)
220/220	400	74	50 (68%)	23 (31%)
240/240	500	62	31 (50%)	12 (19%)
260/260	400	71	29 (41%)	7 (10%)
		Limestone Cobble		
180/180	1000	29	31 (107%)	19 (66%)

13.1.1.3.1.1 Origin of the IR-sensitive grains

The question remains as to whether this IR-sensitive behaviour observed in the Pech IV samples is the result of geological or anthropogenic processes. To test this, a limestone cobble, collected from Layer 5B during the field season, was dissolved in 10% HCl acid to remove the carbonate and liberate the siliclastic grains. These

siliclastic grains were then chemically pre-treated, sieved and HF-etch following the same procedures outlined in Section 8.4. The 1000 individual 180–212 μm HF-acid etched quartz grains were then measured using the SAR procedure outlined in Section 8.5 using PH_1 and PH_2 temperatures of 180°C.

The results are also presented in Table 8.7. Of the 1000 quartz grains measured, 29 (3%) were accepted having passed all rejection criteria. Of the remaining 9971 rejected grains, 31 were observed to be IR-sensitive failing at least the IR-depletion ratio test. Of these 31 grains, 19 failed only the IR-depletion ratio test. Given that 29 grains in total were accepted, the IR-sensitive grains represent 66% (N=19) of the sample with respect to the accepted grains. This proportion is substantially larger than the 40% IR-sensitive grains from Layer 8 (PdLIV-1) measured using the 180°C/180°C preheat combination in Table 8.5. However, it is more in line with the 58% proportion of IR-sensitive grains coming from the same layer (Layer 5B) that the limestone pebble was collected from (Table 8.5). It is apparent that the IR-sensitive nature of the quartz grains is inherited from the host limestone, rather than an artefact of the intensive anthropogenic heating that occurred in Layer 8.

13.1.1.4 SUMMARY

The presence of the IR-sensitive grains in the Pech IV samples is currently not well understood. It has been shown that this IR-sensitive behaviour of the quartz is inherited from the geological host material (i.e., the Coniacien Limestone), rather than an artefact of intensive anthropogenic heating of the sediments. Such quartz grains are more thermally unstable (Figure 8.13) than their IR-insensitive counterparts that had passed all rejection criteria and were accepted for D_e determination. This thermal stability was considered to be the result of thermally unstable UFC and S3 components (Figure 8.15). However, the presence, and dominance, of these two components varies with each individual grain (Figure 8.15). At present, these two observations alone are not able to account completely for the IR-sensitivity of these grains. Regardless of this, these grains had failed the IR-

depletion ratio test, were rejected and, therefore, not considered in the D_e of the Pech IV samples.

13.1.2 PXRF MAPS

This section provides the elemental distributions of U, Th, K, Ca, P and Si obtained using the pXRF for all 15 ROI discussed in Section 8.8.2.1. Please note that the units for U, Th and K (the top row of distribution maps) are given in µg/g, while the units for Si, P and Ca (the bottom row) are given in %. I have also included a macroscopic scan of each region of interest, the name of which can be found in the top left hand corner of each image. The figures are arranged in descending order down the Layer 8 column (see Figure 8.22 main text)

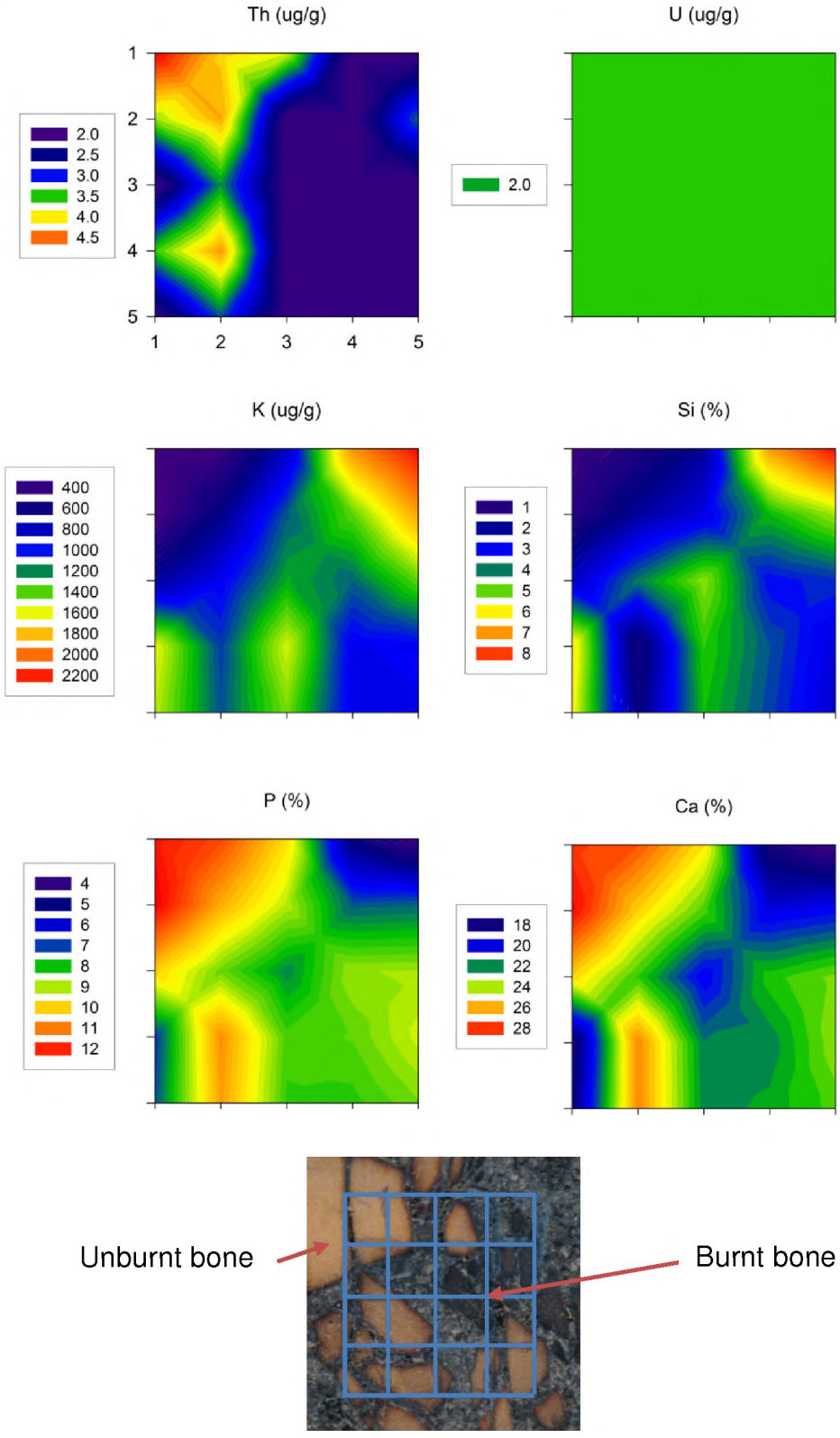

Figure 13.1. A-Lower-01 region of interest elemental distribution maps for Th, U, K, Si, P and Ca using the pXRF. Each region of interest measures 12 mm in length and width and covers an area of 5×5 measurement points.

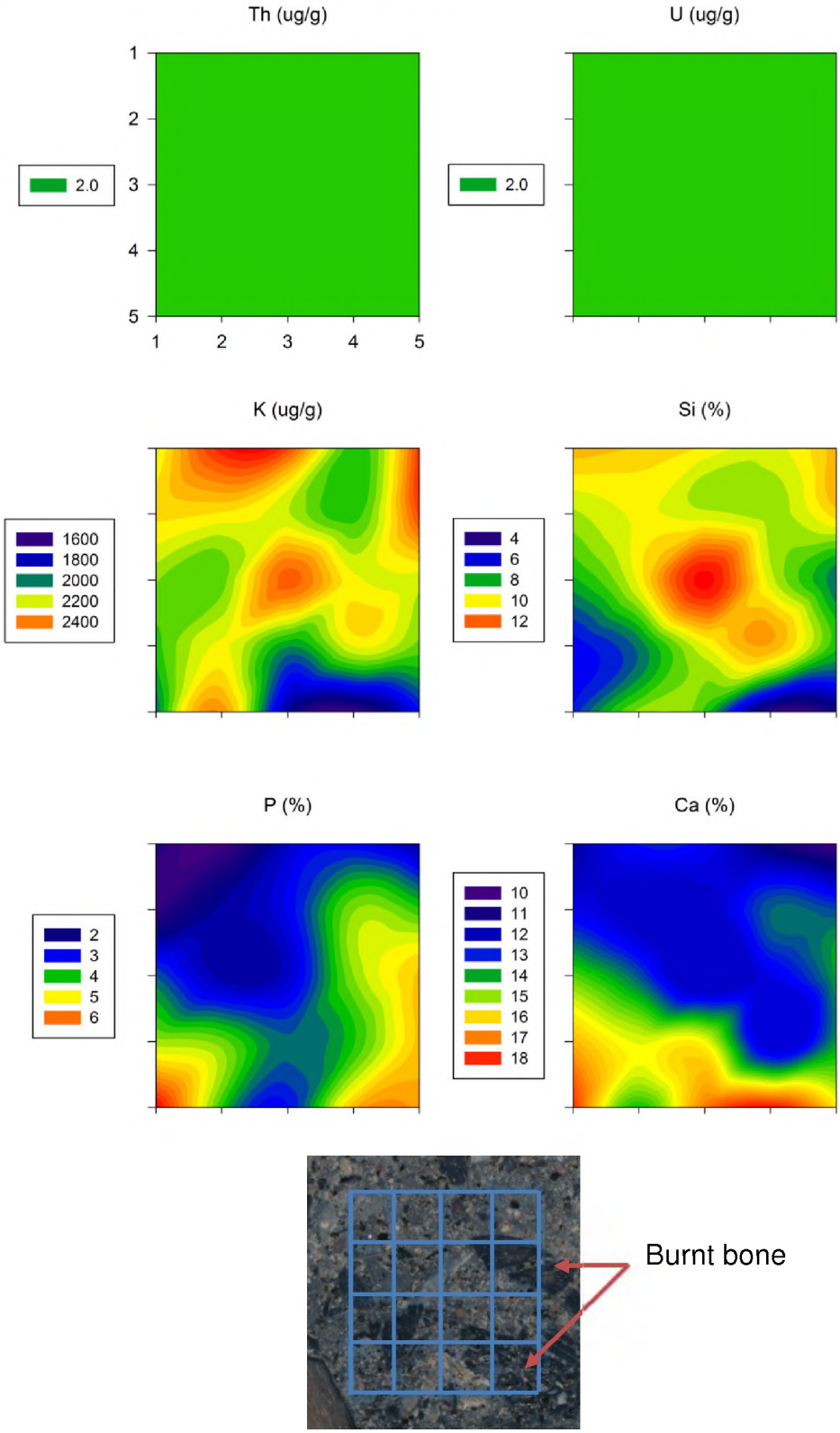

Figure 13.2. A-Lower-02 region of interest elemental distribution maps for Th, U, K, Si, P and Ca using the pXRF. Each region of interest measures 12 mm in length and width and covers an area of 5×5 measurement points.

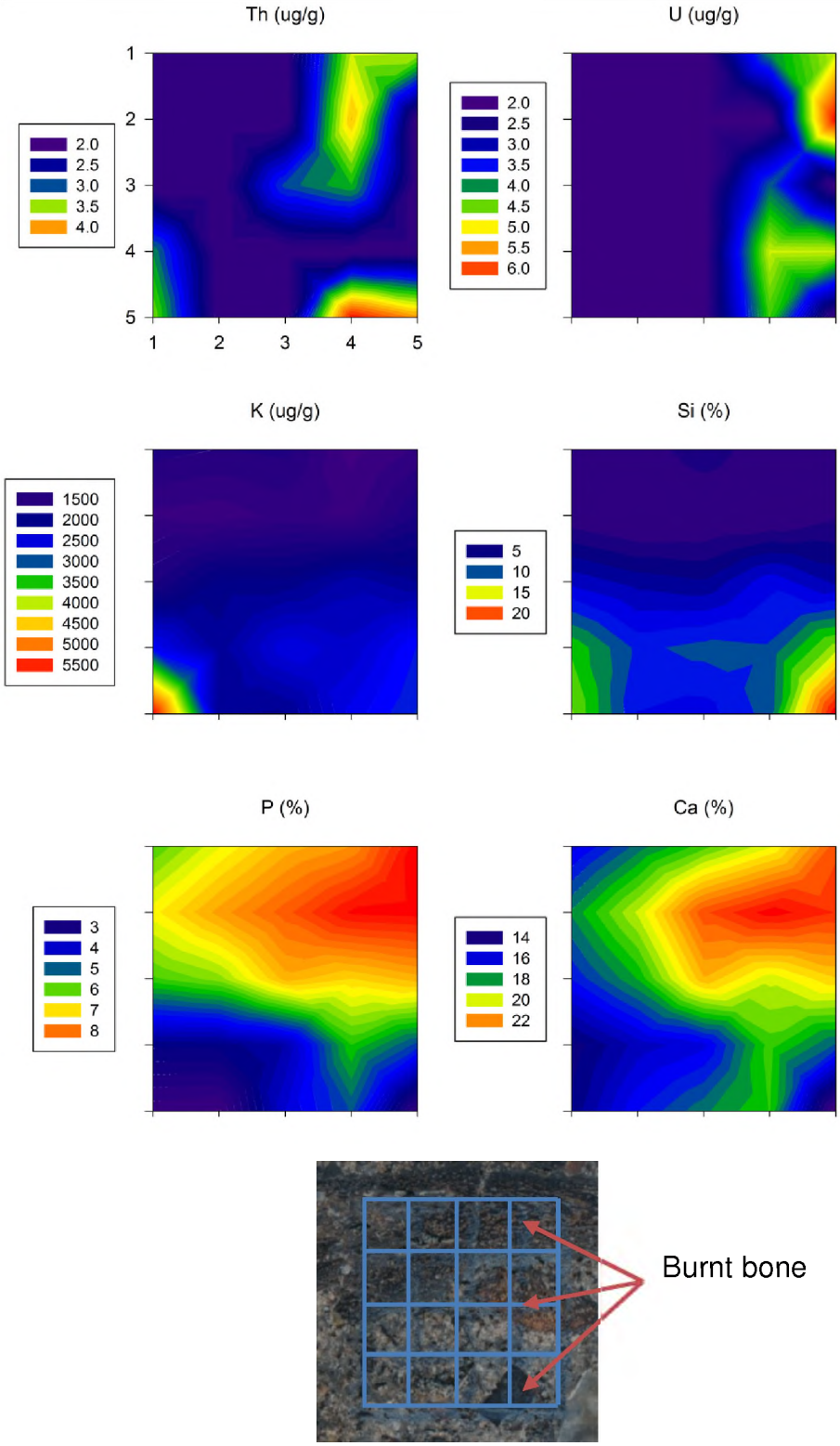

Figure 13.3. A-Upper-01 region of interest elemental distribution maps for Th, U, K, Si, P and Ca using the pXRF. Each region of interest measures 12 mm in length and width and covers an area of 5×5 measurement points.

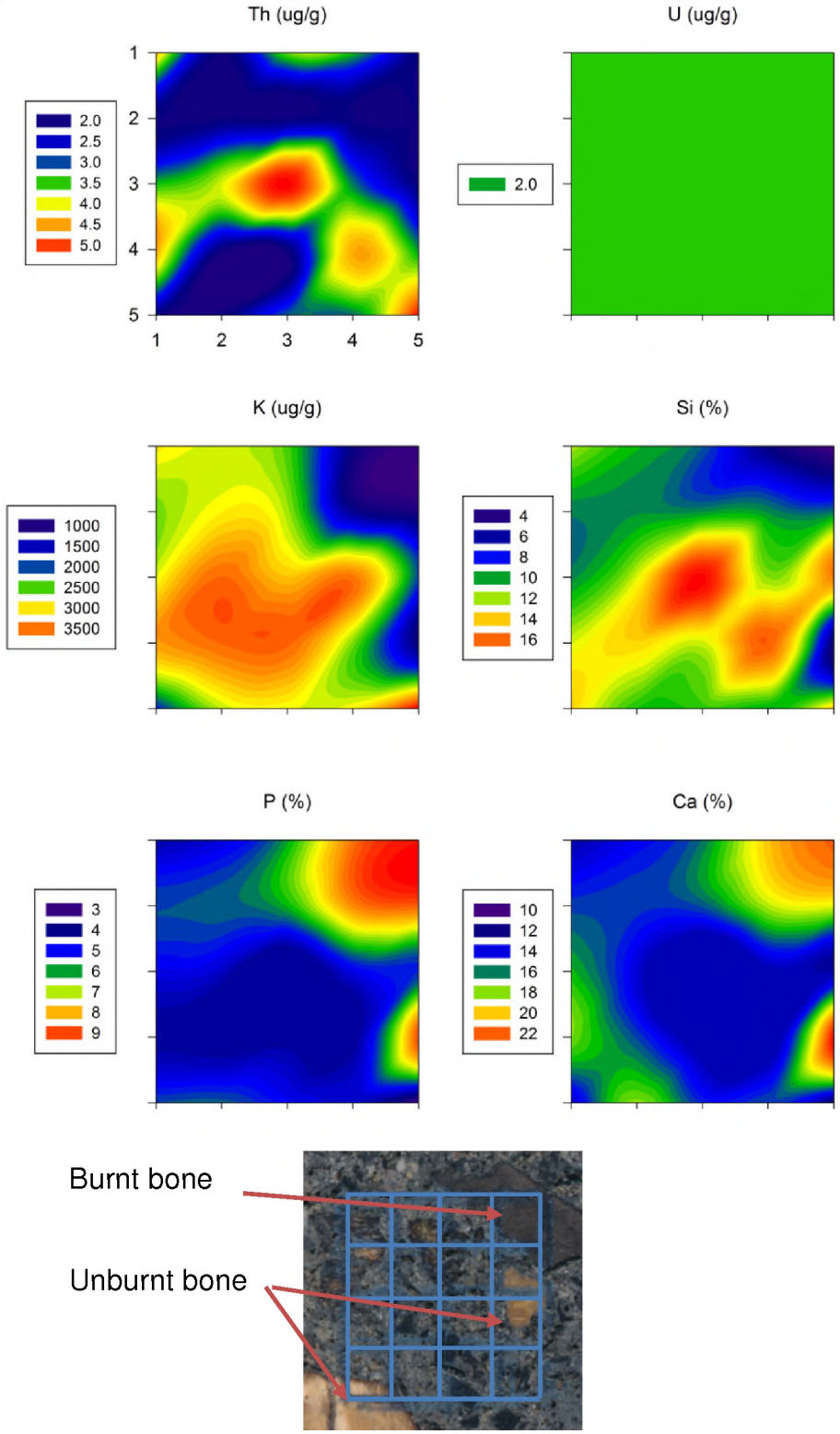

Figure 13.4. A-Upper-02 region of interest elemental distribution maps for Th, U, K, Si, P and Ca using the pXRF. Each region of interest measures 12 mm in length and width and covers an area of 5×5 measurement points.

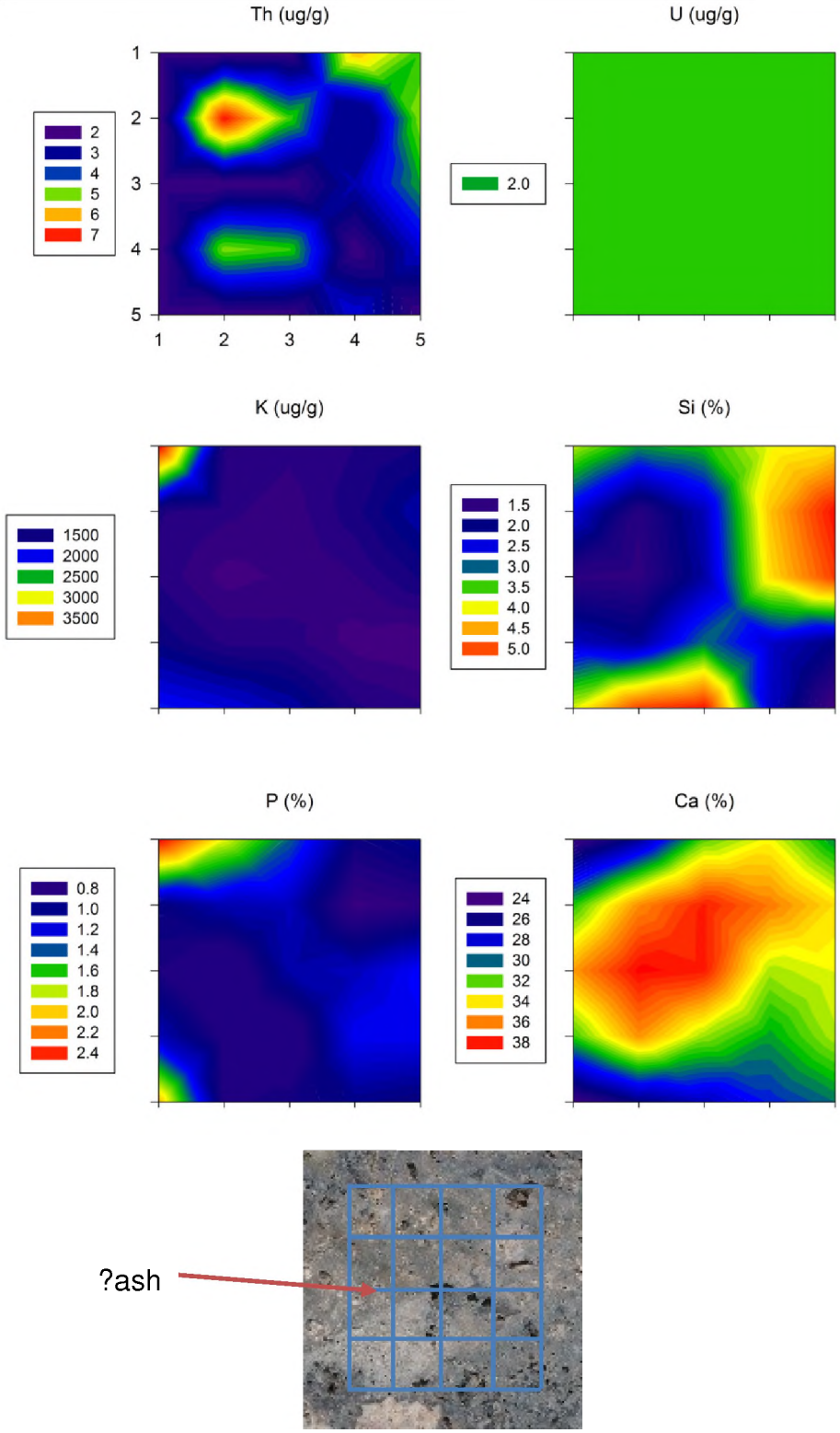

Figure 13.5. B-Lower-01 region of interest elemental distribution maps for Th, U, K, Si, P and Ca using the pXRF. Each region of interest measures 12 mm in length and width and covers an area of 5×5 measurement points.

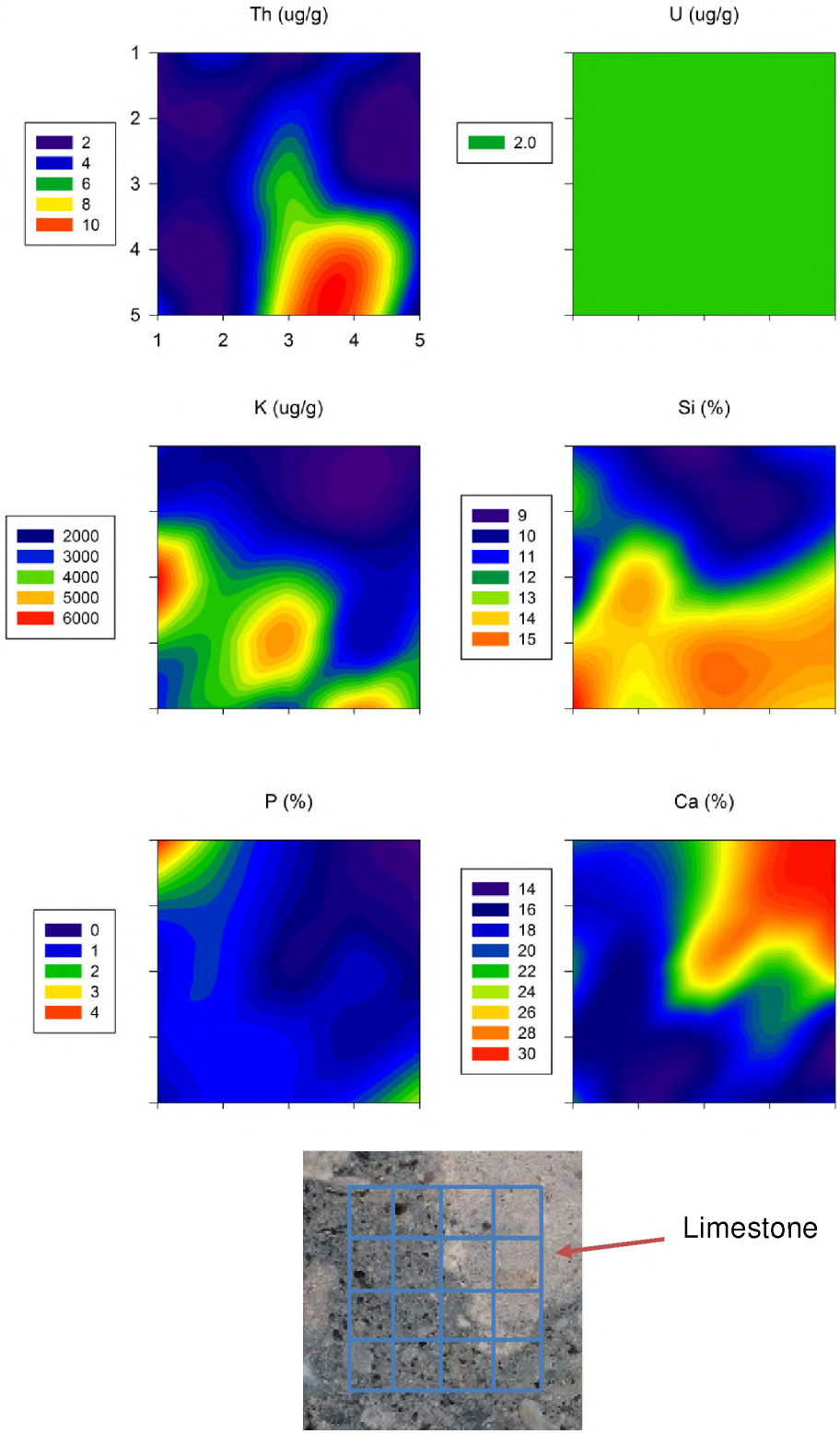

Figure 13.6. B-Lower-02 region of interest elemental distribution maps for Th, U, K, Si, P and Ca using the pXRF. Each region of interest measures 12 mm in length and width and covers an area of 5×5 measurement points.

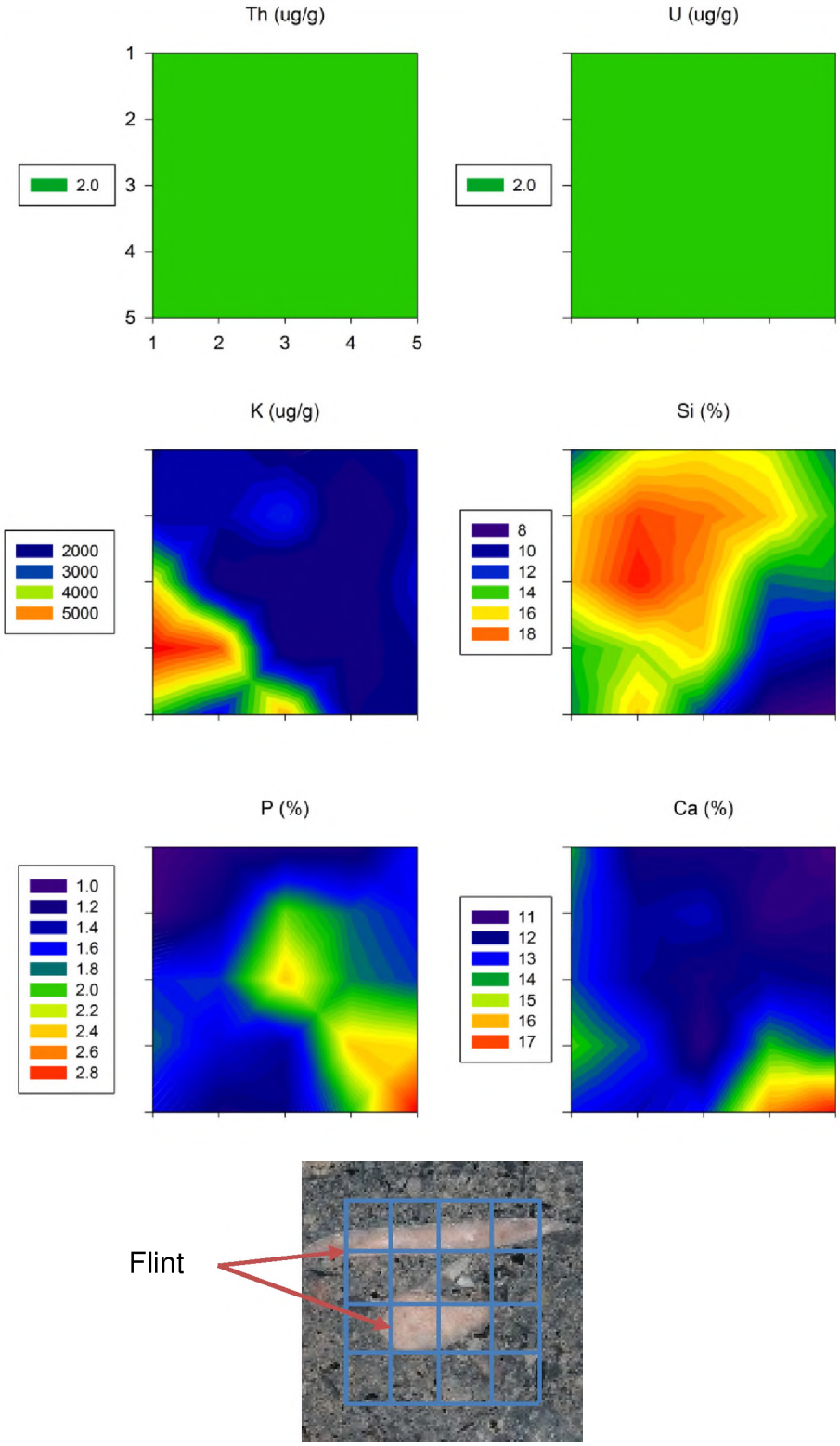

Figure 13.7. B-Upper-01 region of interest elemental distribution maps for Th, U, K, Si, P and Ca using the pXRF. Each region of interest measures 12 mm in length and width and covers an area of 5×5 measurement points.

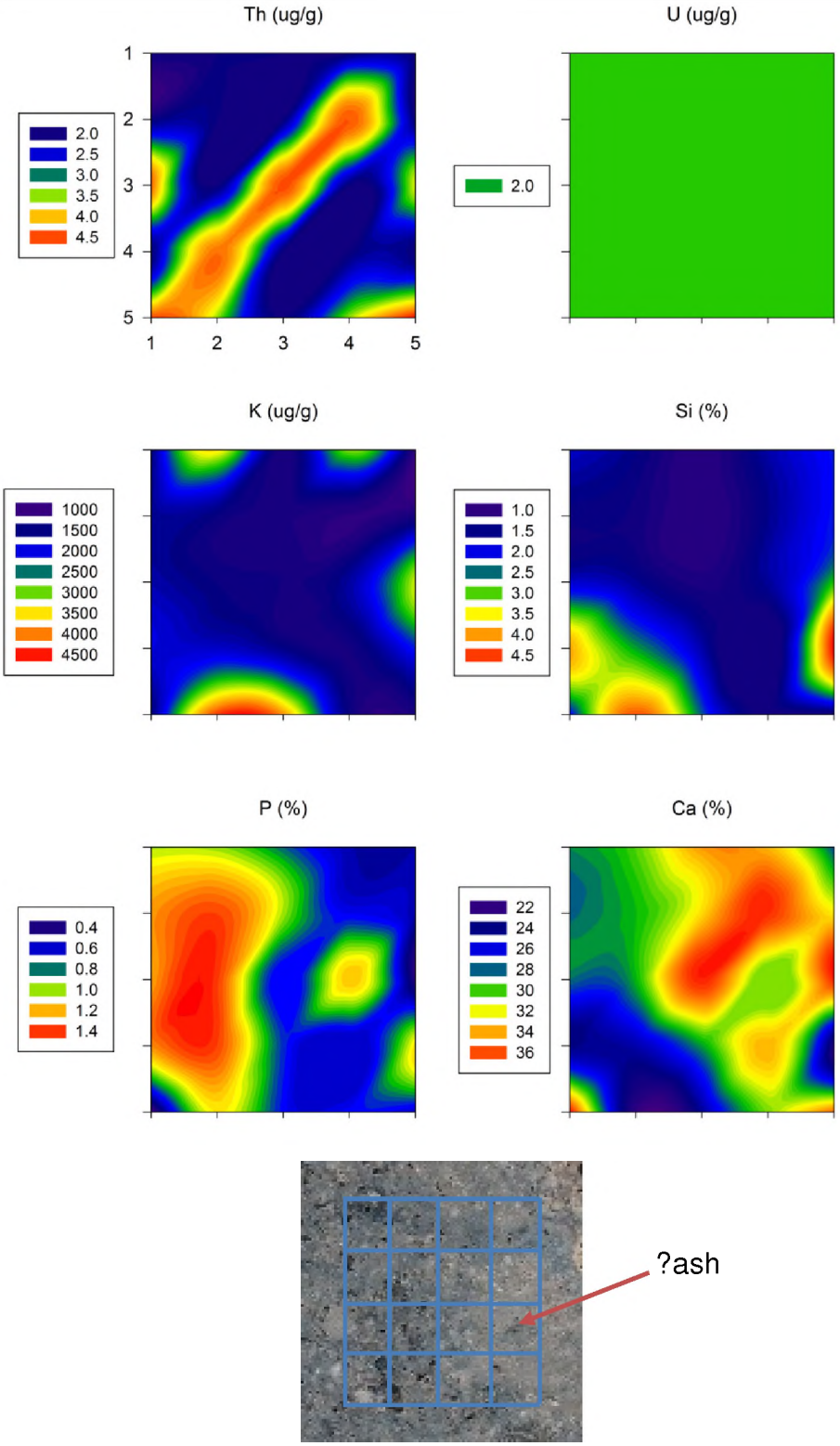

Figure 13.8. B-Upper-02 region of interest elemental distribution maps for Th, U, K, Si, P and Ca using the pXRF. Each region of interest measures 12 mm in length and width and covers an area of 5×5 measurement points.

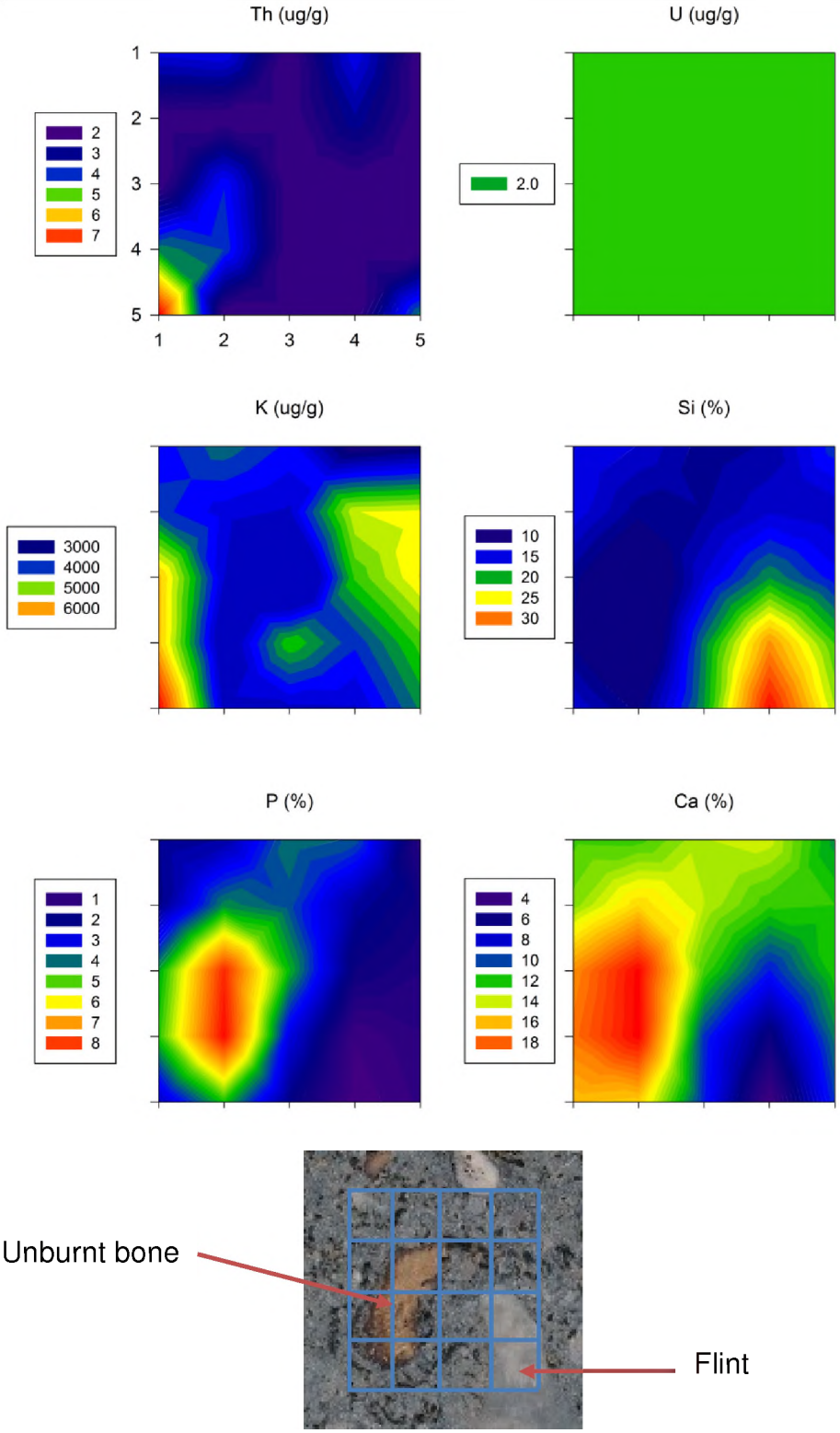

Figure 13.9. C-Lower-01 region of interest elemental distribution maps for Th, U, K, Si, P and Ca using the pXRF. Each region of interest measures 12 mm in length and width and covers an area of 5×5 measurement points.

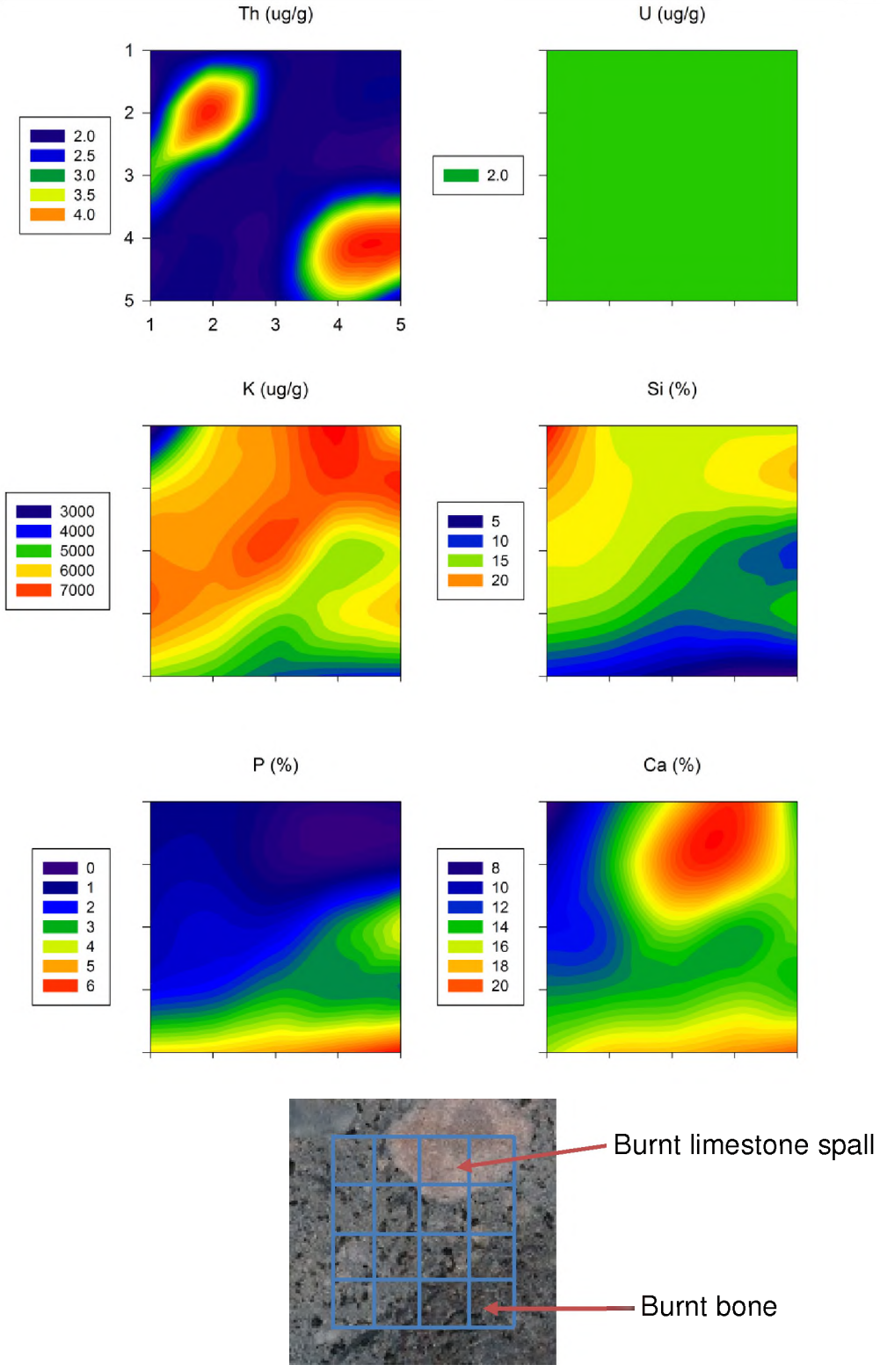

Figure 13.10. C-Lower-02 region of interest elemental distribution maps for Th, U, K, Si, P and Ca using the pXRF. Each region of interest measures 12 mm in length and width and covers an area of 5×5 measurement points.

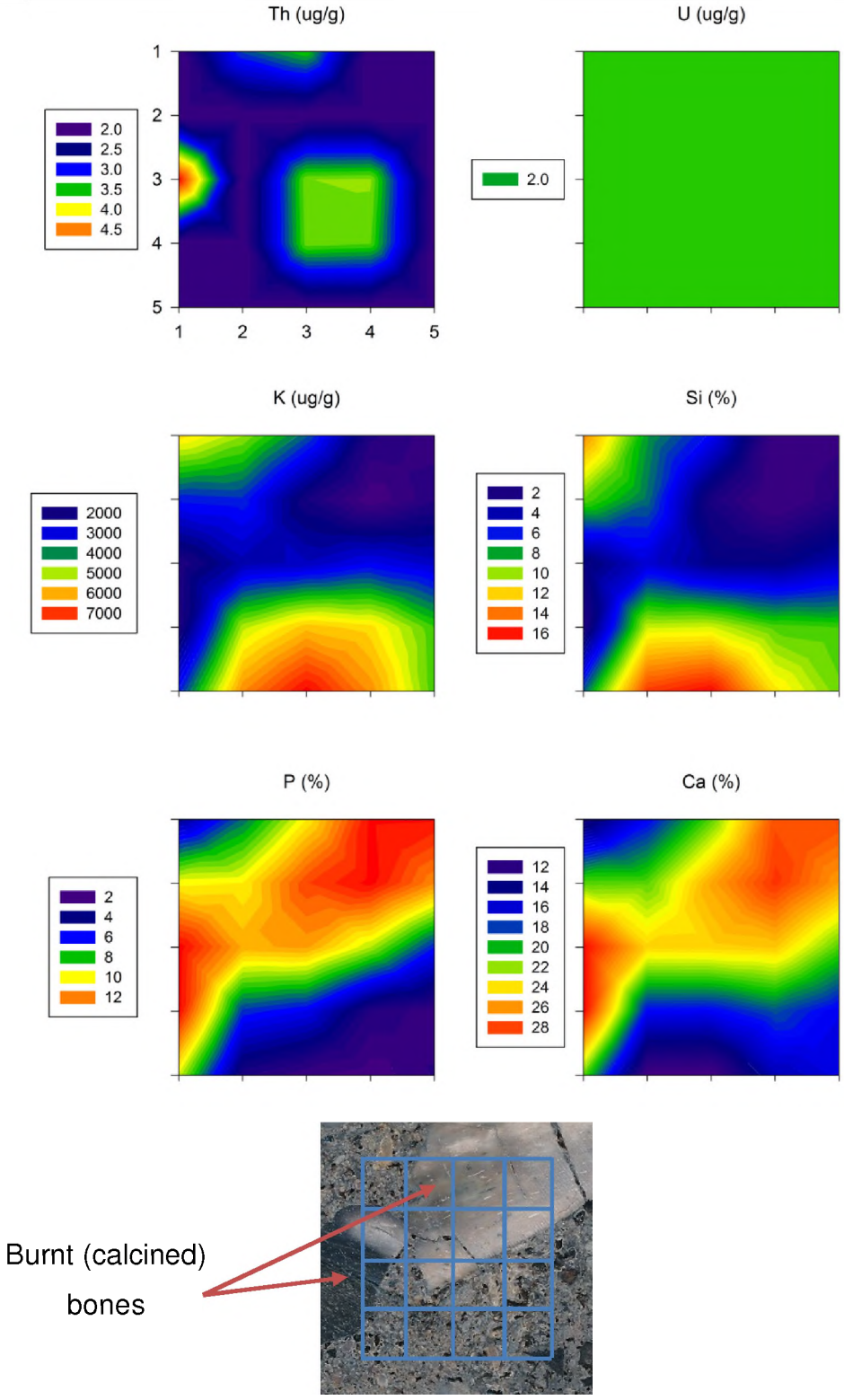

Figure 13.11. C-Upper-01 region of interest elemental distribution maps for Th, U, K, Si, P and Ca using the pXRF. Each region of interest measures 12 mm in length and width and covers an area of 5×5 measurement points.

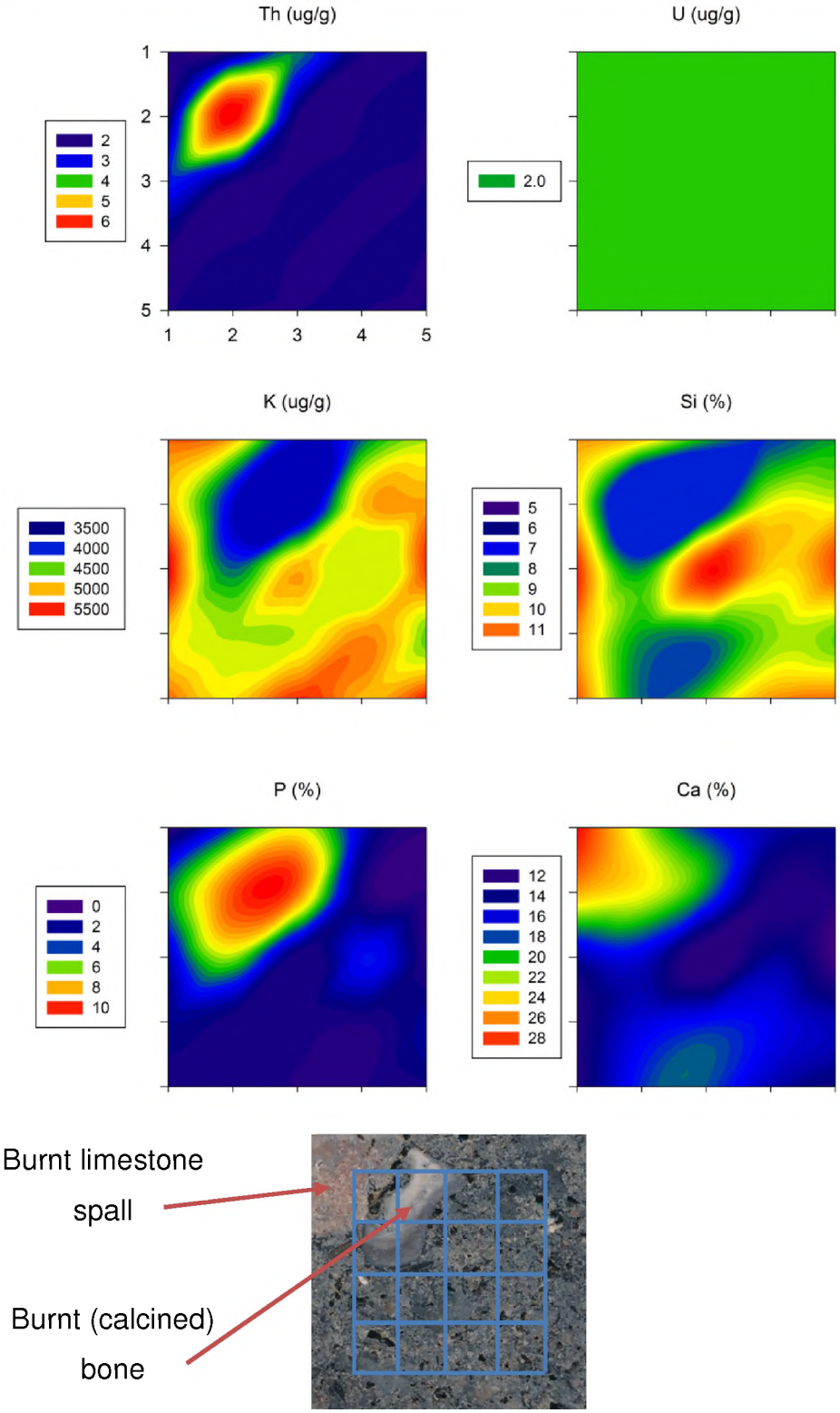

Figure 13.12. C-Upper-02 region of interest elemental distribution maps for Th, U, K, Si, P and Ca using the pXRF. Each region of interest measures 12 mm in length and width and covers an area of 5×5 measurement points.

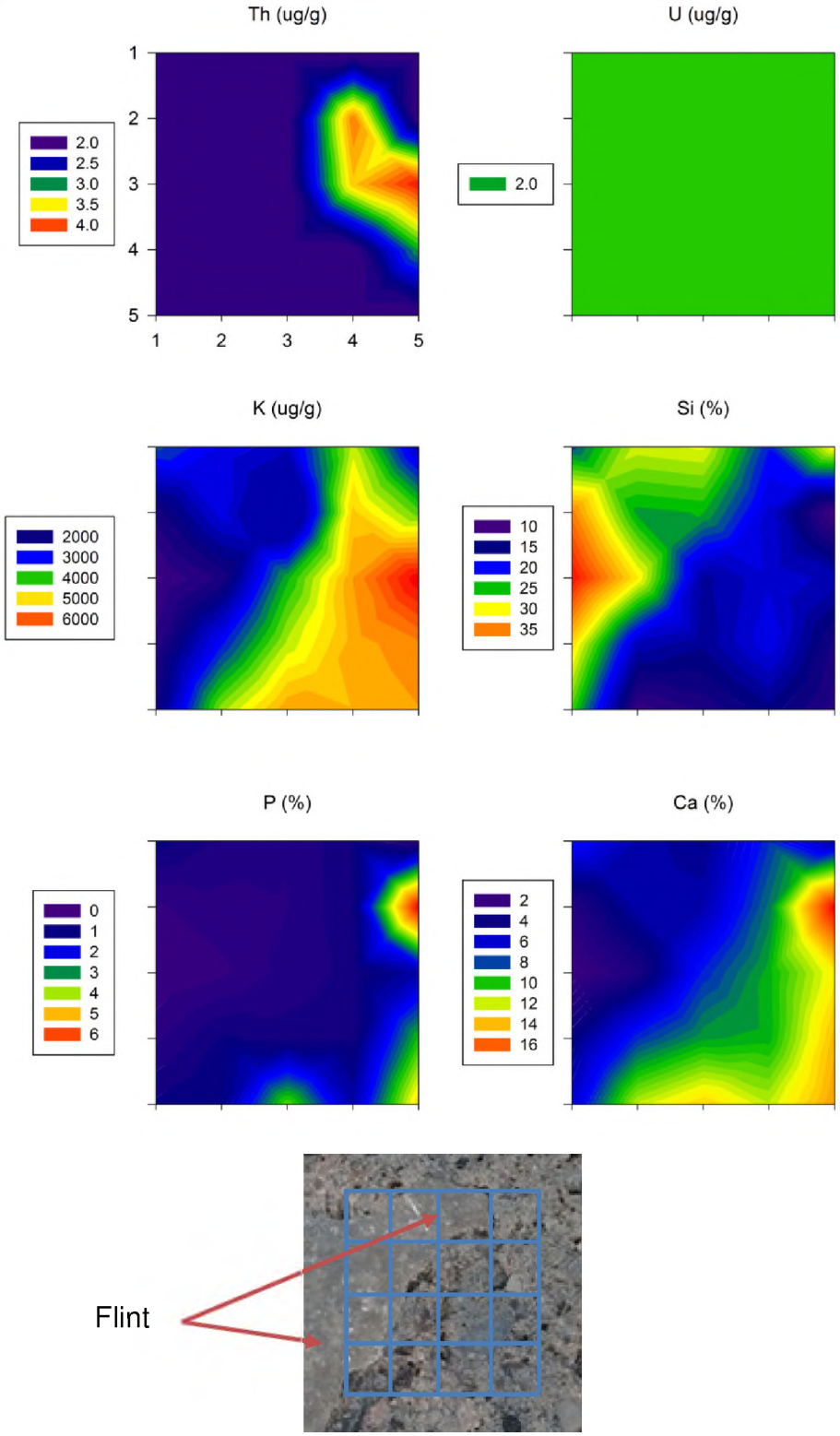

Figure 13.13. D-Lower-01 region of interest elemental distribution maps for Th, U, K, Si, P and Ca using the pXRF. Each region of interest measures 12 mm in length and width and covers an area of 5×5 measurement points.

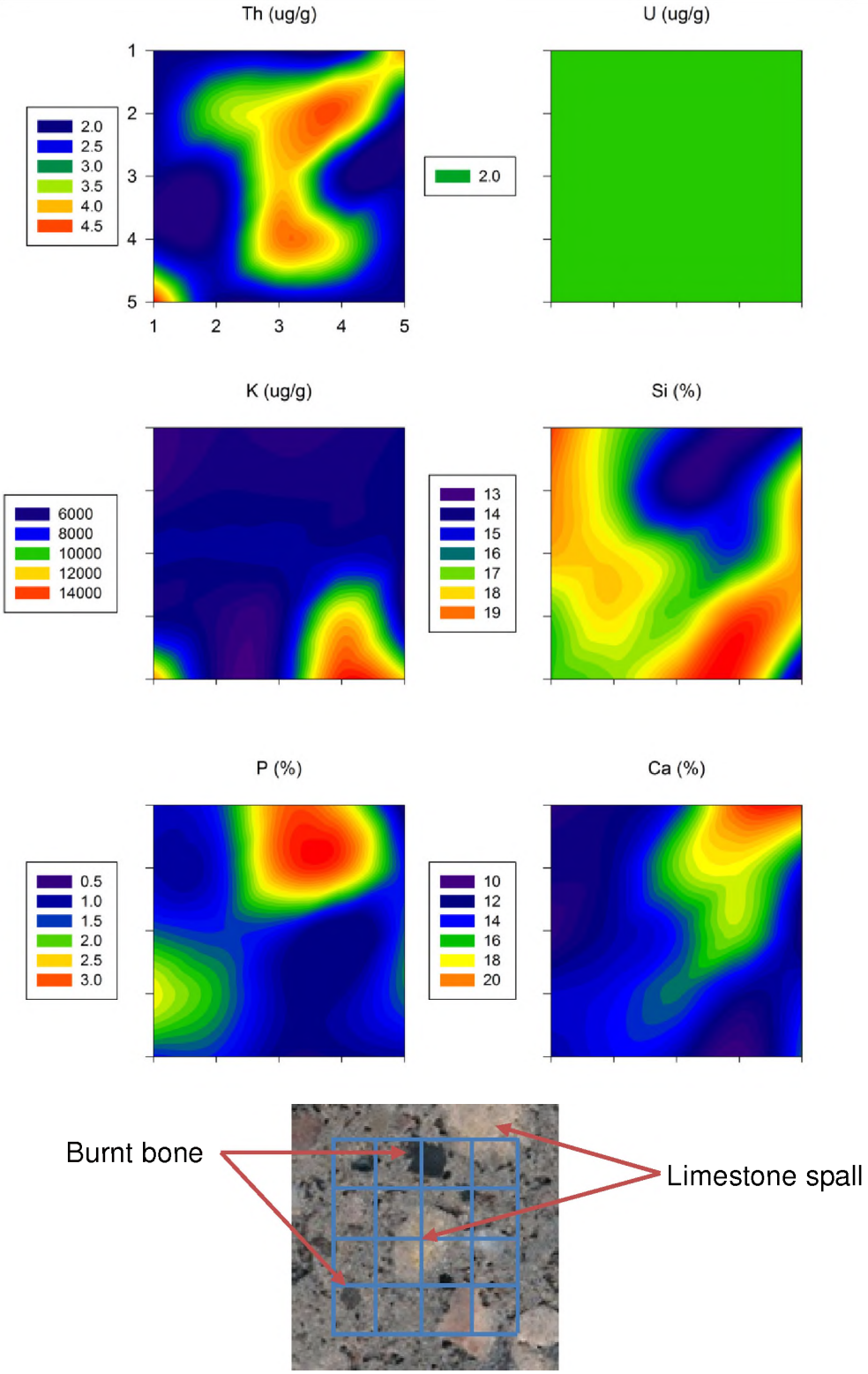

Figure 13.14. D-Lower-02 region of interest elemental distribution maps for Th, U, K, Si, P and Ca using the pXRF. Each region of interest measures 12 mm in length and width and covers an area of 5×5 measurement points.

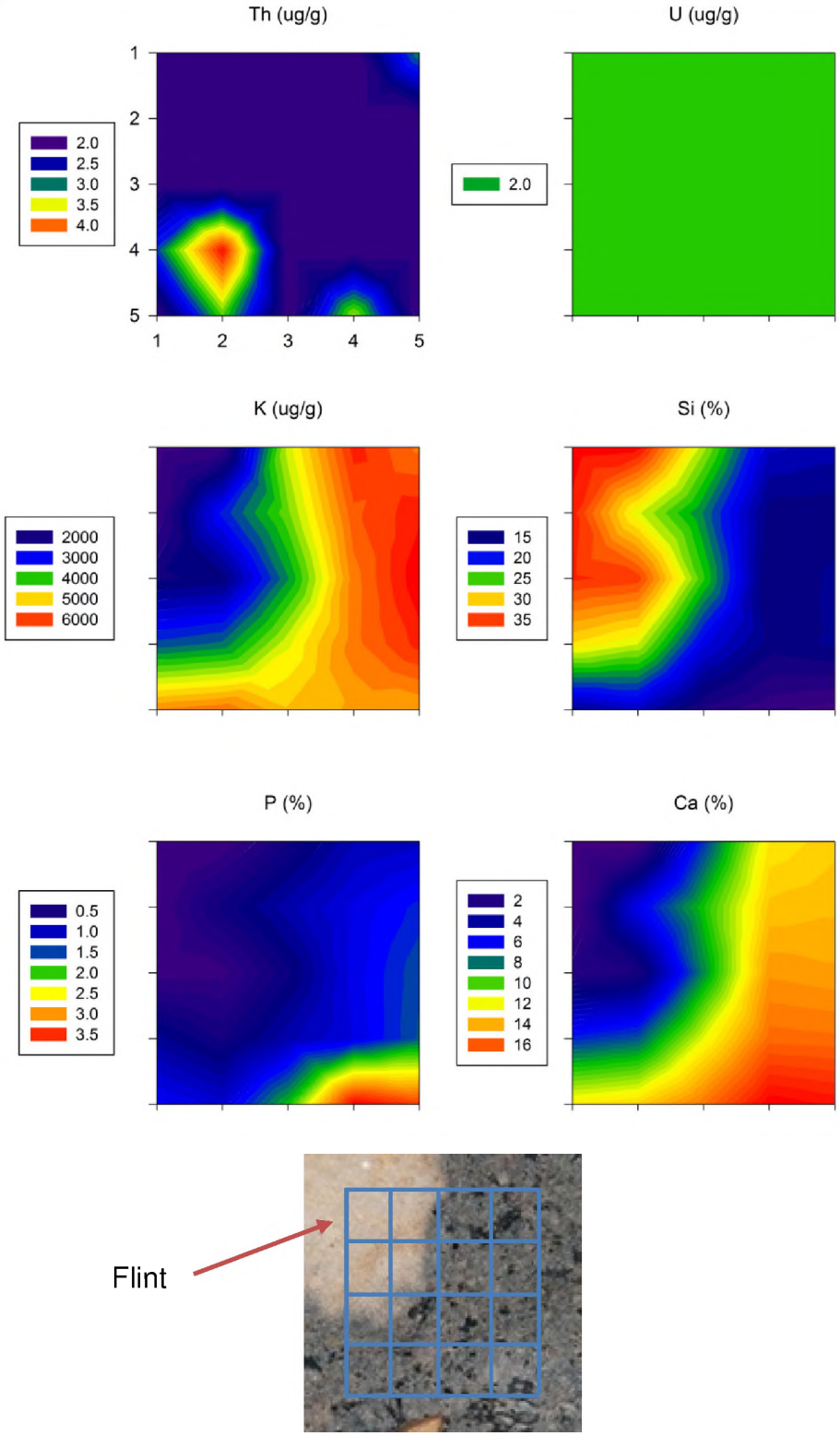

Figure 13.15. D-Upper-01 region of interest elemental distribution maps for Th, U, K, Si, P and Ca using the pXRF. Each region of interest measures 12 mm in length and width and covers an area of 5×5 measurement points.

Appendix V

The age of three Middle Palaeolithic sites: single-grain optically stimulated luminescence (OSL) chronologies for Pech de l'Azé I, II and IV (France)

Zenobia Jacobs[1], Nathan Jankowski[1], Harold L. Dibble[2,3,4], Paul Goldberg[5], Shannon P. McPherron[4], Dennis Sandgathe[6] & Marie Soressi[4,7]

[1] *Centre for Archaeological Science, School of Earth and Environmental Sciences, University of Wollongong, Wollongong, NSW, Australia 2522*

[2] *Department of Anthropology, University of Pennsylvania, Philadelphia, USA.*

[3] *Institute for Human Origins, Arizona State University, USA.*

[4] *Department of Human Evolution, Max Planck Institute for Evolutionary Anthropology, Leipzig, Germany.*

[5] *Department of Archaeology, Boston University, Boston, USA.*

[6] *Human Evolution Studies Program and Department of Archaeology, Simon Fraser University, Burnaby, Canada.*

[7] *Department of Human Origins, University of Leiden, The Netherlands.*

ABSTRACT

Optically stimulated luminescence (OSL) measurements were made on individual, sand-sized grains of quartz from Middle Palaeolithic deposits at three sites (Pech de l'Azé I, II and IV) located in the Dordogne region of France. We were able to calculate OSL ages for 70 samples collected from these three sites. These ages reveal periods of occupation between about 180 and 50 ka ago. Our single-grain OSL chronologies largely support previous age estimates obtained by TL dating of burnt flints at Pech IV, ESR dating of tooth enamel at Pech I, II and IV and ^{14}C dating of bone at Pech I and IV, but provide a more complete picture due to the ubiquitous presence of sand-sized quartz grains used in OSL dating. These complete chronologies for the three sites have allowed us to compare the single-grain ages for similar lithic assemblages among the three sites and test the correlations previously proposed by Bordes in the 1970s. We have also constructed a correlative chronological framework for the three different sites. This shows that similar lithic assemblages occur at around the same time, and that where a lithic assemblage is unique to one or two of the Pech sites, there is no chronological equivalent at the other Pech site(s). We interpret this to mean that, for these three Pech de l'Azé sites, the Mousterian variants show temporal ordering and represent chronological phases.

14.1INTRODUCTION

As one of the sites presented in the seminal work of Lartet & Christy (1875) in the mid-19th century, Pech de l'Azé I has earned its place in the development of the field of Palaeolithic archaeology. Around 150 years have now elapsed since that publication, and during this time many other sites in and around the Dordogne valley have been excavated, including three other Lower and Middle Palaeolithic locales in the immediate area of Pech de l'Azé I (Pech de l'Azé II-IV) (Bordes 1971, Soressi *et al.* 2007, Turq *et al.* 2011). Together, the Pech sites contain examples of most of the classic Mousterian "facies", or industrial variants and thus continue to play a vital role in debates concerning the nature and interpretation of Mousterian assemblage variability (e.g., Bordes 1977, Binford 1973, Rolland & Dibble 1990). With the advent of new dating techniques over the past several decades, numerical ages have been obtained from a large number of sites in southwest France, including the Pech sites, by a variety of methods (e.g., Vogel & Waterbolk 1967, Bowman & Sieveking 1983, Valladas *et al.* 1986, 1987, 1999, 2003, Mellars & Grün 1991, Falgueres *et al.* 1997, Guibert *et al.* 1997, 1999, 2008, Lahaye 2005, Guerin *et al.* 2012). Given the time-depth represented by the Pech archaeological deposits, it is not surprising that some of the earliest numerical ages for the French Mousterian have been obtained at these sites (e.g., Schwarcz & Blackwell 1983, Grün *et al.* 1991), or that these sequences are a continuing focus of attention for both archaeologists and geochronologists (e.g., McPherron & Dibble 2000, McPherron *et al.* 2001, 2012, Dibble *et al.* 2005, 2009, Soressi *et al.* 2007, 2013, Turq *et al.* 2011 Richter *et al.* 2013).

Prior to the present study, a number of dating studies have been undertaken at the Pech sites, including electron spin resonance (ESR) dating of tooth enamel on teeth collected from Pech I, II and IV (Grün *et al.* 1991, 1999, Soressi *et al.* 2007, Turq *et al.* 2011), thermoluminescence (TL) dating of burnt flint from Pech IV (Richter *et al.* 2013), radiocarbon (^{14}C) dating of charcoal and bone from Pech I and IV (Soressi *et al.* 2007, McPherron *et al.* 2012) and uranium-series dating of flowstones in the cave connecting Pech I and II and in deposits at Pech II (Schwarcz

& Blackwell 1983). Only three OSL ages have been reported for the Pech sites and that was for Pech I in Soressi *et al.* (2013) as part of the study fully presented here. At Pech I and II a single technique (ESR dating of tooth enamel) has been used to date the entire sequence. At Pech IV, no single technique was applied to the entire sequence; instead, different techniques have been used to date different portions of the deposit, with only a small amount of overlap. This is because animal teeth (for ESR dating) are not present in abundance in every layer, burnt flints (for TL dating) are only available in those layers where burning is evident, flowstones are rarely preserved in archaeological sections and may be too dirty for uranium-series dating, and most of the deposit is beyond the range of radiocarbon (^{14}C) dating.

In this study, we applied a single dating method to the sedimentary deposits at each of the Pech sites to provide a coherent chronology on a common time scale. We used single-grain OSL dating of quartz because quartz is ubiquitous in geological and archaeological deposits and has an OSL time range that can extend from a few years to a few hundreds of millennia. Because OSL dating can be applied to geological and archaeological sediments, it was also feasible to obtain a complete chronological sequence for these sites – even for those layers that do not contain any archaeological traces. By applying single-grain OSL dating to each and every layer, it is thus possible to discern the history of site formation at a temporal resolution that might allow periods of occupation to be distinguished from periods of site abandonment.

There is also an archaeological imperative to link these sites using a common chronological yardstick. The three Pech sites have lithic assemblages that vary significantly within each site (Pech II and IV), that show some similarities between sites (e.g., Pech I and the top of Pech IV), and that show unique variability (e.g., the Asinipodian at Pech IV). The question thus arises: does the assemblage variability both within and between the Pech sites represent different/similar periods in time or is it because the caves were used for different/similar purposes at the same time? This basic question concerning Mousterian variability remains unresolved with, on the one hand, some stratigraphic and palaeoenvironmental data suggesting that the Mousterian variants represent chronological phases (Mellars 1970, 1989, 1992,

Discamps 2013) while on the other, an increasingly large set of numerical ages have failed to support a chronological succession (e.g., Guibert *et al.* 2008, Richter *et al.* 2013). Although many numerical ages have been obtained for the Pech sites over the past few decades, the differing precisions and possible systematic biases in age determinations make it difficult to correlate the deposits with sufficient resolution based on previous dating evidence alone. A coherent and consistent chronology is required, therefore, to reliably compare the timing of the different artefact assemblages at each of the Pech sites and to overcome any distortion inevitably introduced by different dating methods.

Our goal, then, is to develop an OSL chronology for the three Pech sites that will be able to reveal when the lithic sequences for the three sites are broadly contemporaneous and when they are not. Though three sites are not enough to demonstrate Mousterian variability is chronologically structured, they can falsify the hypothesis. If similar Pech industries are not broadly contemporary or if, in a given time slot, there is significant lithic variability, then it suggests that the chronological phase argument for Mousterian variability cannot be supported. In doing this, we will also test previous correlations of the sites, which were made by Bordes (1975) on the basis of faunal and sedimentological evidence, linked to the Riss-Wurm climatic phase scheme.

14.2SITE BACKGROUND AND STRATIGRAPHY

The hill of Pech de l'Azé contains a complex of four separate late Middle Palaeolithic sites (Figure 1c), located in the Department of the Dordogne in southwest France, situated about 5 km southeast of the city of Sarlat (44°50'N, 1°14'E) (Figure 1a,b). The sites are positioned at the base of an Upper Cretaceous, Coniacian limestone cliff face (Goldberg *et al.* 2012), ~50 m above the valley floor of the Enéa River, a small tributary of the Dordogne River (Figure 1c). Pech I and II are on either side of a still existing karstic tunnel, and Pech IV is thought to be part of the same karst system, though not the same karstic tunnel (Turq *et al.* 2011) (note

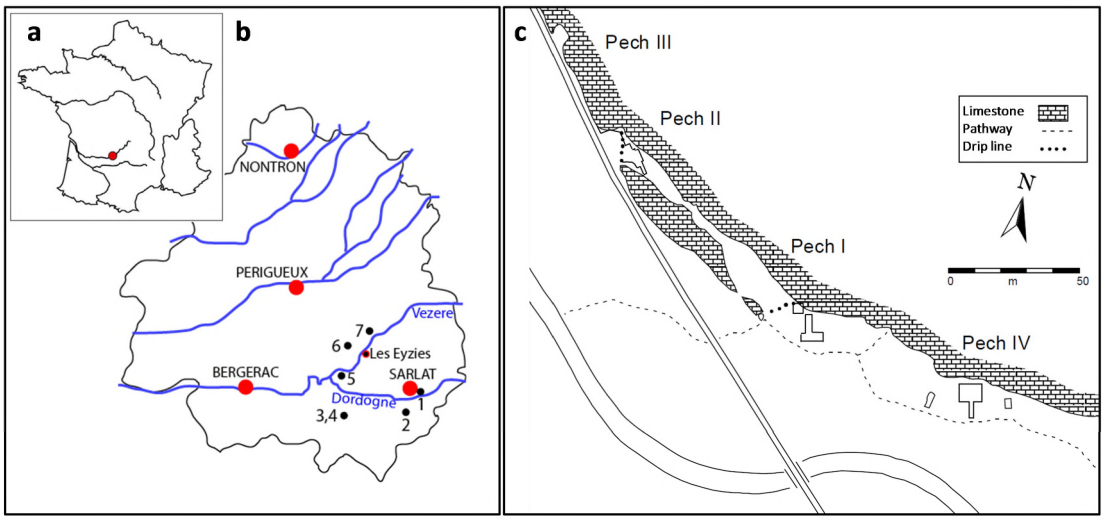

Figure 1. a) Map of France indicating the location of the Department of the Dordogne in southwest France. b) Map of the Dordogne area showing the location of several important site relative to known cities. 1 Pech de l'Azé, 2 Comb Grenal, 3 Comb Capelle Bas, 4 Abri Peyrony, 5 Roc de Marsal, 6 La Ferrassi, 7 Le Moustier. c) Schematic of the limestone cliff and the positions of the three Pech sites.

that Pech III is a small cave not far to the west of Pech II that is now empty of sediment). All three sites had a complex morphological evolution, including periods of cliff retreat and intense roof collapse that significantly changed the configuration of the sites over time (Texier 2009, Turq *et al.* 2011). Understanding the sedimentology and the site formation processes at each of these sites are important for OSL dating, as this directly impacts on what we are dating – the last time sedimentary grains of quartz were exposed to sunlight. The sedimentology and site formation of all three sites have been documented thoroughly in Bordes (1972), Laville (1973), Goldberg (1979), Texier (2009), Turq *et al.* (2011) and Soressi *et al.* (2013). A summary of the stratigraphy, associated archaeological industries and the main sedimentological features of each layer and for each site are provided in Tables 1a, 1b and 1c.

14.2.1 PECH I

Pech I was originally excavated in the early 19th century by Jouannet and later by the Abbé Audierne, followed by excavations in 1909 by Capitan & Peyrony, in 1929-30 by Vaufrey and from 1948 to 1951, and again from 1970 to 1971 by Bordes. In 2004 and 2005 limited excavations were conducted by M. Soressi on the witness section left by Vaufrey in 1930, which has been used as the reference sequence for the site since then. A schematic of the site, location of each of the excavations and the witness section are provided in Figure 2a.

The stratigraphy of Pech I consists of 7 levels (Table 1a; Bordes 1954-1955, Texier 2009). Levels 3-7 are all attributed to the Mousterian of the Acheulian Tradition (MTA). Peyrony used Pech I as one of the type sites to define the MTA (Peyrony 1925) and two variants of the MTA were later described, namely MTA Type A and MTA Type B (Bordes & Bourgon 1951). The MTA Type A is characterised by the production and use of mainly bifaces, whereas the MTA Type B is characterised by fewer bifaces and by the production and use of mainly backed knives and elongated flakes (Soressi 2004). Layers 4-7 are of interest in this study and, in general terms, consist of ~4 m thickness of deposit composed of very coarse blocks of collapsed limestone rubble embedded in a clayey sand matrix (Figure 2b,c). The sediment is mostly derived from the slopes and was deposited as slope-wash, together with continuous large cliff and roof collapse.

The archaeological assemblage in Layer 4 is attributed to the MTA Type A; during the 2004 excavation by Soressi, a juvenile Neandertal tooth was found confirming that the MTA Type A was made by Neandertals (Soressi *et al.* 2007). They also discovered a *lissoir*, a bone tool type likely used for polishing hides, previously thought to have only been made by modern humans and, thus, shedding light on the complexities of late Neandertal behaviour (Soressi *et al.* 2013). Layer 5 has a low density of artefacts of both MTA Types A and B. Layers 6 and 7 are both attributed to MTA Type B; the very top of Layer 7 (the top 1 m of the section), is archaeologically sterile (Figure 2c). During the 1909 excavations by Capitan

&Peyrony, a juvenile Neandertal skull and mandible were uncovered in Layer 6 (Figure 2a; Soressi *et al.* 2007), confirming that the MTA Type B was also made by Neandertals.

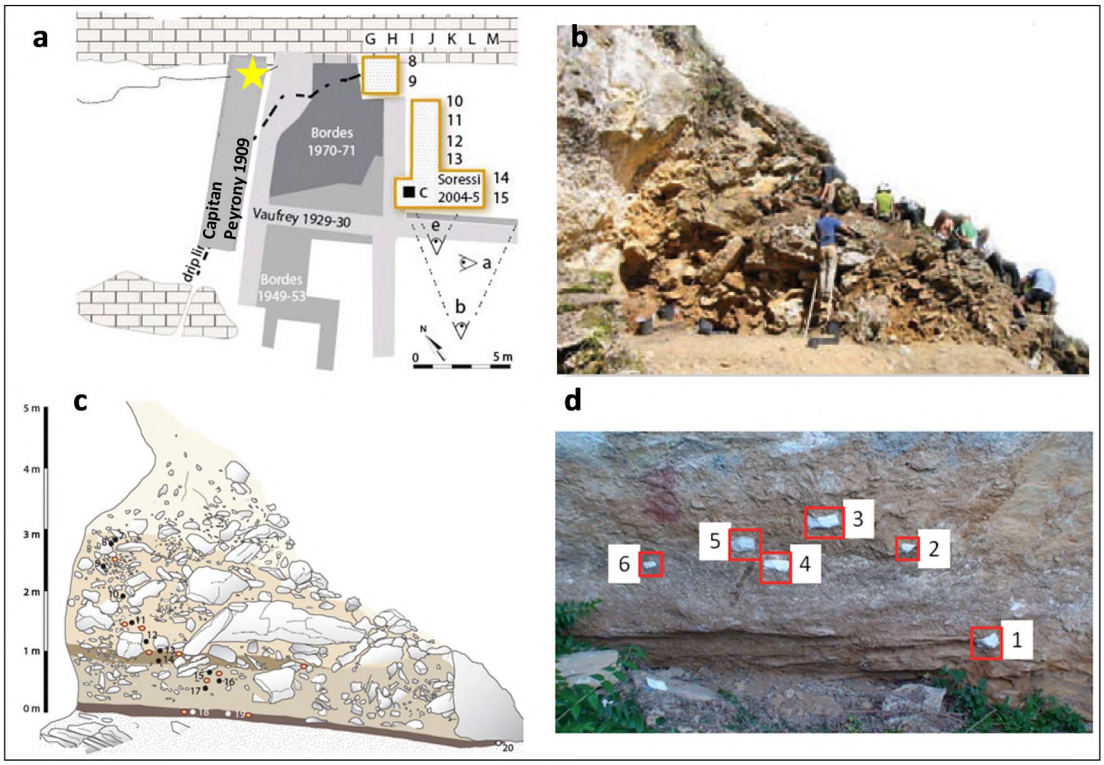

Figure 2: a) Planform map of the different excavations conducted at Pech I. The two areas of interest in this study is the witness section outlined in yellow and the Capitan and Peyrony excavation. The yellow star indicate the relative position from where the juvenile Neandertal baby skull and jaw was found. b) Photograph of the witness section. c) Schematic of the witness section showing the locations of the OSL samples (black filled circles) and gamma spectrometry holes (open red circles) of Rink, reported in Soressi et al. (2007). d) Close-up photograph showing the location of the OSL samples removed from the shelter wall left-over from, and directly related to the Capitan and Peyrony excavation.

Table 1a: Summary of the stratigraphic layers and archaeological industries found at Pech I. Also given is a short synopsis of the most important sedimentological information for each layer.

Stratigraphy	Archaeological Industry	Sedimentology
7	MTA-B	Sandy-clayey matrix; large limestone fragments; voids due to biological activity; carbonate features including calcite impregnation of sediment
6	MTA-B	
5	MTA-A/B	Sandy, slightly clayey sediment matrix; limestone fragments, flint and bone; bone and charcoal less abundant than in layer 4; biological activity in the form of root channels, earthworm casts and mite pellets; some biological voids filled post-depositionally with fine sands.
4	MTA-A	Poorly sorted silty-clayey sand; some limestone fragments, flint, burnt and unburnt bone and traces of charcoal. Clear combustion features towards south. Sediments are bedded, suggesting no significant post-depositional vertical movement of objects
3	MTA-A	Yellow sand; ash lenses
2	Sterile	Pavement of flat limestone slabs
1	Sterile	Light yellow fluvial sand; some small rock fragment near the top of the layer

14.2.2 PECH II

Pech II was excavated by Bordes between 1950 and 1969 (Bordes 1969, 1971, 1972, Bordes & Bourgon 1950, 1951, Laville *et al.* 1980). It contains a total of 5 m of sediment and karstic and associated rock weathering deposits, formed at the entrance of a small cave that penetrates a small tunnel, leading to Pech I at the opposite end of the tunnel (Figure 1b and Figure 3a). The Pech II sequence has previously been studied in detail, including aspects of sedimentology (Laville 1975, Laville *et al.* 1980, Goldberg 1979, Texier 2009), palynology (Paquereau 1969), fauna (Bordes & Prat 1965, Laquay 1981), and the associated archaeological

assemblages (Bordes 1971, 1975, Bordes & Bourgon 1951, Laville *et al.* 1980), but no recent excavations have taken place as was the case for Pech I and Pech IV. A plan map of the site is shown in Figure 3a together with a schematic of one of the sections that best represents the entire sequence (Figure 3d).

The stratigraphy of Pech II was described as 10 layers by Bordes (1972) and Laville (1973), with many of the layers also divided into sub-layers; these are summarised in Table 1b and shown in Figure 3d. Texier (2009) later re-defined the stratigraphy based on his sedimentological observations, and his layer assignations are also provided in Table 1b and Figure 3d. We chose to use the stratigraphic layers of Bordes (1972) because we used Laville's stratigraphic drawing provided in Goldberg (1979) to select our sample locations in order to match the layers with the archaeological industries as closely as possible. The sedimentary and archaeological sequences can be divided into two broad phases, those below and those above the large cryoclastic deposit in Layer 5 (Figure 3d). The deposits below were originally attributed to the Clactonian (Layers 6-8) and Acheulean (Layer 9) archaeological industries, whereas the deposits above comprise a range of different Mousterian facies, including Typical (Layers 3, 4A, 4B and 4D), Denticulate (Layer 4C) and Ferrassie Mousterian (Layer 2A-G).

14.2.3PECH IV

Pech IV was originally discovered in 1952 by F. Bordes, but the first major systematic excavation was not undertaken by him until 1970, and he continued work there for a total of eight years. The Pech IV stratigraphy was first described in a preliminary note by Bordes in 1975. Further investigations of the Bordes collection by McPherron & Dibble (2000) and a new field campaign directed by them from 2000-2003, led to a re-investigation of the site formation processes, sedimentology and stratigraphy. A detailed description of the new stratigraphic framework, and the methods used, are reported in Turq *et al.* (2011).

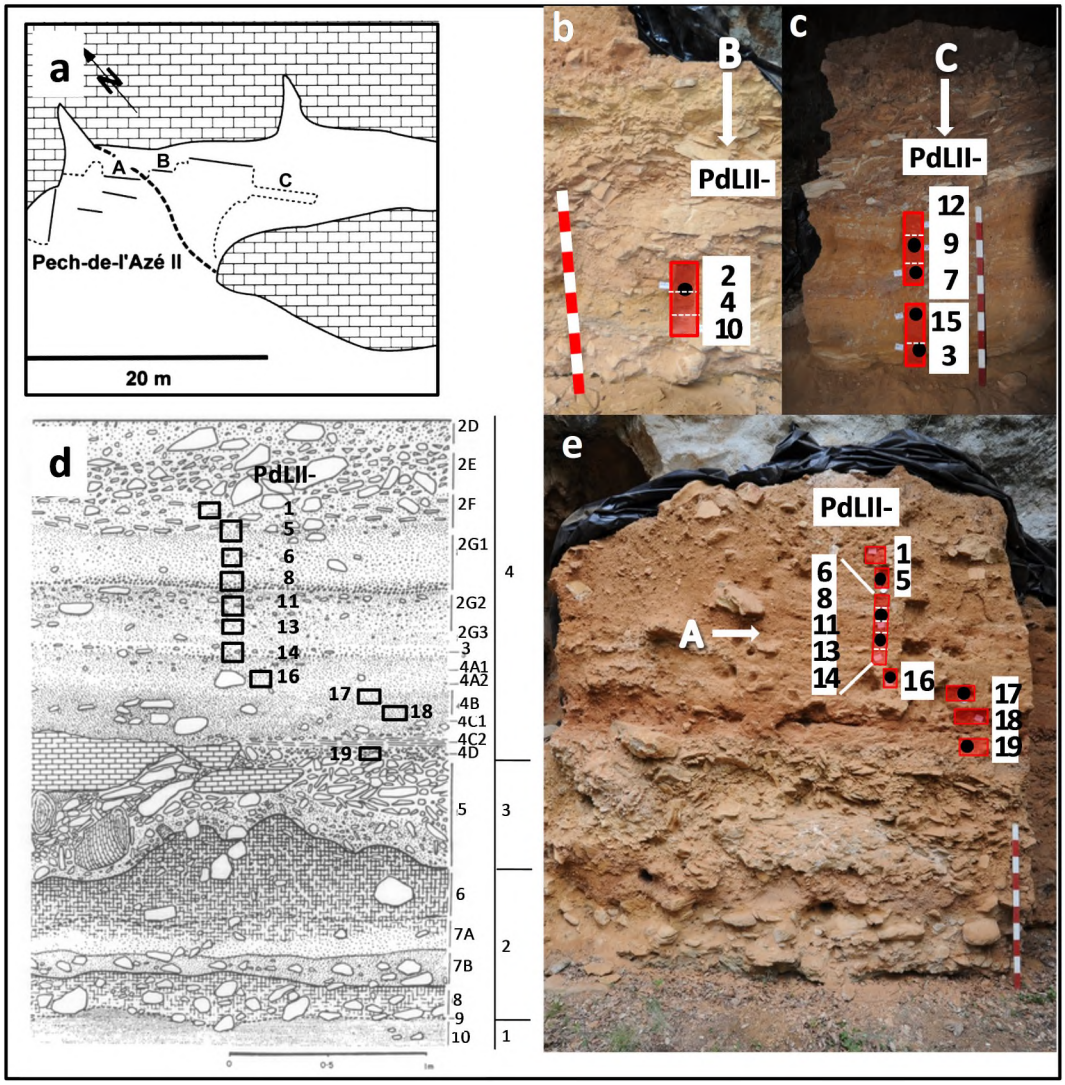

Figure 3: a) Planform map of Pech II, showing the location of the three profiles from which OSL samples were collected. b) Photograph of Profile B and the location of the OSL samples. C) Photograph of Profile C and the location of the OSL samples. d) Stratigraphic drawing of part of Profile A with the OSL sample locations indicated, together with the layer numbers following Bordes (1969) in the left-hand column and Texier (2009) in the right-hand column. e) Photograph of the profile in d) with the locations of the OSL samples. The red boxes denote the position of the OSL samples. The black filled circles show the position of the gamma spectrometry measurements.

Table 1b: Summary of the stratigraphic layers and archaeological industries found at Pech II. Also given is a short synopsis of the most important sedimentological information for each layer. Information on the archaeological industries was taken from Bordes (1972) and for the sedimentology from Bordes (1972), Laville (1972) and Goldberg (1979).

Stratigraphy (Bordes, 1972; Laville, 1973)	**Stratigraphy** (Texier, 2009)	**Archaeological Industry (Bordes, ?)**	**Sedimentology**
S			Modern soil, disturbed by rodents
1		Indeter.	Reddish sandy layer with small archaeological traces
2A	4	Ferrassie-type Mousterian (Levallois flakes and Quina-type scrapers)	Yellow sands with limestone fragments
2B			
2C			
2D			Sandy clay with rare limestone fragments
2E			Brown, clayey silty sand; numerous limestone fragments with sharp edges; smaller rock fragments
2F			Clayey, silty sand; with smaller flat limestone fragments
2G1			Slightly clayey sand with fine rock fragments; scattered limestone fragments in sands
2G2			Slightly clayey sand; discontinuous large and relatively rounded rock fragments
2G3			Clayey sand with small limestone fragments; very friable.
3		TM	Light brown, sandy-clay matrix; some limestone fragments
4A		TM	Reddish-brown, sandy clay, with rare limestone fragments. Some traces of fire
4B		Denticulate Mousterian	Red brown, sandy-clay; very hard when dry; numerous traces of fire
4C		TM	Alternation of clay-like sands and brown clay; numerous traces of fire
4D		TM	Clayey-sand matrix; small rounded rock fragments
5	3	Sterile	Cryoclastic complex; thick layer of large rock fragments, fining upwards; archaeologically almost sterile; stalagmite fragments throughout.
6	2	Clactonian	Brown red sandy silty clay; altered rock fragments and clay coatings
7A		Clactonian	Brown sand with some clay; limestone fragments are rare
7B		Clactonian	Yellow brown sand; more clay than in 7A; some rounded rock fragments.
8		Clactonian	Thin reddish silt (palaeosol (?)); brown clayey sand; well rounded rock fragments.
9		Acheulean	Brown sand, clayey in some areas where not cemented; rounded limestone fragments
10	1	Sterile	Sterile cross-bedded and horizontal fluvial sand; some rounded gravel and iron rich pebbles.

The stratigraphy and basic sedimentological features of each of the layers are summarised in Table 1c. A planform map of the site is shown in Figure 4a together with a schematic representation of the stratigraphy for the west wall (Figure 4b). The archaeological assemblage is comprised of a range of different Mousterian traditions, including Typical Mousterian (Layers 8 and 5), the Asinipodian (Layer 6), the Quina Mousterian (Layer 4A) and the MTA (Layer 3). At the time of deposition of the basal Layer 8, the site was a cave rather than a rock shelter (Goldberg *et al.* 2012), and this layer represents a period of intense anthropogenic activity. The layer is distinctly different from all the other layers in that it consists of numerous hearth features that together give the layer a black and burnt appearance (Dibble *et al.* 2009, Goldberg *et al.* 2012). The first major collapse of the cave roof occurred on top of Layer 7, marked by the presence of a layer of limestone slabs that created a physical and chemical barrier, preserving Layers 7 and 8. This collapse resulted in a more open configuration of the site. A significant break in sedimentation is found between Layers 6 and 5 in the form of a sharp and irregular contact, and the culmination of the collapse of the cave ceiling over the cave mouth occurred at the end of Layer 5 and beginning of Layer 4, resulting in a further enlargement of the cave aperture. The previously poorly-illuminated and sheltered cave is now thought to have become open to the elements and is more akin to a rock shelter (Turq *et al.* 2011). A sharp erosional contact separates Layer 4 from Layer 3; cryoturbation is believed to have been the process responsible for the truncation of Layer 4A. Layer 3 is the last of the layers to contain *in situ* archaeological materials and is overlain by Layer 2 that is only present along the western section. After deposition of Layer 2, a complete collapse of the cave awning occurred and effectively sealed and preserved the site and archaeological sequence. Layer 1 was formed much later in time and is the result of colluvial processes, migrating slowly downhill, mantling the collapsed roof deposit of the site.

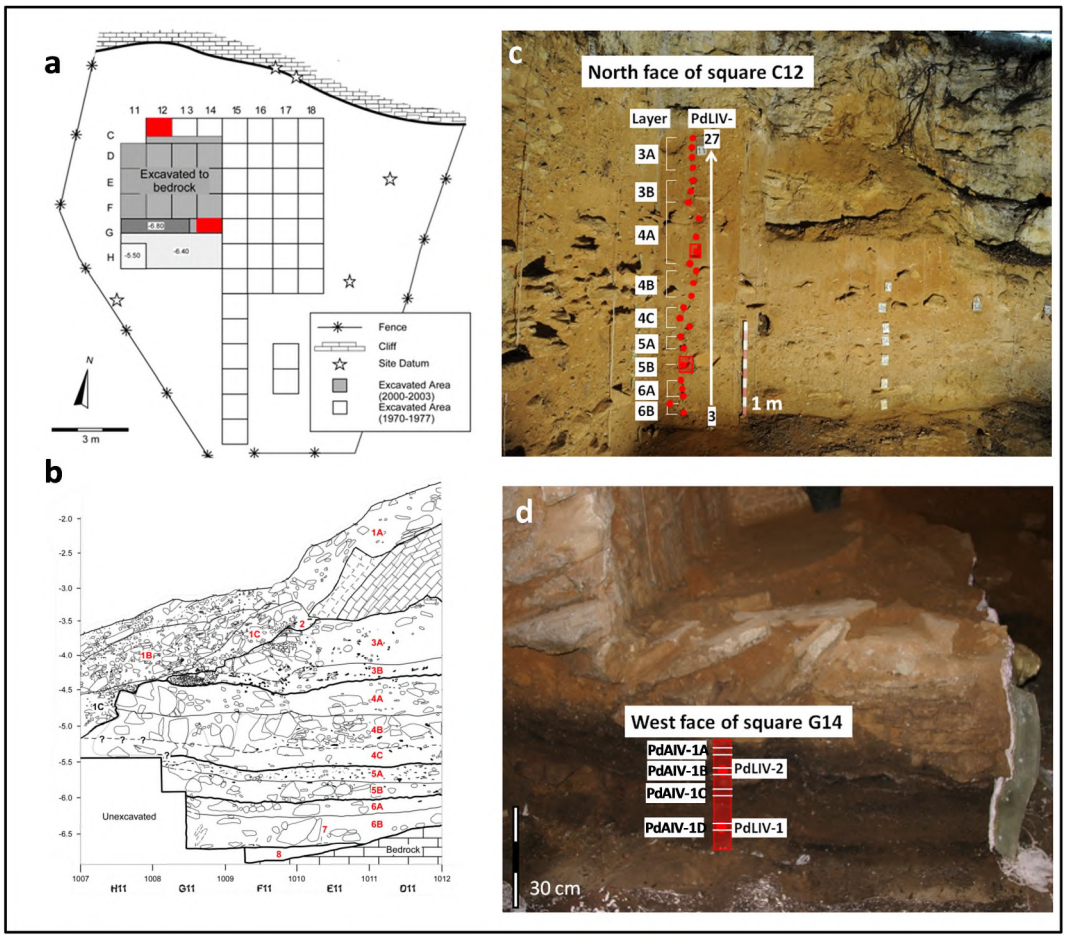

Figure 4: a) Planform map of Pech IV. The two red squares indicate the two squares from which all OSL samples were collected. b) Stratigraphic drawing of the west profile showing the layer numbers and relative depth of the deposit. c) Photograph of the profile from which the majority of the OSL samples were collected together with the layer number and sample numbers. d) Photograph of the profile from which all OSL samples from Layer 8 were collected. The red filled circles indicate the OSL samples, whereas the red square indicate the block sample that were later sub-sampled for OSL dating in the lab. The white lines denote the areas sub-sampled and their corresponding sample names.

Table 1c: Summary of the stratigraphic layers and archaeological industries found at Pech IV. Also given is a short synopsis of the most important sedimentological information for each layer. All information was taken from Turq et al. (2012).

Stratigraphy	Archaeological Industry	Sedimentology
1	None	Part of modern soil profile. Dark brown, organic rich silty to sandy layers with rounded and dissolving limestone fragments.
2	None	Spatially restricted unit of rounded pebbles, and limestone fragments in a sandy, silty matrix.
3A	MTA-B	Red/yellow silty-sand with limestone fragments more compacted and less cemented than underlying layer 4. Limestone fragments are rounded and appear to be dissolved.
	MTA-A/B	
3B	MTA-A	Red/yellow silty-sand with limestone fragments more compacted and less cemented than underlying layer 4. Limestone fragments are rounded and appear to be dissolved.
4A	Quina	Red/yellow silty-sand with limestone fragments. Strongly cemented with calcite in some regions produced a breccia.
4B	TM	Red/yellow silty-sand with greater concentration of limestone fragments than the overlying 4A layer.
Vault collapse		Limestone slabs and blocks
4C	TM	Silty-sand with higher concentrations of small eroded limestone fragments and bone fragments.
5A	TM	Red/yellow silty-sand with angular limestone blocks
5B		Red/yellow silty-sand with limestone fragments, some of which are well-rounded.
6A	Asinipodian	Dark brown to red/yellow silty-sand with large block of limestone occurring in the upper portion
6B		Silty-sand with varying sizes of limestone blocks
Roof collapse		Limestone slabs and blocks
7	?Mousterian	Thin layer of coarse sand with edge damaged stone tools.
8	Typical Mousterian	Black, bedded clayey-sand with major organic anthropogenic component. Charcoal and ash lenses with burnt and unburnt bone fragments.

14.3AGE DETERMINATION BY OSL DATING

OSL dating has been the 'workhorse' in this study because it is able to generate accurate and precise ages over the time span of interest and it provides a means of determining burial ages for sediments and associated artefacts (Huntley *et al.* 1985, Aitken 1998, Duller 2004, Lian & Roberts 2006, Jacobs & Roberts 2007, Wintle

2008). The method is based on the time-dependent increase in the number of trapped electrons induced in mineral grains (such as quartz) by low levels of ionising radiation from the decay of natural uranium, thorium and potassium in the surrounding deposits and from cosmic rays. The time elapsed since the light-sensitive electron traps were emptied can be determined from measurements of the OSL signal – from which the 'equivalent dose' (D_e) is estimated – together with determinations of the radioactivity of the sample and the material surrounding it to a distance of ~30 cm (the 'dose rate'). The OSL 'clock' is reset by just a few seconds of exposure to sunlight. The D_e divided by the dose rate gives the burial time of the grains in calendar years before present, enabling a direct comparison with other numerical age estimates (including calibrated ^{14}C ages and TL, ESR and uranium-series ages). Tests on known-age samples have shown that accurate OSL ages can be obtained from a wide variety of depositional environments (Rittenour 2008) — including cave and rockshelter sediments, which are the focus of this study — provided that appropriate OSL signals are measured and rigorous procedural checks are made.

14.4SAMPLING FOR OSL DATING

Sixty-seven samples were collected for OSL dating from the three sites. Both archaeological and non-archaeological layers were sampled, the latter to provide additional chronological and contextual information. All samples were collected in a manner that prevents inadvertent exposure of the sediment to sunlight that will reset the luminescence 'clock'.

We collected 21 OSL samples from Pech I at night using a red light for illumination. All OSL samples from the witness section (PdLI-7-20) (Figure 2b,c) were excavated using a trowel and/or auger. The samples collected from the rockshelter wall (PdLI-0-6) (Figure 2d), above the Capitan & Peyrony/Bordes excavations (Figure 2a), were stabilised with plaster bandages, and then cut out with a knife at night. The location of each of the OSL samples is shown in Figure 2c, and their positions were also recorded by total station relative to the site datum.

We collected 19 samples from Pech II all during the day. The locations of each of the samples are shown in Figure 3. All samples were collected as blocks of sediments that were stabilised with plaster bandages and cut out using a knife (shown as red squares in Figure 3 where the broken white line indicates the border between samples taken in a continuous column).

We also collected 30 samples from Pech IV all at night using a red light. The location of the two squares (C12 and G15) from which the samples were collected is shown in Figure 4a as red squares, and the location of each of the samples is shown in Figures 4c and 4d. We did not collect a sample from Layer 7 and the samples from Layer 8 are not part of the same continuous column of samples collected from the north face of square C12; instead, we collected the Layer 8 samples from the thickest extent of this layer further to the south into the west face of square G14 (Figure 4d). The section faces were cleaned prior to sample collection to remove light-exposed grains. All samples were excavated using a trowel and placed into a plastic bag. Three samples (PdAIV-1, 2 and 3) were collected as blocks of sediment that were stabilised with plaster bandages and cut out using a knife (shown as red squares in Figure 4c and 4d). One of these samples (PdAIV-1) was further sub-sampled into four samples (PdAIV-1A to 1D). All sample positions were recorded by total station relative to the site datum. Both types of samples were sealed in black plastic bags to prevent light exposure during transport to the laboratory.

In the OSL dating laboratory at the University of Wollongong, the sample bags were opened under dim red light. Where samples were collected as intact sediment blocks, these samples were kept as undisturbed sediment blocks and sub-sampled in the laboratory for OSL measurement. The remainder of the blocks were impregnated with resin and thin sections were made for further study of the sediments. Quartz grains were then extracted from the OSL samples using standard preparation procedures (Wintle 1997, Aitken 1998). First, carbonates were dissolved in 10% hydrochloric acid and then organic matter was oxidised in 30% hydrogen peroxide solution. The remaining sample was dried and then sieved to isolate grains of 180-212 μm in diameter, and feldspar, quartz and heavy minerals were separated by density using sodium polytungstate solutions of 2.62 and 2.70 specific gravities,

respectively. The separated quartz grains were etched with 48% hydrofluoric acid for 40 min to remove the alpha-irradiated rind of each quartz grain and to destroy any remaining feldspars, and then rinsed in hydrochloric acid to remove any precipitated fluorides, dried and sieved again; grains retained on the 180 µm diameter mesh were used for dating.

14.5EQUIVALENT DOSE DETERMINATION AND RESULTS

D_e values were estimated for individual 180-212 µm in diameter sand-sized grains for all samples from all three sites. We used the standard Risø single grain aluminium discs (Bøtter-Jensen *et al.* 2000) for measurement of all individual grains, and confirmed the presence of only one grain in each hole after measurement by systematically checking each disc under a microscope.

All measurements were made in an identical manner and with the same equipment, using the single aliquot regenerative-dose (SAR) procedure described elsewhere (e.g., Murray & Wintle 2000, Jacobs *et al.* 2008). The SAR procedure involves measuring the OSL signals from the natural (burial) dose and from a series of regenerative doses (given in the laboratory by means of a calibrated $^{90}Sr/^{90}Y$ beta source), each of which was preheated at 180°C for 10 s prior to optical stimulation by an intense, green (532 nm) laser beam for 2 s at 125°C. The resulting ultraviolet OSL emissions were detected by an Electron Tubes Ltd 9235QA photomultiplier tube fitted with Hoya U-340 filters. A fixed test dose (~10 Gy, preheated at 180°C for 5 s) was given after each natural and regenerative dose, and the induced OSL signals were used to correct for any sensitivity changes during the SAR sequence. A duplicate regenerative dose was included in the procedure, to check on the adequacy of this sensitivity correction, and a 'zero dose' measurement was made to monitor the extent of any 'recuperation' induced by the 180°C preheat. As a check on possible contamination of the etched quartz grains by feldspar inclusions, we also applied the OSL IR depletion-ratio test (Duller 2003) to each grain at the end of the SAR sequence, using an infrared exposure of 40 s at 50°C.

The D_e values were estimated from the first 0.22 s of OSL decay (see Figure S7 for example decay curves), with the mean count recorded over the last 0.3 s being subtracted as background. The dose-response data were fitted using a saturating exponential function with an extra linear term, and the sensitivity-corrected natural OSL signal was projected on to the fitted dose-response curve to obtain the D_e by interpolation (see Figure S8 for example dose response curves). The uncertainty on the D_e estimate of each grain (from photon counting statistics, curve fitting uncertainties, and an allowance of 2% per OSL measurement for instrument irreproducibility) was determined by Monte Carlo simulation, using the procedures described by Duller (2007) and implemented in Analyst version 3.24. The final age uncertainty also includes a further 2% (added in quadrature) to allow for any bias in the beta source calibration; this error is added as a systematic uncertainty. The $^{90}Sr/^{90}Y$ beta source was calibrated using a range of known gamma-irradiated quartz standards for individual grain positions. Spatial variations in beta dose rate for individual grain positions were taken into account, based on measurements made using the same gamma-irradiated quartz standards (e.g., Ballarini *et al.* 2006). A relative error of 2.8% was added, in quadrature, to the combined random error of each grain to capture the uncertainty associated with the calibration of the individual grain positions for the machine used in this study. The calibration of each grain position is based on multiple estimates of D_e from different grains that received a gamma dose that are then combined to obtain one value using the central age model of Galbraith *et al.* (1999). It is the relative error associated with the combined D_e value that is added as a random error to the D_e of each grain.

Details of the dose recovery and preheat plateau tests to determine the preheat conditions for measurement of the grains are provided in Supplementary Information.

Of all the individual grains measured from all three sites (Pech I - N = 22,900; Pech II – N = 32,900; Pech IV – N = 57,900), only a very small number of grains (N = 1314, 1973 and 2403, respectively) were used for final D_e determination. Aberrant grains were rejected using the quality-assurance criteria described and tested previously (Jacobs *et al.* 2006a). Tables S2, S3 and S4 provide the details for all

samples from all three sites and the reasons for why single grains were rejected. A discussion and examples of why grains have been rejected are provided in Supplementary Information.

The majority of grains (on average ~90%) were rejected because they were too dim following a laboratory dose (T_N signal<3xBG) or the test dose signal was imprecisely known (>20% error on test dose signal). From the ~10% grains that gave a measureable luminescence signal, ~20-30% of the grains were routinely rejected because they were sensitive to infrared radiation, failed the OSL-IR depletion ratio of Duller (2003) and gave D_e values that were half that obtained from quartz grains that behaved in an expected manner (see Figure S5 and S6). Further discussion is provided in Supplementary Information.

The D_e values for the accepted grains are displayed as radial plots in Figure S9 (Pech I), Figure S10 (Pech II) and Figure S11 (Pech IV) for each of the samples. One representative example from each site is also shown in Figure 5a-c. All the single grain D_e distributions are spread more widely than can be explained by measurement uncertainties alone. The single-grain D_e distributions are overdispersed by between 16 ± 2 (PdLI-20) and 53 ± 7% (PdLI-10) for samples from Pech I (Table 2), between 25 ± 3 (PdLII-6) and 40 ± 4% (PdLII-14) for samples from Pech II (Table 3), and between 17 ± 5 (PdLIV-13) and 39 ± 4% (PdLIV-2) for samples from Pech IV (Table 4). There are no discrete patterning observed in any of the distributions that allows us to resolve post-depositional mixing or partial bleaching; all distributions are scattered randomly around a central value of D_e (Figure S9-11). We interpret the spread to be predominantly the result of differences in the intrinsic behaviour of the grains, heterogeneity in the beta-dose delivered to individual grains of quartz and also small-scale disturbances by soil fauna and flora in some of the samples that may mix stratigraphically adjacent sediment through burrowing and root penetration. Investigation of thin sections of stratigraphically equivalent samples for Pech IV, and from the same sample positions for sample PdLI-1 to -6 and all the PdLII samples support the possible effects from the latter two factors.

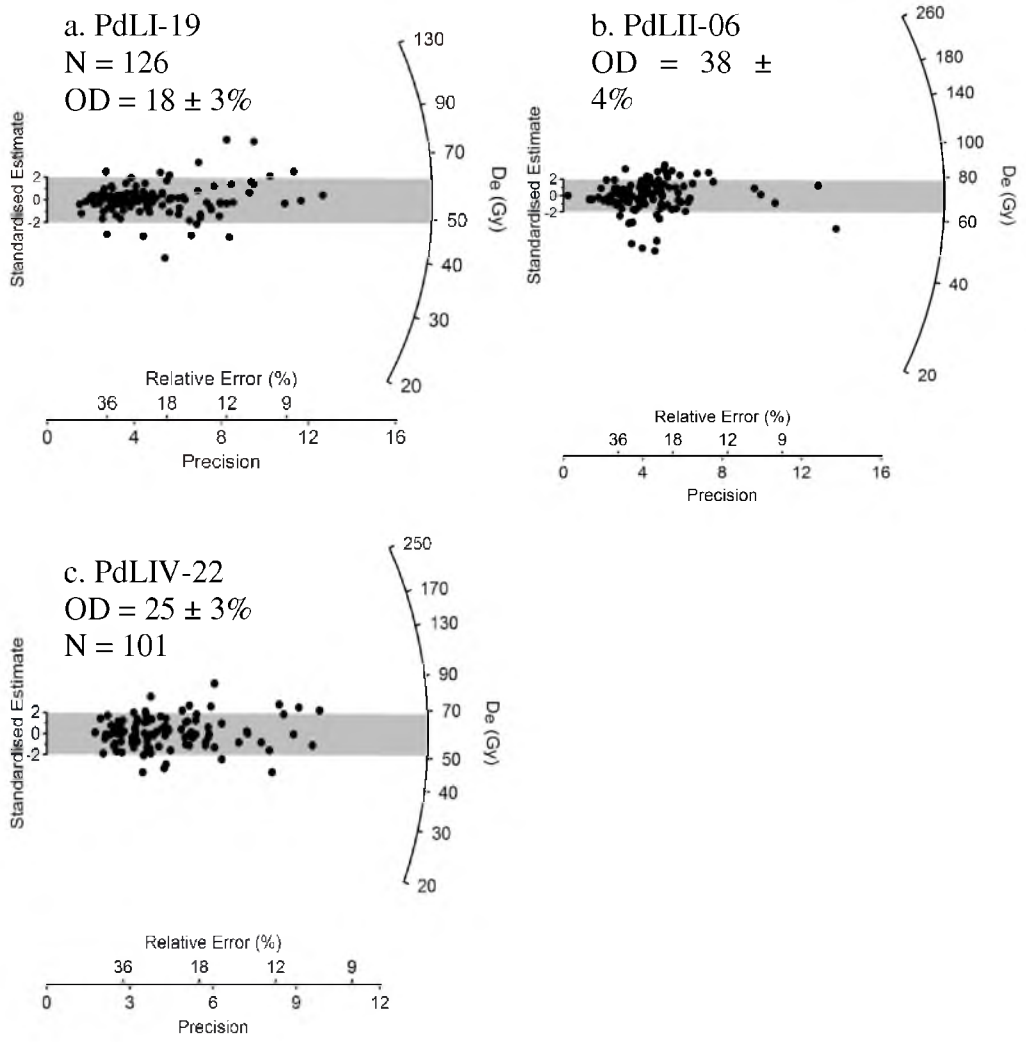

Figure 5: Radial plots of single-grain De distributions for a representative samples measured from a) Pech 1, b) Pech II and c) Pech IV. If the D_e estimates in each distribution were statistically consistent (at 2σ) with a common value, then 95% of the points should fall within any grey band projecting ± 2 units from the standardised estimate axis and the overdispersion (OD) should be consistent with 0%. The grey band is centred on the CAM weighted mean D_e value.

Since we cannot resolve any discrete and large-scale post-depositional mixing in any of our samples, we used the central age model (CAM) of Galbraith *et al.* (1999) to combine the single-grain D_e values meaningfully for all samples in order to obtain the most accurate estimate of D_e for age calculation. The CAM model

assumes that the D_e values for all grains are centred on some average value of D_e (similar to the median) and the estimated standard error takes account of any overdispersion (i.e., the greater the overdispersion, the larger the error) (Galbraith *et al.* 1999). Information about the number of grains measured and used, overdispersion values calculated and the final $D_e \pm 1\sigma$ value for each sample is presented in Tables 2, 3 and 4 for Pech I, Pech II and Pech IV, respectively.

14.6DOSE RATE DETERMINATION AND RESULTS

The total dose rate consists of contributions from beta, gamma and cosmic radiation external to the grains, plus a small alpha dose rate due to the radioactive decay of U and Th inclusions inside sand-sized grains of quartz. To calculate the OSL ages, we have assumed that the measured radionuclide activities and dose rates have prevailed throughout the period of sample burial.

An internal alpha dose rate of 0.032 ± 0.01 Gy/ka has been assumed for all samples.

We have estimated the beta dose rates directly by low-level beta counting of dried, homogenised and powdered sediment samples in the laboratory, using a GM-25-5 multi-counter system (Bøtter-Jensen and Mejdahl, 1988). We have measured all samples in triplicate. The pots were filled to the brim with sediment and left on the bench for 3-4 weeks prior to measurement to allow equilibration of any ^{222}Rn gas with its parent nuclides that may have escaped during the preparation process. For all samples, allowance was made for the effect of sample moisture content (Aitken 1985), as well as grain size (Mejdahl 1979) and hydrofluoric acid etching (Bell & Zimmerman 1978) on beta-dose attenuation.

Table 2: Dose rate data, equivalent doses and OSL ages for sediment samples from Pech de l'Aze I. Also provided are the weighted mean ages for each layer.

Sample code	Moisture content (%)	Dose rates (Gy/ka) Beta	Gamma	Cosmic	Total dose rate (Gy/ka)	D_e (Gy)	Number of grains	Over-dispersion (%)	Optical age (ka)	
Level 7										
PdLI-7	7.4	0.52 ± 0.04	0.43 ± 0.02	0.11	1.08 ± 0.06	51.0 ± 1.9	62 / 1000	20 ± 3	47.2 ± 3.4 (2.9)	
PdLI-8	4.9	0.53 ± 0.04	0.36 ± 0.02	0.11	1.03 ± 0.06	52.6 ± 2.3	73 / 1000	31 ± 4	51.3 ± 3.8 (3.0)	
PdLI-9	1.3	0.48 ± 0.03	0.23 ± 0.01	0.10	0.84 ± 0.04	38.8 ± 2.0	47 / 1000	26 ± 5	46.3 ± 3.4 (2.9)	
PdLI-10	1.9	0.53 ± 0.03	0.26 ± 0.01	0.10	0.93 ± 0.05	46.1 ± 4.5	36 / 1000	53 ± 7	49.7 ± 5.5 (3.4)	
PdLI-11	3.3	0.58 ± 0.04	0.26 ± 0.01	0.10	0.97 ± 0.06	50.2 ± 2.4	55 / 1000	26 ± 4	51.8 ± 4.0 (3.2)	
							Weighted mean =		***49.1 ± 2.9*** (1.4)	$P = 0.78$
PdLI-3	0.5	0.56 ± 0.03	0.39 ± 0.06	0.08	1.06 ± 0.09	54.6 ± 2.8	64 / 1000	36 ± 4	51.7 ± 5.3 (4.6)	
PdLI-2	2.3	0.72 ± 0.04	0.34 ± 0.05	0.08	1.17 ± 0.09	55.4 ± 2.5	63 / 1000	30 ± 4	47.2 ± 4.3 (3.6)	
PdLI-5	3.6	0.75 ± 0.04	0.37 ± 0.06	0.08	1.22 ± 0.10	56.5 ± 3.0	61 / 1000	34 ± 4	46.3 ± 4.5 (3.9)	
							Weighted mean =		***48.0 ± 3.5*** (2.5)	$P = 0.74$
							Grand weighted mean =		***48.8 ± 2.8*** (1.2)	$P = 0.83$
Level 6										
PdLI-12	3.4	0.56 ± 0.04	0.31 ± 0.02	0.12	1.03 ± 0.05	54.7 ± 3.2	43 / 1000	25 ± 6	53.3 ± 4.3 (3.8)	
PdLI-13	2.4	0.54 ± 0.03	0.31 ± 0.02	0.13	1.01 ± 0.05	47.6 ± 3.9	46 / 1000	33 ± 5	47.3 ± 4.6 (4.2)	
PdLI-14	2.8	0.55 ± 0.04	0.34 ± 0.02	0.13	1.04 ± 0.05	56.9 ± 3.2	41 / 1000	38 ± 6	54.6 ± 4.3 (3.6)	
							Weighted mean =		***52.1 ± 3.2*** (2.3)	$P = 0.61$
PdLI-4	1.6	0.57 ± 0.03	0.30 ± 0.05	0.08	0.98 ± 0.08	51.8 ± 2.3	63 / 1000	40 ± 5	52.8 ± 4.9 (4.1)	
							Grand weighted mean = 52.2 ± 3.1 (1.4)			$P = 0.77$
Level 5										
PdLI-15	1.1	0.52 ± 0.03	0.36 ± 0.02	0.13	1.04 ± 0.05	54.7 ± 2.6	53 / 1000	33 ± 5	52.3 ± 3.8 (3.2)	
PdLI-16	1.0	0.55 ± 0.04	0.36 ± 0.02	0.13	1.07 ± 0.06	57.8 ± 3.1	57 / 1000	34 ± 4	53.8 ± 4.2 (3.5)	
PdLI-17	2.0	0.58 ± 0.04	0.54 ± 0.03	0.11	1.26 ± 0.06	68.0 ± 3.3	63 / 1000	31 ± 4	54.2 ± 3.9 (3.4)	
							Weighted mean =		***53.4 ± 2.9*** (2.1)	$P = 0.94$
PdLI-1	4.2	0.66 ± 0.04	0.35 ± 0.05	0.08	1.12 ± 0.09	58.2 ± 2.2	87 / 1000	30 ± 3	52.2 ± 4.9 (4.1)	
							Grand weighted mean = 53.2 ± 2.9 (1.9)			$P = 0.99$
Level 4										
PdLI-18	4.0	0.55 ± 0.03	0.63 ± 0.03	0.08	1.29 ± 0.07	67.6 ± 2.1	90 / 2000	17 ± 3	52.5 ± 3.4 (2.7)	
PdLI-19	3.6	0.48 ± 0.03	0.52 ± 0.03	0.08	1.11 ± 0.06	55.4 ± 1.4	126 / 1900	18 ± 3	50.0 ± 3.1 (2.5)	
PdLI-20	4.0	0.40 ± 0.03	0.36 ± 0.02	0.16	0.94 ± 0.05	48.4 ± 1.0	140 / 2000	16 ± 2	51.3 ± 3.1 (2.4)	
							Grand weighted mean =		***51.2 ± 2.4*** (1.5)	$P = 0.80$
PdLI-0	1.7	0.67 ± 0.03	0.44 ± 0.02	0.08	1.22 ± 0.06	74.4 ± 5.6			60.8 ± 5.6 (5.2)	

Table 3: Dose rate data, equivalent doses and OSL ages for sediment samples from Pech de l'Azé II. Also provided are the weighted mean ages for layers for which more than one age was determined.

Sample code	Layer	Moisture content (%)	Dose rates (Gy/ka)			Total dose rate (Gy/ka)	D_e (Gy)	Number of grains	Over-dispersion (%)	Optical age (ka)
			Beta	Gamma	Cosmic					
PdLII-5	2G1	1.9	0.63 ± 0.03	0.42 ± 0.02	0.07	1.15 ± 0.06	72.9 ± 2.6	113 / 2000	29 ± 3	63.3 ± 4.1 (3.2)
PdLII-6	2G1	8.3	0.67 ± 0.04	0.42 ± 0.02	0.07	1.19 ± 0.07	70.9 ± 3.1	118 / 2000	38 ± 4	59.4 ± 4.3 (3.5)
PdLII-8	2G1	3.1	0.71 ± 0.03	0.43 ± 0.02	0.07	1.24 ± 0.06	80.7 ± 2.8	123 / 2000	28 ± 3	65.3 ± 4.2 (3.2)
PdLII-11	2G2	3.1	0.91 ± 0.05	0.44 ± 0.02	0.07	1.45 ± 0.07	88.9 ± 3.3	118 / 2000	31 ± 3	61.5 ± 4.0 (2.9)
PdLII-13	2G2	2.1	0.63 ± 0.03	0.44 ± 0.02	0.07	1.16 ± 0.06	64.6 ± 1.3	410 / 2000	33 ± 2	55.7 ± 3.2 (2.2)
PdLII-14	3	2.0	0.88 ± 0.05	0.44 ± 0.02	0.07	1.42 ±0.07	86.1 ± 4.4	102 / 2000	40 ± 4	60.5 ± 4.5 (3.9)
PdLII-16	4A1	1.4	0.86 ± 0.04	0.52 ± 0.03	0.06	1.47 ± 0.07	84.8 ± 3.9	68 / 2000	25 ± 4	57.7 ± 4.0 (3.2)
PdLII-17	4B	1.4	0.81 ± 0.05	0.59 ± 0.03	0.06	1.49 ± 0.08	133.7 ± 4.9	110 / 2000	34 ± 3	89.9 ± 5.9 (4.7)
PdLII-18	4B	1.5	0.61 ± 0.03	0.50 ± 0.03	0.06	1.20 ±0.06	96.4 ± 4.3	100 / 2000	36 ± 4	80.3 ± 5.5 (4.6)
PdLII-19	4D	0.7	0.71 ± 0.04	0.41 ± 0.02	0.05	1.21 ± 0.06	135.4 ± 4.8	118 / 2000	24 ± 3	105.3 ± 6.8 (5.2)
PdLII-2	7A	2.8	0.73 ± 0.04	0.48 ± 0.02	0.02	1.26 ± 0.06	180.8 ± 6.5	70 / 2000	16 ± 4	143.3 ± 9.3 (7.1)
PdLII-4	7B	1.7	0.66 ± 0.04	0.48 ± 0.02	0.02	1.22 ± 0.06	192.6± 9.4	71 / 2000	30 ± 5	161.3 ± 11.9 (9.9)
PdLII-10	7B	7.0	0.50 ± 0.03	0.48 ± 0.02	0.02	1.03 ± 0.06	185.1 ± 7.6	78 / 2000	25 ± 4	179.0± 12.9 (11.8)
PdLII-12	7B	3.3	0.51 ± 0.03	0.41 ± 0.02	0.01	0.97 ± 0.05	169.8 ± 8.6	80 / 1900	35 ± 5	176.0± 13.7 (11.8)
PdLII-9	7B	3.1	0.75 ± 0.04	0.41 ± 0.02	0.01	1.21 ± 0.06	204.5 ± 5.6	117 / 2000	13 ± 4	169.5 ± 10.5 (7.5)
PdLII-7	8	3.1	0.52 ± 0.03	0.59 ± 0.03	0.01	1.16 ± 0.06	183.2 ± 6.4	87 / 2000	20 ± 4	158.6 ± 10.5 (7.3)
PdLIV-15	9	2.8	0.52 ± 0.04	0.53 ± 0.03	0.01	1.09 ± 0.07	179.9 ± 13.0	34 / 1000	33 ± 6	165.2 ± 16.1 13.7)

Table 4: Dose rate data, equivalent doses and OSL ages for sediment samples from Pech de l'Aze IV.

Sample code	Layer	Moisture content (%)	Dose rates (Gy/ka)			Total dose rate (Gy/ka)	D_e (Gy)	Number of grains	Over-dispersion (%)	Optical age (ka)
			Beta	Gamma	Cosmic					
PdLIV-27	3A	3.8	0.57 ± 0.03	0.45 ± 0.02	0.12	1.17 ± 0.06	61.1 ± 1.7	112 / 2000	18 ± 3	52.4 ± 3.2 (2.5)
PdLIV-26	3A	3.2	0.64 ± 0.04	0.44 ± 0.02	0.12	1.23 ± 0.07	60.3 ± 1.9	109 / 2000	24 ± 3	49.2 ± 3.2 (2.6)
PdLIV-25	3A	4.7	0.53 ± 0.05	0.43 ± 0.02	0.12	1.10 ± 0.06	55.1 ± 1.8	108 / 2000	31 ± 3	49.9 ± 3.4 (2.9)
PdLIV-24	3A	3.6	0.50 ± 0.03	0.42 ± 0.02	0.12	1.06 ± 0.06	57.3 ± 2.8	91 / 2000	38 ± 4	53.8 ± 4.0 (3.4)
							Weighted mean =			***51.1 ± 2.4*** *(1.4) P* = 0.65
PdLIV-23	3B	2.5	0.67 ± 0.04	0.40 ± 0.02	0.11	1.21 ± 0.06	59.7 ± 2.1	104 / 2000	26 ± 3	49.5 ± 3.2 (2.5)
PdLIV-22	3B	3.5	0.62 ± 0.04	0.39 ± 0.02	0.11	1.15 ± 0.06	60.4 ± 2.1	101 / 2000	25 ± 3	52.5 ± 3.4 (2.7)
PdLIV-21	3B	5.6	0.72 ± 0.05	0.39 ± 0.02	0.10	1.24 ± 0.08	64.0 ± 2.2	79 / 2000	29 ± 4	51.5 ± 3.8 (3.2)
							Weighted mean =			***51.0 ± 2.6*** *(1.6) P* = 0.71
PdLIV-20	4A	3.9	0.78 ± 0.04	0.46 ± 0.02	0.10	1.37 ± 0.07	72.6 ± 3.2	99 / 2000	34 ± 5	52.9 ± 3.7 (3.0)
PdLIV-19	4A	3.4	0.89 ± 0.06	0.53 ± 0.03	0.10	1.54 ± 0.09	88.1 ± 3.5	92 / 1900	34 ± 4	57.1 ± 4.1 (3.5)
PdLIV-18	4A	4.0	0.88 ± 0.05	0.58 ± 0.03	0.10	1.59 ± 0.08	90.3 ± 4.1	66 / 2000	26 ± 4	56.9 ± 4.0 (3.3)
PdAIV-03	4A	4.0	0.84 ± 0.03	0.58 ± 0.03	0.10	1.56 ± 0.08	100.7 ± 4.4	72 / 2600	30 ± 4	64.6 ± 4.6 (3.8)
PdLIV-17	4A	4.2	0.90 ± 0.05	0.51 ± 0.03	0.10	1.54 ± 0.08	92.8 ± 4.6	62 / 3000	28 ± 5	60.4 ± 4.4 (3.6)
PdLIV-16	4B	4.7	0.85 ± 0.05	0.45 ± 0.02	0.10	1.42 ± 0.07	87.5 ± 4.1	46 / 3000	19 ± 5	61.6 ± 4.4 (3.5)
							Weighted mean =			***58.3 ± 2.8*** *(1.4) P* = 0.22
PdLIV-15	4B	6.8	0.83 ± 0.05	0.42 ± 0.02	0.09	1.38 ± 0.07	83.1 ± 3.3	74 / 2000	31 ± 4	60.4 ± 4.2 (3.3)
PdLIV-14	4B	5.8	0.84 ± 0.05	0.40 ± 0.02	0.09	1.37 ± 0.07	86.5 ± 4.4	74 / 2000	34 ± 4	63.1 ± 4.8 (3.9)
							Weighted mean =			***61.5 ± 3.7*** *(2.5) P* = 0.87
PdLIV-13	4C	7.5	0.73 ± 0.05	0.38 ± 0.02	0.09	1.23 ± 0.08	81.1 ± 3.6	46 / 3000	17 ± 5	65.9 ± 5.2 (4.4)
PdLIV-12	4C	5.4	0.53 ± 0.03	0.38 ± 0.02	0.09	1.03 ± 0.06	74.7± 4.0	48 / 2000	33 ± 6	72.4 ± 5.6 (4.8)
PdLIV-11	4C	8.6	0.64 ± 0.04	0.37 ± 0.02	0.09	1.13 ± 0.07	75.8 ± 4.0	72 / 2000	36 ± 4	67.1 ± 5.4 (4.6)
							Weighted mean =			***68.3 ± 3.9*** *(2.7) P* = 0.57
PdLIV-10	5A	8.9	0.50 ± 0.03	0.37 ± 0.02	0.08	0.99 ± 0.06	76.5 ± 3.5	48 / 3000	19 ± 5	77.5 ± 6.0 (5.2)
PdLIV-9	5A	9.1	0.53 ± 0.03	0.36 ± 0.02	0.08	1.01 ± 0.06	70.6 ± 2.7	108 / 2000	31 ± 3	74.3 ± 5.3 (4.2)
PdLIV-8	5B/A	6.6	0.49 ± 0.04	0.39 ± 0.03	0.08	0.99 ± 0.06	77.1 ± 3.1	96 / 3000	38 ± 4	77.7 ± 5.7 (4.9)
PdAIV-02	5B	6.6	0.46 ± 0.03	0.39 ± 0.03	0.08	0.97 ± 0.05	66.4 ± 4.1	61 / 2000	28 ± 4	68.8 ± 5.9 (5.3)
							Weighted mean =			***74.7 ± 3.8*** *(2.4) P* = 0.89
PdLIV-7	6A	7.8	0.61 ± 0.05	0.42 ± 0.02	0.08	1.14 ± 0.07	88.2 ± 2.6	106 / 2000	27 ± 3	77.2 ± 5.6 (4.6)
PdLIV-6	6A	8.1	0.60 ± 0.04	0.41 ± 0.02	0.08	1.13 ± 0.07	83.5 ± 3.6	81 / 2000	31 ± 4	74.1 ± 5.6 (4.7)
PdLIV-5	6B/A	7.1	0.56 ± 0.03	0.41 ± 0.02	0.07	1.07 ± 0.06	82.4 ± 2.9	114 / 2000	28 ± 3	77.0 ± 5.3 (4.2)
PdLIV-4	6B	8.9	0.57 ± 0.04	0.35 ± 0.02	0.07	1.02 ± 0.06	77.8 ± 3.4	83 / 2000	30 ± 4	76.3 ± 5.7 (4.8)
PdLIV-3	6B	9.3	0.41 ± 0.03	0.35 ± 0.02	0.07	0.86 ± 0.06	68.3 ± 2.5	115 / 2000	31 ± 3	79.8 ± 6.1 (5.3)
							Weighted mean =			***76.7 ± 3.7*** *(2.1) P* = 0.99

Table 4 (continued): Dose rate data, equivalent doses and OSL ages for sediment samples from Pech de l'Aze IV.

PdAIV-01-A	8	5.6	0.27 ± 0.03	0.24 ± 0.01	0.05	0.60 ± 0.04	55.1 ± 2.7	90 / 1000	39 ± 4	91.5 ± 7.6 (7.1)
PdLIV-2	8	5.6	0.23 ± 0.03	0.33 ± 0.02	0.05	0.65 ± 0.05	62.7 ± 1.6	84 / 1000	39 ± 4	97.4 ± 7.6 (6.9)
PdAIV-01-B	8	5.6	0.23 ± 0.03	0.33 ± 0.02	0.05	0.64 ± 0.05	63.5 ± 4.5	80 / 1500	72 ± 6	98.6 ± 11.1 (10.7)
PdAIV-01-C	8	6.9	0.29 ± 0.03	0.31 ± 0.02	0.05	0.69 ± 0.05	62.9 ± 3.6	89 / 1000	48 ± 4	91.6 ± 8.8 (8.2)
PdAIV-01-D	8	8.1	0.31 ± 0.02	0.29 ± 0.02	0.05	0.68 ± 0.04	63.7 ± 3.9	77 / 1000	49 ± 5	93.1 ± 8.4 (7.7)
PdLIV-1	8	8.1	0.41 ± 0.03	0.29 ± 0.02	0.05	0.79 ± 0.05	73.9 ± 2.2	112 / 1000	23 ± 2	93.8 ± 6.7 (5.6)
							Weighted mean =			***93.9 ± 4.4*** *(3.0) P* = 0.99

To test the accuracy of our beta dose rate estimates we have also determined the beta dose rates in two additional ways. For the majority of samples from all three sites we obtained estimates of U and Th from ICP-MS and K from ICP-OES to calculate the first additional set of beta dose rates. For all samples from Pech I and Pech II, we also obtained estimates of U and Th from thick source alpha counting (TSAC) and K from X-ray fluorescence (XRF) to determine the second additional set of beta dose rates. All elemental concentrations were converted to dose rates using the conversion factors of Guerin *et al.* (2011). We do not expect perfect agreement between the three different methods, but prefer GM-25-5 beta counting and the combined TSAC and XRF estimates over the ICP-MS measurements since the latter only measures the parent radionuclide in the U and Th decay series. Since the vast majority of the beta dose rate from U is derived from the daughter nuclides lower down the decay series (e.g., post-^{226}Ra) and it is known that disequilibrium in the U decay series is commonplace in limestone environments, it is likely that estimates of U from ICP-MS will result in inaccurate estimates of the beta dose rate. Comparisons of the estimates derived using the different methods will also provide a relative idea of the extent of disequilibrium.

Gamma dose rates were measured directly at the vast majority of sample locations by *in situ* gamma spectrometry, to take into account any spatial heterogeneity in the gamma radiation field within 30 cm of each OSL sample (as gamma rays can penetrate this distance through sediment and rock). Counts were collected for 60 min with either a 1-inch (Pech II and Pech IV) or a 2-inch (Pech I) NaI(Tl) crystal. We measured the gamma dose rate of the limestone wall from which we collected the samples in Pech I and used this as an estimate of the gamma dose rate for half of the gamma sphere; we calculated the gamma dose rate for the other half of the gamma sphere from laboratory measurements of the sediment and combined those two estimates. The detectors were calibrated using the concrete blocks at Oxford University (Rhodes & Schwenninger 2007) and the gamma dose rates were determined using the 'threshold' technique (Mercier & Falguerès 2007). This approach gives an estimate of the combined dose rate from gamma-ray emitters in the U and Th chains and from ^{40}K.

Account was also taken of the cosmic-ray contribution, which was adjusted for an average site altitude (~165 m), geomagnetic latitude (47.3°), the density and thickness of rock and sediment overburden (Prescott & Hutton 1994), and the $\cos^2$-Φ zenith angle dependence of cosmic rays (Smith *et al.* 1997). We also took into account the morphological evolution of the sites (see Texier 2009 and Turq *et al*, 2011).

The beta, gamma and cosmic-ray dose rates were corrected for long-term water contents. We used the current measured field values that ranged between 0.5 and 7.4% at Pech I (Table 2), between 0.7 and 8.3% at Pech II (Table 3) and between 2.5 and 9.3% at Pech IV (Table 4). A relative uncertainty of ±25% (at 1σ) was assigned to each estimate of water content. As a general rule, the total dose rate will decrease, and the OSL age will increase, by ~1% for each 1% increase in water content.

14.6.1 PECH I

The dose rate results for all samples from Pech I are provided in Table 2. The total dose rates for all the samples show only a modest amount of variation, ranging between 0.82 ± 0.05 (PdLI-9) and 1.28 ± 0.08 Gy/ka (PdLI-18), with the majority of values ranging between 0.9 and 1.1 Gy/ka.

Many of the OSL sample positions at Pech I were determined by the location of previously made large holes for gamma spectrometry by W.J. Rink in 1999/2000. There is not a lot of sediment left at Pech I, so to preserve as much of the deposit as possible, but still being able to make the required *in situ* gamma spectrometry measurements, we collected some of our samples inside and adjacent to his gamma spectrometry holes, and did our own gamma spectrometry measurements inside these same holes. This allowed us to check the consistency of the gamma dose rate measurements conducted by two different laboratories more than a decade apart, and also gave us the estimate of the gamma dose rate at the point of sampling. We compared our estimates of the gamma dose rate with those of Jones (2001) and Soressi *et al.* (2007) obtained for the same holes and the results are shown in Figure

6. From here it can be seen that there is good consistency between the measurements made by the different laboratories. On average, the gamma dose rate ratio of Rink / this study is 0.95 with a standard deviation of 0.05. What is interesting is the significant range in gamma dose rates between ~0.20 and 0.65 Gy/ka, especially between the sediments near the top and bottom of the ~4 m witness section, but also for sediments within the same layer. For example, two gamma dose rate measurements in Layer 4, taken ~50 cm apart gave gamma dose rates of 0.65 and 0.49 Gy/ka, respectively. This is directly related to the proximity of the samples to blocks of limestone. Such variations may prove problematic when the gamma dose rate has to be reconstructed for stone or tooth samples that were collected from museum collections and for which only an average estimate would be used for age estimation. This is one of the advantages of OSL dating of sediment in settings where there are gross inhomogeneities in the gamma sphere of influence, because the gamma dose rate can be determined in the field at the point of sampling.

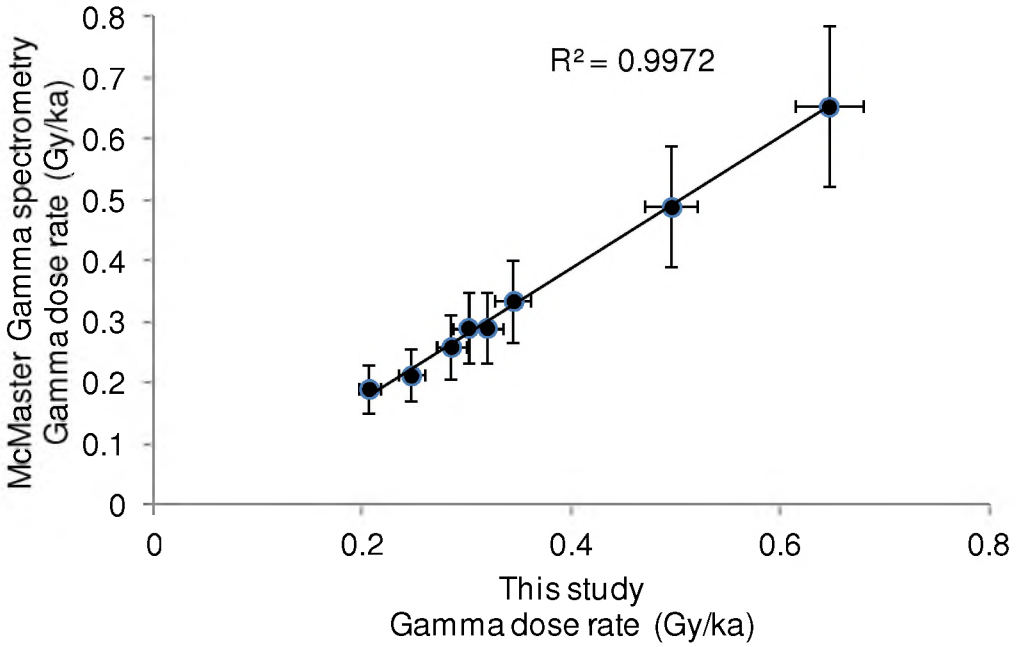

Figure 6: Comparison of the gamma dose rate results obtained from two different laboratories a decade apart. The gamma dose rate measurements were made in the same holes.

The beta dose rates determined in three different ways are shown as ratios in Figure 7 for all samples from Pech I. From here it can be seen that the beta dose rates derived using elemental concentrations from ICP-MS are systematically smaller than those derived using the two alternative methods; average ratios of 0.93 ± 0.03 and 0.92 ± 0.03 (one significant outlier was omitted) were calculated when these beta dose rates are compared to those obtained from GM-25-5 beta counting and a combination of TSAC and XRF, respectively. The latter two techniques show good consistency, resulting in an average beta dose rate ratio of 1.01 ± 0.03. The reported uncertainty is the standard deviation of the average ratio. The systematically lower beta dose rates derived using ICP-MS is likely the result of uranium leaching.

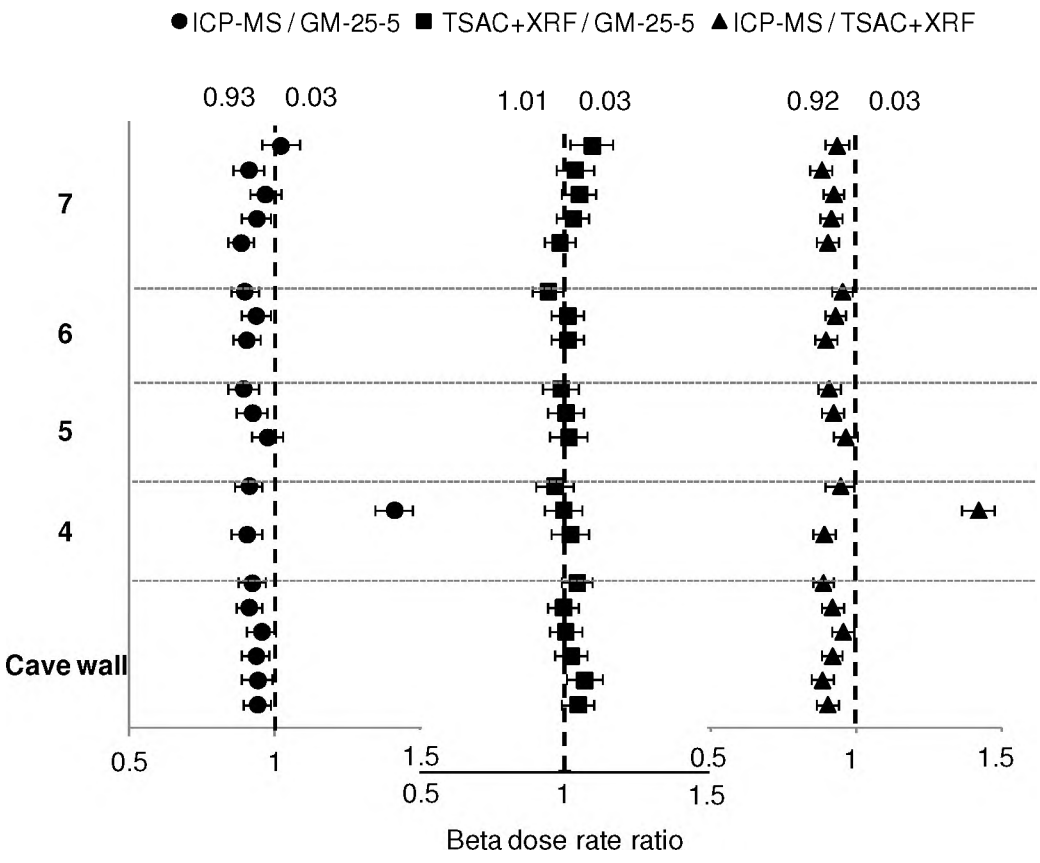

Figure 7: The ratio of beta dose rates obtained for the same samples using three different methods. The filled circles show the ratio of the results obtained from ICP-MS(OES) and GM-25-5 beta counting. The filled squares show the results of the results obtained from TSAC and XRF against GM-25-5 beta counting and the filled

triangles show the results obtained from ICP-MS(OES) against TSAC and XRF. The samples are plotted in stratigraphic order and per layer for the witness section (Figure 2c) and separately for the samples collected from the cave wall (Figure 2d).

14.6.2 PECH II

The dose rate results for all samples from Pech II are provided in Table 3. The total dose rates for all the samples range between 1.09 ± 0.07 (PdLII-15) and 1.49 ± 0.08 Gy/ka (PdLII-17), with one lower value at 0.97 ± 0.05 Gy/ka (PdLII-12). Most values appear to fall into two groupings centred on ~1.2 and ~1.45 Gy/ka. From studies of the thin sections made on the same samples, it appears that the difference relates directly to the relative proportion of clay and limestone in the sediment.

No *in situ* gamma spectrometry results have previously been reported for this site. The values reported in Grün *et al.* (1991) were based on measurement of parental concentrations of U, Th and K of sediment attached to the dated tooth samples, using neutron activation analysis (NAA). It does not take into account any possible disequilibrium that may exist in the U-series decay chain or inhomogeneity in the gamma sphere (~30 cm around a sample), and is similar to what would be obtained with ICP-MS. We measured the *in situ* gamma dose rate for a number of our samples and these are indicated as filled circles in Figure 3 and the results are provided in Table 3.

The beta dose rates determined in three different ways are shown as ratios in Figure 8 for all samples from Pech II. No systematic trends in any of the methods can be seen; rather, the beta dose rate ratios are spread randomly around unity with the occasional significant outlier, resulting in average beta dose rate ratios and standard deviations of 1.01 ± 0.13, 1.02 ± 0.15 and 0.99 ± 0.11 (Figure 8).

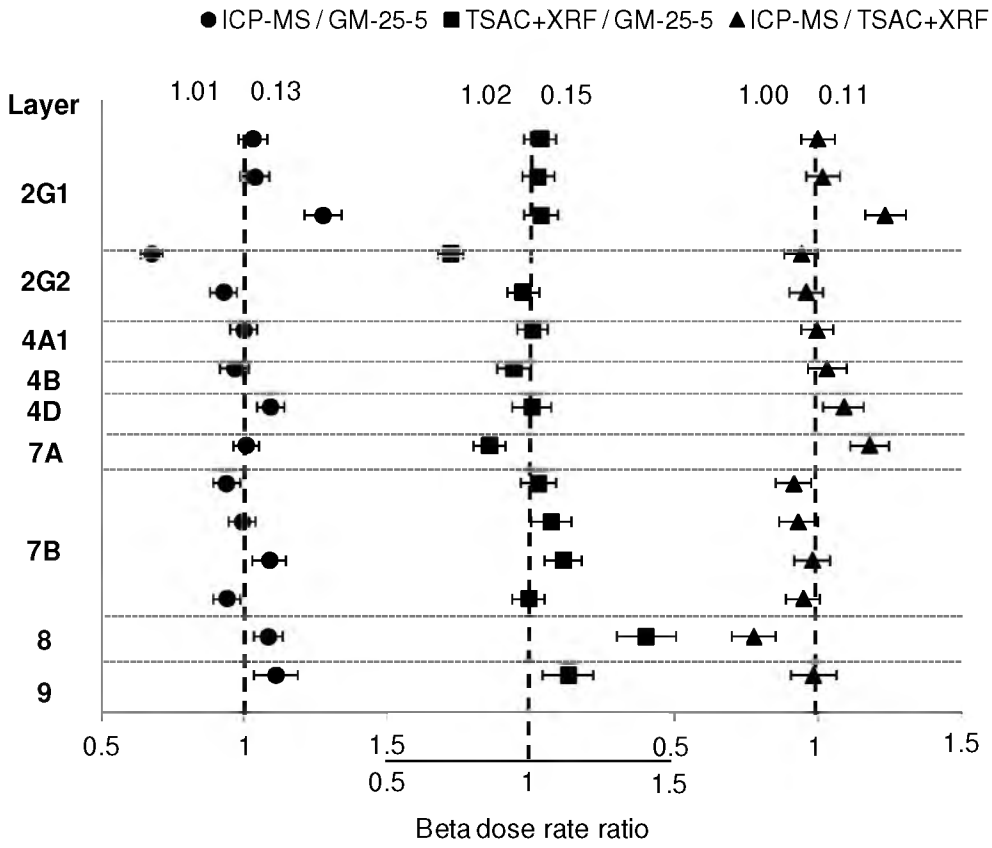

Figure 8: The ratio of beta dose rates obtained for the same samples using three different methods. The filled circles show the ratio of the results obtained from ICP-MS(OES) and GM-25-5 beta counting. The filled squares show the results of the results obtained from TSAC and XRF against GM-25-5 beta counting and the filled triangles show the results obtained from ICP-MS(OES) against TSAC and XRF. The samples are plotted in stratigraphic order and the corresponding layer name is noted.

14.6.3 Pech IV

The dose rate results for all samples from Pech IV are provided in Table 4. The total dose rates for all the samples ranges between 0.78 ± 0.04 (PdLIV-1) and 1.58 ± 0.08 Gy/ka (PdLIV-18). Richter *et al.* (2013) reported *in situ* gamma dose rate results

based on measurement of α- Al_2O_3:C dosimeters with OSL. Their results are presented in Figure 9 as closed circles, where each circle represents the result from one dosimeter. Also shown, as open triangles, are the *in situ* gamma spectrometry measurements made in this study. We measured the gamma dose rates for each of our samples whose locations are shown in Figure 4. Note that the results from the two studies are not directly comparable as was the case for Pech I (Figure 6), but rather the measurements were made on similar sediment from the same layers at Pech IV, but from different profiles within the cave (see Figure 4 and Figure 3 in Richter *et al.* (2013) for exact locations). The average gamma dose rate for each layer derived from each of the methods is shown inside the stippled boxes, and the ratio of the two average values is provide above each of the boxes. The results from Layers 4C and 5A show good consistency. The two TL dosimeter results for Layer 3B were quite different; all the *in situ* gamma spectrometry results are consistent with the lower dose rate value.

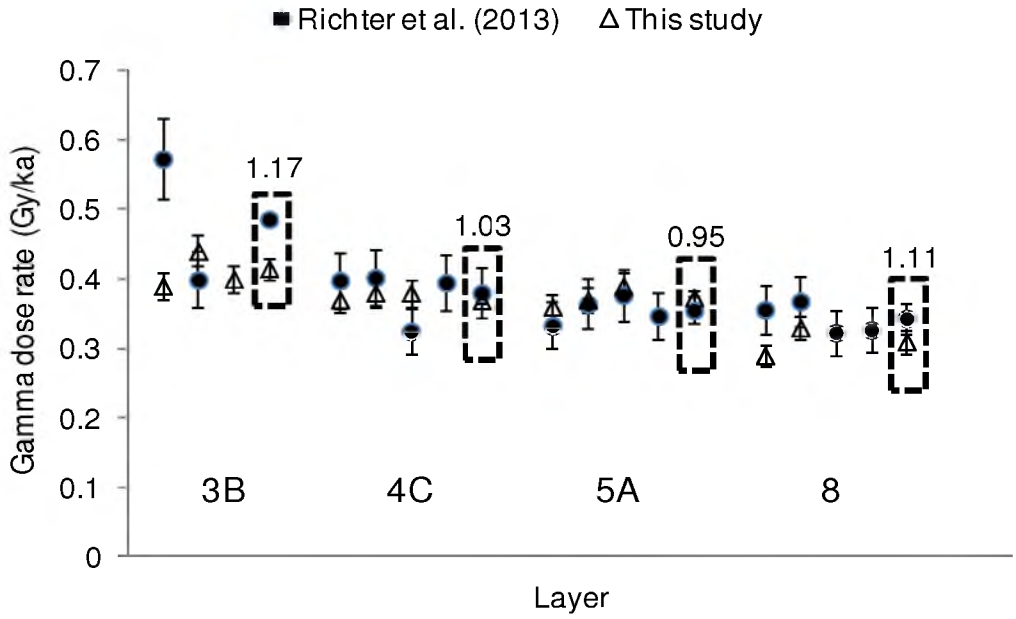

Figure 9: Gamma dose rate results for sediment from Pech IV using an in situ gamma spectrometer (this study) or α- Al_2O_3:C dosimeters (Richter et al., 2013). The results are not for exactly the same position and measurements were made for different profiles in the site. The average for each layer and for each method is provided in the square boxes and shown on top of each box is the ratio of the two averages.

The beta dose rates were only determined using two different methods for the samples from Pech IV, namely GM-25-5 beta counting and conversion of measured concentrations of U, Th (ICP-MS) and K (ICP-OES) to beta dose rates. The ratio of the beta dose rate derived using these two methods is presented in Figure 10a. The results for Pech IV are quite different from those obtained for Pech I and II. The beta dose rate ratios for some layers (e.g., 4A and 4C) are consistent with unity, whereas the ratios for sediment from other layers (e.g., 3A, 4B and 6A) deviate significantly from unity. The same bow-shaped curve can also be seen when uranium concentrations (ppm) derived from ICP-MS are plotted (Figure 10b). We interpret this similarity in shape to mean that the difference in the two beta dose rates relate directly to the state of disequilibrium in the uranium-decay series. Where there is an excess of parental U, the beta dose rate derived using ICP-MS will overestimate relative to GM-25-5 beta counting and *vice versa*. If this is correct, then the beta dose rate derived using GM-25-5 beta counting is the more accurate estimate as this takes into account disequilibrium, assuming that this has been the case for the entire period of burial.

14.7 AGES AND COMPARISONS WITH EXISTING CHRONOLOGIES AT PECH DE L'AZÉ

The final ages for all samples from all three sites are listed in Tables 2, 3 and 4, together with the supporting D_e and dose rate estimates. Uncertainties on the ages are given at 1σ (standard error on the mean) and were derived by combining, in quadrature, all known and estimated sources of random and systematic error. The 1σ error on the age provided in brackets only includes the random errors and is the error to be used for comparison of ages among the three sites. For all other comparisons the full error should be used. For the sample D_e, the random error was obtained from the CAM used to determine the weighted mean, and a systematic error (of 2%) was included for any possible bias associated with calibration of the laboratory beta source. The total uncertainty on each dose rate was obtained as the quadratic sum of

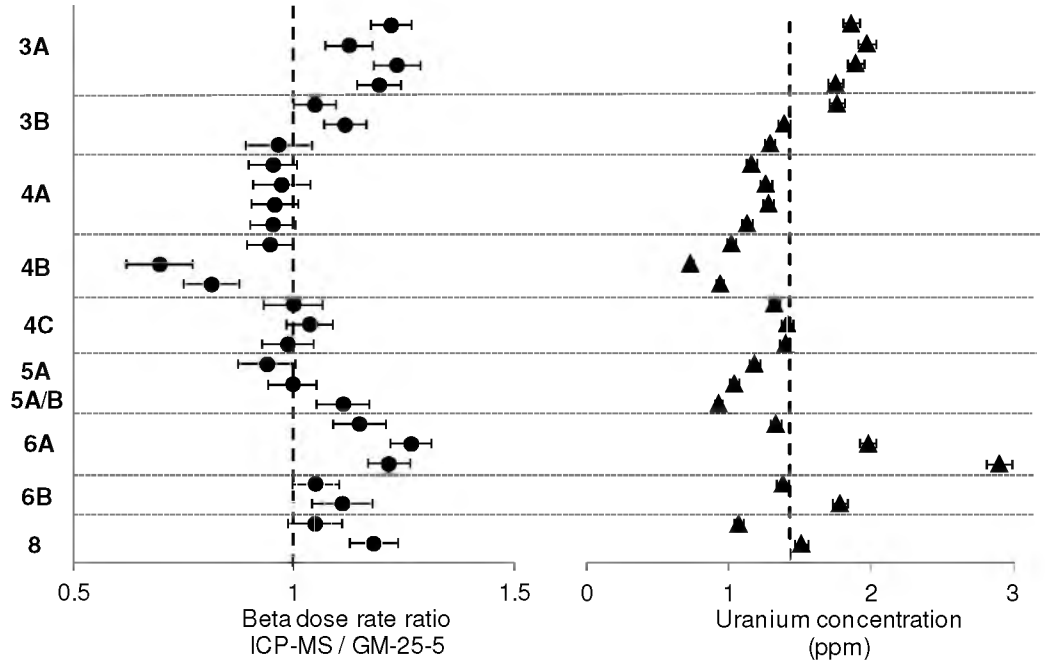

Figure 10: a) The ratio of beta dose rates obtained from ICP-MS (U and Th) and ICP-OES (K) and GM-25-5 beta counting plotted in stratigraphic order and the layers are demarcated. The broken vertical line indicated unity. b) Uranium concentrations (ppm) obtained from ICP-MS measurements plotted for all samples and in stratigraphic order.

all random (measurement) errors and the systematic errors associated with estimation of the beta and cosmic-ray dose rates.

We used the statistical (homogeneity) test of Galbraith (2003), and the resulting *P*-values to test whether the independent estimates obtained within each stratigraphic unit are self-consistent (i.e., the spread in ages are compatible with the size of the uncertainties). If self-consistency is demonstrated (i.e., $P = >0.05$), we then calculated a weighted mean age estimate for each layer or sub-layer. Both *P*-values and weighted mean ages were calculated by combining all ages using only their random uncertainties (the errors provided in brackets after the age in Tables 2, 3 and 4). The final error on the weighted mean, however, includes the systematic error

that was added in quadrature to the random error on the mean age. In calculating a weighted mean age for each layer, we assume that the individual age estimates within a layer represent either a single event, or a series of events spread over a period of time that is short compared to the size of the age uncertainties.

14.7.1 PECH I

We were able to obtain reliable ages for all samples collected from Pech I, including those sediment remnants from the Capitan & Peyrony excavations that were left on the shelter wall. An age of 61 ± 6 ka was obtained for the lowermost sample (PdLI-0) collected from an ochre-coloured sterile sediment pocket left against the wall. Very little variation in age was obtained for the remainder of the samples collected from Layers 4, 5, 6 and 7 from both the witness section and the shelter wall. The individual ages are plotted in Figure 11a (closed symbols represent samples from the witness section and open symbols those samples collected from the shelter wall). The ages range between ~46 and 55 ka.

The *P*-values for each layer are provided in Table 2 and range between 0.61 and 0.99, far greater than the accepted value of >0.05, thus supporting self-consistency of ages within each layer. Accordingly, we calculated weighted mean ages for each of the layers and obtained ages of 51.2 ± 2.4 (Layer 4), 53.2 ± 2.9 (Layer 5), 52.2 ± 3.1 (Layer 6) and 48.8 ± 2.8 ka (Layer 7). The weighted mean ages for each layer are provided in Table 2 and plotted in Figure 11b. In Table 2, the weighted mean ages for those layers where samples were collected from both the witness section and the shelter wall were calculated separately to check for age consistency over space; the results support the consistency. A grand weighted mean was then calculated to include both samples from the wall and the witness section for that particular layer; it is these grand weighted mean ages that are plotted in Figure 11b. It is apparent from Figure 11b that the weighted mean ages for all four layers are consistent at 1σ uncertainty and when all the ages are combined a *P*-value of 0.99 is obtained, suggesting that there is no statistical difference in age between the top and the bottom and that the deposits, therefore, represent a relatively short duration

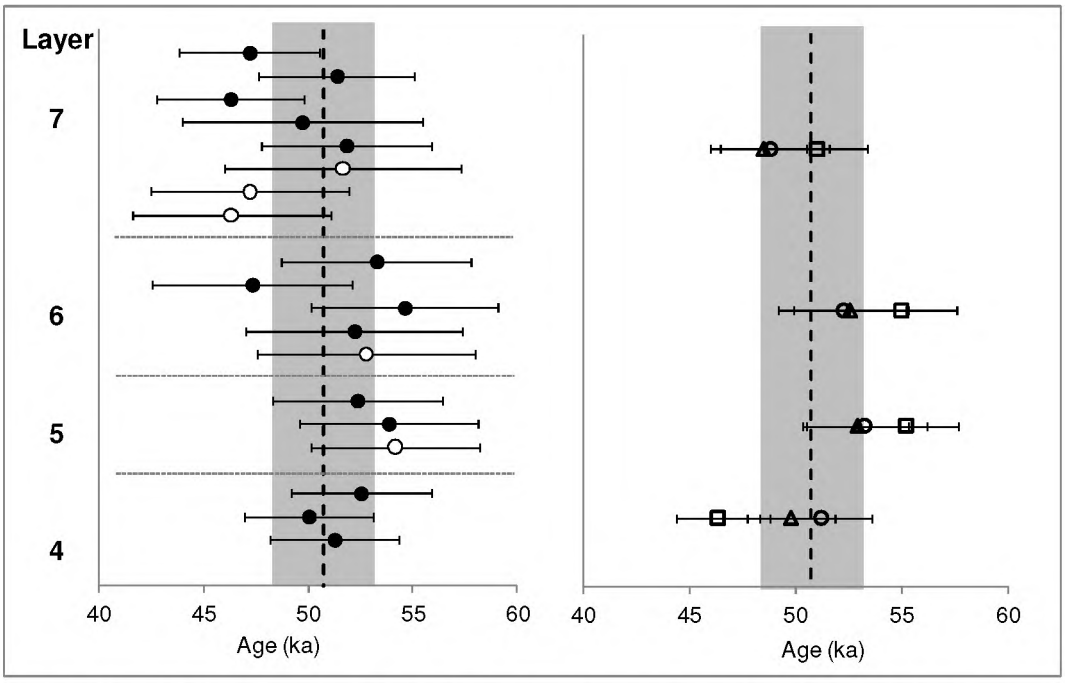

Figure 11: a) All ages for Pech I plotted in stratigraphic order with the layers demarcated with stippled lines. The filled symbols represent ages for samples collected from the witness section (Figure 2c) and the open symbol those samples collected from the cave wall (Figure 2d). The broken vertical line shows the weighted mean age calculated for all 20 samples and the grey shaded bar the 1σ standard error on the weighted mean. b) The weighted mean ages for each layer. The weighted mean ages include all samples from the witness section and the cave wall. Weighted mean ages were calculated using three different beta dose rates (open circles—GM-25-5 beta counting, open triangles—TSAC+XRF and open squares—ICP-MS and ICP-OES). The same weighted mean and 1σ standard error as in a).

of time; a weighted mean age of 50.7 ± 2.5 ka is obtained when all 20 age estimates (excluding PdLI-0 from the lowermost unit) are combined and is indicated as a stippled line and grey shading in both Figure 11a and 11b.

It can be seen from Figure 11b that when the weighted mean ages are plotted for each of the layers, that there is a slight tendency, albeit within statistical

uncertainty, for the middle two layers (Layers 5 and 6) to be older than the lowest layer (Layer 4); this was also the case for the ESR ages presented in Soressi *et al.* (2007). To further investigate this, we have also plotted the weighted mean ages for the same set of samples, but when the two alternative estimates of beta dose rate are used instead to calculate the age (see Figure 7); the results are also plotted in Figure 11b. This same tendency is observed for all three data sets with the most extreme tendency demonstrated for those ages for which the beta dose rates are based on measured elemental concentrations determined with ICP-MS (U and Th) and ICP-OES (K). This supports our interpretation of the beta dose rates in Figure 7 (and discussed above), that at some point in the past, there was leaching of U and that the best estimate beta dose rate, and, hence, best-estimate age for these samples, are those using the beta dose rate obtained from GM-25-5 beta counting (plotted as open circles).

The data suggests that the age of the MTA Type B and A at Pech I span a relatively short period of time (~2-4 ka), and all the ages are statistically consistent with a mean age of 50.7 ± 2.5 ka.

14.7.1.1 PECH I COMPARISONS WITH PUBLISHED CHRONOLOGIES

A series of ESR ages and three ^{14}C ages were previously reported by Soressi *et al.* (2007) for Pech I. They reported the mean ESR age and standard deviation for three layers (Layers 5, 6 and 7) using two different uranium uptake models, namely the early-uptake (EU) and linear-uptake (LU) models. Soressi *et al.* (2007) also reported coupled ESR/U-series ages for two of the samples, one each from Layers 6 and 7 and three ^{14}C ages on bone from Layers 4 and 6. These ages are plotted, together with the OSL ages of this study, in Figure 12. The EU and LU ages are shown as closed and open triangles, respectively and are treated as a single age range with the most likely age being somewhere between those two estimates. The ^{14}C ages are plotted with their 2σ ranges where the symbol denotes the midpoint value and the positive and negative error bars the entire calibration range.

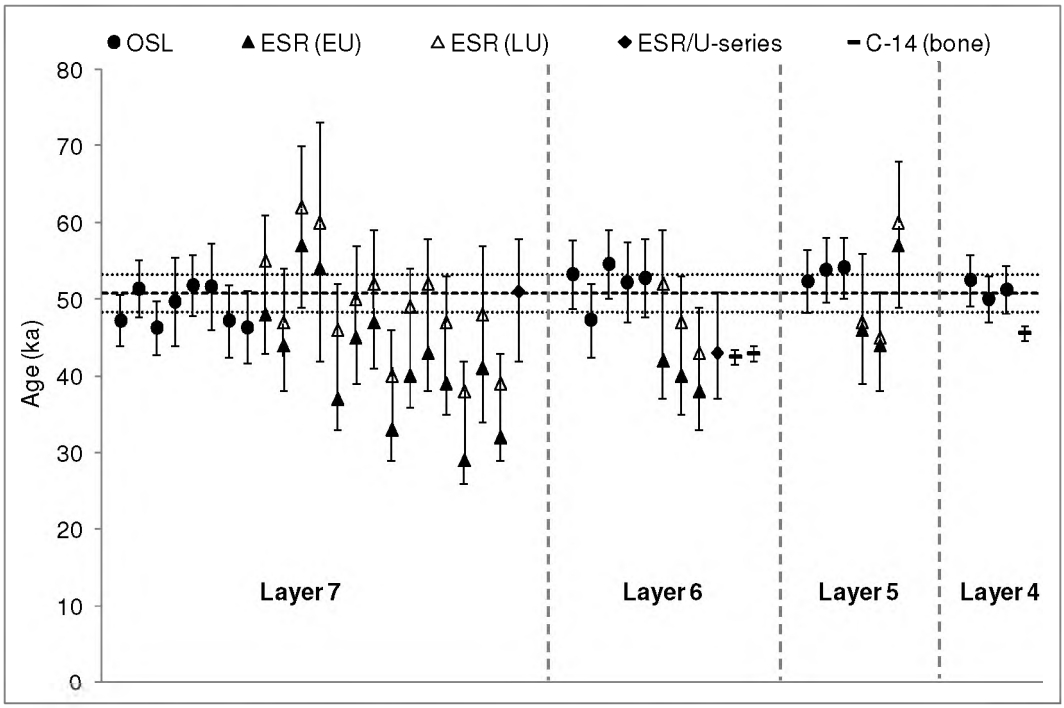

Figure 12: All OSL ages for Pech I together with all independent ages published previously for Pech I, shown per layer. Ages are plotted with 1σ uncertainties. The EU and LU ages are plotted as a range and the ^{14}C ages are plotted where the line is the midpoint value of the calibrated range and the error bars represent the entire range. The broken line is the weighted mean age calculated for all the OSL ages and the stippled lines are the 1σ standard error on the weighted mean age.

A mean EU and LU age for Layer 5 of 49 ± 6 and 51 ± 7 ka, respectively, is entirely consistent with the weighted mean OSL age of 53 ± 3 ka. Mean EU and LU ages of 40 ± 2 and 47 ± 5 ka, respectively for Layer 6 and a single coupled ESR/U-series age of 43 $\frac{+8}{-6}$ ka for one of the two measured teeth gave ages that are systematically younger than the weighted mean OSL age of 52 ± 3 ka; the ages are, however, consistent within their margins of error. The mean EU and LU ages of 42 ± 8 and 49 ± 7 ka, respectively and the single coupled ESR/U-series age of 51 $\frac{+7}{-9}$ for Layer 7 is consistent with the weighted mean OSL age of 49 ± 3 ka. It is important to point out that the uranium concentrations for the enamel from the teeth were very low and that the external beta, gamma and cosmic-ray dose rates (i.e., the same dose

rates that apply to the OSL ages) were responsible for at least half of the total dose rates. This means that the ESR ages will suffer from the same dosimetry issues related to the OSL samples (discussed above and shown in Figure 7); this is in addition to the problem of recreating a dose rate environment that does not exist anymore because the sediments in which the teeth were buried have already been excavated. These issues may account for the variability in age between individual teeth from the same layer and also the larger errors associated with the ESR ages. Regardless, the two independent chronologies show good consistency and it appears that the LU modelled ages are more consistent with the OSL than the EU ages (Figure 12).

The two ^{14}C ages on unburnt bone from the top of Layer 6 ranged at 2σ between ~ 44 and 41 cal BP and is younger than both the ESR and OSL ages for this layer (Figure 12); there is no statistical overlap between the ^{14}C and OSL ages even at 2σ. The ^{14}C age from Layer 4 range at 2σ between 47 and 44 cal BP and is similarly younger than the corresponding OSL ages. The bone samples were not prepared using molecular ultrafiltration, so the underestimation may be due to small-scale contamination, now known to be a prevalent problem (e.g., Higham 2011).

14.7.2 PECH II

The ages for 18 samples from Pech II are provided in Table 3. The ages range between ~ 55 and 100 ka for the 11 sediment samples located above the thick cryoclastic complex (Figure 3), and then again between ~140 and 180 ka for the seven sediment samples located below the cryoclastic complex. The ages are also displayed in Figure 13 as a function of layer.

We did not attempt to date the fluvial sands at the base of the deposit in Layer 10 because we do not believe that these sands were exposed to sunlight prior to deposition. We obtained a single age of 165 ± 16 ka for Layer 9 associated with an

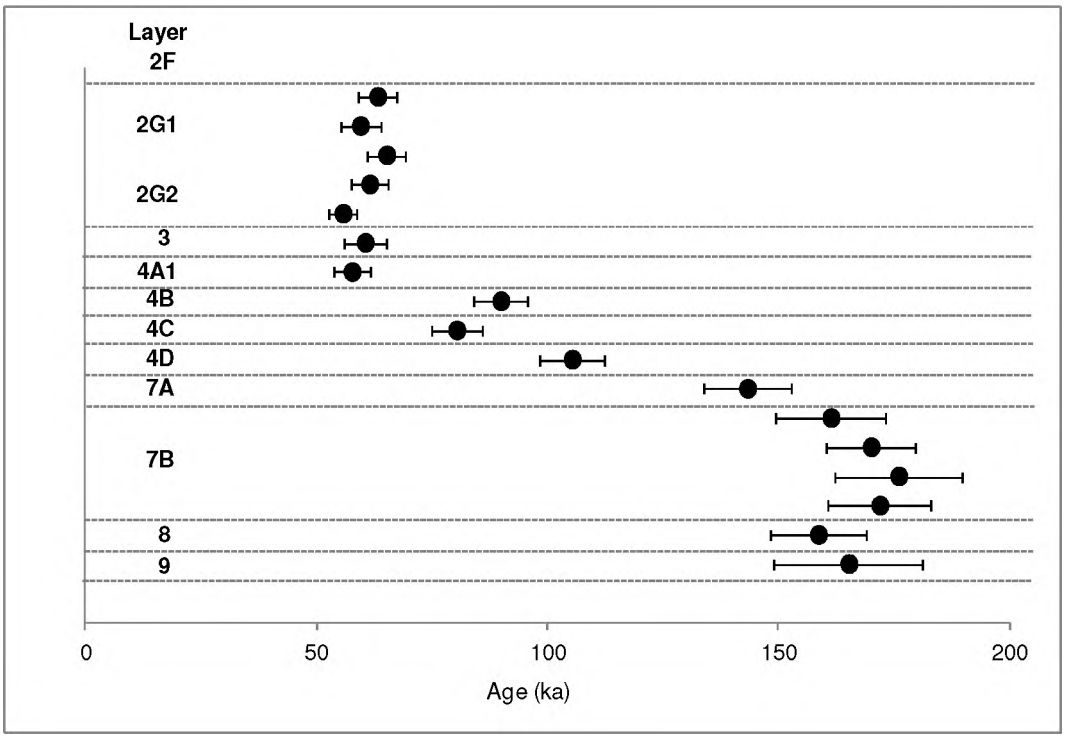

Figure 13: All ages for Pech II plotted in stratigraphic order with the layers demarcated with stippled lines. All samples from Layers 2G to 4D were collected from Profile A in Figure 3a,d and e and samples from Layers 7A to 9 are for samples collected from Profiles B and C (Figure 3b and c) below the large cryoclastic deposit in Layer 5.

Acheulean with handaxes (PdLII-15). We also obtained a single age of 159 ± 11 ka for Layer 8 (PdLII-7). We calculated a weighted mean age of 170 ± 8 ka for four samples from Layer 7B and the sample from Layer 7A gave an age of 143 ± 9 ka (PdLII-2). Layers 8, 7B and 7A are all associated with the Clactonian, which contained choppers and chopping tools but no handaxes. It, therefore, appears that the sediment below the cryoclastic deposit in Layer 5 was deposited during the penultimate glacial period (oxygen isotope stage (OIS) 6). Although we could not date Layer 5, the cryoclastic layer, it was likely a result of the severity of the end of OIS 6, when temperatures increased rapidly by ~14°C from a mean palaeotemperature of ~7°C to a mean palaeotemperature of ~21°C at the beginning of MIS 5 in southwestern France (Wainer *et al.* 2011). The rapidity and significant

change in temperature may have led to the significant rock shatter from the cave roof and concomitant cryoturbation of the deposit.

Immediately above the cryoclastic deposit, the first evidence for occupation occurred at the base of Layer 4 in Layer 4E and 4D. Bordes (1972) described these layers, and the associated archaeological assemblages, as being significantly damaged by cryoturbation. Our first samples were collected across Layers 4D and 4C2 for which micromorphological analysis of our sample (PdLII-19) shows only limited evidence for cryoturbation in the form of coatings and some banded fabrics. The deposits appear quite fresh and intact with perhaps some of the fine fraction removed by water. We obtained an OSL age of 105 ± 7 (PdLII-19) for initial re-occupation of the site, associated with a Typical Mousterian industry. Layer 4B is associated with a lithic assemblage that is quite different from the preceding Typical Mousterian and was assigned to the Denticulate Mousterian. We obtained ages of 80 ± 6 ka (PdLII-18) and 90 ± 6 ka (PdLII-17) for Layer 4B. There is a significant age gap separating the age for Layer 4B and that obtained for Layer 4A1. The samples were collected only cm apart in depth (Figure 3d and e), thus suggesting that there was also a significant break in sedimentation, or an erosional event that removed sediment from the site. An age of 58 ± 4 ka (PdLII-16) was obtained for this layer, associated with the Typical Mousterian, albeit rather poor in lithics, and an age of 61 ± 5 ka (PdLII-14) was obtained for the Typical Mousterian in the overlying Layer 3, much richer in lithics. Five ages from Layer 2G, associated with a scraper-rich Mousterian, gave a weighted mean age estimate of 60.1 ± 2.9 ka. The rest of Layer 2 was not sampled and was almost devoid of tools. Importantly, no MTA industry was identified in Pech II.

14.7.2.1 PECH II COMPARISONS WITH PUBLISHED CHRONOLOGIES

A series of ESR ages and two U-series ages were previously reported by Grün *et al.* (1991) and Schwarcz & Blackwell (1983) for Pech II, respectively. Grün *et al.* (1991) reported ages for 27 individual teeth collected from all major stratigraphic units and for the majority of the teeth, sub-samples were also measured. The U-series

ages were reported for one *in situ* flowstone at the top of Layer 3 and a broken off stalagmite found within the cryoclastic deposit in Layer 5. All the ages are shown together with the OSL ages of this study in Figure 14a and b where Figure 14a shows

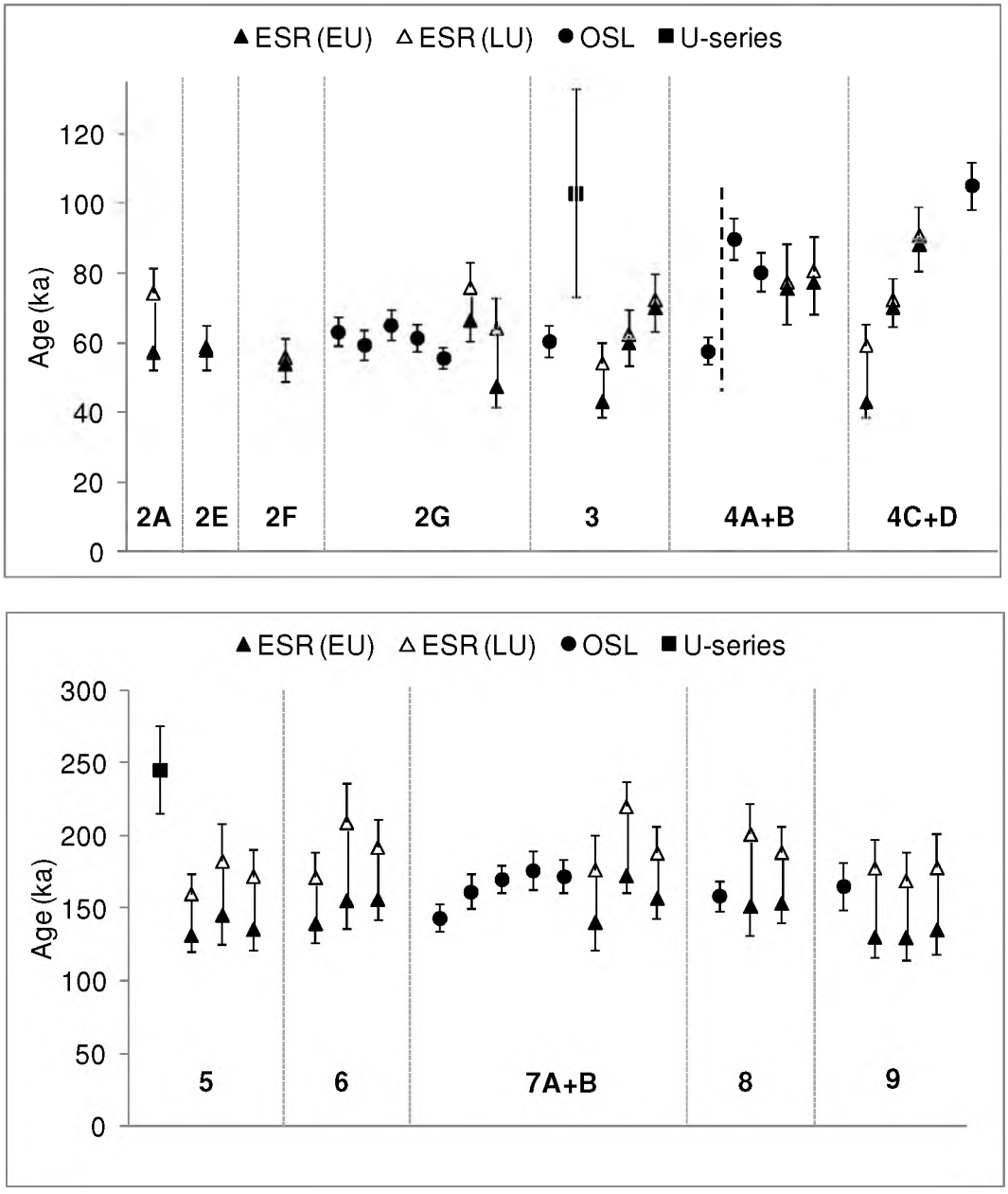

Figure 14: All OSL ages for Pech II together with the previously published ESR (EU and LU) and U-series ages. Ages are plotted with 1σ uncertainties. The EU and LU ages are plotted as a range. Each ESR age is the average of 2 to 4 different fragments of the same tooth (see Grün et al., 1991) for each individual age estimate. a) All ages for deposits above Layer 5 and b) all ages for deposits in Layer 5 and below.

the ages above the cryoclastic deposit and Figure 14b those within and below this layer. The ESR ages represent averages of the different individual fragments of each tooth that was measured.

The ESR ages above the cryoclastic deposit (Layer 5) range between ~40 and ~90 ka, and the majority of the samples show excellent agreement between the EU and LU modelled ages, but there appear to be some age reversals. The ages from within and below Layer 5 range between ~ 130 and 220 ka. These EU and LU modelled ages show less agreement, but Grün *et al.* (1991) made a case for the EU modelled ages to be the more accurate. This was later further investigated in Grün *et al.* (1999) where it was apparent that it is difficult to choose one or the other and that further studies are required to refine the chronology.

In a general sense, the ESR ages are in broad agreement with the OSL ages reported in this study. Both methods suggest two major phases of occupation above and below the cryoclastic deposit. The OSL ages in Layers 2, 3 and 4, however, show improved stratigraphic consistency and also indicate a major hiatus within Layer 4 that was not resolved with the ESR ages.

Schwarcz & Blackwell (1983) also reported U-series ages for Pech II. They dated an *in situ* flowstone at the top of Layer 3 and reported an age of 103^{+30}_{-25} ka. This age is much older than the corresponding ESR and OSL ages, but the errors are large and is, thus, broadly consistent. They also obtained an age of 240 ka on a broken stalagmite in Layer 5, but this stalagmite is not in primary position and can only be used as a maximum age for the deposit.

14.7.3 PECH IV

We were able to obtain reliable ages for all 27 samples collected from Pech IV. We also obtained an additional six ages from three different block samples (denoted as PdAIV in Table 4) from Layers 4A, 5B and 8. The ages range from ~50 ka near the top of the sequence in Layer 3A to ~100 ka at the base of the sequence in Layer

8. The ages and their associated uncertainties are listed in stratigraphic order in Table 4, together with the *P*-values and weighted mean ages for each layer.

The individual ages are plotted in Figure 15 as a function of depth from where it can be seen that the ages are all in good stratigraphic order. Figure 15b shows the weighted mean ages for each layer to which a two period moving average regression line was fitted. This line clearly indicates that the sedimentation rate was not constant over time (as would be expected) and that during periods of most intense occupation (e.g., Layer 8, 6, 5A and 3) the sediment accumulated rapidly compared to the much slower accumulation rate associated with Layer 4 in which evidence of occupation was also sparse.

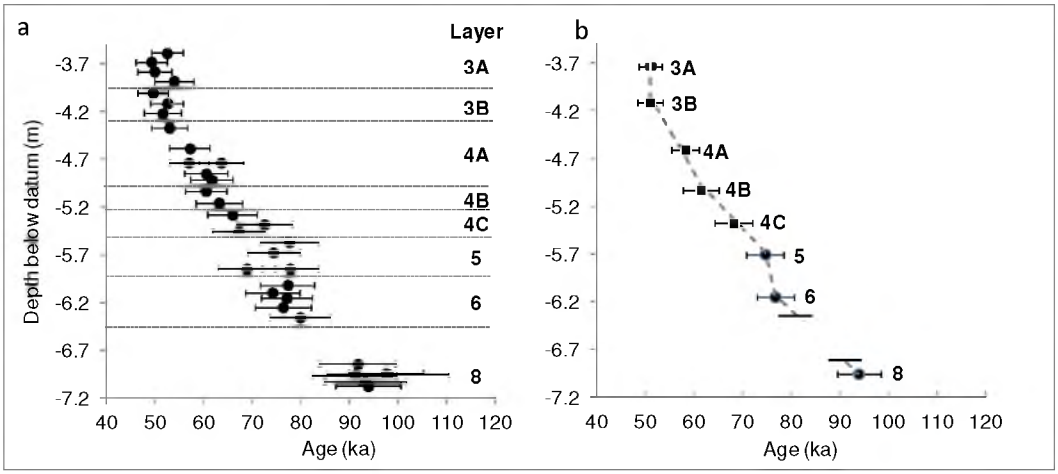

Figure 15: a) All OSL age estimates with their 1σ errors for samples collected from Pech IV shown as a function of their depth below datum and in stratigraphic order with the layer boundaries demarcated. b) Weighted mean ages for each layer plotted as a function of their depth below datum. The stippled line is a two period moving average line fitted to the data. The two horizontal black marks indicate a break between layers 6 and 8 because the samples were not collected from the same stratigraphic profile.

We have demonstrated in Figure 10a that the beta dose rate results, when measured in two different ways, show significant divergence from each other in some parts on the sediment profile possibly because of the mobility of uranium (Figure 10b). We postulated that the beta dose rates derived using GM-25-5 beta counting is superior and this is further supported in Figure 16a where the ages for all the samples from Pech IV are plotted twice, once using the beta dose rate derived from GM-25-5 beta counting (closed circles) and the other using the beta dose rate derived from ICP-MS measurements (open triangles); for clarity the associated errors are not shown in this Figure, but they are included in the age ratios shown in Figure 16b. Figure 16a clearly shows an increase in age with an increase in depth using GM-25-5 beta counting, compared to the occasional significant age reversals obtained using ICP-MS measurements, especially for samples from Levels 6A, 4B and 3A.

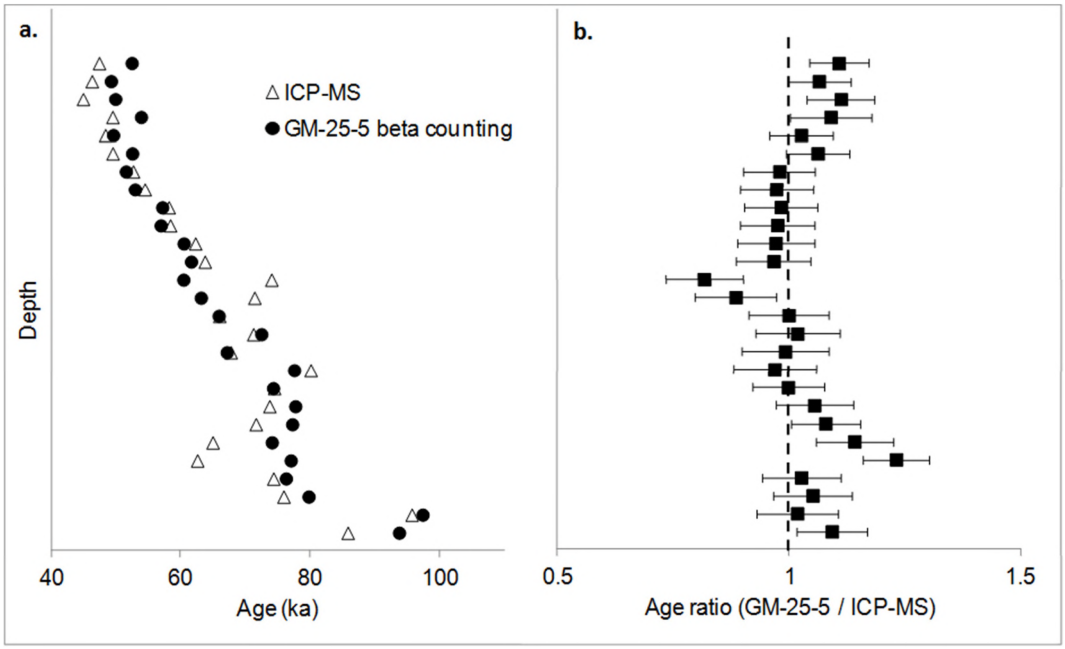

Figure 16: a) Two sets of OSL ages plotted for the same samples from Pech IV. One set (filled circles) were calculated using GM-25-5 beta counting for estimation of the beta dose rate, whereas the other set (open triangles) used ICP-MS measurements for beta dose rates instead. Uncertainties are not shown for clarity. b) Ratio of the two age estimates plotted in a). The broken line indicates unity.

We are, therefore, confident in our ages presented in Table 4 that use GM-25-5 beta counting for estimation of the beta dose rate and in the weighted mean age estimates determined for each of the layers. A weighted mean age of 93.9 ± 4.4 ka (Layer 8) was obtained for the lowermost archaeological deposit that contains Typical Mousterian. We did not collect a sample from Layer 7, so its age remains unknown. An age of 76.3 ± 3.7 ka was obtained for Layer 6 that contains an Asinipodian industry and is significantly younger than the underlying Layer 8. This time gap may be represented by the undated Layer 7, or the site may have been abandoned before or after the initial collapse of the cave roof that covers these two layers. The age of 76.2 ± 4.1 ka for Layer 5 (Typical Mousterian) is almost identical to the age obtained for Layer 6 (Asinipodian) and does not support the macroscopic observation of a sharp and irregular contact between these two layers (Turq *et al.* 2011). A significant break in sedimentation was suggested (Turq *et al.* 2011), but it may be that the duration of this break is shorter than the uncertainties on our age estimates. Based on the ages alone, it appears to have instead been a period of rapid sedimentation (Figure 15b). Chronologies, however, should never be interpreted in isolation from other proxies and information. With OSL, we estimate the last time the sedimentary grains were exposed to sunlight. If the sediment in Layer 5 was re-deposited from sediment inside the cave as a result of groundwater re-working the sediment (as proposed in Turq *et al.* 2011), and was not re-exposed to sunlight, then this age may well be an overestimate of the age for this layer, but its minimum age can be constrained by the age of 68 ± 4 ka for the overlying Level 4C.

Layer 4 shows a continuum of ages from ~70 through to ~58 ka, and the sedimentation was relatively slow compared to periods before and after. It is also the layer with the sparsest archaeological evidence. Three sub-levels were identified based on differences in sedimentology. The weighted mean ages of 68.3 ± 3.9 (Level 4C), 61.5 ± 3.4 (Level 4B) and 57.7 ± 2.9 ka (Level 4A), best constrain the age of this layer. Levels 4C and 4B are representative of the Typical Mousterian, where Level 4A contains Quina Mousterian (Turq *et al.* 2011), so our best age estimate of the Quina Mousterian at Pech IV is 57.7 ± 2.9 ka.

The final occupation in Pech IV – Layer 3 – has been attributed to the MTA, for which we obtain weighted mean ages of 51.0 ± 2.6 (Level 3B) and 51.1 ± 2.4 ka (Level 3A).

14.7.3.1 PECH IV COMPARISONS WITH PUBLISHED CHRONOLOGIES

Three other independent dating techniques have been employed at Pech IV — ^{14}C dating of bone, ESR dating of tooth enamel and TL dating of burnt flints. All three techniques were used to obtain ages for Layer 3, but only TL dating was used to date three of the other layers (Layers 4C, 5A and 8). All the OSL ages are plotted in Figure 17 together with the ^{14}C, ESR and TL ages. The ages are plotted for each layer and also shown, as stippled lines, are the weighted mean ages and 1σ standard errors calculated for the OSL ages for each layer. All OSL ages are shown as filled circles, EU- and LU-modelled ages are shown as closed and open triangles, respectively, TL ages as open diamonds and ^{14}C ages as lines where the line denotes the mid-point value of the 2σ calibration range.

It can be seen for Layer 3 that both the EU and LU modelled ESR ages and the TL ages are statistically consistent with the OSL ages, but all the ^{14}C ages that could be calibrated are systematically too young. The weighted mean OSL age is only slightly older than the 2σ lower range values of 49.5 ka cal BP start age for Layer 3 calculated using a Bayesian model and presented in McPherron *et al.* (2013). There are, however, two ^{14}C estimates for Layer 3B that fall beyond the capability of the currently accepted ^{14}C calibration curve, and these are shown with an arrow pointing upwards to indicate that they are minimum ages. Both these ages must be >50 cal BP, the current upper range of the calibration curve, and are thus consistent with the other independent ages. This suggests that the other ^{14}C ages may be very slight underestimates of the true ages due to small-scale contamination.

The TL and OSL ages for Layers 4C, 5A and 8 also show excellent agreement. Richter *et al.* (2013) reported two TL ages for Level 4C of 69 ± 7 and 72 ± 7 ka, and these agree with the weighted mean OSL age of 68 ± 4 ka. They also reported a

weighted mean TL age (N = 4) for Level 5A of 74 ± 5 ka that is in agreement with the OSL weighted mean age of 76 ± 4 ka, and a weighted mean TL age for Layer 8 (N = 6) of 96 ± 5 ka that is consistent with the OSL weighted mean age of 94 ± 4 ka.

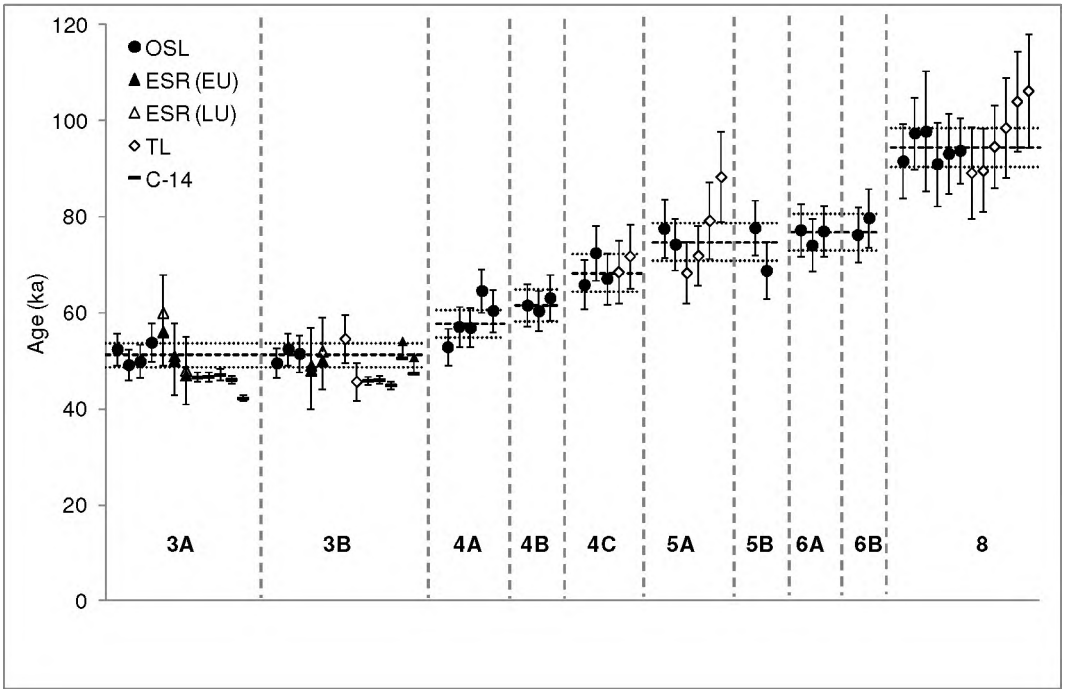

Figure 17: All OSL ages for Pech IV together with all independent ages published previously for Pech IV, shown per layer. Ages are plotted with 1σ uncertainties. The EU and LU ages are plotted as a range and the ^{14}C ages are plotted where the line is the midpoint value of the calibrated range and the error bars represent the entire range. The broken line is the weighted mean age calculated for all the OSL ages in a layer and the stippled lines are the 1σ standard error on the weighted mean age.

14.8DISCUSSION

Bordes (1975, 1978) used the information he gathered based on the archaeological industries, fauna and, in particular, the geological work of Laville (1973) to correlate the three sites and to place the archaeological deposits within a

climatic framework using the Würm and Riss climatic phases that was in vogue in Europe at the time. His proposed correlations are presented in Table 5. Bordes placed all of Pech I in Würm II (similar to marine isotope stage (MIS) 3), together with the uppermost layers of Pech IV (Layers F1-4). These layers contain MTA Type A and B industries. The rest of Pech IV and the deposits above the large cryoclastic deposit in Pech II were all placed in Würm I (similar to MIS 4). The deposits below the cryoclastic layer in Pech II were all placed within the Riss (similar to MIS 6). Bordes drew direct parallels between only a few layers, including the MTA layers in both Pech I and Pech IV, in particular Layer 4 at Pech I and F4 at Pech IV (MTA-A) and Layers 6 and 7 at Pech I and F1 and F2 at Pech IV (MTA-B), as well as Layer 4C at Pech II and Layer X at Pech IV (Typical Mousterian). He recognised these to be typologically similar and suggested these belong to the same climatic and chronological phases. He also recognised that some assemblages had no equivalents among the three different sites, and saw these as assemblages made by different groups of people occupying the sites during the same climatic phase, but perhaps centuries earlier or later. Bordes, thus, interpreted the deposits to span a relatively short, and almost continuous, period of time and remarked that *"Our temporal control is not fine enough, and probably will never be"* (Bordes 1978). These correlations have since drawn substantial criticism (Mellars 1988, Texier 2000, Bertran & Texier 1995).

The common chronology for all three Pech sites presented here now enables us to test the correlations proposed by Bordes (1975, 1978). In this study, we made measurements on individual sand-sized grains of quartz to maximise the benefits inherent in single-grain OSL dating. These include the identification of contaminant grains in a sample and their exclusion before final age determination, and the ability to directly check the stratigraphic integrity of archaeological sequences and take into account any post-depositional sediment mixing (Jacobs & Roberts 2007). We also measured all samples using the same GM-25-5 beta counter, OSL equipment and irradiated the grains using the same laboratory radiation source, and all the data were analysed by a single operator using a common set of procedures (a subset of the samples were cross-checked for operator bias). By holding constant all of these

Table 5: Correlations between the three sites proposed by Bordes (1975, 1978) based on the climate, fauna, geology and archaeological industries. Also shown for Pech IV is the current stratigraphic units proposed in Turq et al. (2011) and used in the rest of this study.

Climatic Phase	**Pech I**		**Pech II**		**Pech IV**		
Würm / Périgord	Layer	Industry	Layer	Industry	Layer (Bordes, 1975)	Layer (Turq *et al.*, 2011)	Industry
II / V (less cold, damp)	Rock fall	—	—	—	E	1	—
II/ IV (very cold, dry)	7	MTA-B	—	—	F1	2	MTA-B
II / III (less cold, damper)	6	MTA-B	—	—	F2	3A	MTA-B
II / II (cold, dry)	5	MTA-A/B	—	—	F3	3A	MTA-A/B
II / I (very cold, damp)	4	MTA-A	—	—	F4	3B	MTA-A
I / IX (cold, very dry)	—	—	2A–2C	Mousterian	G	4A	Mousterian
I / VIII (milder)	—	—	2D	Mousterian	H1–H2	4A	TM
I / VII (cold, dry)	—	—	2E–2F	TM	I1–I2	4B (I1) 4C (I2)	TM
I / VI (mild)	—	—	2G	Mousterian	J1	5A	TM
I / V (short, cold)	—	—	2G' top	Mousterian	J2	5B	TM
I / IV (mild, damp)	—	—	2G' base	Mousterian	J3a–c	6A (J3a-b) 6B (J3c)	Asinipodian
I / III (cold, dry)	—	—	3	TM	Rock fall		—
I / II (mild, damp)	—	—	4A	TM	X	7 (X top)	TM
	—	—	4B	DM	X		TM
	—	—	4C	TM	X		TM
I / I (short, cold)	—	—	4D–E	TM	Y–Z	8 (X base, Y-Z)	TM

experimental variables for all samples, it was possible to remove much of the unwanted 'noise' in OSL data that typically prevents high-resolution ages from being obtained. In addition, the sources of error that apply to all samples (i.e., systematic errors) could be removed using this systematic approach, allowing all ages to be placed on the same calibrated timescale with improved precision (e.g., Jacobs *et al.*

2008c). For purposes of comparison we have, therefore, used the random errors only and these are provided in brackets in Tables 2, 3 and 4. We have plotted the three stratigraphic profiles of the sites together with the OSL ages for all samples in Figure 18 where we used different colours to indicate age equivalence or not. We also summarised our proposed correlations based on chronology only in Table 6, together with the corresponding marine isotope stages (MIS).

Table 6: Correlations between the three Pech sites based on the chronologies constructed in this study, together with the broad age range and corresponding marine isotope stages.

Climatic Phase	**Pech I**		**Pech II**		**Pech IV**	
Marine Isotope Stage (MIS) / Approximate age	Layer	Industry	Layer	Industry	Layer	Industry
	Rock fall	—			1	—
MIS 3 (~51 ka)	7 6 5 4	MTA-B MTA-B MTA-A/B MTA-A			2 3A 3A 3B	MTA-B MTA-B MTA-A/B MTA-A
End of MIS 4, beginning of MIS 3 (~63 to ~55 ka)	Yellow-red sand (Layer 3(?))	—	2A–2G 3 4A	FM with Levallois flakes and Quina scrapers TM TM	4A 4B (I1)	Quina TM
End of MIS 5a, all of MIS 4 (~77 to ~65 ka)					4C 5A 5B 6A 6B	TM Asinipodian
MIS 5d to MIS 5b (~105 to ~80 ka)			4B 4C 4D–E	DM TM	7 8	? TM
MIS6 (~180-~140 ka)			6-9	Clactonian and Acheulian		

The oldest dated deposits are found only at Pech II in Layers 6-9 (below the large cryoclastic deposit represented by Layer 5) and are indicated in purple in Figure 18. These deposits date to between ~140 and 180 ka, which falls within the

penultimate glacial period, MIS 6; the associated lithic assemblages have been assigned to the Clactonian and Acheulian by Bordes (1972). We have not plotted these ages in Figure 18 for clarity, but they are provided in Table 3. We did not directly date Layer 5, but it likely relates to the penultimate glacial maximum at ~ 132 ka, and this is supported by a number of ESR ages on tooth enamel.

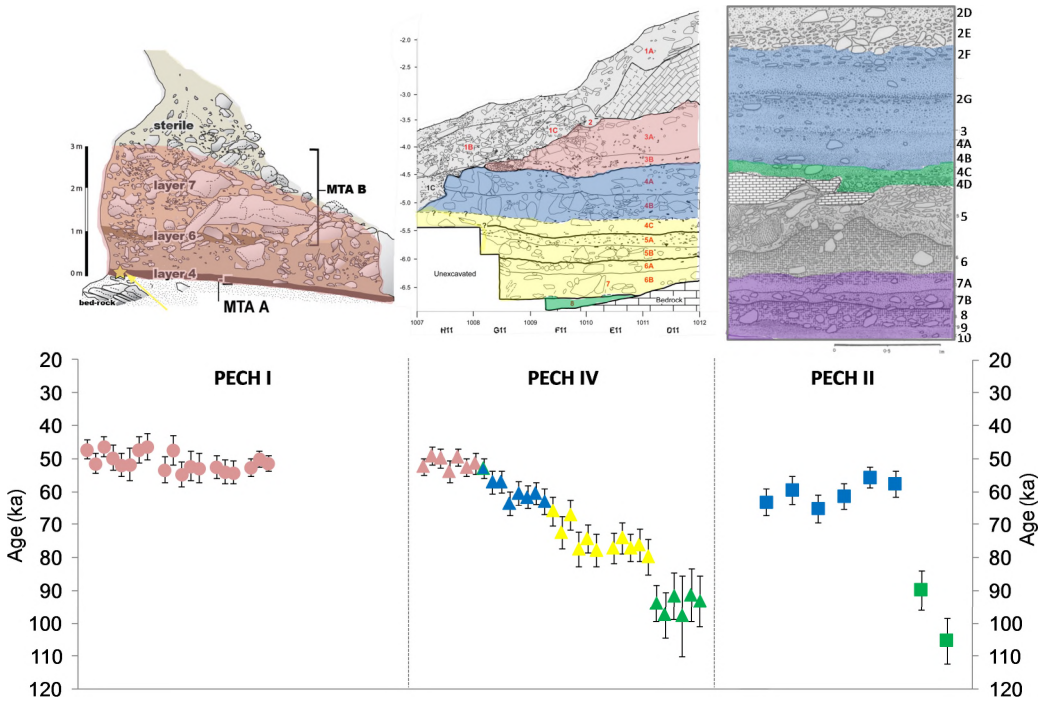

Figure 18: Composite figure of all three sites indicating where there is overlap with regards to age (shown as the same colour; pink, blue and green), where deposits are only represented in one site (yellow and purple) and those parts of the sequences that remains undated (shown in grey). We omitted the ages for the deposits below cryoclastic layer in Pech II (shown in purple) for clarity, but these ages are provided in Table 3.

The first dated intact deposit in Figure 18 is from Pech II in Layer 4D for which we obtained an age of 105.3 ± 5.2 ka (MIS 5d). This suggests either that the Pech sites were not occupied during the last interglacial (MIS 5e) or that no evidence for occupation at this time is preserved at any of the three sites (perhaps having been

washed out of the sites). Significant flowstone deposits can be found in the tunnel between Pech I and Pech II and these have been dated to MIS 5e at ~125 ka (Schwarcz & Blackwell 1983), and post-depositional flowstone into the cryoclastic deposit in Layer 5 can also be seen. It is also evident from thin sections of Layer 4D that water might have washed out the fine fraction, providing further support that water action was at work in at least Pech II. The absence of evidence, however, does not necessarily support an evidence of absence at Pech II and even perhaps Pech IV.

The age for Layer 4D (105.3 ± 5.2 ka) is statistically consistent with the two ages for Layer 4B (80 ± 6 and 90 ± 5 ka; MIS 5b/c) and also the weighted mean age of 93.9 ± 3.0 ka (MIS 5c) for 6 samples from Layer 8 in Pech IV. This correlation is shown in green in Figure 18. The ages for Layers 4B and 4D from Pech II bracket Layer 4C that Bordes thought was equivalent to Layer X (=Layers 7 and 8) in Pech IV based on typological similarities. Our correlations, thus, supports his, even though it is older than he anticipated (e.g., he place it in Würm I, roughly equivalent to MIS 4). He also suggested that the archaeological assemblage in Layer 4B in Pech II, a Denticulate Mousterian, had no equivalent in Pech IV. Our ages for Layer 4B suggest that it might be a little later than Layer 4C/4D (Pech II) and Layer 8 (Pech IV), but we don't have the precision to resolve the difference statistically.

In Pech IV there is no evidence for occupation or sediment deposition during MIS 5b between ~90 and 80 ka (Figures. 13 and 14). Pech IV is then re-occupied again at the end of MIS 5a at ~77 ka in Layer 6B and shows continuous sediment deposition with sparse archaeological evidence throughout MIS 4 in Levels 6A, 5A, 5B and 4C (shown in yellow in Figure 18). There is no chronological parallel in Pech II where the age hiatus suggests no sediment deposition during MIS 4. Bordes (1978) explicitly mentioned that his Layers J3a-J3c (corresponding to Layers 6A and 6B in the recent excavations) in Pech IV containing the Asinipodian are very different from anything seen in Pech I or Pech II, and we have now confirmed in this study that there is no age equivalent.

It is only at the start of MIS 3 at ~60 ka that chronological parallels can again be drawn between Pech II and Pech IV (shown in blue in Figure 18). Age estimates

for Layers 4A, 3, 2G and 2F at Pech II are indistinguishable from each other at 57.7 ± 3.2 (Layer 4A), 61 ± 5 (Layer 3), and 60.1 ± 1.3 (Layer 2G) (see Table 3). We did not obtain any age estimates for Layers 2A-2F at Pech II; Layers 2A-2C were not present in the profile we sampled and Layers 2D to 2F were very friable and full of large limestone spall (Figure 3d and e). ESR ages for Layer 2A and 2E (Figure 14), however, are indistinguishable from each other and from ages for Layers 2F and 2G (Figure 14; Grün *et al.* 1991). Bordes also noted that the upper part of Layer 2 contained very little archaeological material and that Layer 2G was archaeologically the densest part of Layer 2. We are, thus, treating all of Layers 2, 3 and 4A as age equivalent deposits. These deposits are comparable to the ages obtained for Levels 4A (58.3 ± 1.4 ka) and 4B (61.5 ± 2.5 ka) at Pech IV (Table 4). Our correlations are shown in blue in Figure 18, and, thus, differ from Bordes' correlation of the entire Layer 2 (A-G') at Pech II to Levels 4A through to 6B at Pech IV (see Table 5). As discussed above, Layers 4C, 5 and 6 at Pech IV have no age parallels at Pech II. Interestingly, Bordes described the archaeological assemblages from Layer 2 (Pech II) as Ferrassie-type Mousterian with Levallois flakes and Quina-type scrapers (Bordes, 1972) and Layer 4A (Pech II) as Typical Mousterian. Layer 4A in Pech IV is now known to be Quina Mousterian, whereas Layer 4B has been defined as Typical Mousterian (Turq *et al.* 2011). The co-occurrence of Quina scrapers in coeval deposits at Pech II and Pech IV overlying Typical Mousterian deposits might be meaningful.

We also obtained an age of ~61 ka for a pocket of yellow-red sand sampled from the cave wall at Pech I. This layer underlies Layers 4-7 and cannot currently be seen in the witness section, but it was observed by Soressi (pers. comm.) during her excavations between Layer 4 and the fluvial sands at the very base of the sequence (Texier 2009). At present we do not know anything more about its sedimentological characteristics or whether or not it contains any archaeological materials. But, it is interesting that it matches in age and in colour the sedimentary deposits at the top of Pech II and is, apart from the fluvial sands at the base of both sites (Texier, 2009), currently the only connection between all three sites.

Pech I and Pech IV show chronological overlap at the top of their respective archaeological sequences (shown as pink in Figure 18) and the archaeological assemblages in both these sites belong to the MTA. We obtained identical ages at both sites and dated the MTA to ~51 ka in MIS 3. This supports the correlation drawn by Bordes (Table 5). Also, Bordes did not identify any MTA at Pech II, and in our chronology we see no occupation at Pech II during the MTA time period of Pech I and IV. We could not resolve the ages of the MTA-A and MTA-B, suggesting that in these sites the duration of these two assemblage types is probably shorter than the uncertainties associated with our ages. If we make the assumption that the MTA is a chronological phase in southwest France, then at Pech IV the start of the MTA is constrained by the underlying Quina Mousterian dated to ~58 ka. The end of the MTA is constrained by the start of the Chatelperronian and Proto-Aurignacian in southwest France. Dates of both of these entities are debated and under revision, but the Proto-Aurignacian of the nearby site of Isturitz can be dated to XX and the start date for the Chatelperronian at the more northern sites of Grotte du Renne and Les Cottés is ~45 ka (Hublin *et al.* 2012, Talamo *et al.* 2012). These ages in combination with the Pech I and IV dates leave some time for a longer duration of the MTA-B or for another archaeological entity as some have suggested (Jaubert *et al.* 2011, Discamps *et al.* 2011). The TL ages for the base of the MTA-B from Le Moustier (Level H1) fall within this gap (Valladas *et al.* 1986).

14.9CONCLUSIONS

The archaeological sequences at Pech de l'Azé provide insights into the timing and nature of the Mousterian in southwestern France during the Late Pleistocene. By dating individual grains of quartz, we have been able to construct a detailed and reliable chronology for all three sites (Pech I, II and IV) that are consistent with, and support, the previous TL, ESR and, to a lesser extent, the ^{14}C chronologies. The advantage of the new single-grain OSL chronologies is that it provides a linked temporal framework for the vast majority of layers and levels in all three sites, and these new ages are directly comparable at a higher temporal resolution due to the systematic study design.

None of the sites were occupied continuously or preserve a complete and continuous sedimentary record. There is no archaeological overlap linking all three sites. There is some chronological overlap between Pech I and IV, and between Pech II and IV, but none between Pech I and II, even though the latter two sites are situated adjacent to each other and separated only by a karstic tunnel.

Together, the three sites contain 5 of the 6 known Mousterian variants, namely the MTA (Pech I and IV), Quina Mousterian (Pech II and IV), the Asinipodian (Pech IV), Typical Mousterian (Pech II and IV) and the Denticulate Mousterian (Pech II). The single-grain OSL chronologies constructed for these three sites suggest that, at least locally, these variants form a time sequence. This conclusion is in contrast to the recent suggestions of Guibert *et al.* (2008) and Richter *et al.* (2013), who compared ages obtained from a range of sites, constructed using a variety of techniques and different laboratories to support an emerging pattern of considerable temporal overlap among different Mousterian variants.

14.10 ACKNOWLEDGEMENTS

This research was funded by the Australian Research Council through Discovery Project grant DP1092843 to Jacobs, Dibble and McPherron. We would like to specially thank The National Museum at Les Eyzies and its Director, Mr Cleyet-Merle and the Pech IV property owner, Mr LaPlanche. Sam Lin assisted with the survey to get accurate locational information for the OSL samples. Yasaman Jafari and Terry Lachlan helped with all aspects of the OSL dating program. We also thank all members of the excavation and research teams for valuable information that has helped us to understand and interpret the OSL data.

14.11 REFERENCES

AITKEN M. J. 1985. *Thermoluminescence Dating.* Academic Press.

Aitken M.J. 1998. *An Introduction to Optical Dating*. Oxford University Press, Oxford.

BALLARINI M., WINTLE A.G. & WALLINGA J. 2006. Spatial variation of dose rates from beta sources as measured using single grains. *Ancient TL* **24**, 1-8.

BELL W.T. & ZIMMERMAN, D.W. 1978. The effect of HF acid etching on the morphology of quartz inclusions for thermoluminescence dating. *Archaeometry* **20**, 63-65.

BØTTER-JENSEN L. & MEJDAHL V. 1988. Assessment of beta dose-rate using a GM multicounter system. *Nuclear Tracks and Radiation Measurements* **14**, 187-191.

BØTTER-JENSEN L., BULUR E., DULLER G.A.T. & MURRAY, A.S. 2000. Advances in luminescence instrument systems. *Radiation Measurements* **32**, 523-528.

BERTRAN P. & TEXIER, J.-P. 1995. Fabric Analysis: application to Paleolithic Sites. *Journal of Archaeological Sciences* **22**, 521-535.

BINFORD L. 1973 Interassemblage variability: The Mousterian and the functional argument. *In*: Renfrew C. ed., *The Explanation of Culture Change*. London : Duckworth, pp 227-254.

BORDES F. 1954-55. Les gisements du Pech de l'Azé (Dordogne). In: Le Mousterien de tradition acheuléenne I et suite, avec une note paleontologique de J.Bouchud. *L'Anthropologie* **58-59**, 401-432 & 401-438.

BORDES F. 1969. Os percé moustérien et os grave acheuléen du Pech de l'Azé II. *Quaternarian* **XI**: 1-6.

BORDES F. 1971 Physical evolution and technological evolution in man: a parallelism. *World Archaeology* **3**, 1-5.

BORDES F. 1972. *A Tale of Two Caves*. Harper and Row, New York.

BORDES F. 1975. Le gisement de Pech de l'Azé IV: Note préliminaire. *Bulletin de la Société Préhistorique Française* **72**: 293–308.

BORDES F. 1977. Time and space limits in the Mousterian. *In*: Wright R.V.S. ed., *Stone Tools as Cultural Markers*. Canberra: Australian Insitute of Aboriginal Studies, pp 37-39.

BORDES F. 1978. Typological variability in the Mousterian layers at Pech de l'Azé I , II and I V. *Journal of Anthropological Research* **34**, 181-193.

BORDES F. & BOURGON M. 1950. Le gisement du Pech de l'Azé-Nord : prise de date et observations preliminaries. *BSPF* **47**, 381-383.

BORDES F. & BOURGON M. 1951. Le gisement du Pech de l'Azé-Nord, campagnes 1950-1951: les couches inférieures à Rhinoceros mercki. *BSPF* **48**, 520-538.

BORDES F. & PRAT, F. 1965. Observations sur les faunes du Riss et Würm I en Dordogne. *L'Anthropologie* **69**, 31-45.

BOWMAN S.G.E. & SIEVEKING, G.D.G. 1983. Thermoluminescence dating of burnt flint from Combe Grenal. *PACT* **9**, p. 253-268.

DIBBLE H.L., RACZEK T.P. & MCPHERRON S.P. 2005. Excavator bias at Pech de l'Azé IV, France. *Journal of Field Archaeology* **30**, 317-328.

DIBBLE H., BERNA F., GOLDBERG P., MCPHERRON S., MENTZER S., NIVEN, L., RICHTER D., THÉRY-PARISOT I.,SANDGATHE D. & TURQ, A. 2009. A Preliminary Report on Pech de l'Azé I V, Layer 8 (Middle Paleolithic,France). *PaleoAnthropology*, 182-219.

DISCAMPS E., JAUBERT J. & BACHELLERIE F. 2011. Human choices and environmental constraints: deciphering the variability of large game procurement from Mousterian to Aurignacian times (MIS 5e3) in southwestern France. *Quaternary Science Reviews* **30**, 2755-2775.

DISCAMPS E. In press. Ungulate biomass fluctuations endured by Middle and Early Upper Paleolithic societies (SW France, MIS 5-3): The contributions of modern analogs and cave hyena paleodemography. *Quaternary International* doi: 10.1016/j.quaint.2013.07.046.

DULLER G.A.T. 2004. Luminescence dating of Quaternary sediments: recent advances. *Journal of Quaternary Science* **19**, 183-192.

DULLER G.A.T. 2007. Assessing the error on equivalent dose estimates derived from single aliquot regenerative dose measurements. *Ancient TL* **25**, 15-24.

DULLER G.A.T. 2003. Distinguishing quartz and feldspar in single grain luminescence measurements. *Radiation Measurements* **37**, 161-165.

FALGUERES C., BAHAIN J.-J. & SALEKI, H. 1997. U-Series and ESR dating of teeth from Acheulian and Mousterian levels at La Micoque (Dordogne, France). *Journal of Archaeological Science* **24**, 537-545.

GALBRAITH R.F., ROBERTS R.G., LASLETT G.M., YOSHIDA H. & OLLEY J.M. 1999. Optical dating of single grain and multiple grains of quartz from Jinmium rock shelter, Northern Australia: Part I, experimental design and statistical models. *Archaeometry* **41**, 339-364.

GALBRAITH R.F. 2003. A simple homogeneity test for estimates of dose obtained using OSL. *Ancient TL* **21**, 75-77.

GOLDBERG P. 1979. Micromorphology of Pech de l'Azé II: sediments. *Journal of Archaeological Sciences* **6**, 17-47.

GOLDBERG P., DIBBLE H., BERNA F., SANDGATHE D., MCPHERRON S.J.P. & TURQ A. 2012. New evidence on Neandertal use of fire: Examples from Roc de Marsal and Pech de l'Azé IV. *Quaternary International* **247**, 325-340.

GRÜN R., MELLARS P. & LAVILLE H. 1991. ESR chronology of a 100,000 year archaeological sequence at Pech de l'Azé II (France). *Antiquity* **65**, 544-551.

GRÜN R., YAN G., MCCULLOCH M. & MORTIMER G. 1999. Detailed mass spectrometric U-series analyses of two teeth from the archaeological site of Pech de l'Azé II : Implications for uranium migration and dating. *Journal of Archaeological Science* **26**, 1301-1310.

GUÉRIN G., MERCIER N. & ADAMIEC G. 2011. Dose-rate conversion factors: update. *Ancient TL* **29**, 5-8.

GUÉRIN G., DISCAMPS E., LAHAYE C., MERCIER N., GUIBERT P., TURQ A., DIBBLE H.L., MCPHERRON S.P., SANDGATHE D., GOLDBERG P., JAIN M., THOMSEN K., PATOU-MATHIS M., CASTEL J. & SOULIER M. 2012. Multi-method (TL and OSL), multi-material (quartz and flint) dating of the Mousterian site of Roc de Marsal (Dordogne, France): correlating Neanderthal occupations with the climatic variability of MIS 5-3. *Journal of Archaeological Science* **39**, 3071-3084.

GUIBERT P., BECHTEL F. & SCHVOERER M., 1997. Déséquilibre des séries de l'uranium, implications sur la dose annuelle en datation par thermoluminescence : une étude à la grotte XVI, Cénac et Saint-Julien, Dordogne, France. *Quaternaire* **8**, 377-389.

GUIBERT P., BECHTEL F., SCHVOERER M., RIGAUD J.-P. & SIMEK J.-F. 1999. Datation par thermoluminescence de sediments chauffés provenant d'une aire de combustion moustérienne (Grotte XVI, Cénac et St-Julien, Dordogne, France). *Revue d'Archéométrie* **23**, 163-175.

GUIBERT P., BECHTEL F., BOURGUIGNON L., BRENET M., COUCHOUD I., DELAGNES A., DELPECH F., DETRAIN L., DUTTINE M., FOLGADO M., JAUBERT J., LAHAYE C., LENOIR M., MAUREILLE B., TEXIER J.-P., TURQ A., VIEILLEVIGNE E. & VILLENEUVE G. 2008. Une base de données pour la chronologie du Paléolithique moyen dans le Sud-Ouest de la France. *In*: Jaubert J., Bordes J.-G. & Ortega I. eds. *Les sociétés du Paléolithique dans un Grand Sud-Ouest de la France: nouveaux gisements,nouveaux résultats, nouvelles méthodes* **47**. pp 19-40. Sociéte préhistoriques française Bordeaux,

HIGHAM T. 2011. European Middle and Upper Palaeolithic radiocarbon dates are often older than they look: problems with previous dates and some remedies. *Antiquity* **85**, 235-249.

HUBLIN J.-J., TALAMO S., JULIEN M., DAVID F.,CONNET N., BODU P., VANDERMEERSCH B. & RICHARDS M.P. 2012. Radiocarbon dates from the Grotte du Renne and Saint-Césaire support a Neandertal origin for the Châtelperronian. *Proceedings of the National Academy of the USA* **109**, 18743-18748.

HUNTLEY D.J., GODFREY-SMITH D.I. & THEWALT M.L.W. 1985. Optical dating of sediments. *Nature* **313**, 105–107.

JACOBS Z., ROBERTS R.G., GALBRAITH R.F., DEACON H.J., GRÜN R., MACKAY A., MITCHELL P., VOGELSANG R. & WADLEY L. 2008. Ages for the Middle Stone Age of Southern Africa: Implications for Human Behavior and Dispersal. *Science* **322**, 733-735.

JACOBS Z. & ROBERTS R.G. 2007. Advances in Optically Stimulated Luminescence Dating of Individual Grains of Quartz from Archeological Deposits. *Evolutionary Anthropology* **16**, 210-223.

JACOBS Z., DULLER G.A.T. & WINTLE A.G. 2006a. Interpretation of single grain D_e distributions and calculation of D_e. *Radiation Measurements* **41**, 264-277.

JAUBERT J., BORDES J.-G., DISCAMPS E. & GRAVINA B. 2011. A new look at the end of the Middle Palaeolithic sequence in southwestern France. *In*: Derevianko A.P. & Shunkov M.V. eds. *Characteristic features of the Middle to Upper Paleolithic transition in Eurasia*. Asian Palaeolithic Association, Novosirbirsk.

JONES H.L. 2001. Electron Spin Resonance (ESR) dating of tooth enamel at three Palaeolithic archaeological sites. Unpublished M.Sc. thesis, McMaster University, Canada.

LAHAYE C. 2005. Nouveaux apports de la thermoluminescence à la chronologie du Paléolithique dans le Sud-Ouest de la France. Études en milieu hétérogène et en présence de déséquilibres radioactifs dans les séries de l'uranium. Thèse de Doctorat, Université Bordeaux 3, 428 p.

LAQUAY G. 1981. Recherches sur les faunes du Würm I en Périgord, Thèse de 3e cycle, Université deBordeaux 1, 506 p.

LARTET E. & CHRISTY H. 1864. Cavernes du Périgord. *Revue Archéologique* **1**, 233-267.

LAVILLE H., RIGAUD J.-P. & SACKETT J. 1980. *Rock Shelters of the Perigord: Geological Stratigraphy and Archaeological Succession*. Academic Press, New York.

LAVILLE H. 1975. Climatologie et chronologie du paléolithique en Périgord: Etude sédimentologique de depots en grottes et sous abris. Marseilles: Université de Provence.

LAVILLE H. 1973. The relative position of Mousterian industries in the climatic chronology of the Early Würm in the Périgord. *World Archaeology* **4**, 323-329.

LIAN O.B. & ROBERTS R.G. 2006. Dating the Quaternary: progress in luminescence dating of sediments. *Quaternary Science Reviews* **25**, 2449-2468.

MCPHERRON S. & DIBBLE H.L. 2000. The lithic assemblages of Pech de l'Azé IV (Dordogne, France). *Préhistoire Européenne* **15**, 9–43.

MCPHERRON S., SORESSI M. & DIBBLE H. 2001. Deux nouveaux projets de recherché à Pech de l'Azé (Dordogne, France). *Préhistoire du Sud-Ouest* **8**, 11-30.

MCPHERRON S.P., TALAMO S., GOLDBERG P., NIVEN L., SANDGATHE D., RICHARDS M.P., RICHTER D., TURQ A. & DIBBLE H.L. 2012. Radiocarbon dates for the late Middle Palaeolithic at Pech de l'Azé IV, France. *Journal of Archaeological Science* **39**, 3436-3442.

MEJDAHL V. 1979. Thermoluminescence dating: beta-dose attenuation in quartz grains. *Archaeometry* **21**, 61–72.

MELLARS P. & GRÜN R. 1991. A Comparison of the electron spin resonance and thermoluminescence dating methods: the results of ESR dating at Le Moustier (France). *Cambridge Archaeological Journal* **1**, 269-276.

MELLARS P. 1969. The chronology of Mousterian industries in the Périgord region of southwest France. *Proceedings of the Prehistoric Society* **35**, 134-171.

MELLARS P. 1970 Some comments on the notion of "functional variability" in stone-tool assemblages. *World Archaeology* **2**, 74-89.

MELLARS P. 1988. The chronology of the South-West French Mousterian: A review of the current debate. In: Binford L. & Rigaud J.-P. eds., *L'Homme de Neandertal* -4- La technique, p. 97-120. ERAUL, Liège.

MELLARS P. 1989 Technological changes across the Middle-Upper Palaeolithic transition: economic, social and cognitive perspectives. *In*: Mellars P. & Streinger C. eds., *The Human Revolution* p. 339-365. Princeton University Press, New Jersey.

MELLARS P. 1992 Technological Changes in the Mousterian of Southwest France. *In*: Dibble H.L. & Mellars P.A. eds., *The Middle Paleolithic : adaptation, behaviour, and variability.* p. 29-43. Monograph of the University of Pennsylvania Museum, n° 78.

MERCIER N. & FALGUÈRES C. 2007. Field gamma dose-rate measurement with a NaI(Tl) detector: re-evaluation of the 'threshold' technique. *Ancient TL* **25**, 1-4.

MURRAY A.S. & WINTLE A.G. 2000. Luminescence dating of quartz using an improved single-aliquot regenerative-dose protocol. *Radiation Measurements* **32**, 57-73.

PAQUEREAU M.M. 1969. Étude palynologique du Würm I du Pech de l'Azé (Dordogne). *Quaternaria* **XI**, 227-235.

PEYRONY D. 1925. Le gisement préhistorique du haut de Combe-Capelle. Moustérien de Tradition Acheuléen. *Association Française pour l'Avancement des Sciences* **49**, 484-487.

PRESCOTT J.R. & HUTTON J.T. 1994. Cosmic ray contributions to dose rates for luminescence and ESR dating: Large depths and long term time variations. *Radiation Measurements* **23**, 497-500.

RHODES E. J. & SCHWENNINGER J.-L. 2007. Dose rates and radioisotope concentrations in theconcrete calibration blocks at Oxford. *Ancient TL* **25**, 5-8.

RICHTER D., DIBBLE H., GOLDBERG P., MCPHERRON S.P., NIVEN L., SANDGATHE D., TALAMO S. & TURQ A. 2013. The late Middle Palaeolithic in southwest France: New TL dates for the sequence of Pech de l'Azé IV. *Quaternary International* **294**, 160-167.

RITTENOUR T.M. 2008. Luminescence dating of fluvial deposits: applications to geomorphic, palaeoseismic and archaeological research. *Boreas* **37**, 613-635.

ROLLAND N. & DIBBLE H. 1990. A new synthesis of Middle Paleolithic variability. *American Antiquity* **55**, 480-499.

SCHWARCZ H.P. & BLACKWELL B. 1983. $^{230}Th/^{234}U$ age of a Mousterian site in France. *Nature* **301**, 236-237.

SMITH M.A., PRESCOTT J.R. & HEAD M.J. 1997. Comparison of ^{14}C and luminescence chronologies at Puritjarra rock shelter, central Australia. *Quaternary Science Reviews* **16**, 299-320.

SORESSI M. 2004. From Mousterian of Acheulian tradition type A to type B: technical tradition, raw material, task, or settlement dynamic changes? *In*: Conard N.J. ed., *Settlement Dynamics of the Middle Paleolithic and Middle Stone Age* **2**, pp. 343-366. Tübingen Publications in Prehistory, Tübingen.

SORESSI M., MCPHERRON S.P., LENOIR M., DOGANDŽIĆ T., GOLDBERG P., JACOBS Z., MAIGROT Y., MARTISIUS N., MILLER C.E., RENDU W., RICHARDS M.P., SKINNER M.M., STEELE T.E., TALAMO S. & TEXIER J.-P. 2013. Neandertals made the first specialized bone tools in Europe. *Proceedings of the National Academy of Sciences of the USA* **110**, 14186-14190.

SORESSI M., JONES H.L., RINK W.J., MAURILLE B. & TILLIER A.-M. 2007. The Pech-de-l'Azé I Neandertal child: ESR, uranium-series, and AMS ^{14}C dating of its MTA type B context. *Journal of Human Evolution* **52**, 455-466.

TALAMO S., SORESSI M., ROUSSEL M., RICHARDS M. & HUBLIN J.-J. 2012. A radiocarbon chronology for the complete Middle to Upper Palaeolithic transitional sequence of Les Cottés (France). *Journal of Archaeological Science* **39**, 175-183.

TEXIER J.-P. 2000. À propos des processus de formation des sites préhistoriques. *Paléo* **12**, 379-386.

TEXIER J.-P. 2009. *Histoire Géologique de Sites Préhistoriques Classiques du Périgord: Une Vision Actualisée.* Éditions du Comité des travaux historiques et scientifiques, Paris.

TURQ A., DIBBLE H.L., GOLDBERG P., MCPHERRON S.P., SANDGATHE D., JONES H., MADDISON K., MAUREILLE B., MENTZER S., RINK J. & STEENHUYSE A. 2011. Les Fouilles Récentes du Pech de l'Azé IV (Dordogne). *Gallia Préhistoire* **53**, 1-58.

VALLADAS H., GENESTE J.-M., JORON J.-L. & CHADELLE J.-P. 1986. Thermoluminescence dating of Le Moustier (Dordogne, France). *Nature* **322**, 452-454.

VALLADAS H., CHADELLE J.-P., GENESTE J.-M., JORON J.-L., MEIGNEN L. & TEXIER P.-J. 1987. Datations par la thermoluminescence de gisements moustériens du sud de la France. *L'Anthropologie* **91**, 211-226.

VALLADAS H., MERCIER N., FALGUERES C. & BAHAIN J.-J. 1999. Contribution des méthodes nucléaires à la chronologie des cultures paléolithiques entre 300 000 et 35 000 ans BP. *Gallia Préhistoire* **41**, 153-166.

VALLADAS H., MERCIER N., JORON J.-L., MCPHERRON S. P., DIBBLE H. L. & LENOIR M. 2003. TL dates for the Middle Paleolithic site of Combe-Capelle Bas, France. *Journal of Archaeological Science* **30**, 1443-1450.

VOGEL J.C. & WATERBOLKT. 1967. Groningen radiocarbon dates VII. *Radiocarbon* **9**, 107-155.

WINTLE A.G. 2008. Fifty years of luminescence dating. *Archaeometry* **50**, 276-312.

WINTLE A.G. 1997. Luminescence dating: Laboratory procedures and protocols. *Radiation Measurements* **27**, 769-817.

14.12 SUPPLEMENTARY INFORMATION

14.12.1 SINGLE GRAIN OSL MEASUREMENTS AND ANALYSIS

Details about the sample preparation, equipment and measurement procedures for single grain OSL are provided in the main text. Here we provide further details about dose recovery tests conducted to determine the optimum measurement parameters and also the characteristics of the individual grains and reasons for why some of the grains were rejected.

14.12.2 DOSE RECOVERY TESTS

We conducted a number of different dose recovery tests on four of the samples (PdLI-20, PDLII-2, PdL10-8 and PdLIV-8) to determine the optimum laboratory measurement parameters for the samples collected from the three sites at Pech de l'Aze. All grains were exposed to natural sunlight to empty the electron traps and were then given a known laboratory dose (60 Gy; PdLI-20, PdLIV-8, and PdL10-8 and 80 Gy; PdLII-2). We measured two samples from PdLIV, one from a burnt layer (Layer 8) and one from an unburnt layer (Layer 5B). A range of different preheat (PH) combinations were tried where PH-1 is that prior to measurement of the natural and regenerative dose OSL signals and PH-2 that prior to measurement of the test dose OSL signals. The combinations were:

PH-1 = 160°C for 10 s; PH-2 = 160°C for 5 s
PH-1 = 180°C for 10 s; PH-2 = 180°C for 5 s
PH-1 = 220°C for 10 s; PH-2 = 160°C for 5 s
PH-1 = 240°C for 10 s; PH-2 = 160°C for 5 s
PH-1 = 260°C for 10 s; PH-2 = 160°C for 5 s
PH-1 = 260°C for 10 s; PH-2 = 220°C for 5 s
And the results are provided below in Table S1.

Although none of the combinations show a >10% deviation from unity, it does appear that an increase in PH temperature results in a decrease in our ability to recover a dose accurately. We obtained, between the different samples, the best dose recovery results using a PH-1 of 180°C for 10 s and a PH-2 of 180°C for 5 s, and decided to use this combination for measurement of all our samples.

Table S1: Results for dose recovery tests using a range of different PH combinations. Provided are the measured/given dose ratio at each combination for each sample, the overdispersion calculated for each test and the number of grains included in the estimate.

Sample	Measured/Given dose ratios and Overdispersion values (%)					
	1	2	3	4	5	6
PdLI-20	—	0.97 ± 0.02 OD = 7 ± 2 N = 104)	—	—	—	—
PdLII-2	0.97 ± 0.02 OD = 11 ± 3 N = 82	0.97 ± 0.02 OD = 6 ± 2 N =102	0.92 ± 0.02 OD = 8 ± 4 N = 82	0.92 ± 0.02 OD = 9 ± 3 N = 67	0.90 ± 0.02 OD = 12 ± 3 N = 93	0.92 ± 0.04 OD = 23 ± 4 N= 57
PdL10-8	1.06 ± 0.06 OD = 20 ± 4 N = 24	0.97 ± 0.03 OD = 11 ± 3 N = 39	—	—	0.92 ± 0.03 OD = 5 ± 3 N = 31	0.93 ± 0.03 OD = 9 ± 2 N = 51
PdLIV-8	—	1.02 ± 0.05 OD = 19 ± 4 N = 53	—	—	—	—

To confirm that this preheat combination is also appropriate for measurement of the natural dose in our samples, we conducted a PH plateau test on one of the samples (PdLIV-1). The results are shown in Figure S1, where it can be seen that a plateau is obtained in the lower temperature range (160-220°C), but significant deviation from the plateau is observed for higher temperatures. This result mimics the results obtained from the dose recovery tests and, thus, confirms our choice of PH combination (PH-1 = 180°C for 10 s; PH-2 = 180°C for 5 s) for measurement of our samples.

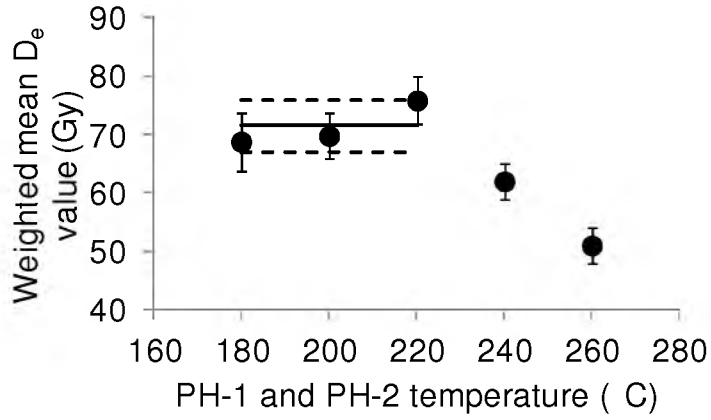

Figure S1: Preheat plateau test results for samples PdLIV-1. The solid line is the arithmetic mean of the weighted mean D_e values for PH-1 and PH-2 temperatures at 180-220°C that form a plateau. The broken lines indicate the 2σ error associated with this mean.

14.12.3 REJECTION OF GRAINS

A total of 115,700 grains were measured for samples from Pech, but it is well-known that not every measured grain will result in an accurate estimate of D_e (e.g., Thomsen et al., 2005; Jacobs et al., 2006; 2013). So, a series of internal tests and criteria for rejection of individual grains have been developed that result in the routine elimination of grains with aberrant OSL characteristics (Jacobs et al., 2006). Table S2, S3 and S4 provides details for all samples from the three different sites and reasons for why grains were rejected. Grains were rejected if they exhibited one or more of the following properties:

14.12.3.1 WEAK TEST-DOSE OSL SIGNALS

(i.e., the initial intensity of the test dose signals was less than three times the background intensity and/or the error on the test dose measurement was more than 20%). The majority of grains from Pech I (88.5%), Pech II (87.8%) and Pech IV (91.6%) were discarded on the basis of this criterion. Examples of the decay curves for a typical grain that failed this criterion, selected from a representative sample (PdLI-20, PdLII-16 and PdLIV-7 (unburnt) and PdLIV-1 (burnt)) from each site are

Table S2: Pech I: Number of single-grains measured, rejected and accepted, together with the reasons for their rejection.

Sample name	No. of grains measured	T_N signal <3xBG	0 Gy dose >5% of L_N	Poor recycling ratio	No L_N/T_N intersection	Depletion by IR	Sum of rejected grains	Acceptable individual D_e values
PdLI-0	1000	870	2	21	22	41	956	44
PdLI-1	1000	820	3	19	6	65	913	87
PdLI-2	1000	877	4	19	5	32	937	63
PdLI-3	1000	872	3	16	1	44	936	64
PdLI-4	1000	857	5	22	3	50	937	63
PdLI-5	1000	857	3	18	3	58	939	61
PdLI-7	1000	849	3	26	9	51	938	62
PdLI-8	1000	836	4	14	8	65	927	73
PdLI-9	1000	919	2	3	8	21	953	47
PdLI-10	1000	927	2	4	1	30	964	36
PdLI-11	1000	903	3	6	3	30	945	55
PdLI-12	1000	940	3	6	1	7	957	43
PdLI-13	1000	911	2	10	5	26	954	46
PdLI-14	1000	920	2	6	5	26	959	41
PdLI-15	1000	898	3	9	8	29	947	53
PdLI-16	1000	901	4	10	3	25	943	57
PdLI-17	1000	892	3	13	7	22	937	63
PdLI-18	2000	1786	6	21	41	56	1910	90
PdLI-19	1900	1660	6	23	25	60	1774	126
PdLI-20	2000	1781	6	21	6	46	1860	140
Total	22900	20276	69	287	170	784	21586	1314
% total		88.5	0.3	1.3	0.7	3.4	94.3	5.7
% accept			2.6	10.9	6.4	29.9		50.2

T_N is the OSL signal measured in response to the test dose given after measurement of the natural OSL signal.

L_N is the natural OSL signal.

Recycling ratio is the ratio of the sensitivity-corrected OSL signals measured from duplicate doses to test the efficacy of the test dose correction used in the SAR procedure.

IR is the infrared stimulation used to erase any part of the signal that may be derived from IR-sensitive (e.g., feldspar) grains.

Table S2: Pech II: Number of single-grains measured, rejected and accepted, together with the reasons for their rejection.

Sample name	No. of grains measured	T_N signal <3xBG	0 Gy dose >5% of L_N	Poor recycling ratio	No L_N/T_N intersection	Depletion by IR	Sum of rejected grains	Acceptable individual D_e values
PdLII-2	2000	1771	10	23	55	71	1930	70
PdLII-4	2000	1790	23	25	39	52	1929	71
PdLII-5	2000	1812	9	16	10	40	1887	113
PdLII-6	2000	1784	17	21	19	41	1882	118
PdLII-7	2000	1723	13	53	46	78	1913	87
PdLII-8	2000	1746	15	23	22	71	1877	123
PdLII-9	2000	1783	14	18	21	47	1883	117
PdLII-10	2000	1794	16	19	44	49	1922	78
PdLII-11	2000	1762	18	23	37	42	1882	118
PdLII-12	1900	1686	28	24	34	48	1820	80
PdLII-13	2000	1193	34	108	208	47	1590	410
PdLII-14	2000	1792	24	27	27	28	1898	102
PdLII-15	1000	905	14	9	13	25	966	34
PdLII-16	2000	1826	11	13	38	44	1932	68
PdLII-17	2000	1775	20	19	24	52	1890	110
PdLII-18	2000	1724	23	32	50	71	1900	100
PdLII-19	2000	1759	13	33	28	49	1882	118
Total	32900	28625	302	486	715	855	30983	1917
% total		87.0	0.9	1.5	2.2	5.6	94.2	5.8
% accept			7.1	11.4	16.7	20.0		44.8

Table S4: Pech IV: Number of single-grains measured, rejected and accepted, together with the reasons for their rejection.

Sample name	No. of grains measured	T_N signal <3xBG	0 Gy dose >5% of L_N	Poor recycling ratio	No L_N/T_N intersection	Depletion by IR	Sum of rejected grains	Acceptable individual D_e values
PdLIV-1	1000	751	8	66	6	57	888	112
PdLIV-2	2000	1717	11	49	23	58	1858	142
PdLIV-3	2000	1788	7	19	11	60	1885	115
PdLIV-4	2000	1835	4	19	7	52	1917	83
PdLIV-5	2000	1739	5	33	9	96	1886	114
PdLIV-6	2000	1839	5	9	17	49	1919	81
PdLIV-7	2000	1805	5	17	10	57	1894	106
PdLIV-8	3000	2793	5	19	13	76	2906	94
PdLIV-9	2000	1771	5	17	10	89	1892	108
PdLIV-10	3000	2904	4	6	7	31	2952	48
PdLIV-11	2000	1865	6	13	8	36	1928	72
PdLIV-12	2000	1879	3	14	10	47	1953	47
PdLIV-13	3000	2906	4	9	9	26	2954	46
PdLIV-14	2000	1799	4	24	3	96	1926	74
PdLIV-15	2000	1830	4	18	13	48	1913	87
PdLIV-16	3000	2898	4	6	10	30	2948	52
PdLIV-17	3000	2885	4	11	13	25	2938	62
PdLIV-18	2000	1834	4	19	14	63	1934	66
PdLIV-19	1900	1719	4	24	11	50	1808	92
PdLIV-20	2000	1803	4	19	9	66	1901	99
PdLIV-21	2000	1823	6	18	12	63	1922	78
PdLIV-22	2000	1819	5	15	14	46	1899	101
PdLIV-23	2000	1802	6	18	8	62	1896	104
PdLIV-24	2000	1825	4	13	5	62	1909	91
PdLIV-25	2000	1811	6	15	8	52	1892	108
PdLIV-26	2000	1801	6	21	4	59	1891	109
PdLIV-27	2000	1793	7	21	11	56	1888	112
Total	57900	53034	140	532	275	1512	55497	2403
% total		91.6	0.2	0.9	0.5	2.6	95.8	4.2
% accept			2.9	10.9	5.7	31.1		49.4

shown in Figure S2. It does not matter how much laboratory dose is added to such grains, no significant increase in the OSL signal can be discerned. These grains are not responsive to light stimulation and are, therefore, not useful for dating. Rejecting such grains does not cause any bias in the results, because they do not contribute to the luminescence signal. They will also not bias the results of single aliquots.

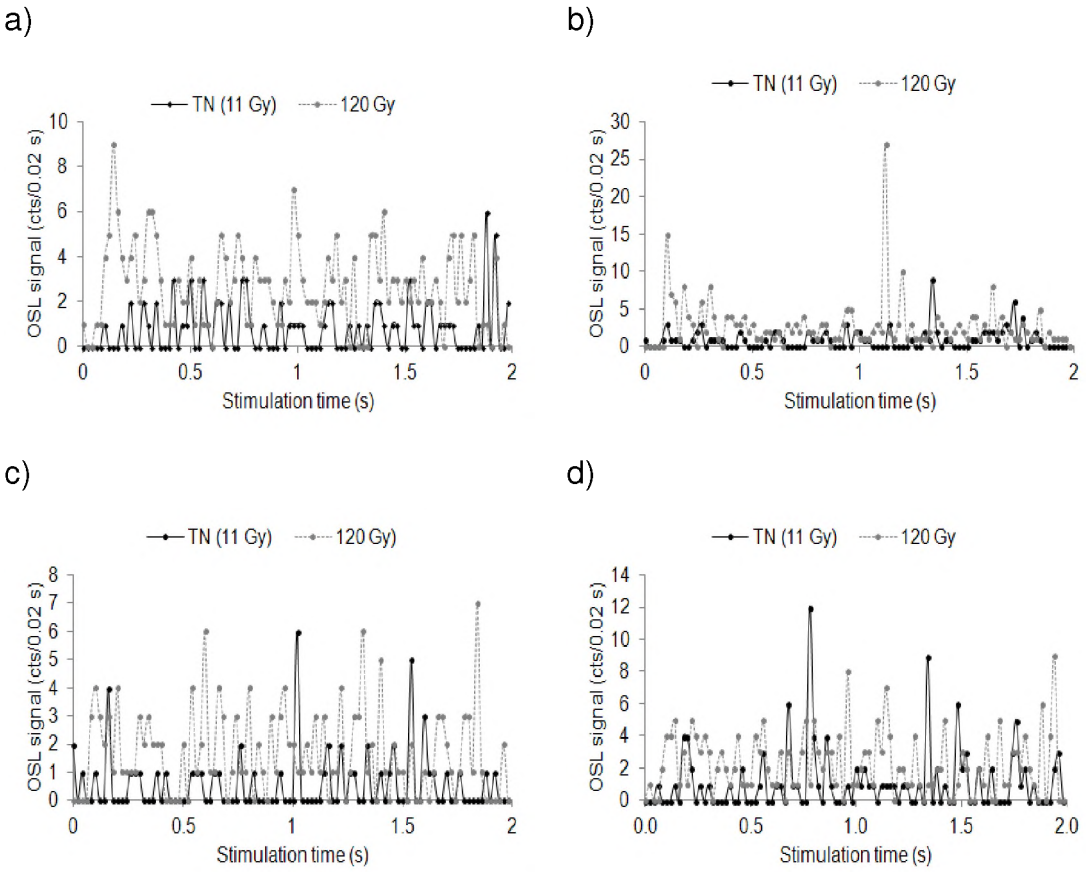

Figure S2: Optical decay curves for a typical grain from each site (a) PdLI-20, b) PdLII-16, c) PdLIV-7 and d) PdLIV-1) that gets rejected because they have a weak luminescence signal. There is no significant increase in signal even with a ten-fold increase in dose.

After rejection of all these grains that gave no discernable luminescence signal, we were left with only a small proportion of the grains that were measured and these are the grains that were further scrutinised for their behaviour. The remaining grains amounted to 2624 out of 22900 grains measured from Pech I (11.5%), 4243 out of 34900 grains measured from Pech II (12.2%) and 4866 out of 57900 grains measured from Pech IV (8.4%). In the following sections, the percentage grains that failed each

of the criteria is expressed as a percentage of the grains with a luminescence signal (% accept in Tables S2, S3 and S4), rather than all grains measured (% total in Tables S2, S3 and S4).

The next rejection criteria involved grains with:

14.12.3.2 HIGH LEVELS OF RECUPERATION

(i.e., the sensitivity-corrected OSL intensity measured in the 0 Gy regenerative-dose cycle was more than 5% of the sensitivity-corrected natural OSL intensity). A very small proportion of the grains from Pech I (2.6%), Pech II (2.4%) and Pech IV (2.9%) were rejected on this basis. Most of these grains are very dim, and there is no common characteristic amongst these grains that we can use to explain the behaviour.

14.12.3.3 POOR RECYCLING RATIOS

(i.e., the sensitivity-corrected OSL values for duplicate regenerative doses differed by more than 2σ). A larger number of grains failed this criterion; 10.9% (Pech I), 12.1% (Pech II) and 10.9% (Pech IV) (Tables S2, S3 and S3). An analysis of the grains that failed this criterion revealed two broad patterns. A) A small number of the grains have decay and dose response curves typical of well-behaved quartz grains, but a recycling ratio inconsistent with unity at 2σ. There is no obvious reason why the recycling ratios are poor and it is unlikely that either the rejection or inclusion of these grains will impact on the final D_e distribution and value used for age determination. An example decay and dose response curve is shown in Figure S3a and d for a representative grain from sample PdLI-20. B) The larger number of grains that got rejected using this criterion has slower decay curves, indicative of the presence of medium and/or slow components. The shape of the decay curves for these grains also change from measurement cycle-to-cycle, suggesting that one or more of these slower components change sensitivity at a different rate to the others,

and, in particular, the fast component that is used in OSL dating. This result in poor recycling ratios. Many of these grains also show a zero dose signal that is significantly greater than zero. We assume this is because of the build-up of signal over the different measurement cycles. An example decay and dose response curve for a grain from PdLI-20 that is on the extreme end of the range is shown in Figure S3b and e, and a further example, on the less extreme part of the spectrum of this behaviour, is shown for a grain from sample PdLIV-7 in Figure S3c and f. The inset curves are the same decay curves that are normalised to the initial 0.02 s of optical stimulation to clearly show the changes in shape. We conclude that this second type of grain that failed the recycling ratio test must be eliminated as it can adversely affect the results if included, either as a single-grain or as part of a multi-grain single aliquot.

14.12.3.4 NATURAL OSL SIGNALS EQUAL TO OR GREATER THAN THE SATURATION LIMIT OF THE DOSE-RESPONSE CURVE

(i.e., the sensitivity-corrected natural OSL intensity exceeded that induced by the largest regenerative dose ('Class 3' grains of Yoshida et al. (2000)) or lay in the saturated region of the dose-response curve, so a finite estimate of D_e could not be obtained). A relatively small number of grains failed this criterion in the samples from Pech I (6.4%) and Pech IV (5.7%), whereas a larger number failed for the samples from Pech II (17.5%) (Tables S2, S3 and S3). For Pech II, this was not necessarily related to the age of the sample (i.e., older samples did not have more of these grains than younger samples). The grains from Pech that failed this criterion did not exhibit typical 'Class 3' behaviour, rather the grains were all fully saturated and can, but do not necessarily, have small D_0 values, the characteristic saturation dose of the data fitted with a saturating-exponential function (see Figure S4). This may suggest that these grains are genuinely 'old' and may be derived from the limestone that occurs ubiquitously within the sediments as small and large chunks and that may liberate old grains that have not been exposed to sunlight into the otherwise well-bleached sediment. A typical decay and dose response curve for a grain from Pech I is shown in Figure S4. These grains all had decay curves very

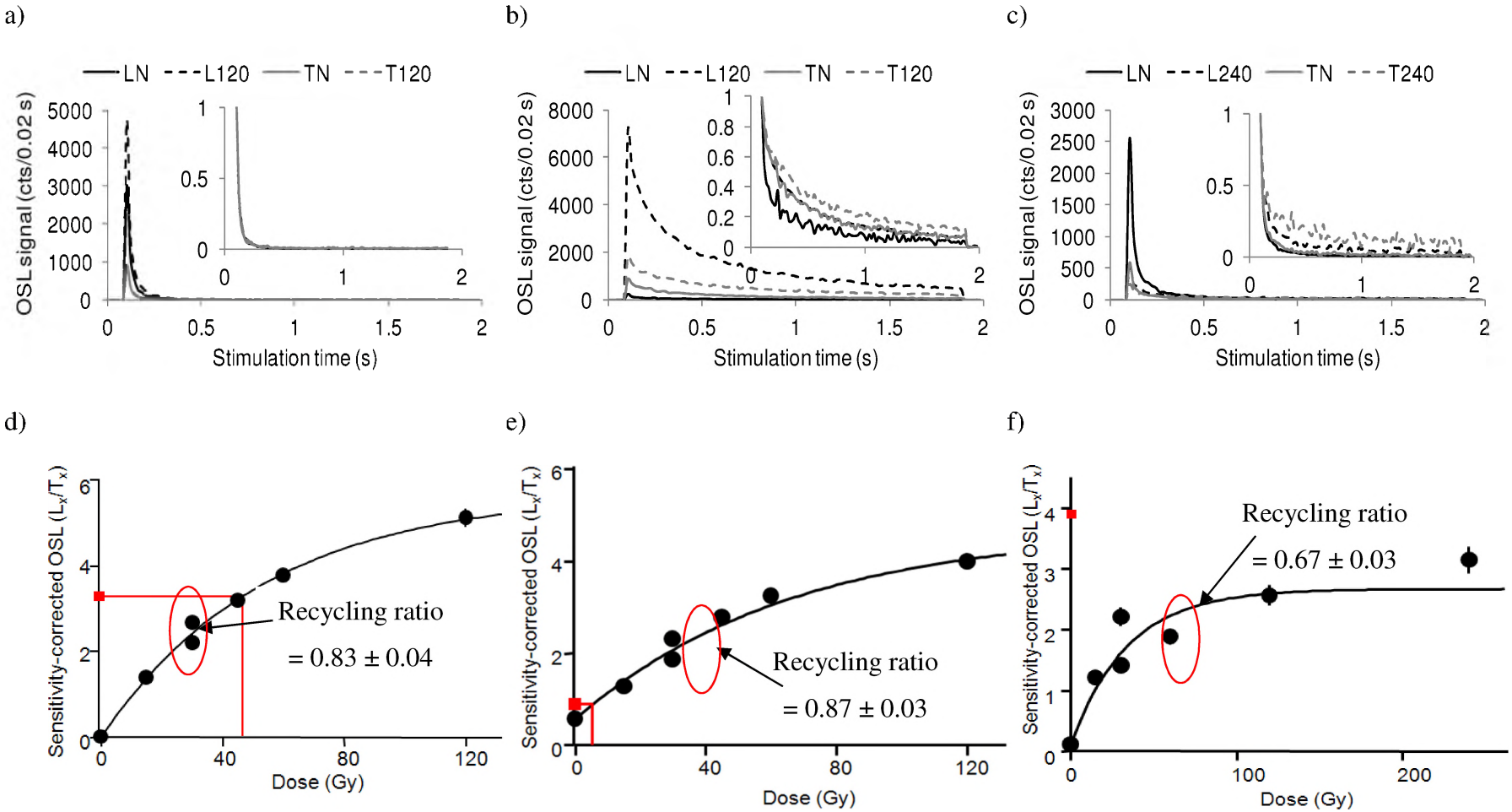

Figure S3: Example data for three grains that failed the recycling ratio criterion. a-c) Natural and the highest regenerative-dose decay curve and their respective test dose OSL decay curves. The inset curves show the same decay curves, but normalised to their respective maximum signal intensities. d-f) Dose response curves for the three grains whose decay curves are shown in a-c.

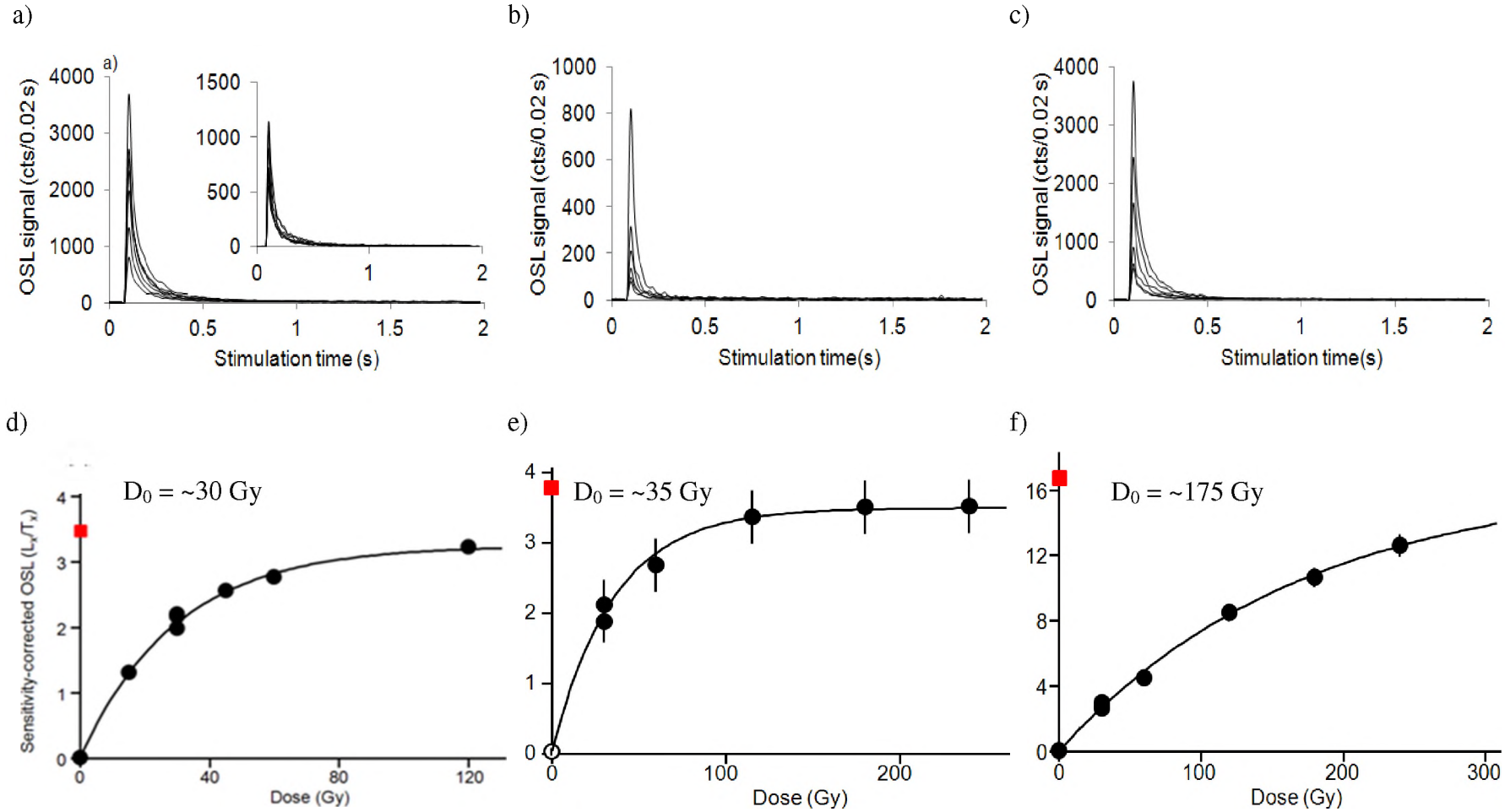

Figure S4: Example decay curves (a) and the corresponding dose response curve (d) for a typical grain from Pech I that failed one of the rejection criteria because the luminescence signals (L_x/T_x) are saturated. b), c), e) and f) show the same type of grains, but these are two examples from quartz grains extracted from a chunk of limestone. The example in b) and e) has a low D_0 value, whereas the other example in c) and f) has a high D_0 value. Both grains have a natural dose that is saturated.

typical of quartz grains dominated by the fast component (Figure S4a) and that stayed stable from cycle to cycle in both the regenerative and test dose responses(Figure S4a). To explicitly test whether these grains may be unbleached quartz grains within the limestone, we prepared and measured a sample of the limestone collected from the archaeological deposit in the same way. Figure S4c and d show an example of a grain from the limestone that has a similar D_0 value of ~35 Gy to that for the example grain from Pech I shown in Figure S4a and d, and also one that has a high D_0 value of 175 Gy. These two extreme examples encompass the range of acceptable and saturated grains measured from the limestone. We, therefore, assume that the saturated grains present in our samples from all three sites are derived from the *in situ* dissolution of limestone and that these grains should be eliminated. If not, it may lead to an overestimation of the D_e value for the sample.

14.12.3.5 Significant loss of OSL signal after exposure to infrared stimulation

(i.e., the OSL IR depletion ratio of Duller (2003) was less than unity by more than 2σ). The largest number of grains (after those with no luminescence response; criterion 1) was rejected on this basis; 29.9% (Pech I), 21.5% (Pech II) and 31.1% (Pech IV). This was surprising, since the samples were first density separated to separate out the quartz from the feldspar grains and this resulted in a small proportion of grains identified as feldspar. All grains that were thought to be quartz were then also subjected to an HF acid etch that will at least partially, if not completely, dissolve any remaining feldspar grains. The samples were then sieved again, to remove the partially dissolved feldspar grains that will now fall through the sieves. But, despite this rigorous treatment, we still had significant 'contamination'. Furthermore, a detailed petrographic investigation of the sediments revealed that there is some, but not a great abundance of feldspar grains present in the sediment or in the limestone. So, what do these grains that fail this criterion actually represent? Are they feldspar grains? Are they quartz grains with a peculiar behaviour? Or, are they a different mineral grain? We have looked at these IR sensitive grains in a number of different ways. First, the OSL-IR depletion ratios of the grains are

significantly less than unity. For the IR sensitive grains from sample PdLIV-5 (displayed in Figure S5 and S6), the ratios range between 0.22 ± 0.03 and 0.74 ± 0.04. These grains were, therefore, not rejected because the criterion is too stringent, but rather indicate significant sensitivity to IR stimulation. Second, the decay curve characteristics are very typical of quartz grains. In Figure S5, we have plotted a selection of IR sensitive grains from sample PdLIV-5 and divided them into two categories – the 6 brightest grains that decay the fastest (Figure S5a) and the 6 brightest grains that had the slowest decay rates (Figure S5b). The former resulted in a loss of ~85-90% within the first 0.1 s of optical stimulation, whereas the latter resulted in a loss of ~55-65%; these represent the two extreme ends of a spectrum of variability. The shapes and rates of decay fall within the range of variability observed for the quartz grains that were accepted for D_e determination and that have passed all criteria (Figure S7). Third, their corresponding dose response curves are also shown in Figures S5d, and e. There are two important characteristics: a) the growth with dose is more linear over the measured dose range than that observed for the typical quartz grain dominated by a fast component and is, therefore, more typical of feldspar grains (Figure S8c). Their D_0 values are also much higher (between 120 and 310 Gy), and their between grain dose response curves more reproducible compared to that usually observed for quartz (see Figure S8). Fourth, to estimate the impact of these grains on D_e determination, we have calculated D_e values for the grains that failed the OSL-IR depletion ratio test and compared those against the grains from the same sample (PdLIV-5) that passed all criteria. The results are presented in Figure S6a-c, where the D_e values for the accepted quartz grains are presented in Figure S6a, the D_e values for the IR sensitive grains in Figure S6b and the two data sets together in Figure S6c, with the accepted quartz grains as open triangles and the IR sensitive grains as closed circles. Also provided are the CAM D_e values and overdispersion values for each data set. From here it can be seen that the IR sensitive grains significantly underestimate the D_e value compared to that obtained for the accepted quartz grains. Should these grains not be rejected, the radial plot will appear to have two discrete dose components and the average D_e value will be somewhere between the two values.

Although we are not absolutely sure what these grains represent at this stage, it is important that these need to be omitted from the data set as they will lead to underestimation of the age. Also, because these grains represent a sizable proportion of the luminescent grains of a sample (20-30%), they may potentially skew the results, should De values be based on measurements of multi-grain aliquots. The nature of these grains is currently investigated and a detailed account of their thermal, optical and mineralogical properties will be reported elsewhere.

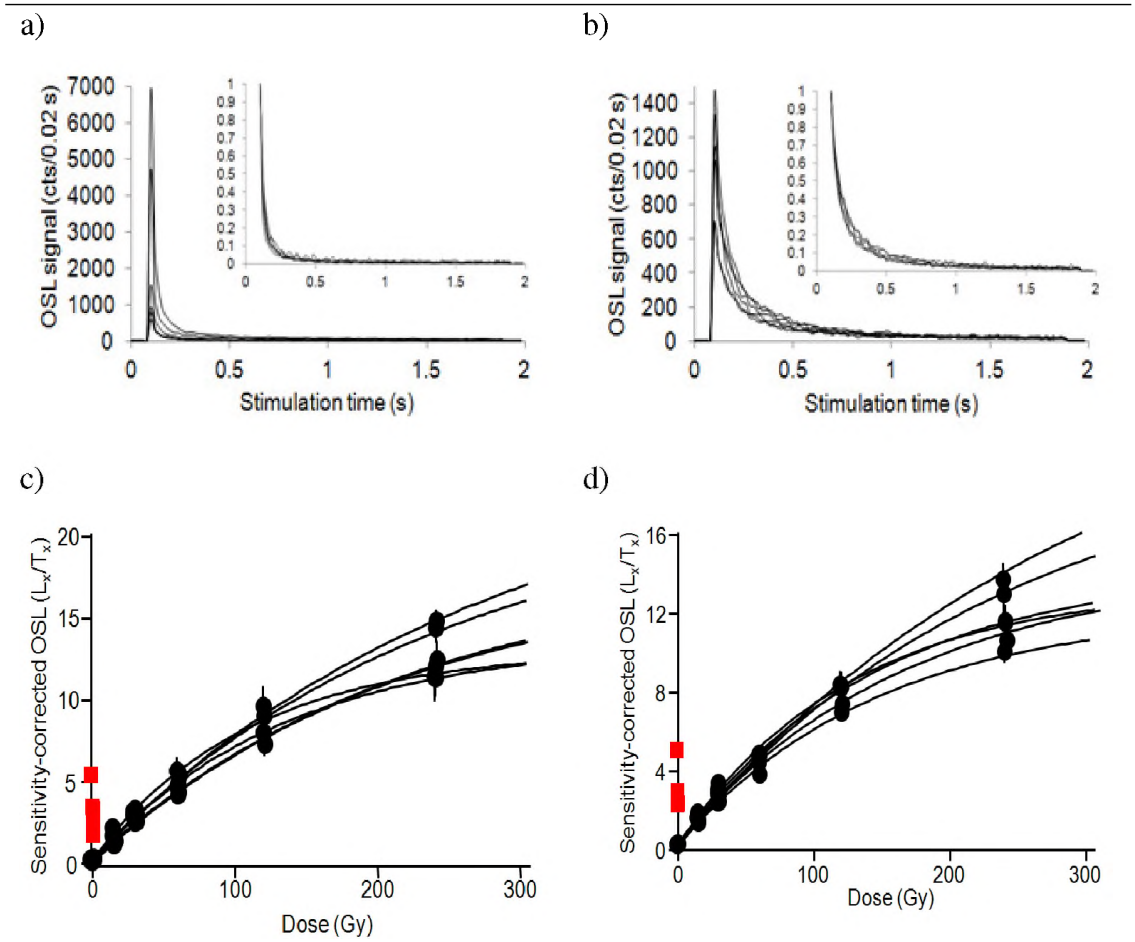

Figure S5: The decay curves for a) the five brightest and fastest decaying grains, and b) the five brightest, but slowest decay grains measured for sample PdLIV-5 that failed the OSL-IR depletion ratio test and that was rejected. C) and d) show their corresponding dose response curves.

a) b)

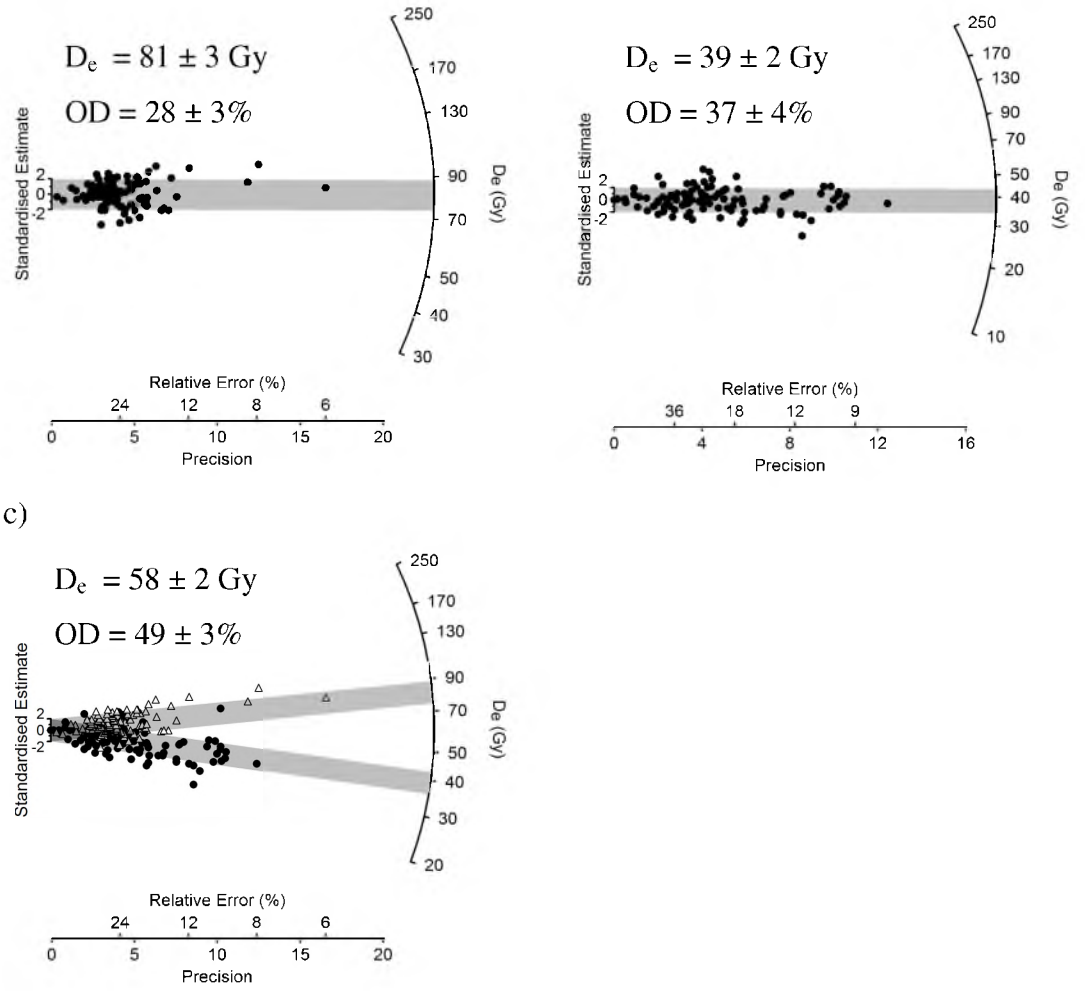

Figure S6: D_e values presented as radial plots for a) all accepted quartz grains for sample PdLIV-5, b) all grains that failed the OSL-IR depletion ratio for sample PdLIV-5, and c) both data sets combined with a) shown as open triangles and b) as closed circles. The grey bands in the radial plots in a) and b) are centred on the weighted mean D_e value, determined using the CAM. The grey bands in c) are centred on the respective CAM De values for the two data sets (i.e., the same as in a) and b)).

14.12.4 ACCEPTED GRAINS – DECAY CURVE CHARACTERISTICS

About 4.9% of the measured grains were in the end used for D_e determination. All D_e values were estimated from the first 0.22 s of OSL decay, with the mean count recorded over the last 0.3 s being subtracted as background. Figure S7a-d shows the decay curves for 140 grains of sample PdLI-20, 68 grains of sample PdLII-16, 114

grains of PdLIV-5 and 112 grains of sample PdLIV-1; these are all the grains in each of these representative samples that were accepted for D_e determination after application of the rejection criteria, discussed above. The decay curves are those following a regenerative dose of 120 Gy, and a preheat temperature of 180°C for 10 s. There are four important features to note: 1) the decay curve shapes are generally quite reproducible, but 2) there are a few grains in each sample that haveslower rates of decay. 3) The majority of the grains have OSL signals that have decayed to instrumental background level and there is little chance for build-up of background from measurement cycle-to-cycle. 4) There is no relationship between rate of OSL decay and D_e value.

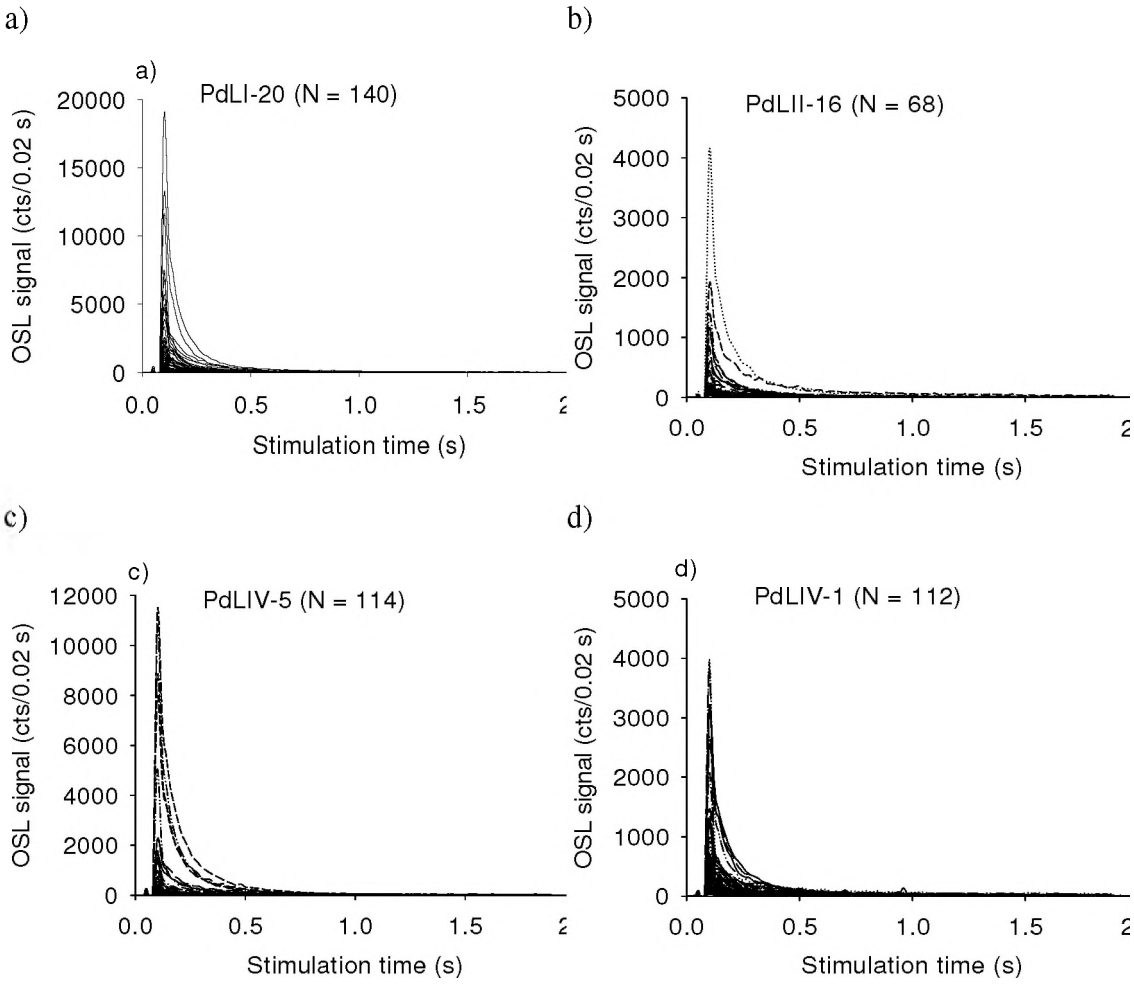

Figure S7: OSL decay curves following a regenerative dose of 120 Gy and a Ph of 180°C for 10s for all accepted grains included in the final De value for a) PdLI-20, b) PdLII-16, c) PdLIV-5 and d) PdLIV-1.

14.12.5 ACCEPTED GRAINS – DOSE RESPONSE CURVE CHARACTERISTICS

We next compared the dose-response curves for individual grains and again used the accepted grains from samples PdLI-20, PDLII-16, PDLIV-5 and PdLIV-1 as representative of the samples from the three sites at Pech de l'Aze. Each grain was given successive regenerative doses of 60, 30, 120, 180, 240, 320, 0 and 60 Gy to obtain L_x values, together with test doses of ~11 Gy to obtain values of T_x, to monitor and correct for any sensitivity changes. Sensitivity-corrected (L_x/T_x) dose response curves were then constructed from these induced L_x and T_x OSL signals, using a single saturating-exponential function of the form $I = I_0(1\text{-}\exp^{-D/D0})$, and an extra linear time which was suitable for the majority of the accepted grains. In this function, I is the L_x/T_x value at regenerative dose D, I_0 is the saturation value of the exponential curve and D_0 is the characteristic saturation dose; I_0 and D_0 are estimated from the data.

The fitted dose-response curves for 10 of the brightest accepted grains from each of the samples are presented in Figure S8. These grains have dose response curves that show a wide range of shapes and saturation doses and is typical of the range observed for all the samples. Some of the grains continue to grow with increasing dose (up to the maximum applied doses of 120 and 240 Gy), whereas others seizes to increase at much lower doses.

14.12.6 SINGLE GRAIN EQUIVALENT DOSE RESULTS

The D_e values for all the accepted grains (Tables S2, S3 and S4) are displayed as radial plots in Figure S9 (Pech I), S10 (Pech II) and S11 (Pech IV), for each of the samples. In such plots, the most precise estimates fall to the right and the least precise to the left. If these independent estimates are consistent with statistical expectations, then 95% of the points should scatter within a band of width ±2 units

projecting from the left-hand ('standardised estimate') axis to any chosen D_e value on the right-hand, radial axis. The radial plot, thus, provide simultaneous information about the spread, precision and statistical consistency of the D_e values (Galbraith 1988, 1990). Although there are more spread than can be explained with measurement uncertainties alone, no discrete dose components or patterns akin to samples that may have suffered from partial bleaching has been detected. So, to obtain a single meaningful D_e value for age calculation, we determined the weighted mean of all the accepted individual D_e values from a sample, using the central age model (CAM) of Galbraith et al. (1999). The standard error on the CAM estimates of D_e takes into account the measured overdispersion.

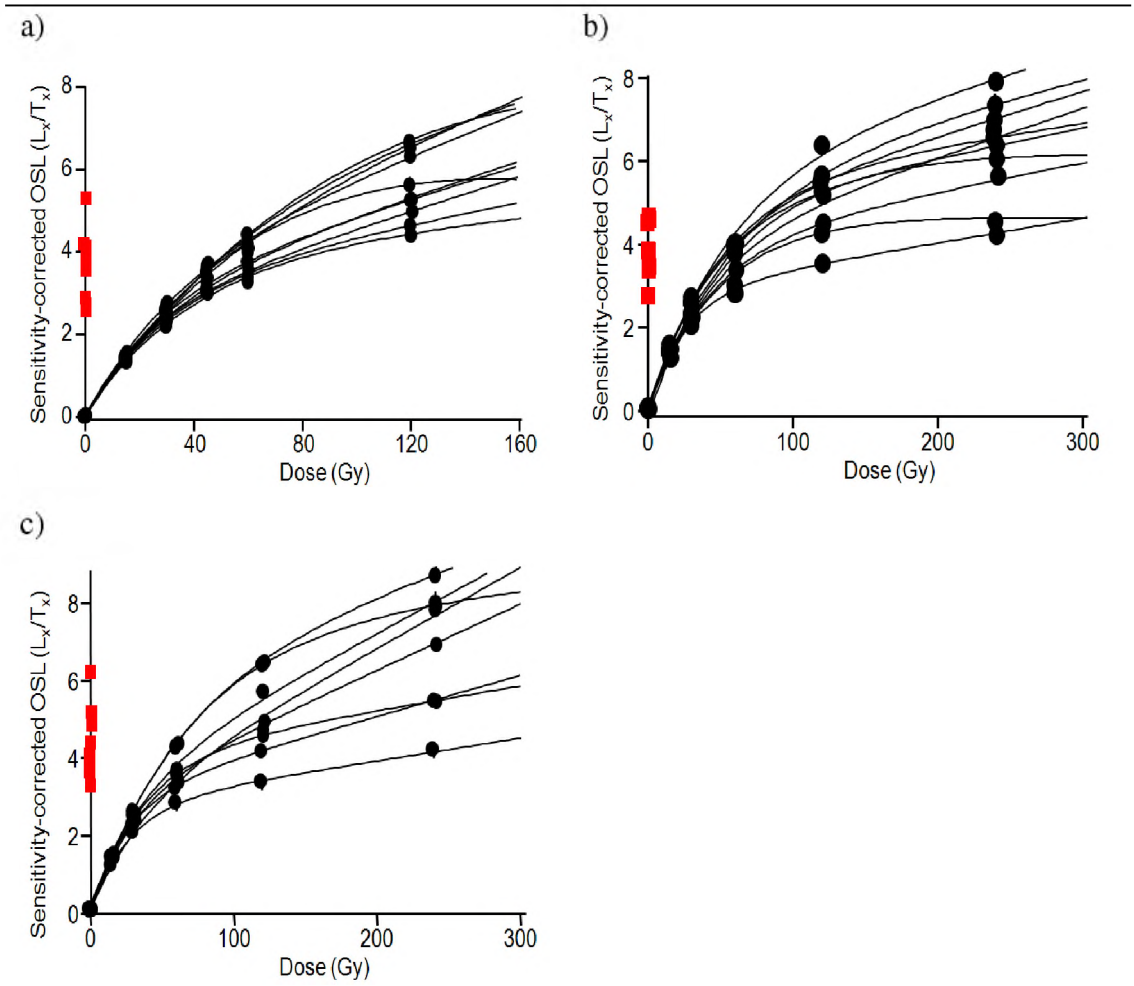

Figure S8: A range of dose response curves for a selection of the brightest accepted quartz grains from a) PdLI-20, b) PdLII-16, c) PdLIV-5 and d) PdLIV-1.